MICROWAVE PERIODIC STRUCTURES BASED ON MICROELECTROMECHANICAL SYSTEMS (MEMS) AND MICROMACHINING TECHNIQUES

THÈSE N^{O} 3969 (2007)

PRÉSENTÉE LE 23 NOVEMBRE 2007

À LA FACULTÉ DES SCIENCES ET TECHNIQUES DE L'INGÉNIEUR

Laboratoire d'électromagnétisme et d'acoustique

SECTION DE GÉNIE ÉLECTRIQUE ET ÉLECTRONIQUE

ÉCOLE POLYTECHNIQUE FÉDÉRALE DE LAUSANNE

POUR L'OBTENTION DU GRADE DE DOCTEUR ÈS SCIENCES

PAR

Julien PERRUISSEAU-CARRIER

ingénieur électricien diplômé EPF

de nationalités française et suisse originaire de Epalinges (VD)

acceptée sur proposition du jury:

Prof. J. R. Mosig, président du jury

Prof. A. Skrivervik Favre , directrice de thèse

Prof. G. Elefteriades, rapporteur

Prof. M. A. Ionescu, rapporteur

Dr H. Legay, rapporteur

ÉCOLE POLYTECHNIQUE
FÉDÉRALE DE LAUSANNE

Lausanne, EPFL

2007

"Le courage, c'est de chercher la vérité et de la dire, c'est de ne pas subir la loi du mensonge triomphant qui passe et de ne pas faire écho de notre âme, de notre bouche et de nos mains aux applaudissements imbéciles et aux huées fanatiques."

J. Jaurès

... freely translated to english to ...

"Courage is to seek the truth and tell it, not to suffer the law of triumphant and accepted lies and not to give away our soul, our mouth and our hands to foolish applause and fanatic booing."

J. Jaurès

Abstract

As a result of the ever growing number of functionalities and standards to be supported by communication systems, as well as the constant development of radar and imaging technologies, a key research area in the field of microwaves and millimeter waves is the achievement of *reconfigurability* capabilities. In recent years, the progress of MicroElectroMechanical Systems (MEMS) fabrication techniques has allowed radically challenging the performances of reconfigurable devices based on established technologies such as controllable ferrite material, semiconductor pin diodes or FET transistors. Consequently, there is presently significant effort to apply MEMS technology to the microwave field; in the case of high-cost applications (e.g. radars, satellites), the main reason is the state-of-the-art performances that MEMS technology can offer; namely, low losses, high linearity, large bandwidth. In the case of mass market (e.g.: mobile phone, GPS receiver), it is rather pushed by the increasing demand for the integration of numerous microwave functionalities into a monolithic, small, low-power consuming and low-cost device.

In this context, the objective of this thesis is to contribute to the development of new *periodic or cascadable* microwave devices reconfigurable by means of MEMS. Indeed, numerous microwave devices take advantage of the particular propagation properties of a wave in periodic structures to achieve given functionalities (e.g. phase shifters, frequency selective surfaces, periodic antennas, antenna arrays and reflectarrays, metamaterials). For this purpose, analysis and design methods were developed based on the theory of waves propagating in periodic structures to help in dealing with different kinds of periodic or cascadable MEMS structures in an integrated approach. The method comprises the following main steps: the setup of efficient full-wave simulations of MEMS blocks, the derivation of physical and accurate circuit models, and the development of hybrid full-wave–circuit model design methods based on periodic structure modeling. It is noticeable that several theoretical developments presented are not restricted to micromachined and MEMS devices, but could be of use for many other microwave designs.

Three main classes of devices have been studied and designed to illustrate the versatility of the approach, as well as the various potentialities of MEMS in microwave applications. The first structure addressed is an existing microwave MEMS structure, the distributed MEMS transmission line (DMTL), for which design methods based on the periodic structure modeling were developed. Analog and digital devices were fabricated, showing excellent agreement with the circuit modeled results. We also introduce and analyze a new topology for the reduction of the mismatch in multi-bit DMTLs.

The results presented next consist mainly in theoretical developments on the metamaterial composite right/left handed transmission line (CRLH-TL) structure, carried out to overcome the limitations of existing models, which were shown to be inappropriate in the case of MEMS CRLH-TL implementations. Fixed micromachined devices were successfully designed based on the new theory, which also allowed the demonstration of the possibility to design especially low/high impedance CRLH-TLs. Next, MEMS implementations of variable CRLH-TLs are presented. Analog and digital devices were designed, and excellent agreements between full-wave simulations and circuit models are obtained in both cases. For fabrication reasons, only the analog device could be

measured to exhibit the expected performances. This constitutes —to the author's knowledge— the first implementation of a MEMS-reconfigurable metamaterial structure.

The last device studied is a MEMS-reconfigurable reflectarray cell. A comprehensive assessment of the numerous requirements for such a cell with regard to the functioning of a reconfigurable reflectarray is first presented, as well as detailed discussions on the rigorous simulation and measurement of the device. A monolithic MEMS reflectarray cell was then designed based on these considerations, and exhibits excellent performances in comparison with other reconfigurable reflectarray cells based on MEMS and other technologies.

Keywords: *Microwaves, Millimeter waves, Micromachining, MicroElectroMechanical Systems (MEMS), Periodic structure, Phase shifters, Metamaterial, Antennas, Reflectarray.*

Resumé

Le développement de systèmes *reconfigurables* constitue une direction de recherche particulière dans le domaine des hyperfréquences et ondes millimétriques, en conséquence du nombre croissant de fonctionnalités et standards requis dans les systèmes de communications, ainsi que du développement constant des technologies radar et d'imagerie. Ces dernières années, le développement des techniques de fabrication de MicroElectroMechanical Systems (MEMS) a permis d'améliorer les performances de systèmes reconfigurables basés sur des technologies existantes telles que ferrites, diodes p-i-n et transistors FET. On assiste donc actuellement à un effort particulier envers l'application des MEMS au domaine des hyperfréquences; dans le cas d'applications à coût élevé (ex.: radars, satellites), la raison principale en sont les exceptionnelles performances que la technologie MEMS peut potentiellement offrir. Dans le cas de marchés de masse (ex.: téléphonie mobile, récepteurs GPS), c'est la nécessité d'intégrer de plus en plus de fonctionnalités dans un système monolithique, petit, à faible consommation et à bas coût de production.

Dans ce contexte, l'objectif de cette thèse est de contribuer au développement de nouveaux systèmes hyperfréquence *périodiques*, reconfigurables grâce à la technologie MEMS. En effet, de nombreux systèmes hyperfréquence permettent d'obtenir de très intéressantes fonctionnalités en utilisant les propriétés particulières de la propagation d'une onde électromagnétique dans un milieu périodique (ex.: déphaseurs, surfaces à sélection de fréquence, antennes périodiques, réseaux d'antennes, métamateriaux). Dans ce but, des méthodes d'analyse et de design ont été développées sur la base de la théorie des ondes se propageant dans un milieu périodique, pour traiter de différents types de structure périodiques MEMS dans une approche unifiée. Celle-ci comprend les principaux points suivants: la mise en place de simulations numériques efficaces de blocs MEMS, la déduction de modèles circuit physiques précis, ainsi que le développement de procédures de design hybrides simulation - circuit, basées sur la théorie des structures périodiques. Cependant, on notera que la plupart des développements théoriques conduits dans ce contexte ne se limite pas aux structures MEMS ou micro-usinées, mais aussi à beaucoup de systèmes similaires bases sur d'autre technologies.

Trois principaux types de systèmes ont été étudiés pour illustrer la polyvalence des méthodes développées, ainsi que les diverses potentialités des MEMS dans les applications hyperfréquences. La première structure concernée est un système MEMS préalablement existant, la ligne retard à MEMS distribués (DMTL), pour laquelle des méthodes de design basées sur la modélisation de structures périodiques ont été développées. Des démonstrateurs analogiques et digitaux ont alors été réalisés, démontrant une excellente corrélation avec les performances modélisées. Finalement, Une nouvelle topologie pour la réduction de la désadaptation dans les structures multi-bit est présentée et analysée.

Dans un second temps, nous présentons des résultats principalement théoriques liés à la structure 'métamatériau' appelée composite right/left handed transmission line (CRLH-TL). Ces développements sont nécessaires pour maîtriser les limitations de modèles existants dans le cas d'implémentation de CRLH-TLs en technologie micro-usinée et MEMS. Des démonstrateurs fixes micro-usinés ont été tout d'abord réalisés avec succès sur la base de cette théorie, qui a aussi per-

mis de démontrer la possibilité de concevoir des CRLH-TLs d'impédance particulièrement basse ou élevée. Puis, des implémentations MEMS analogiques et digitales ont été conçues, pour lesquelles un excellent accord entre model circuit et simulations numériques est obtenu. Pour des raisons de fabrication, seuls les démonstrateurs analogiques ont pu être mesurés avec succès. Cela constitue, à notre connaissance, les premières réalisations de métamatériaux reconfigurables au moyen de MEMS.

Le dernier type de structure étudié consiste en une cellule de 'reflectarray' contrôlable par MEMS. Une évaluation complète des nombreuses exigences pour de telles cellules est tout d'abord proposée, ainsi que des considérations sur la simulation et mesure rigoureuse d'une telle structure. Une cellule monolithique a alors été conçue sur la base de ces développements, et présente d'excellentes performances en comparaison d'autres cellules de reflectarray basées sur la technologie MEMS ou autre.

Mots clés: *Hyperfréquences, Ondes millimétriques, Micro-usinage, MicroElectroMechanical Systems (MEMS), Structure périodique, Déphaseur, Métamatériaux, Antenne, Reflectarray.*

Acknowledgements

My thanks go first to Prof. Anja Skrivervik, my boss through these years, for her advice, kindness, and for her support through some hard times. To our amazing laboratory director Prof. Juan Mosig, for hiring me at LEMA and always trusting me, but especially for his world-renowned great human qualities.

I would also like to acknowledge my other committee members, Prof. George Eleftheriades from the University of Toronto, Dr. Hervé Legay from Thales Alenia Space, and Prof. Mihai Adrian Ionescu from EPFL, for having accepted to examine this work and for their valuable insights.

Hail to king Frédéric Bongard!, for –in addition to being a great friend— his outstanding contribution to this thesis through our endless technical discussions and the reviewing of most of the papers and reports I have written. Well deserved appreciation also goes to Pedro Crespo-Valero for the very stimulating talks, to Michael Mattes and Sarah Suter for their very valuable thesis proof-reading, and to J-F Zürcher for the much useful technical help. I also wish to thank my present and former office mates and all the LEMA team for the wonderful atmosphere there. Last but not least, to Daniel Llorens del Río, who, as a great supervisor of my first student project, taught me how to walk in the electromagnetic world.

I would also like to thank all the people I had the chance to work with in other EPFL labs, especially at the Laboratory of Micro and Nanoelectronics Devices (LEG2) and the Center of MicroNanoTechnology (CMI). Special 'bravo' to my friends Raphael Fritschi and Montserrat Fernandez-Bolaños for the discussions and the time spent in the cleanroom.

Finally, big hug to my family and friends, for your integrity and the support you have given me in theses years—to you I dedicate this work.

Contents

1. General introduction

1.1. Context of the work

1.1.1. MEMS in microwave applications

The acronym MEMS, for *MicroElectroMechanical Systems*, does not refer to a class of devices sharing the same functionalities or domain of applications, but rather to a common set of fabrication techniques. Based on further developments of the fabrication processes established in the field of microelectronics, MEMS processes allow the combination—at a microscopic scale—of mechanical, optical or even fluidic elements along with electrical components [1]. Thus, common features to MEMS in terms of components characteristics are the microscopic size of at least some part of the device geometry, and the requirement of the presence of some mobile part in the structure for mechanical interaction with any other 'field' (this second characteristic differentiates MEMS devices from simple *micromachined* ones).

With earliest developments tracing back to the 1970s, MEMS fabrication techniques made it possible for systems of all kinds to be more efficient in terms of raw performances, energy-consumption, size, cost, etc. MEMS-based products were then first commercialized in the 1990s. Subsequently, they have been successfully applied to various fields, such as electromechanical sensors (e.g. accelerometers for automobile airbags, gyroscopes), integrated fluidic systems (e.g. so called 'lab-on-chip'), optics (e.g. optical switches, low-power small area displays), acoustics (e.g. MEMS microphones) and other kinds of sensors and actuators (e.g. pressure sensors, ink jet printer heads). Figure 1.1 shows the forecasted MEMS market up to year 2011, with the detailed contribution of each of the aforementioned application fields [2].

More recently, MEMS have also been developed for radio frequency (RF) applications, for instance in the case of resonators [3, 4]. The related class is referred to as RF MEMS and the various actors active in 2006 in this field are shown in Figure 1.2. Nevertheless, the term RF MEMS is generally employed so that it also encompasses much higher frequency applications, namely, in the microwave and millimeter bands. For clarity, we will differentiate here such range of application and simply refer to the corresponding MEMS as *microwave MEMS*, which is the class of MEMS concerned in the present work.

Until recent years, the reconfigurability capabilities of microwave and millimeter wave devices were solely based on controllable ferrite material, semiconductor pin diodes or field effect transistor (FET) transistors. However, the development of MEMS technology allowed radically challenging the performances of reconfigurable microwave devices based on the aforementioned established technologies [3, 7]. In addition, this process will be further encouraged by the growing interest

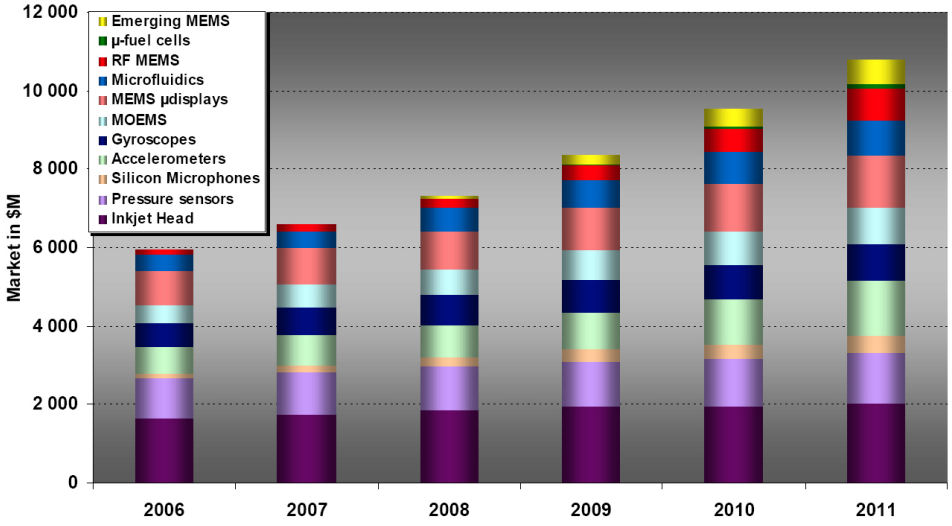

Figure 1.1: Foreseen global MEMS market 2006-2011 (courtesy: Yole Développement [2]).

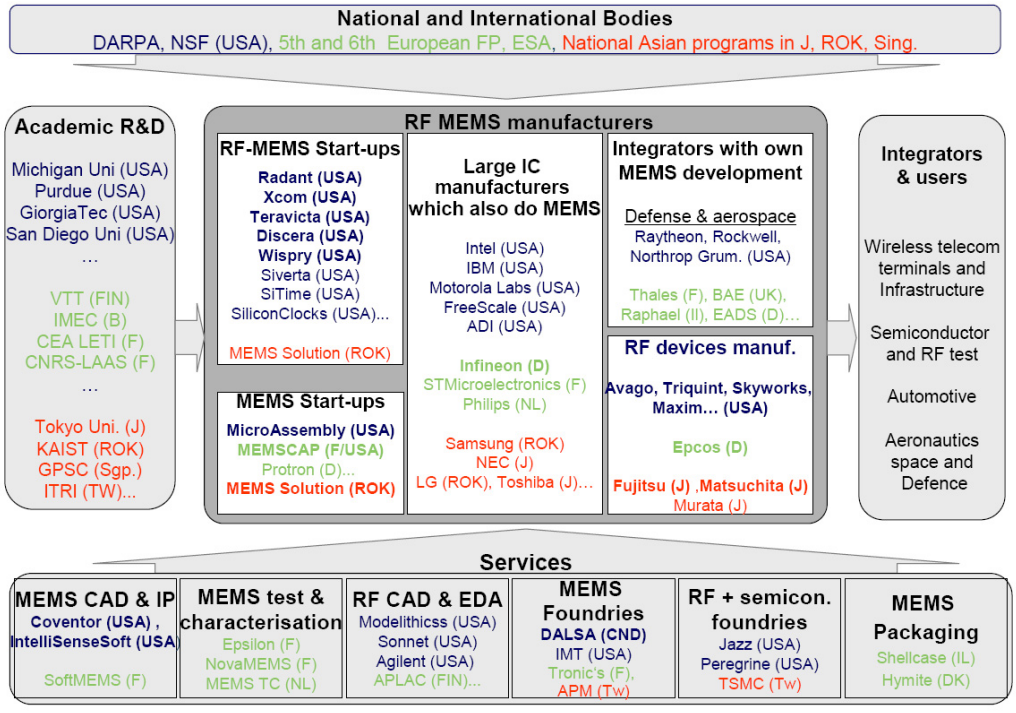

Figure 1.2: Worldwide supply chain for RF MEMS in 2006 (courtesy: Arrro project [5]).

in the high frequency millimeter wave band (for instance for imaging/sensing and communication applications [8]), for which the advantage of MEMS proves to be even more significant. Rather than pushing for the development of completely new microwave and millimeter wave devices, MEMS technology has mainly allowed increasing dramatically the performances of established topologies by replacing, for instance, solid state devices by MEMS ones. As an example, Figure 1.3 shows the numerous sub-functionalities in a telecom repeater that could potentially benefit from a MEMS implementation. Here is a brief overview of demonstrated benefits of the use of MEMS in microwave and millimeter wave devices, with regard to established technologies for reconfigurability such as ferrite materials, pin diodes or FET transistors:

- **Low insertion loss**: especially towards high frequencies.
- **Large bandwidth:** no fundamental frequency limitation.
- **Low drive power**: no DC power consumption outside switching.
- **Monolithic integration** of microwave actives and passives, which reduces assembly cost as well as losses and parasitics.
- **Good Linearity:** possibility to use linear materials only.
- **Low cost:** use of microelectronics batch fabrication techniques.
- **Small size and weight.**

Nevertheless, there are as well some causes for concern for the application of microwave MEMS in 'real life' applications:

- **Limited power handling.**
- **Reliability, lifetime.**
- **Requirement of hermetic package.**

Compared with other classes of MEMS, microwave MEMS are still in their early developments. Nevertheless, there has been in recent years a significant effort in this direction; in the case of high cost applications (e.g. radars, satellites), the main reason is the state-of-the-art performances that MEMS technology can offer; in the case of mass market (e.g.: mobile phone, GPS receiver), it is rather pushed by the increasing demand for the integration of numerous microwave functionalities in a single, small, low-power consuming and low-cost device. As can be observed in Figure 1.1, it is expected that the market for RF MEMS will significantly increase in the coming years.

1.1.2. Research projects

The work carried out in this thesis was mainly funded by the 6^{th} Framework Program of the European Union on Information Society Technology (IST). A good overview of worldwide public funding in the domain of RF MEMS is shown in the left hand side of Figure 1.4. The right hand side of the figure shows the different projects funded by the European Commission in this field, among which the three projects the author of this thesis was involved in (the names of these projects are boxed in the legend of the figure). In the first project, entitled *WIDE-RF:*

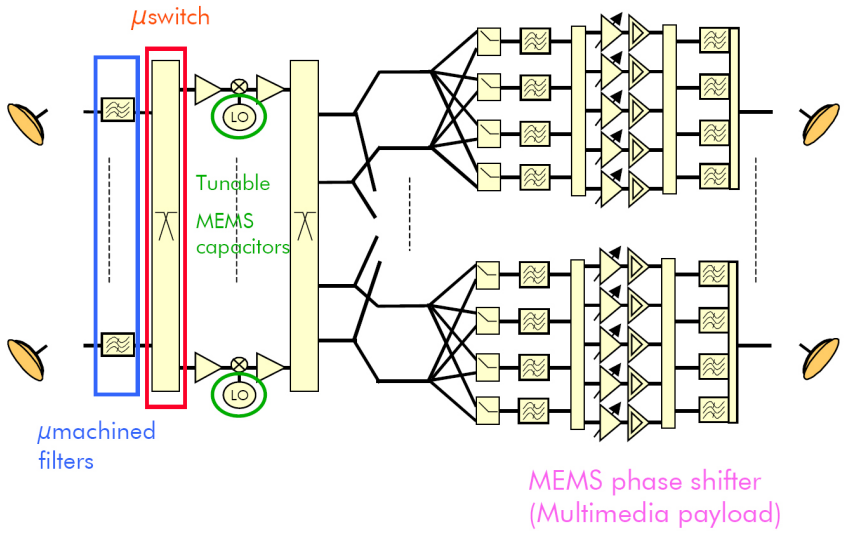

Figure 1.3: Sub-functionalities in a transparent satellite telecom repeater that could benefit from a MEMS implementation (courtesy: Thales Alenia Space, source: [6]).

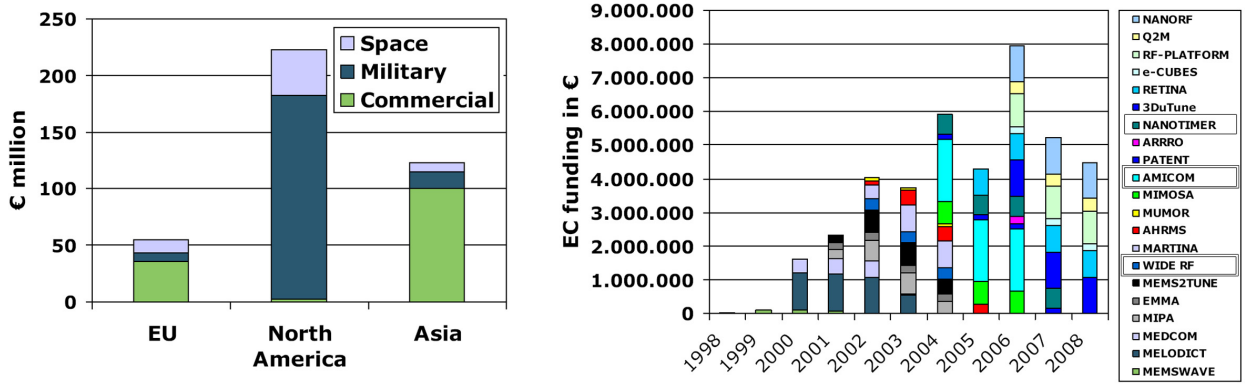

Figure 1.4: Left: worldwide estimated cumulative public funding of RF MEMS research between 2000 and 2006. Right: European Commission RF MEMS research projects funding since 1998 (Courtesy: Arrro project [5]).

Innovative MEMS for Wideband Reconfigurable RF Microsystems [9], our task was to model, design and measure MEMS variable capacitors and DMTLs. The most relevant results obtained in this project are presented in this thesis. In the second project, *NanoTIMER: Nanotechnology in Mechanical-electrical Resonators* [10], we designed an optimal package for MEMS resonators, as well as characterized the parasitics for the overall packaged resonators. This work is however not reported in this thesis, since quite out of the scope of the rest of the here presented work.

The third source of funding was somehow different from the aforementioned ones since it consists in a so-called Network of Excellence, meant to improve synergies and collaborations in the field of RF MEMS in Europe. Entitled *AMICOM: European Network of Excellence on RF MEMS and RF Microsystems* [11], the network's impact on this work was mainly to provide some multi-project MEMS fabrication runs. More precisely, the participation of EPFL in AMICOM allowed us to design devices on three different runs, on available surfaces ranging from 1 to 2 cm^2. Two of these runs were used for the design of MEMS composite right/left handed transmission lines (V-CRLH-TLs), whereas the third run was employed for the design of monolithic reflectarray cells. The choice of these designs was thus not imposed by external funding or constraints; they were selected as very interesting microwave periodic structures, to which MEMS technology could be beneficial to reconfigurability capabilities and integration. Finally, within AMICOM was launched the smaller scale project *RARPA: Reflectarrays and Reconfigurable Printed Antennas* [12]. There, we designed MEMS-controllable RA antenna cells on low temperature co-fired ceramics (LTCC) technology.

1.2. Objectives and organization of the thesis

1.2.1. Motivation and objectives

As a result of the very interesting features of MEMS for microwave applications listed above, there has been in the last years intensive research effort in the developments of microwave MEMS switches, tunable capacitors, phase shifters, filters and reconfigurable antennas. Nevertheless, this research is still in its early stage, compared with other aforementioned application domains for MEMS. Indeed, although numerous interesting works have been published, very few devices have so far reached the market, and these almost only consist in MEMS switches[1], namely, the most simple of the above microwave MEMS.

In this context, the objective of this thesis is to contribute to the development of new microwave functionalities as well as to improve existing architectures of microwave structures using MEMS devices. More precisely, we will focus here on *periodic or cascadable microwave devices*. Indeed, numerous microwave devices take advantage of the particular propagation properties of a wave in periodic structures to achieve given functionalities; one can name: distributed phase shifters, frequency selective surfaces (FSSs), periodic antennas, antenna arrays and reflectarrays, and more recently, metamaterials. The idea here is to develop analysis and design methods based

[1] We do not consider FBARs and MEMS resonators here, as they are not properly speaking microwave MEMS due to their generally low operating frequency.

on the theory of waves propagating in periodic structures to help in dealing with different kinds of periodic or cascadable MEMS structures in an integrated approach. It should be emphasized here that the term periodic as used in the title of this thesis is rather linked with the theory usually employed for periodic structure but is not limited to real periodic structure only. Indeed, we will show that this approach is also very interesting for the design of any finite periodic structure. At the limit, a single *cascadable* device can be seen as a 1-cell periodic and treated accordingly.

These concepts will be applied to three main classes of devices which will be designed, fabricated, and fully characterized. The first two are 1-dimensional transmission line structures, namely, the distributed MEMS transmission line (DMTL) and the MEMS composite right/left handed transmission line (V-CRLH-TL)[1]. Then, we develop MEMS-controlled reflectarray antenna elements, which are different from the previous devices in the sense that they are the unit cells of 2-dimensional periodic structures illuminated by a plane wave.

The development of MEMS microwave devices requires not only an efficient electromagnetic design but also some electromechanical modeling and fabrication process development. Although these issues obviously had to be addressed in this work to realize functioning devices — in practice, electromechanical and electromagnetic designs are not fully independent— the emphasis in this work is put on the electromagnetic design and other aforementioned issues will only be briefly commented. Finally, let us note that a large part of the original contributions in this thesis are not limited to MEMS devices only. Indeed, in the process of developing particular MEMS devices, general theoretical results for a given class of structure were obtained, which could be of use for the implementation of such type of device in other technologies than MEMS.

1.2.2. Outline and original contributions

In this section, we describe the organization of this thesis and provide some comments about the original contributions linked with each chapter. The first part of the thesis (Chapters 2 to 7) focuses on the 1-D TL structures — the DMTLs, fixed CRLH-TLs and V-CRLH-TLs, whereas the second deals with the reflectarray application, namely, a 2-D periodic structure interacting with a field in free space rather than guided waves (Chapters 8 and 9).

Chapter 2: Periodic Structure Modeling

Description: First, this chapter studies the fundamental properties of periodic TL structures composed of identical cascaded unit cells, the results of which will be employed for the development of design methods for the 1-D MEMS devices. Particular solutions especially useful for the design of the following MEMS structures are also provided. The theory is then extended to the multimode case, which allows us to take into account the inter-cell coupling through higher order modes —whether propagating or evanescent— of the waveguide comprising the ports of the cell.

Original contribution: The basis of the theory presented in this chapter, usually referred to as Bloch wave theory is not new and addressed in several textbooks. However, the developments are carried out here in a way which allows the clear identification of the link between

[1]Note that fixed micromachined composite right/left handed transmission line (CRLH-TL) will also be designed

the different mathematical solutions in the light of physical considerations. Some other intuitive and analytical considerations are also made to show that the Bloch wave periodic structure modeling is not only valid for infinite periodic structures but also allows dealing with terminated finite-size periodic structures without any further assumption. Finally, new contributions are brought to the considerations of higher order modes interactions in the periodic structure modeling.

Chapter 3: Building Blocks

Description: In order to design efficiently devices such as DMTLs, MEMS V-CRLH-TLs, or MEMS-based reflectarray cells, it is necessary to work first on a 'building block' level, these blocks being the different MEMS or micromachined 'units' constituting the microwave device. Since most of the design methods presented afterwards are based on equivalent circuits, we especially wish to derive simple and accurate circuit models for such blocks. In this context, this chapter discusses the simulation, measurement, and extraction of lumped elements for several 'building blocs' to be employed in the MEMS devices presented in later chapters. This includes a comprehensive characterization of micromachined coplanar waveguides with regard to non-conventional materials used in MEMS processes.

Original contribution: This chapter does not present major innovative results but rather several practical issues linked with the simulation, measurement and method of extraction for any integrated 'block'. In addition, we present here several new MEMS devices that were designed for the particular applications treated in this thesis in Chapters 4 to 9.

Chapter 4: DMTLs Design

Description: In this chapter, we present the design strategies and results obtained for the single-bit DMTL. First, applications for DMTLs are discussed along with related calculations, in order to deduce relevant information for the optimization strategies. The two design algorithms developed, based on the periodic structure modeling, are then explained step-by-step. Finally, some measurement results for an analog and a digital DMTL are presented, along with circuit model results.

Original contribution: Several points in the design algorithms presented here are inspired from previous works on 'non-MEMS' distributed delay lines and DMTLs. However, the methods also include several new aspects and improvements, mostly thanks to the periodic structure modeling approach. Finally, the two methods presented allow targeting different goals in the optimization procedure.

Chapter 5: Multi-bit DMTLs

Description: Here we present a simple solution to improve the matching of multi-bit DMTLs, which is an important limitation of digital DMTL implementations. First, we discuss the issue of matching in conventional multi-bit DMTL and introduce the new topology. The advantages of the latter are then explained both intuitively and based on detailed analytical developments. Afterwards, a design strategy for the new topology is discussed, based on the design method presented in the previous chapter. Finally, complete designs of DMTLs of the conventional and new types are carried out to validate the design method and demonstrate the advantages of the new topology.

Original contribution: To our knowledge, the advantageous multi-bit topology presented in this chapter was first introduced by the author. The corresponding analysis and design method are thus obviously new, and not limited to MEMS-based phase shifters only.

Chapter 6: CRLH-TLs: Theory and Micromachined Implementation

Description: In this chapter, we first study in detail the CRLH-TL structure from a theoretical point of view and discuss the notion of effective media for this particular metamaterial structure. Then, we present a simple method to design optimally matched CRLH-TLs, based on the computation of the Bloch wave equivalent impedance of the corresponding unit cell circuit. The modeling and design strategies are then validated by measurements on micromachined CRLH-TLs realizations.

Original contribution: Here we show that the theory for CRLH-TL as developed in the literature is based on assumptions not suited to micromachined realization as well as some other useful CRLH-TL implementations, and that this is linked with the effective medium assumption commonly employed for the analysis of such structures. Thus, a new theoretical approach is developed, which is exact on the basis on the CRLH-TL unit cell circuit while providing very simple design expressions. Finally, we show that this new approach allows designing CRLH-TLs whose impedance is much beyond the range achievable in the usual case of effective CRLH-TLs.

Chapter 7: MEMS V-CRLH-TLs

Description: In this chapter, we present the MEMS-variable counterpart of the micromachined CRLH-TL described in the previous chapter. We show that an efficient design can be made using a Bloch wave formalism, accurate circuit models and a limited number of full-wave simulations. Both analog and digital devices are designed and fully characterized. In the second step, we present some applications of the designed MEMS V-CRLH-TL, which consist in differential phase shifters with interesting phase properties.

Original contribution: The devices presented are, to the author's knowledge, the first reported MEMS V-CRLH-TLs. The applications proposed are inspired from a previous work but generalized for reconfigurability and versatility in the phase response.

Chapter 8: Reconfigurable Reflectarray Cell Theory

Description: In this chapter, we first discuss in detail the various requirements for the design of MEMS-based reconfigurable RA cells. We then discuss the theory and modeling of 2-D periodic structures interacting with a field in free space, which are based on Floquet's theorem. Then, a comprehensive theoretical discussion of the possibilities and limitations in the simulations and measurements of such cells in an array environment is provided. These developments and the simulation methods are finally validated using dedicated passive test devices.

Original contribution: Although based on results available in the literature, this chapter brings new contributions to the different topics addressed. In the case of the requirements for the RA cells, we integrate some well-known issues linked with fixed-beam RA with new ones related to the design of *reconfigurable* devices. Concerning the characterization of such cells, we provide a comprehensive theoretical assessment of the requirements on the device

and correct measurement/simulation setups for a valid comparison and interpretation of the results.

Chapter 9: MEMS Reflectarray Cells

Description: This chapter presents the design of RA cells controlled by MEMS and fabricated in a monolithic process. The design procedures are detailed with regard to the requirements highlighted in the previous chapter. In addition, we explain the strategy employed to dramatically reduce the computation time, which would otherwise be prohibitive.
Original contribution: In view of the very fragmented results on MEMS RA cells available in the literature, the devices designed here present, to the author's knowledge, the most comprehensive and state-of-the-art performances.

Chapter 10: Conclusions and perspectives We conclude with some summary and general assessment of the work achieved in this thesis, and discuss the perspectives of MEMS technology in microwave and millimeter wave applications.

Appendices

Two appendices are provided, briefly treating some electromechanical issues and describing the different MEMS fabrication processes employed for the realization of the demonstrators presented in this thesis.

2. Periodic Structure Transmission Line Theory

2.1. Introduction

First, this chapter studies the fundamental properties of periodic structures composed of identical cascaded 2-port networks, which will hereafter be referred to as the *cells* of the structure. The associated theory, known as the Bloch wave theory[1], is well known and addressed in numerous textbooks such as [13] and [14]. Thus, the first part of this chapter mainly consists in rewriting Bloch theory in the notation that will be used throughout this thesis. However, we also pay particular attention to the signs within the developments, in order to subsequently link the different mathematical solutions to physical considerations.

Some additional developments to the ones available in the aforementioned references are also provided to show that the Bloch wave periodic structure modeling is not only valid for infinite periodic structures but also allows dealing with terminated finite-size periodic structures without any further assumption. Then, we develop in more detail the expressions in the particular case where the cell is composed of an 'obstacle' loading a TL, since this is the case of several micromachined and MEMS structures to be studied in this thesis.

In the last part of this chapter, the theory is extended to the multimodal case and an example and comments about the necessity of taking into account higher order modes are discussed.

2.2. General developments

2.2.1. Naming convention

For clarity in the following discussion, let us first explicitly write the naming conventions employed here about the propagation of waves:

***Propagating* vs. *evanescent* waves:** A non-attenuated *propagating wave* exhibits $\alpha = 0$ and $\beta \neq 0$. However, a propagating wave can also be attenuated so that $\alpha \neq 0$ and $\beta \neq 0$. An *evanescent wave* is characterized by $\alpha \neq 0$ and $\beta = 0$.

Purely *traveling* waves: A purely *traveling* wave is a 'single' wave propagating either toward the positive or negative direction of the axis of the periodic structure, hence according to $U(z) = U_0 \exp(\pm\gamma z)$. This traveling wave can be propagating or evanescent.

[1] by analogy with the quantum-mechanical electron waves that propagate through periodic crystal lattice in a solid.

***Forward* vs. *backward* propagation:** We refer to a *forward* propagation when the phase and group velocity of a purely traveling wave are in the same direction, whereas a *backward* propagation means that phase and group velocities are antiparallel. Let us note that *forward* and *backward* propagations are also sometimes referred to as *direct* and *inverse*, respectively.

Concerning the naming of the parameters describing the propagation in the periodic structure, they are referred to as *periodic structure equivalents*, or *Bloch wave equivalents* and are thus denoted with the subscript *equ* as follows:

γ_{equ}:	Periodic structure (Bloch wave) equivalent propagation constant.
$\alpha_{equ}, \beta_{equ}$:	Real and imaginary parts of γ_{equ}.
Z_{equ}:	Periodic structure (Bloch wave) equivalent characteristic impedance.

2.2.2. Transmission matrix eigenvalue problem

Let us imagine that a periodic structure supports the propagation of a purely traveling wave. In this case, voltage and current corresponding to the traveling wave must obviously have the same dependence on the direction of propagation z, and this dependence must be of the usual exponential form $\exp(\mp\gamma_{equ}d)$ with $\gamma_{equ} = \alpha_{equ} + j\beta_{equ}$ so that we write :

$$\begin{cases} U(z+d) = U(z)\exp(\mp\gamma_{equ}d) \\ I(z+d) = I(z)\exp(\mp\gamma_{equ}d) \end{cases} \tag{2.1}$$

This means that γ_{equ} is the propagation constant of the wave supported by the periodic structure and we verify that the attenuation is $|U(z+d)/U(z)| = \exp(\mp\alpha_{equ}d)$ and the phase shift $\arg[U(z+d)/U(z)] = \mp\beta_{equ}d$.

Formula (2.1) links voltage and current between cell ports, but gives no information about the electrical quantities inside the cells. The $\pm$ sign means that two waves propagating in opposite directions are supported by the structure and that these waves are described by the same propagation constant[1] in the case of reciprocal structures. We must now prove that there exists γ_{equ} so that (2.1) is true. If we compare the above expressions with the definition of the transmission matrix of a cell T_{cell}, we deduce that:

$$\begin{bmatrix} U(z) \\ I(z) \end{bmatrix} = \exp(\pm\gamma_{equ}d) \begin{bmatrix} U(z+d) \\ I(z+d) \end{bmatrix} = [T_{cell}] \begin{bmatrix} U(z+d) \\ I(z+d) \end{bmatrix} \tag{2.2}$$

Some observation of the above equation shows that the equivalent propagation constant γ_{equ} of the loaded line is found by solving an eigenvalue problem, where $\exp(\pm\gamma_{equ}d)$ are the two eigenvalues of the matrix T_{cell}. In other words, we have:

$$\det\{[T_{cell}] - \exp(\pm\gamma_{equ}d)[I]\} = 0 \tag{2.3}$$

[1] This is not exactly equivalent to writing γ_{equ} and implicitly considering that this parameter can be either positive or negative. Indeed, by writing the equation for two different opposite solutions, we will be able to determine if different signs in some following results are linked with the sign of γ_{equ} or independent from it.

With the definition $T_{cell} = [A_{cell}\ B_{cell}\ ;\ C_{cell}\ D_{cell}]$, we find:

$$A_{cell}D_{cell} - B_{cell}C_{cell} + \exp\left(\pm 2\gamma_{equ}d\right) - \exp\left(\pm\gamma_{equ}d\right)\left(A_{cell} + D_{cell}\right) = 0 \tag{2.4}$$

2.2.3. Equivalent propagation constant γ_{equ}

a. General case

Any reciprocal network transmission matrix (reciprocity is assumed in these developments) has the property $A_{cell}D_{cell} - B_{cell}C_{cell} = 1$, which allows simplifying (2.4). Then, multiplying by $\exp\left(\mp\gamma_{equ}d\right)$ and making use of the definition of the cosh function leads to (2.5), *whichever the sign preceding* γ_{equ}.

$$\cosh\left(\gamma_{equ}d\right) = \frac{1}{2}\left(A_{cell} + D_{cell}\right) \tag{2.5}$$

As we found solutions for γ_{equ}, we actually proved that the periodic structure supports traveling waves according to (2.1). This result is a simple form of Floquet's Theorem, which will be addressed in its general form in Chapter 8. The wave supported by the structure can be purely propagating, evanescent, or propagating and attenuated, depending on the properties of the cell cascaded and the frequency. We also observe that the same propagation constant is obtained if A_{cell} and D_{cell} are inverted. Since inverting A_{cell} and D_{cell} is equivalent to physically revert the reciprocal two-port described by the matrix T_{cell}, this confirms that the propagation constant is the same for both propagation directions in the structure, as the solution above in cosh is equally found for each eigenvalue $\exp(\pm\gamma_{equ}d)$.

b. Symmetrical cells

By definition of the transmission matrix, $A_{cell} = D_{cell}$ for symmetrical cells. In this case, the expression for the propagation constant reduces to:

$$\cosh\left(\gamma_{equ}d\right) = A_{cell} \tag{2.6}$$

2.2.4. Equivalent characteristic impedance Z_{equ}

a. Eigenvalues method

In practice, a periodic structure will be terminated and it is necessary to set appropriate boundary conditions at the extremities of the structure. For that reason, it is most important to derive not only the propagation constant, but also the characteristic impedance of the periodic structure, which is defined as follows:

$$Z_{equ} = \frac{U\left(z\right)}{I\left(z\right)} \tag{2.7}$$

Note: By definition of the characteristic impedance, $U\left(z\right)$ *and* $I\left(z\right)$ *in (2.7) must be associated with a purely traveling wave. We observe that this is consistent with the initial definition of* $U\left(z\right)$ *and* $I\left(z\right)$ *in (2.1).*

If we now write again the eigenvalue equation (2.2) as follows[1]:

$$\begin{bmatrix} U(z) \\ I(z) \end{bmatrix} = \exp(\pm\gamma_{equ}d) \begin{bmatrix} U(z+d) \\ I(z+d) \end{bmatrix} = \begin{bmatrix} A_{cell} & B_{cell} \\ C_{cell} & D_{cell} \end{bmatrix} \begin{bmatrix} U(z+d) \\ I(z+d) \end{bmatrix} \tag{2.8}$$

we see that:

$$U(z) = A_{cell}U(z+d) + B_{cell}I(z+d) = \exp(\pm\gamma_{equ}d)U(z+d) \tag{2.9}$$

$$I(z) = C_{cell}U(z+d) + D_{cell}I(z+d) = \exp(\pm\gamma_{equ}d)I(z+d) \tag{2.10}$$

respectively yield:

$$Z_{equ1} = \frac{U(z)}{I(z)} = \frac{U(z+d)}{I(z+d)} = \frac{-B_{cell}}{A_{cell} - \exp(\pm\gamma_{equ}d)} \tag{2.11}$$

$$Z_{equ2} = \frac{U(z)}{I(z)} = \frac{U(z+d)}{I(z+d)} = \frac{\exp(\pm\gamma_{equ}d) - D_{cell}}{C_{cell}} \tag{2.12}$$

Now, let us write the solution of the eigenvalue problem (2.4) as (making use of the reciprocity assumption):

$$\exp(\pm\gamma_{equ}d) = \frac{1}{2}\left[A_{cell} + D_{cell} \pm \sqrt{(A_{cell} + D_{cell})^2 - 4}\right] \tag{2.13}$$

Note that it is, at this stage, impossible to associate the sign before the square root to one of the signs before $\gamma_{equ}d$. Indeed, each sign preceding the square root is solution for each sign initially set to $\gamma_{equ}d$. Finally, we find by substituting (2.13) in (2.11) and (2.12):

$$Z^{\pm}_{equ1} = +\frac{-2B_{cell}}{A_{cell} - D_{cell} \pm \sqrt{(A_{cell} + D_{cell})^2 - 4}} \tag{2.14}$$

$$Z^{\pm}_{equ2} = +\frac{A_{cell} - D_{cell} \pm \sqrt{(A_{cell} + D_{cell})^2 - 4}}{2C_{cell}} \tag{2.15}$$

Here, the sign preceding the expression of Z_{equ} is + because the + (respectively -) sign in the exponential argument of (2.13) corresponds to the + (respectively -) sign of (2.11). This issue is however not to be mistaken with the sign before the square root, which will be discussed later on.

By definition, Z_{equ1} and Z_{equ2} are the same quantity. However, the ± sign in each expression actually leads to four 'couples' $Z_{equ1} = Z_{equ2}$, which might not be all true. By the following method, we can verify if $Z_{equ1} = Z_{equ2}$, and in which cases:

Case 1: $Z^{+}_{equ1} = Z^{+}_{equ2}$ and $Z^{-}_{equ1} = Z^{-}_{equ2}$

We substitute (2.14) and (2.15) into these equalities and find:

$$A^2_{cell} + D^2_{cell} \pm (A_{cell} - D_{cell})\sqrt{(A_{cell} + D_{cell})^2 - 4} - 2 = -2B_{cell}C_{cell} \tag{2.16}$$

[1] Remark: The transmission matrix can also be defined in the other direction (i.e. so as to transform current and voltage from z to $z+d$). Consequently, it is important to define properly the signs when calculating the elements of the transmission matrix, so that they correspond to the convention used in these developments.

Let us consider the symmetrical case, hence $A_{cell} = D_{cell}$. We obtain:

$$A_{cell}^2 + B_{cell}C_{cell} = 1 \tag{2.17}$$

This is not possible for a reciprocal symmetrical network, for which $A_{cell}^2 - B_{cell}C_{cell} = 1$ is always true. Consequently, the two assumptions $Z_{equ1}^+ = Z_{equ2}^+$ and $Z_{equ1}^- = Z_{equ2}^-$ above are not true since not true in the particular case of a symmetrical two-port network.

Case 2: $Z_{equ1}^+ = Z_{equ2}^-$ and $Z_{equ1}^- = Z_{equ2}^+$

Similarly, but in the general asymmetrical case, we find after some calculations:

$$A_{cell}D_{cell} - B_{cell}C_{cell} = 1 \tag{2.18}$$

This is always true and verifies that the two expressions found for the characteristic impedances are actually the same, with the restriction of choosing the appropriate sign before the square root. Practically we can use either of the expressions and we choose:

$$Z_{equ}^{\pm} = +\frac{-2B_{cell}}{A_{cell} - D_{cell} \pm \sqrt{\left(A_{cell} + D_{cell}\right)^2 - 4}} \tag{2.19}$$

Note: Z_{equ} can be normalized or not, depending on the transmission matrix normalization. The transmission parameters are themselves normalized if the impedances/admittances from which they are deduced are normalized.

Since Z_{equ} is by definition the ratio $U(z)/I(z)$ and $[U(z)\ ;\ I(z)]$ the eigenvector of the matrix T_{cell} [see (2.7) and (2.2), respectively], the eigenvectors of the operator T_{cell} can be written as a function of Z_{equ} as follows:

$$v^{\pm} = \begin{bmatrix} Z_{equ}^{\pm} \\ 1 \end{bmatrix} \tag{2.20}$$

So, we showed that the equivalent propagation constant γ_{equ} is linked with the eigenvalues $\exp(\mp\gamma_{equ}d)$ of the unit cell transmission matrix T_{cell}, whereas the equivalent impedance Z_{equ} corresponds to the eigenvectors of the system $\left[Z_{equ}^{\pm}\ ;\ 1\right]$.

b. Single cell method

This section presents a simple and intuitive, alternative way to calculate the equivalent impedance of the periodic structure, based on the analysis of a cell connected to a given load impedance Z_L, as depicted in Figure 2.1. The input impedance of the system is called Z_{IN}. By definition of the T_{cell} matrix:

$$\begin{bmatrix} U(z) \\ I(z) \end{bmatrix} = [T_{cell}] \begin{bmatrix} U(z+d) \\ I(z+d) \end{bmatrix} = \begin{bmatrix} A_{cell}U(z+d) + B_{cell}I(z+d) \\ C_{cell}U(z+d) + D_{cell}I(z+d) \end{bmatrix} \tag{2.21}$$

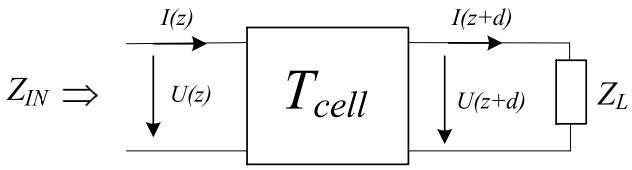

Figure 2.1: Circuit for the 'single cell' method determination of the equivalent Bloch impedance.

By inspection of Figure 2.1, we have:

$$Z_{IN} = \frac{U(z)}{I(z)} \quad \text{and} \quad Z_L = \frac{U(z+d)}{I(z+d)} \tag{2.22}$$

Making use of (2.21) and (2.22), we obtain the input impedance as a function of the load impedance:

$$Z_{IN} = \frac{U(z)}{I(z)} = \frac{A_{cell} Z_L + B_{cell}}{C_{cell} Z_L + D_{cell}} \tag{2.23}$$

If $Z_{IN} = Z_L$, this means that the two-port network transforms the impedance seen at its right terminal to the same impedance at its left input. If now more than one cell are cascaded at the left of the load, the same input impedance will be repeated at each connection. Consequently, this means that that the load impedance Z_L such that $Z_{IN} = Z_L$ is the equivalent characteristic impedance Z_{equ} of the structure. So, we introduce the condition $Z_{equ} \equiv Z_{IN} = Z_L$ in the last expression and we find after some calculations:

$$Z_{equ} = \frac{A_{cell} - D_{cell} \pm \sqrt{(A_{cell} + D_{cell})^2 - 4}}{2C_{cell}} \tag{2.24}$$

This result is the same as the one found by means of the eigenvalues method (it is actually one of the solutions, which was proven to be equivalent to the other one), which concludes the demonstration.

Finally, let us note that the propagation constant given by (2.5) can also be found using this method. Indeed, when $Z_{equ} = Z_L$, there is no reflected wave and we simply have:

$$\frac{U(z+d)}{U(z)} = \exp(-\gamma_{equ} d) \tag{2.25}$$

Using then the definition $\cosh(x) = (\exp(+x) + \exp(-x))/2$ and (2.21) allows obtaining (2.5), after some algebraic operations.

c. Symmetrical cell

If a cell is reciprocal and symmetrical, we know that $A_{cell}D_{cell} - B_{cell}C_{cell} = 1$ and $A_{cell} = D_{cell}$, respectively. In this case the impedance reduces as follows:

$$Z_{equ} = \frac{-2B_{cell}}{A_{cell} - D_{cell} \pm \sqrt{(A_{cell} + D_{cell})^2 - 4}} = \frac{-2B_{cell}}{\pm 2\sqrt{(A_{cell})^2 - 1}} = \frac{-B_{cell}}{\pm\sqrt{B_{cell}C_{cell}}} = \pm\sqrt{\frac{B_{cell}}{C_{cell}}} \tag{2.26}$$

2.3. Solutions and signs discussion

2.3.1. Equivalent propagation constant γ_{equ}

The mathematical developments for the propagation constant γ_{equ} in the periodic structures led to two solutions given by (2.5), which thus only differ by their sign. We noted that both solutions exist at any frequency and correspond to the two possible directions of propagation. The question we face now is how to link each solution to a given propagation direction, since this information could not be deduced from the mathematical developments. As will be shown below, a good physical interpretation of the solutions is not trivial when *forward*, *backward* or even *negative group velocity* bands exist (see this chapter's appendix). Understanding that propagation behavior with regard to the mathematical results will be especially important to select the right solution for the impedance among the two solutions found previously. Finally, another illustration of the need of these results will be given in Chapter 6 in the case of the CRLH-TL structure.

For that purpose, we will now discuss two possible sign conventions in the light of physical considerations. First, let us recall the definitions of phase and group velocities:

$$v_\phi = \omega/\beta \tag{2.27}$$

$$v_g = \left(\frac{\partial\beta}{\partial\omega}\right)^{-1} \tag{2.28}$$

Positive group velocity ($v_g > 0$) convention: The first convention proposed here is to force a positive group velocity ($v_g > 0$) to choose the sign of the γ_{equ} solution. According to (2.28), this means that the sign chosen is the one corresponding to a positive $\beta(\omega)$ slope. This does not mean that we restrict the solution to one direction of propagation, since $+z$ and $-z$ remain in the expression for $U(z)$, and is only a question of consistency in the definitions since waves can actually propagate in both directions at any frequency.

Positive phase velocity ($v_\phi > 0$) convention: Usually, purely traveling waves $U_+(z)$ and $U_-(z)$ propagating in the $+z$ and $-z$ directions, respectively, are written as follows:

$$U_+(z) = U_{0+}\exp(-\gamma z) \quad \text{and} \quad U_-(z) = U_{0-}\exp(+\gamma z) \tag{2.29}$$

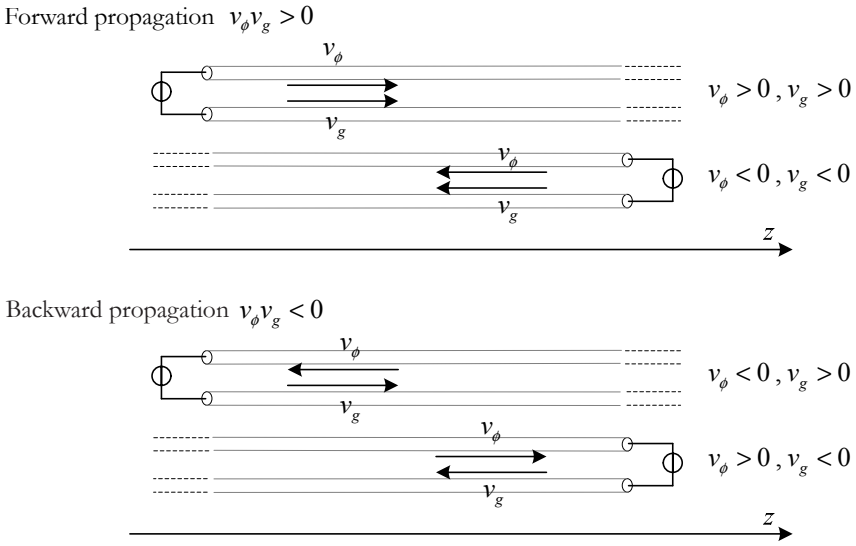

Figure 2.2: Intuitive illustration of the signs of phase and group velocities in *forward* and *backward* bands.

with $\gamma = \alpha + j\beta$. To be consistent with the convention that $U_+(z)$ and $U_-(z)$ are respectively propagating in the $+z$ and $-z$ directions, inspection of the above equations shows that β *must always be positive*. According to (2.27), the sign of the phase velocity is obviously that of β and this convention is thus referred to as *positive phase velocity* ($v_\phi > 0$).

In the case of a *forward* propagation, which is the usual TL behavior, the phase velocity v_ϕ is in the same direction as the group velocity v_g so that $v_\phi v_g > 0$. We can see in Figure 2.2 that if an energy source is placed at one end of a semi-infinite line, a purely traveling wave propagates away from the source. The two reverse lines in the figure represent the two possible directions of propagations, with the associated velocities signs with regard to the z axis, which is identically defined for both propagation directions. In the case of *backward* propagation, the phase velocity v_ϕ is opposite to the group velocity v_g so that $v_\phi v_g < 0$. Except for very particular cases[1], the energy/information propagates in the same direction as the group velocity. Consequently, it is physically sensible to set the convention that the group velocity is directed from the source to the load (here the infinite line). By doing so, we set the convention that $v_g > 0$, both in *forward* and *backward* bands. We can also think from a group delay point of view, which represents the time for the energy/information carried by the signal to travel through the line. It is logical that this quantity is always positive, which is the case only with this convention. According to this convention and due to the conservation of energy, the attenuation coefficient α will always

[1] The group velocity can be antiparallel with the energy/information propagation in very particular cases. This issue is treated in this chapter's appendix. However, these special cases can be identified by observation of the propagation characteristic and are also very rare. Therefore, and for the sake of simplicity, all present developments consider that the energy propagates in the same direction as the group velocity, and any extraordinary behavior will be treated in a second stage.

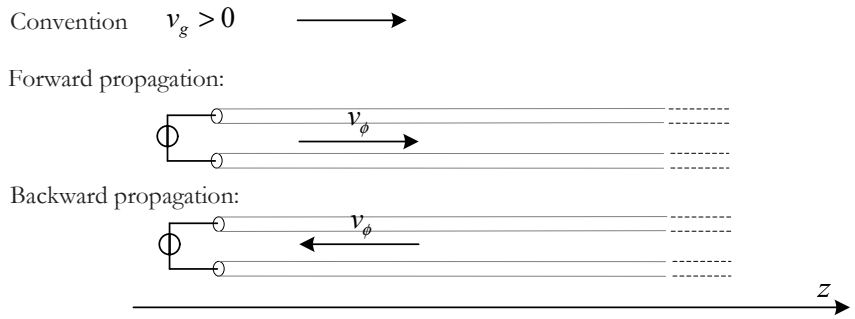

Figure 2.3: Intuitive illustration of the signs of phase and group velocity in *forward* and *backward* bands, using the convention of positive group velocity ($v_g > 0$).

be positive for a positive group velocity, whatever the type of propagation, namely *forward* or *backward*.

All cases for the signs of v_ϕ and v_g are depicted in Figure 2.2. In the general case of a finite periodic structure, there are waves propagating in both direction but we can consider only one direction to set the convention, as we know that we only need to change the sign of α and β to describe propagation of the energy in the other direction. With regard to the intuitive illustration of Figure 2.2 this means that we can choose a certain position for the source. We decide to put it at the left end of the line (toward $-z$) so that $v_\phi > 0$ corresponds to the *forward* band. Figure 2.4(a) shows a numerical example of the computed γ_{equ} with adequate post processing regarding the selection of solution, according to the $v_g > 0$ convention discussed above. The structure concerned here consists of a TL loaded with shunt loading elements with a mainly capacitive behavior. As can be seen in the figure, it exhibits stop and passbands, themselves either corresponding to *forward* or *backward* propagations.

If we had chosen the $v_\phi > 0$ convention, it would mean that we deal with waves whose phase velocity is always in the $+z$ direction. We will now give an example which shows that this convention is physically inadequate. Let us consider a finite structure having both *forward* and *backward* bands. We connect a source to the left termination of the structure (toward $-z$) and a perfect load to the right one (toward $+z$). This situation is obviously equivalent to the infinite line presented above but practically more realistic. As the convention sets that the phase velocity is always positive, this means that in the *forward* band, the group velocity and energy flow are positive. This is physically correct since the energy then flows from the source to the load. Now let us consider an *backward* band, defined by $v_\phi v_g < 0$. Since in this case $v_\phi v_g < 0$, using the $v_\phi > 0$ convention means that the group velocity is negative and that the energy travels towards the $-z$ direction. In other words, this means that the energy is transmitted from the load to the source, which is obviously not true and a consequence of the $v_\phi > 0$ convention.

This problem is overcome by using the $v_g > 0$ convention. However, the representation 'β positive' is sometimes used in the literature. In this case, the sign of α must be negative in the *backward* bands in order to fulfil the requirement that the energy carried by a propagating wave

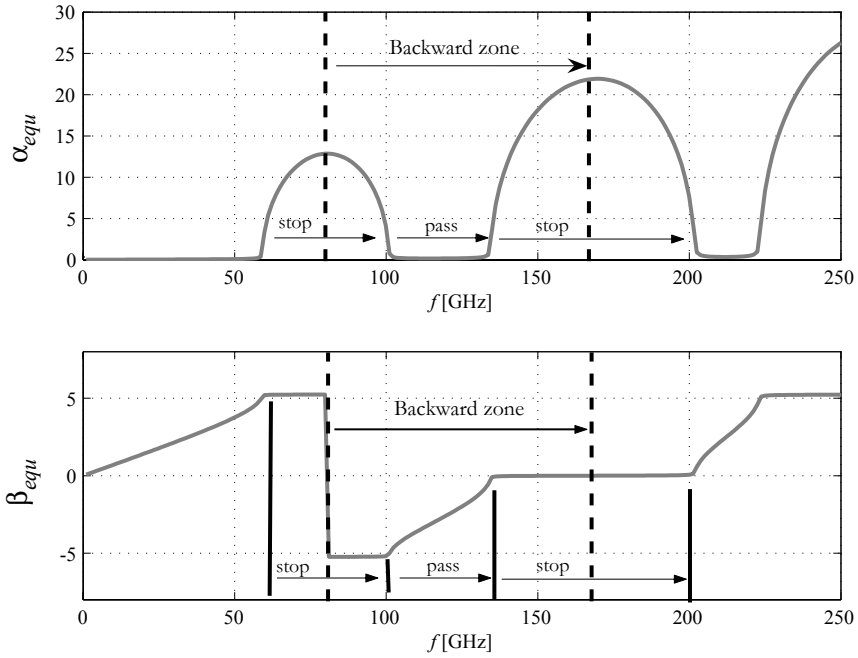

(a) positive group velocity ($v_g > 0$).

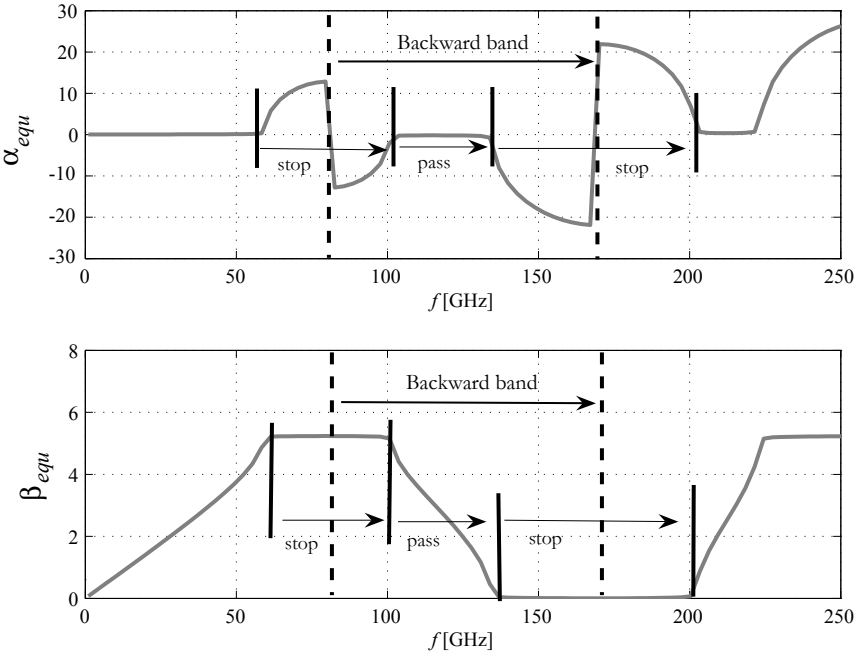

(b) positive phase velocity ($v_\phi > 0$).

Figure 2.4: Example of a band structure with different sign conventions $v_g > 0$ and $v_\phi > 0$.

is attenuated in the direction of propagation of the energy. Consequently, α is positive within the 'forward' bands but negative within the 'backward' bands. With this convention, the graphs of Figure 2.4(a) become the ones shown in Figure 2.4(b).

2.3.2. Equivalent characteristic impedance Z_{equ}

Concerning now the equivalent characteristic impedance Z_{equ}, not only the sign is to be determined since two solutions different in magnitude were found in the general case [see (2.19)]. However, (2.26) shows that in the symmetrical case, only the sign of the impedance changes. Although it is in general understood that these two solutions are linked to different propagation directions, developments available in the literature do not provide any convincing explanation to support this statement. Indeed, a careful attention paid to the signs in the previous calculations showed that both solutions for Z_{equ} are found for *each* eigenvalue. Moreover, the problem of determining which impedance solution corresponds to which propagation direction remains and we will now try to address these questions with regard to our convention.

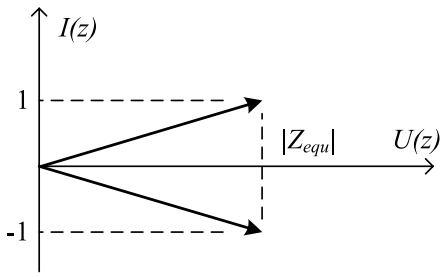

Figure 2.5: Representation of the eigenvectors in the U-I plane for a symmetrical cell.

Figure 2.5 is a graphical representation, in the U-I plane, of the two eigenvectors of the cell transmission matrix in the symmetrical case [see (2.20)]. We see that in this case, and for a given voltage at a point of the line, the two eigenvectors correspond to opposite currents. On the other hand, we know that in the case of uniform lines (which are degenerate periodic structures), two waves exhibiting the same voltage but opposed currents correspond to traveling waves propagating in opposite directions. Therefore, we can conclude that each solution found for the impedance actually corresponds to a particular direction of propagation. Nevertheless, we must now establish some criterion to deduce which solution should be selected in each particular propagation type, in relation with the set convention.

Energy propagation toward $+z$: First, let us again consider a semi-infinite line with a source located at its left terminal. By doing so, we consider a pure propagating wave with energy propagating toward $+z$, as shown in Figure 2.6. The convention for the sign of the current and the voltage is also depicted in the figure. Except for the aforementioned *negative group velocity* propagation, the group velocity and Poynting vector are directed toward $+z$, *for both forward and backward bands*, as a result of the conservation of energy and causality. We can write the active

power transmitted at any point in the line, which is necessarily positive:

$$P_{act} = Re\left[U\left(z\right)I^{*}\left(z\right)\right] > 0 \tag{2.30}$$

For this wave propagating to the right, we link voltage and current by the impedance Z^{+}_{equ}:

$$U\left(z\right) = Z^{+}_{equ}I\left(z\right) \tag{2.31}$$

and we develop:

$$P_{act} = Re\left[U\left(z\right)I^{*}\left(z\right)\right] = Re\left[Z^{+}_{equ}I\left(z\right)I^{*}\left(z\right)\right] = \left|I\left(z\right)\right|^{2} Re\left[Z^{+}_{equ}\right] > 0 \tag{2.32}$$

which shows that the real part of the characteristic impedance Z^{+}_{equ} must be positive.

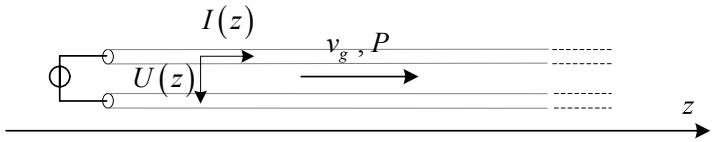

Figure 2.6: Sign definition of current and group velocity for a wave propagating toward $+z$.

Energy propagation toward $-z$: If we now locate the source at the right end of the line and keep the same conventions for the axis z and for $U\left(z\right)$ and $I\left(z\right)$, we obtain the situation depicted in Figure 2.7. As the convention for $U\left(z\right)$ and $I\left(z\right)$ is the same, and that the energy is propagating in the other direction, we obviously have a change of sign in the expression of the transmitted active power, which is now negative:

$$P_{act} = Re\left[U\left(z\right)I^{*}\left(z\right)\right] < 0 \tag{2.33}$$

The impedance definition is still the same, since the convention for $U\left(z\right)$ and $I\left(z\right)$ is the same:

$$U\left(z\right) = Z^{-}_{equ}I\left(z\right) \tag{2.34}$$

So, if we develop the expression of transmitted active power:

$$P_{act} = \left|I\left(z\right)\right|^{2} Re\left[Z^{-}_{equ}\right] < 0 \tag{2.35}$$

We see that the real part of the characteristic impedance Z_{equ} must now be negative.

The convention we chose concerning the propagation constant was to keep the same direction for the group velocity ($v_g > 0$) whether in *forward* or *backward* bands. This corresponds to the first case studied for the impedance (Energy propagation toward +z), and the solution for Z_{equ} must consequently be chosen so that *its real part is always positive*. Once again, only the case of negative group velocity is an exception to this rule (see Section 2.8). Let us also note that, with the rejected convention that β is always positive, the sign of the real part of Z_{equ} must be positive for a *normal* propagation, but negative in *backward* bands. If now Z_{equ} is purely imaginary, no active energy is transferred and the above criteria can obviously not be used. In this case, a more complicated 'sign tracking' strategy is possible, based on the condition that the imaginary part of the refractive index is positive [15].

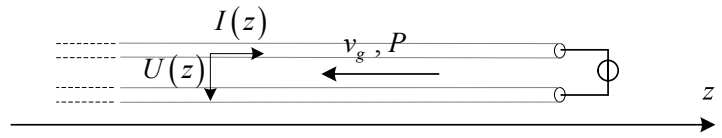

Figure 2.7: Sign definition of current and group velocity for a wave propagating toward $-z$.

2.4. Finite periodic structure

2.4.1. Transmission matrix

a. General case

This section examines the properties of finite periodic structures, which in practice must be connected to given loads at its terminals. First, let us write the transmission matrix for the N identical cascaded cells:

$$T_{cell}^{N} = \begin{bmatrix} A_{cell} & B_{cell} \\ C_{cell} & D_{cell} \end{bmatrix}^{N} \tag{2.36}$$

We make us of the decomposition of a matrix by means of its eigenvalues and eigenvectors:

$$T_{cell} = \begin{bmatrix} A_{cell} & B_{cell} \\ C_{cell} & D_{cell} \end{bmatrix} = \begin{bmatrix} v_1^+ & v_1^- \\ v_2^+ & v_2^- \end{bmatrix} \begin{bmatrix} \kappa^+ & 0 \\ 0 & \kappa^- \end{bmatrix} \begin{bmatrix} v_1^+ & v_1^- \\ v_2^+ & v_2^- \end{bmatrix}^{-1} \tag{2.37}$$

where the the eigenvalues $\kappa^{\pm}$ and eigenvectors $v^{\pm}$ were found to be:

$$\kappa^{\pm} = \exp\left(\pm\gamma_{equ} d\right) \tag{2.38}$$

$$\begin{bmatrix} v_1^{\pm} \\ v_2^{\pm} \end{bmatrix} = \begin{bmatrix} Z_{equ}^{\pm} \\ 1 \end{bmatrix} \tag{2.39}$$

with this decomposition, the N^{th} power of the matrix T_{cell} can be written as:

$$\begin{aligned} T_{cell}^{N} = &\begin{bmatrix} v_1^+ & v_1^- \\ v_2^+ & v_2^- \end{bmatrix} \begin{bmatrix} \kappa^+ & 0 \\ 0 & \kappa^- \end{bmatrix} \begin{bmatrix} v_1^+ & v_1^- \\ v_2^+ & v_2^- \end{bmatrix}^{-1} \begin{bmatrix} v_1^+ & v_1^- \\ v_2^+ & v_2^- \end{bmatrix} \begin{bmatrix} \kappa^+ & 0 \\ 0 & \kappa^- \end{bmatrix} \begin{bmatrix} v_1^+ & v_1^- \\ v_2^+ & v_2^- \end{bmatrix}^{-1} \ldots \\ &= \begin{bmatrix} v_1^+ & v_1^- \\ v_2^+ & v_2^- \end{bmatrix} \begin{bmatrix} \kappa^+ & 0 \\ 0 & \kappa^- \end{bmatrix}^{N} \begin{bmatrix} v_1^+ & v_1^- \\ v_2^+ & v_2^- \end{bmatrix}^{-1} \end{aligned} \tag{2.40}$$

Substituting the eigenvalues and eigenvectors in the general asymmetrical case ($Z_{equ}^{+} \neq -Z_{equ}^{-}$) leads to:

$$T_{cell}^{N} = \frac{1}{Z_{equ}^{+} - Z_{equ}^{-}} \begin{bmatrix} Z_{equ}^{+} & Z_{equ}^{-} \\ 1 & 1 \end{bmatrix} \begin{bmatrix} \exp\left(+\gamma_{equ} d\right)^{N} & 0 \\ 0 & \exp\left(-\gamma_{equ} d\right)^{N} \end{bmatrix} \begin{bmatrix} 1 & -Z_{equ}^{-} \\ -1 & Z_{equ}^{+} \end{bmatrix} \tag{2.41}$$

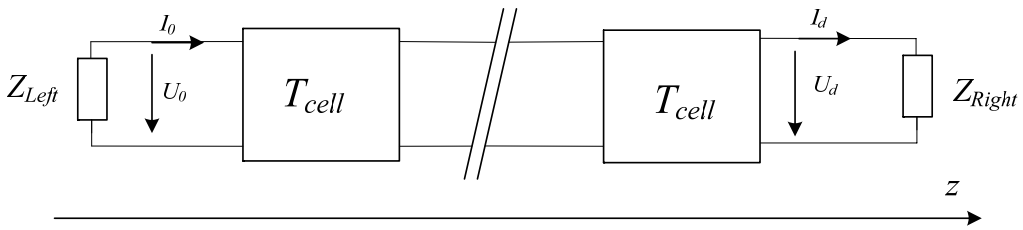

Figure 2.8: Representation of a finite and terminated periodic structure.

after some calculations, we obtain:

$$T_{cell}^{N} = \frac{1}{Z_{equ}^{+} - Z_{equ}^{-}} \begin{bmatrix} Z_{equ}^{+} \exp\left(N\gamma_{equ}d\right) - Z_{equ}^{-} \exp\left(-N\gamma_{equ}d\right) & \\ 2\sinh\left(N\gamma_{equ}d\right) & \\ -2Z_{equ}^{+}Z_{equ}^{-} \sinh\left(N\gamma_{equ}d\right) & \\ -Z_{equ}^{-} \exp\left(N\gamma_{equ}d\right) + Z_{equ}^{+} \exp\left(-N\gamma_{equ}d\right) & \end{bmatrix} \tag{2.42}$$

b. Symmetrical cell

In the symmetrical case, we saw that the two eigenvectors have opposed U-components, which also means that $Z_{equ}^{+} = -Z_{equ}^{-} \equiv Z_{equ}$. Consequently (2.41) and (2.42) become:

$$T_{cell}^{N} = \frac{1}{2Z_{equ}} \begin{bmatrix} Z_{equ} & -Z_{equ} \\ 1 & 1 \end{bmatrix} \begin{bmatrix} \exp\left(+\gamma_{equ}d\right)^{N} & 0 \\ 0 & \exp\left(-\gamma_{equ}d\right)^{N} \end{bmatrix} \begin{bmatrix} 1 & Z_{equ} \\ -1 & Z_{equ} \end{bmatrix} \tag{2.43}$$

$$T_{cell}^{N} = \begin{bmatrix} \cosh\left(N\gamma_{equ}d\right) & Z_{equ}\sinh\left(N\gamma_{equ}d\right) \\ \frac{1}{Z_{equ}}\sinh\left(N\gamma_{equ}d\right) & \cosh\left(N\gamma_{equ}d\right) \end{bmatrix} \tag{2.44}$$

We observe that this transmission matrix is exactly equivalent to the transmission matrix of a uniform line of length Nd, with characteristics γ_{equ} and Z_{equ}. This result is very important and will be further commented below.

2.4.2. Reflection coefficient

a. General case

A finite periodic structure is, by definition, terminated by given impedances. The situation is depicted in Figure 2.8, together with the definition of voltages and currents for the following developments. The reflection coefficient at the left termination of the line ($z = 0$) is defined as the ratio of reflected and incident currents, when a wave propagating in the $-z$ direction reaches the impedance Z_{Left}. The reflection coefficient can also be defined as the ratio of the *voltages*, and it is straightforward to show that the only difference resulting from this choice is the sign of

the reflection coefficient. Using the 'current' definition, we write, with the superscript '+' and '-' respectively referring to waves propagating towards the $+z$ and $-z$ directions:

$$\rho_{I,Left} = -\rho_{U,Left} = \frac{I_0^+}{I_0^-} \tag{2.45}$$

We must now write incident and reflected currents at Z_{Left} in terms of the total voltages and currents:

$$\begin{cases} I_0 = I_0^+ + I_0^- \\ U_0 = U_0^+ + U_0^- = Z_{equ}^+ I_0^+ + Z_{equ}^- I_0^- \end{cases} \tag{2.46}$$

In accordance with the developments carried out previously, the reflected voltage U^+ (resp. U^-) is linked to the current I^+ (resp. I^-) by the impedance of a wave propagating in the $+z$ direction (resp. $-z$). The corresponding impedances Z_{equ}^+ and Z_{equ}^- are the equivalent characteristic impedances of the line, and must not be mistaken with the termination impedances. We now transform the last expressions into:

$$\begin{cases} I_0^+ = \frac{U_0 - Z_{equ}^- I_0}{Z_{equ}^+ - Z_{equ}^-} \\ I_0^- = \frac{-U_0 + Z_{equ}^+ I_0}{Z_{equ}^+ - Z_{equ}^-} \end{cases} \tag{2.47}$$

and observe in Figure 2.8 that $U_0/I_0 = -Z_{Left}$. Substitutions in (2.45) then yield:

$$\rho_{I,Left} = -\rho_{U,Left} = -\frac{Z_{Left} + Z_{equ}^-}{Z_{Left} + Z_{equ}^+} \tag{2.48}$$

Similarly, we find at the right hand termination (incident and reflected wave are now respectively traveling in the $+z$ and $-z$ directions, respectively):

$$\rho_{I,Right} = -\rho_{U,Right} = \frac{I_d^-}{I_d^+} = -\frac{Z_{Right} - Z_{equ}^+}{Z_{Right} - Z_{equ}^-} \tag{2.49}$$

b. Symmetrical cell

We proved previously that in the case of symmetrical cells, the equivalent characteristic impedances satisfy:

$$-Z_{equ}^- = Z_{equ}^+ \equiv Z_{equ} \tag{2.50}$$

Substitutions in the expression for $\rho_{I,Right}$ and $\rho_{I,Left}$ lead to:

$$\rho_{I,Left} = -\rho_{U,Left} = \frac{Z_{equ} - Z_{Left}}{Z_{equ} + Z_{Left}} \tag{2.51}$$

$$\rho_{I,Right} = -\rho_{U,Right} = \frac{Z_{equ} - Z_{Right}}{Z_{equ} + Z_{Right}} \tag{2.52}$$

As expected, the reflection coefficients are now identical. We also found the well-known expression for the reflection coefficient in a uniform line.

c. Calculation example

Here, we will calculate the input impedance of a structure consisting of a single symmetrical cell ($N = 1$) connected to a load Z_L. This is done by means of both the equivalent TL parameters and a direct calculation, thereby allowing us to draw interesting conclusions in the next section.

Direct calculation: a direct calculation with the transmission matrix immediately gives the input impedance according to (2.53).

$$Z_{IN} = \frac{A_{cell} Z_L + B_{cell}}{C_{cell} Z_L + D_{cell}} = \frac{Z_L + B_{cell}/A_{cell}}{\frac{A_{cell}^2 - 1}{A_{cell} B_{cell}} Z_L + 1} \tag{2.53}$$

Equivalent line calculation: The two-port network is now seen as a TL of length d with parameters γ_{equ} and Z_{equ}. The input impedance of the device is consequently [16] (this is the usual loaded TL input impedance formula, written in a convenient form for the following substitutions):

$$Z_{IN} = Z_{equ} \frac{Z_L \left(1 + \exp\left(-2\gamma_{equ} d\right)\right) + Z_{equ} \left(1 - \exp\left(-2\gamma_{equ} d\right)\right)}{Z_{equ} \left(1 + \exp\left(-2\gamma_{equ} d\right)\right) + Z_L \left(1 - \exp\left(-2\gamma_{equ} d\right)\right)} \tag{2.54}$$

From the eigenvalue solution for the equivalent propagation constant and impedance, and making use of the reciprocity and symmetry assumptions, we have:

$$\exp\left(-2\gamma_{equ} d\right) = \left(\exp\left(-\gamma_{equ} d\right)\right)^2 = \left(A_{cell} - \sqrt{A_{cell}^2 - 1}\right)^2 \tag{2.55}$$

$$Z_{equ} = \frac{B_{cell}}{\sqrt{A_{cell}^2 - 1}} \tag{2.56}$$

We substitute these expressions into (2.54) and obtain, after some calculation, exactly the same expression as the one found with the direct calculation, namely, (2.53). This shows that the representation of the cell by a TL of length d with γ_{equ} and Z_{equ} is equivalent to its initial transmission matrix definition.

2.5. Summary and conclusions

A periodic structure consisting of a cascade of identical two-port networks defined by their transmission matrix $T_{cell} = [A_{cell}\ B_{cell}\ ;\ C_{cell}\ D_{cell}]$ can be modeled as a TL of propagation constant and impedance γ_{equ} and Z_{equ} according to (2.5) and (2.19). We showed, in the symmetrical case, that the transmission matrix of the cascade of N two-ports is exactly the same as the one of a TL of length Nd, with characteristics γ_{equ} and Z_{equ}. The corresponding transmission matrix is given by (2.44) and the equivalence is illustrated in Figure 2.9. Consequently, the only difference that the structure exhibits, when compared to a uniform line, is that its characteristic parameters γ_{equ} and Z_{equ} might have highly dispersive behavior and that the voltages and currents are only defined at the connections of the periodic cells, whereas they are defined everywhere in the case of the uniform line.

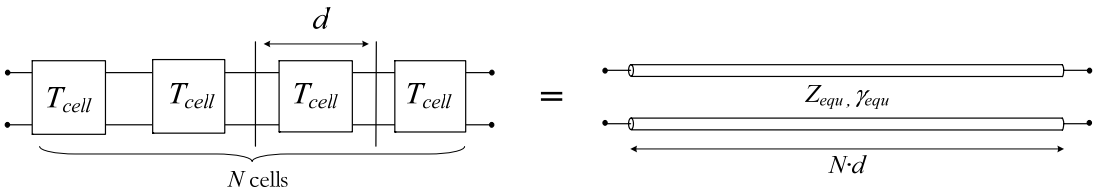

Figure 2.9: Illustration of the exact equivalence between the N cascaded cell two-port and its equivalent TL model using the Bloch periodic structure equivalents.

It should be emphasized here that the aforementioned equivalence is exact *regardless of the number of cells cascaded*, although this fact is sometimes misunderstood (e.g. [17]). Indeed, several examples of calculations were made to illustrate and confirm this result; we showed that the reflection at the termination of the periodic structure is similar to a uniform line. It was also observed that the equivalent impedance could be deduced for a single cell ('single cell method'), and that the impedance of a 'super-cell' composed of any number of such cascaded cells exhibit the same impedance. This is a straightforward way to show that the impedance does not depend on the number of cascaded cells. A more powerful demonstration example, taking γ_{equ} and Z_{equ} into account, was shown above: the calculation of the input impedance based on the equivalent line parameters provided an exact result for the input impedance, although the number of cells in the example is only $N = 1$.

In conclusion, *usual TL theory, and more specifically the analysis of boundary conditions (matching), can be correctly applied to symmetrical periodic structures which are described by their Bloch equivalent characteristic impedance and propagation constant.* In the case of asymmetrical cells, some modifications must be made to basic formulas, because the characteristic impedance has a different magnitude for two waves propagating in opposite directions. The corresponding expressions for the propagation and reflection have been derived.

2.6. Particular case: TL with loading element

2.6.1. Introduction

In this section, we study some particular case of interest for the design of micromachined or MEMS structures; namely, an 'obstacle' periodically loading a TL, as depicted in Figure 2.10(b). Under the assumption that this loading element is symmetrical, it is then modeled by a T-network [Figure 2.10(c)] and corresponding periodic structure Bloch wave equivalents are provided for use in the design and analysis of such structures.

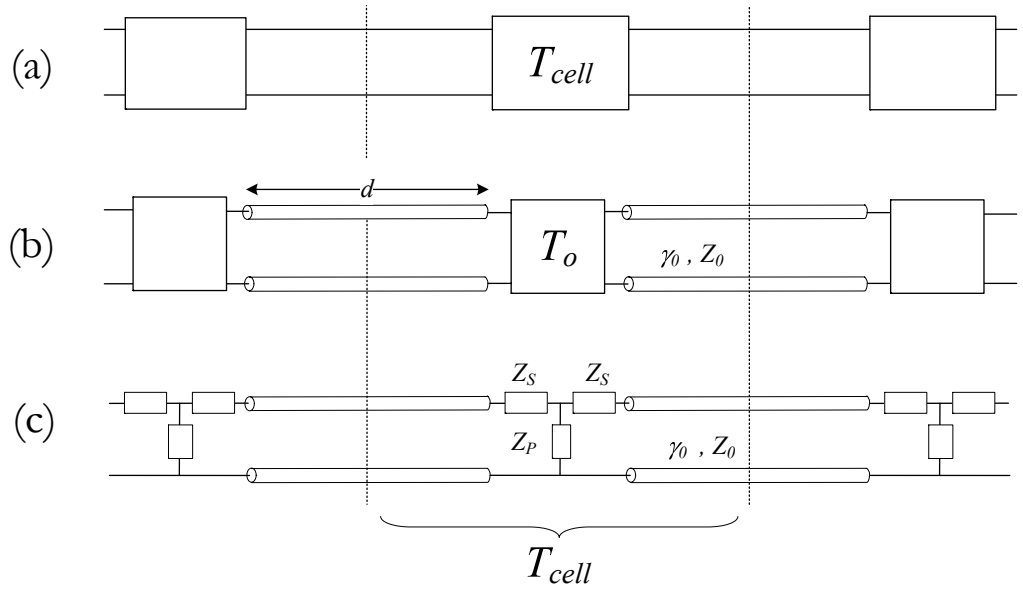

Figure 2.10: Particular case of a symmetrical 'obstacle' periodically loading a TL.

2.6.2. Calculations

a. Cell transmission matrix

With the loading element represented by its transmission matrix $T_o = [A_o\ B_o\ ;\ C_o\ D_o]$, the transmission matrix of the cell is simply:

$$T_{cell} = \begin{bmatrix} A_{cell} & B_{cell} \\ C_{cell} & D_{cell} \end{bmatrix} = \begin{bmatrix} X & V \\ U & X \end{bmatrix} \begin{bmatrix} A_o & B_o \\ C_o & D_o \end{bmatrix} \begin{bmatrix} X & V \\ U & X \end{bmatrix} \tag{2.57}$$

$$T_{cell} = \begin{bmatrix} A_{cell} & B_{cell} \\ C_{cell} & D_{cell} \end{bmatrix} = \begin{bmatrix} A_oX^2 + B_oXU + C_oXV + D_oVU & A_oXV + B_oX^2 + C_oV^2 + D_oXV \\ A_oXU + B_oU^2 + C_oX^2 + D_oXU & A_oVU + B_oXU + C_oXV + D_oX^2 \end{bmatrix} \tag{2.58}$$

with the transmission matrix of a TL section being:

$$T_L = \begin{bmatrix} X & V \\ U & X \end{bmatrix} = \begin{bmatrix} \cosh\psi & Z_0 \sinh\psi \\ Y_0 \sinh\psi & \cosh\psi \end{bmatrix} \tag{2.59}$$

with $\psi = \gamma_0 \cdot d/2$, where γ_0 is the unloaded TL propagation constant and Z_0 the complex unloaded TL characteristic impedance.

b. Propagation constant γ_{equ}

General case

By substitution into the general expression for the propagation constant (2.5), we have:

$$\cosh(\gamma_{equ} d) = \frac{1}{2}\left(A_0\left(X^2 + UV\right) + 2B_0XU + 2C_0XV + D_0\left(X^2 + UV\right)\right) \tag{2.60}$$

Symmetrical loading element

In most practical cases, the loading element is symmetrical and we are interested in finding reduced solutions. We decide here to represent the symmetrical loading element by a T-model, as shown in Figure 2.10(c), so that:

$$T_o = \begin{bmatrix} A_o & B_o \\ C_o & D_o \end{bmatrix} = \begin{bmatrix} 1 + Z_S Y_P & 2Z_S + Z_S^2 Y_P \\ Y_P & 1 + Z_S Y_P \end{bmatrix} \tag{2.61}$$

By substitution of (2.59) and (2.61) into the general solution (2.60), and making use of several hyperbolic trigonometrical formulas, we find the general solution (2.62) for the circuit of Figure 2.10(c).

$$\cosh(\gamma_{equ} d) = (1 + Z_S Y_P)\cosh(\gamma_0 d) + \frac{1}{2}\left[(2 + Z_S Y_P)(Z_S/Z_0) + Z_0/Z_P\right]\sinh(\gamma_0 d) \tag{2.62}$$

Shunt loading element

If the loading element is purely shunt so that $Z_S = 0$, the last expression can be simplified and validated by the result provided in [16].

$$\cosh(\gamma_{equ} d) = \cosh(\gamma_0 d) + \frac{1}{2}\left[Z_0/Z_P\right]\sinh(\gamma_0 d) \tag{2.63}$$

c. Characteristic impedance Z_{equ}

General case

The general expression for the characteristic impedance of the loaded line is obtained by substituting (2.58) into (2.19). The resulting expressions for the impedance are easily obtained but very long. They are thus not presented here, and the substitutions can be directly implemented in any software. Nevertheless, we present some developed expressions for the model of Figure 2.10(c).

Symmetrical loading element

Making use of the simplified impedance formula (2.26) for symmetrical loading elements, we obtain, after some calculation using the hyperbolic functions properties:

$$Z_{equ} = \pm\sqrt{\frac{2Z_0 A\sinh(\gamma_0 d) + \left(B + Z_0^2/Z_P\right)\cosh(\gamma_0 d) + \left(B - Z_0^2/Z_P\right)}{(2/Z_0)\,A\sinh(\gamma_0 d) + \left(1/Z_P + B/Z_0^2\right)\cosh(\gamma_0 d) + \left(1/Z_P - B/Z_0^2\right)}} \tag{2.64}$$

with $A = 1 + Z_S/Z_P$ and $B = 2Z_S + Z_S^2/Z_P$

Shunt loading element

The impedance for a line loaded with a purely shunt loading element is obtained by introducing $Z_S = 0$ in the last expression:

$$Z_{equ} = \pm Z_0 \sqrt{\frac{2\sinh(\gamma_0 d) + Z_0/Z_P\,(\cosh(\gamma_0 d) - 1)}{2\sinh(\gamma_0 d) + Z_0/Z_P\,(\cosh(\gamma_0 d) + 1)}} \tag{2.65}$$

d. Case study: Low-frequency reduced expressions in the case of purely shunt load elements

Here, we show that working with the general expressions developed above, we can also deduce intuitive expressions corresponding to the case of short TL sections cells (low-frequency limit) loaded with purely shunt elements.

Propagation constant γ_{equ}

Let us start with the general expression for (2.63) found for a purely shunt element loading a TL:

$$\cosh(\gamma_{equ} d) = \cosh(\gamma_0 d) + \frac{1}{2}\,[Z_0/Z_P]\sinh(\gamma_0 d) \tag{2.66}$$

We introduce the simplified notation:

$$A = \frac{Z_0}{2Z_P} \quad , \quad y = \gamma_{equ} d \quad \text{and} \quad x = \gamma_0 d \tag{2.67}$$

Doing then the Taylor expansions (associated assumptions are commented below) $\sinh(t) \cong t + t^3/6$ and $\cosh(t) \cong 1 + t^2/2$ in (2.63), and neglecting 3^{rd} order terms, we find:

$$y = \sqrt{2Ax + x^2} \tag{2.68}$$

We write now the line parameters Z_0 and γ_0 in terms of the distributed parameters of a uniform TL R'_L, L'_L, G'_L, and C'_L, so that:

$$x = \gamma_0 d = d\sqrt{\left(R'_L + j\omega L'_L\right)\left(G'_L + j\omega C'_L\right)} \tag{2.69}$$

$$A = \frac{Z_0}{2Z_P} = \frac{1}{2Z_P}\sqrt{\frac{\left(R'_L + j\omega L'_L\right)}{\left(G'_L + j\omega C'_L\right)}} \tag{2.70}$$

after some calculations, we find the following approximation of the equivalent propagation constant:

$$\gamma_{equ} = \pm\sqrt{\left(R'_L + j\omega L'_L\right)\left(G'_L + j\omega C'_L + \frac{1}{Z_P d}\right)} = \pm\sqrt{Z'Y'} \tag{2.71}$$

In order to obtain this result, we made use of the conditions $|\gamma_0 d| \ll 1$ and $|\gamma_{equ} d| \ll 1$ for the above Taylor expansions to be valid. The first condition obviously means that the TL sections in

the unit cell of the structure are electrically short. If this condition is verified, the second condition is equivalent to requiring that the following simpler condition is *not* true:

$$\frac{1}{Z_P d} \gg G'_L + j\omega C'_L \tag{2.72}$$

Result (2.71) is very intuitive; indeed, if the wavelength is large enough compared to the distance d between loading elements, we can distribute the admittance of this shunt loading element over the line. This distributed admittance $1/(Z_P d)$ is then added to the admittance of the line and we get the effective admittance Y'. As will be explained in more detail in Chapter 4, the simple but approximate Formula (2.71) was intuitively proposed in [18] for the design of distributed microwave structures.

Characteristic impedance Z_{equ}

We now want to find a low frequency simplified expression for (2.65). Using the same simplified notation and Taylor developments as for the propagation constant γ_{equ}, we find:

$$Z_{equ} = \pm Z_0 \sqrt{\frac{x}{x+2A}} \tag{2.73}$$

We write now the line parameters Z_0 and γ_0 in terms of the distributed parameters of a uniform TL R'_L, L'_L, G'_L, and C'_L, and obtain:

$$Z_{equ} = \pm \sqrt{\frac{\left(R'_L + j\omega L'_L\right)}{1/(Z_P d) + \left(G'_L + j\omega C'_L\right)}} = \pm \sqrt{\frac{Z'}{Y'}} \tag{2.74}$$

Again, the result is directly interpreted by seeing the equivalent loaded line admittance Y' as a superposition of loading element and unloaded line admittance. The assumptions for the validity of this expression are the same as for γ_{equ}.

2.7. Multimode periodic structure theory

2.7.1. Introduction

In this section, we extend the periodic structure modeling as previously presented in the monomode case, to a multimodal one. This is obviously necessary to treat periodic structures whose ports TLs support more than one propagating mode. However, we will show that the most interesting feature of the approach is that it allows taking into account higher order *evanescent* modes at the port TL while keeping a *monomode* periodic structure equivalent model. The approach is validated by simulations on a packaged coplanar waveguide (CPW) and applied to the modeling of a DMTL in such a package.

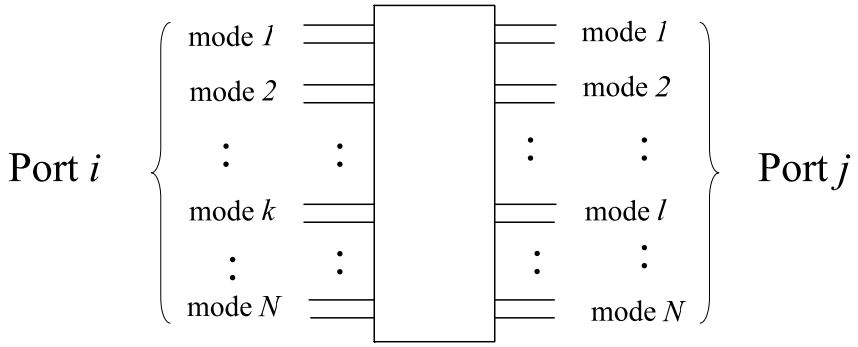

Figure 2.11: Multimode two-port network.

2.7.2. Multimode two-port networks matrices

a. Generalities and notation

For all following considerations, we assume the same number N of *TL modes*[1] at each port. This, of course, is not a limitation since the formulation is also valid in the case where some modes are not considered at one of the ports: in this case some of the terms in the matrix corresponding to those modes will be null. Such a N-mode two-port is depicted in Figure 2.11.

b. Multimode Scattering S matrix

The following notation is used here for the input waves, output waves, and scattering matrix elements:

$$a_{\text{port}}^{(\text{mode})} \quad , \quad b_{\text{port}}^{(\text{mode})} \quad \text{and} \quad s_{\text{port\_out,port\_in}}^{(\text{mode\_out,mode\_in})} \tag{2.75}$$

The multimode scattering matrix can be written by gathering the different modes for each port as follows:

$$\begin{bmatrix} b_1^{(1)} \\ b_1^{(2)} \\ \vdots \\ b_1^{(N)} \\ b_2^{(1)} \\ b_2^{(2)} \\ \vdots \\ b_2^{(N)} \end{bmatrix} = \begin{bmatrix} s_{11}^{(11)} & s_{11}^{(12)} & \cdots & s_{11}^{(1N)} & s_{12}^{(11)} & s_{12}^{(12)} & \cdots & s_{12}^{(1N)} \\ s_{11}^{(21)} & s_{11}^{(22)} & & \vdots & s_{12}^{(21)} & s_{12}^{(22)} & & \vdots \\ \vdots & & \ddots & \vdots & \vdots & & \ddots & \vdots \\ s_{11}^{(N1)} & \cdots & \cdots & s_{11}^{(NN)} & s_{12}^{(N1)} & \cdots & \cdots & s_{12}^{(NN)} \\ s_{21}^{(11)} & s_{21}^{(12)} & \cdots & s_{21}^{(1N)} & s_{22}^{(11)} & s_{22}^{(12)} & \cdots & s_{22}^{(1N)} \\ s_{21}^{(21)} & s_{21}^{(22)} & & \vdots & s_{22}^{(21)} & s_{22}^{(22)} & & \vdots \\ \vdots & & \ddots & \vdots & & & \ddots & \vdots \\ s_{21}^{(N1)} & \cdots & \cdots & s_{21}^{(NN)} & s_{22}^{(N1)} & \cdots & \cdots & s_{22}^{(NN)} \end{bmatrix} \begin{bmatrix} a_1^{(1)} \\ a_1^{(2)} \\ \vdots \\ a_1^{(N)} \\ a_2^{(1)} \\ a_2^{(2)} \\ \vdots \\ a_2^{(N)} \end{bmatrix} \tag{2.76}$$

[1] Throughout this chapter, we will always refer to the modes supported by the waveguide at the ports as the *TL modes*, which can equivalently be propagating or evanescent. This is to avoid any confusion with the Floquet's modes to be defined later.

This notation corresponds to the definition of an element of the scattering matrix as follows:

$$s_{ij}^{(kl)} = \frac{b_i^{(k)}}{a_j^{(l)}} \quad \text{with} \quad \begin{cases} a_{p=j}^{(q\neq j)} = 0 \quad \text{(other modes)} \\ a_{p\neq j}^{(q)} = 0 \quad \text{(other ports)} \end{cases} \tag{2.77}$$

The detailed scattering matrix expression (2.76) can be written in a compact way as follows:

$$\begin{bmatrix} \bar{b}_1 \\ \bar{b}_2 \end{bmatrix} = \begin{bmatrix} \tilde{S}_{11} & \tilde{S}_{12} \\ \tilde{S}_{21} & \tilde{S}_{22} \end{bmatrix} \begin{bmatrix} \bar{a}_1 \\ \bar{a}_2 \end{bmatrix} \tag{2.78}$$

where:

- $\bar{a}_i$ is a vector, whose k-th component is the k-th mode incident wave at the i-th port.
- $\bar{b}_i$ is a vector, whose k-th component is the k-th mode reflected or transmitted wave at the i-th port.
- $\tilde{S}_{ij}$ is a sub-matrix, coupling the waves at port j and at port i, for all modes combinations.

c. Multimode impedance Z matrix

Here we will use the same compact notation as in the case of the scattering matrix. We choose to define $\bar{I}_2$ as the vector of currents flowing out of port 2, while writing $-\bar{I}_2$ in the right hand side of (2.79). In this way, the impedance matrix actually links currents flowing inward the two-port, which is the usual convention used for Z matrices (see Figure 2.12). This notation will be useful when transforming Z to ABCD matrices.

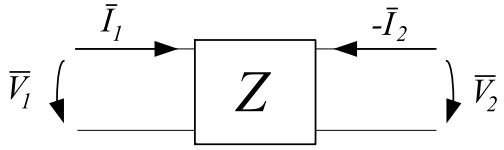

Figure 2.12: Definition of currents and voltages signs for the multimode impedance matrix.

$$\begin{bmatrix} \bar{V}_1 \\ \bar{V}_2 \end{bmatrix} = \begin{bmatrix} \tilde{Z}_{11} & \tilde{Z}_{12} \\ \tilde{Z}_{21} & \tilde{Z}_{22} \end{bmatrix} \begin{bmatrix} \bar{I}_1 \\ -\bar{I}_2 \end{bmatrix} \tag{2.79}$$

where:

- $\bar{V}_i$ is a vector, whose k-th component is the k-th mode voltage at the i-th port.
- $\bar{I}_i$ is a vector, whose k-th component is the k-th mode current at the i-th port.
- $\tilde{Z}_{ij}$ is a sub-matrix, coupling the currents at port j and voltages at port i, for all modes combinations.

d. Multimode transmission ABCD matrix

The transmission matrix concerned here is the transmission (ABCD) matrix defined in the voltage-current domain as follows[1]:

$$\begin{bmatrix} \bar{V}_1 \\ \bar{I}_1 \end{bmatrix} = \begin{bmatrix} \tilde{A} & \tilde{B} \\ \tilde{C} & \tilde{D} \end{bmatrix} \begin{bmatrix} \bar{V}_2 \\ \bar{I}_2 \end{bmatrix} \tag{2.80}$$

The definitions of $\bar{V}_i$ and $\bar{I}_i$ are the same as for the impedance matrix (2.79). Moreover, the current $\bar{I}_2$ is defined in the same direction as for the matrix Z, so the notation is consistent.

e. Matrices transformations

The method explained below to deduce the *multimode* periodic structure equivalents is based on the ABCD matrix, in a similar way as in the monomode case. As full-wave simulation tools usually provide results only in terms of scattering or impedance matrix, it is necessary to deduce how to transform multimode S or Z matrices into multimode ABCD matrices. In the next subsections, we recall the S-Z transformation formula (this transformation is available in textbooks). Concerning the Z-ABCD transformation, the required developments to deduce the transformation formula are provided, since such transformations were not found in the literature in the multimode case.

S – Z matrices transformation

The formula for this transformation is:

$$\begin{bmatrix} \tilde{Z}_{11} & \tilde{Z}_{12} \\ \tilde{Z}_{21} & \tilde{Z}_{22} \end{bmatrix} = \sqrt{Z_0} \left(\tilde{U} - \begin{bmatrix} \tilde{S}_{11} & \tilde{S}_{12} \\ \tilde{S}_{21} & \tilde{S}_{22} \end{bmatrix} \right)^{-1} \left(\tilde{U} + \begin{bmatrix} \tilde{S}_{11} & \tilde{S}_{12} \\ \tilde{S}_{21} & \tilde{S}_{22} \end{bmatrix} \right) \sqrt{Z_0} \tag{2.81}$$

where $\tilde{U}$ is the identity matrix and Z_0 is the diagonal matrix having the characteristic impedance of each port as diagonal values.

S – ABCD matrices transformation

First, Let us recall the definitions of the multimode matrices proposed above:

$$\begin{bmatrix} \bar{V}_1 \\ \bar{I}_1 \end{bmatrix} = \begin{bmatrix} \tilde{A} & \tilde{B} \\ \tilde{C} & \tilde{D} \end{bmatrix} \begin{bmatrix} \bar{V}_2 \\ \bar{I}_2 \end{bmatrix} \quad \text{and} \quad \begin{bmatrix} \bar{V}_1 \\ \bar{V}_2 \end{bmatrix} = \begin{bmatrix} \tilde{Z}_{11} & \tilde{Z}_{12} \\ \tilde{Z}_{21} & \tilde{Z}_{22} \end{bmatrix} \begin{bmatrix} \bar{I}_1 \\ -\bar{I}_2 \end{bmatrix} \tag{2.82}$$

We can now solve for the sub-matrices $\tilde{A}$, $\tilde{B}$, $\tilde{C}$ and $\tilde{D}$ as follows:

Subsystem 1: we place an open-circuit at Port 2 for all modes so that $\bar{I}_2 = 0$ and (2.82) becomes

$$\begin{cases} \bar{V}_1 = \tilde{A}\bar{V}_2 \\ \bar{I}_1 = \tilde{C}\bar{V}_2 \end{cases} \quad \text{and} \quad \begin{cases} \bar{V}_1 = \tilde{Z}_{11}\bar{I}_1 \\ \bar{V}_2 = \tilde{Z}_{21}\bar{I}_1 \end{cases} \tag{2.83}$$

[1] This matrix should not be mistaken by the matrix sometimes referred to as the *wave transmission* matrix [13], which links wave parameters ($\bar{a}_i$ and $\bar{b}_i$) in a different way than the scattering matrix.

By substitution in (2.83), we obtain:

$$\bar{I}_1 = \tilde{Z}_{11}^{-1}\tilde{A}\tilde{Z}_{21}\bar{I}_1 \tag{2.84}$$

Which means that, $\tilde{U}$ being the unit matrix:

$$\tilde{Z}_{11}^{-1}\tilde{A}\tilde{Z}_{21} = \tilde{U} \tag{2.85}$$

The transformation from (2.84) to (2.85) is obviously true only if $\bar{I}_1$ is not an eigenvector (with eigenvalue equal to 1) of the left hand of (2.85). However, the calculation must hold true for any excitation and the relative amplitudes of the excitation of the modes (i.e the different components of the vector $\bar{I}_1$) are therefore not fixed. Consequently, the only general solution is the one proposed above and we finally write $\tilde{A}$ as a function of the $\tilde{Z}$ sub-matrices as follows:

$$\tilde{A} = \tilde{Z}_{11}\tilde{Z}_{21}^{-1} \tag{2.86}$$

Also, by substitution using (2.77) and (2.79):

$$\tilde{C} = \tilde{Z}_{21}^{-1} \tag{2.87}$$

Subsystem 2: we place an short-circuit at Port 2 for all modes so that $\bar{V}_2 = 0$

$$\begin{cases} \bar{V}_1 = \tilde{B}\bar{I}_2 \\ \bar{I}_1 = \tilde{D}\bar{I}_2 \end{cases} \quad \text{and} \quad \begin{cases} \bar{V}_1 = \tilde{Z}_{11}\bar{I}_1 - \tilde{Z}_{12}\bar{I}_2 \\ 0 = \tilde{Z}_{21}\bar{I}_1 - \tilde{Z}_{22}\bar{I}_2 \end{cases} \tag{2.88}$$

This system can also be reduced by substitution and we obtain:

$$\tilde{B} = \tilde{Z}_{11}\tilde{Z}_{21}^{-1}\tilde{Z}_{22} - \tilde{Z}_{12} \tag{2.89}$$

and

$$\tilde{D} = \tilde{Z}_{21}^{-1}\tilde{Z}_{22} \tag{2.90}$$

Summary

The complete set of transformation formulas is thus:

$$\begin{cases} \tilde{A} = \tilde{Z}_{11}\tilde{Z}_{21}^{-1} \\ \tilde{B} = \tilde{Z}_{11}\tilde{Z}_{21}^{-1}\tilde{Z}_{22} - \tilde{Z}_{12} \\ \tilde{C} = \tilde{Z}_{21}^{-1} \\ \tilde{D} = \tilde{Z}_{21}^{-1}\tilde{Z}_{22} \end{cases} \tag{2.91}$$

A comparison with literature results is possible in the case where only one mode is considered [14]:

$$\begin{cases} A = Z_{11}/Z_{21} \\ B = (Z_{11}Z_{22} - Z_{12}Z_{21})/Z_{21} \\ C = 1/Z_{21} \\ D = Z_{22}/Z_{21} \end{cases} \tag{2.92}$$

2.7.3. Multimode periodic structure

Now that we have set the definition and transformation for multimode matrices, we can deduce the periodic structure equivalents in a multimode case. First, let us write the electric field at the ports of the structure as:

$$\begin{aligned} \vec{E}_1 &= \vec{E}\,(x, y, z = 0) \\ \vec{E}_2 &= \vec{E}\,(x, y, z = d) \end{aligned} \tag{2.93}$$

where $\vec{E}$ is the total field written in the most general way. The Floquet condition of periodicity on the total electric field in the structure is given by (2.94). Let us note that there is a different equation (2.94) for each Floquet's mode, namely a different γ_{equ}. These different γ_{equ} solutions will be found when solving the multimode eigenvalue problem.

$$\vec{E}_1 = \exp(\gamma_{equ} d)\, \vec{E}_2 \tag{2.94}$$

We decompose the total transverse field at the ports in terms of the N modes of the port TL (see Figure 2.11), which leads to (2.95), where $\vec{e}_i^{(k)}$ and $V_i^{(k)}$ are defined as in [19]. It is clear that the equivalence between (2.94) and (2.95) is only exact if an infinite number of these TL modes are considered.

$$\sum_{k=1}^{N} V_1^{(k)} \vec{e}_1^{(k)} = \exp(\gamma_{equ} d) \sum_{k=1}^{N} V_2^{(k)} \vec{e}_2^{(k)} \tag{2.95}$$

If the modes of the TL constitute an orthonormal base, namely $\vec{e}_i^{(k)} \cdot \vec{e}_i^{(l)} = \delta_{kl}$, the condition of periodicity applies to the amplitude of each mode individually :

$$V_1^{(k)} = \exp(\gamma_{equ} d)\, V_2^{(k)} \tag{2.96}$$

Since Floquet's theorem equivalently applies to the magnetic field, with the same γ_{equ} as for the electric field, we write:

$$\vec{H}_1 = \exp(\gamma_{equ} d)\, \vec{H}_2 \tag{2.97}$$

and, following the same procedure as for the electric field, we can write:

$$I_1^{(k)} = \exp(\gamma_{equ} d)\, I_2^{(k)} \tag{2.98}$$

The mode amplitudes in (2.96) and (2.98) correspond to the generalized $\bar{V}$ and $\bar{I}$ vectors in the multimode ABCD representation so we can combine the above condition with the definition of the ABCD matrix and obtain:

$$\begin{bmatrix} \tilde{A} & \tilde{B} \\ \tilde{C} & \tilde{D} \end{bmatrix} \begin{bmatrix} \bar{V}_2 \\ \bar{I}_2 \end{bmatrix} = \exp(\gamma_{equ} d) \begin{bmatrix} \bar{V}_2 \\ \bar{I}_2 \end{bmatrix} \tag{2.99}$$

a. Conclusion and discussion

Eigenvalue problem solutions

Equation (2.99) is the fundamental eigenvalue problem to be solved in order to obtain the Floquet modes —or Bloch waves— description for a given unit cell described by its multimode ABCD matrix. When considering N TL modes, this system leads to $2N$ eigenvalues and eigenvectors solutions, collected in a matrix form as (2.100) and (2.101), respectively:

$$\left[\begin{array}{cccc} \exp\left(\gamma_{equ,m=1}d\right) & \exp\left(\gamma_{equ,m=2}d\right) & ... & \exp\left(\gamma_{equ,m=2N}d\right) \end{array} \right] \tag{2.100}$$

$$\left[\begin{array}{cccc} \bar{V}_{equ,m=1} & \bar{V}_{equ,m=2} & ... & \bar{V}_{equ,m=2N} \\ \bar{I}_{equ,m=1} & \bar{I}_{equ,m=2} & ... & \bar{I}_{equ,m=2N} \end{array} \right] \tag{2.101}$$

with:

$$\bar{V}_{equ,m} = \left[\begin{array}{c} V_{equ,1,m} \\ ... \\ V_{equ,N,m} \end{array} \right] \quad \text{and} \quad \bar{I}_{equ,m} = \left[\begin{array}{c} I_{equ,1,m} \\ ... \\ I_{equ,N,m} \end{array} \right] \tag{2.102}$$

We can note that in the case where the 2-port is reciprocal, there will only be N independent eigenvalues (the other N solutions corresponding to solutions with opposite sign of the Bloch wave propagation constant $\gamma_{equ,n}$). However, two eigenvalues with opposite signs do correspond to different eigenvectors and there are indeed $2N$ solutions to be considered. If the 2-port is now not only reciprocal but also symmetric, the eigenvectors corresponding to opposite eigenvalues will only differ by their sign, as was already observed in the monomode case.

TL modes and Floquet's modes

First, for a clear understanding and interpretation of the results, it is important to differentiate:

TL modes: modes (propagating or evanescent) of the TL that constitutes the port.

Floquet's modes: modes (propagating or evanescent) supported by the periodic structure. These are not to be mistaken with Floquet's *harmonics*, which will be introduced in Chapter 8.

We observe that the number of Floquet's modes —or Bloch waves— found here is linked to the number of TL modes considered. The reason for this is not physical —there is no direct link between both number of modes— but rather mathematical. Indeed, the above developments are only exact if an infinite number of TL modes are considered. If so, there is also an infinite number of Floquet's mode and, in both cases, this can be seen as expansions of the field on a complete basis. For a finite number of TL modes N, the mathematical development above allows finding the solutions of the $2N$ first Floquet's modes.

2.7.4. Results

a. Tests and method validations

The resolution of the eigenvalue problem (2.99) has been implemented in Matlab, so as to obtain the $2N$ eigenvalues and eigenvectors from the multimode matrix of Z parameters, obtained from a full-wave simulation. In order to test the method, a *uniform* waveguide, consisting of a CPW embedded in a metallic package (see Figure 2.13), was simulated. Indeed, in this case, the device simulated is a simple multimode TL section and the Floquet modes are theoretically exactly equivalent to the TL modes. Since the simulator employed (HFSS) also provides the propagation constant and impedance of each TL mode at the port, this allows a simple verification of the method.

Figure 2.14 shows the electric field of the 4 first waveguide modes found by the cross-solver of HFSS. The propagation constant of the 3 first modes is shown in solid lines in Figure 2.15 (since the cutoff frequency of the 4^{th} mode is well above the maximum frequency considered here, it has not been considered for the rest of these developments). As was already clear from the pattern of the field in Figure 2.14 the first mode is the usual quasi-transverse electromagnetic (TEM) CPW fundamental mode, whereas the second is a rectangular waveguide-like mode. The 3^{rd} mode has a less obvious pattern, but it can be seen from Figure 2.15 that it has a quite similar propagation constant as Mode 2.

Figure 2.15 also indicates the $2N$ eigenvalues found at each frequency point. Since we consider $N = 3$ TL modes here, we have 6 solutions for each frequency point. The structure is obviously reciprocal, so there are actually 3 pairs of propagation constants of opposite signs that are solutions. It is observed that these results match the 3 positive solutions found by the cross-solver of HFSS (shown in solid lines in Figure 2.15), hence validating the method. The different types of markers used in Figure 2.15 represent the eigenvalues position in the eigenvalue vector. It is observed that the eigenvalues location corresponding to two opposite solutions are randomly inverted in the vector. This is due to the fact that the eigenvalue matrix is found independently for each frequency point, based on the S or Z matrix at that frequency. In order to overcome that problem, further post-processing was implemented in Matlab to reorganize eigenvalues and eigenvectors in their matrix so that they are sorted according to Floquet's modes. The results after sorting are shown in Figure 2.16 (we now only show the three positive solutions).

The structure of the Floquet modes is given by the eigenvector matrix (2.101). More precisely, to each eigenvalue in the eigenvalue vector (2.100) corresponds an eigenvector in the same column in the eigenvector matrix (2.101). It is noticeable that this matrix was also reorganized in the same way as the eigenvalue matrix, so that each eigenvector location still corresponds to the right eigenvalue in their respective matrices. Since the structure simulated here is a *uniform* TL, the eigenvector matrix is degenerated so that only one pair of element in each vector is non-null, these elements being $V_{equ,n,m}$ and $I_{equ,n+N,m}$, following the notation of (2.101). The ratio $V_{equ,n,m}/I_{equ,n+N,m}$ must obviously correspond to the impedance of each of the modes of the TL, which is verified in Figure 2.17 and concludes the verification.

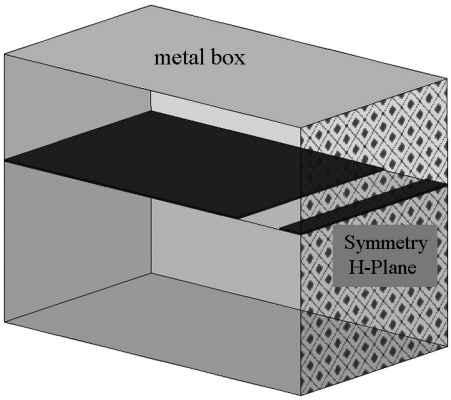

Figure 2.13: Half-geometry of the boxed CPW test structure.

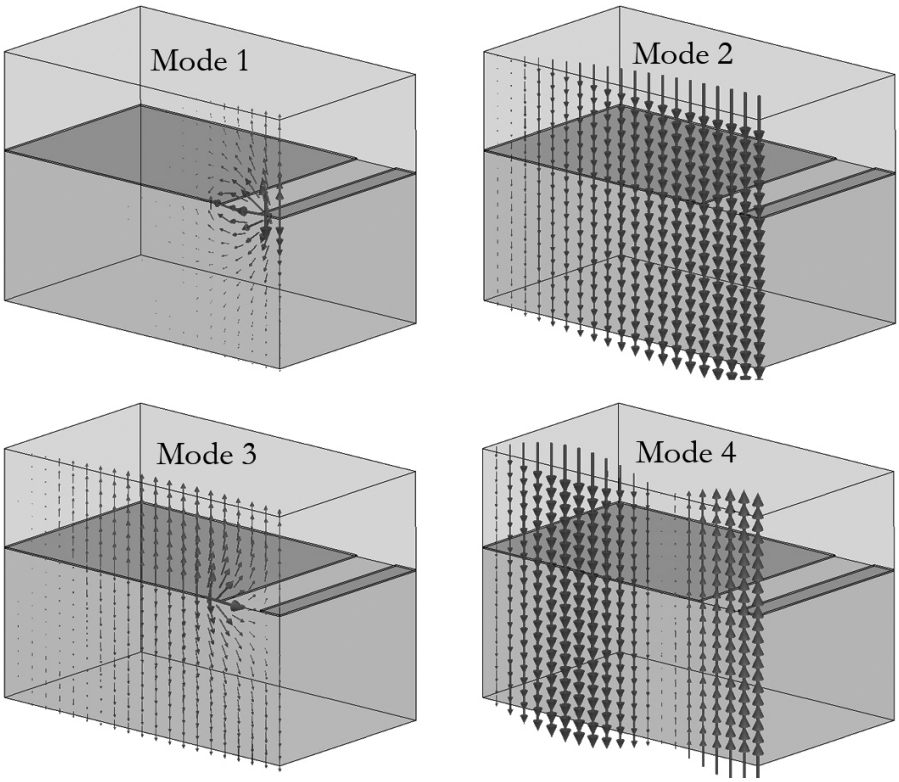

Figure 2.14: Electric field of the 4 first modes of the boxed CPW.

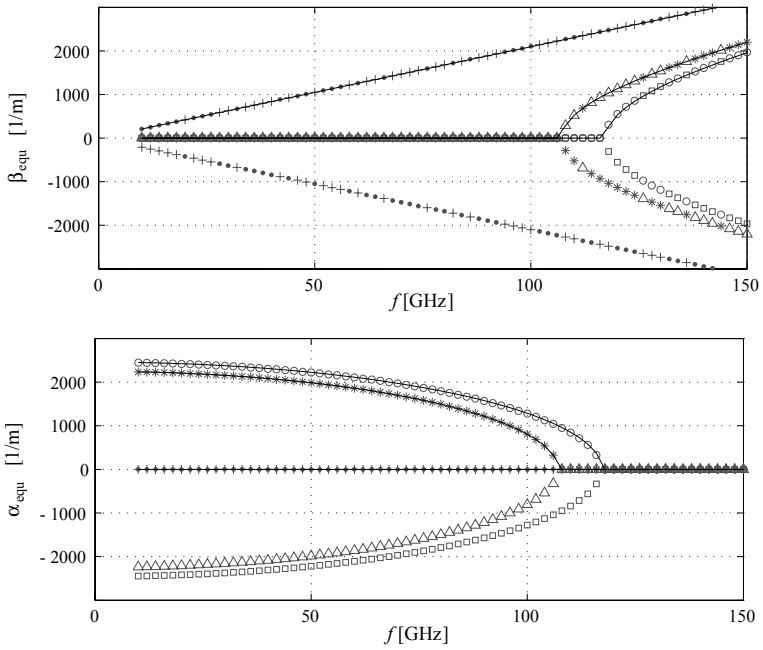

Figure 2.15: Mode structure of the boxed CPW. Solid lines: direct port solution, markers: reconstruction by the multimode eigenvalue problem.

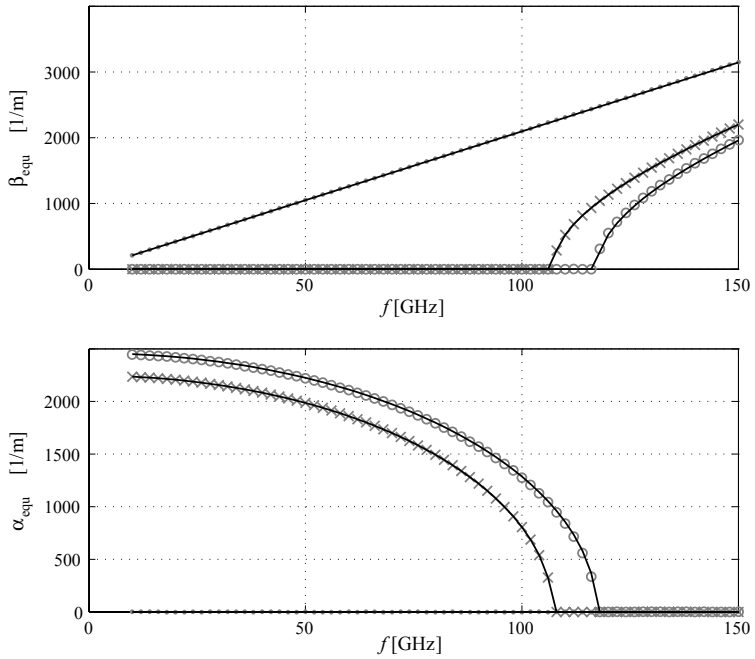

Figure 2.16: Same as Figure 2.15, after post-processing.

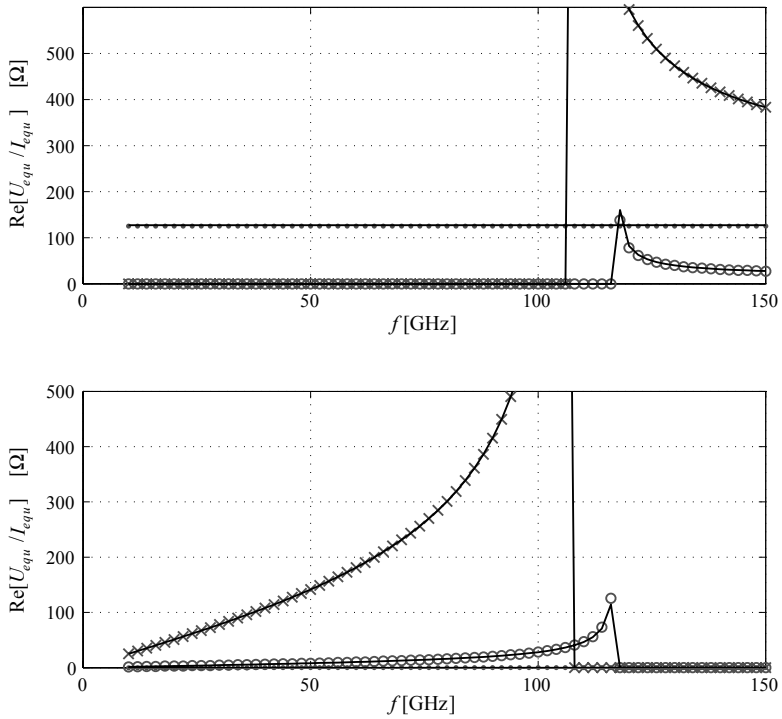

Figure 2.17: Modes impedances of the boxed CPW. Solid lines: direct port solution, markers: reconstruction by the multimode eigenvalue problem, after post-processing.

b. Test case

The method has been tested on a uniform TL, where the solution to be found were already known and this example thus merely consisted in a verification of the calculation procedure. We will now apply the method to a given non-uniform unit cell to derive some qualitative and quantitative observations. The test case structure used here consists of a 'bridge' loading a CPW, the CPW being exactly the boxed CPW previously employed (see Figure 2.18). It should be noted that this example is of real practical interest, for the following two main reasons. The first one is linked with the fact that, in real-life applications, MEMS always require a hermetic package for protection from external environment. Thus, the boxed CPW can simply represent a *packaged* CPW. Second, the bridge over CPW structure is the unit cell of the DMTL (see Chapter 4), which is a major application of microwave MEMS. In conclusion, the design of DMTL that are packaged could require the use of the multimode method presented here and is the reason why this structure was selected here for the following developments.

The mode structure of the TL was shown in Figure 2.16 and the band simulated can be separated into two main regions. The first region goes from DC to about 100 GHz; this is below the cutoff of the two superior modes. This is the region where a typical design will be made, since we prefer in general working with a TL that supports a single propagating mode only. In this case, the usual approach is to carry out simulations considering only the fundamental mode at the ports. However, the effect of the higher modes coupling between cells is obviously not exactly zero in the associated periodic structure, although they are evanescent. The importance of these effects depends on:

- The attenuation level of the evanescent modes.
- The obstacle loading the TL.
- The distance between successive elements.

This is symbolically illustrated in Figure 2.19, which depicts the amplitude of an evanescent wave propagating from an obstacle at $z = 0$ to the adjacent one at $z = d$. The obstacle loading the TL influences the amplitude of the excitation, A_0, whereas the attenuation is represented by ξ in the graph. The impact of this phenomenon will be tested here in the particular case of the structure of Figure 2.18.

The second region is above 100 GHz, where more than one propagating mode is supported by the TL. This is a classical multimode problem, where a monomode method will obviously not only lead to some possible imprecision, but wrong results. In this case the multimode approach must obviously be employed.

The results for the DMTL unit cell of Figure 2.18, with $d = 80$ μm and $d = 800$ μm, were computed considering first the CPW dominant mode only. The same process was then repeated considering the 3 first modes previously commented. The results for the propagation constant are plotted in Figure 2.20. In colors are presented all 3 positive solutions for the 3 modes case, while the monomode one is shown in black. The comparison between both methods is, for the reason explained above, only relevant below the cutoff frequency of the first higher order mode and the

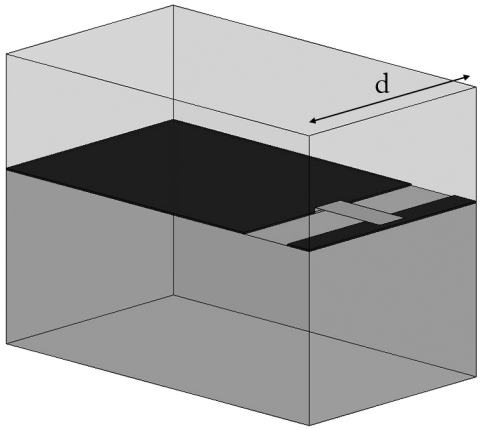

.

Figure 2.18: Simulated half geometry of the bridge loading a CPW (CPW dimensions 100 μm / 100 μm / 100 μm, bridge width $w = 40$ μm).

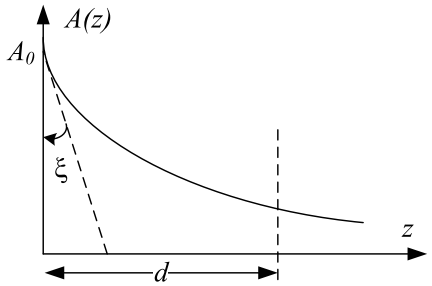

Figure 2.19: Illustration of the parameters influencing the coupling through higher order evanescent modes

results are thus plotted here up to 100 GHz. It is observed that only one of the 3 Floquet modes is non-evanescent for both $d = 80$ μm and $d = 800$ μm. This means that the TL higher order evanescent modes only 'create' evanescent Floquet's modes, which in general do not need be taken into account in a practical design since they will not couple to surrounding structures.

Second, we observe that this propagating Floquet mode is influenced by the inter-cell coupling through evanescent TL modes, since there is some difference between the results obtained with one and 3 TL modes. We observe that this difference is significant when $d = 80$ μm, whereas it is very small with $d = 800$ μm. This result is perfectly consistent since the longer distance between the obstacles loading the TL (here the 'bridges') makes the coupling through evanescent modes much smaller.

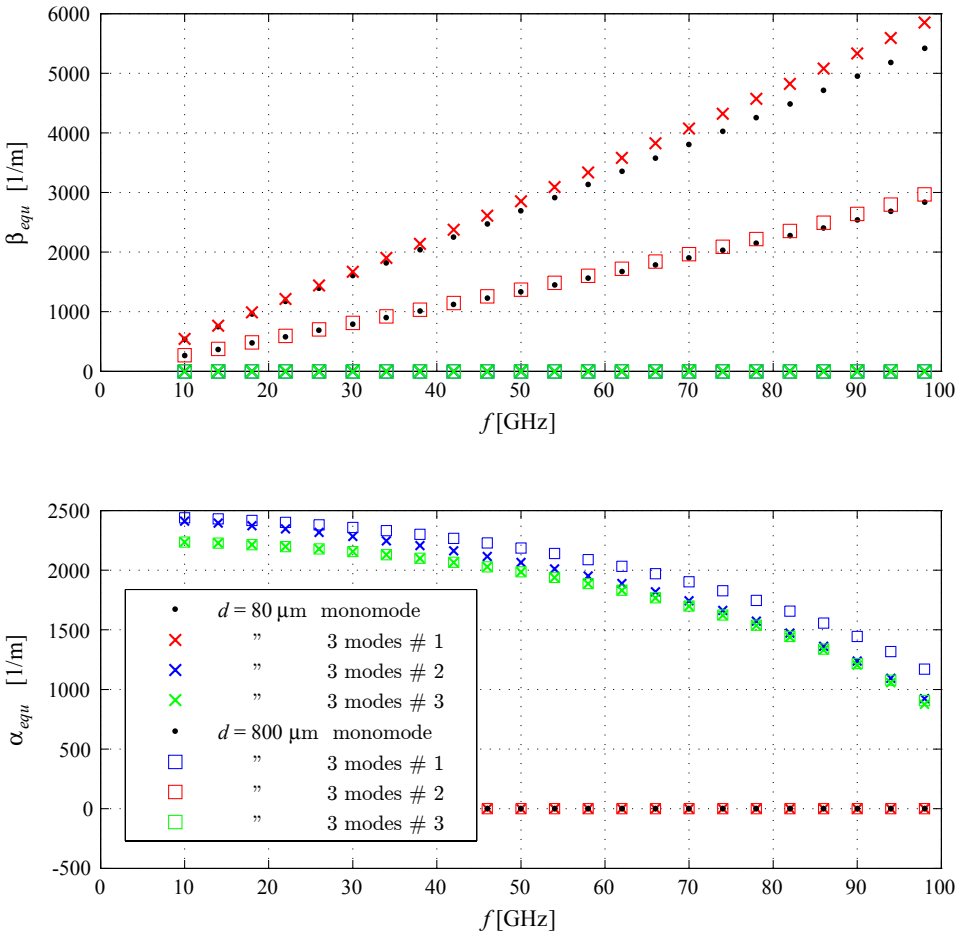

Figure 2.20: Comparison of the monomode and multimode Bloch propagation constants for the structure of Figure 2.18

2.7.5. Conclusion

We extended the periodic structure approach to the multimode case, which allows taking into account the inter-cell coupling through higher order modes —whether propagating or evanescent— of the TL comprising the ports of the cell. The method was validated by an unloaded multimode TL.

This is a further illustration of the power of periodic structure equivalents and Bloch wave modeling. Indeed, in most practical cases the unit cell TL ports support only one propagating mode and higher order modes are evanescent. In this case, only the first Floquet mode is non-evanescent and we thus have *a monomode periodic structure equivalent model, while taking into account more than one mode at the cell level.* As a result, most of the concepts and design methods presented in this thesis in the monomode case (which is in most cases sufficient) could easily be upgraded to take into account higher order mode inter-cell coupling without a significant increase in complexity.

From a quantitative point of view, the method was tested on a structure of interest in the framework of this thesis, namely a packaged DMTL. We showed that, for realistic dimensions (a bridge width of $d = 40$ μm for a unit cell length of $d = 80$ μm), the packaging of the structure would have a significant impact on the delay of the line since it is directly linked with the imaginary part of the Bloch wave propagation constant.

2.8. Chapter conclusion

In this chapter, we first explained that a finite periodic structure consisting of a cascade of identical two-port networks can be modeled as a TL of propagation constant and impedance γ_{equ} and Z_{equ} according to (2.5) and (2.19), regardless of the number of cells cascaded. As a result, usual TL theory, and more specifically the analysis of boundary conditions, can be used for the analysis or the design of such structures.

Then, some physically-based considerations for the right selection of the signs of γ_{equ} and Z_{equ} were proposed, and we showed that the most logical choice was to select the sign of γ_{equ} so that the group velocity is positive both in forward and backward bands. In this case, the corresponding sign of Z_{equ} must be chosen so that its real part is always positive.

After having deduced some useful expressions for γ_{equ} and Z_{equ} in some particular cases relevant to the design of micromachined and MEMS periodic structures, we finally showed how the periodic structure approach can be extended to the multimode case, which allows taking into account the inter-cell coupling through higher order modes of the TL comprising the ports of the cell.

Appendix: Group velocity and abnormal propagation

Introduction

In Section 2.3, we deduced a simple and physically-based convention for the signs of the Bloch wave equivalents. It was explained that associated considerations were always valid, except for the very particular case of *negative group velocity*, which will be discussed in this appendix. For that purpose, we first recall some important considerations with regard to phase and group velocities. Then, we summarize some results available in the literature and interpret them to allow us identifying a possible so-called *abnormal group velocity* with regard to our convention.

Generalities

Definitions

Let us consider a transmission medium with wave number $\beta(\omega)$ and the spectrum of an incident wave $A(\omega)$. If a pure monochromatic wave with constant amplitude is considered, the function $A(\omega)$ is a Dirac function and a single parameter, for instance the phase velocity, is sufficient to describe the propagation of the wave. For a pulse of finite length, which can be in its simplest form a monochromatic wave modulated by a 'time window' function, the frequency domain peak has a finite width, such as depicted in Figure 2.21. The frequency range of interest is then the region where the spectral components of the transmitted wave are sufficiently significant. This is will be called the bandwidth of the signal (or pulse) and is highlighted in the figure as $\Delta\omega$. In a general case, namely when β is not proportional to ω, the different components of the pulse do not have the same phase velocity, which induce a distortion of the pulse as it is transmitted through the medium.

First order development ($\beta(\omega)$ linear in the $\Delta\omega$ band)

In the case where $\beta(\omega)$ is approximately linear in the bandwidth of the signal, one can use the first order approximation of $\beta(\omega)$ to describe the propagation of the wave. Indeed, according to [20], which uses the Fourier transform to treat the propagation in the frequency domain and obtain a space-time domain solution, a given incident signal $u(x, t = 0)$ traveling through a given medium takes the form:

$$u(x,t) = u(x - v_g t, 0) \cdot \exp\{j(\beta_0 v_g - \omega_0)t\} \tag{2.103}$$

with $v_g = (\partial\beta/\partial\omega)^{-1}$. The first term in the right hand side of 2.103 is the magnitude —or envelop— of the signal. It is observed that this envelop remains unchanged and propagates at the velocity v_g. Consequently we can state that: *if a signal propagates through a medium whose $\beta(\omega)$ is linear in the bandwidth $\Delta\omega$ of the signal, the envelop of the signal remains unchanged in shape and propagates at the velocity $v_g = (\partial\beta/\partial\omega)^{-1}$*. Nevertheless, the attenuation of the signal was not considered here; it is clear that the attenuation must be weakly frequency dependant in the bandwidth $\Delta\omega$ in order that the different components have approximately the same attenuation

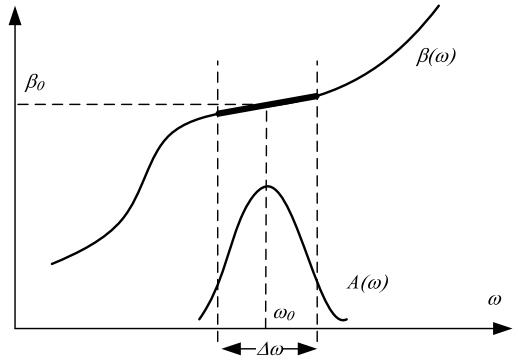

Figure 2.21: Spectrum diagram for the propagation of a pulse $A(\omega)$ through a medium of wave number $\beta(\omega)$.

and the envelop is not distorted. Concerning the phase variation, we can readily show that it is null only if the phase velocity is constant since:

$$(\beta_0 v_g - \omega_0)\, t = 0 \quad \rightarrow \quad v_g = \frac{\omega_0}{\beta_0} = v_\phi \tag{2.104}$$

In other words, the signal is not distorted in magnitude *and in phase* only if the phase velocity is constant in the bandwidth.

Conclusions

If $\beta(\omega)$ is not linear in the bandwidth of the pulse, the pulse shape is distorted as it propagates and describing the special propagation of the pulse by a single velocity quantity is not possible. In this case, a Fourier transform into the space or time domain is needed to deduce the shape of the pulse after transmission through the media. This consists in treating separately each frequency component of the pulse and reconstructing the overall pulse after transmission.

As a conclusion to this section, the group velocity has an intuitive and useful meaning only if the pulse distortion is negligible, which occurs if $\beta(\omega)$ is approximately a linear function in the bandwidth of the transmitted signal. If this is not the case, a computation of the group velocity can be used to assess the distortion undergone by the envelop of a pulse in a given frequency range.

Finally, one must keep in mind that a constant group velocity in the signal bandwidth is sufficient for the envelop of the signal not to be distorted, which is usually sufficient for the transmission of data in communication systems demodulation (e.g.: delay lines before A/D sampling, PLLs). In contrast, if the phase of the carrier within the envelop must be constant, not only the group velocity must be constant but also the phase velocity (e.g.: corporate feeding network for phased array).

Abnormal group velocity

General description

This section treats some special propagation characteristic leading to so-called *abnormal group velocity*, in connection with the sign discussion carried out previously. It can be read in several textbooks such as [13] that the group velocity as defined above is equal to the flow of energy or information carried by a propagating wave, except for a positive constant factor. This is true in almost all practical cases but theoretically not valid for any transmission medium at any frequency. More specifically, it is not true in media exhibiting losses, where the group velocity might be negative or larger than the speed of light.

By *negative group velocity*, we mean here that the group velocity of a pure traveling wave is directed toward the source of this very wave. Although this might seem non-causal in the first place, it is possible and well understandable if we associate this phenomenon with pulse reshaping. In this case, the group velocity represents the velocity of the maximum amplitude of the pulse. The causality principle is not violated since the wavefront itself still exhibit a positive and subluminal velocity. All these concepts are especially well treated in [20] and [21]. Therefore, they will not be detailed here as we only want to deduce the necessary condition to interpret correctly the computed characteristic of a given periodic structure.

Abnormal velocity identification

In Section 2.3, it was chosen to use the convention of a positive group velocity for both *backward* and *forward* bands of a given structure. This approach is sufficient in almost all cases but we need a criterion to identify if an abnormal *negative* group velocity occurs somehow in order to exclude any erroneous interpretation of the results. It is noticeable that the abnormal superluminal velocity is already well treated by our approach, since the only possible error is about the sign of the velocity.

The abnormal *negative* velocity can occur only in the case where the periodic structure contains a lossy resonant element, such as described in [21]. It is noticeable that the resonant element will lead to an abnormal velocity only for very particular numerical values of the elements. Therefore, we already know that a structure will not exhibit a negative group velocity by inspection of their equivalent circuit, if known. Still, such a resonant element might be hard to identify in a structure containing lossy lines and parasitics. For this purpose, we make use of the following theorem demonstrated in [22], re-written here in the case of passive structures only: *'In any medium, the group velocity is abnormal for a frequency at which the absorption is a maximum. In contrast, the group velocity is normal for a frequency at which the absorption is a minimum'*

This theorem allows the verification of the curves obtained for β. First, let us consider the propagation constant plot of Figure 2.4(a), which corresponds to a TL loaded with shunt loading element with a mainly capacitive behavior. We observe an abnormal velocity at the point of maximum attenuation, which consists in a null slope in the β plot, hence an infinite group velocity. This observation is consistent with the first part of the above theorem. On the other hand, normal velocity is observed for the attenuation minima, and the second part of the theorem is also verified.

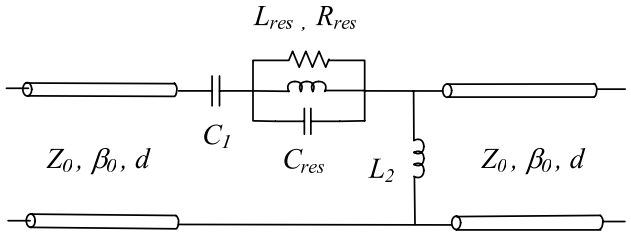

Figure 2.22: Unit cell presenting an abnormal negative group velocity. $Z_0 = 150\ \Omega$, $d = 10$ mm, $\beta = \beta_0$, $C_2 = 1$ nF, $C_{res} = 1$ pF, $R_{res} = 300\ \Omega$, $C_{res} = 5$ pF, $L_{res} = 2.7$ nH, $L_2 = 11$ pH.

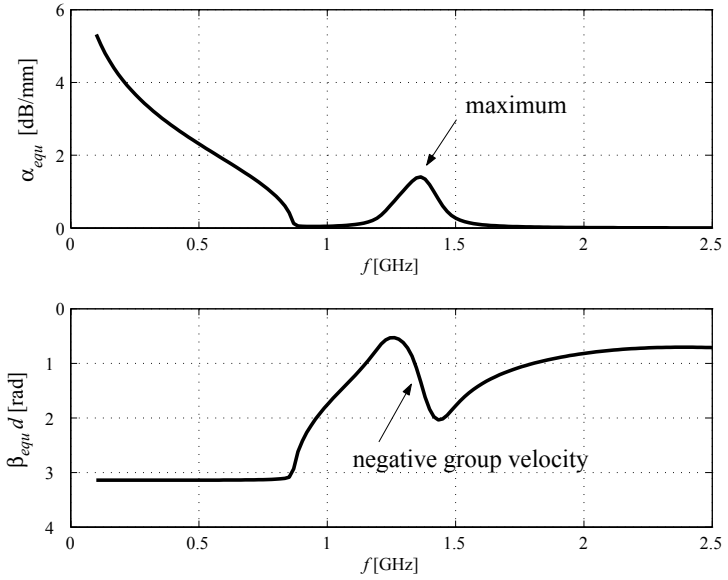

Figure 2.23: Propagation constant for the unit cell of Figure 2.22

As a result, we can conclude that this structure does not exhibit extraordinary behavior and our criterion and sign convention is suitable for this structure.

Now, let us consider the structure presented in [21], with numerical values tuned in order to observe an abnormal negative propagation. The corresponding circuit and associated lumped element values are shown in Figure 2.22, and the computed propagation constant is depicted Figure 2.23. We observe that the maximum in the attenuation is not associated with an abnormal *infinite* group velocity. Consequently, according to the aforementioned theorem, the maximum must be associated to an abnormal *negative* group velocity. As a result, and only in this case, we must modify our '$v_g > 0$' convention so as to allow for a negative slope of $\beta(\omega)$ in the region of the maximum attenuation.

3. Building Blocks

3.1. Introduction

3.1.1. Motivation and organization of the chapter

Microwave TL periodic structures such as DMTLs, CRLH-TLs, MEMS filters [23], or MEMS matching networks [24], consist of TLs periodically loaded with shunt or series capacitors, inductors, or more complicated MEMS systems. Here, we refer to these loading elements as the constitutive *building blocks* of the structures, which are defined in the most general way as given geometries connected to the ports of the building block by TLs. In addition, note that the host TL sections of the structures will be considered as building blocks as well.

In order to analyze and design DMTLs, MEMS CRLH-TLs, or MEMS-based reflectarray cells, it is obviously much more efficient to work first on a building block level. However, even more important is to derive lumped element models from the S-parameters of the block[1]. Indeed, this allows designing a given device on a circuit level first, using methods such as presented in this thesis. In a next step, the required lumped element values are translated into building block layouts by a given number of simulation-extraction cycles. The second advantage of the lumped circuit representation is for computational efficiency. This is especially relevant for MEMS-based devices since such structures exhibit very different scales and critical aspect-ratios; for example, as will be explained in detail in Section 3.8, a reflectarray cell with several MEMS can only be simulated in reasonable time and accuracy if the MEMS are represented by lumped elements, which have been previously deduced from the simulation of a single isolated MEMS building block.

In this chapter, we first comment on the simulation, extraction and measurement methods employed to characterize such building blocks, together with their precision with regard to some targeted applications. Some examples of building blocks designed and realized for concrete applications within this thesis are then presented. The comparison between measurements, full-wave simulation and circuit model results is discussed. Nevertheless, in order to limit this chapter to a reasonable size, not all building blocks are presented. For the same reason, not all issues linked with the building blocks (measurement results, full-wave simulations, circuit models, lumped models in full-wave simulation, etc) are addressed for each device but are treated to give a good overview of the methods employed and resulting efficiency. Table 3.1 shows which building blocks are presented here, along with their application in the context of this thesis. The table also lists the building blocks designed but not described in this chapter.

[1] This remark does not concern the 'host TL' building block.

Table 3.1: Overview of the building blocks designed in this thesis.

Building block	Device application	Presented results
CPW	All DMTLs + CRLH-TLs	Measurements, full-wave sim.
Shunt analog MEMS C	Analog DMTL	Measurements, full-wave sim., circuit model
Shunt digital MEMS C	Digital DMTL	Measurements, full-wave sim.
Shunt fixed L (1)	CRLH-TL	Measurements, full-wave sim.
Series analog MEMS C	Analog V-CRLH-TL	Measurements, full-wave sim., circuit model
Series digital MEMS C	Digital V-CRLH-TL	Measurements, full-wave sim., circuit model
Series switch	RA cell	Full-wave detailed + '*RLC*' sim., circuit model
Series fixed C	*CRLH-TL*	*Not shown*
Shunt fixed L (2)	*Analog V-CRLH-TL*	*Not shown*
Shunt digital MEMS L	*Digital V-CRLH-TL*	*Not shown*

3.1.2. Note on the EM full-wave simulation of MEMS blocks

The majority of building blocks considered here cannot be designed nor characterized using analytical formulas, but require full-wave EM simulations. The particularities of these MEMS blocks, with regard to typical microwave devices for which full-wave EM solvers are commonly employed, are the following:

- The small electrical size of the whole simulated block.
- The (very) large aspect-ratios in the geometry.
- The presence of electrically very small but physically significant geometrical details.
- The non-conventional materials sometimes present in MEMS processes.

Thus, significant effort was made in the determination of optimal simulation setups and testing of the solvers employed with regard to the particular class of devices concerned here. It should be mentioned that, although the elements are small in terms of wavelength, static or quasi-static (e.g. Ansys and ADS momentum *RF module*, resp.) solutions are either not sufficient to assess all EM effects in the block or proved not to be as efficient as their full-wave counterparts.

The two full-wave solvers employed in this thesis are *Agilent ADS Momentum* and *Ansoft HFSS*. *ADS* is based on the method of moments (MoM) and suffers important limitations for the simulation of MEMS devices. First, the MoM is not appropriate for the very thin dielectric layers and dimensions present in MEMS processes, because of the numerical instabilities linked with the computation of the Green's function in such cases [25]. Second, MEMS devices usually comprise metal layers as thick as, or thicker than, dielectric ones. Although this is not an inherent problem for the MoM solution, it is a limitation with regard to commercially available MoM-based codes such as *ADS Momentum* or *Ansoft Designer*. Indeed, metal patterns are only defined as 2-D structures in these software, which is not appropriate if the thickness of the metal is comparable with that of surrounding dielectrics (although pseudo 3-D metal structure can be defined in these codes using 'vias', a real 3-D approach is preferable here, see below).

Also problematic is the fact that these solutions can only consider infinite dielectric layer, which is often not realistic here (e.g. SiO_2 layer in the 'Al-Si EPFL' process, see Appendix A). Finally, the MoM classifies materials either as conductors or dielectric, which then have completely different 'roles' in the numerical computation. This is problematic when 'intermediate' materials, such as low-resistivity silicon, are present in the technology.

As a result of these important limitations, it was in general preferred to use the finite elements method (FEM) based HFSS software. Indeed, although this method is usually not as fast as a MoM solution, HFSS allows an exact 3-D description of the complete MEMS structures, as well as arbitrary material definitions, thus overcoming the aforementioned limitations of ADS. Finally, some tests were carried out to verify that HFSS does not suffer from instabilities when solving for electrically very small patterns in the design. This is an important feature of this FEM solution for MEMS devices, which was even validated for the simulation of MEMS structure in the low MHz range[1].

3.1.3. Lumped model extractions

This paragraph summarizes the principle of the method employed here to extract lumped element models from measured or simulated S-parameters of a 'building block'. For this we assume that the block is small in terms of wavelength so that it can accurately be described by an RLC circuit, which is always the case for the micromachined and MEMS devices building blocks considered in this thesis.

In general, the block can be well described either by a T or π-model, as shown in Figure 3.1. In this case, the values of the corresponding impedances can easily be deduced from the S-parameters and the reference impedance [14]. For each impedance, a model is chosen (for instance, RC series or RLC parallel ...), and the values of the corresponding R, L and C elements are extracted in a least mean square sense. These regressions are applied separately on the real and imaginary parts of the impedances. Note that if neither the T or the π-model is a good model for the device, a more complicated circuit might be employed. However, in this case, the method for the extraction cannot be as simple and numerical algorithms such as available in Matlab or ADS schematics must be used. It should be noted that our method considers *frequency-independent lumped element* only, which is necessary for the circuit models to have a physical meaning, and thus to be advantageously used in circuit-based design methods.

The accuracy of the extracted model can be graphically evaluated by comparing —over the frequency range of interest and for each impedance—the value given by the extracted model with the initial data. However, in order to get a quantitative estimation of the accuracy of the whole extracted model, the S-parameters of the T- or π-network can also be calculated with the extracted impedances. In this reconstitution process, there is the possibility of neglecting some elements that have been extracted but the effect of which is expected to be small (parasitic elements, for instance). Then, the reconstituted S parameters ($\tilde{S}$) are compared to the original ones (S), by means of two

[1]These simulations were carried out in the context of the design of the package of MEMS resonators within the NanoTimer EU project, the results of which are not reported in this thesis; see Chapter 1 and [10].

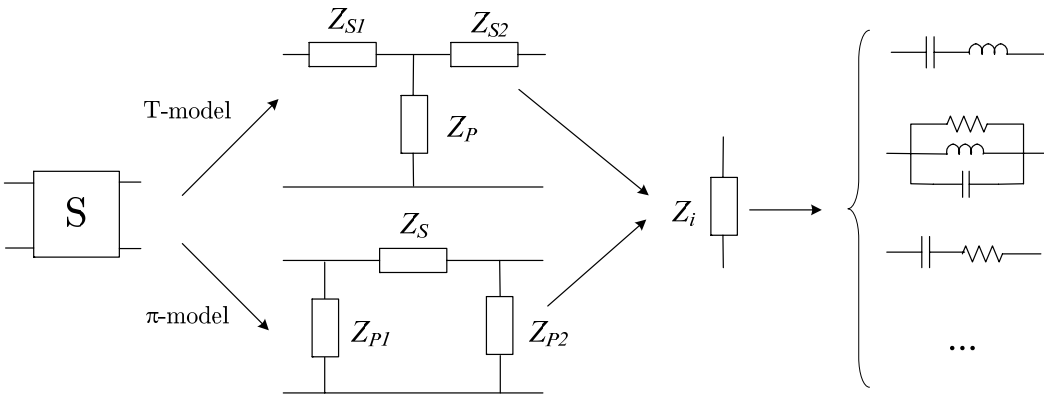

Figure 3.1: extraction process on T or π *RLC* two-port networks.

quantities which involves the four S-parameters at all the N_f frequency points of interest: the mean square error ΔS_{MSE} and the maximal error $\Delta S_{\max}$, defined as:

$$\begin{cases} \Delta S_{\mathrm{MSE}} = \sqrt{\mathrm{mean}\left|S-\tilde{S}\right|^2} = \sqrt{\frac{1}{4}\sum_{i,j}\left[\frac{1}{N_f}\sum_{f}\left|S_{ij}-\tilde{S}_{ij}\right|^2\right]} = \sqrt{\frac{1}{4N_f}\sum_{i,j}\sum_{f}\left|S_{ij}-\tilde{S}_{ij}\right|^2} \\ \Delta S_{\max} = \max\left(\left|S-\tilde{S}\right|\right) = \max_{i,j}\left[\max_{f}\left(\left|S_{ij}-\tilde{S}_{ij}\right|\right)\right] = \max_{i,j,f}\left(\left|S_{ij}-\tilde{S}_{ij}\right|\right) \end{cases} \tag{3.1}$$

It is important to emphasize here that the models chosen to represent given building blocks are not chosen in the sole goal that a regression on this model fits the S-parameter data, but chosen prior to the regression based on a *physical* understanding of the building block. Of course, a good fit should be obtained if the physical representation is valid. However, it is important to have a relevant physical model to get a good understanding of the link between the layout geometry and lumped element value. Indeed, design processes such as developed in this thesis (e.g. MEMS CRLH-TLs) provide lumped element values that must then be translated into layout elements. It is clear that this process can only be done in a limited number of simulation-extraction cycles if the link between the physical geometry and lumped element value is well understood. Finally, let us mention that the model chosen should be a good tradeoff between precision and simplicity (namely a small number of R, L, and C, since it is obviously preferable to have a compact model to develop efficient analytical or numerical circuit-based design methods.

3.1.4. On-wafer measurements and TRL calibration

a. Thru-Reflect-Line (TRL) calibration

This section concerns the TRL calibration [26], which was employed in this work to carry out on-wafer and rectangular waveguide measurements. This issue is addressed in this chapter because the TRL calibration exhibits particular features, which must be clearly understood prior to any building block characterization based on this calibration technique. Figure 3.2 shows a typical

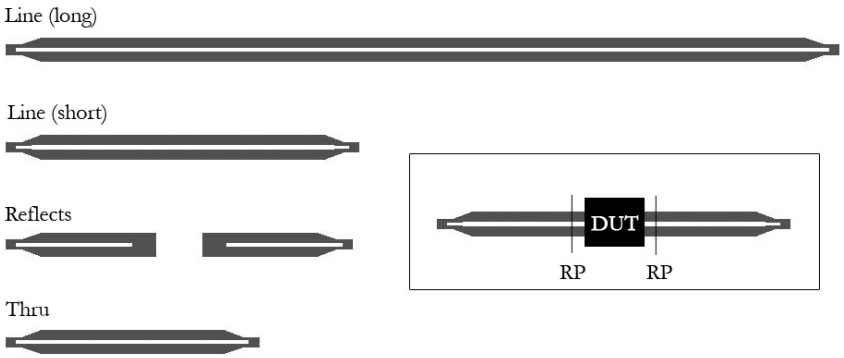

Figure 3.2: TRL calibration standards and TRL-calibrated measurement of a device under test (DUT). The letters RP show the *reference planes* of the measurement.

CPW TRL calibration kit, which must be designed on each wafer to be measured and according to the CPW characteristics and frequency band [26]. This calibration method presents the advantage that the calibration is done on the wafer where the devices to be measured have been fabricated, avoiding calibration problems due to inter-wafer variability. Second, the TRL calibration is especially convenient for on-wafer measurements since it allows placing the reference planes at an arbitrary location with regard to the device under measurement (see the inset of Figure 3.2).

Due to the TRL algorithm, the *S-parameters obtained from the TRL-calibrated measurements are always referred to the characteristic impedance of the TL on which the calibration is carried out.* As is well known, the reference impedance of the scattering matrix must be known to transform the S-parameters to the Z domain, which is necessary in any lumped elements extraction. Thus, in order to carry out some precise extraction from the measurements of a building block loading the TL, it is necessary to know precisely the characteristics of the CPW. The problem is that the value of the reference impedance is not directly calculated by the calibration algorithm and is therefore not accessible from the measurements. Nevertheless, we will show here how we can obtain some measurements, or pseudo-measurements, of the calibration line characteristics.

Let us finally mention that the knowledge of the host TL is not only important with regard to the treatment of TRL-calibrated measurements, but also because the TL is itself a building block whose characteristics will significantly influence the performance of the microwave periodic structure it hosts.

b. Measurement precision assessment

The various on-wafer measurements in this thesis were taken with a HP8510XF network analyzer and a Cascade Microtech 42 probe station. The measurement of a building block is pictured in Figure 3.3(a), where one clearly sees the two RF probes, as well as a DC actuation needle probe. A simple way to assess the precision of such measurement is to measure a 'Thru' standard. Indeed, as can be seen in Figure 3.3(c), in this case the two reference planes are degenerated and the

measurement should ideally yield $|s_{11}| = -\infty$ dB, $|s_{21}| = 0$ dB and $\arg(s_{21}) = 0$. In order to test the precision of such measurement, we first carried 3 different calibrations on a given calibration kit. Then, 3 different 'Thru' standards were measured, using the 3 different calibration sets previously determined. The results, referred to as A, B and C, in terms of S-parameters are presented in Figure 3.4.

For each measurement, the error is the superposition of the calibration imprecision (i.e. the errors in the calibration set data) and the error in the measurement itself, mainly due to the limited precision in the placement of the probes. We observe that typical values for $|s_{11}|$ are -40 dB to -50 dB, and 0.01 dB to 0.02 dB for $|s_{21}|$, which is good enough for typical measurements to be carried out in this work. Concerning $\arg(s_{21})$, a linear response is obtained, which means that the error is mainly due to the placement of the probes; indeed, a simple calculation shows that the 2^o error at 20 GHz observed in the worst case A corresponds to a misplacement of the probes of about 35 μm only. More precisely, it is probable that the two probes were located 35 μm too close to each other for this measurement since the phase is positive. In contrast, the best measurement (C in Figure 3.4) correspond a total misplacement of 10 μm. These values were deduced from the measurements but are realistic with regard to achievable precision on the manual probe station used here.

However, these results can be better interpreted with regard to the extraction of lumped elements by carrying out some extraction following the method explained in Section 3.1.3. If we assume that the measurement of the 'Thru' corresponds to the measurement a TL section whose length correspond to the error in the placement of the probes, a usual TL section model (shunt C, series L) should fit the raw impedances. This is confirmed by Figure 3.5 (taking into account that the measurement 'noise' is important with regard to the very small values extracted) and the results are consistent with the observations made above and based on $\arg(s_{21})$. Indeed, we observe in case A that the probes were too close too each other and the series L and shunt C extracted values are negative. In case B the probes were slightly too far and L and C are thus positive. Numerically, we obtain in case A (resp. B) $C_P = -5$ fF and $L_S = -7$ pH (resp. $C_P = 2$ fF and $L_S = 6$ pH). In case C, the measurement is almost perfect since we have $C_P = -1$ fF and $L_S = -2$ pH. These values are useful in the way that they provide a rough assessment of the incertitude on the extracted parameters. For instance, the shunt digital capacitive MEMS presented hereafter in this chapter is about 20 fF; although this value is very small (even for a MEMS device), it can still be extracted from such measurement. However, the incertitude will be quite large since we showed that a minimal imprecision in the placement of the probes already results in an error of some fF in the shunt capacitance extracted.

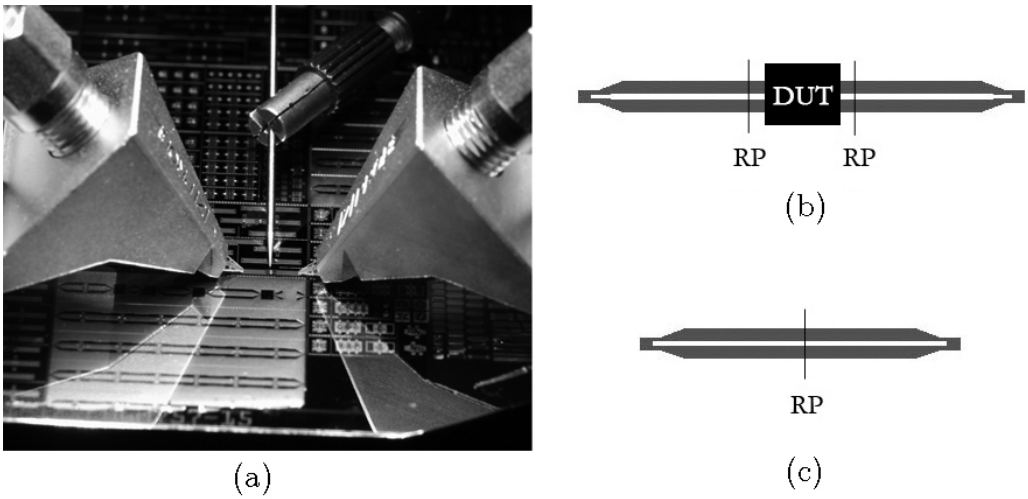

Figure 3.3: (a) On-wafer TRL-calibrated measurement of a building block. (b) reference planes (RP) and device under test (DUT) between TRL calibration lines. (c) 'Thru' reference.

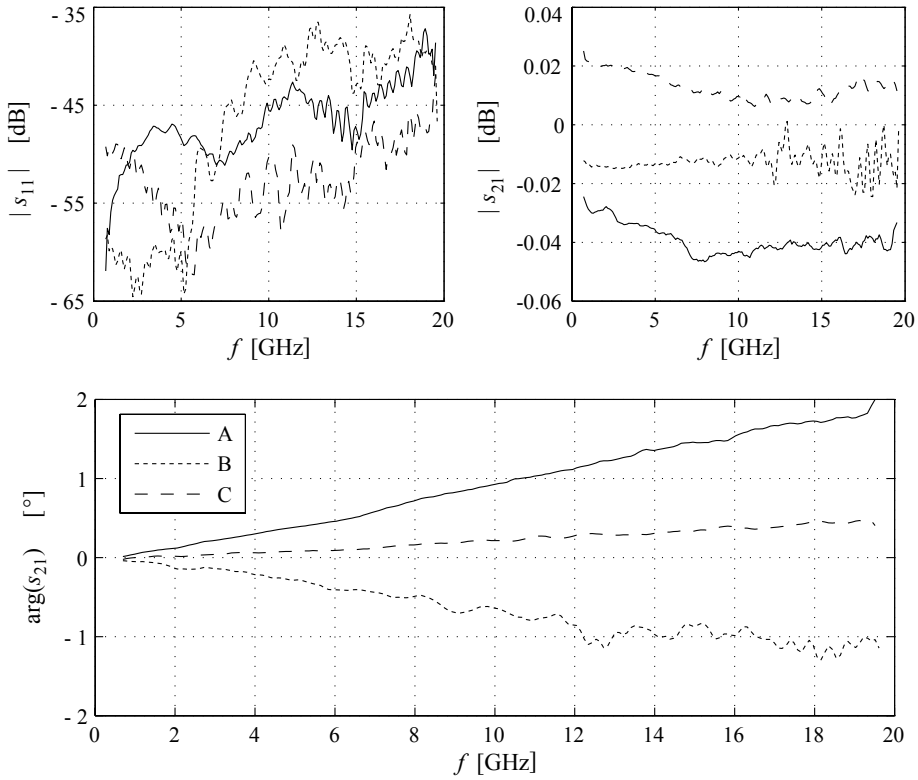

Figure 3.4: Measured TRL-calibrated S-parameters for 3 different 'Thru' standards.

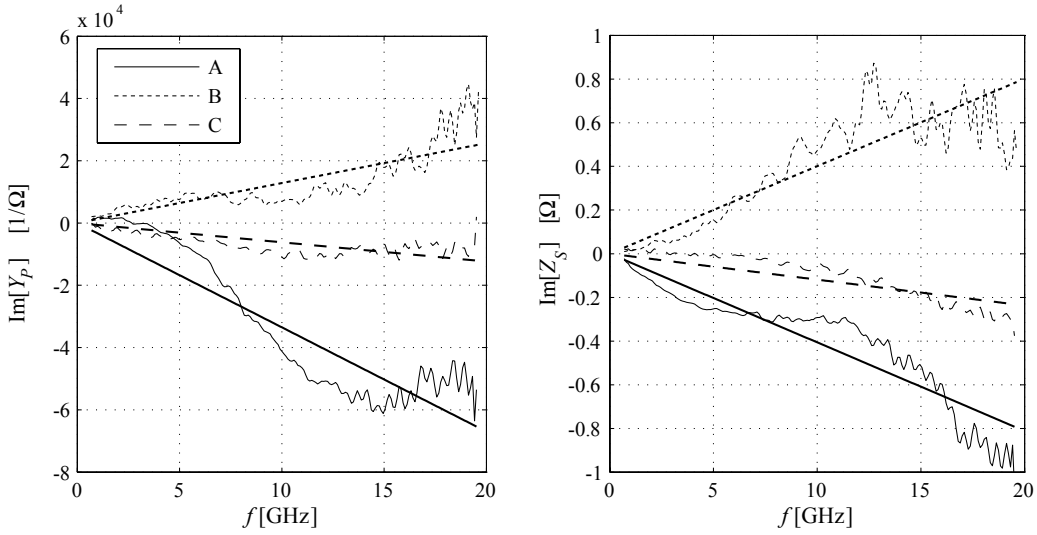

Figure 3.5: Measured extracted impedances (straight lines: interpolations) for 3 different 'Thru' standards.

3.2. Host TL

3.2.1. Introduction

a. Context

First, we discuss the characterization of the 'host TL' building block. In all devices presented from Chapter 4 to 7, this host TL is a CPW. The CPW presents well-known advantages over microstrip lines: low dispersion, low radiation, low coupling between adjacent lines, etc. Nevertheless, the main reason here for the use of CPW is linked with fabrication issues. Indeed, it is very difficult to make MEMS *shunt* loading element in microstrip technology. For instance, a MEMS variable shunt capacitor can easily be implemented in CPW technology (see Section 3.3 of this chapter), whereas an implementation in microstrip would be much more complicated. Concerning shunt inductances, they can also hardly be designed in microstrip because of the quasi impossibility to draw vias in standard wafers. Therefore, this section discusses the modeling and measurements of CPWs in micromachined technology. First, let us make some comments on the analytical and numerical methods for the computation of the CPW parameters:

- *Analytical methods* are limited by the fact that variations of the geometry from the standard CPW, such as the presence of non-uniform substrate layers, cannot be taken into account. These methods are also unable to compute dielectric losses and do not take the thickness of the metallization into account. Such limitations are not of prime importance in most PCB designs; in contrast, they have significant impact when considering CPWs in micromachining technologies.
- *Numerical methods* can handle all these limitations (although most of them do have some limitation in terms of material definition, metal thickness vs. skin depth, etc.), but are of

course much more time consuming. This is not a problem if a single CPW is to be designed, but is inconvenient in an optimization process since in this case, it is necessary to have a fast calculation method that can be integrated in the optimization parent program (see Chapter 4).

Now, let us summarize the special needs and difficulties in the precise assessment of the TL characteristics in the context of this work:

- As explained in Section 3.1.4, the impedance of the TL must be precisely known to carry out some extraction of lumped elements on TRL-calibrated measurements.
- In micromachining technologies, materials definitions are not as simple and precisely known as in standard PCB technologies (e.g. inversion layer in semiconductor substrates, see Section 3.3). Thus, even if an 'ideal' modeling tool is available, it is necessary to experimentally assess if the expected materials definitions are appropriate. We will thus discuss here how the TL characteristics can be experimentally determined.
- As mentioned above, there was here the need for a fast solver that can be integrated within a larger optimization procedure. For that purpose, the well-known conformal mapping approach was employed, with some additional steps to obtain a reasonable accuracy of the computed values. These particularities of the method are described in the Appendix of this chapter.

3.2.2. Theory

The approach presented here relies on the measurement of a TL using a TRL calibration made on this *same* TL. In other words, this means that the 'Line' standard of the TRL calibration kit can simply be used, although a longer line is generally preferred, for precision reasons. In this way, no discontinuity and higher order effects occur in the measurement, as would be the case if the measured line was different from the TRL calibration line.

a. Propagation constant

As the device under test is the same line as the one on which the TRL calibration is carried out, there is no mismatch at the ports and we have:

$$s_{21} = \exp(-\gamma_0 l) \quad \rightarrow \quad \gamma_0 = -\frac{1}{l} \cdot \ln_{\mathbb{C}}(s_{21}) \tag{3.2}$$

Where $\gamma_0 = \alpha_0 + j\beta_0$ and l are the TL propagation constant and length, respectively, and where the notation $\ln_{\mathbb{C}}$ represents the logarithm of a complex number. Now, as $\ln_{\mathbb{C}}(s_{21}) = \ln|s_{21}| + j\arg(s_{21})$, we have:

$$\alpha_0 = -\frac{1}{l}\ln|s_{21}| \quad \text{and} \quad \beta_0 = -\frac{1}{l}\arg(s_{21}) \tag{3.3}$$

The propagation constant of the TL is thus immediately deduced from the S-parameters. The only source of imprecision in this measurement is the non-perfect repeatability of the probes placement in the calibration and measurement processes, which can be assessed by inspection of s_{11} and s_{22} (these are zero in the case of a perfect calibration and repeatability).

b. Characteristic impedance

From TLs basics [14], we know that:

$$\frac{\gamma_0}{Z_0} = j\omega C + G \tag{3.4}$$

where Z_0 is the characteristic impedance and C and G the distributed capacitance and conductance of the TL. Combining (3.4) with (3.2), we find:

$$Z_0(f) = \frac{\gamma_0}{(j\omega C + G)} = \frac{1}{(j\omega C + G)} \left[-\frac{1}{l} \cdot \ln_{\mathbb{C}} (s_{21}) \right] \tag{3.5}$$

Since s_{21} is the only parameter obtained from the measurement ($s_{11} = 0$ by definition), we observe that Z_0 cannot be deduced from the measurement alone as C and G are present in the right member of (3.5). However, in the case of lines with reasonably low losses, it is observed that C is extremely weakly dependent on the frequency and the conductivity and that $G \ll \omega C$ [27]. With these approximations, (3.5) becomes:

$$Z_0(f) \cong \frac{\gamma_0}{j\omega C} = \frac{j}{l \cdot \omega C} \cdot \ln_{\mathbb{C}} (s_{21}) = \frac{j}{l \cdot \omega C} \cdot (\ln |s_{21}| + j \arg (s_{21})) \tag{3.6}$$

We can therefore deduce a pseudo-measured characteristic impedance Z_0 from the line S-parameter measurements, making use of a theoretical value for C. Nevertheless, C is the easiest line parameter to obtain and can be computed with good accuracy. Let us remark finally that, when computing Z_0 according to (3.6), one must previously unwrap the phase of s_{21} so that it decreases continuously with the frequency even below $-\pi$. For this purpose it is preferable to separate real and imaginary parts:

$$\mathrm{Re}\,[Z_0] = -\frac{1}{l \cdot \omega C} \cdot \arg (s_{21}) \tag{3.7}$$

with $\arg (s_{21})$ replaced by $\arg (s_{21}) + 2n\pi$ for frequencies above the n-*th* 'phase jump' in the wrapped $\arg (s_{21})$. Concerning the imaginary part of the impedance, it is similarly given by:

$$\mathrm{Im}\,[Z_0] = +\frac{1}{l \cdot \omega C} \cdot \ln |s_{21}| \tag{3.8}$$

c. Computation of the distributed capacitance C

We just explained that there is a need for a precise computation of the distributed capacitance C of the line. However, few numerical software deal with finite-thickness metallization and non-infinite dielectric layers, and it was observed that these are determining issues as far as the distributed capacitance is concerned. It is possible to do 2-D electrostatic analysis for such geometries using a software like *ANSYS*. However, the approach that was preferred and presented here is to use HFSS. Indeed, HFSS provides a versatile and powerful cross-section solver for the ports. This solver does not directly provide C to the user but gives access to the characteristic impedance Z_0 and propagation constant γ_0. However, Z_S and Y_P being the distributed series impedance and shunt admittance of the TL, we know that:

$$Z_0 = \sqrt{\frac{Z_S}{Y_P}} \quad \text{and} \quad \gamma_0 = \sqrt{Z_S Y_P} \tag{3.9}$$

Taking the ratio of these, we get:

$$\frac{\gamma_0}{Z_0} = \sqrt{Z_S Y_P}\sqrt{\frac{Y_P}{Z_S}} = Y_P \tag{3.10}$$

As $Y_P = j\omega C + G$, C can be deduced from the outputs given by HFSS:

$$C = \frac{1}{2\pi f}\mathrm{Im}\left[\frac{\gamma_0}{Z_0}\right] \tag{3.11}$$

Let us also note that the distributed series inductance of the line can be found in a similar way by calculating the product $Z_0 \cdot \gamma_0$ out of (3.9), and, with $Z_S = j\omega L + R$, we have:

$$L = \frac{1}{2\pi f}\mathrm{Im}\left[\gamma_0 \cdot Z_0\right] \tag{3.12}$$

3.2.3. Results

Different types of CPWs that will be used as host TLs in the devices presented in this thesis have been simulated and measured using the approach explained in the previous section. In this paragraph, we illustrate some of these results to validate the methods, as well as to draw important conclusions with regard to the losses in micromachined CPWs on standard MEMS substrates. Figure 3.6 shows simulated and measured impedance and propagation constant results, for CPWs of dimensions 20/110/20 μm with 475 μm-wide ground planes, made out of the patterning of a 3 μm-thick aluminum layer on the following substrates:

- 'Quartz': Fused silica quartz wafer.
- 'Si-standard': high resistivity ($>$ 10 kΩ.cm) silicon wafer with 500 nm SiO_2 insulator.
- 'Si-passivated': Same as 'Si-standard', but with the creation of an amorphous silicon layer at the Si-SiO_2 interface (see below).

A very important issue concerns the losses obtained with the different technologies, since these will directly impact on the insertion loss of the MEMS devices. Here, the particular following procedure was employed to clearly identify the origin of the losses in each case, using measured results and HFSS. The quartz wafer is first analyzed; in this case, the losses in the substrate are negligible because the quartz conductivity is nearly zero. As a result, measured losses on the quartz wafer can be attributed to the metal alone, and we can deduce the conductivity of the deposited aluminum by comparison with HFSS simulations (cross-checked by other simulators). Doing so results in an Al conductivity σ = 3.2e+7 S/m, for which we observe in Figure 3.6(b) a good agreement between simulated and measured results. As the Al deposition on both silicon wafers was made with exactly the same equipment and recipe as for the quartz wafer, we can safely assume that the conductivity of the Al is close to σ = 3.2e+7 S/m in all three cases.

Comparing now measured and simulated results for the 'Si-standard' technology, we observe that measured losses are much larger than simulated ones with the minimal specified silicon resistivity of the wafers (10 kΩ.cm). This phenomenon is linked with the formation of conductive surface channels at the Si-SiO_2 interface, which degrades the 'effective' substrate conductivity of

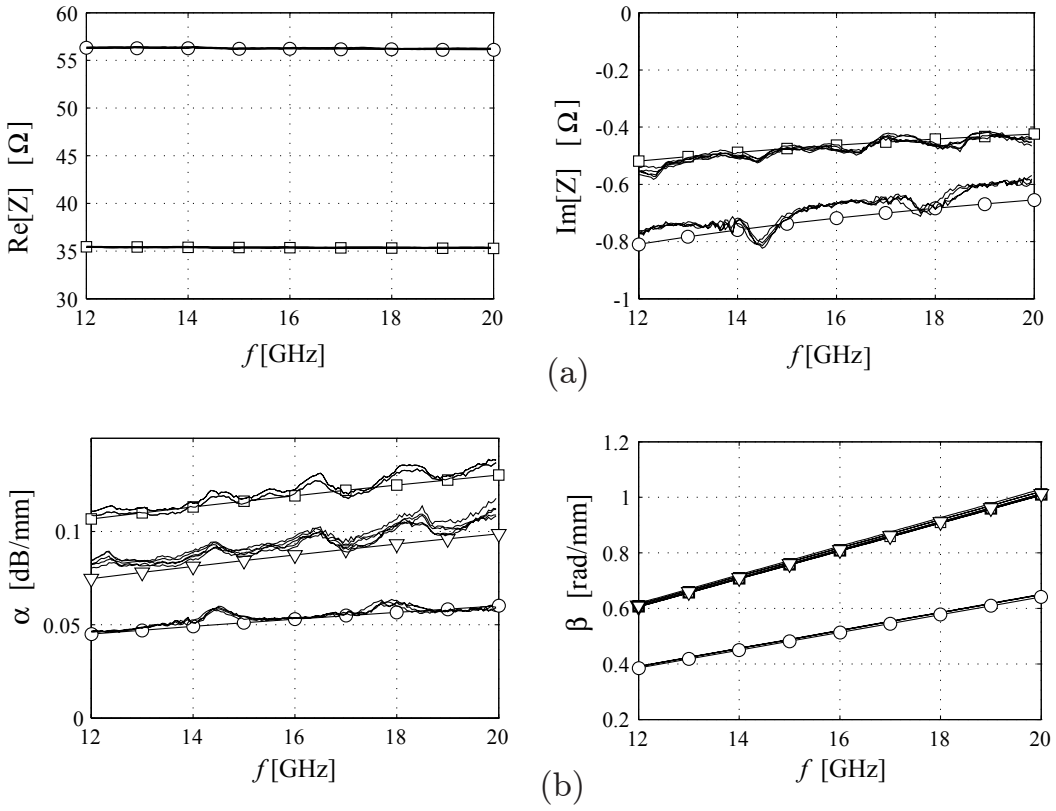

Figure 3.6: Simulated and measured (a) CPW impedance. (b) CPW propagation constants. (◯) 'quartz', (□) 'Si-standard', (▽) 'Si-passivated'.

the high-resistivity silicon [28]. As shown in Figure 3.6(b), measured losses on this substrate actually correspond to the simulation with a silicon resistivity of less than 0.7 kΩ.cm, namely, 13 times smaller than expected. It is possible to alleviate this problem by depositing a thin highly defective silicon layer at the Si-SiO_2 interface, which was done here by means of a 300 nm thick amorphous silicon [29]. The corresponding 'Si-passivated' measured loss is also shown in Figure 3.6(b), and we observe that the loss is indeed significantly reduced. This new measured results actually fits the simulated ones with the specified Si conductivity, which demonstrates the effectiveness of the amorphous silicon deposition.

From a practical point of view, the first conclusion to draw from these observations is that the best substrates for low-loss MEMS devices are quartz wafers. Much higher losses occur for standard high-resistivity silicon, although this is not suggested by the theoretical bulk resistivity of this material. In order to reduce the loss on silicon, it is necessary to 'passivate' the Si wafer, but the losses remain larger than with quartz substrates. Unfortunately, the two silicon-based MEMS processes employed in this thesis[1] did not include such passivation step, and losses in the corresponding devices are thus higher than what could have been achieved otherwise.

3.3. Shunt analog MEMS capacitors (for DMTL applications)

After having characterized the host TL for our periodic MEMS structures, we present here the first building block in the sense of a given geometry loading the TL. This block is one of the simplest one and consists of a shunt analog MEMS capacitor implemented by a mobile membrane connected one each ground plane side of the CPW and providing a variable capacitance to the central conductor (see Figure 3.7, [30]). This MEMS structure, also called *bridge*, is used as the basic element in the DMTLs presented in Chapter 4 and the principle of the actuation of such a MEMS is explained in the original paper [30] and in Appendix A.

3.3.1. 'Dimensionless' discontinuity model

The discontinuity constituted by the capacitor is considered dimensionless; that is, the distance between the reference planes of the discontinuity is zero, as illustrated in Figure 3.7. In concrete terms and referring to the sketch of Figure 3.7, this means that:

- In a full-wave simulation: a reference plane shift of half of the simulated length d_{ref} between ports is carried out at each port.
- In a TRL-calibrated measurement: the reference planes are degenerated in the middle of the cell. In other words, the whole measured device comprising the calibration lines has the same length as the 'Thru' standard.

It should be emphasized that this approach is perfectly valid and not less accurate than setting the reference planes at a finite distance with respect to each other and adding a small TL section on

[1] 'Al-Si EPFL' process for the DMTLs of Chapter 4 and 'Au-Si ISiT' process for the V-CRLH-TLs of Chapter 7, see Appendix.

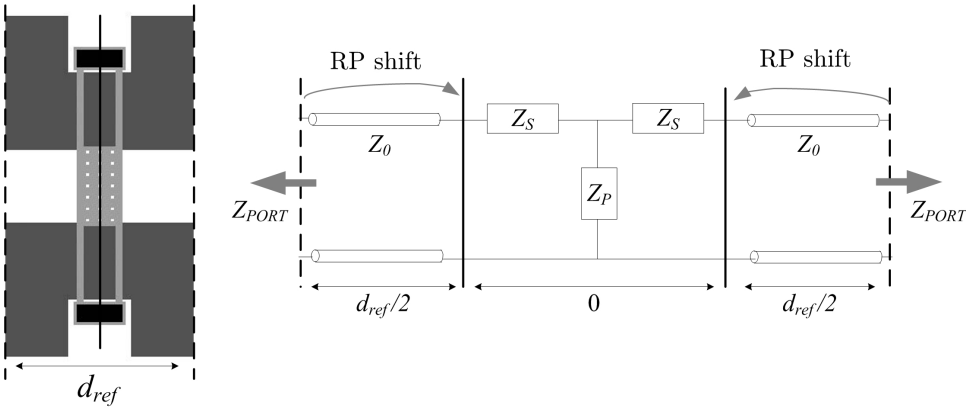

Figure 3.7: Illustration of the 'dimensionless' model for the bridge (dark grey: metal1 slots, light grey: metal2, black: anchoring).

each side of the discontinuity circuit model. The only requirement is to *ensure consistency between the extraction process and use of the extracted model*; here, the bridge loading a given TL section length L will be modeled by the dimensionless element model (namely the Z_S and Z_P T-network of Figure 3.7), with two TL sections of length $L/2$ on each side, which is thus consistent with the method employed for the extraction.

3.3.2. Shunt components (Z_P)

The capacitor of Figure 3.7 was realized and measured on the Al-Si EPFL process (see Appendix A). The measured S-parameters are plotted in Figure 3.8 and are typical of the low-pass behavior of a shunt capacitance. The imaginary part of the shunt admittance is shown in Figure 3.9, along with the regression lines and some of the regressed capacitance values. It is observed that the MEMS capacitor pull-in occurs between 12 V and 13 V since the capacitance value dramatically change in that region [7]. However, the capacitance still increases when the voltage is further increased, which shows that the membrane is not flat enough to achieve a good contact for a voltage only slightly larger than the pull-in voltage. The resistance of the bridge, in series with the capacitance, is more difficult to extract than the capacitance. Nevertheless, the values extracted for the different voltage are all between 1 and 1.5 Ω, which gives some estimate of the bridge resistance.

We observed that the shunt impedance measured is well modeled by a capacitance in series with a resistance alone. However, there is obviously also an inductive component linked with the current flowing through the bridge suspension beams, which could not be identified due to the limited precision and frequency range of the measurements. In order to extract this inductance, the frequency range must be increased so that the effect of the inductance becomes significant enough to be easily extracted. Associated results are shown in Figure 3.10 with two different full-wave simulators (corresponding measurements could not be carried out due to the 20 GHz limitation of the available measurement setup). The effect of the inductance is clearly seen in the upper part of the band, and the inductance value can now be extracted (see Figure 3.10).

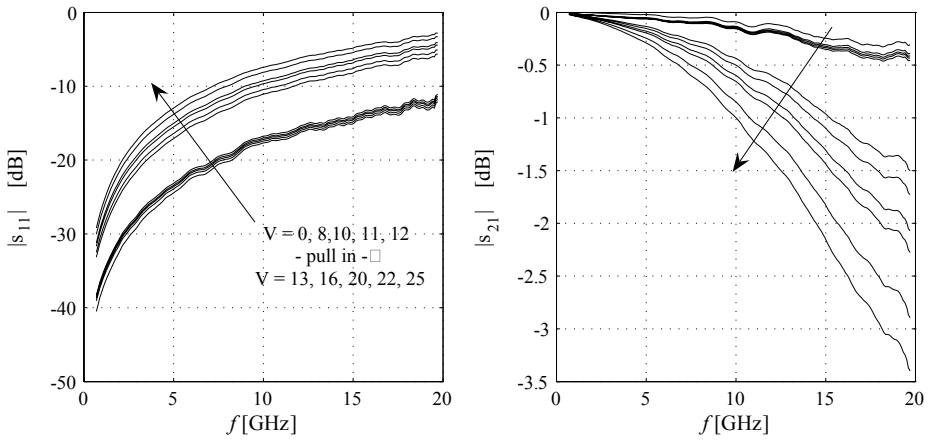

Figure 3.8: Measured S-parameter of an analog capacitor (referred to the calibration impedance).

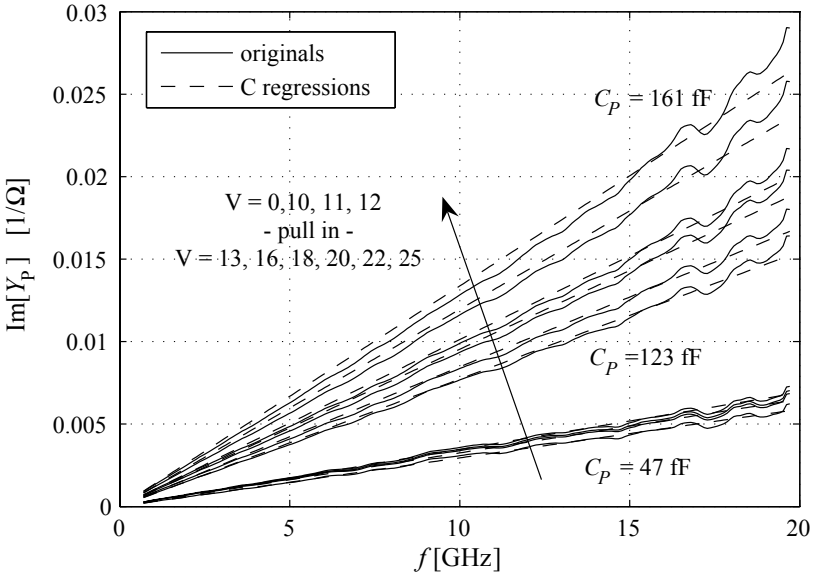

Figure 3.9: Measured imaginary part of the shunt impedance for an analog capacitor.

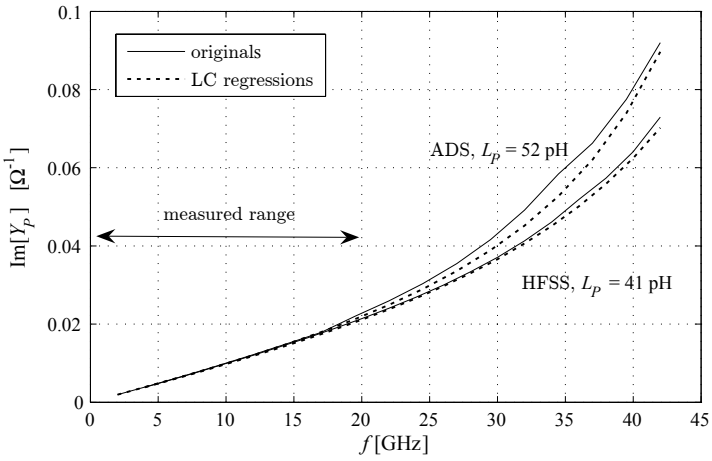

Figure 3.10: Simulated imaginary part of the shunt impedance for an analog capacitor.

3.3.3. Series components (Z_S)

a. Limitation of a purely shunt model

In the previous section, the MEMS bridge was modeled as a purely shunt component (i.e. $Z_S = 0$ in Figure 3.7), as was already done in previous works on DMTLs or MEMS switches [7,31]. However, the purely shunt model is only accurate enough for small bridge widths and larger ones require the introduction of series components. Indeed, in this case, non-negligible currents *parallel* with the axis of CPW are induced in the bridge. These currents are linked with series components, since the shunt modeling only accounts for current in the bridge perpendicular to the CPW axis. This assumption is confirmed by [32], which models the bridges by sections of transmission lines consisting of a CPW *with top-cover*. By doing so, currents in both directions are implicitly taken into account and any bridge width can be modeled. However, although such model can be of use for the analysis of DMTLs, its complexity makes it inappropriate for a design procedure such as presented here in Chapter 4. Consequently, we first propose here to model the effect of the series currents in an *approximate* way (namely using only R, L and C elements), so that the corresponding circuit can be directly introduced in a design procedure. Second, this simpler model is used to show that the undesirable series components can be significantly reduced by carrying appropriate cuts in the bridges.

b. Introduction of corrective series elements

The approach proposed here is to keep the length of the discontinuity to zero in the modeling, whilst introducing the series components ΔL_S and ΔR_S. As a result, the detailed model for the analog bridge with shunt and series elements is as depicted in Figure 12. This approach is valid as long as the series elements are considered as *corrective* elements to distributed series parameters of the plain CPW (hence the notation ΔL_S and ΔR_S). Considering again the bridge as a *CPW*

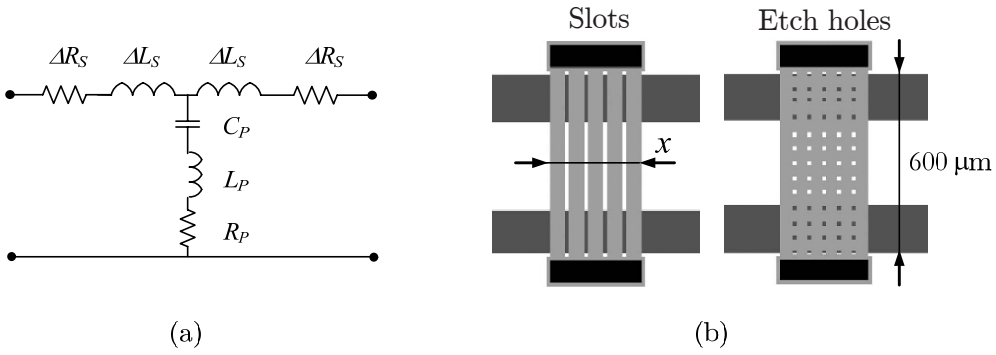

Figure 3.11: (a) Complete circuit model for the shunt MEMS capacitance [with degenerate reference planes, see Figure 3.7]. (b) layout of a bridge with etch holes and with slots (dark grey: metal1 slots, light grey: metal2, black: anchoring).

with top-cover line section, the corrective elements ΔL_S and ΔR_S represent the difference between the distributed series elements of the unloaded CPW and the top-covered one. If this is true, this means that $\Delta L_S < 0$ since it can be shown that the distributed inductance of a top-covered CPW is lower than the one of the simple CPW with same dimensions [33]. Similarly, it is expected that $\Delta R_S > 0$.

c. Simulations

Bridge with etch holes

These assumptions were first confirmed by simulation, which also confirmed that $\Delta L_S$and ΔR_S increase with the bridge width x. The considered bridge is shown in Figure 3.11(b) and includes the etch holes that are necessary for the sacrificial layer etching. Corresponding simulated results for three different bridge widths are depicted in Figure 3.12. The real part of the extracted series impedance increases with the frequency, as expected since the surface resistance does so. The imaginary part is negative and proportional to the frequency, and can consequently be modeled by the negative inductor ΔL_S.

Bridge with slots

As mentioned previously, the corrective series elements are linked with currents *parallel* with the axis of CPW. As a result, it was believed that preventing such currents to flow should allow the reduction of ΔL_S and ΔR_S and narrow slots were cut in relatively wide bridges, such as depicted in Figure 3.11(b). Comparing simulation results for the plain bridge and the bridge with slots (Figure 3.12), it is observed that the slots have the effect of significantly reducing both the resistive and inductive part of the series component. It is also worth mentioning that the bridge with slots is exactly equivalent to the bridge with etch holes from a capacitance point of view. Indeed, as a result of the fringe field, the effect of the slots on the parallel capacitance is very small when the bridge is not stuck to the central conductor (analog capacitor or digital capacitor in the Up state). In the case where the bridge is pulled-in on the central conductor,

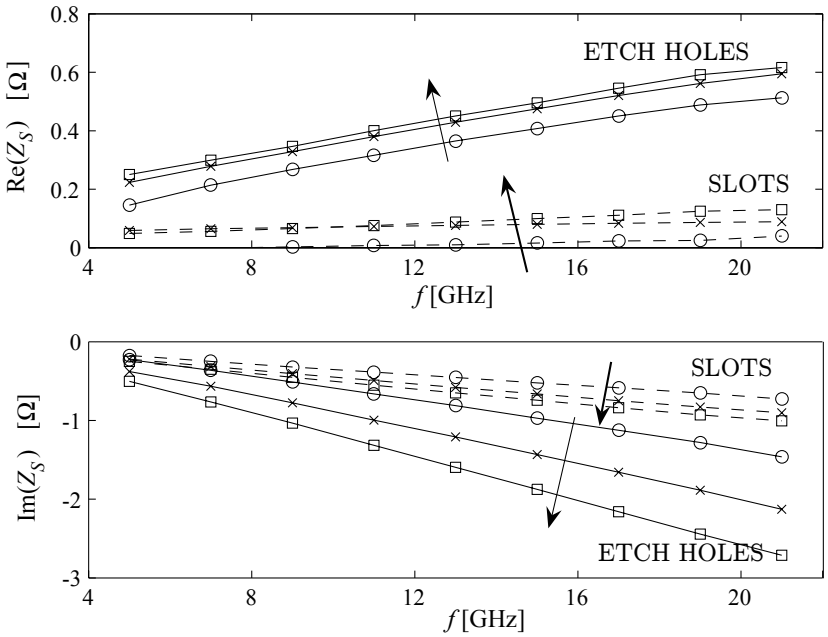

Figure 3.12: Series impedance of the bridge with and without slots as a function of frequency and bridge width x. (The arrows show increasing bridge widths x = 90, 120, and 150 μm).

the effect of the slots is close to the one produced by the etching holes that must be cut in a bridge without slots and consequently does not result in a reduction of the parallel capacitance. Finally, it is noticeable that the series components can also apparently be reduced by reducing the bridge width and compensating the reduction of the capacitance by enlarging the central conductor under the bridge. However, this approach modifies the CPW structure and would also introduce corrective series elements; consequently, it does not result in any improvement with regard to the performance of the DMTL.

d. Measurements

Figure 3.13 shows the regressed value for ΔL_S as a function of the bridge width. Some measurements on different samples of the same bridge and with different calibrations were taken for the bridge width x = 122 μm and are plotted on the same graph. As explained in Section 3.1.4, the limited precision in the placement of the probes results in some error in the extraction of a series inductance. Since the corrective inductances to be measured are very small, the relative error is here significant. Anyway, the measurements clearly confirm that the slots significantly reduce ΔL_S. Concerning ΔR_S, no clear confirmation of the simulations could be drawn from single bridge measurements, due to the importance of the incertitude with regard to the small resistive values highlighted by the simulations. However, the importance of ΔR_S can be observed when modeling a complete DMTL, as will be shown in Chapter 4.

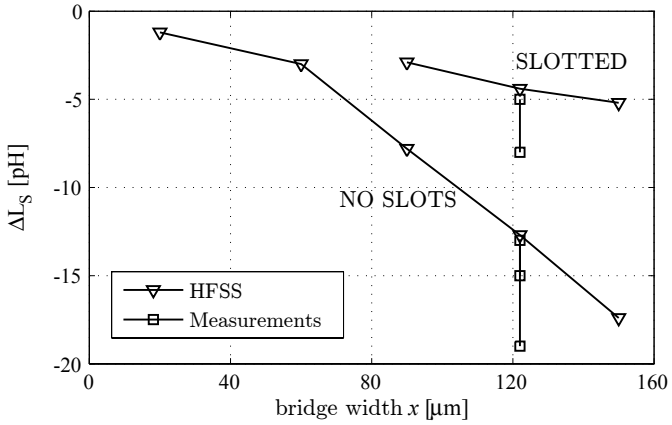

Figure 3.13: Simulated and measured corrective series inductance as function of the bridge width (only one bridge width was available for measurement).

3.4. Shunt digital MEMS capacitors (for DMTL applications)

The shunt *digital* capacitor concept for use in DMTLs was introduced in [34]. It is basically the same structure as the analog capacitor, except for two additional fixed capacitance in series with the mobile MEMS one. These fixed capacitance can be metal-insulator-metal (MIM) capacitors such as in [34] or metal-air-metal (MAM), as is the case of the digital shunt MEMS capacitor whose layout is presented in Figure 3.14(a). This digital capacitor was used for the design of digital DMTLs.

The model for this bridge is the same as for the analog capacitor, except that the capacitance C_P in Figure 3.11(a) must now include the two fixed MAM capacitances C_F in series with C_M so that the overall shunt capacitance is now $C_P = (1/C_M + 1/2C_F)^{-1}$. Compared with the analog case previously shown, this capacitor is meant to be operated in digital mode. In the Up state, the membrane is not actuated and the total capacitance is the series combination of C_F and $C_{M,Up}$. However, in the Down state, a voltage sufficient to pull-in the C_M capacitance is applied and the total capacitance is now the series combination of C_F and $C_{M,Down}$. In [34], $C_{M,Down}$ is assumed large enough so that $C_{M,Down} \gg 2C_F$ so that $C_{F,Down} \approx 2C_F$, although this assumption is not necessary and not employed in the design method of Chapter 4. As explained in [34], the digital capacitor allows a larger tuning range than its analog counterpart. It also exhibits better properties in terms of repeatability and sensitivity to the actuation voltage imprecision. More details about the actuation voltage and power handling for such digital MEMS bridge can be found in Appendix A.

Figure 3.14(b) shows the imaginary part of the shunt admittance in the circuit of Figure 3.11(a). The measurements of two instances of the same device are presented, along with HFSS and ADS simulation results. The curves exhibit a good agreement, taking into account the very small capacitance value extracted (20 fF) and the measurement incertitude (see section 3.1.4). Concerning the inductance L_P, simulations with both simulators have been carried out on extended

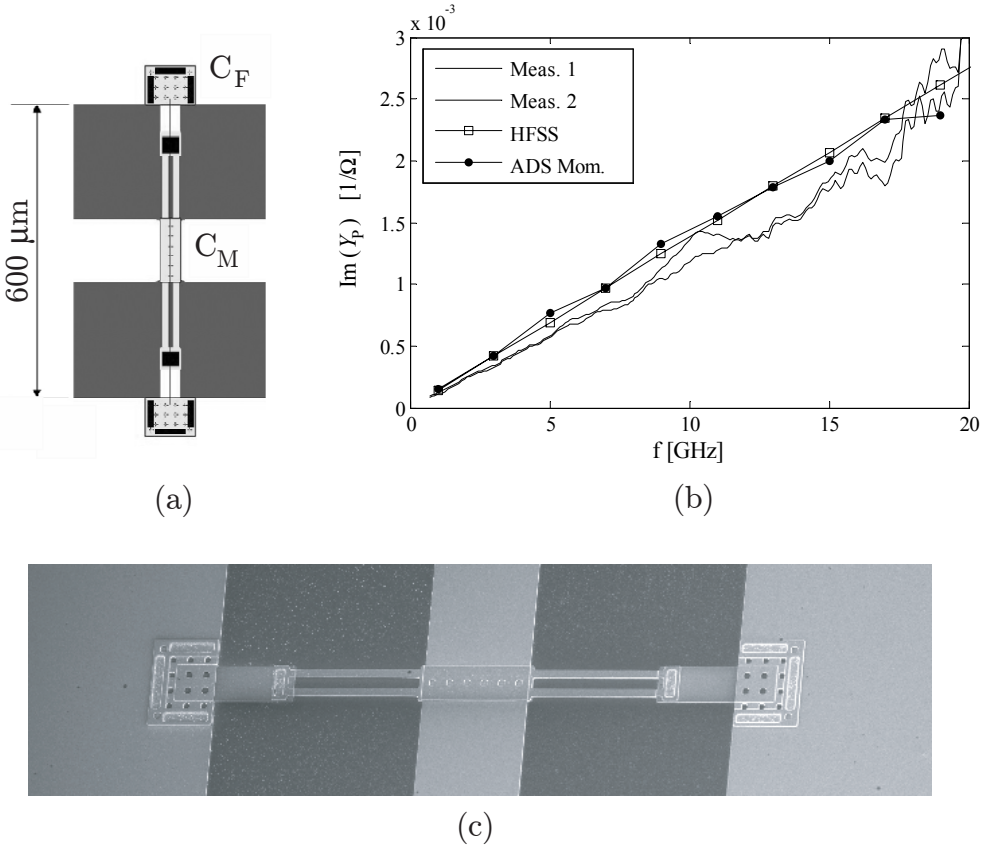

Figure 3.14: (a) Digital shunt MEMS capacitor layout [dark grey: metal1 slots, light grey: metal2, black: anchoring]. (b) Extracted imaginary part of the shunt admittance. (c) SEM picture of the fabricated device.

frequency ranges, which allowed the extraction of the inductance value. It was shown that L_P is only weakly dependant on the capacitance value and on the type of suspensions [full bridge or 4 beams structure as depicted in Figure 3.14(a)]. From a practical point of view, this means that a constant value for L_P can be used while optimizing C_P, as done within the DMTL design procedures presented in Chapter 4.

3.5. Shunt fixed inductor (for CRLH-TL applications)

Figure 3.15(a) shows the layout of a shunt inductor made with stubs in the CPW central conductor, as proposed in [35]. This basic block is employed for the realization of the fixed CRLH-TLs presented in Chapter 6 and was also fabricated on the Al-Si EPFL process. The inductor dimensions were chosen targeting the value $L_P = 115$ pH using HFSS. Both real and imaginary parts of the shunt impedance Z_P are shown in the graph of Figure 3.15(b), along with their measured counterparts. A linear regression on the imaginary part leads to a measured $L_P = 119$ pH, which is close to the design target. The real part of Z_P represents the parasitic resistance R_P in series with

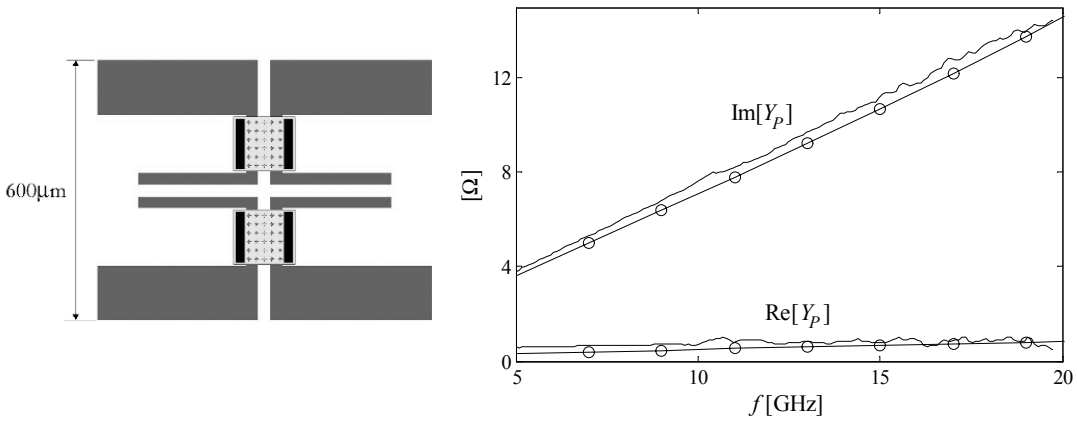

Figure 3.15: (a) Shunt inductance layout [dark grey: metal1 slots, light grey: metal2, black: anchoring], (b) simulated and measured shunt impedance: (—) measurement, (○) HFSS simulation.

L_P. A good agreement between simulations and measurements is also obtained in this case and the results show that this resistance is non-negligible due to the small dimensions and significant loss in the 'Al-Si EPFL' process (see Section 3.2.3). In general, higher L_P values are associated with higher resistive parts R_P, therefore limiting the practical range of L_P value.

Shunt fixed and variable inductors were also employed for the design of the MEMS V-CRLH-TL. In this case, more complicated models were required due to the more complex geometries and larger inductance values (in this case longer stubs are needed and the capacitive component in the TL line model of the stub must also be taken into account). These devices are not described in this chapter for space consideration, but the relevant models can be found as a part of the overall MEMS CRLH-TL circuits of Chapter 7.

3.6. Series MEMS analog capacitor (for V-CRLH-TL applications)

3.6.1. Description

Here we present a new *series* MEMS capacitor topology, designed for the implementation of the MEMS V-CRLH-TLs of Chapter 7. These V-CRLH-TLs are to be fabricated on the 'Au-Si ISiT' process and it was thus necessary to design a series capacitor based on this technology. Considering electromechanical issues and the requirement of achieving particular capacitances values with regard to the V-CRLH-TL application, the topology depicted in Figure 3.16 was selected (instead of a more straightforward cantilever approach, [7]). The overall series capacitance depends on the interdigited capacitor in the central conductor of the CPW [see the inset in Figure 3.16(a)], but also on the parallel plate capacitances between the 1st metal and the bridge; it is therefore possible to control the overall series capacitance by changing the height of the bridge membrane. As shown in the figure, in the final V-CRLH-TL structure the shunt inductive loading elements of

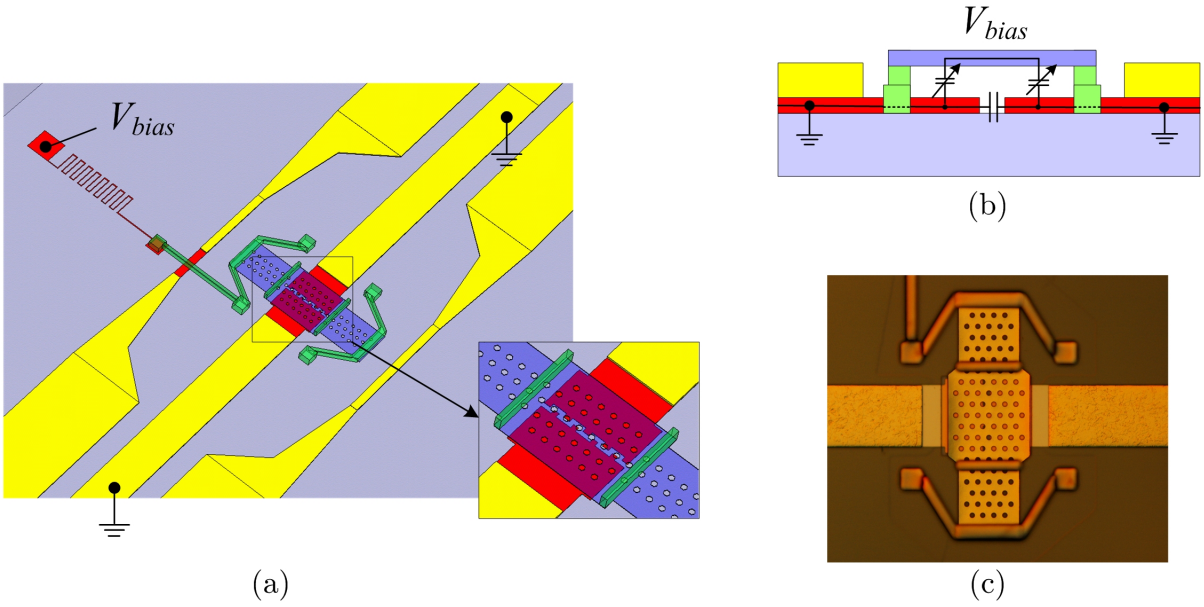

Figure 3.16: Principle of the series MEMS analog capacitor for V-CRLH-TL applications. (a) 3-D view, (b) cut along the central CPW central conductor, (c) optical microscope picture.

the V-CRLH-TL will DC ground the CPW central conductor sections. As a result, it is possible to actuate the structure by applying a DC voltage to the bridge by means of a DC pad, as depicted in Figure 3.16(a).

3.6.2. Modeling and results

Figure 3.17(a) shows the physical model deduced for this analog series capacitor. Note that here, a finite length between reference planes was chosen because of the CPW cross-section variation in the MEMS area, which prevents the use of 'degenerate' reference planes such as done for the devices previously presented in this chapter. Here is a brief description of the different lumped elements in the circuit:

- C_{SUB} represents the coupling capacitance through the substrate between both electrodes of the interdigited capacitor.
- C_{GAP} represents the variable capacitance between each electrode and the bridge.
- C_A represents the coupling between the bridge anchors and the CPW ground.
- C_L, R_L and L_L account for the CPW-like propagation in the MEMS area.

This physical model can obviously be reduced to the T-model shown in Figure 3.17(b), and Figure 3.18 shows the regressed results based on this model. Looking first at the full-wave simulation results, we observe that the model accounts very well for the simulated structure since the regression curves are almost indistinguishable form the raw impedance and admittance data. On the

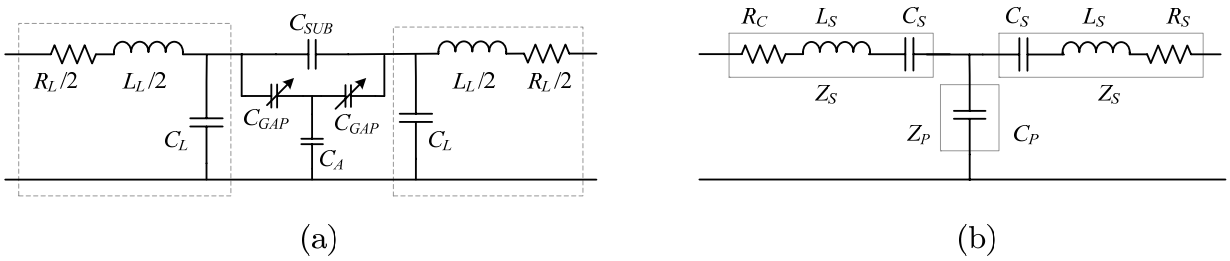

Figure 3.17: Circuit model of the analog MEMS series capacitor of Figure 3.16. (a) detailed physical model. (b) reduced model.

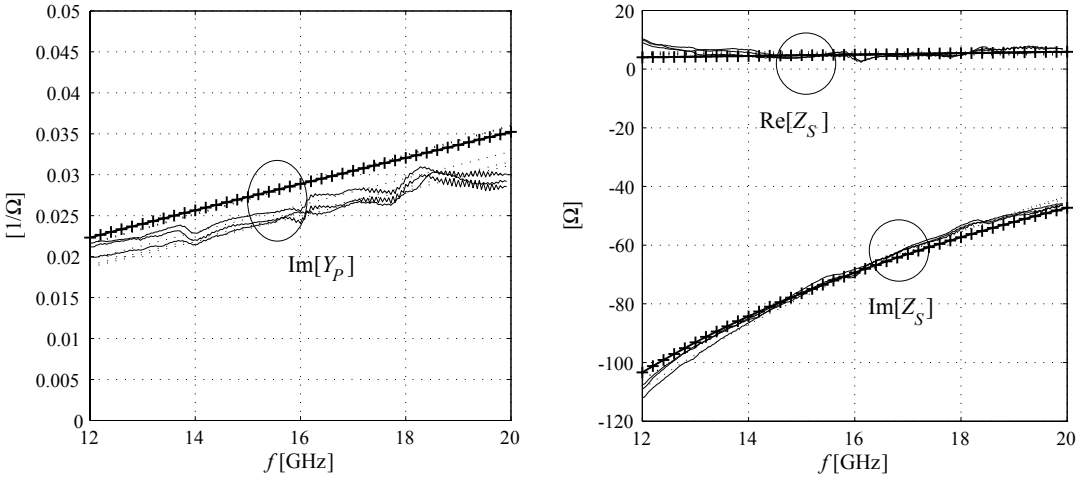

Figure 3.18: Extracted shunt admittance Y_P and series impedance Z_S of the T-model of Figure 3.17, in the Up state. (—) raw data, (· · ·) circuit model regressions. (+) full-wave, (no marker) 3 different devices measurements.

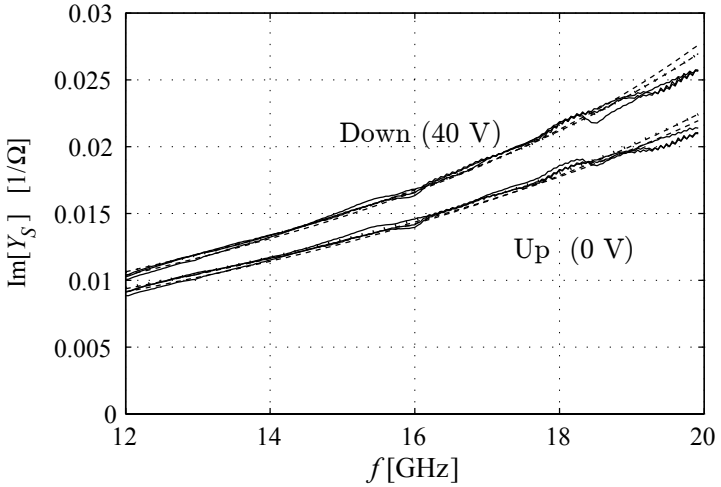

Figure 3.19: Extracted shunt admittance Y_P in Up and Down states for 3 different measurements. (—) raw data, (- -) circuit model regressions.

graph are also plotted three different measurements. A very good agreement with the simulation is observed for the series impedance. Concerning the shunt admittance, some discrepancy with the simulated result is observed, and is attributed to some fabrication tolerances.

Let us now observe the behavior of the imaginary part of the series impedance under actuation. Measured results for 3 instances of the same MEMS are presented Figure 3.19, which indicates that good 'intra-wafer' repeatability is obtained (all fabricated devices were processed on the same wafer). The MEMS is here actuated in its analog range, and the Down state curve presented corresponds to the maximum deflection before pull-in of the membrane (at about 40 V). As expected, the actuation of the MEMS corresponds to an increase of the series capacitance value, which is however limited to about 10% here due to the contribution of the fixed coupling capacitance between both electrodes of the interdigited capacitor [C_{SUB} in Figure 3.19(a)].

3.7. Series MEMS digital capacitor (for V-CRLH-TL applications)

3.7.1. Description

The device presented in this section consists in an evolution of the MEMS of the previous paragraph and is depicted in Figure 3.20. As can be seen in the inset, MIM capacitors have been added in series with the MEMS central capacitor, following the concept already employed for the digital shunt MEMS capacitor. This allows operating the MEMS in two stable states while accurately controlling the overall series capacitance in each state, although the main reason here is to extend the range of tunability of the capacitor. In this digital realization, the actuation of the bridge is achieved by applying a DC voltage between both CPW central conductors, as shown in Figure 3.20. In this case, there is no DC actuation pad and the corresponding physical circuit model employed is shown in Figure 3.21, along with its reduced π-model.

3.7.2. Results

a. Full-wave and circuit model

Figure 3.22 shows the full-wave simulation results for this digital capacitor, along with regressed circuit model data. Again, we observe that the model accounts very well for the simulated structure since the regression curves fit the raw admittances very well. In contrast with the analog capacitor, a large capacitance ratio is obtained here, namely 54.2 fF/21.8 fF=2.1.

b. Measurements

The series digital capacitor was fabricated in a 2$^{\text{nd}}$ run on the 'ISiT Au-Si' process. Figure 3.23 shows corresponding measured results, along with simulated ones already shown in Figure 3.22 (for clarity, the regression curves are not shown here). A very large discrepancy is observed, and it was thus decided to measure the topology of the device using some interferometry profilometer, in

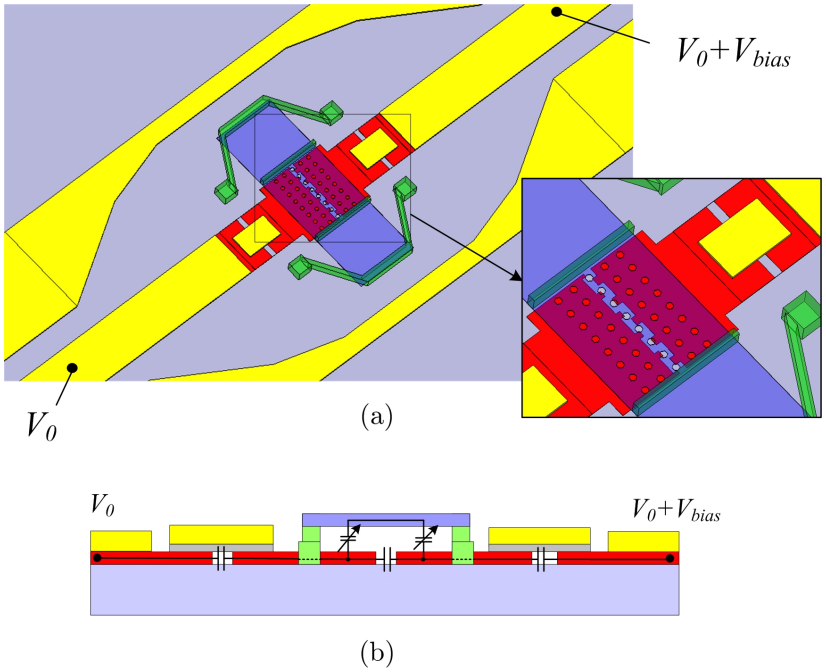

Figure 3.20: Principle of the series MEMS digital capacitor for V-CRLH-TL applications, (a) 3-D views (b) cut along the central CPW central conductor.

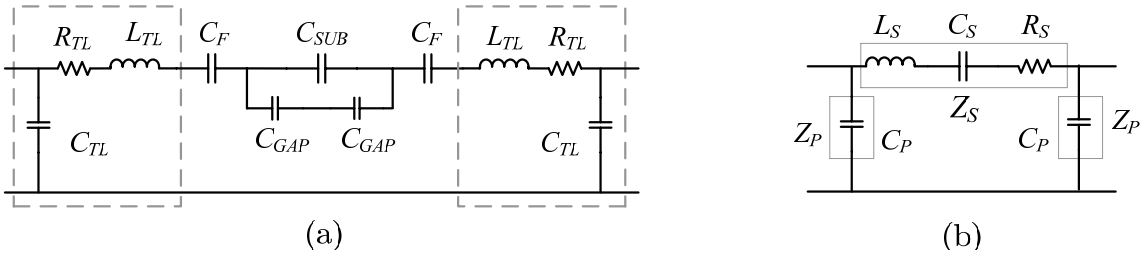

Figure 3.21: Circuit model of the digital MEMS series capacitor of Figure 3.20. (a) detailed physical model. (b) reduced model.

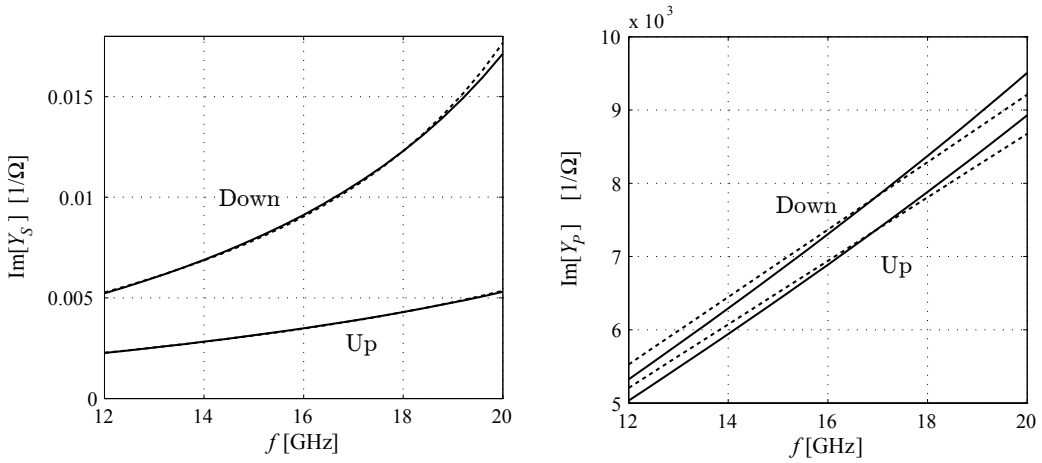

Figure 3.22: Extracted series and shunt admittances of the π-model of Figure 3.19(b). (—) raw data, (- -) circuit model regression.

order to identify possible problems in the fabricated devices. The 3-D view corresponding to this measurement is shown in Figure 3.24. A set of particular cuts in this profile allows determining the thickness of the different layers and the following observations were made:

- One of the dielectric layers (AlN) was damaged during the process.
- The annealing of the membrane done as a last step in the process led to some lateral bending of the membrane, hence a poor contact in down state.
- The dielectric stack used to fabricate the MIM capacitor was thicker than expected, namely, 700 nm – 800 nm instead of a targeted value of 500 nm.

We can reasonably assume that these are the main causes for the discrepancies since the observed defects obviously lead to smaller capacitances both in the Down and Up state, which translates into the smaller imaginary part of the series admittance observed in Figure 3.23. It is interesting to note that these issues would not have been detrimental in the case of the analog capacitor: concerning the two first points above, it is because they only have a significant effect when the membrane is pulled-in, which only occurs in the digital case. Concerning the third item, it is because the MIM capacitor is not implemented in the analog version of the device. However, the impact of these process faults is very significant for the digital MEMS. For instance, the difference in the MIM capacitor dielectric thickness will obviously greatly reduce the overall capacitance, especially in the Down state. In order to verify these statements, the simulations were run again with the measured MIM dielectric thickness, and assuming a poor contact of the pulled-in membrane. The results are shown in Figure 3.23 as well; although these simulations are not meant to precisely account for the measured device, they show that the large discrepancy between targeted performance and measured results can indeed be mainly attributed to the above process faults. This failure in obtaining the desired performances with this MEMS capacitor is a good illustration of the difficulty of designing performing microwave devices based on MEMS, even using a quite mature fabrication process. The case of the MIM capacitor is exemplary. Indeed, two different steps were taken in the design stage to minimize the effect of fabrication tolerances on the capacitance value. First,

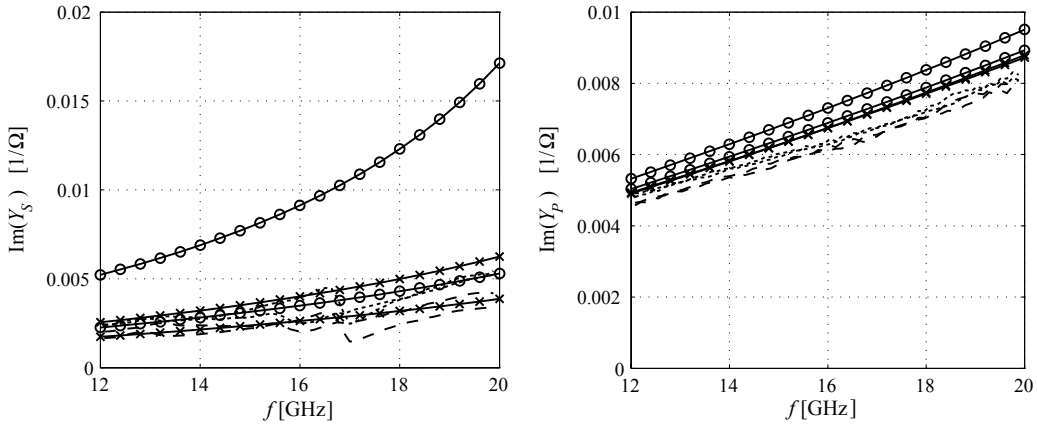

Figure 3.23: Extracted imaginary part of shunt and series admittances. Simulations: expected dimensions (○), corrected dimensions (×). Measurements: Up states (- -), Down state (· · ·) [two different measurement results are shown here].

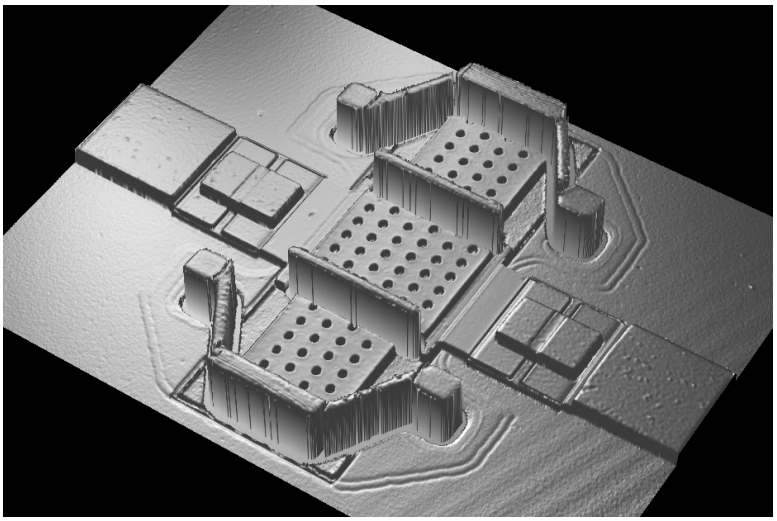

Figure 3.24: 3-D view of the profile measurement of a fabricated series digital MEMS capacitance. A set of particular cuts in this profile allows determining the thickness of the different layers.

both dielectrics were used so that a larger active surface is patterned for a given capacitance value (lower sensitivity to both the dielectric thickness and the metal surface patterning imprecision). Second, each MIM capacitance actually consists of two capacitances in series (see Figure 3.20), which reduces the geometrical tolerances on each capacitance. Nevertheless, these steps proved not to be sufficient here, and it is believed that a better solution would have been to implement the fixed capacitor of the MEMS as metal-air-metal (MAM) capacitors, using the sacrificial layer for the gap (such as done in the case of the *shunt* digital capacitor of Section 3.4).

3.8. Series MEMS switch (for reflectarray application)

3.8.1. Introduction

The last building block presented in this chapter is the series MEMS capacitor shown in Figure 3.25(a). Although the MEMS itself resembles a usual shunt topology, the way the electrodes below the membrane are connected obviously results in a series capacitance between the two accesses to the MEMS. This capacitor is to be inserted in a controllable reflectarray element in Chapter 9, and is realized on the 'Al-Quartz VTT' technology. In contrast with the previous MEMS capacitors, this one is referred to here as a *switch*. The reason is that, although this capacitor has the same structure as a usual analog capacitor, it will be operated as a switch in the reflectarray element: the membrane will be either left with no actuation voltage (Up state) or completely pulled-in (Down state).

However, this example also differs from the previous ones in the sense that the MEMS studied here is not meant to load a transmission line but is part of a radiating element. In this case, several of the MEMS concerned here are to be inserted in a single reflectarray cell, and a simulation of such a cell including all the MEMS detailed geometry is extremely time consuming. On the other hand, and in contrast with the previous TL applications (DMTL, CRLH-TL), it is in this case not possible to deduce the relevant parameter of the reflectarray cell working only on a circuit level. As a result, an intermediate approach is necessary, which consists in *including lumped models representing the MEMS in a full-wave simulation of the reflectarray cell*. This is possible in HFSS using so-called RLC boundaries, which are actually surface impedances. However, in order to do so, we must first deduce the appropriate circuit model for the MEMS, which was done here following the procedure:

1. Full-wave detailed simulation of a single switch.
2. Deduction of a circuit model for the switch.
3. Implementation of this circuit model by RLC boundaries in the full-wave simulation of a single switch (the detailed geometry of 1. is replaced by the RLC boundary).
4. Verification that the result of 3. corresponds to the result of 1.

Consequently, the organization of this section is different from the previous one since emphasis is put here on some theoretical and practical aspects of the substitution of the detailed MEMS geometry by a simple lumped model in HFSS.

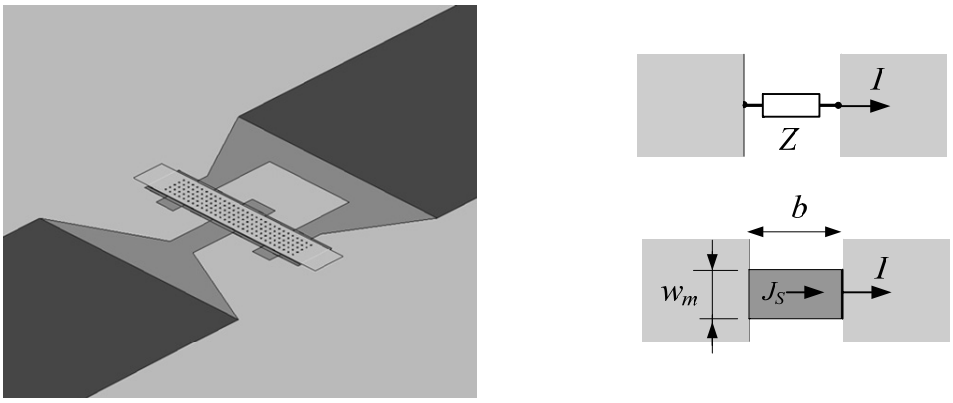

Figure 3.25: (a) 3-D view the series MEMS switch for reflectarray application. (b) Illustration of the implementation of a lumped element by a surface impedance in a full-wave simulator.

a. Representation of lumped elements with RLC boundaries

It is not possible to include a real lumped element as shown in the top of Figure 3.25(b) in a FEM software like HFSS. Nevertheless, it is possible to setup RLC boundaries to model lumped elements, where the R, L and C elements are connected in parallel. Such a boundary actually consists in a surface with given surface impedance and is depicted in Figure 3.25(b) as well. Formally, the equivalence between the lumped and boundary approach can be expressed by first writing the continuity of the tangential electric field at the boundary:

$$n \times (E_1 - E_2) = 0 \tag{3.13}$$

The tangential electric field on the boundary $\mathbf{E_{2T}}$ is linked to the surface impedance Z_S and surface current J_S by:

$$\mathbf{E_{2T}} = \rho \mathbf{J} = (Z_S dx)\,(\mathbf{J_S}/dx) = Z_S \mathbf{J_S} \tag{3.14}$$

Substituting (3.14) in (3.13) yields the tangential component of the E field at the boundary:

$$\mathbf{E_{1T}} = Z_S \mathbf{J_S} \tag{3.15}$$

Assuming a constant surface impedance within the boundary, and that a non-zero net current only exists in the direction of the current of the lumped element, we have:

$$V = ZI \rightarrow E_{Tx} b = Z \cdot (J_S w_m) \tag{3.16}$$

with b and w_m as defined in Figure 3.25(b). The relation between the lumped impedance Z and the surface impedance Z_S of the boundary is finally obtained using (3.15) and (3.16):

$$Z_S = Z \cdot \left(\frac{w_m}{b}\right) \tag{3.17}$$

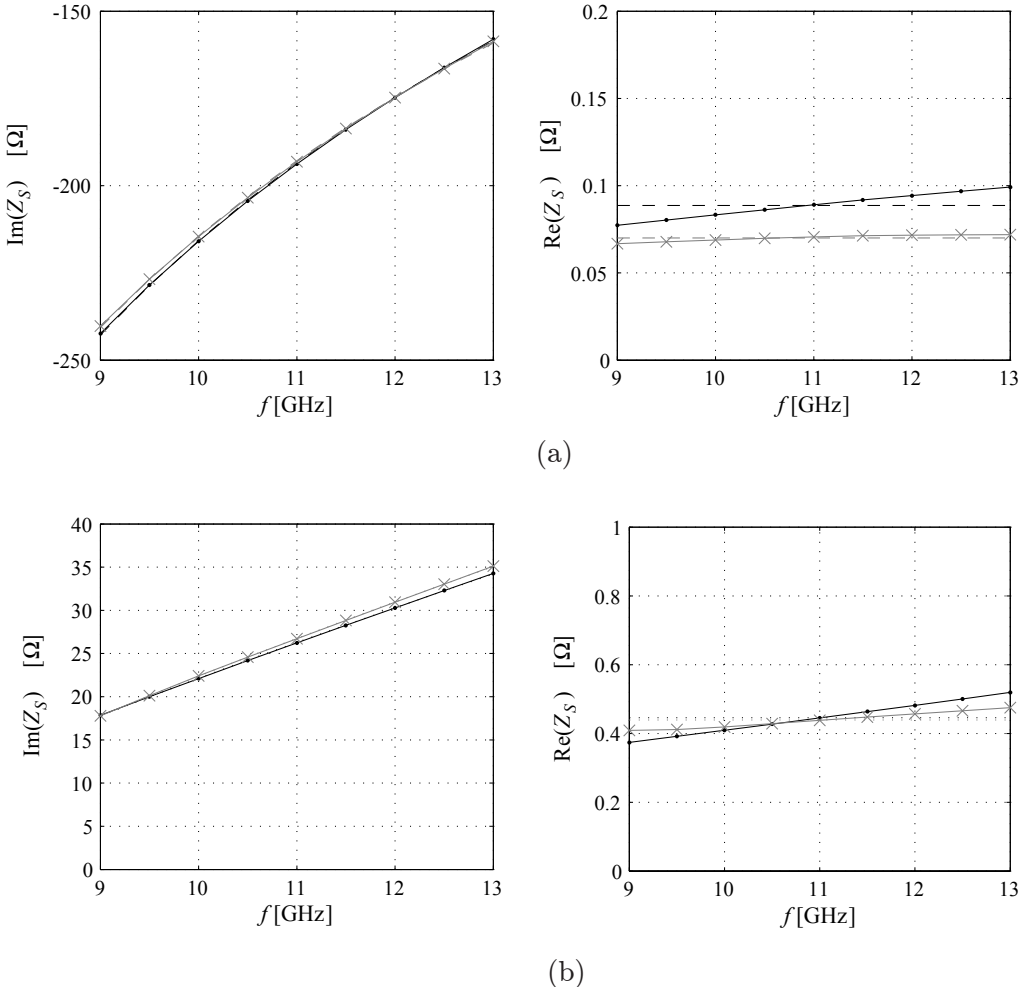

Figure 3.26: Comparison of the simulation results with detailed MEMS geometry (•) and *RLC* boundary (×). (a) Up state, (b) Down state. (—) raw data, (- -) regressions.

3.8.2. Results

As explained previously, the first step here was to simulate the MEMS switch in its detailed geometry, shown in Figure 3.25(a). Note that the biasing line for the MEMS is not present in the simulation, since it was previously tested that it has no influence on the RF response of the device, due to the very high resistivity of the dedicated layer in the 'Al-quartz VTT' process.

First, Let us consider the Up state, namely when the membrane is not actuated. The raw impedance of the MEMS switch is plotted in Figure 3.26(a). Some extraction on this result shows that the device is very well modeled by a series *RLC* network with the following lumped elements values $R = 0.1\ \Omega$, $L = 225$ pH, and $C = 71$ fF, since we observe in Figure 3.26(a) that the regression curves fit very well the simulated impedance (compare solid and dashed lines). As expected, the switch mainly behaves as a series capacitance in the Up state.

The next step is now to replace this MEMS geometry by some lumped RLC boundaries in HFSS. However, this is not as straightforward as putting in series boundaries with the above regressed values, for the following reasons; first, the capacitance value extracted comprises the capacitance due to the MEMS, but also the contribution resulting from the coupling through the substrate between the access lines on each side of the MEMS. This can be checked by carrying out the same simulation but without the MEMS structure [namely, with an 'open' between the two access lines visible in the darkest grey in Figure 3.25(a)]. In this case we extract a series capacitance of $C = 33$ fF, which means that the contribution of the MEMS is only about $C = 71 - 33 = 38$ fF, since it is in parallel with the 'open' capacitance. As a result, the boundary must be set to a lumped capacitance value of 38 fF rather than 71 fF. Concerning the inductance, it results from the currents flowing in the electrodes and membrane of the MEMS. However, when the MEMS is replaced by an equivalent capacitive boundary as proposed here, current still flows through the boundary and the inductive effect remains. In other words, the inductance extracted above should not be included as an L boundary in the simulation since this would mean 'accounting twice' for the inductive effect in the MEMS.

These affirmations are simply verified by comparing the results for the detailed geometry with the simulation where the MEMS is replaced by a boundary condition corresponding to a lumped C element of 38 fF in series with a lumped R boundary of 0.1 Ω. This is done in Figure 3.26(a): a very good agreement between both simulation setup is obtained, which confirms the above considerations and validates the possibility to replace the detailed MEMS geometry by a simple boundary condition in HFSS. It is noticeable that a similar verification is also carried out in Chapter 9, considering then the whole reflectarray cell.

The same approach was employed in the Down state and is thus not detailed here. The lumped model for the MEMS is again a RLC series network (but behaves now mainly as an inductance), with numerical values for the boundary conditions $C = 1500$ fF, $L = 150$ pH, and $R = 0.3$ Ω. In Figure 3.26(b) are compared the extracted results from the detailed simulation and simplified RLC boundaries setup. Here again, we observe that the simplified setup accounts very well for the detailed geometry.

3.9. Chapter appendix: Enhanced conformal mapping CPW modeling

The method employed to compute the characteristics of the CPW lines in the optimization procedure of Chapter 4 is based on the conformal mapping method. Most of the formulas used are presented in [33] and will consequently not be repeated. However, some particular steps were taken to obtain reasonable accuracy of the computed values and are described in this appendix.

1: Skin depth and surface resistance

In order to calculate the conductor losses, it is necessary to assess the skin depth δ over the frequency range of interest:

$$\delta = \sqrt{\frac{2}{\omega\mu\sigma}} \tag{3.18}$$

Usually, the calculation of the surface resistance is made under the assumption that the conductor thickness t is much greater than the skin depth, hence the formula for the surface resistance in [Ω/square]:

$$R_{S,HF} = \frac{1}{\delta\sigma} \tag{3.19}$$

where σ is the metal conductivity. However, in the case where the ratio t/δ is not large enough for the above formula to be valid, the formula is 'corrected' in order to take the finite thickness of the metallization into account [36].

$$R_{S,LF} = \frac{1}{\delta\sigma}\left[\frac{\sinh(2t/\delta)+\sin(2t/\delta)}{\cosh(2t/\delta)+\cos(2t/\delta)}\right] \tag{3.20}$$

Finally, we can calculate the DC surface resistance. This is straightforward and we obtain:

$$R_{S,DC} = \frac{1}{t\sigma} \tag{3.21}$$

The resistance calculated with these three different formulas, so together with the ratio t/δ, are plotted in Figure 3.27 for a typical micromachined line with 1 μm aluminium on Hi-Res silicon. We observe that:

- At high frequencies, $R_{S,HF}$ is equal to $R_{S,BF}$. This means that the ratio t/δ is large enough to consider the skin depth negligible when calculating the surface resistance. This occurs for a relatively small ratio $t/\delta = 2.5$.
- Below $t/\delta = 1.2$, $R_{S,BF}$ becomes larger than $R_{S,HF}$, which was expected and means that the thickness is small enough compared to the skin depth so that the resistance increases with reduced thickness.
- $R_{S,BF}$ tends to $R_{S,DC}$ at very low frequency, which validates the formula for $R_{S,BF}$ at low frequencies.

As a conclusion, it is necessary to use Formula (3.20), which takes into account a finite conductor thickness, in order to compute correctly the characteristics of the line at rather low frequency. It is important to remind here that the conductor losses of a CPW line are proportional to the surface resistance. Therefore, using wrongly the high frequency formula for the resistance would lead to a very significant under-estimation of the line losses under the frequency where $t/\delta = 1.2$. For instance, for typical lines on the 'Al-Si EPFL' process, an error of 300% occurs at 1GHz.

2: Perturbation method

The impedance calculated with a conformal mapping method is real, which means that the losses are not taken into account in its calculation. The losses are computed in a second step and we can use a perturbation method in order to obtain a complex impedance taking the losses into account. The impedance calculated with the conformal mapping corresponds to the real part Z_{0R} of the impedance so we have:

$$\frac{\gamma_0}{Z_0} = j\omega C + G \quad \rightarrow \quad \beta_1 = Im\left[Z_{0R}\left(G + j\omega C\right)\right] = Z_{0R}\omega C \tag{3.22}$$

where C and G are the CPW distributed capacitance and conductance. α is calculated separately by the conformal mapping method, and since we also know that $\alpha_d = G_t Z_0/2$ (α_d this is the substrate loss only) [33], the complex characteristic impedance Z_{0C} is:

$$\frac{\gamma_0}{Z_0} = j\omega C + G \quad \rightarrow \quad Z_{0C} = \frac{\gamma_0}{G + j\omega C} = \frac{\alpha + j\beta_1}{G + j\omega C} = \frac{\alpha + jZ_{0R}\omega C}{2\alpha_d/Z_{0R} + j\omega C} \tag{3.23}$$

Figure 3.28 shows an example of complex impedance obtained with this simple method, which corresponds to a CPW designed on a *low-resistivity* silicon substrate. In this case, the losses are very important and Z_{0C} is far from being a frequency-constant, real parameter. The agreement with a full-wave simulation is very good.

3: Conformal mapping capacitance correction

One limitation of the conformal mapping method is that it is unable to consider non-infinite dielectric layer such as the SiO_2 insulator layer of the Al-Si EPFL process. However, the removal of this dielectric in the slots of the CPW has a non-negligible impact on the distributed capacitance of the line, since most of the electric field is concentrated at the edges of the CPW. So, a possibility is to calculate the capacitance by neglecting the insulator layer. The error introduced depends on the insulator thickness, the difference between substrate and insulator permittivities and also on the dimensions of the CPW with regard to the thickness of the insulator. However, for a given technology, the only parameter that varies is the size of the CPW. Thus, for a reasonable range of CPW dimensions, we can introduce a corrective factor in the calculation of the capacitance, deduced from a simple static 2-D capacitance solution or using HFSS and the method explained previously. In practice, this correction is about 2-3% on the capacitance value in the case of the 'Al-Si EPFL' process.

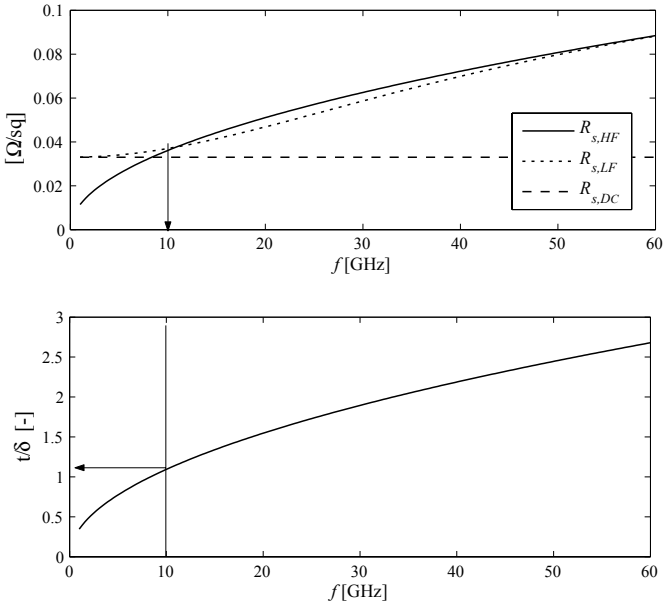

Figure 3.27: Illustration of the surface resistance as a function of frequency using different formulas.

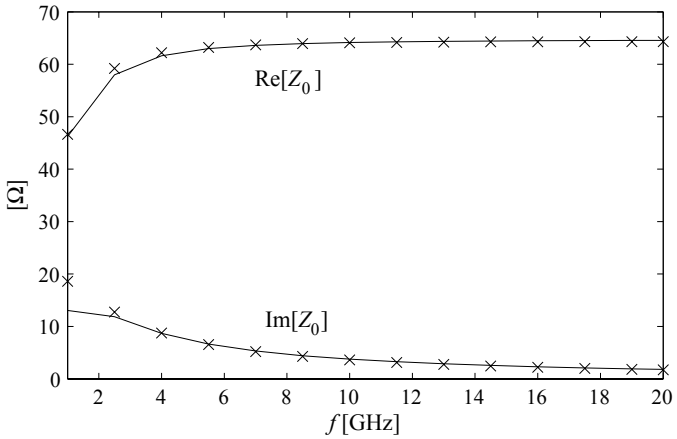

Figure 3.28: illustration of the complex impedance obtained by the perturbation method (×) and comparison with simulated results (—) for a 85/60/85μm CPW on low-resistivity silicon.

4. Distributed MEMS Transmission Lines (DMTLs)

4.1. Introduction

4.1.1. Content and organization of the chapter

In this chapter, we present the design strategies and results obtained for the distributed MEMS transmission line (DMTL), which is a typical microwave MEMS periodic structure. The organization of the chapter is as follows: first, we introduce the DMTL in the more general context of MEMS variable true-time delay lines (V-TTDLs). Applications for V-TTDLs are then discussed along with related calculations, in order to deduce relevant information for the DMTL optimization strategies. The developed design algorithms based on the periodic structure approach are then explained step-by-step. Finally, some measurements for an analog and a digital DMTL are presented, along with circuit model results.

4.1.2. MEMS-based V-TTDLs

There is a significant amount of publication concerning MEMS-based V-TTDL topologies. Here, we first describe the main features of the most popular V-TTDL configurations and introduce the structure of interest in this chapter, namely, the DMTL.

The *switched type* V-TTDL is based on transmission lines of different length which are switched to produce different delays. It has good performance over a large bandwidth but device size is its major drawback. The bandwidth (BW) is not limited by the dispersion in the line but rather by the quality of the switching devices. A high-performance device using microstrip technology and based on the switched lines principle is presented in [37], and is depicted in the left hand side of Figure 4.1. The *switched type* V-TTDL uses the 'space' to produce a change in the delay while the 'velocity' is kept constant. In contrast, the *distributed type* V-TTDL takes advantage of the possibility to control the wave velocity, while keeping the length of the propagation path constant. This approach is the best in terms of space but also provides a very wide BW. Regarding these advantages, the *distributed type* delay lines have been the most widely studied and many results can be found in the literature (e.g. [18,31,34]). The easiest way to control the velocity in such lines is by using MEMS to vary the distributed capacitance. Usually, this control is made by means of MEMS variable capacitors connected periodically in parallel with the TL. The corresponding structure was thus named the *distributed MEMS transmission line* (DMTL) in [30].

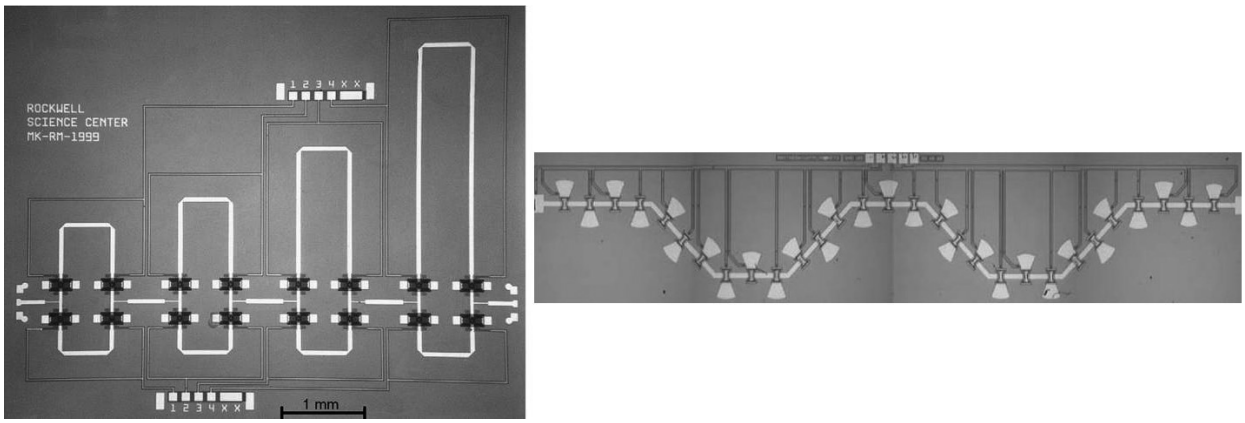

Figure 4.1: Pictures of the switched-type MEMS V-TTDL of [37] (left) and distributed-type V-TTDL of [38] (right).

It is finally noticeable that, although most designs have been done on CPW lines, it is also possible to realize microstrip distributed TTDL [39] (see the right hand side of Figure 4.1). Another kind of distributed delay line is presented in [38]. In this case, the variation of the distributed capacitance is achieved by controlling the strip to group plane distance. When compared to the aforementioned distributed types, this realization reveals to be more complex in terms of design, fabrication complexity, and requires hundreds of volts for the actuation.

4.1.3. V-TTDLs Applications

a. Introduction

This section first discusses some applications of V-TTDLs. Although there are some possible applications in ultra wideband (UWB) telecommunication subsystems, it is generally understood that the main field of application of V-TTDLs is for the feed networks of phased arrays. By briefly showing why and in which feed network configuration V-TTDLs are useful for phased arrays, we intend to show how the phase error of the V-TTDL should be characterized with regard to this particular application. These results will be of use when developing methods for the optimization of DMTLs in the next sections of this chapter.

b. Communication system

In UWB systems, there is a need for increased sampling rates. For instance, in the case of an all-digital UWB receiver, the received signal is immediately converted by high speed A/D converters. However, the maximum sampling rate is determined by the speed of the conversion (not to be confused with the acquisition speed). In order to design UWB systems where a very high sampling rate is required, there is a need to overcome the limitation of the speed of the converter by operating different converters in parallel, as shown in Figure 4.2. This requires a precise control of the true-time delay blocks between antenna and converters. In advanced architectures, it can be envisioned

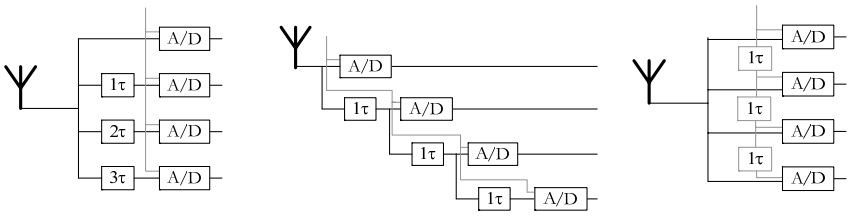

Figure 4.2: Parallel sampling strategies in UWB systems

to use V-TTDL to substitute for the numerous delay lines for space saving in mobile receivers. In practice, such parallel acquisition also suffers from imprecision in the delays, which could then be corrected by a real-time correction of the delays thanks to V-TTDLs.

c. Array corporate feed network

Introduction

Figure 4.3 shows the example of a 1-D array with its *corporate* (or *parallel*) feed network. The BW of arrays and phase arrays depends on the radiating elements, but also on the feed network. In general, the radiating elements are matched over a broad band and the array BW is mostly determined by the feed network and phase shifters [40]. It is important to observe that while the matching of the radiating element limits the BW of the array from a *reflected energy* point of view (*matching BW*), the feed network structure induces another form of limitation to the BW, which is a dependence of the scan angle on the frequency (named here *scan angle BW*). As will be shown below, the scan angle BW is linked with the phase properties of the feed network.

There are naturally also other limitations to the BW of arrays, which are beyond the scope of this document. Nevertheless, it is noticeable that they are not only 'phase' issues in the role of the feed network in the array BW since the performance of the power splitter and the matching of the different lines in the feed network will also influence the matching BW of the array. For instance, in digital operation, the phase shifter in each branch of the feed network must actually be constituted of a cascade of sub-phase shifters in order for several angles to be scanned (with a single digital phase shifter in each branch, the array would only be able to scan at 0^o, $-\alpha$ and $+\alpha$ with regard to broadside). Consequently, the mismatch can be a very limiting factor in the feed network if the scan angle resolution is high.

For the sake of simplicity, let us consider a 1-D array such as depicted in Figure 4.3. This is not a limitation since the concepts developed here are also valid for 2-D arrays. If the array is scanned to the angle α_s with regard to azimuth, this means that the waves from each antenna interfere constructively in the plane perpendicular to that direction and, referring to Figure 4.3, we can write:

$$\theta_{space} = \theta_{el} + 2n\pi \tag{4.1}$$

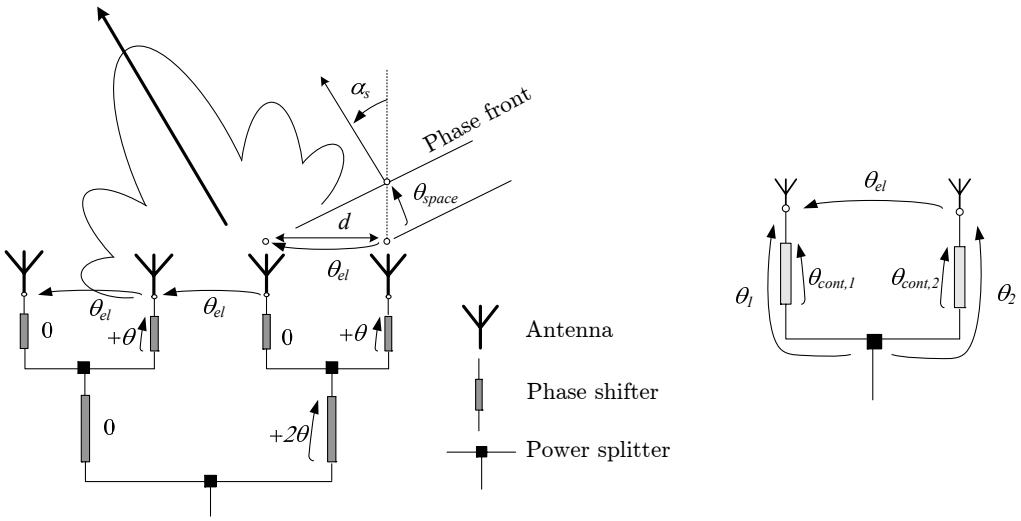

Figure 4.3: Principle of a corporate-fed phased array and some variables definition.

where θ_{el} is the inter-element electrical phase shift and n can be negative or positive. It is easily shown that the phase shift associated with the propagation from the antenna to the given phase front is:

$$\theta_{space} = -\frac{2\pi d \sin \alpha_s}{c} f \tag{4.2}$$

where d is the inter-elements spacing and c the speed of light in the surrounding medium. So, we obtain an expression for the electrical phase shift to be imposed between elements in order to obtain a given scan angle α_s:

$$\theta_{el} = -\frac{2\pi d \sin \alpha_s}{c} f + 2n\pi \tag{4.3}$$

Corporate feed phase scanning

True-time delay: The right hand side of Figure 4.3 shows the phase shifts of interest θ for the following analysis in the last level of the corporate feed 'tree'. The developments will be done only for this stage, but it is straightforward that they apply to the whole network, if the phase shift is doubled when decreasing one level in the 'tree' (see Figure 4.3).

We use here the notation:

$\theta_{cont,i}$:	Total phase shift of the controlled phase shifter i.
$\theta_{line,i}$:	Phase shift produced by the line section i, except for the controllable part [see (4.4)].
$\Delta\theta$:	Phase difference between two *states* of the phase shifter.

From the figure, we easily deduce that (for simplicity, a perfectly matched structure can be considered at this stage):

$$\theta_{el} = \theta_1 - \theta_2 = \theta_{line,1} + \theta_{cont,1} - \theta_{line,2} - \theta_{cont,2} \tag{4.4}$$

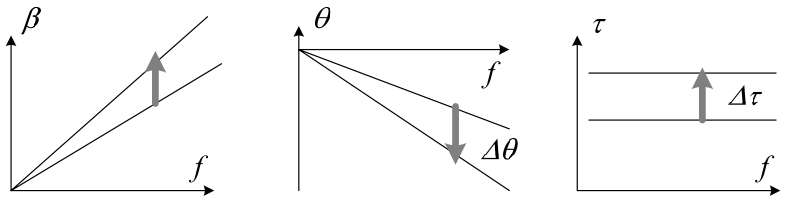

Figure 4.4: Ideal phase and delay properties of a V-TTDL

In the case of this corporate feed, the 'non-controllable' phase shifts $\theta_{line,i}$ cancel each other out in the above subtraction, so we have:

$$\theta_{el} = \theta_{cont,1} - \theta_{cont,2} \equiv \Delta\theta \tag{4.5}$$

Finally, we make use of expression (4.3), where n can obviously be set zero in this case, and find:

$$\Delta\theta = -\frac{2\pi d}{c} \cdot \sin\alpha_s \cdot f \tag{4.6}$$

Inspection of (4.6) shows that, for a narrowband array, a simple device producing the required phase shift $\Delta\theta$ between different states at the operation frequency f allows to scan the desired angle. However, in the case of a wide band phased array, we want the scan angle to be frequency independent. An observation of the above expression readily shows that this means that the phase shift $\Delta\theta$ must be proportional to the frequency. This will be the case for a phase shifter whose phase shift is proportional to the frequency, as shown in Figure 4.4, which is called a variable true-time delay line (V-TTDL) since the associated propagation delay is frequency independent.

In conclusion, the *scan angle BW* of a corporate-fed array with V-TTDL controllable elements corresponds to the band where the V-TTDL dispersion is below a certain level, determined by the maximum error allowed for the scan angle. If a good performance is achieved from this point of view, the actual BW of the array will in general be determined by the input return loss BW. Finally, it should be noted that V-TTDL are also of use in the case of narrow band arrays, where the use of V-TTDL results in a signal modulating the carrier to be appropriately delayed, hence limiting the dispersion in the demodulated signal [41].

Error quantification: Here we want to determine how the deviation of a V-TTDL from its ideal behavior should be characterized, with regard to the resulting scan angle error in a corporate feed application. In other words, the question we address is: is it right to characterize the V-TTDL by the *phase error* in the BW, such as done in almost all V-TTDL publications (except [37])? To answer this question, let us rewrite equation (4.6) as follows:

$$\alpha_s = \arcsin\left[-\frac{c}{2\pi d} \cdot \frac{\Delta\theta}{f}\right] \tag{4.7}$$

A mere observation of this expression shows that an error in α_s is directly related to the ratio $\Delta\theta/f$ rather than the phase shift $\Delta\theta$ alone. This difference is fundamental for DMTLs since such devices can reach BW greater than a decade. For instance, a phase error of 5°at $f = 1$ GHz results in a

scan angle error 4 times greater than at $f = 4$ GHz, with the same 5°phase error. Consequently, the quality of a true-time delay line (TTDL) in the BW should be given in terms of the $\Delta\theta/f$ error and not in terms of phase error, as long as the corporate feed application is concerned. Finally, let us note that the aforementioned ratio $\Delta\theta/f$ is proportional to the *differential* phase delay ΔD_ϕ of the V-TTDL, which can therefore be used to assess the phase imperfection of the device:

$$\Delta D_\phi = l\left(\frac{1}{v_{\phi 1}} - \frac{1}{v_{\phi 2}}\right) = l\left(\frac{\beta_1}{\omega} - \frac{\beta_2}{\omega}\right) = l\frac{\Delta\beta}{2\pi f} = -\frac{\Delta\theta}{2\pi f} \tag{4.8}$$

where l is the length of the controlled line.

Mismatch: In practice, and particularly in the case of the DMTLs considered in this chapter, the V-TTDLs are not perfectly matched in all states. In order to take into account the effect of the mismatch on the phase of the signals, we must write the differential phase shift between two states i and j as $\Delta\theta_{mis} = \arg(s_{21,i}) - \arg(s_{21,j})$ where $\arg(s_{21,i})$ and $\arg(s_{21,j})$ are the insertion phases of the delay line in two different states of the V-TTDL, referred to the impedance of the reference lines. We can now define a delay which simply corresponds to the phase shift but reported to the time domain:

$$\Delta D_{\phi,mis} = -\frac{\Delta\theta_{mis}}{2\pi f} = -\frac{\arg(s_{21,i}) - \arg(s_{21,j})}{2\pi f} \tag{4.9}$$

If the mismatch effect on the transmission phase is neglected, and only in this case, $\arg(s_{21}) = -l\beta$ and $\Delta D_{\phi,mis}$ stands for the difference between the propagation delays of pure traveling waves as given by (4.8). However, the scan angle is indeed linked with the phase shift *including* the mismatch, and we finally write the scan angle as a function of $\Delta D_{\phi,mis}$ as defined in (4.9), using (4.6):

$$\alpha_s(f) = \arcsin\left[\frac{c_0}{d}\Delta D_{\phi,mis}(f)\right] \tag{4.10}$$

In conclusion, the error in the scan angle is directly linked with the delay error rather than with the phase error and it is thus more appropriate to define the DMTL phase error in terms of delay than in terms of phase. Second, the delay must include the mismatch and must not be considered as the insertion phase βl alone.

4.2. Design

4.2.1. Introduction

In order to explain the design strategies presented in this section, it is useful to first recall the principle of the DMTL and deduce some general characteristics of this device by means of approximate formulas. The principle of the DMTL is sketched in Figure 4.5; MEMS variable capacitors C_P periodically load a TL of unloaded characteristics Z_0, β_0 and distributed parameters L, C. This allows controlling the phase velocity in the line, as suggested by (4.11), which is valid under the assumption that the capacitors are electrically very close to each other ($d \ll \lambda_0$). However, (4.12) shows that varying C_P to control the velocity also results in some modification of the structure characteristic impedance and thus in some mismatch. In practice, there will be losses in the device

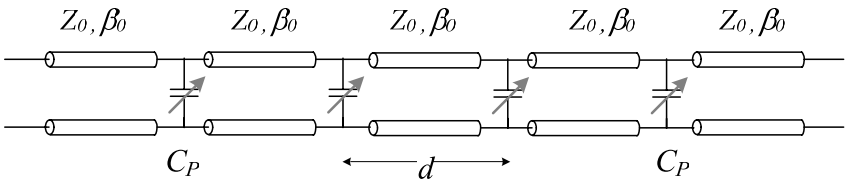

Figure 4.5: Principle of the distributed MEMS transmission line (DMTL).

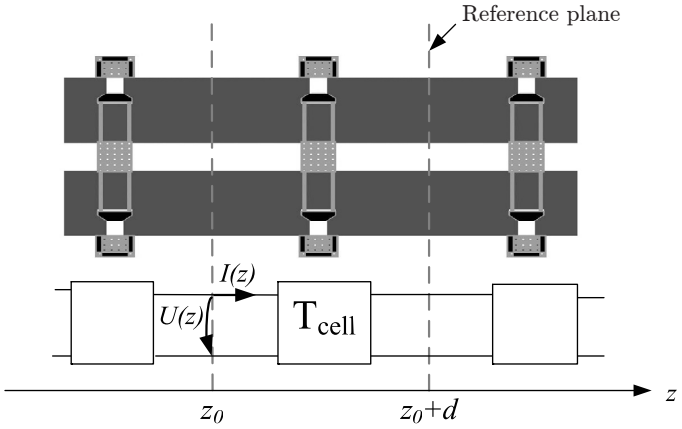

Figure 4.6: Periodic structure representation of a DMTL.

as well. As a result, the design of DMTL mainly consists of optimizing the circuit element values so that a large delay is obtained while guaranteeing minimum mismatch and insertion loss.

$$\beta_0 \approx \omega\sqrt{L\,(C + C_P/d)} \tag{4.11}$$

$$Z_0 \approx \sqrt{\frac{L}{C + C_P/d}} \tag{4.12}$$

We will now explain in detail the design of DMTLs based on the requirements for V-TTDL that were just deduced. More precisely, two systematic design algorithms are explained, which are based on the periodic structure concepts presented in Chapter 2. Indeed, the DMTL is inherently a periodic structure, as suggested in the illustration of Figure 4.6. A very important aspect for a good efficiency of the method is to get a precise circuit modeling of a cell in the periodic structure that the DMTL constitutes. This issue was already addressed in chapter 3, where we presented two 'building blocks' directly intended to this application, namely the analog and digital shunt MEMS capacitor. The equivalent circuit models for these blocks were deduced and the circuit of the digital shunt capacitor is recalled in Figure 4.7.

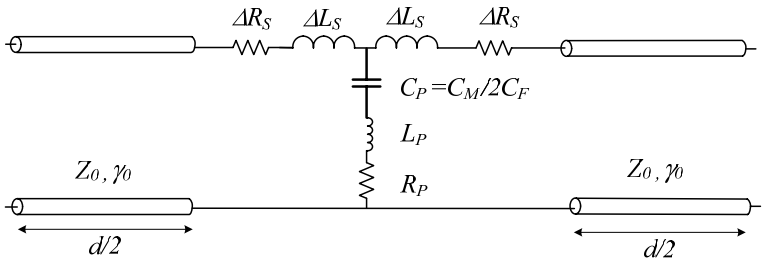

Figure 4.7: Equivalent model for a bridge loading a CPW guide.

4.2.2. Design algorithms

The two design algorithms presented here differ in their optimization goals; the first method, called Minmis, is inspired from developments presented in [42] and [7], while taking advantage of the periodic structure modeling. We also introduce the series elements of the unit cell circuit of Figure 4.7 in the design. In this method, the insertion loss is minimized, but the main requirement is to achieve optimal matching. The second method, called Minloss, minimizes the insertion loss of the line while relaxing the constraint of minimum mismatch.

Note: The methods described here are valid for both analog and digital designs. When referring to the Down state in the case of an analog DMTL, we consider the state corresponding to the maximum deflection in the stable analog range of the MEMS.

a. Minimum mismatch design (Minmis)

All variable definitions and the different steps of this first design algorithm are summarized in Table 4.1 and 4.2, respectively. In step 1, the design starts with making initial choices for the targeted differential delay, the Bragg frequency and the bandwidth for which the optimization is to be carried out. The Bragg frequency of the DMTL periodic structure is the frequency at which the first stopband occurs, as illustrated in Figure 4.8 for a typical DMTL. Obviously, a DMTL will be operated below this frequency. However, the closer the Bragg frequency to the upper limit of the operation band, the larger the dispersion. Therefore, the Bragg frequency given as input here will mainly set the delay distortion in the upper part of the bandwidth of the DMTL.

Concerning the capacitance ratio between Down and Up states C_r, it differs greatly depending on the type of the used loading capacitor, namely up to about 1.3 for an analog MEMS and between 1.5 and 3 for a digital one (see Chapter 3). Thus, the choice of the exact value given as input to the algorithm is made with regard to electro-mechanical considerations and physical limitations for the capacitances. Also, as can be easily understood from the approximate expression (4.11) and (4.12), it is important to consider that higher capacitance ratios will result in larger ratios of differential delay over losses, at the cost of increased mismatch.

For the next steps, the unloaded line impedance Z_0 is left variable, in order to be optimized. The loaded line impedances are temporarily approximated in step 3, by distributing the loading

Table 4.1: Notation

Variable name	Description
$\gamma_0,\ Z_0,\ L_{CPW},\ C_{CPW}$	Unloaded CPW parameters
C_r	Capacitance ratio
f_B	Bragg frequency
Z_{Ref}	Reference impedance
$C_u,\ C_d$	'Up' and 'down' states capacitance
ΔL_S	Bridge series inductance
$Z_u,\ Z_d$	Up and Down approximate impedance
$Z_{equ,u},\ Z_{equ,d}$	Up and Down equivalent impedance
$\gamma_{equ,u},\ \gamma_{equ,d}$	Up and Down equivalent prop. constants
$\Delta\tau$	Differential delay *per unit length*
ΔD	'target' differential time delay
d, l	Cell length, total DMTL length

Table 4.2: MINMIS design method

	Description	Formulas, comments
1	Inputs	Choice of $C_r,\ f_B,\ \Delta D$ and BW
With Z_0 variable (step 2-9):		
2	$\gamma_0,\ Z_0$	Enhanced conf. mapping (see Chapter 3)
3	$C_r \mapsto Z_u,\ Z_d$	$Z_u^4\left(Z_0^2/Z_{ref}^4\right) + Z_u^2(C_r-1) - C_r Z_0^2 = 0$ $Z_d = Z_{ref}^2/Z_u$
4	$f_B \mapsto d$	$d = \frac{Z_d - 2\pi f_B \Delta L_S}{\pi f_B L_{CPW}}$
5	$d,\ Z_u \mapsto C_u,\ C_d$	$C_u = d\left(\frac{L_{CPW}+2\Delta L_S/d}{Z_u^2} - C_{CPW}\right)$ $C_d = C_r C_u$
6	$\gamma_{equ,u},\ \gamma_{equ,d},\ Z_{equ,u},\ Z_{equ,d}$	Formulas (2.6) and (2.19)
7	$\gamma_{equ,u},\ \gamma_{equ,d} \mapsto \Delta\tau$	$\Delta\tau_p = \frac{1}{2\pi f}\left(\beta_{equ,d} - \beta_{equ,u}\right)$ $\Delta\tau_g = \frac{1}{2\pi}\left(\frac{\partial\beta_{equ,d}}{\partial f} - \frac{\partial\beta_{equ,u}}{\partial f}\right)$
8	$\Delta D,\ \Delta\tau \mapsto l$	$l = \underset{f}{mean}\left(\frac{\Delta D}{\Delta\tau}\right)$
9	$\Delta\tau/\alpha_{equ,d} \mapsto Z_0$	Selection of optimum (Z_0 choice)

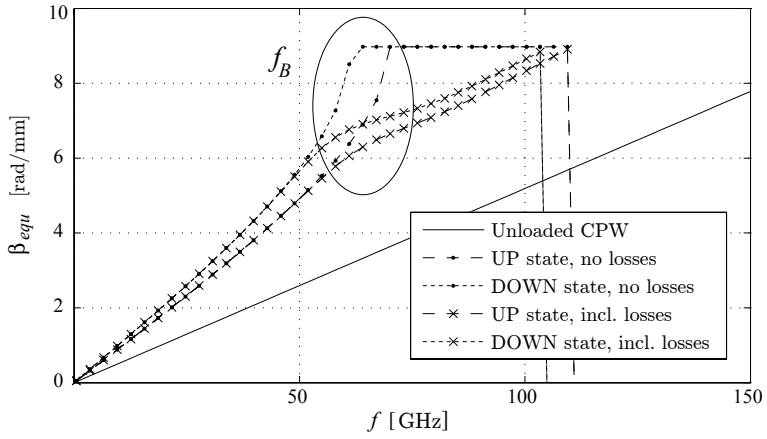

Figure 4.8: Illustration of the Bragg frequency effect for a typical DMTL.

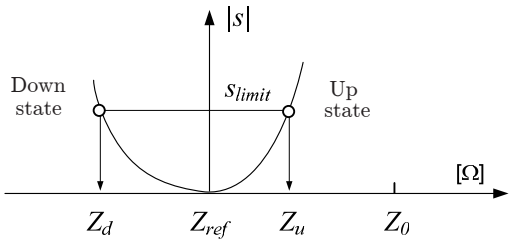

Figure 4.9: Symbolic representation of the impedances of the DMTL.

MEMS capacitance and neglecting ΔL_S in this case (exact calculation of the impedances is made in step 6, but is not convenient at this stage).

As explained previously, the impedances in Up and Down state are different and thus there is necessarily some mismatch in at least one state. Different kind of matching circuits could be imagined in order to match the loaded lines to the reference impedance. Nevertheless, matching circuits based on frequency-dependent properties of stubs [43] or lines are not adequate since we want to design a very wide-band V-TTDL. Moreover, these would have to be reconfigurable. We will come back to this issue in more details in Chapter 5; here, as a result of the evident difficulty in designing a satisfactory wideband, low-loss, and reconfigurable matching network, we will not use any matching circuit but minimize the mismatch as already suggested in [7]. The optimal solution is thus to set the impedances in Up and Down so that there is a minimum mismatch considering both states together. In this case, the mismatch is the same in both states, as symbolically illustrated in Figure 4.9, and some calculation shows that this is equivalent to setting the condition $Z_d = Z_{ref}^2/Z_u$ on the unloaded and loaded impedances. This condition is used in step 3 and this is the reason why this first design method is referred to as Minmis for *minimum mismatch*.

The second order polynomial in Z_u^2 in step 3 of Table 4.2 allows computing Z_u as a function

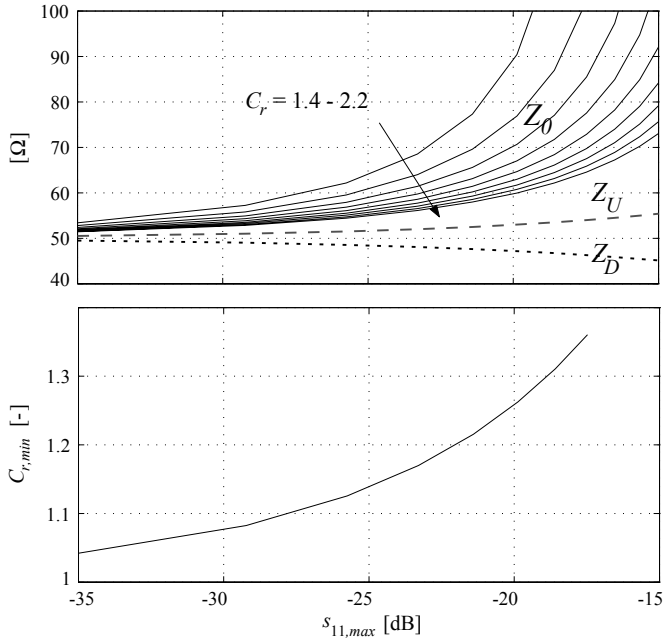

Figure 4.10: Illustration of the relation between impedances, mismatch and capacitance ratio.

of Z_0, C_r and the reference impedance chosen for the design. It can be easily deduced from the distribution of the capacitances in the different states and $Z_d = Z_{ref}^2/Z_u$. Basically, this expression links the impedances illustrated in Figure 4.10 as functions of the mismatch. Obviously, the larger the mismatch, the further away Z_u and Z_d from the reference impedance (which is 50 Ω in the graph). We also observe that when the capacitance ratio decreases, the impedance of the unloaded line gets closer to Z_u. Finally, it should be noted that in order to find a solution for this equation, condition (4.13) must be satisfied, and $C_{r,\min}$ is also plotted in Figure 4.10.

$$C_{r,\min} = \left(\frac{Z_u}{Z_d}\right)^2 \tag{4.13}$$

Step 4 is a closed-form expression for choosing the spacing d between bridges as a function of the Bragg frequency (see above) and Step 5 allows choosing the Up state capacitance C_u from formulas (4.14)-(4.16) [44], where we also include a term accounting for the series inductive component of the bridge.

$$Z_0^2 \simeq \frac{L_{CPW}}{C_{CPW}} \tag{4.14}$$

$$Z_u^2 \simeq \frac{L_{CPW} + 2\Delta L_S/d}{C_{CPW} + C_u/d} \tag{4.15}$$

$$Z_d^2 \simeq \frac{L_{CPW} + 2\Delta L_S/d}{C_{CPW} + C_r C_u/d} \tag{4.16}$$

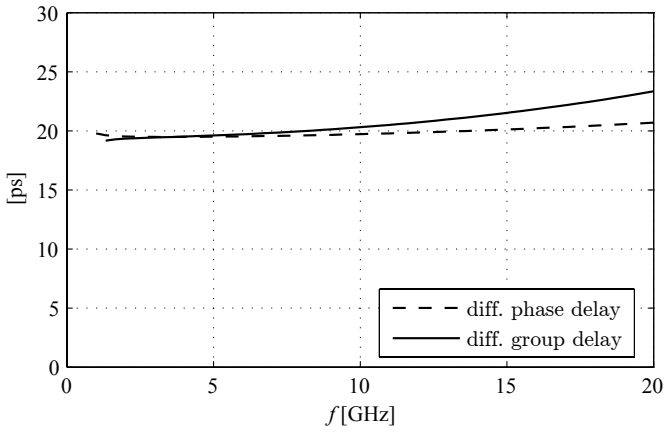

Figure 4.11: Illustration of the effect of the finite Bragg frequency on the differential delay dispersion

The precision of the last design steps is maximized by making use of the periodic structure propagation constant γ_{equ} in step 6[1]. As no assumption is made in this calculation with regard to the circuit model, it allows calculating the losses and the phase properties (respectively related to real and imaginary parts of γ_{equ}) precisely and at any frequency. In contrast, and as mentioned in [44], the expression used for the losses of the DMTL with TL sections modeled with lumped elements [42] is less accurate, especially for frequencies approaching the Bragg frequency. More important in the case of the DMTL, the approach proposed here takes into account series elements such as ΔL_S when computing the losses and the delay (ΔL_S and ΔR_S will be shown to have a significant impact on the delay and losses, respectively). In addition, any model for bias lines or other parasitics can be easily included. Finally, it is noticeable that the use of a full-wave simulator is not convenient at this stage since this calculation is included in an optimization loop. For fast computation, 3-D transmission matrices are used, whose 3$^{\text{rd}}$ dimension accounts for the frequency. In step 7, designs based on the phase delay $\Delta\tau_\phi$ or group delay $\Delta\tau_g$ can be made, depending on the target application ($\Delta\tau_\phi$ for phased array feed, whereas $\Delta\tau_g$ could be preferred in some transmission application).

In step 8, the line length that will produce the goal delay is calculated. In practice, a multiple of the cell length d is chosen by the algorithm so that the equivalent characteristic impedance is known at the input and output of the structure (see Chapter 2). In step 9, the impedance of the CPW line is chosen so as to maximize the delay/losses ratio $\Delta\tau/\alpha$, which concludes the design.

The differential delay can be plotted at this stage, giving a quantitative assessment of the dispersion in the BW. In the upper part of the band, this consists of observing accurately the effect of the choice of the Bragg frequency. An example is plotted of Figure 4.11 for a design with

[1]There are in general sign ambiguities in the periodic Bloch equivalents, which must be appropriately treated as explained in Chapter 2. However, such considerations are not necessary in the case of DMTL structures in the frequency range of interest, namely where they behave as TTDL. Indeed, in this case, each sign can be easily selected by analogy with a continuous transmission line.

a Bragg frequency of 80 GHz. The dispersion is clearly visible in the plot and is, as expected, more important in the group delay. If this dispersion is too important, the design algorithm should be re-run with an increased Bragg frequency. The delay defined by (4.9) also includes the mismatch. In multi-bit operation, the mismatch is especially important in the states where the cascaded lines have different equivalent impedances, and leads to significant oscillations in the differential delays. The method presented allows assessing precisely these oscillations, which can be reduced by decreasing C_r chosen for the design, at the cost of a reduced delay/losses ratio.

b. Minimum losses design (Minloss)

We propose here another design method, called MINLOSS, which minimizes the insertion loss of the line, while relaxing the constraint of minimum mismatch (step 3 in method MINMIS). This approach leads to designs with even reduced insertion loss, which can be useful for applications where the mismatch is not the main requirement. The method MINLOSS is presented in Table 4.3, where only the steps different from the MINMIS method are shown. Relaxing the minimum mismatch condition results in the pseudo-independence of Z_u and Z_d and there is one more degree of freedom for the optimization of the insertion loss. Therefore, it was chosen here to let Z_0 and Z_u variable for optimization. Since the mismatch is not 'fixed' here as it was in case with the method MINMIS, it is also necessary to include its influence on the insertion loss, which is due to the ohmic losses in the line but also to the energy reflected to the source. Therefore, the delay/losses optimization coefficient K_{opt} is written as a function of $|s_{21}|$, as described in step 9b. The insertion loss $|s_{21}|$ is calculated by means of the formula in step 9a for one-bit operation. In the case of multi-bit operation, the most straightforward way to calculate $|s_{21}|$ is to cascade transmission matrices, with each matrix representing a bit line section (in contrast with the transmission matrix of a cell in the periodic structure). These matrices are simple TL section transmission matrices, where the line parameters are the periodic structure Bloch equivalents.

An example of the optimization coefficient K_{opt} as a function of the variables Z_u and Z_0 is depicted in Figure 4.12, in an analog mode ($C_r = 1.22$). The maximum is selected by the algorithm and provides the optimum values for Z_0 and Z_u, which are here 73.7 Ω and 46.5 Ω, respectively (the resulting Z_d is 43.7 Ω). It is noticeable that both Z_d and Z_u are now below the reference impedance 50 Ω, which is a consequence of the fact that losses in the CPW reduce as the impedance decreases. Indeed, in this case, the MINLOSS method selects the solution with minimum insertion loss, while relaxing the mismatch performance. Figure 4.13 shows the insertion loss results obtained with the MINMIS and MINLOSS methods. The curves corresponding to the MINLOSS method exhibit, as expected, lower insertion loss. However, the increased mismatch in the MINLOSS case leads to oscillations in the differential delay. In this example, the amplitude of the maximum oscillation is only 0.2 ps for an overall differential delay of 20 ps. Let us note here that the coefficient K_{opt} is actually optimized with regard to the curve corresponding to the local minima of $|s_{21}|$, which is also plotted in Figure 4.13 (This curve was obtained by some filtering on $|s_{21}|$ implemented in MATLAB). The length of the delay line designed with the MINLOSS method is 10% shorter than its MINMIS counterpart.

Table 4.3: MINLOSS design method (steps different from MINMIS only).

	Description	**Formulas, comments**
With Z_0 and Z_u variable:		
3	$C_r \rightarrow Z_d$	$Z_d = \frac{Z_u \cdot Z_0}{\sqrt{Z_u^2(1-C_r)+C_r Z_0^2}}$
9a	$\gamma_{equ,d},\ Z_{equ,d} \mapsto \lvert s_{21}\rvert$	$\lvert s_{21}\rvert = \frac{1}{\lvert\cosh(\gamma_{equ,d}l)+0.5(Z_{equ,d}/Z_{ref}+Z_{ref}/Z_{equ,d})\sinh(\gamma_{equ,d}l)\rvert}$
9b	$\Delta\tau,\ \lvert s_{21}\rvert \rightarrow K_{opt}$	$K_{opt} = \frac{\Delta\tau \cdot l}{-20\log\lvert s_{21}\rvert}$ Selection of opt. ($Z_0,\ Z_u$ choice)

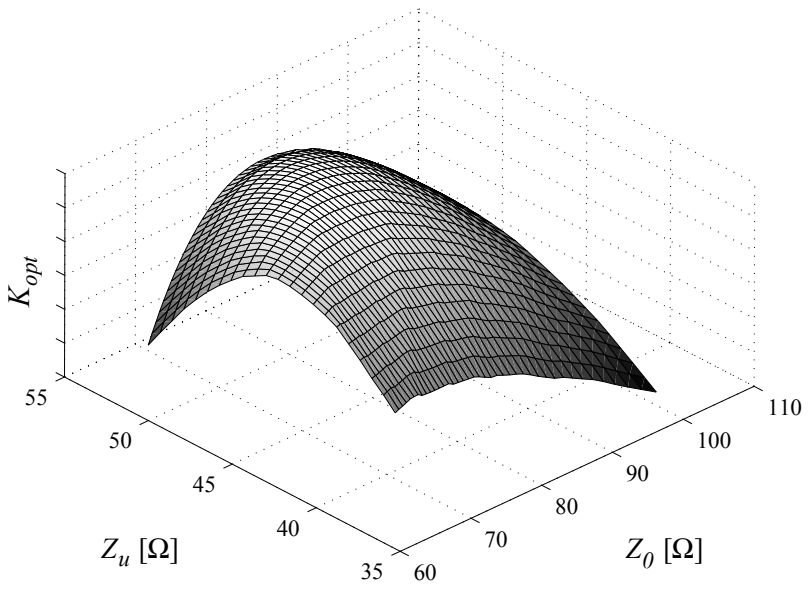

Figure 4.12: Optimization coefficient K_{opt} as a function of the variables Z_u and Z_0.

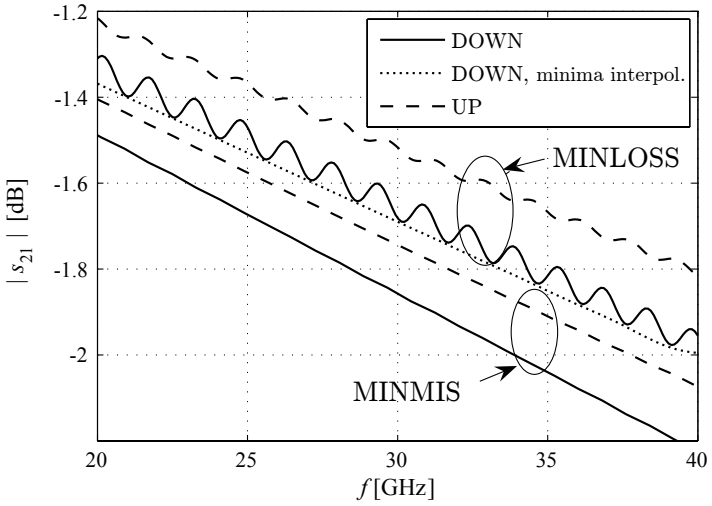

Figure 4.13: Comparison of the MINMIS and MINLOSS design methods results.

4.3. Results

First, we briefly present the measured results for a fabricated analog DMTL. In a second step, we present a digital design along with design details and comparison with circuit model results. All realized DMTLs were designed for operation in the 0.8 - 20 GHz frequency range, the upper limit of this bandwidth being determined by the probe station available for the measurements at the time of this work. The technology employed for the fabrication of the device basically consists of aluminum on high resistivity silicon (details available in Appendix A, 'Al-Si EPFL process')

4.3.1. Analog DMTL

Figure 4.14 shows the layout of the analog DMTL whose measured results are presented in this section. Figure 4.15 to 4.18 present the results for this analog DMTL for actuation voltages varying from 0V to 19V. All those voltages are below the pull-in voltage of the bridges, as is required for analog DMTLs. The insertion phase, shown in Figure 4.15, is linear with frequency and becomes larger when the voltage is increased. The dispersion is better observed with the differential delay plotted in Figure 4.16. The line was designed for achieving a delay of 10 ps (for a capacitance ratio of 1.3), which occurs for a voltage of 19V. The dispersion in the lowest frequency is due to the CPW characteristic impedance frequency variation whereas the dispersion in the highest frequency is linked with the periodic structure of the DMTLs (Bragg frequency).

Figure 4.17 shows the input return loss of the line, which is excellent within the whole bandwidth but limited at lower frequencies by the important imaginary part of the CPW characteristic impedance at such frequencies. The graph also shows that the design method properly 'sets' the loaded line impedances since all the intermediate states from 9 to 18V are better matched than the extreme positions 0 and 19V. Indeed, this means that the equivalent impedances have been

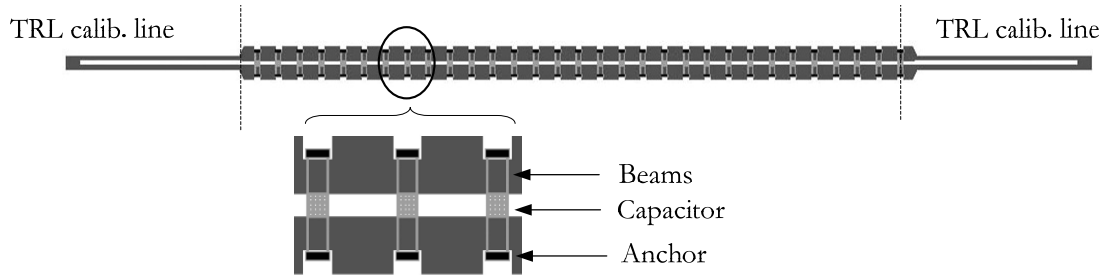

Figure 4.14: Layout of the presented analog DMTL (white: first metal, light grey: second metal, dark grey: slots, black: anchoring).

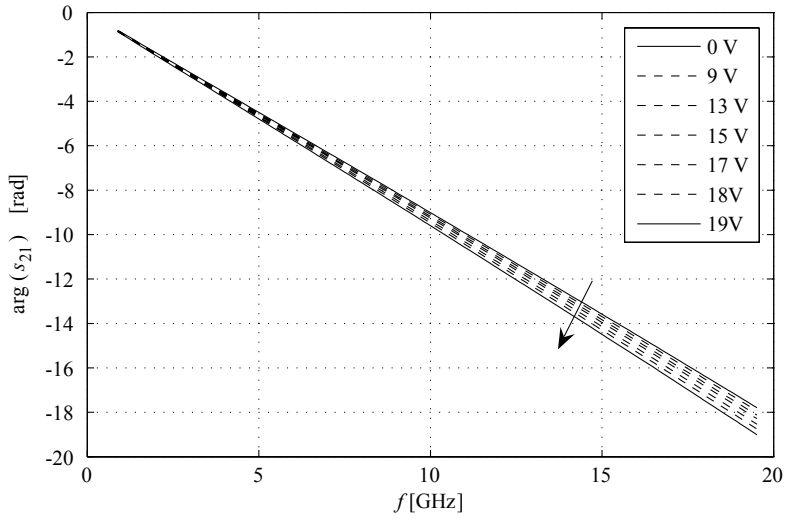

Figure 4.15: Analog DMTL: measured absolute phase shift.

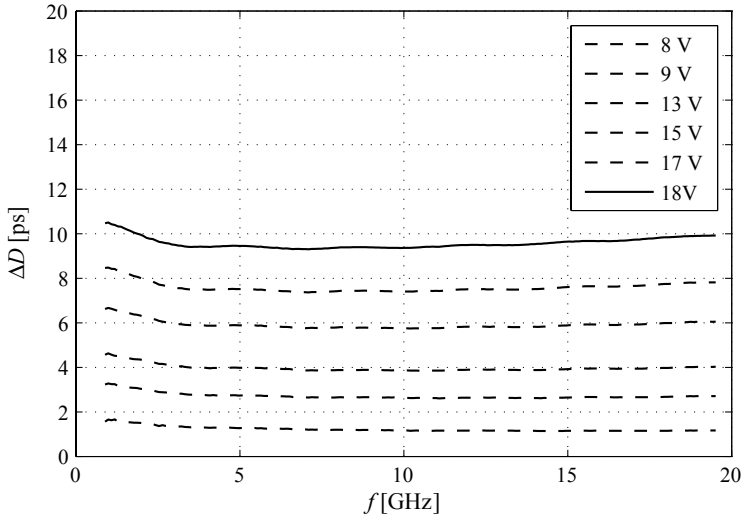

Figure 4.16: Analog DMTL: measured differential phase delay.

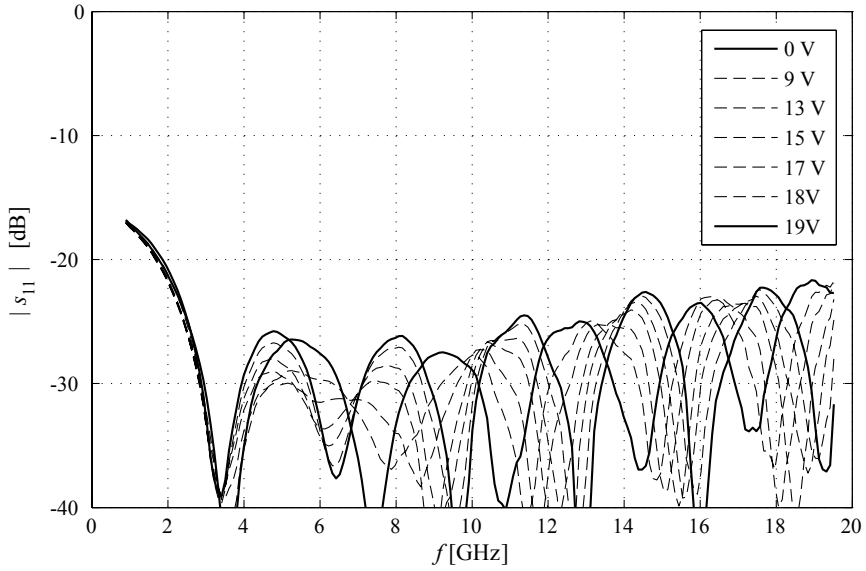

Figure 4.17: Analog DMTL: measured input return loss.

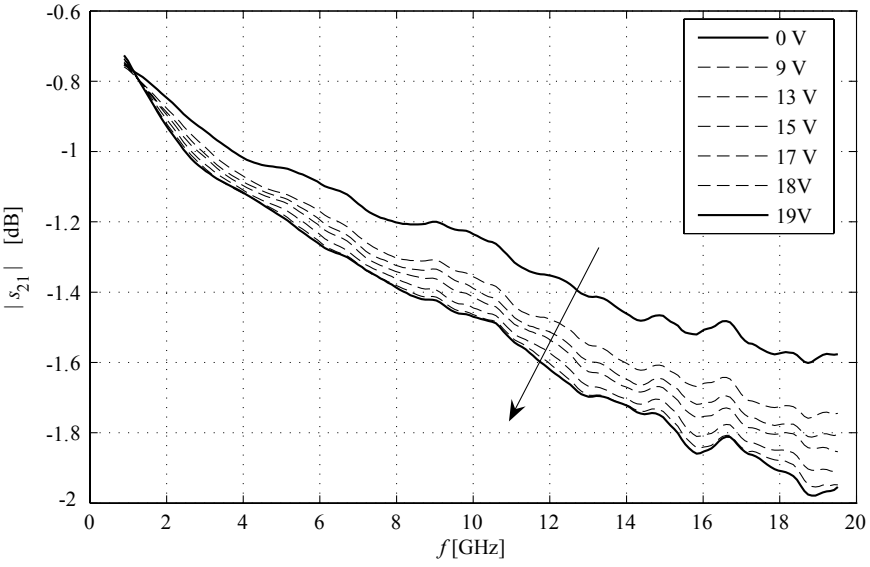

Figure 4.18: Analog DMTL: measured insertion loss.

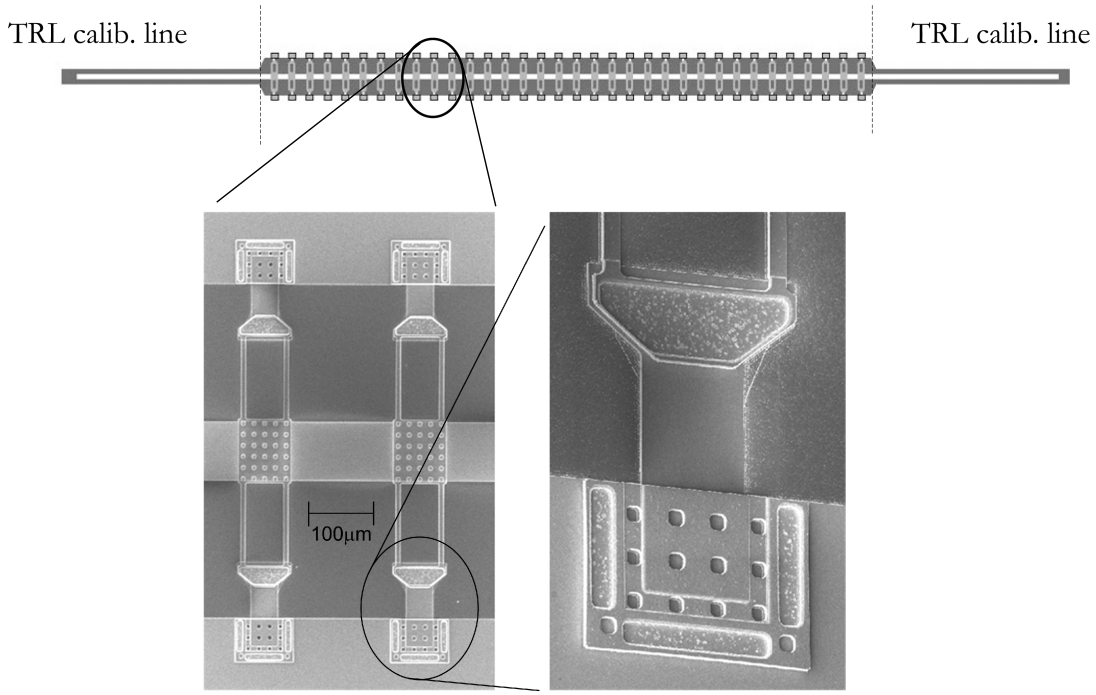

Figure 4.19: Layout and SEM pictures of the presented digital DMTL.

'placed' in an optimal way above and below (resp. for 0V and 19V) the reference impedance of 50 Ω, as suggested by Figure 4.9.

4.3.2. Digital DMTLs

Here we present the measurements and circuit model results for the digital design whose layout and SEM pictures are shown in Figure 4.19. The inputs for the design of the line are a differential delay $\Delta D = 20$ ps, a Bragg frequency $f_B = 80$ GHz and capacitance ratio $C_r = 2$. The circuit model of a cell was presented in Figure 4.7 and the numerical values of the associated lumped elements are $C_u = 58$ fF, $C_F = 29$ fF, $N = 34$ cells of $d = 288$ μm, $R_P = 1\Omega$, $L_P = 50$ pH, $\Delta L_S = -4$ pH and $\Delta R_S = 0.1$ Ω at 20 GHz. The computation of the CPW characteristics is done by means of the enhanced conformal mapping method described previously in Chapter 3.

Figure 4.20 depicts the measured and simulated delay results in terms of phase shift and differential delay. As mentioned previously, this second representation is preferred with regard to the phased array application. It is also noticeable that, although the dispersion is invisible when observing the phase shift, it is well highlighted by the delay plot. The dispersion in the upper part of the band (linked with the periodic structure of the DMTL) and in the low frequencies (due to the dispersion of the CPW characteristic impedance) is perfectly modeled when the mismatch is included in the computation of the delay.

The modeled designed capacitances values have been slightly tuned in order to fit the mea-

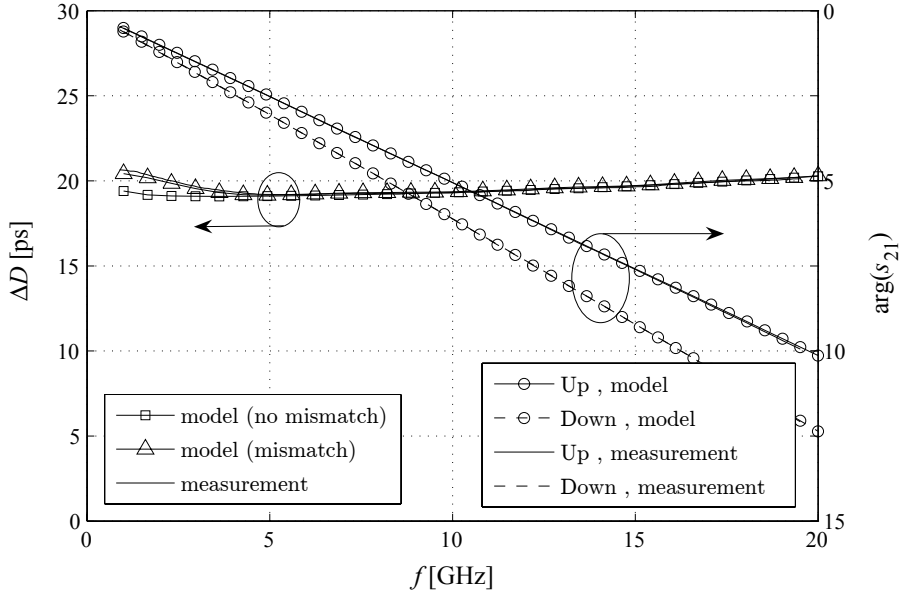

Figure 4.20: Absolute phase shift and differential delay of the digital DMTL, measured and modeled.

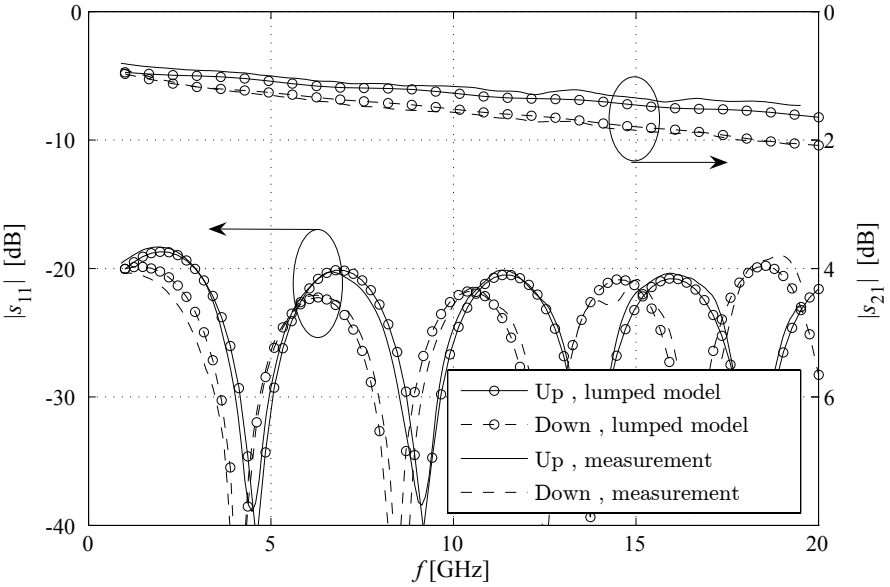

Figure 4.21: Matching and insertion loss of the digital DMTL, measured and modeled.

surements. The difference is not due to modeling issues but linked with the limited precision in the height of the free-standing parts of the structure after sacrificial layer etching, which obviously results in some deviation in the capacitances values. In the case of the DMTL results presented here, the capacitance values have been tuned of about 10% on average. Figure 4.21 exhibits the matching and insertion loss of the delay line. The matching is better than -20 dB in both states. The insertion loss performance is about -2 dB at 20 GHz, which is not as good as state-of-the-art DMTL insertion loss performance [31][1]. This is linked with the fact that the optimized delay/losses performance of DMTLs mainly depends on the losses in the technology on which the design is based. Here, the DMTLs are implemented on the Al-Si EPFL process and it was shown in Chapter 3 that this process exhibits higher losses than a process on quartz substrates for instance, hence the lower performance of our device in comparison with [31].

a. Influence of the series elements on the DMTL performances

In Chapter 3, we commented on the series elements ΔL_S and ΔR_S of the circuit of Figure 4.7 in the context of the simulation or measurement of a single MEMS capacitor. Concerning ΔR_S, no clear confirmation of the simulations could be drawn from such a measurement, due to the importance of the incertitude with regard to the small resistance values highlighted by the simulations. However, the importance of ΔR_S can be observed when modeling a complete DMTL, taking into account or neglecting ΔR_S in the bridge model, as shown in Figure 4.21 in the case of the digital DMTL presented here. It is observed that the insertion loss is very sensitive to ΔR_S and that neglecting ΔL_S results in some error in the computation of the mismatch $|s_{11}|$, which means that the series elements should be considered in both the modeling and in the optimization process.

4.3.3. Electromechanical properties

Although the mechanical design and analysis of the structure was not the focus of this work, the repeatability of the device characteristics (i.e. the similarity between the results for two instances of the same design) was tested and is shown in Figure 4.23 to be very good. The narrow suspension beams (10 μm) were designed for an actuation voltage of 20 V. This is already low for digital capacitors [31, 34], but could even be reduced by means of a 'separate actuation' as explained in Appendix A. No degradation in mechanical behavior was observed by the use of such narrow beams.

[1] Note that in general, DMTLs performances are given in terms of the differential phase shift per dB of insertion loss. This figure of merit is however misleading because it increases with frequency for a given design, as a result of the proportionality between phase shift and frequency in the DMTL, whereas the losses increase less rapidly with f, namely with $\sqrt{f}$ as long as metal losses are concerned).

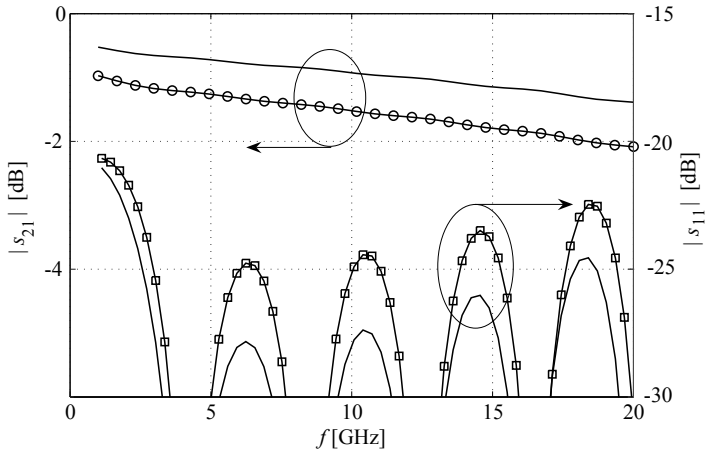

Figure 4.22: Effect of the bridge series element in a DMTL structure (Down). No series elements (—), $\Delta R_S\,(20\text{ GHz}) = 0.1\ \Omega$ (○), $\Delta L_S = -4$ pH (□).

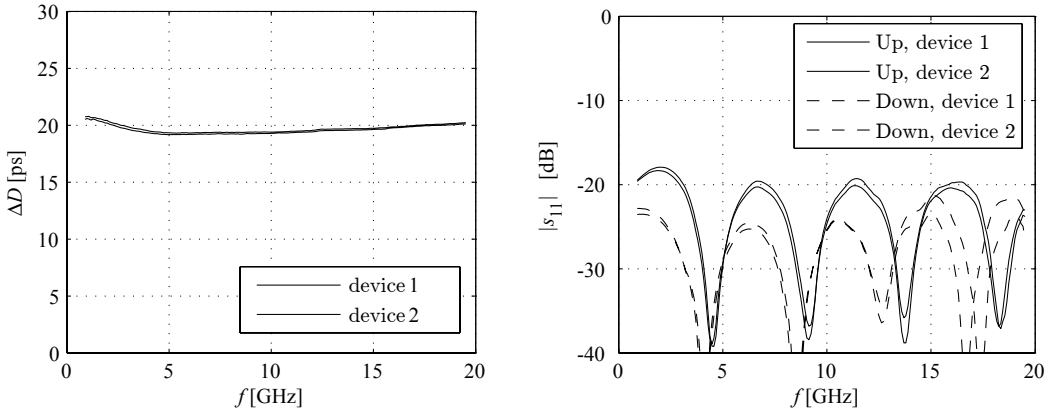

Figure 4.23: Test of the repeatability: measurements of two instances of the same digital design.

4.4. Conclusion

Powerful methods for the design of DMTLs have been presented, based on the periodic structure theory addressed in Chapter 2. In addition, the accurate analysis of the building block of the DMTL, presented in Chapter 3, allowed for a better analysis and reduction of the parasitics. The designed analog and digital devices have been successfully measured and the detailed circuit models used for the design proved to account very precisely for the measured results. The approach was applied to an existing DMTL structure. However, the analysis does not focus on a particular DMTL topology or MEMS equivalent circuit. Therefore, it could be of use for other types of DMTLs, such as the one presented in [45].

5. Multi-bit DMTLs: the interlaced-bits topology

5.1. Introduction

5.1.1. Organization of the chapter

In this chapter, we present a new and simple solution to improve the matching of multi-bit DMTLs, which is an important limitation of digital DMTL implementations. First, we will discuss the issue of matching in conventional multi-bit DMTL and introduce the new topology. The advantage of the latter will then first be intuitively explained by means of the periodic Bloch wave equivalents. Secondly, an analytical approach based on realistic approximations and the concept of small reflections will demonstrate the advantages and limitations of the new topology over its usual counterpart, in a very general manner. These results will be validated by actual DMTL numerical applications.

Next, a design strategy for the new topology will be discussed, based on the design method presented in Chapter 4. Finally, complete designs of 2-bit phase shifters of the conventional and new types will be carried out to validate the design method proposed and demonstrate the advantages of the new topology on a concrete basis.

5.1.2. Mismatch in multi-bit DMTLs

We explained in the previous chapter that the performance of DMTLs in terms of differential delay over losses was significantly improved by increasing the MEMS capacitance ratio, which is one of the advantages of replacing the loading analog capacitors with digital ones. However, it was also shown that this improvement is necessarily at the cost of a larger impedance difference between Up and Down states, hence a larger mismatch.

In the example of digital DMTL realized in the previous chapter, the input return loss was satisfactory, namely about -20 dB. However, this figure corresponds to a single bit DMTL only, whereas most practical applications require multi-bit resolution. For instance, and as already mentioned, each branch in a corporate array feed network must have several bits in order to scan more than 2 angles in addition to broadside. In this case, the mismatch can become prohibitive for good delay/losses performance, at least in some of the states operated. Indeed, although states 0000 and 1111 of a 4-bit phase DMTL will be correctly matched, it will not be the case for states 0101 and 1010, for which 3 additional important impedance discontinuities occur at the transition

between the different bit sections 0 and 1.

Since the main reason for implementing a DMTL is to obtain a constant delay over a very wide bandwidth, it is not possible to use conventional, frequency-dependant matching techniques. Even if operated over a relatively narrow band, the matching circuits would have to be reconfigurable, and such complicated structures would introduce losses larger than the ones of the DMTL itself. Concerning the tapered match, it requires a length comparable with the wavelength. This solution is therefore too space consuming for most monolithic microwave integrated circuit (MMIC) applications and would also increase the overall insertion loss of the DMTL. In [45], the matching of the DMTL is improved by using a loading element that is not purely capacitive but also modifies the distributed inductance in the line, thus controlling the velocity while preserving an impedance close to the reference impedance. However, this very interesting solution is much more complex than the one proposed here and also introduces some small degradation of the other parameters of the DMTL with regard to a conventional implementation. In summary, the problem with the existing matching strategies is linked with the fact that the DMTL itself exhibits very good linearity and insertion loss performance thanks to its simplicity; thus, any improvement in terms of matching is generally overshadowed by additional losses or non-linearities in the delay. In this context, the solution proposed here improves the matching of multi-bit DMTL without significantly increasing the complexity of the device.

5.1.3. IB-DMTL structure description

When multi-bit operation is required for DMTL ($N > 1$ bits), the usual approach is to cascade a number N of DMTLs as presented in Chapter 4, each of those providing a delay corresponding to a bit weight (e.g. [31, 46]). This structure is schematically depicted in the upper part of Figure 5.1 in the case $N = 2$ and will be referred to here as the CB-DMTL for *cascaded bits DMTL*. In the lower part of the figure, we propose a new structure where the bridges actuated by the different bits are not cascaded, but interlaced. This structure will be referred to as the *interlaced bits DMTL* (IB-DMTL). Both structures are operated in four different states determined by the value of each control bit, named AB in the CB-DMTL case and CD in the IB-DMTL case (see Figure 5.1). These different states will be referred to in this document using the bit values, i.e. 00, 01, 10 and 11. The bits '0' and '1' mean that the corresponding MEMS capacitors are in the Up and Down states, respectively.

It should be noted here that the evolution from CB to IB-DMTL does not simply consist of operating a single section of the CB-DMTL with 'four-state MEMS capacitors' since there are line sections between the two types of bridges C and D, in order to limit the dispersion at the high frequencies (Bragg frequency). In addition, it is clear that although the bridges for bits A and B are the same in the CB-DMTL topology, it is not the case for the bridges controlled by the bits C and D in the IB-DMTL case. More details about these issues will be given when presenting the design method for IB-DMTLs later in this chapter.

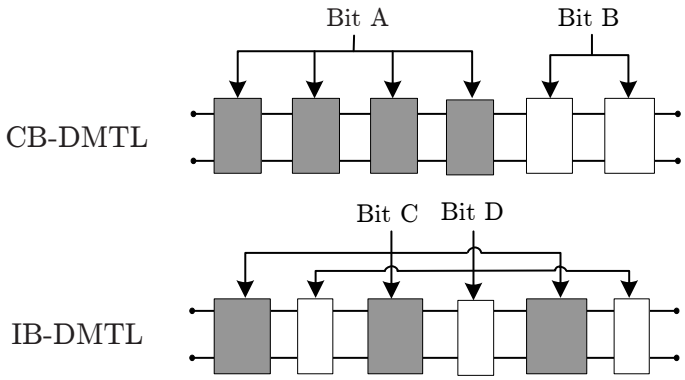

Figure 5.1: Illustration of the cascaded-bit (CB) and interlaced-bit (IB) topologies in a 2-bit case

5.2. Performance analysis of the IB-DMTL structure

5.2.1. Intuitive periodic structure approach

In order to understand the main difference between both DMTL types, let us qualitatively study the equivalent characteristic impedances of the structures, based on the diagrams of Figure 5.2. First, we consider the case of the 2-bit CB-DMTL, which can be modeled by two cascaded TL sections in the sense of the Bloch wave equivalence explained in Chapter 2, as shown in the left of Figure 5.2(c). In order to minimize the mismatch in the four states altogether, the equivalent characteristic impedance of each section in the state 0 (Up state, high impedance Z_u) is placed above the reference impedance Z_{ref}, while the impedance in state 1 (Down state, low impedance Z_d) is below Z_{ref} according to $Z_d = Z_{ref}^2/Z_u$, as explained in Chapter 4. In the case of the IB-DMTL, there is only one periodic structure Bloch TL, but with four different characteristic impedances, which will be 'placed' by an appropriate design method as schematically shown in the right of Figure 5.2(d).

In states 00 and 11, both structures will exhibit approximately the same matching properties since they correspond to single lines of very similar impedances [see Figure 5.2(d)]. Now, let us observe that in the case of the CB-DMTL and for states 01 and 10, the mismatch will be larger than in states 00 and 11, because there is an additional impedance discontinuity at the transition between the two line sections. States 01 and 10 are therefore the critical ones for the matching performances of the CB-DMTL structure. This problem is solved by the IB-DMTL topology since there is no discontinuity in the line in terms of Bloch impedance, and that the impedance in the states 01 and 10 is close to the reference impedance. Intuitively, this can be understood by the fact that an IB-DMTL unit cell is small in terms of wavelength, which results in some *averaging* of the impedance along the structure in states 01 and 10. This is not the case of the CB-DMTL, where an important impedance discontinuity occurs at an electrically long distance from the ports.

These intuitive interpretations will be confirmed by the analytical approach of the next section and validated by comparison of detailed designs of IB and CB-DMTL at the end of this chapter.

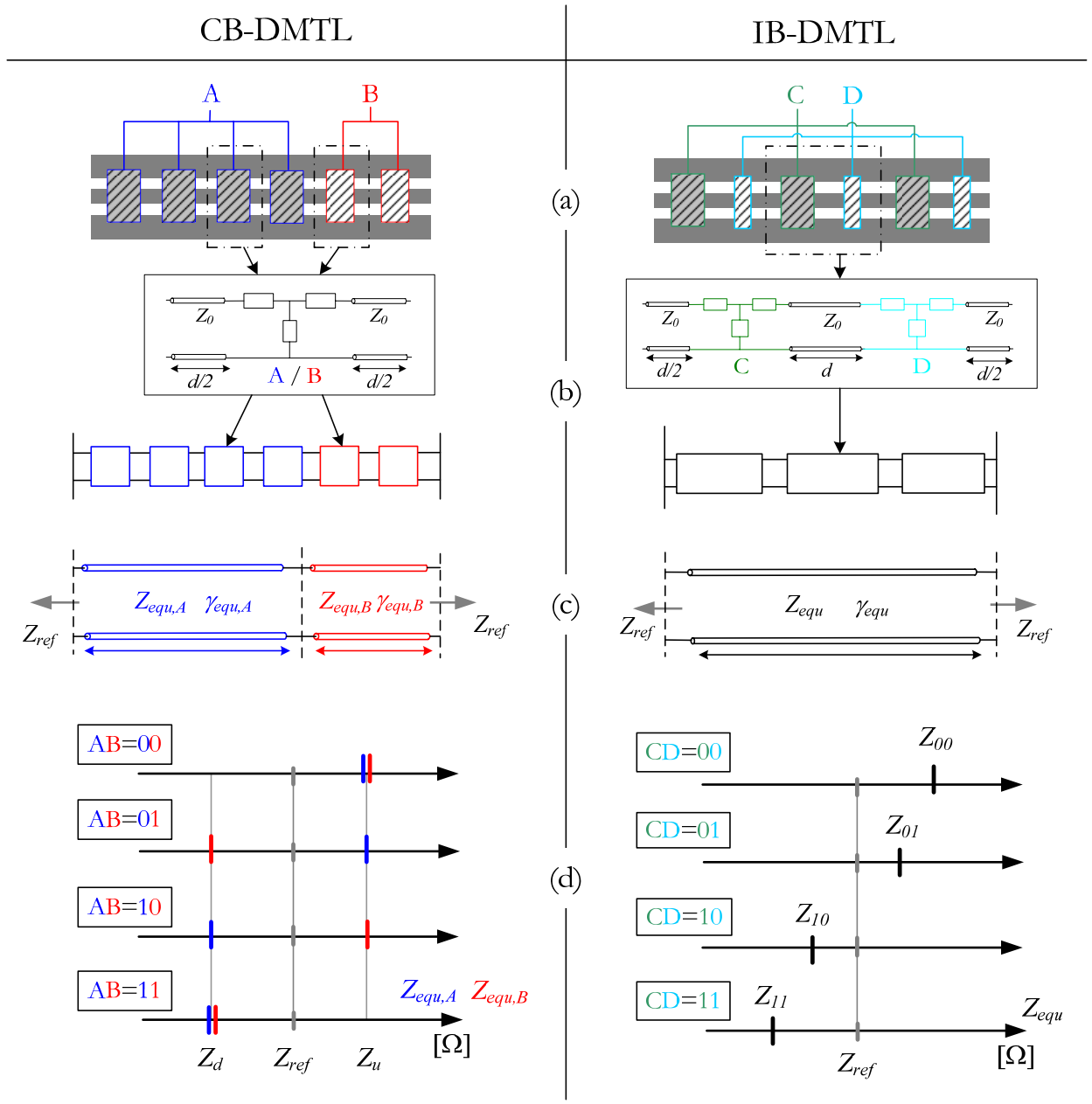

Figure 5.2: Description and intuitive comparison of IB and CB-DMTL topologies. (a) Physical structure representation, (b) Detailed circuit models, (c) Bloch wave TL equivalent models, (d) optimal location of the impedances.

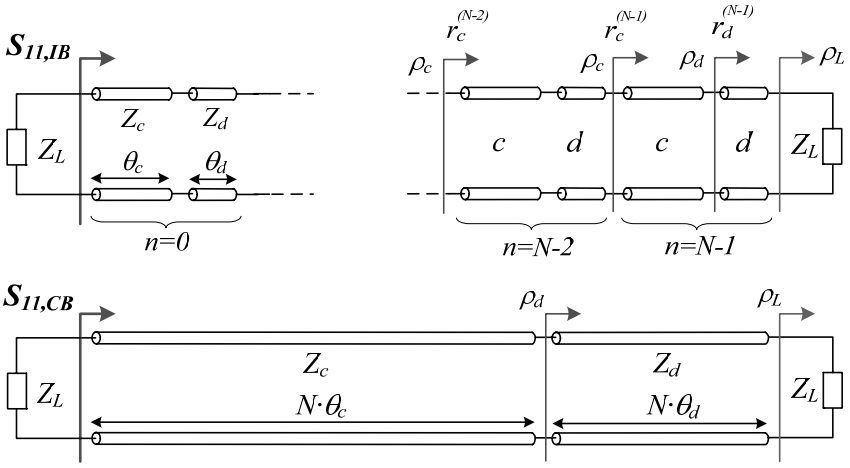

Figure 5.3: Periodic Bloch wave TL models for the analytical study of IB and CB DMTL structures (top and bottom, respectively).

5.2.2. Analytical small reflection approach

In this section, we propose an analytical approach based on equivalent circuits and using the concept of small reflections [13] to demonstrate the advantages and limitations of the IB topology over its usual CB counterpart. Using appropriate approximations, we deduce simple and general expressions for the performance of both structures, allowing a fast quantitative assessment of the advantage of the IB over the CB topology as a function of frequency.

a. Models

Figure 5.3 depicts the models for the 2-bit IB and CB structures on which the following analysis is based. It must be emphasized here again that the TL sections in these circuits are TLs in the sense of the Bloch wave equivalence demonstrated in Chapter 2 and that the analysis is thus not limited to cascades of 'conventionnal' TLs. Therefore, each TL section in the IB model represents one smallest unit cell of the device —i.e. a single bridge loading a CPW— but N of these cells in the CB case.

In the case of actual DMTLs, both topologies are operated in 4 four different states, which means that each of the parameters of the model Z_c, Z_d, θ_c and θ_d takes 2 different values. In practical DMTLs, the variations of θ_c and θ_d are small with respect to their average value (see the results of the DMTLs of Chapter 4, in particular Figure 4.15). As the total electrical length of the line is larger than 2π for all actual DMTLs and that we are interested in the input return loss (IRL) *maximum* in the bandwidth, the phase change resulting of the actuation of the bridges will not impact significantly on the result and we can therefore choose to fix θ_c and θ_d , which accounts for the mean value between the different states.

As explained previously, the critical states for the matching are states 01 and 10 and the analysis is thus made for these states only, hence the condition $Z_d = Z_L^2/Z_c$ on the impedances of

Figure 5.3, where Z_L is the reference impedance. These impedances are considered constant with frequency. Therefore, the analytical developments hold true only much below the Bragg frequency of both the IB-DMTL and CB-DMTL, namely where the equivalent impedance of the cells can indeed be considered as constant. This is no limitation with regard to the matching of DMTL, since the requirement of a quasi constant delay already limits their useful bandwidth toward the upper frequencies to a fraction of their Bragg frequency. Finally, let us note that we will consider only real impedances Z_c and Z_d, which is very realistic for systems with reasonable losses. Finally, the choice made for the length of the lines in both cases are made such that both topologies exhibit the same electrical length:

$$\theta_{tot} = N\left(\theta_c + \theta_d\right) \tag{5.1}$$

Also, a 2-bit operation with equidistant delays means that the *average* phase shift of the most significant bit (c line here) is twice that of the less significant one (d line here). Therefore, we will use the following relation between the phase shifts:

$$\theta_c = 2\theta_d \tag{5.2}$$

And the total electrical length of both structures is thus:

$$\theta_{tot} = 3N\theta_c \tag{5.3}$$

A last assumption used here is to neglect the losses in the phase shifter. This assumption is very realistic when considering matching issues since the IRL of a phase shifter essentially depends on the equivalent impedance of the phase shifter, which is weakly dependent on ohmic losses. In contrast, these losses obviously impact on the insertion loss performances and this issue is addressed in Section 5.4 below.

b. Numerical case studies

For some numerical validations of these assumptions and to illustrate the following analytical developments, we will use the parameters of the two following concrete DMTL designs:

Example A

In [34] were designed 1-bit CB-DMTLs with two different impedances pairs $Z_u/Z_d = 70/38\ \Omega$ and $60/44\ \Omega$, in the 1-10 GHz band. These two pairs of impedances correspond, *in a 1-bit configuration*, to IRLs of -10 dB and -15 dB, respectively. The first pair, used for our study, can be considered as the maximum impedance difference for practical cases since the IRL is already about -6 dB if such impedance ratio is used for 2-bit CB structures. The number of cells is $N = 18$ and the absolute average phase shift by unit cell can be deduced from other data provided in [34] and is $\theta\left(f_{max} = 10\text{ GHz}\right) = 26°$.

Example B

This second example is related to the actual designs that will be presented at the end of this chapter. In this case, the impedances are $Z_u/Z_d = 56.4/44\ \Omega$, which guaranties a minimum mismatch since the relation $Z_d = Z_L^2/Z_c$ is satisfied (this is not exactly the case for example A).

The number of cells is $N = 15$. The absolute average phase shift by unit cell is $\theta\,(10\text{ GHz}) = 6°$, which is much lower than for example A, meaning that the Bragg frequency is higher and that a higher limit for the bandwidth can be set in this case, for a given delay dispersion. The BW is here 1-30 GHz and the cell phase shift at the maximum frequency is thus $\theta\,(f_{max} = 30\text{ GHz}) = 18°$.

c. IB-DMTL

In order to analyze the mismatch at the input of the IB structure, let us first define, in accordance with Figure 5.3, the following *partial* reflection coefficients:

$$\rho_c = -\rho_d = \frac{Z_c - Z_d}{Z_c + Z_d} \tag{5.4}$$

$$\rho_L = \frac{Z_L - Z_d}{Z_L + Z_d} \tag{5.5}$$

An optimal matching is obtained with $Z_d = Z_L^2/Z_c$ and some calculations, not detailed here, show that this condition leads to (5.6) with a very small relative error, given by (5.7). For instance, in the case of example B, this error is only 0.4%.

$$\rho_c \simeq 2\rho_L \tag{5.6}$$

$$e_r = \frac{1}{2}\frac{(Z_L - Z_d)^2}{Z_L^2 + Z_d^2} \tag{5.7}$$

Let us now write the virtual IRL at the first transition between the line sections c and d at the right end of the structure, as depicted in Figure 5.3. This IRL is called *virtual* here because it is the IRL that would be obtained if there was a load of value Z_c at the left of the transition, which is obviously not the case here. This virtual IRL is:

$$r_d^{(N-1)} = \frac{\rho_d + \rho_L \exp(-2j\theta_d)}{1 + \rho_d\rho_L \exp(-2j\theta_d)} \tag{5.8}$$

Using the small reflection approximation (5.9), which leads to a very small error for usual DMTL (e.g. 0.8% in example B), (5.8) can be reduced to (5.10).

$$|\rho_d\rho_L| \ll 1 \tag{5.9}$$

$$r_d^{(N-1)} = \rho_d + \rho_L \exp(-2j\theta_d) \tag{5.10}$$

If we now shift to the next discontinuity in the left direction, we write the equivalent of (5.10) at this discontinuity as:

$$r_c^{(N-1)} = \rho_c + r_d^{(N-1)} \exp(-2j\theta_c) \tag{5.11}$$

We now substitute (5.10) into (5.11) and obtain:

$$r_c^{(N-1)} = \rho_c + \rho_d \exp(-2j\theta_c) + \rho_L \exp(-2j\,(\theta_c + \theta_d)) \tag{5.12}$$

Making use of (5.6), we can write:

$$r_c^{(N-1)} = \rho_c A + \rho_L B \tag{5.13}$$

where we introduced the compact notation:

$$\begin{cases} A = (1 - \exp(-2j\theta_c)) \\ B = \exp(-2j(\theta_c + \theta_d)) \end{cases} \tag{5.14}$$

This operation can then be repeated for each transition until the left load Z_L. In order to obtain a compact analytical expression, we deduce the following recursive expression by analogy with (5.13):

$$r_c^{(i)} = \rho_c A + r_c^{(i+1)} B \tag{5.15}$$

with the following 'limit condition':

$$r_c^{(N)} = \rho_L \tag{5.16}$$

Solving the recursive problem of (5.15) and (5.16), we deduce a general virtual IRL at any transition between a line c (left) and a line d (right) along the structure:

$$r_c^{(N-n)} = \rho_c A \sum_{j=0}^{n-1} B^j + \rho_L B^n \tag{5.17}$$

We are particularly interested in the virtual IRL at the very left hand of the structure, which is obtained, according to Figure 5.3, by introducing $n = N$ in (5.17):

$$r_c^{(0)} = \rho_c A \sum_{j=0}^{N-1} B^j + \rho_L B^N \tag{5.18}$$

It is interesting to observe that the first term in the right hand side of (5.18) is linked with the mismatch at the $2(N-1)$ discontinuities between the lines of impedance Z_c and the lines of impedance Z_d (hence ρ_c in the considered term), whereas the second term is linked with the mismatch at the right hand of the line (hence ρ_L). We now make use of the following formula:

$$\sum_{k=0}^{K} x^k = \frac{1 - x^{K+1}}{1 - x} \tag{5.19}$$

From which we can eliminate the sum in (5.18) and obtain:

$$r_c^{(0)} = \rho_c A \frac{1 - B^N}{1 - B} + \rho_L B^N \tag{5.20}$$

For practical cases, we are interested in finding an expression for the IRL $s_{11,IB}$ of the structure when connected to two identical loads Z_L, such as depicted in Figure 5.3. However, $r_c^{(0)}$ given by (5.20) is referred to the impedance Z_d, due to the recursive approach used for the calculation. Therefore, we need to change the reference impedance of the IRL from Z_d to Z_L, which is done by making use of the following formula:

$$s_{11,IB,0} = \frac{r_c^{(0)} - \rho_L}{1 - r_c^{(0)} \rho_L} \tag{5.21}$$

Substituting (5.20) in (5.21), we finally obtain:

$$s_{11,IB,0} = \frac{\left(1 - B^N\right)\left[\rho_c \frac{A}{1-B} - \rho_L\right]}{1 - \rho_L \rho_c A \frac{1-B^N}{1-B} - \rho_L^2 B^N} \tag{5.22}$$

For simplicity, we shall now consider the particular case of interest $\theta \equiv \theta_c = 2\theta_d$ [see (5.2)], so we have:

$$\begin{cases} A = \left(1 - \exp\left(-2j\theta_c\right)\right) \\ B = \exp\left(-6j\theta_c\right) \end{cases} \tag{5.23}$$

We can then show that:

$$B = \exp\left(-2j\left(\theta_c + \theta_d\right)\right) \quad \rightarrow \quad \left|1 - B^N\right| \leq 2 \tag{5.24}$$

$$\frac{A}{1-B} = \left|\frac{\sin 2\theta}{\sin 3\theta}\right| \exp\left(j\theta\right) \quad \rightarrow \quad \left|\frac{A}{1-B}\right| = \left|\frac{\sin 2\theta}{\sin 3\theta}\right| \tag{5.25}$$

which is bounded and close to 2/3 for small θ values. Therefore, (5.22) can be simplified by using the small reflection condition that was already used in a previous stage of this very development, namely $|\rho_L \rho_c| \ll 1$, and with the similar condition $\left|\rho_L^2\right| \ll 1$, which is also verified for practical impedances values. We obtain:

$$s_{11,IB} = \left(1 - B^N\right)\left[\rho_c \frac{A}{1-B} - \rho_L\right] \tag{5.26}$$

Or, by expanding A and B for use in further developments:

$$s_{11,IB} = \left(1 - \exp\left(-j6N\theta\right)\right)\left[\rho_c \left|\frac{\sin 2\theta}{\sin 3\theta}\right| \exp\left(j\theta\right) - \rho_L\right] \tag{5.27}$$

In order to assess the performance of the IB-DMTL in terms of matching, it is logical to consider the level of the *local maxima* of $|s_{11,IB}|$ in the bandwidth. As mentioned previously, actual wideband DMTLs will always have at least one local minimum and maximum of IRL in their bandwidth and the value of the maxima is the quantity of interest here, to be compared with its CB-DMTL structure counterpart. Although these maxima could be found by some derivation of $|s_{11,IB}|$, the location of the maxima can be found in a much simpler way by separating $|s_{11,IB}|$ as follows:

$$|s_{11,IB}| = \underbrace{\left|1 - \exp\left(-j6N\theta\right)\right|}_{T1} \cdot \underbrace{\left|\rho_c \left|\frac{\sin 2\theta}{\sin 3\theta}\right| \exp\left(j\theta\right) - \rho_L\right|}_{T2} \tag{5.28}$$

It can be shown that the term 'T2' is a monotonous function for $0 < \theta < \pi/3$, which means that the *location* of the local maxima in the band of interest (which is in the lower part of the $0 < \theta < \pi/3$ range for acceptable delay dispersion/ Bragg frequency) is determined by the term T1. Therefore, the location of the maxima is given by:

$$\theta_{\max,IB} = \left(2m + 1\right)\frac{\pi}{6N} \quad m \in \mathrm{N} \tag{5.29}$$

As the total electric length of the structure is $3N\theta$, this means that the maxima and minima are located at approximately the same frequencies as for a continuous structure of constant equivalent impedance and electrical length $3N\theta$. This approximation is linked with the assumption made in previous steps leading to (5.28), namely the small reflection assumption. From (5.29) we deduce the condition on the total electrical length of the IB-DMTL for having at least one local IRL maxima in the bandwidth:

$$\theta\left(f_{max}\right) > 3N\left(2m+1\right)\frac{\pi}{6N}\bigg|_{m=0} \quad \rightarrow \quad \theta_{tot}\left(f_{max}\right) = 3N\theta > \frac{\pi}{2} \tag{5.30}$$

At these maxima, the module of T1 in (5.28) is obviously equal to 2. Thus, we can define the determining quantity for the matching of the IB-DMTL as the value of the local maxima of the module of $s_{11,IB}$. In other words, this quantity corresponds to the curve fitting the local maxima of (5.28), and is given by:

$$s_{11,IB,\max} = 2\cdot\left|\rho_c\left|\frac{\sin 2\theta}{\sin 3\theta}\right|\exp\left(j\theta\right)-\rho_L\right| = 2\cdot\left(\rho_c^2\left|\frac{\sin 2\theta}{\sin 3\theta}\right|^2+\rho_L^2-2\rho_c\rho_L\left|\frac{\sin 2\theta}{\sin 3\theta}\right|\sin\theta\right)^{1/2} \tag{5.31}$$

We will now verify these developments by means of the numerical examples proposed above. Figure 5.4(a) and Figure 5.4(b) compare the exact circuit solution (calculated by cascading transmission matrices for each TL periodic equivalent section of Figure 5.3) and the approximations deduced here, for examples A and B, respectively. In example A, there is a shift in the position of the maxima due to the large impedance difference between Z_c and Z_d. However, it is seen that this phenomenon is very small in case B. Nevertheless, this does not impact on the precision of the relevant parameter calculated, namely the expression for the maxima of the mismatch (5.31). This is due to the calculation method and we observe that $s_{11,IB,\max}$ given by (5.31) is indeed a very good approximation of the level of mismatch in the BW, even in example A (as explained previously, example A can be considered as an extreme case for the validity of the small reflection assumption).

The dependence of $s_{11,IB,\max}$ on the frequency, represented by the angle θ here, is complex. Different Taylor expansions can be made to obtain polynomial functions of θ, which will be of use later in this document. In (5.32) and (5.33) are the corresponding 3$^{\text{rd}}$ and 1$^{\text{st}}$ order expansions (3$^{\text{rd}}$ and 1$^{\text{st}}$ order terms are null and the expression deduced are therefore 2$^{\text{nd}}$ and 0$^{\text{th}}$ order polynomials):

$$s_{11,IB,\max}^{3rd} = 2\cdot\left(\rho_c^2\left(\frac{4}{9}+\frac{20}{27}\theta^2\right)+\rho_L^2-2\rho_c\rho_L\left(\frac{2}{3}+\frac{2}{9}\theta^2\right)\right)^{1/2} \tag{5.32}$$

$$s_{11,IB,\max}^{1st} = 2\left|\frac{2}{3}\rho_c-\rho_L\right| \tag{5.33}$$

It is observed in Figure 5.5 that the 2$^{\text{nd}}$ order expression is a very good approximation of the level of the maxima, whereas the 1$^{\text{st}}$ order approximation gives the maximum level of the mismatch at low frequencies.

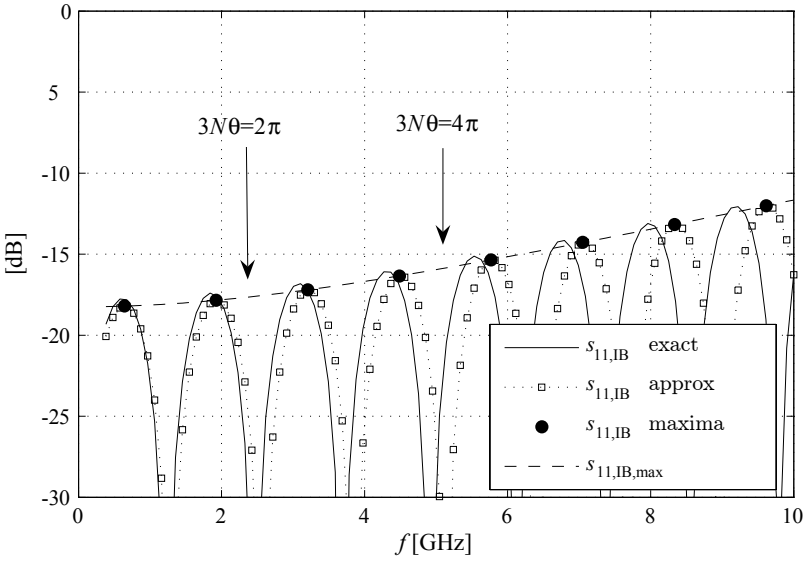

(a) example A

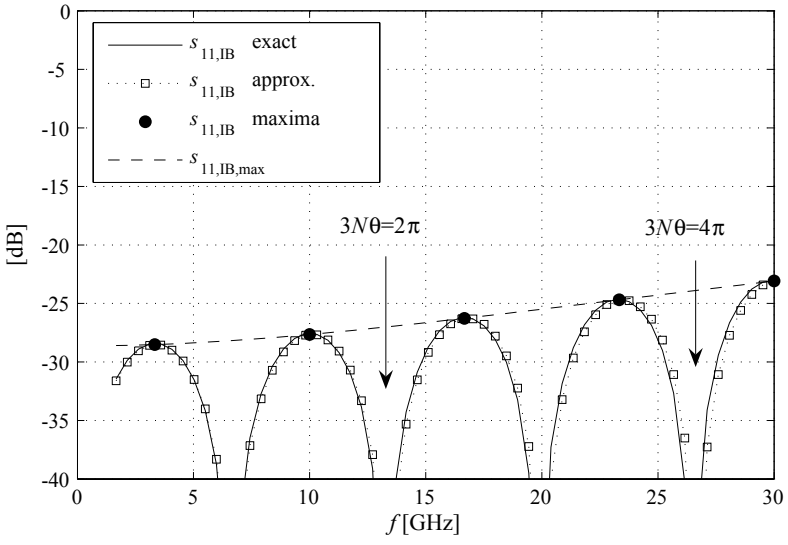

(b) example B

Figure 5.4: Numerical validations of the approximate expressions for the matching of the IB-DMTL.

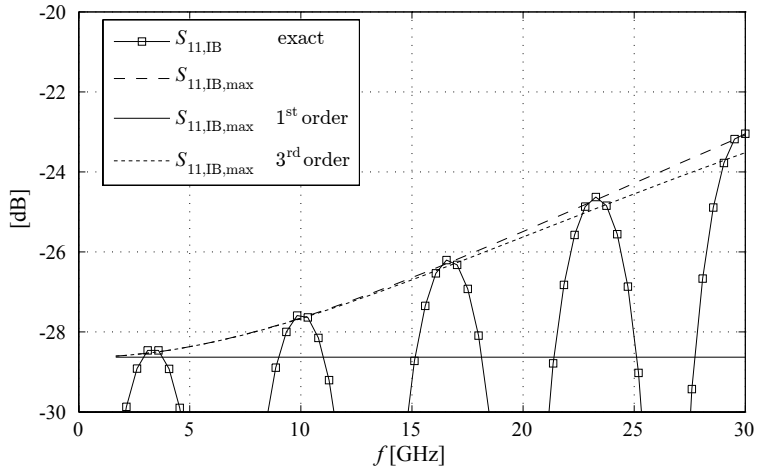

Figure 5.5: Numerical validation of the Taylor expansion on the approximate expression for the matching of the CB-DMTL (example B).

d. CB-DMTL

The CB-DMTL case is studied using the same approach as for IB-DMTL. In this case, no recursion is needed as the structure is only constituted of two line sections and we can write the IRL at the left of the structure as:

$$r_c = \rho_c \left(1 - A'^N\right) + \rho_L B^N \tag{5.34}$$

where a notation consistent with the IB-DMTL developments has been introduced:

$$\begin{cases} A' = 1 - A = \exp\left(-2j\theta_c\right) \\ B = \exp\left(-2j\left(\theta_c + \theta_d\right)\right) \end{cases} \tag{5.35}$$

Again, the reference impedance of this IRL must be changed from Z_d to Z_L, and the IRL of interest is then, using (5.21):

$$s_{11,CB,0} = \frac{\rho_c \left(1 - A'^N\right) + \rho_L \left(B^N - 1\right)}{1 - \rho_L \rho_c \left(1 - A'^N\right) - \rho_L^2 B^N} \tag{5.36}$$

We observe that:

$$B = \exp\left(-2j\left(\theta_c + \theta_d\right)\right) \quad \rightarrow \quad \left|B^N\right| = 1 \tag{5.37}$$

$$A' = \exp\left(-2j\theta_c\right) \quad \rightarrow \quad \left|1 - A'^N\right| \leq 2 \tag{5.38}$$

Therefore, (5.36) can be simplified by using the same small reflection condition as used in the IB-DMTL case, namely $|\rho_L \rho_c| \ll 1$ and $\left|\rho_L^2\right| \ll 1$:

$$s_{11,CB} = \rho_c \left(1 - A'^N\right) + \rho_L \left(B^N - 1\right) \tag{5.39}$$

Again, we need find the level of the *local maxima* of $|s_{11,CB}|$ in the bandwidth. An exact analytical solution for this problem is lengthy but it can be shown that the maxima of $|s_{11,CB}|$ are

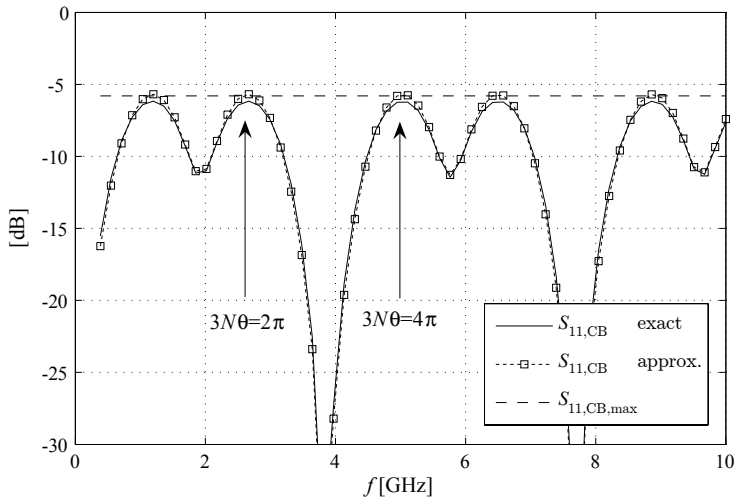

(a) example A

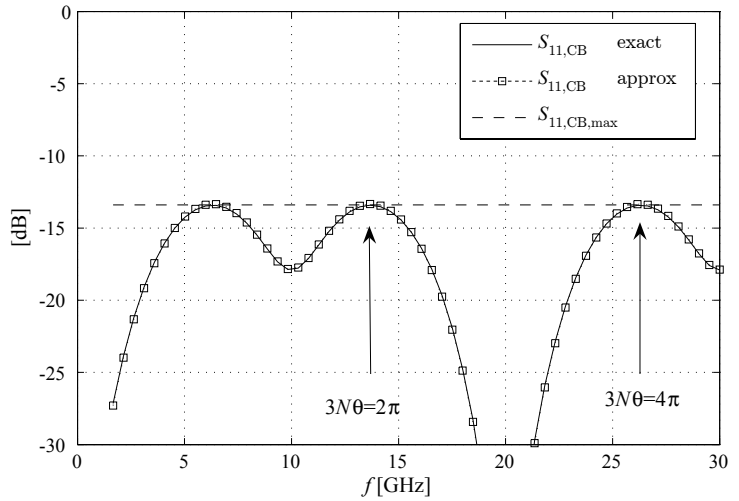

(b) example B

Figure 5.6: Numerical validations of the approximate expressions for the matching of the CB-DMTL.

approximately located at:

$$\theta_{\max,CB} = \begin{cases} (3m+1)\,\frac{\pi}{3N} \\ (3m+2)\,\frac{\pi}{3N} \end{cases} \qquad m \in \mathrm{N} \tag{5.40}$$

It is noticeable that the small error in terms of the location of the maxima (frequency or θ) has a very small impact on the error in terms of the value of the maximum, as $|s_{11,CB}|$ is a slowly varying function in the local maxima regions (see Figure 5.6(a) and Figure 5.6(b)). From this expression we can deduce the condition on the total electrical length of the CB-DMTL for having at least one local minimum in the bandwidth:

$$\theta\left(f_{max}\right) > 3N\,(3m+1)\,\frac{\pi}{3N}\Big|_{m=0} \quad \rightarrow \quad \theta_{tot}\left(f_{max}\right) = 3N\theta > \pi \tag{5.41}$$

The value of $|s_{11,CB}|$ is the same at all maxima (since $|s_{11,CB}|$ it is actually periodic, with a period $3N\theta = 3\pi$), and is deduced from (5.39):

$$s_{11,CB,\max} = \rho_c\sqrt{3} \tag{5.42}$$

Figures 5.6(a) and 5.6(b) show the good agreement between the exact circuit solution and the approximation deduced here. The location of the maxima is also depicted and it is observed that (5.42) precisely account for the maximum level of mismatch.

e. Performance comparison

Influence of N

Before comparing the matching performances of IB and CB topologies, it is useful to discuss the influence of the number of cells N in the IB-DMTL structure. We observe that the final results of these developments, namely the levels of IRL given by (5.31) and (5.42), do not depend on N. However, it seems obvious that the difference between CB-DMTL and IB-DMTL depends on N (at the extreme limit, we can even note that the CB and the IB structures are exactly the same for $N = 1$!). This apparent contradiction can nevertheless be easily explained as follows: in order to base our comparison of the mismatch on the level of the *local maxima* of the IRL in the BW, we assumed that there is at least one local maximum in the BW for both topologies, which is true if [see (5.30) and (5.41)]:

$$\theta_{tot}\left(f_{max}\right) = 3N\theta > \frac{\pi}{2} \tag{5.43}$$

Let us now illustrate this matter by means of our 2 numerical examples, for which (5.43) means that the results found in the previous section for the maximum level of IRL are true as long as the number of cells is at least $N = 3$ (example A) and $N = 4$ (example B). As explained before, actual DMTLs have indeed a much larger number of cells, here $N = 18$ (example A) and $N = 15$ (example B) and the assumption is well verified. Nevertheless, it is interesting to illustrate these considerations graphically as done in Figure 5.7, which corresponds to example B. For $N = 15$ and $N = 4$, there is a large difference between the maximum levels of CB and IB topologies, as

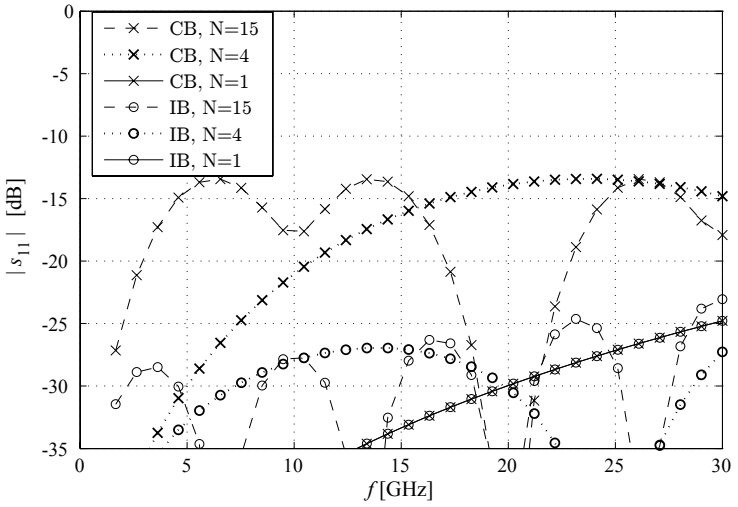

Figure 5.7: Influence of the number of Cells N (example B).

	CB-DMTL	IB-DMTL
LF limit	$s_{11,CB,\max} = \rho_c\sqrt{3}$	$s_{11,IB,\max}^{1st} = 2\left\lvert\frac{2}{3}\rho_c - 2\rho_L\right\rvert$
Whole BW		$s_{11,IB,\max} = 2\cdot\left(\rho_c^2\left\lvert\frac{\sin 2\theta}{\sin 3\theta}\right\rvert + \rho_L^2 - 2\rho_c\rho_L\left\lvert\frac{\sin 2\theta}{\sin 3\theta}\right\rvert\sin\theta\right)^{1/2}$

Table 5.1: Summary of the final results obtained for the IRL of CB and IB-DMTLs.

calculated in the previous developments. In the case where $N = 4$, we see that this is indeed the limit case, since below that value the local maximum of the IB-DMTL will be shifted outside the BW considered. Finally, both curves are, as expected, exactly the same in the case $N = 1$.

Matching performance

Table 5.1 summarizes the final results (5.31), (5.33), and (5.42) obtained for the level of mismatch of both structures. At the low-frequency limit, the difference between IB and CB-DMTLs is:

$$\Delta_{LF} = \frac{s_{11,IB,\max}^{1st}}{s_{11,CB,\max}} = \frac{2\left|\frac{2}{3}\rho_c - \rho_L\right|}{\rho_c\sqrt{3}} \tag{5.44}$$

which, using (5.6), yields:

$$20\log_{10}\Delta_{LF} = -14.3\ dB \tag{5.45}$$

It is remarkable that, thanks to the approximations used, this result is independent from the impedances Z_u and Z_d. Indeed, although these impedances obviously influence the mismatch of each structure, the *difference* between the IRL of both structures is itself independent from the impedances, as long as they are optimally 'positioned' above and below the reference impedance according to $Z_d = Z_L^2/Z_c$.

Since $s_{11,IB,\max}$ given by (5.31) increases with θ, the difference between IB and CB topologies reduces as the frequency increases. In this context, it is interesting to calculate at which frequency the level of mismatch of the IB structure reaches that of the CB topology. Mathematically, this means that we must solve the following equation for θ_{lim}:

$$\Delta_{LF} = \frac{s_{11,IB,\max}(\theta_{lim})}{s_{11,CB,\max}(\theta_{lim})} = 1 \tag{5.46}$$

After some calculation, and using again (5.6), it is seen that this result is also independent from the impedances and is given by:

$$\theta_{lim} = 0.23\pi \tag{5.47}$$

This means that when the electrical length θ of the unit cell of the IB structure reaches about 45°, the 'averaging' effect explained in the intuitive interpretation of the advantage of the IB topology is lost.

We will now again illustrate the final results (5.45) and (5.47) with our numerical examples. Figure 5.8(a) shows the results for example B on an extended frequency range. On the graph are plotted the exact circuit solutions as well as the maxima curves (5.31) and (5.42). It is verified that the IB topology exhibits better matching than its CB counterpart below the calculated limit of 69 GHz [which is directly deduced from (5.47)]. At the LF limit, the difference is about -14 dB, which also confirms the calculated result (5.45). Practically, this means that the IB structure exhibits a much better matching than the CB topology on the whole operation BW (in this case, this upper limit of the BW can be set between 20 GHz and up to about 40 GHz, depending on the requirement on the delay dispersion). Figure 5.8(b) plots the results in example A, on the whole operation bandwidth for which the corresponding DMTL was designed [34]. Here again, it is observed that the IB topology exhibits much better matching than its CB counterpart on the whole BW.

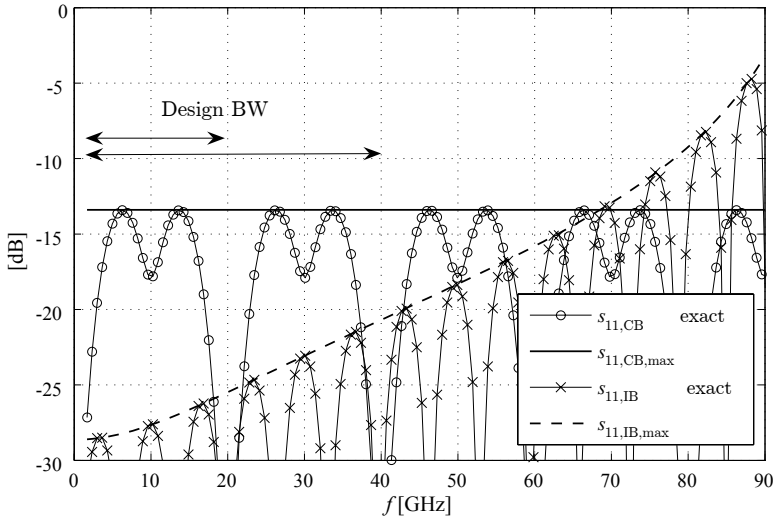

(a) example B

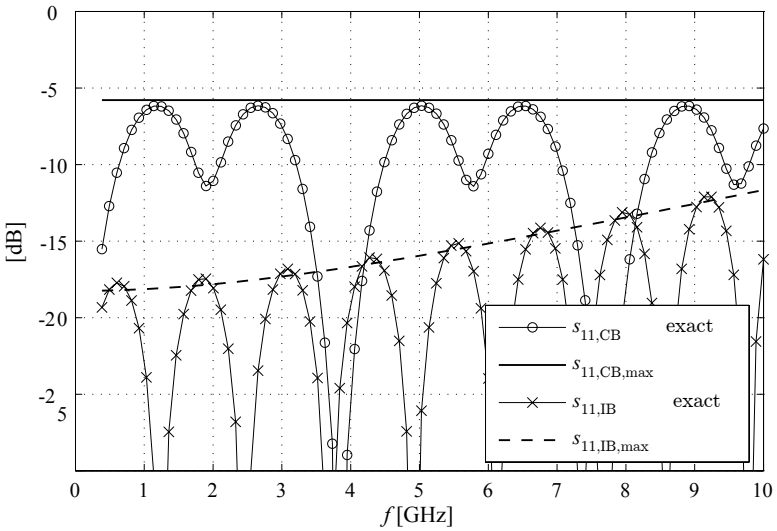

(b) example A

Figure 5.8: Comparison of the matching of CB and IB topologies.

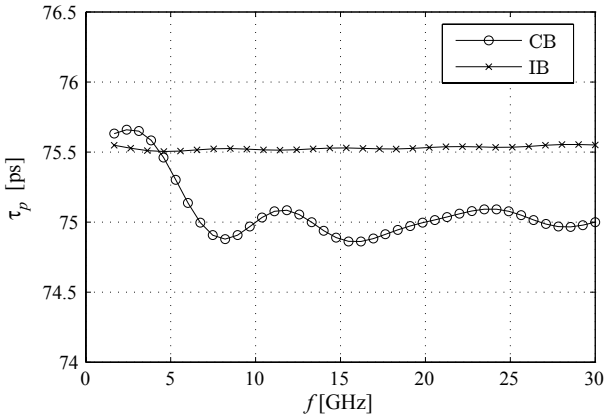

Figure 5.9: Comparison of the phase delay of CB and IB topologies (example A).

Delay performance

This section studies how the difference in terms of mismatch between IB and CB topologies affects the phase shift. First, let us note that in the case of a perfectly matched phase shifter, only a pure traveling wave propagates in the structure. In this case, $\arg(s_{21}) = -\theta_{tot}$, where θ_{tot} is the total electrical length of the phase shifter (e.g. $3N\theta$ in the models of Figure 5.3). However, the mismatch of the structures considered here results in the superposition of reflected waves to the 'main' one, hence some oscillations in $\arg(s_{21})$. These oscillations can be clearly highlighted by computing the phase delay, in the time domain, including reflected waves and defined as:

$$\tau_p = \frac{-\arg(s_{21})}{2\pi f} \qquad [\text{s}] \tag{5.48}$$

Figure 5.9 depicts the exact τ_p circuit solutions in the IB and CB cases using Example B numerical data. As expected, it is observed that the reduced mismatch of the IB structure leads to a significant reduction of the oscillations in τ_p.

5.3. Design

For simplicity, the design of the IB-DMTL consists of an extension of the design method presented in Chapter 4 for 'conventional' DMTLs. In order to do so, we need to assume that the cell of the digital IB-DMTL as shown in the left hand side of Figure 5.10 can be first approximated by the same structure, but where the 2 pairs of loading capacitances are averaged and considered identical (right hand side of the figure). It can be shown that this approximation has a small impact on the calculation since the unit cell length is small in terms of wavelength. Moreover, once the design solutions are found by the approximate method, an exact periodic analysis of the designed circuit is made and the actual structure performances are immediately assessed (this also allows quantifying the impact of the approximation).

Using the assumption that the mobile capacitance in the Down state is much larger than

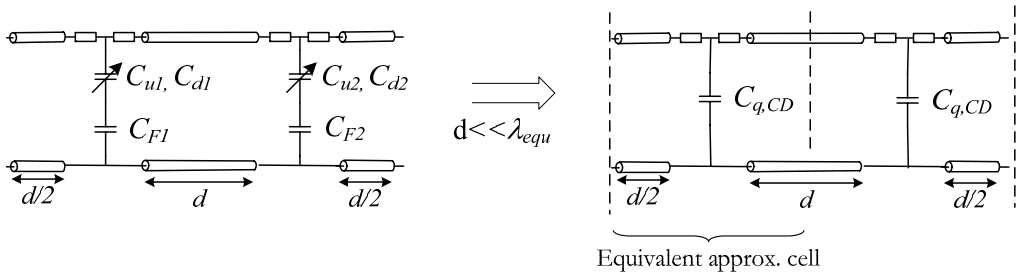

Figure 5.10: Approximation employed for a simple design of the IB-DMTL.

the fix one, namely, $C_d \gg C_F$[1] , the averaging of the capacitance as illustrated in Figure 5.10 is translated into the following design capacitances values:

$$C_{q,CD} = \begin{cases} C_{q,00} = \frac{1}{2}\left(\frac{C_{F1}C_{u1}}{C_{F1}+C_{u1}} + \frac{C_{F2}C_{u2}}{C_{F2}+C_{u2}}\right) \\ C_{q,01} = \frac{1}{2}\left(\frac{C_{F1}C_{u1}}{C_{F1}+C_{u1}} + C_{F2}\right) \\ C_{q,10} = \frac{1}{2}\left(C_{F2} + \frac{C_{F2}C_{u2}}{C_{F2}+C_{u2}}\right) \\ C_{q,11} = \frac{1}{2}\left(C_{F2} + C_{F2}\right) \end{cases} \tag{5.49}$$

So, we first use (5.50), derived from the design formulas of Chapter 4, to deduce the four capacitances $C_{q,CD}$ within the design method for conventional DMTLs. The values of the actual capacitances of the IB-DMTL in the left of Figure 5.10 are then obtained using (5.49).

$$C_{q,CD} = d\left(\left(L_{CPW} + \frac{2\Delta L_S}{d}\right)\left(\frac{1}{Z_{00}} + \frac{c_0}{\sqrt{\varepsilon_{eff}}Z_0}\Delta\tau_{CD}\right)^2 - C_{CPW}\right) \tag{5.50}$$

However, (5.49) implies that:

$$C_{q,00} + C_{q,11} = C_{q,10} + C_{q,01} \tag{5.51}$$

which means that it is not possible to deduce a solution C_{F1}, C_{u1}, C_{F2}, C_{u2} for any four capacitances $C_{q,CD}$ (C_{d1} and C_{d2} are linked to C_{u1} and C_{u2} by the capacitance ratio used as an input in the design). Now, let us write the approximate propagation constant under the assumption that $2d \ll \lambda$ as (5.52), where C_P accounts for each capacitance connected in parallel with the TL of the unit cell of length $2d$. From this expression we deduce the absolute delay given by (5.53), where $(1 + C \cdot \Delta C_{r,c}) = C_{r,c}$ with $C_{r,c}$ being the capacitance ratio as usually defined (here the new notation allows including the value 0 or 1 of the bits C and D in the general expression for the delay). Since this delay is not a linear function of the capacitances values, it is clear that (5.51) is not compatible with a condition of equidistant delays.

$$\beta \approx \omega\sqrt{L_{CPW}\left(C_{CPW} + \sum C_P \Big/ 2d\right)} \tag{5.52}$$

$$D\left(C,B\right) = Nd\sqrt{L_{CPW}}\sqrt{C_{CPW} + \frac{C_C\left(1 + C \cdot \Delta C_{r,c}\right)}{2d} + \frac{C_D\left(1 + D \cdot \Delta C_{r,d}\right)}{2d}} \tag{5.53}$$

[1]but we do not use the approximation $C_F \gg C_u$ as sometimes proposed, since not accurate in many design cases.

There is therefore one degree of freedom missing in order to have equally spaced delays. This issue could be solved by adding a free parameter in the structure in different ways (e.g. adding a fixed capacitance in the circuit) and modifying the design method accordingly. However, this was not done here, for the following reasons:

- As will be shown with the design example presented below, it possible to achieve almost equally spaced delays by some fine tuning after the design method is completed, since this one comprises some approximations.
- Although all published CB-DMTL results (e.g. [31, 46]) exhibit equally spaced delays, this is not a requirement set by the main application for DMTLs, namely the corporate feed network. Indeed, as shown in Section 4.1.2, such equally spaced delays would lead to non-constant steps in the scan angle since this angle is linked to the delay by a *sine* function. On the other hand, compensating this *sine* dependence by the delays is not possible with the CB-DMTL structure either, which also lacks a degree of freedom to select independently the different delays, since we necessarily have $\Delta D_{11-00} = \Delta D_{10-00} + \Delta D_{01-00}$, where ΔD_{IJ-00} is the differential delay between states IJ and 00.

5.4. IB-DMTL design results

In this last part of the chapter, we design actual 2-bits CB and IB-DMTLs in order to test the presented design method for IB-DMTLs as well as verifying its superior performances with regard to its CB counterpart. Although such tests were already carried out numerically based on the circuits of Figure 5.3, here the verification is made on a full-wave simulation level after a detailed design. The designed structures were however not measured nor fabricated, since the multi-bit DMTLs require the use of high resistivity bias lines not available in the 'Al-Si EPFL' MEMS process employed here[1]. Indeed, since there must be two independent control voltages here, it is not possible to apply the DC bias voltage between central conductor and ground planes of the CPW, as was done in the case of the single-bit DMTLs of Chapter 4. As a result, and as shown in Figure 5.12, it is necessary to feed each type of bridge by a separate feed line, which must necessarily be of a highly resistive material as available in several MEMS processes such as the 'Al-Quartz VTT' presented in Appendix A. Nevertheless, although the simulations will not be verified by measurements here, the agreement between these was previously tested in the case of single-bit DMTL and must obviously be verified here as well.

For fair comparison, the designs were made using the same materials, delays, and bandwidth. The results obtained from the model used for the design are verified by full-wave simulations with Ansoft HFSS. Plotted in Figure 5.12 and Figure 5.13 are the absolute delay and IRL obtained. We observe that the circuit model and the full-wave simulations are in very good agreement. Table 5.2 reports the performances for each topology, along with the corresponding values of the various periodic Bloch impedances. As can be seen in this table and Figure 5.13, the CB-DMTL and

[1] the use of this process for the design of DMTLs was set by the corresponding research project WIDE-RF, see Chapter 1.

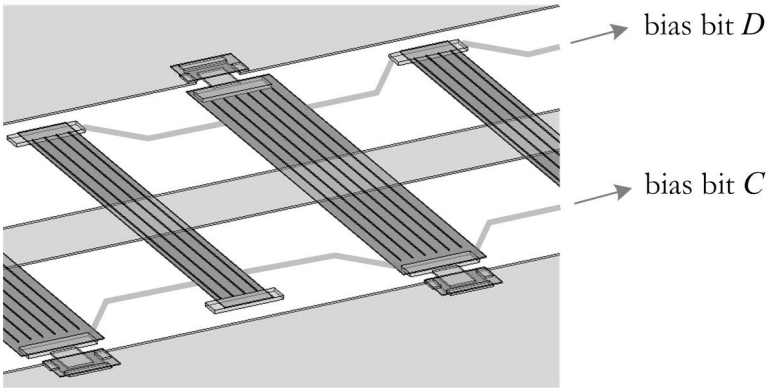

Figure 5.11: 3-D view of the designed IB-DMTL with bias lines. *Note: the small fixed capacitors of the bridges corresponding to Bit C are realized by the coupling through the substrate alone.*

IB-DMTL exhibit approximately the same IRL in states 00 and 11 as there is no mismatch at the transition between the two bit sections in the CB-DMTL. However, in the states 01 and 10, an important mismatch occurs in the CB case, since two lines of impedances 44 Ω and 56.4 Ω are cascaded. As expected, this problem is solved by the IB-DMTL approach, where the states 01 and 10 correspond to intermediate impedances (52.5 Ω and 46.7 Ω), hence a low IRL. In Section 5.2.2, we showed theoretically that the difference of IRLs between states 01 and 10 of IB and CB-DMTL is about 14 dB at low frequency and slowly decreases with frequency. Looking at Table 5.2, we see that this difference is here about 11 dB and 13 dB, which is perfectly consistent with the theoretical result since the whole bandwidth is considered and that these values are slightly lower that the low-frequency limit of 14 dB[1].

These improvements of 11 dB and 13 dB occur for the critical states of the CB-DMTL structure, namely states 01 and 10. However, since the IB-DMTL allows achieving a very good matching for these states, the critical ones in the case of the IB-DMTL are 00 and 11, as can be observed in Figure 5.13 or Table 5.2. Consequently, the improvement in terms of mismatch considering all four states together is the difference between the IRL of the CB structure in states 01 and 10 and the IRL of the IB structure in states 00 and 11. As a result, the improvement based on the criteria of the maximum IRL of the four states is $-12-(-18)=6$ dB, which is lower than the improvement considering states 01 and 10 only.

As mentioned previously, some oscillations in the delay are due to the mismatch and are therefore lower in the IB-DMTL case. Another important parameter for DMTL is the insertion loss and it is seen that both configurations exhibit approximately the same performance from this point of view. The reason is the predominance of ohmic losses over mismatch losses in the overall insertion losses.

[1]In addition, note that the difference of matching is calculated on the basis of IRLs as low as -25 dB, for which imprecisions of 1 or 2 dB can be expected.

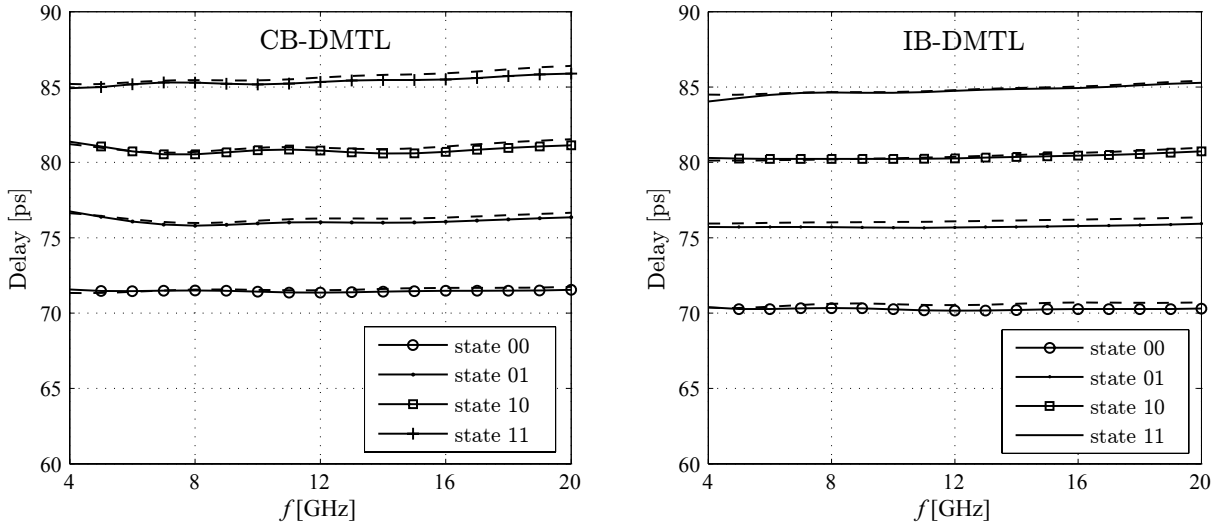

Figure 5.12: Absolute delays of the CB-DMTL and IB-DMTL, HFSS simulation (—) and lumped model (– –).

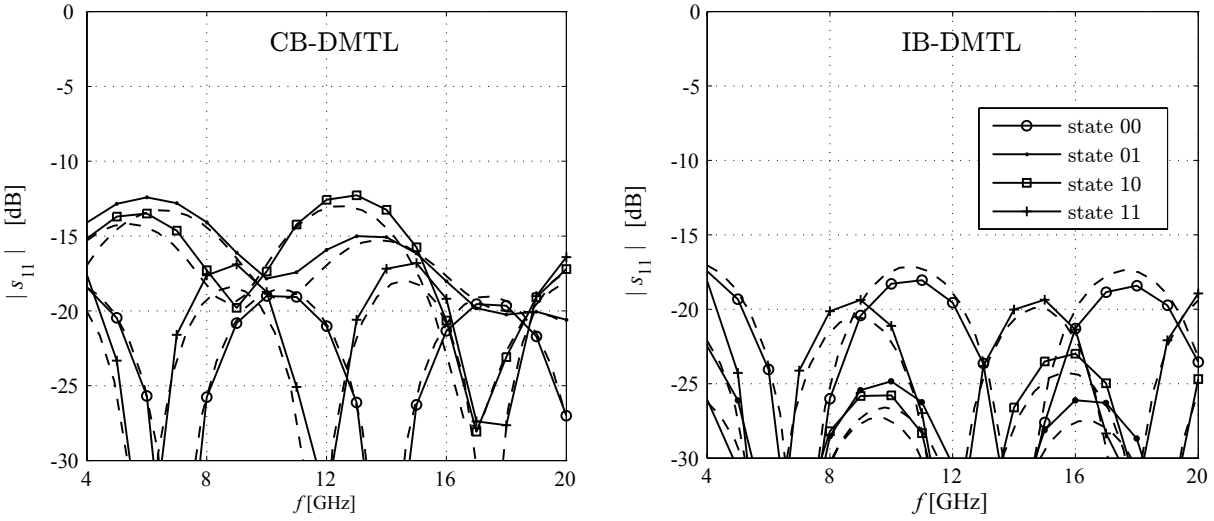

Figure 5.13: Input return loss of the CB-DMTL and IB-DMTL, HFSS simulation (—) and lumped model (– –).

	CB-DMTL				**IB-DMTL**		
	$Z_{equ,A}$	$Z_{equ,B}$	S_{11max}	S_{21min}	Z_{equ}	S_{11max}	S_{21min}
00	56.4	56.4	-19	-0.7	56.7	-18	-0.8
01	56.4	44.0	**-12**	-0.7	**52.5**	**-25**	-0.7
10	44.0	56.4	**-12**	-0.8	**46.7**	**-23**	-0.7
11	44.0	44.0	-17	-0.7	44.2	-19	-0.6

Table 5.2: Comparison of the two types of DMTL in terms of the equivalent impedances in Ω, the max. of s_{11} and the min. of s_{21} in dB.

5.5. Conclusion

In this chapter, we introduced the IB-DMTL structure and demonstrated its advantages over its CB-DMTL counterpart from matching and delay distortion points of view, in a two bit operation. The cost of this improvement is an increased design complexity. Although the method could be extended to a larger number of bits, the complexity of the design might become prohibitive. However, it is possible in this case, for instance for a 4-bits DMTL, to cascade 2 sections of 2-bit IB-DMTLs as designed here, which would obviously exhibit much better matching properties than a 4-bit CB-DMTL. Nevertheless, the best solution in terms of mismatch when a large number of bits are required is probably the one proposed in [45] (which was commented in Section 5.1.3). Indeed, in this case the mismatch only weakly depends on the number of bits, as a result of the quasi-independence of the impedance to the state operated.

Let us finally note that the generality of the IB method presented here makes the results directly applicable to most multi-bit microwave distributed phase shifters whose equivalent impedance depends on the state operated. This is the case of a wide class of phase shifters; namely, phase shifters relying on the control of the effective permittivity of a TL, since the impedance of the line will also vary if the effective permittivity is changed. This is the case of DMTL, but also of devices based on ferroelectric [47] or piezoelectric actuation [48], or even phase shifters based on variable metamaterials structures such as presented in this thesis in Chapter 7.

6. CRLH-TLs: Theory and Micromachined Implementation

6.1. Introduction

6.1.1. The composite right/left handed transmission line (CRLH-TL)

In recent years, there have been tremendous developments in the realization and characterization of artificial materials exhibiting negative permittivity and/or permeability. Such materials are usually referred to as *metamaterials* and were conceptually proposed by Veselago [49]. Nevertheless, they were only recently implemented using either particular geometries such as arrays of metal wires and split ring resonators (SRRs) [50, 51] (for $\varepsilon < 0$ and $\mu < 0$, respectively), or lumped L and C elements loading a transmitting medium [52, 53]. These artificial dielectrics were named by Veselago as left-handed media, as a result of the left-handed triplet formed by the vectors **E**, **H** and **k** of the wave propagating in the metamaterial.

In the case of the LC-loaded transmitting medium approach, the reversed properties of metamaterials are rather observed in terms of the opposition of the phase and group velocities of a propagating wave ('backward wave' propagation, see Chapter 2). In the left hand side of Figure 6.1 is shown a possible 1-D unit cell of such metamaterial, which is made of the composition of classical 'right-handed' TL loaded by dual 'left-handed' elements (shunt L and series C). Such metamaterials are usually referred to as composite right/left handed TL (CRLH-TLs) [54], which is also the naming we will use here. Upon given conditions on the circuit elements values, this structure exhibits both 'forward' and ' backward' bands (denoted as FW and BW) in a common passband, with a continuous transition between FW and BW band at the frequency f_0 of 0^o phase shift. This band structure is illustrated in the right hand side of Figure 6.1. If there is no stopband between BW and FW band, as is the case in the figure, it is usually said that the CRLH-TL is *balanced*. In this work, we decided to address the micromachined implementation of this CRLH-TL metamaterial rather than the one based on metal wires and SRRs. The reason is twofold: first, the SRR-based realization as proposed in [55] is not suitable for a micromachined implementation because the miniaturization of the SRRs leads to prohibitive losses as a result of the large currents flowing in the SRRs. The second —and more fundamental— reason is the narrow band of operation associated with the resonance of the SRRs[1] (there is no such resonance in the case of the

[1] [56] describes a so-called 'broadband resonant-type metamaterial TL', which shows that it is possible to realize a broadband metamaterial-TL using the SRR approach. Nevertheless, this is done by working the SRRs off their resonance and thus actually consists of mimicking the CRLH-TL approach by a SRR one (the correspondence between these structures is established in [57]). In this context, the CRLH-TL approach is preferable due to its

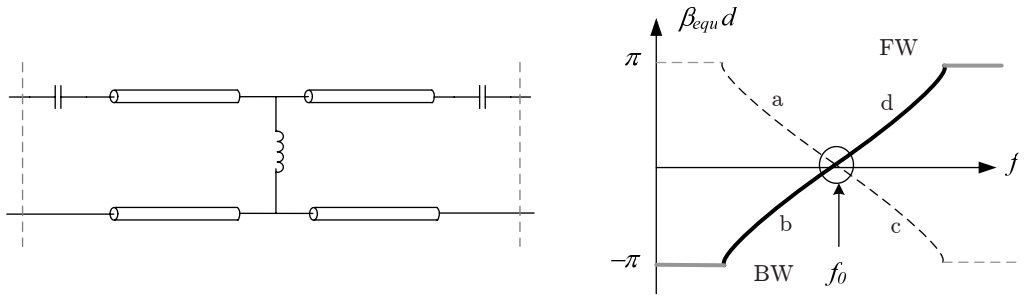

Figure 6.1: Possible 1-D unit cell circuit and band structure of a balanced CRLH-TL.

CRLH-TL). From a more general perspective, most useful applications of metamaterials are based on the aforementioned particular dispersion of the CRLH-TL structure, which cannot be achieved with the SRR approach. Here is a non-exhaustive list of applications advantageously using the properties of the CRLH-TL:

- 2-D applications: negative refraction for focusing application [52].
- 1-D phase shifters for various applications:
  - Arrays feed networks [58].
  - Dual-band couplers [59].
  - Resonators [60].
  - Baluns [61].
  - Etc.
- Antennas:
  - Microstrip patch miniaturization [54].
  - Leaky-wave antennas [54, 62].
  - Etc.

Thus, for miniaturization purposes, or for a monolithic integration of these devices with active components, it is necessary to study the implementation of CRLH-TLs in micromachining technology, which is the topic of this chapter. In addition, let us note that the knowledge acquired in this process will be of use for the development of MEMS-based reconfigurable CRLH-TL presented in the following chapter of this thesis.

This chapter is organized as follows: first, we study the band structure of the CRLH-TL based on the calculation of its periodic equivalent Bloch propagation constant. Then, we compare the results to the ones obtained in previous works on CRLH-TL and explain in which case and why the new formulation must be used. We link this issue to the notion of *effective media*, which will be discussed in the case of the CRLH-TL structure and with regard to its most common applications. These considerations are then validated by the design and measurements of silicon-integrated CRLH-TLs.

unequalled performances and design ease, which are discussed in the present chapter.

Next, we study the Bloch impedance of the CRLH-TL and show that this parameter must also be considered for the design of micromachined CRLH-TLs with a wide bandwidth. Based on all aforementioned developments, we eventually provide a simple design procedure for an optimal CRLH-TL design and demonstrators are measured on quartz substrates.

In a next section, we show that our general approach also allows designing CRLH-TLs with extreme impedance values, which have been fabricated and measured. Finally, we also discuss the design of CRLH-TL optimized for operation at a different frequency than the one of the transition between FW and BW bands (f_0 in Figure 6.1). The modified design method is applied to the design of multi-sectional quarter-wavelength transformer (QWT) used for antenna matching.

6.2. Equivalent periodic propagation constant γ_{equ}

6.2.1. CRLH-TL band structure

A CRLH-TL is realized by cascading any number of unit cells whose equivalent circuit is a TL loaded with shunt inductances and series capacitors, as shown in Figure 6.2. When considering an infinite periodic structure, the two unit cell definitions shown in the figure are possible, depending on the choice of the location of the reference planes of the cells. In practice, the structure is finite and the choice of the model corresponds to the actual structure so that the input and output of the finite periodic structure correspond to the reference plane of the first and last cells. Losses in the TL and loading elements are not considered in this section but will be introduced when comparing modeled and measured results on some realized micromachined CRLH-TLs.

Here again, we base our analysis on the computation of the periodic Bloch equivalents of the CRLH-TL unit cell. Since the cells are symmetrical, we can use the reduced expression recalled in (6.1) and (6.2), where A_{cell}, B_{cell}, C_{cell} and D_{cell} are the four elements of the transmission matrix.

$$\cosh\left(\gamma_{equ} d\right) = A_{cell} \tag{6.1}$$

$$Z_{equ} = \pm\sqrt{\frac{B_{cell}}{C_{cell}}} \tag{6.2}$$

The transmission matrices of the unit cells of Figure 6.2 are easily obtained by cascading the five matrices associated with the sub-elements of a cell. The equivalent propagation constant γ_{equ} is then calculated using (6.1):

$$\cosh\left(\gamma_{equ} d\right) = \frac{1}{2} Y_L Z_L \cos^2\left(\theta_h\right) + \cos\left(2\theta_h\right) + \frac{1}{2} j \left(Y_L Z_C + \frac{Z_L}{Z_C}\right) \sin\left(2\theta_h\right) \tag{6.3}$$

with $\theta_h = \beta_0 \left(d/2\right)$, and where β_0 is the unloaded host TL phase constant. Although Z_{equ} depends on the reference plane choice (as will be seen later in these developments), it is not the case of the equivalent propagation constant γ_{equ} and (6.3) is thus found equivalently for the two circuits of Figure 6.2. We will now develop (6.3) using:

$$Y_L = \frac{1}{j\omega L_P} \quad \text{and} \quad Z_L = \frac{1}{j\omega C_S} \tag{6.4}$$

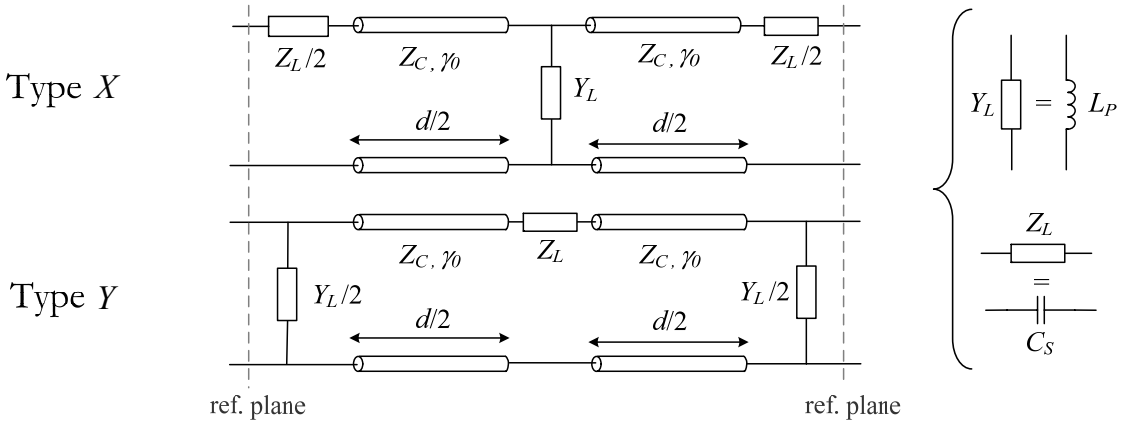

Figure 6.2: General models for unit cells made up of series/shunt loaded TL.

For reasons that will be clarified below, we also explicitly write the frequency dependence of the phase shift through the unloaded TL sections as follows:

$$\theta_h = \beta_0 (d/2) = \tau\omega \tag{6.5}$$

where τ corresponds to the propagation delay through *each* of the two line sections in a cell. With c_0 being the speed of light in vacuum and $\varepsilon_{r,eff}$ the effective permittivity of the unloaded TL sections, τ is given by:

$$\tau = \frac{d/2}{v_\phi} = \frac{d/2\sqrt{\varepsilon_{r,eff}}}{c_0} \tag{6.6}$$

Eventually, substituting (6.4) and (6.5) in (6.3) yields:

$$g' \equiv \cosh(\gamma_{equ} d) = -\frac{1}{2C_S L_P}\frac{1}{\omega^2}\cos^2(\tau\omega) + \cos(2\tau\omega) + \frac{1}{2}\left(\frac{1}{C_S Z_C} + \frac{Z_C}{L_P}\right)\frac{1}{\omega}\sin(2\tau\omega) \tag{6.7}$$

where we defined the function g'. Now let us define g as $g = g' - 1$ and rewrite (6.7) as:

$$\gamma_{equ} = \alpha_{equ} + j\beta_{equ} = \frac{1}{d}\text{acosh}\left(g' = g + 1\right) \tag{6.8}$$

It is observed that the particular network studied here leads to a *real* function g. From (6.8) we express the relation between the type of propagation in the periodic structure and the sign of the function g:

$$\begin{aligned} &\text{if } g > 0 && \rightarrow && \gamma_{equ} = \alpha_{equ} \\ &\text{if } g = 0 && \rightarrow && \gamma_{equ} = 0 \\ &\text{if } -2 < g < 0 && \rightarrow && \gamma_{equ} = j\beta_{equ} \\ &(\text{if } g < -2 && \rightarrow && \gamma_{equ} = \alpha_{equ} + j\pi) \end{aligned} \tag{6.9}$$

So, the Bloch waves guided by the structure depicted in Figure 6.2 are either purely attenuated or propagating without attenuation, provided that no losses are considered. As is the case for any periodic structure, a spatial harmonic solution for the propagation constant γ_{equ} is obtained [see the *acosh* function in (6.8)].

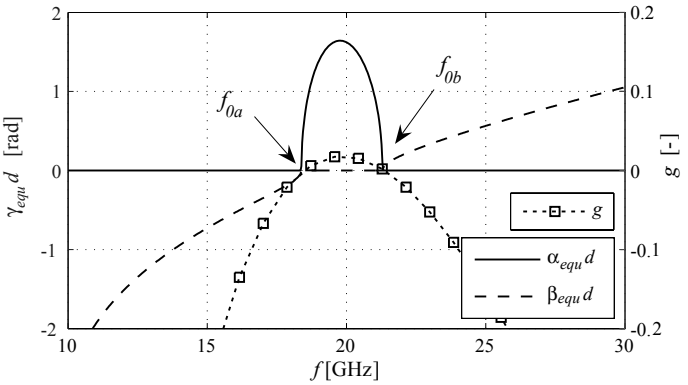

Figure 6.3: Example of function g and corresponding $\alpha_{equ}d$ and $\beta_{equ}d$.

An example of the function g and the resulting γ_{equ} is given in Figure 6.3 in the region of interest in the fundamental harmonic range. The numerical values for the circuit elements were chosen arbitrarily but are typical for micromachined designs. Below f_{0a}, the function g is negative and corresponds to a *negative* β_{equ} solution with the convention of a positive group velocity v_g (see Chapter 2). This means that the corresponding band is 'backward' since the sign of the phase velocity v_ϕ is obviously that of β_{equ}. Above f_{0b}, β_{equ} is positive (with the same convention for v_g) and this band is therefore 'forward' since v_ϕ and v_g are in the same direction. Finally, g is positive between f_{0a} and f_{0b} and the wave is purely attenuated.

It should be emphasized that the sign analysis and associated convention explained in detail in Chapter 2 is useful here for a correct physical interpretation of the mathematical results obtained. Indeed, let us imagine that the stopband in Figure 6.3 is closed such as depicted in the Figure 6.1. Mathematically, there are always two opposite solutions for β_{equ}, such as shown in Figure 6.1 by the a-b and c-d solutions below and above f_0, respectively. Now, what is the propagation of a given signal traveling in such a structure and whose spectrum covers a finite bandwidth including the transition frequency f_0? If solution 'a' is linked with solution 'd', this means that the frequency components above and below f_0 have different group velocity signs. In contrast, if 'a' is linked with solution 'c', this means that there are different phase velocity signs, but that the group velocity is approximately constant around f_0. This question is simply answered following the approach of Chapter 2; for a given traveling wave, the group velocity is always positive [except for the case of abnormal propagation, which is not the case here (see Chapter 2)]. Thus the curve selected below f_0 is that of positive slope and negative β_{equ} ('b' in Figure 6.1) and corresponds, for a given traveling wave, to that of positive slope and positive β_{equ} above f_0 ('b' in Figure 6.1). Thus, the components of the signal on a finite bandwidth below and above f_0 actually travel with an almost constant, positive, group velocity. However, the frequencies below f_0 have negative phase velocities whereas the ones above f_0 exhibit positive ones.

6.2.2. Phase shift continuity condition and 0º phase shift frequency

The location of the frequencies where both real and imaginary parts of γ_{equ} are zero determine the limits of the stopband of the structure, which are shown as f_{0a} and f_{0b} in Figure 6.3. These frequencies are therefore determined by introducing $\gamma_{equ} = 0$ in (6.8), which means that $g' = g + 1 = 1$, hence:

$$g = -1 - \frac{1}{2C_S L_P}\frac{1}{\omega_0^2}\cos^2(\tau\omega_0) + \cos(2\tau\omega_0) + \frac{1}{2}\left(\frac{1}{C_S Z_C} + \frac{Z_C}{L_P}\right)\frac{1}{\omega_0}\sin(2\tau\omega_0) = 0 \qquad (6.10)$$

As explained in [63], we wish to 'close' the stopband between f_{0a} and f_{0b} in order to obtain a continuous β_{equ} (hence a continuous phase shift) around a single solution f_0 for $\gamma_{equ} = 0$. This means that we can write:

$$f_0 \equiv f_{0a} = f_{0b} \qquad (6.11)$$

and the associated condition for closing the stopband will be referred to in this document as the *phase continuity condition*[1]. Consequently, based on expression (6.10), we are interested in:

- Finding the phase continuity condition.
- Determining the circuits elements as functions of the 0º phase shift frequency f_0 (for design purposes).

a. Existing solution

Both these issues were treated in [63] by doing Taylor expansions of the trigonometric functions of the right hand of (6.3) on the variable θ_h and around $\theta_h = 0$ (note the difference of a factor of 2 in the definition of θ_h with θ of [63]). By doing so, other variables in (6.3) are implicitly considered independent from θ_h, which is however not the case since θ_h is proportional to frequency and Y_L and Z_L are also frequency dependent (see (6.4) and (6.5)). Therefore, a Taylor expansion of a given order should rather be made on expression (6.7) and on the variable $\tau\omega$, where all the frequency dependences have been explicitly written and provided that L_P and C_S are lumped elements independent of frequency.

Nevertheless, the method presented in [63] works well under suitable conditions on the values of the parameters of the circuit (which will be derived later in this chapter and are valid in the case of [63]). The resulting phase continuity condition linking the characteristic impedance of the unloaded TL to the loading elements is given by (6.12), whereas the resulting 0º phase shift frequency f_0 is obtained with (6.13):

$$Z_C = \sqrt{\frac{L_P}{C_S}} \qquad (6.12)$$

$$f_0 = \frac{1}{2\pi\left(\tau\sqrt{4L_P C_S}\right)^{\frac{1}{2}}} \qquad (6.13)$$

[1] Saying that a CRLH-TL is *balanced* [53] means that this phase continuity condition is met.

b. Exact solution

In the approach presented here, we solve (6.10) in an exact way, namely, without doing Taylor expansions on the trigonometric functions in (6.10). Indeed, a Taylor expansion around $\omega_0 = 0$ is only precise if $\theta_h = \tau\omega_0 \ll 1$, which is usually not true in the case of designs free of surface-mount technology (SMT) elements, as will be explained later in this chapter. In addition, an expansion around the frequency f_0 (unknown of the problem) leads to a system that cannot be solved with reasonable complexity. Therefore, we start by writing $\cos^2(\tau\omega_0)$ in terms of $\cos(2\tau\omega_0)$ and obtain, after some algebraic operations:

$$\omega_0^2 (a-1) + \omega_0 \frac{1}{2} b \left(\frac{1}{C_S Z_C} + \frac{Z_C}{L_P} \right) - (a+1) \frac{1}{4 C_S L_P} = 0 \tag{6.14}$$

with

$$\begin{cases} a = \cos(2\tau\omega_0) \\ b = \sin(2\tau\omega_0) \end{cases} \tag{6.15}$$

We want (6.14) to have only one solution in ω_0 in order to close the stopband. As a and b are functions of ω_0, the left term of (6.14) is rigorously not a polynomial in ω_0. However, we can consider the electrical length $2\tau\omega_0$ as a constant at the *single* solution angular frequency ω_0, since τ is an adjustable parameter in the problem. Therefore, we can determine the condition for the pseudo-polynomial (6.14) to have a single solution by cancelling its discriminant Δ:

$$\Delta = \frac{b^2}{4} \left(\frac{1}{C_S Z_C} + \frac{Z_C}{L_P} \right)^2 + \left(a^2 - 1\right) \frac{1}{C_S L_P} = 0 \tag{6.16}$$

Due to the definition of a and b we have $a^2 + b^2 = 1$ and:

$$\Delta = \left(a^2 - 1\right) \left[\frac{1}{C_S Z_C} - \frac{1}{4} \left(\frac{1}{C_S Z_C} + \frac{Z_C}{L_P} \right)^2 \right] = 0 \tag{6.17}$$

Therefore, the first possibility for (6.10) to have only one solution ω_0 is $a = \pm 1$, which means that $2\tau\omega_0 = 0 + n\pi$, $n \in \mathrm{N}$. However, substituting a and b according to $2\tau\omega_0 = n\pi$ in (6.14) leads to non-physical solutions and we must therefore cancel the term in square brackets in (6.17) which, solved for Z_C, yields :

$$Z_C = \sqrt{\frac{L_P}{C_S}} \tag{6.18}$$

This condition is now used to substitute Z_C in (6.10), which leads to (6.19). As a result, (6.19) has a unique fundamental harmonic solution $\omega_0 = 2\pi f_0$.

$$-\left(A\omega_0^2 + \frac{1}{2} \right) + \left(A\omega_0^2 - \frac{1}{2} \right) \cos(2\tau\omega_0) + \sqrt{2A}\omega_0 \sin(2\tau\omega_0) = 0 \tag{6.19}$$

with

$$A = 2 L_P C_S \tag{6.20}$$

Expression (6.19) is a transcendental equation and solving for ω_0 is only possible numerically. However, for design purposes, it is especially useful to derive formulas providing the values of the

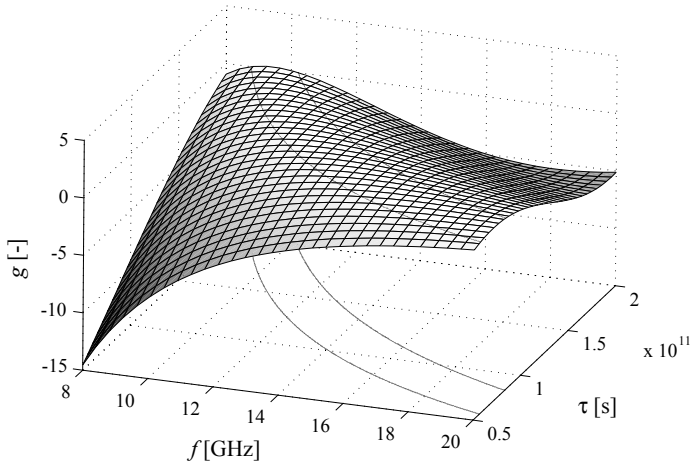

Figure 6.4: g function and $g = 0$ solutions for typical micromachined design values $Z_C = 50\ \Omega$, $L_P = 115$ pH, $C_S = 92$ fF.

circuit parameters as functions of the frequency f_0. This is possible in an exact way, since solving (6.19) for τ yields:

$$\tau = \frac{1}{2\omega_0}\arccos\left(\frac{2A\omega_0^2 - 1}{2A\omega_0^2 + 1}\right) \tag{6.21}$$

The τ solution given by (6.21) is harmonic and there are consequently an infinite number of line lengths which are solutions. However, for losses and space considerations, the most interesting solution is obviously the one corresponding to the smallest line length and is bounded within 0 and $\pi/(2\omega_0)$.

We finally present some graphical illustration of the function g on which the above calculation was based; Figure 6.4 exhibits the $g(f, \tau)$ function and the fundamental harmonic solutions to $g(f, \tau) = 0$ (which are found here numerically) with parameters as reported in the relevant caption. On the graph shown here, condition (6.18) is *not* met and two solutions curves $\tau(f)$ for which $\gamma_{equ} = 0$ are found. However, if one of the elements values is changed so that (6.18) is met, it is verified that the two curves tend to a unique solution corresponding to the analytical formula (6.21).

6.2.3. Discussion and notion of effective media

a. Conditions of equivalence

It is observed that the exact solution (6.18) to the phase continuity condition is the same as the solution found in [53, 63], despite the approximation made in the latter calculation method. In contrast, the expression linking circuit elements values and frequency f_0 are not the same [see (6.13) and (6.21)]. Here, we will discuss the correspondence between these approaches both from mathematical and physical point of views.

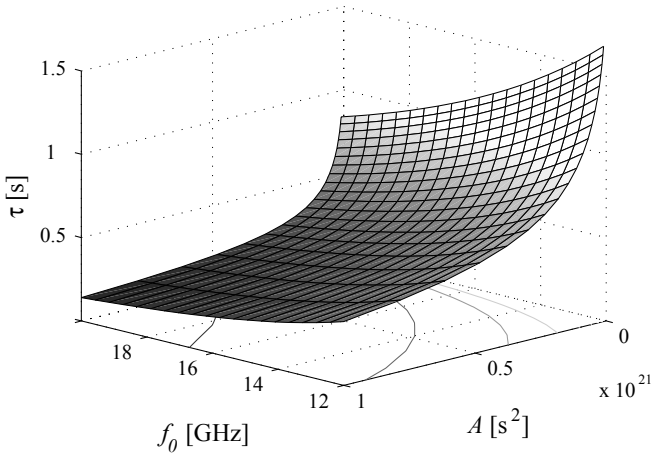

Figure 6.5: Graphical representation of formula (6.21).

With the assumption used in [63], formula (6.21) counterpart is directly deduced from (6.13):

$$\tau = \frac{1}{\sqrt{2A}\omega_0^2} \tag{6.22}$$

Now, some inspection of (6.21) shows that the conditions (6.23) and (6.24) below are equivalent in the case of balanced CRLH-TLs:

$$2A\omega_0^2 = 4L_P C_S \omega_0^2 \gg 1 \tag{6.23}$$

$$\tau\omega_0 = \beta_0 \left(d/2\right) \ll 1 \tag{6.24}$$

If we now introduce these conditions in the exact τ solution (6.21), we obtain the approximate expression (6.22), which demonstrates that (6.22) is only valid if condition (6.23) is met.

For illustration purposes, Figure 6.5 shows a plot of the exact solution for τ given by (6.21) and indicates that, for a given f_0, small line length τ are associated with large A, thus illustrating the correspondence between conditions (6.23) and (6.24).

b. Discussion

Need for the exact formulation

The practical conclusions to be drawn from the above developments for the design of CRLH-TLs are as follows: if it is possible to design large C_S and L_P —they cannot be independently maximized, due to the phase continuity condition (6.18)— at the given 0^o phase shift frequency f_0 so that condition (6.23) is met, the expressions given in [63] are suitable for the design of the CRLH-TL. For example, in [64], a design at $f_0 = 0.9$ GHz made of SMT elements mounted on a

printed CPW allows large $C_S = 22$ pF and $L_P = 54$ nH so that condition (6.23) and (6.24) are met.

In contrast, if C_S or L_P are too small for (6.23) to be met —as will be shown to be the case in a typical micromachined design— (6.24) is also not true and the exact expression (6.21) must be used for the design.

Link with the notion of effective medium

We will now show that these considerations are linked with the notion of *effectively homogeneous medium*[1], which is well known in the field of metamaterials [52, 53]. But prior to this, it is useful to clarify the different possible definitions of what is an effective medium and the corresponding conditions on the structure parameters. The criterion used in this document is as follows: *A CRLH-TL is effective if the wavelength in the host medium of the metamaterial is much larger than the unit cell dimensions.* Nevertheless, the notion of effective medium is also sometimes assessed considering the 'effective wave' propagating in the periodic structure that constitutes the metamaterial. Indeed, it is shown in [65] that effective parameters cannot be defined in a physically rigorous manner in some SRRs and wires type metamaterial in the region of resonance, namely where the Bloch wavelength is too small. However, this problem does not occur in the case of the particular metamaterial structure studied here; namely, the CRLH-TL. Indeed, the equivalent Bloch propagation constant in the frequency range of interest of such structures is close to zero, which means that the Bloch wavelength will always be much larger than the unit cell size. In conclusion, the only relevant condition for determining if a CRLH-TL is an effective medium *from a phase shift modeling point of view* is the one stated above.

This definition being clarified, we can observe that condition (6.24) is mathematically exactly equivalent to the above definition of an *effective* CRLH-TL. Thus, since we showed that (6.24) is equivalent to (6.23) for a balanced CRLH-TL, we can conclude that the CRLH-TL will be effective if it is possible to design sufficiently large C_S and L_P at the given 0^o phase shift frequency f_0. In other words, developments presented in previous works on CRLH-TL such as [53, 64] are valid as long as the CRLH-TL is effective. If it is not the case, the exact expressions hereby deduced must be employed.

Non-effective CRLH-TLs

We will now make several comments with regard to the effective and non-effective CRLH-TLs, both from vocabulary and physical point of views. First, let us comment on the use of the term 'metamaterial' in the present context. It is often stated that a structure must be effective to be referred to as a metamaterial. This seems quite logical, in the sense that the word 'material' refers in our common understanding to a structure that is homogenous, and that a metamaterial behaves as a *homogenous* transmission media for the propagating wave only if it is effective [52,53]. Indeed, in this case only, it is possible to define *effective parameters* for the propagation of the wave in the metamaterial, which are valid at any point in the structure [52, 65]. For that reason, and also because a 1-D structure should rather not be referred to a 'material', it seems appropriate here to

[1] In this thesis, by abuse of language, the terms *(non-)effectively homogeneous* will usually be replaced by the simpler expression *(non-)effective.*

refer to our non-effective CRLH-TL as a meta-transmission line but not as a metamaterial.

Although this question of vocabulary is important for a good communication in the field, more important here is to understand if a CRLH-TL which is not effective according to (6.23) and (6.24) is still useful from an application point of view. In other words, can we employ non-effective CRLH-TLs for the applications listed in the introduction of this chapter or is there some special requirement in terms of modeling or performance that prevents such use ?

First, from a modeling point of view, we showed here that it is possible to describe the propagation in non-effective CRLH-TL in a similarly convenient way as with effective parameters by using the periodic structure Bloch equivalents of the structure. The main difference between the effective and non-effective medium situations is that the effective parameters are defined anywhere in the structure for the former, whereas the latter is described by its periodic structure equivalents only at the reference planes between unit cells[1]. Keeping this in mind, it is clear that all CRLH-TL applications based on phase shifting (arrays feed networks [58], dual-band couplers [59], resonators [60], baluns [61]) can be implemented using non-effective CRLH-TL provided an appropriate placement of the reference planes.

More complicated is the case of applications where the CRLH-TL is not a purely 'wave guiding' structure but interacts with some 'external' field, such as in the case of an antenna. In this case, it is expected that there is some requirement for the structure to be effective for a proper radiation and modeling of this one with simple 'effective' concepts. However, even in this case, several groups have published results showing that metamaterial structures that *cannot* be considered as effective media regarding the modeling of the propagation in the structure, can still behave as effective media from a scattering point of view. A first example is the CRLH-TL leaky-wave antenna presented in [62], which exhibits a phase shift in the unloaded TL sections of $\tau\omega_0 = \beta_0 d/2 \simeq 0.9$, which is obviously not $\ll 1$ and thus do not meet (6.24). Second, similar considerations as the ones made here in the case of the CRLH-TL structure were also observed in the case of SRR-based metamaterials. Indeed, it was shown that such structures presenting unit cell dimensions *not very small* in terms of free space wavelength —namely, $\lambda/6$ [66], $\lambda/10$ [67]— can still behave as effective media from a scattering point of view, although their size makes the usual effective parameters modeling less accurate [68].

6.2.4. Experimental validation

a. Design

This section presents a numerical and experimental validation of the formulation derived above based on a micromachining implementation. Let us start the design by setting the unloaded line impedance Z_C to the reference impedance of 50 Ω; we will see later that this is not an optimal choice for a large CRLH-TL bandwidth but this is sufficient for the present validation. We then select an inductance $L_P = 115$ pH and we find $C_S = 46$ fF with (6.18) and $A = 1.06e-23$ s^2 with

[1] In fact, the periodic structure equivalents represent a general approach from which the effective parameters can be derived on the condition that the wavelength is much larger than the unit cell dimension.

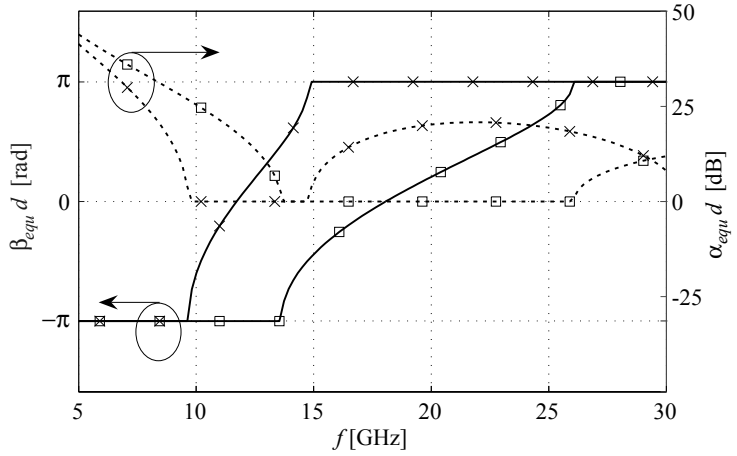

Figure 6.6: Equivalent propagation constant γ_{equ} of CRLH-TLs designed using formula 6.22 ($\times$) and formula 6.21 ($\square$).

(6.20). We must now choose τ as a function of the desired frequency $f_0 = 17.5\,\text{GHz}$, which is done using (6.21) and yields $\tau = 1.00e-11$ s. All circuit parameters are now known and Figure 6.6 exhibits the corresponding equivalent propagation constant. Also plotted is the result that would be obtained using the effective media approximation, namely, using (6.22) instead of (6.21). As expected, this second solution leads to an actual $f_0 \simeq 11\,\text{GHz}$, which is very far from the targeted value of $f_0 = 17.5\,\text{GHz}$. In contrast, we observe in the graph that using the exact solution (6.21) results in a 0^o phase shift at the target frequency $f_0 = 17.5\,\text{GHz}$.

We will now present the measurements of two integrated CRLH-TLs based on these numerical results. We decide to use the type X unit cell of Figure 6.2, which means that the inductor is placed at the center of the cell and the capacitors at the reference planes. An inspection of the circuit in Figure 6.2 shows that the series impedances at the reference planes of the cell are $Z_L/2$, hence capacitances values of $2C_S$. Therefore, a 1-cell CRLH-TL comprises two capacitors of $2C_S$ whereas CRLH-TLs with more than one cell are made up of $2C_S$ capacitors at their external ports but C_S at the connections between successive cells within the structure. As a result, and according to the numerical design above, we designed a shunt inductor $L_P = 115$ pH and series capacitors $C_S = 46$ fF and $2C_S = 92$ fF.

The design is based on the 'Al-Si EPFL' process described in Appendix A. The corresponding shunt inductor was presented as a 'building block' in Chapter 3, and the measured associated resistance in series with L_P is $R_P = 1.2\ \Omega$. We also designed interdigited capacitors C_S and $2C_S$ and measured values of 49 fF and 88 fF, for targeted values of 46 fF and 92 fF, respectively (this corresponds to gaps in the range of $6-10\ \mu$m here). Finally, the CPW sections length are chosen using (6.21) for a 0^o phase shift at $f_0 = 17.5\,\text{GHz}$ and a total cell length of 2.5 mm is obtained.

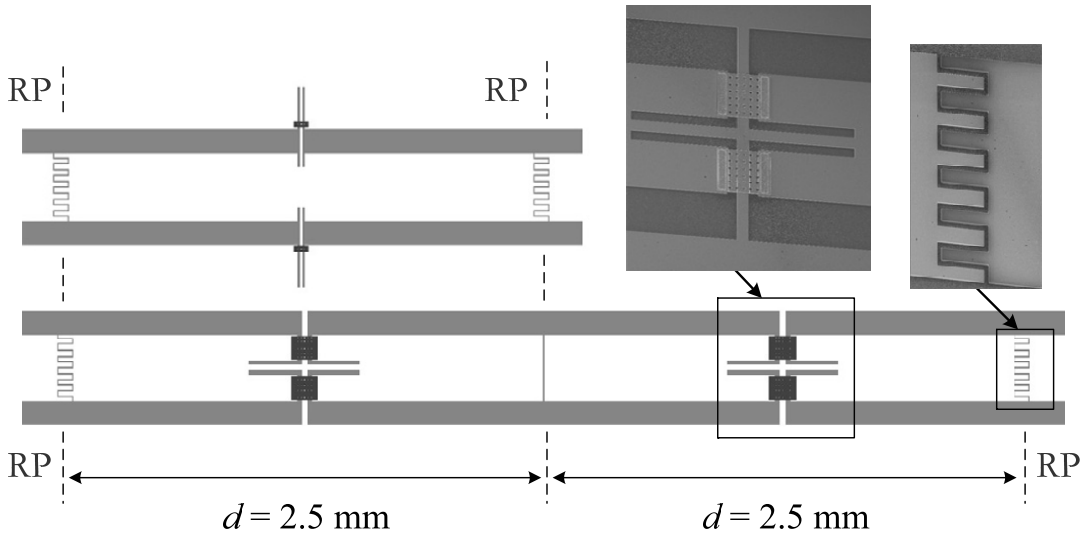

Figure 6.7: Layouts and SEM pictures of the measured 1-cell (top) and 2-cell (bottom) micromachined CRLH-TL.

b. Results

The 1-cell and 2-cell designed CRLH-TL layouts, which have been made with different inductor types, are shown in Figure 6.7. In Figure 6.8 is plotted the equivalent propagation constant of the 1-cell CRLH-TL. The measured data is obtained by converting the measured S-parameters into ABCD matrices and applying (6.2). Modeled results are also obtained using (6.1), but the unit cell ABCD matrix is calculated by cascading the five ABCD matrices associated with the sub-elements of a cell and visible in the circuits of Figure 6.2.

The useful part of the measured frequency range is the passband around $f_0 = 17.5\,\text{GHz}$, denoted as 'CRLH band' in the figure. The measured γ_{equ} is similar to the modeled one with the ideal unit cell model used for the design and visible in Figure 6.2 (dashed line). In order to get an even more precise modeling of the device, CPW losses and inductor parasitics R_P and L_S can be included in the circuit, as shown in Figure 6.9. The CPW losses were measured on an unloaded line to be 0.6 dB/cm. R_P and L_S were extracted from a measurement on an *isolated* shunt inductor and are 1.2 Ω and 4 pH, respectively. It is seen in Figure 6.8 that modeled curves (dashed squared line) are now almost indistinguishable from the measured one, except outside the useful band and when the attenuation reaches about 30 dB. It is also interesting to observe that a very good agreement between model and measurements is obtained in the stopband. As the whole device is well modeled by simply cascading TL sections and loading elements separately characterized, it is understood that higher order mode coupling effects between successive elements are negligible.

We present in Figure 6.10 modeled and measured results in terms of S-parameters. Here again, a good agreement between simulation and measurements is observed. The performances in terms of matching and insertion loss are satisfactory. However, we will present later in this chapter similar devices exhibiting much better performances, due to the use of a fabrication technology

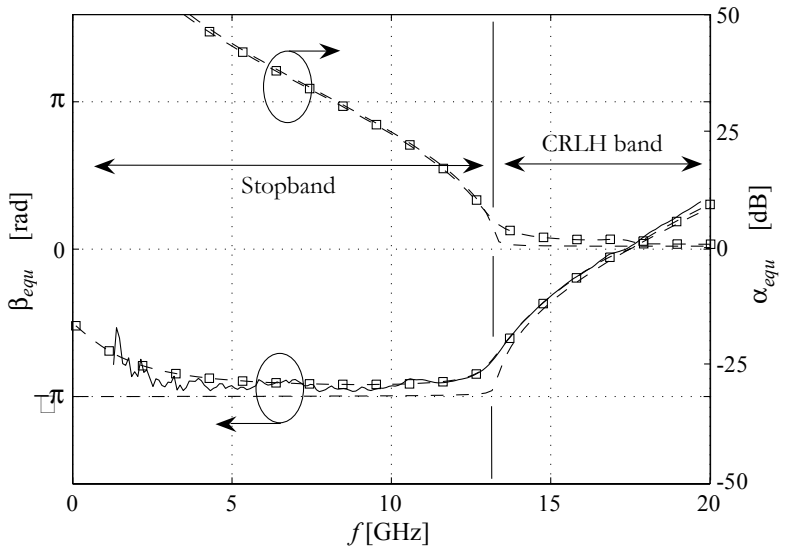

Figure 6.8: Measured (—) and modeled (– –) equivalent propagation constant of the 1-cell CRLH-TL of Figure 6.7. The modeled results are based on the circuit of Figure 6.9. Squared modeled results include CPW losses and shunt inductor parasitics R_P and L_S.

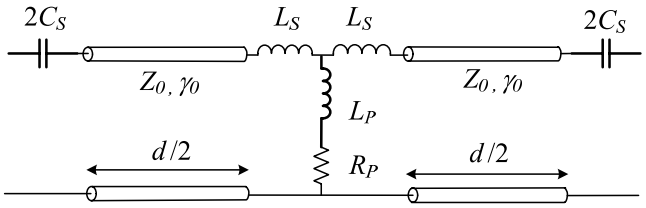

Figure 6.9: Unit cell model including CPW losses and shunt inductor parasitics. $C_S = 49$ fF, $L_P = 119$ pH, $\tau = 1.00e{-}11$ s, CPW losses: 0.6 dB/cm at 17.5 GHz, $R_P = 1.2\ \Omega$ and $L_S = 4$ pH.

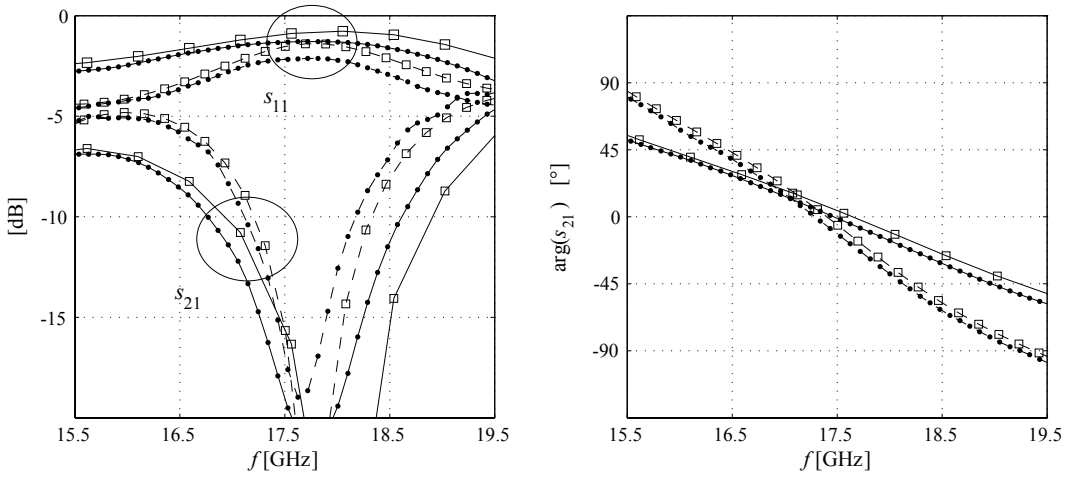

Figure 6.10: S-parameters of the 1-cell (—) and 2-cells device (– –), circuit model (□) and measurements (•).

with reduced losses and a design method improving considerably the matching performances of the CRLH-TL. Nevertheless, these first implementations allowed validating the modeling of micromachined non-effective CRLH-TLs.

6.3. Equivalent periodic impedance Z_{equ}

6.3.1. Theory

This section studies the Bloch impedance Z_{equ} of the CRLH-TL unit cells of Figure 6.1. This impedance, which can be seen as the equivalent *characteristic* impedance of an infinite or finite CRLH-TL structure, is obtained by computing (6.2) from the unit cell transmission matrices. We obtain general expressions for the equivalent impedances of both circuits X and Y of Figure 6.2, named $Z_{equ,X}$ and $Z_{equ,Y}$:

$$Z_{equ,X} = \pm 2\sqrt{\frac{L_P^2\omega^2 Z_C^2 \cos(\tau\omega)\, H(\omega)}{G(\omega)}} \tag{6.25a}$$

$$Z_{equ,Y} = \pm\frac{1}{2}\sqrt{\frac{H(\omega)\, G(\omega)}{\cos(\tau\omega)\, C_S^2\omega^2}} \tag{6.25b}$$

with:

$$G(\omega) = \left(4C_S L_P\omega^2 - 1\right) Z_C \cos(\tau\omega) + 2\omega\left(L_P + C_S Z_C^2\right)\sin(\tau\omega) \tag{6.26}$$

$$H(\omega) = \frac{2C_S\omega Z_C \sin(\tau\omega) - \cos(\tau\omega)}{2L_P\omega \sin(\tau\omega) - Z_C \cos(\tau\omega)} \tag{6.27}$$

Here it should be noted that the Bloch impedance of a CRLH-TL structure was already introduced in [69] for structure Y in a general 2-D case. Here, (6.25a) and (6.25b) provide this impedance for both X and Y circuits in a 1-D case in a particular convenient form for a linear design procedure (see below).

a. Particular case: balanced CRLH-TLs

We are especially interested in matching *balanced* CRLH-TLs, namely, CRLH-TLs satisfying the phase continuity condition (6.18). Thus we introduce (6.18) in the general Z_{equ} expressions (6.25a) and (6.25b), which yields:

$$Z_{equ,X} = \pm \frac{2L_P\omega}{\sqrt{K(\omega)}} \tag{6.28a}$$

$$Z_{equ,Y} = \pm \frac{\sqrt{K(\omega)}}{2C_S\omega} \tag{6.28b}$$

with

$$K(\omega) = 4C_S L_P \omega^2 - 1 + 4\sqrt{C_S L_P}\omega \tan(\tau\omega) \tag{6.29}$$

The aforementioned sign ambiguity of the Bloch impedance is visible in (6.28a) and (6.28b). However, the condition that the transfer of active energy P_{act} toward the direction of positive group velocity is also positive –this is true for the type of structure studied here [21, 64]– makes it possible to identify the right sign for given numerical values of the parameters. This issue was treated in Section 2.3.2 and we showed that the sign in (6.28a) or (6.28b) must be chosen so that $Re[Z_{equ}] > 0$. Here, $K(\omega) > 0$ above the cutoff frequency[1] f_c and choosing the positive solution of $\sqrt{K(\omega)}$ means that the right sign in (6.28a) and (6.28b) is the '+' sign. Below f_c, Z_{equ} is purely imaginary and no energy is transferred, making the use of the same approach impossible. However, any real device exhibits some losses and the positive active transmitted power can be used to determine the right solution sign. Here, the sign of the imaginary part is negative below f_c for topology Y whereas it is positive for circuit X.

b. Effective medium limit

We now first show that the general expressions for Z_{equ} (6.28a) and (6.28b) can be simplified in the case of an effective CRLH-TL. In order to do so, we firstly use the 1st-order approximation $\tan(\tau\omega) \simeq \tau\omega$ since we have $\tau\omega_0 \ll 1$ in this particular case. Secondly, we introduce (6.22) in condition (6.23), which are also both true in the case of an effective CRLH-TL, and obtain:

$$2\sqrt{L_P C_S} \gg \tau \tag{6.30}$$

As a result, expressions (6.28a) and (6.28b) are, in the case of an effective medium CRLH-TL (hence the *EM* subscript in the expression below):

$$Z_{equ,EM,X} = \pm \frac{2L_P\omega}{\sqrt{4C_S L_P\omega^2 - 1}} \tag{6.31a}$$

[1] which corresponds to $K(\omega) = 0$ in (6.28a) and (6.28b).

$$Z_{equ,EM,Y} = \pm\frac{\sqrt{4C_S L_P \omega^2 - 1}}{2C_S\omega} \tag{6.31b}$$

Employing now (6.23) in (6.31a) or (6.31b) equally yields (6.32), which gives the value of the impedance at f_0 in the particular case of an effective CRLH-TL.

$$Z_{equ,EM,X}\left(f_0\right) = Z_{equ,EM,Y}\left(f_0\right) = \sqrt{\frac{L_P}{C_S}} \tag{6.32}$$

c. Examples

Figure 6.11 numerically illustrates expressions (6.28a), (6.28b) and (6.31a), (6.31b) in the cases of an effective and a non-effective CRLH-TL. The circuit parameters for the comparison were chosen so that both structures exhibit the same frequency of 0° phase shift $f_0 \approx 22$ GHz. For that purpose, we introduce the variable m and plot the results for $L_P = m \cdot 115$ pH, $C_S = m \cdot 46$ fF and $\tau = (1/m)\, 1e-11$ s. In the left row of Figure 6.11 , $m = 8$ and the parameters of the circuit satisfy condition (6.24) since $\tau\omega_0 = 0.03 \ll 1$ and the approximate effective medium impedances (6.31a) and (6.31b) closely match the exact solutions. However, if C_S and L_P are reduced, (6.31a) and (6.31b) differ from solutions (6.28a) and (6.28b). This is shown in the right hand side of Figure 6.11 ($m = 2$), where a significant discrepancy is observed, although the TL sections are still relatively short in this case ($\tau\omega_0 = 0.11 \ll 1$).

6.3.2. Optimal design of CRLH-TLs

a. Principle

In order to optimally match a CRLH-TL, the parameters of the circuit must be chosen so that its Bloch equivalent impedance is equal to the reference impedance. Therefore, this requirement must be combined with the phase shift continuity condition in order to get an optimal matching around the frequency of 0° phase shift f_0.

Case 1: Effective CRLH-TL

Introducing the phase continuity condition (6.18) in (6.32) yields:

$$Z_{equ,EM,X-Y}\left(f_0\right) = \sqrt{\frac{L_P}{C_S}} = Z_C \tag{6.33}$$

Equating the impedance $Z_{equ,EM,X-Y}\left(f_0\right)$ to the reference impedance Z_{ref} simply gives:

$$Z_C = \sqrt{\frac{L_P}{C_S}} = Z_{ref} \tag{6.34}$$

which means that an optimal matching at f_0 is simply obtained by choosing unloaded TL sections of characteristic impedance Z_C equal to the reference impedance and, of course, C_S and L_P according to (6.33). This simple condition, valid in the case of effective CRLH-TLs, was already presented and discussed in several works such as [63] or [59].

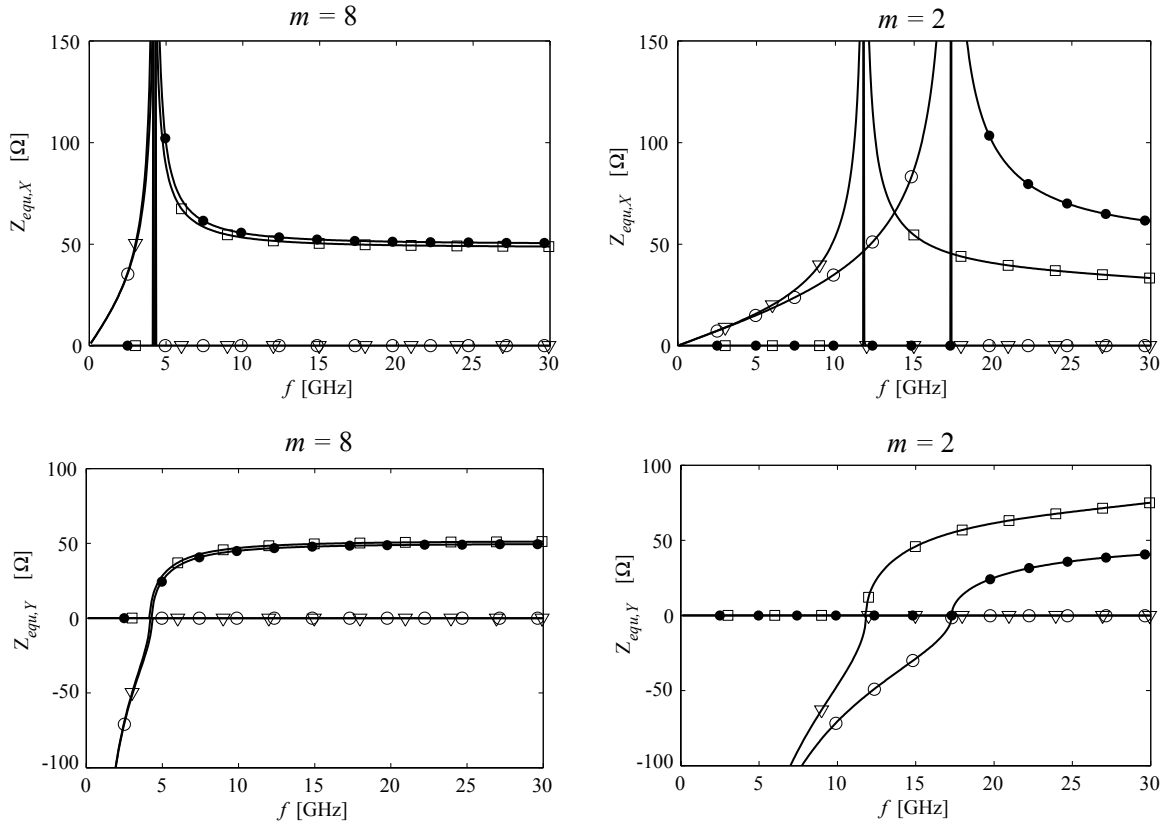

Figure 6.11: Bloch wave equivalent impedance (real part: □, imag. part: ▽) and effective medium approximation (real part: •, imag. part: ○) for $m = 8$ and $m = 2$.

Case 2: Non-effective CRLH-TL

In this case, we observe that Z_{equ}, given by (6.28a) or (6.28b), is strongly frequency-dependent around f_0 and cannot simplified as in the above effective case. In this context, we show in the next section how to achieve an optimal matching in this general case.

b. Design Method

An optimal matching at f_0 requires that the equivalent impedances $Z_{equ}(f_0)$ given by (6.28a) or (6.28b) is equal to the reference impedance Z_{ref}. This equality is written as (6.35a) and (6.35b), where we also eliminated τ using (6.21):

$$Z_{equ,X}(f) = \frac{2L_P\omega}{\sqrt{4C_SL_P\omega^2 - 1 + 4\sqrt{C_SL_P}\omega\tan\left(\frac{1}{2}\arccos\left(\frac{4L_PC_S\omega_0^2-1}{4L_PC_S\omega_0^2+1}\right)\right)}} = Z_{ref} \tag{6.35a}$$

$$Z_{equ,Y}(f) = \frac{\sqrt{4C_SL_P\omega^2 - 1 + 4\sqrt{C_SL_P}\omega\tan\left(\frac{1}{2}\arccos\left(\frac{4L_PC_S\omega_0^2-1}{4L_PC_S\omega_0^2+1}\right)\right)}}{2C_S\omega} = Z_{ref} \tag{6.35b}$$

In these expressions, and in comparison with (6.31a) and (6.31b), the '+' sign has been selected since it is the right one in the passband of the structure (see Section 6.3.1). We are here particularly interested in obtaining an optimal matching at $f = f_0$ (or $\omega = \omega_0$); At this frequency, it is possible to reduce (6.35a) and (6.35b) by some successive algebraic operations. We finally obtain:

$$Z_{equ,X}(f_0) = \frac{2L_P\omega_0}{\sqrt{4C_SL_P\omega_0^2 + 1}} = Z_{ref} \tag{6.36a}$$

$$Z_{equ,Y}(f_0) = \frac{\sqrt{4C_SL_P\omega_0^2 + 1}}{2C_S\omega_0} = Z_{ref} \tag{6.36b}$$

Equations (6.36a) and (6.36b) can now be solved for C_S or L_P, which will allow deriving a purely analytical and linear design method. The choice of the parameter C_S or L_P to solve for depends on which circuit element we wish to fix as a first step in the design. Here, we decide to set L_P and thus solve (6.36a) and (6.36b) for C_S:

$$C_{S,X}(L_P, \omega_0, Z_{ref}) = \frac{(2L_P\omega_0)^2 - Z_{ref}^2}{4Z_{ref}^2L_P\omega_0^2} \tag{6.37a}$$

$$C_{S,Y}(L_P, \omega_0, Z_{ref}) = \frac{L_P\omega_0 + \sqrt{\omega_0^2L_P^2 + Z_{ref}^2}}{2Z_{ref}^2\omega_0} \tag{6.37b}$$

As a result, the following simple design procedure can be employed to design a balanced CRLH-TL with a frequency of 0^o degree phase shift f_0 and an impedance at f_0 equal to the reference impedance Z_{ref}:

1. Choose L_P (or C_S) according to technological issues and considering losses and precision.
2. Since $\omega_0 = 2\pi f_0$ and Z_{ref} are targets in the design, we can directly deduce C_S from (6.37a) or (6.37b) (L_P can be computed here as well if it was chosen to fix C_S in step 1.).
3. Finally the characteristic impedance Z_C of the TL sections is chosen using the phase continuity condition (6.18) and the length of these TL sections is calculated using (6.21) and (6.5).

It is noticeable that (6.37a) only yields a positive, namely, realizable solution for $C_{S,X}$ if $2L_P\omega_0 > Z_{ref}$. Thus, the value of L_P chosen in the first step of the design must meet this condition in order to complete the design. This design procedure is simple and mainly differs from the effective medium case in the way that the characteristic impedance of the TL sections Z_C is not necessarily equal to the reference impedance Z_{ref}.

6.3.3. Results

a. Topologies and design solutions

In the examples given here, we set $f_0 = 18$ GHz and the reference impedance Z_{ref} to 50 Ω. Figure 6.12 shows the left part of (6.35a) and (6.35b), i.e. the equivalent Bloch impedance of the structure in both configurations X and Y of Figure 6.2, as functions of C_S and for different L_P values. For instance, if we want to match our structure to $Z_{ref} = 50\ \Omega$ with $L_P = 4 \cdot 130$ pH and using circuit X, the solution to (6.35a) is $C_S \simeq 167$ fF and is found analytically using (6.37a).

This graphical illustration provides some other interesting information; if it is not possible to achieve sufficiently large L_P value, it might be impossible to match exactly the structure of type X at f_0. For instance if $L_P = 130$ pH, Z_{equ} is always smaller than 50 Ω for any realizable value of C_S. However, the graph shows that type Y is preferable in this situation since it is possible to match the structure even for rather low L_P values. It is also observed that the two types of curves X and Y converge when C_S and/or L_P are large, thus confirming previous developments; indeed, a large $C_S L_P$ product at a given frequency —so that (6.23) is true— means that we tend to an effective medium case, for which it was shown that the two types of structures exhibit the same characteristic impedance (6.32). On the graph is also plotted the characteristic impedance Z_C of the unloaded TL sections providing a continuous phase shift at f_0, according to (6.18). Here again we graphically observe that Z_C is only equal to Z_{ref} and Z_{equ} in the case of an effective medium design ($m = 16$).

b. Experimental validation

This section compares the design method described above, which takes into account the equivalent impedance of the structure (*matched* method), with a design method that does not consider this parameter, referred to as the *unmatched* method. In the second case, we simply choose $Z_C = Z_{ref}$, which is the optimal choice in the case of an 'effective design'.

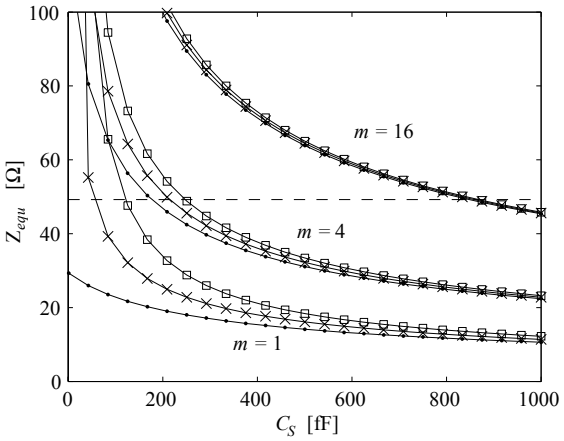

Figure 6.12: Impedances considered in the design of a CRLH-TL: $Z_{equ,X}$ (•), $Z_{equ,Y}$ (□), Z_C (×), Z_{ref} (– –). $L_P = m \cdot 130$ pH.

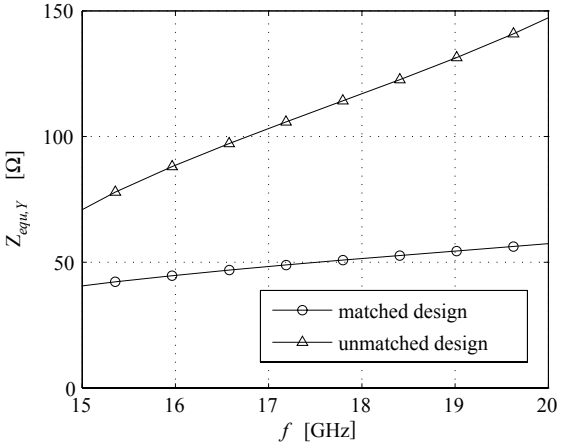

Figure 6.13: Impedance of a CRLH-TL in the case of a *matched* (○) and *unmatched* (△) design with $Z_{ref} = 50$ Ω.

For this study, we choose again $f_0 = 18$ GHz, $Z_{ref} = 50$ Ω and consider the structure Y, which was shown to be preferable for designs with small L_P. With $L_P = 130$ pH we find $C_S = 118$ fF, $Z_C = 33.2$ Ω and $\tau = 7.48e-12$ with the *matched* method and $C_S = 52$ fF, $Z_C = Z_{ref}$ and $\tau = 9.19e-12$ with the *unmatched* method. The resulting equivalent impedances for these designs are calculated using (6.28b) and are shown in Figure 6.13; the *unmatched* design presents an equivalent impedance of more than 100 Ω whereas the *matched* method results in an impedance of exactly 50 Ω at f_0.

Two-cell CRLH-TLs have been designed and fabricated to demonstrate experimentally the advantage of the *matched* design over its *unmatched* counterpart. The layout of each loading element (L_P, C_S and $2C_S$) for both structures was determined by full-wave simulations using HFSS and circuit extraction to achieve the above numerical values. For a good precision, underetching in the process was compensated for in the masks and the typical wirebond height was measured to be precisely accounted for in the simulations. The technology used for the designs is the 'Al-quartz EPFL' process described in Appendix A and Figure 6.14 shows the fabricated 2-cell *unmatched* and *matched* CRLH-TLs. The measured S-parameters, obtained on-wafer by means of a TRL calibration, are shown in Figure 6.15. First, it is observed that the measured frequency of 0° phase shift f_0 is close to the design frequency of 18 GHz for both devices. Since the structures exhibit an electrical length that is zero at this frequency, the matching and insertion loss are good for both structures in a narrow band around f_0. The insertion loss at this frequency is about -0.8 dB, so only -0.4 dB per unit cell. This is much better than for the devices fabricated on silicon wafers and previously presented in this chapter, due to the reduced losses of quartz implementations over silicon ones (see Chapter 3).

Now, let us observe the performances of both *matched* and *unmatched* structures on a certain

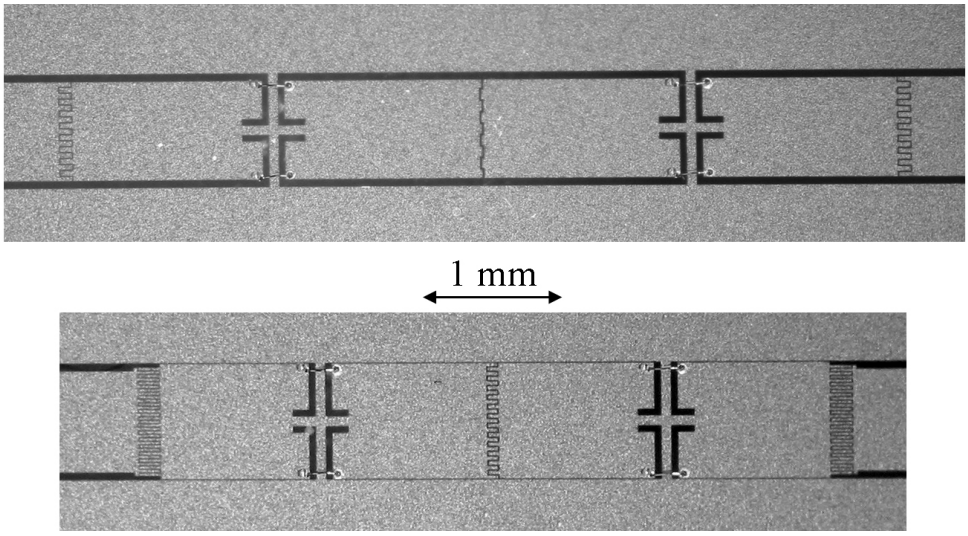

Figure 6.14: Pictures of the measured unmatched (top) and matched (bottom) 2-cell CRLH-TLs.

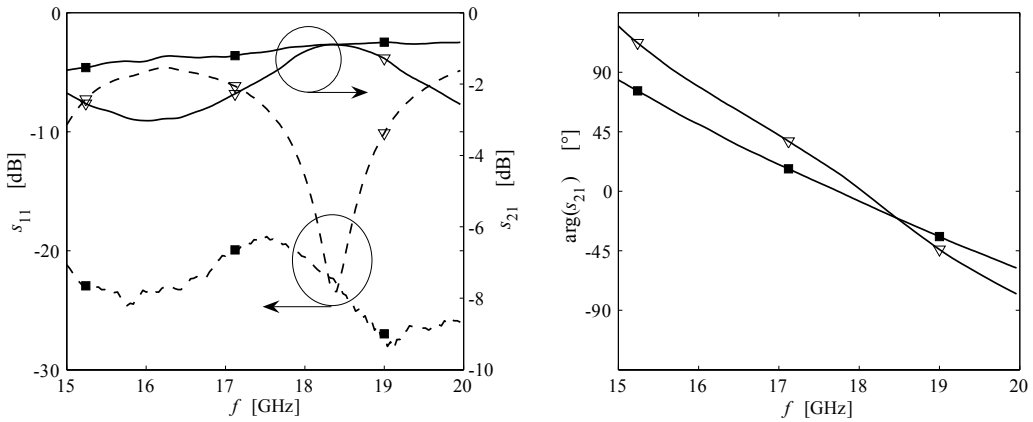

Figure 6.15: Comparison of the measured S-parameters for 2-cell CRLH-TLs designed with unmatched and matched design methods. Matched method (■), unmatched method (▽).

bandwidth around f_0. The -10 dB input return loss bandwidth is about 1.2 GHz in the *unmatched* case whereas the *matched* structure presents a mismatch lower than -20 dB on the whole measured bandwidth (15 GHz - 20 GHz). This means that the input return loss bandwidth is at least four times larger thanks to the *matched* design method. The reason for this very large relative bandwidth is not only that Z_{equ} is exactly 50 Ω at f_0 but also that it exhibits little variation around f_0, as can be seen in Figure 6.13. It is also noticeable that the insertion loss is much better than in the case of the *unmatched* design as well, which results from the difference in terms of matching rather than ohmic losses.

Finally, the *matched* design method results in a better linearity of the phase shift around f_0, as can be seen in the right hand side of Figure 6.15. This is due to the poor matching of the unmatched structure, which results in some oscillations in the phase shift expressed in terms of S-parameters. In the case of the *matched* design, the very good matching on the whole bandwidth results in $\arg(s_{21}) \simeq 2(-\beta_{equ} d)$, where the factor 2 accounts for the two cells cascaded here.

c. Leaky wave antenna (LWA) application

The inherent dispersion property of the CRLH-TL makes it a very interesting candidate to realize leaky wave antennas (LWAs) [62, 70]. Indeed, a wave propagating in a CRLH-TL structure gives rise to a main radiated beam in the backward or forward direction, depending on whether the frequency is located in the left or right-handed band of the CRLH-TL, respectively. The radiation angle from broadside θ_{ML} of the main lobe of a matched LWA is linked to the Bloch wave phase constant β_{equ} and free-space wavenumber k_0 by [70]:

$$\sin\theta_{ML} = \frac{\beta_{equ}}{k_0} \tag{6.38}$$

As a result, scanning in both backward and forward directions can be obtained either by frequency scanning on a fixed CRLH-TL, or, preferably, by an additional control of the unit cell phase shift at a fixed frequency. Such a control is done in [70] by means of varactors diodes but could also be implemented using MEMS.

This section illustrates the use of the CRLH-TL design approach presented in this chapter in the case of LWAs. First, let us note that some LWAs implementations cannot be considered as effective media regarding the propagation in the structure, according to condition (6.24). Indeed, data provided in [62] and [70] lead to $\beta_0(d/2) = 0.9$ and 0.6, respectively. In this context, the design method presented here allows designing CRLH-TL LWA with an accurate control of the 'broadside frequency' f_0 and a control of the antenna impedance around f_0. It should be noted here that, as explained in [66], metamaterials that do not meet the effective medium condition regarding the propagation in the structure can still behave as an effectively homogeneous media regarding scattering effects (hence the good radiation properties of the LWAs of [62] and [70]).

A LWA that exhibits a Bloch wave impedance different from the reference impedance must be matched, for instance, using $\lambda/4$ transformers. The advantage of designing a LWA with a well controlled Bloch impedance is twofold; first, no matching circuit is required, which can result in some important space saving in particular cases (e.g. LWAs array for pencil scanning). Second,

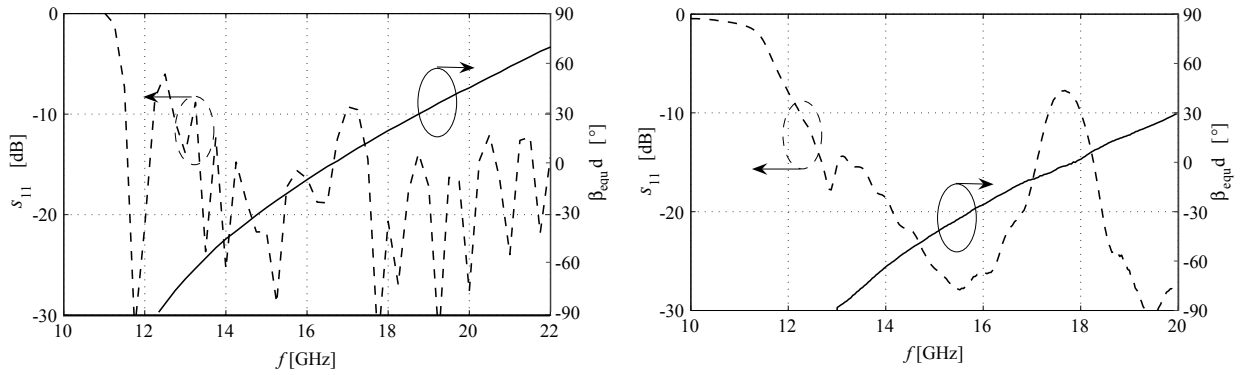

Figure 6.16: Input return loss and unit cell phase shift for a 16-cell LWA designed with the presented method and without matching network. (a) Simulated, (b) measured, by extrapolation from a 2-cell measurement.

Table 6.1: Unit cell phase shift and radiation angle

f	$\beta_{equ}d$	θ_{ML} (6.38)	θ_{ML} pattern	$\Delta\theta_{ML}$
15 GHz	-27°	-31°	-34°	-3°
16 GHz	-10°	-10°	-14°	-4°
18 GHz	19°	17°	14°	-3°
20 GHz	45°	39°	35°	-4°

a wider BW can be achieved than using frequency-dependant matching networks such as $\lambda/4$ transformers.

Figure 6.16(a) shows the simulated input return loss of a 16-cell LWA that radiates at broadside at about 17 GHz and whose Bloch impedance was set equal to the reference impedance of 50 Ω. The antenna is terminated on a 50 Ω load and a very wide BW is obtained since the matching is better than -10 dB on almost the whole band from 13 GHz to 22 GHz. It is noticeable that this band corresponds to a very wide range of unit cell phase shift $\beta_{equ}d$ since it is about -70° and +70° at the limit of the BW. The radiation patterns at different frequencies within the BW are shown in Figure 6.17. The simulated angles of radiation of the main beam are compared with formula (6.38) in Table 6.1; a small discrepancy of no more than 4° is observed for all frequencies.

Integrated LWA have been designed and fabricated on the 'Al-Quartz EPFL' process. However, due to some problem in obtaining a good connection from wafer to SMA connector at frequencies up to 20 GHz, no radiation pattern or connected measurement were taken. Nevertheless, some experimental data for the input return loss of the 16-cell LWA can be deduced from on-wafer measurements by cascading 8 identical measured 2-cell networks. The corresponding results are shown in Figure 6.16(b); the phase response is shifted from 17 GHz to 18 GHz, which is believed

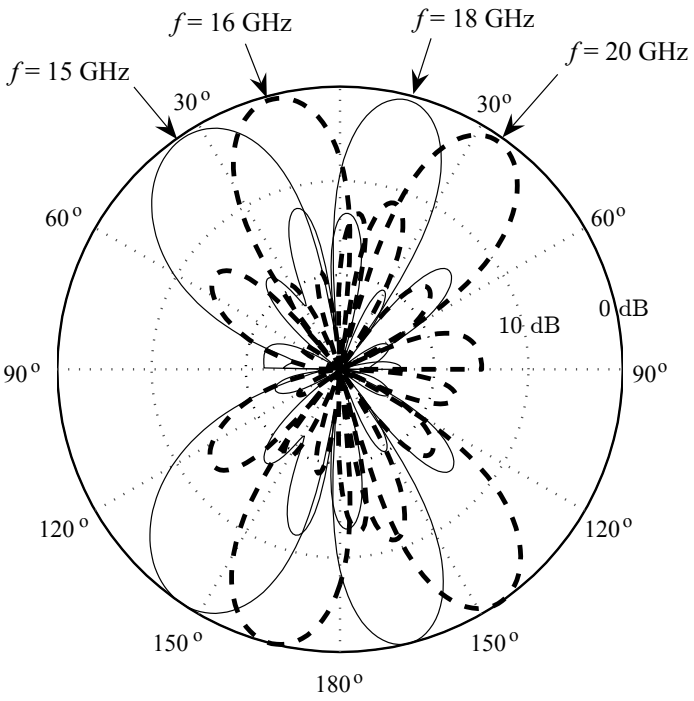

Figure 6.17: Simulated radiation patterns at different frequencies.

to be due to the modeling of the wirebonds shape in the structure. The measured -10 dB BW is similar to the simulated one, although the measurements are limited to 20 GHz due to the measurement setup. The measured BW is therefore at least 12-20 GHz, except for a small degradation to about -8 dB around 17.7 GHz.

In conclusion, a LWA designed to exhibit the appropriate Bloch impedance can be well matched—without the need of a matching network—on a very wide BW, comprising a wide range of radiation angles.

6.4. High/low impedance CRLH-TLs

6.4.1. Introduction

Metamaterial TLs with extreme impedance values have recently been studied in [71]. These were implemented using a microstrip line with complementary split ring resonators (CSRRs) etched in the ground plane. Here we show that the CRLH-TL structure also allows achieving especially high or low impedances. Although the CSRR approach allows designing TLs with a very wide range of impedance at a given frequency, the impedance obtained is strongly frequency-dependent. This is due to the resonant nature of the CSRRs and severely limits the bandwidth. In contrast, the CRLH-TL is a non-resonant structure, and we show here that the design method previously employed,

free from the effective media assumption, allows designing CRLH-TLs with an impedance beyond the range achievable using conventional design, and this on a very wide BW. Finally, the CRLH-TL low/high-impedance TL presents the advantage over the CSRR implementation that it can be used for the various applications of CRLH-TL, whenever extreme impedance values are required.

6.4.2. Theory

First, we calculate the product of the Bloch impedance of the type X and type Y CRLH-TLs at the frequency f_0, respectively given by (6.36a) and (6.36b), which yields:

$$Z_{equ,X}(f_0) \cdot Z_{equ,Y}(f_0) = Z_C^2 \tag{6.39}$$

Dividing now (6.36a) by (6.36b) and considering that lumped elements values and frequency are always positive, we get:

$$\frac{Z_{equ,X}(f_0)}{Z_{equ,Y}(f_0)} = \frac{4C_S L_P \omega_0^2}{4C_S L_P \omega_0^2 + 1} < 1 \tag{6.40}$$

Finally, combining (6.39) and (6.40), we obtain:

$$Z_{equ,Y}(f_0) > Z_C > Z_{equ,X}(f_0) \tag{6.41}$$

a. Discussion

From these simple calculations we deduce that:

(i) Result (6.41) means that a CRLH-TL of type X (resp. Y) will always exhibit a lower (resp. higher) impedance $Z_{equ}(f_0)$ than the unloaded TL impedance Z_C. Thus, topology X should be selected if the minimum host impedance Z_C achievable in the technology considered is larger than the desired CRLH-TL impedance. In contrast, topology Y must be selected if the technology does not allow sufficiently high unloaded TL impedance values.

(ii) Some inspection of (6.39) shows that the difference between Z_{equ} and Z_C is only significant if $4L_P C_S \omega_0^2 \gg 1$ is *not* true. Now, this condition was shown to be the one required for a CRLH-TL to be effective. We can thus conclude that we can only extend the range of achievable CRLH-TL impedance much beyond the limit of the technology Z_C in the case of non-effective CRLH-TLs. This obviously also means that a CRLH-TL design strategy based on the effective medium assumption does not allow designing low or high impedance CRLH-TLs. However, the general method presented in Section 6.3.2 can be directly employed for the design of high/low impedance since it provides all circuit element values for achieving any CRLH-TL Bloch impedance value.

6.4.3. Applications

The range of achievable unloaded impedances in conventional technologies is usually limited, due to fabrication or space constraints. As a result, two main fields of applications can be envisioned for the results presented here. The first one concerns applications based on the CRLH-TL particular

dispersion characteristic. In this case, the method allows designing CRLH-TLs with an extended impedance range when compared to usual CRLH-TLs (for which $Z_{equ}(f_0)$ is necessarily equal to Z_C). For example, this would allow controlling the impedance of the different line sections in a CRLH-TL-based series feed network for optimal matching [72]. Similarly, a slab of metamaterial embedded in air for focusing application should exhibit the free space impedance of 377 Ω for optimal matching.

Second, the CRLH-TL can be used to mimic low or high impedance conventional —or *true-time* delay— TLs. For instance, a matching network might require impedance values not achievable in a given technology; this problem can be overcome by using a CRLH-TL and the presented design procedure. It is however obvious that the CRLH-TL dispersion is different from a conventional TL; thus, it cannot be used to mimic a conventional TL in all applications (for instance, it would lead to beam squint if used in an array corporate feed network). However, as will be verified experimentally below, a balanced CRLH-TL as designed here exhibits a linear phase shift on a wide BW and can therefore be used in several applications in this second category.

6.4.4. Experimental example

Depending on the substrate characteristics, process resolution, and the type of waveguide (e.g. CPW, microstrip), it is usually difficult to realize *either* high or low characteristic impedance values. The technology employed here to design a demonstrator is the same as for the previous CRLH-TLs presented, namely, the 'Al-quartz EPFL' process. Due to the low permittivity of quartz ($\varepsilon_r = 3.8$) and the use of a CPW as the host TL for the CRLH-TL, it is in this case difficult to achieve a *low* impedance. Thus, in this section, we quantify the practical limitation of this technology to realize low impedance TLs and demonstrate how this limitation is overcome by the appropriate CRLH-TL design.

a. Design

The total width of the CPW is set to $G + 2W = 1000\,\mu$m, where G and W are the width of the central conductor and the slots of the CPW, respectively. If we want to realize a 20 Ω CPW in this technology, this means that the slots width G must be only about 0.3 μm, which is not a realistic value in any conventional process. Even in the case of an impedance of 30 Ω, the slot would have to be 6 μm-wide, which is already very critical from a precision point of view. Although there are some techniques to obtain low-impedance TL, they are based on sophisticated multi-layer fabrication processes (e.g. [73]). Thus, we will employ the method presented here to design a 20-Ω CRLH-TL based on the aforementioned single-layer technology and CPW size.

First, let us observe from (6.41) that topology X of Figure 6.2 should be selected in order to realize a CRLH-TL with a lower impedance than the achievable unloaded TL impedance Z_C. We can now use the design method detailed in Section 6.3.2, using the design expression for the topology X. We start the design by choosing $L_P = 120$ pH and consider the design targets $f_0 =$ 15 GHz and an impedance of 20 Ω. Using these inputs, the design method gives $C_{S,X} = 65.4$ fF,

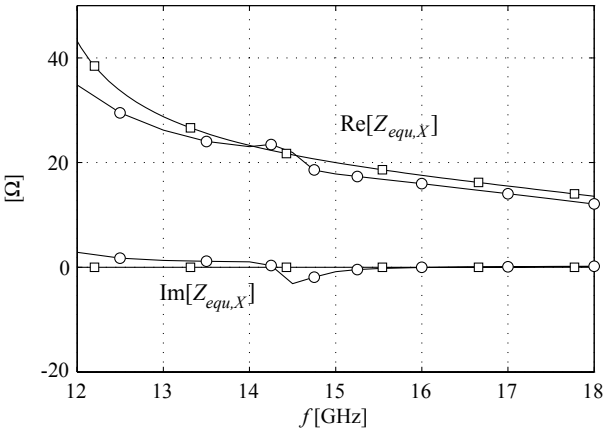

Figure 6.18: Bloch wave impedance of the designed CRLH-TL, ideal circuit model (□) and full-wave simulation (○).

the impedance $Z_C = 42.8\ \Omega$ and the TL length $d/2 = 2.27$ mm. As expected, we can verify that the condition of effective media is not verified here; indeed, as explained previously, only a CRLH-TL that is not effectively homogenous allows achieving a Bloch impedance of 20 Ω significantly smaller than the host TL impedance $Z_C = 42.8\ \Omega$ (which is easily realized with a conventional precision).

Figure 6.18 shows the resulting Bloch wave impedance $Z_{equ,X}$ on a wide BW around $f_0 =$ 15 GHz. First, the results for the ideal circuit of Figure 6.2 with the above design values show that the impedance is exactly 20 Ω at f_0 and smoothly varying with frequency. As no losses are considered in the circuit, the imaginary part of the impedance is exactly zero. The graph also shows the HFSS full-wave simulation results on the exact designed structure. A good agreement is observed, despite some discrepancies due to the losses and parasitics of the actual simulated structure, which were for simplicity not included in the circuit here.

b. Results

Figure 6.19 shows the designed low impedance CRLH-TL unit cell. The measurements were taken on-wafer using a TRL calibration with 50 Ω reference lines (see Figure 6.19). The reference impedance of the S-parameter was then changed from 50 Ω to 20 Ω. These measurements are shown in Figure 6.20 and compared to full-wave simulations using Ansoft HFSS, which were also simulated using 50 Ω CPW 'waveports' ports subsequently re-normalized to 20 Ω.

An excellent agreement between full-wave simulations and measurements is observed. These results slightly differ from the ideal circuit model results since no losses and parasitics elements were introduced here in the circuit. The measured -10 dB matching BW is almost 5 GHz around the $f_0 = 15$ GHz target frequency, which corresponds to a 30% BW. This means that the Bloch wave impedance is close to 20 Ω on a wide band, as suggested by Figure 6.18. The measured insertion loss is -0.6 dB on a 17% BW and is better than -1 dB on the whole matching BW. The

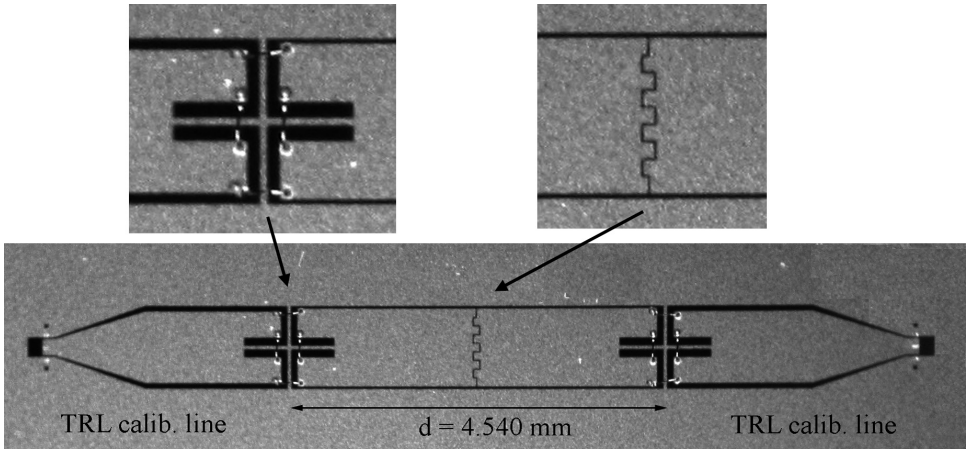

Figure 6.19: Picture of the fabricated type X 1-cell low-impedance CRLH-TL. The loading shunt inductance (incl. wirebond bridges) and series capacitance are shown in the left and right insets, respectively.

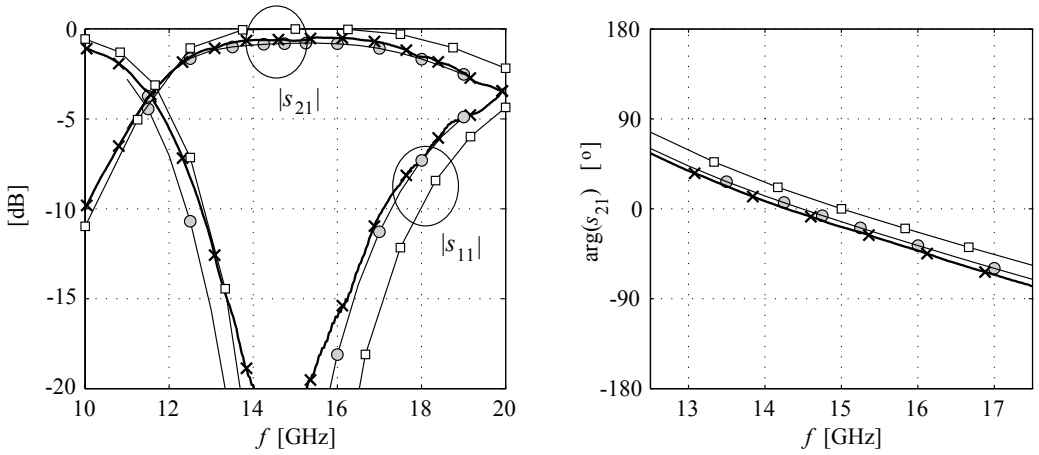

Figure 6.20: S-parameters of the low-impedance CRLH-TL with a reference impedance of 20 Ω. Ideal circuit model (□), full-wave simulation (○), and measurement (×).

right-hand side of Figure 6.20 shows the phase shift within the BW (12.5 GHz - 17.5 GHz); very good phase shift continuity at f_0 is achieved, as well as good phase linearity within the whole band.

6.5. Non-zero phase shift CRLH-TLs

6.5.1. Introduction

The design method and associate demonstrators presented so far in this chapter concerned balanced CRLH-TLs whose matching was optimized around the frequency of 0° phase shift, which was called f_0. This is obviously the optimal solution for structures operating on a bandwidth centered around f_0, such as the array series feed network [58], the patch and broadside leaky-wave antennas of [54] and [62], or for some so called 0^{th}-order resonator [60]. However, in some other applications, the CRLH-TL is not operated at f_0 but at some frequency f_1 where the phase shift is not zero, either in the 'backward' or 'forward' propagation region, which are below and above f_0, respectively (see Figure 6.21).

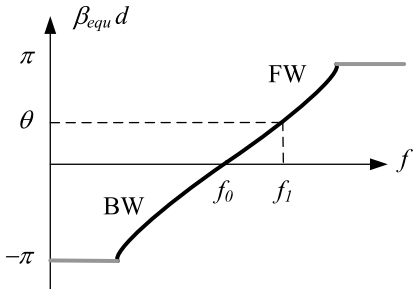

Figure 6.21: Balanced CRLH-TL operating at a non-zero phase shift frequency f_1 (here in the 'forward' zone).

This is for instance the case of the CRLH-TLs used in [61] to realize a very broadband balun. Indeed, in this device, the output ports of a classical Wilkinson divider are respectively connected to $+90°$ and $-90°$ meta-TLs. Another example is the implementation of a quarter-wavelength transformer (QWT) matching network using CRLH-TL. For such applications, a CRLH-TL unit cell must exhibit a phase shift $\theta = \pm 90°/N$ if N cells are to be cascaded in the corresponding branch, Thus, referring to Figure 6.21, the matching should be optimized at f_1 rather than f_0. In [61], good matching is obtained straightforwardly because the device is effective. However, for the reasons explained earlier in this chapter, this 'effectiveness' is made possible here by the use of SMT elements and the rather low frequency of operation (1-2 GHz). If such a device is to be implemented in micromachined technology and/or at much higher frequency, the condition of effective media would not be met and a design approach based on the Bloch wave equivalents is necessary.

Therefore, we first show in this section how the design method presented in Section 6.3.2 for an optimal matching at f_0 can be updated to design CRLH-TL with a given non-zero phase shift θ at the frequency f_1, while simultaneously enforcing the Bloch impedance of the structure

to the desired value at this same frequency f_1. In a next step, the theory is applied to the matching of antennas using multi-sectional QWTs; indeed, in this case, it is necessary that the phase shift incurred in each matching section is $N\theta = \pm 90°$. In addition, this application is especially challenging since the CRLH-TL must exhibit the impedance required by the proper functioning of the QWT, determined by the antenna input impedance.

It should however be noted that in a dual-band operation coupler such as in [59], the same CRLH-TL is used at two different operation frequencies corresponding to $+90°/N$ and $-90°/N$ phase shifts. One of this frequency is necessarily above f_0 and the other below. Thus, in this case, it is a good solution to achieve a good, wideband matching around f_0 so that both aforementioned frequencies are still in the bandwidth of the CRLH-TL. For instance, we can observe that CRLH-TL whose measured results are presented in Figure 6.15 exhibits very good matching (below -20 dB) on a 15-20 GHz bandwidth, which also covers the necessary phase shift range for such an application.

6.5.2. Theory

Let us first remark that in the case of operation around f_1, the phase continuity condition is not always necessary if the bandwidth does extend up (or down) to f_0. However, for the sake of generality we will design here CRLH-TLs with a continuous phase shift at f_0 and a given phase shift and impedance at another frequency f_1. Following the periodic structure analysis explained in Section 6.2, we can express the propagation constant of the *balanced* CRLH-TL by introducing (6.18) in (6.10):

$$\cosh\left(\gamma_{equ} d\right) = -\left(\frac{1}{2A\omega^2}\right) + \left(1 - \frac{1}{2A\omega^2}\right)\cos\left(2\tau\omega\right) + \frac{\sqrt{2}}{\sqrt{A}\omega}\sin\left(2\tau\omega\right) \tag{6.42}$$

with

$$A = 2L_P C_S \tag{6.43}$$

Now, we can solve this expression for τ to obtain the required TL length to achieve a given phase shift θ at the frequency f_1. Since this frequency must obviously be in the passband of the CRLH-TL, we can write[1]:

$$\cosh\left(\gamma_{equ}\left(f_1\right) d\right) = \cos\left(\beta_{equ}\left(f_1\right) d\right) = \cos\left(\theta\right) \tag{6.44}$$

And solving (6.42) yields:

$$\tau = \frac{1}{\omega_1}\text{acos}\left(\frac{\omega_1\sqrt{A}}{1+2A\omega_1^2}\sqrt{\left(3 - Q + 2A\left(1+Q\right)\omega_1^2\right) \pm 2\sqrt{-2\left(Q-1\right)\left(1+A\left(Q+1\right)\omega_1^2\right)}}\right) \tag{6.45}$$

with $Q = \cos\left(\theta\right)$ and where the + and - signs of the $\pm$ correspond to $\theta < 0$ and $\theta > 0$, respectively. However, note that in the case $\theta < 0$, there is not always a valid solution since, in very particular cases, the values of the parameters of the circuits and design targets make the design impossible. More details about this issue and the associated condition of validity for (6.45) are given below.

[1]Note: here, $\theta > 0$ corresponds to a 'forward' propagation and hence to a negative phase shift in terms of $S-$parameters $\arg\left(s_{21}\right)$.

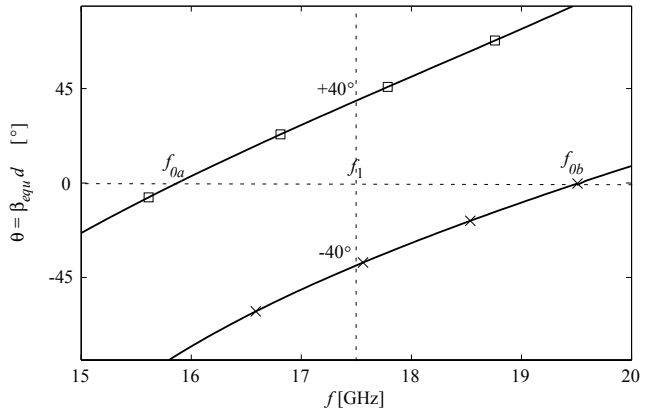

Figure 6.22: Phase shift of CRLH-TLs designed to exhibit +40° and -40° phase shifts at $f_1 = 17.5$ GHz.

Example

For illustration purposes, let us choose the parameters $Z_C = 50\ \Omega$, $L_P = 115$ pH, and $C_S = 46$ fF, a frequency of operation $f_1 = 17.5$ GHz, and two different target phase shifts $\theta = 40°$ and $\theta = -40°$. Using (6.45), we find $\tau =$ 1.14e-11 s and $\tau =$ 8.6e-12 s, respectively, and the validity of the calculation is verified by plotting the phase shift $\cos(\beta_{equ} d)$of the designed structures (see Figure 6.22).

It can be verified that these CRLH-TLs are non-effective. For that reason, and since we simply chose $Z_C = 50\ \Omega$ without considering the structure impedance, the very poor matching visible in Figure 6.23(a) is obtained; namely, about -3.5 dB and -10 dB for $\theta = 40°$ and $\theta = -40°$, respectively. This phenomenon was already observed in the case of the design at f_0 if the Bloch impedance is not considered. However, here the phase shift at the design frequency is not null; thus, the mismatch results in a some discrepancy between $\beta_{equ} d$ and the phase shift in terms of S-parameters, namely $-\arg(s_{21})$, even at the design frequency. The error is in this case really significant since $\arg(s_{21})$ is about -55° and +45° for $\theta = 40°$ and $\theta = -40°$, respectively. As a result, here again we must enforce the Bloch impedance $Z_{equ}(f_1)$ to the desired reference impedance Z_{ref}. By analogy with the method for matching CRLH-TLs designed for a 0° phase shift, we obtain the design expressions:

$$Z_{equ,X}(f_1) = \frac{2L_P\omega_1}{\sqrt{4C_S L_P \omega_1^2 - 1 + 4\sqrt{C_S L_P}\omega_1 \tan(\tau\omega_1)}} = Z_{ref} \tag{6.46a}$$

$$Z_{equ,Y}(f_1) = \frac{\sqrt{4C_S L_P \omega_1^2 - 1 + 4\sqrt{C_S L_P}\omega_1 \tan(\tau\omega_1)}}{2C_S\omega_1} = Z_{ref} \tag{6.46b}$$

with τ given by (6.45). Consequently, the design procedure for a non-zero phase shift at f_1 is very similar to the design method at f_0 and only step 2 below slightly differs from the original procedure:

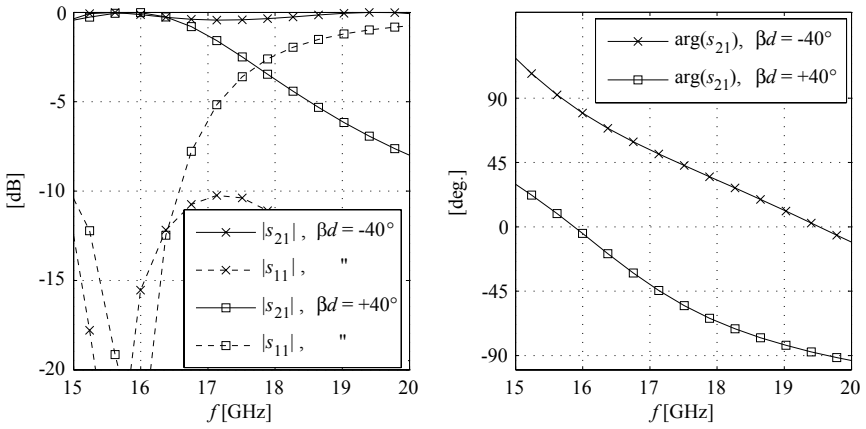

(a) *unmatched* method

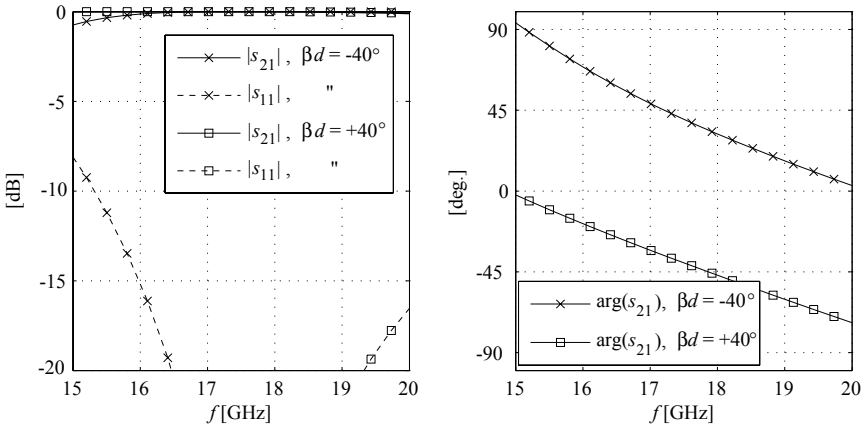

(b) *matched* method

Figure 6.23: *S*-parameters of CRLH-TLs designed with and without matching considerations to exhibit +40° and -40° phase shifts at $f_1 = 17.5$ GHz.

1. Choose L_P (or C_S), for instance according to technological issues and considering losses and precision.
2. Since $\omega_1 = 2\pi f_1$, θ and Z_{ref} are inputs for the design, we can directly deduce C_S from (6.46a) or (6.46b) (or L_P, if C_S was fixed in step 1.). Although (6.46a) and (6.46b) are not a closed-form expression for C_S, they can be easily solved numerically.
3. Finally the characteristic impedance of the TL sections is chosen using the phase continuity condition (6.18) and the length of these TL sections is calculated using (6.45) and (6.5).

We will now briefly illustrate the design method, using the same design targets as in the case of the above unmatched example. In the case of structure Y, with $Z_C = 50\ \Omega$, $L_P = 115$ pH and targets $\theta = 40°$ and $\theta = -40°$ at $f_1 = 17.5$ GHz, we now find $\tau =$ 9.53e-12, $C_S =$ 163 fF, $Z_C =$ 26.6 Ω and $\tau =$ 7.17e-12 s, $C_S =$ 81 fF, $Z_C =$ 37.7 Ω, respectively. The corresponding S-parameters results are shown in Figure 6.23(b) and it is observed that an optimal matching is obtained at $f_1 = 17.5$ GHz and on a very wide bandwidth. In addition, as the structure is now perfectly matched at f_1, $\arg(s_{21})$ is equal to the phase shift of a pure propagating wave in the structure $-\beta_{equ}d$, hence $\arg(s_{21}) = -\beta_{equ}d = \pm 40°$.

a. Limitation to negative phase shift designs

As mentioned previously, there is some limitation to the validity of the design formula (6.45) in the case $\theta = \beta_{equ}d < 0$. In this section, we explain this limitation and derive the associated analytical condition for the validity of (6.45).

In the case $\theta < 0$, we have $f_1 < f_0$ since a negative phase shift is targeted at f_1 and that the 0° phase shift frequency f_0 is therefore above f_1 (see Figure 6.24). For such a structure it can be observed in Figure 6.24 that f_0 increases very significantly with L_P, for a given θ phase shift at f_1. Also linked with this increase in L_P is a decrease of τ (which is proportional to the TL section length). Eventually, there is a superior limit to L_P for which $\tau = 0$ and $f_0 \to \infty$, and the CRLH-TL only operates in its 'backward' region. Above this value for L_P, the right solution to the calculation is τ as given by (6.45) but with a minus sign:

$$\tau = -\frac{1}{\omega_1}\mathrm{acos}\left(\frac{\omega_1\sqrt{A}}{1+2A\omega_1^2}\sqrt{\left(3-Q+2A\left(1+Q\right)\omega_1^2\right)+2\sqrt{-2\left(Q-1\right)\left(1+A\left(Q+1\right)\omega_1^2\right)}}\right) \tag{6.47}$$

with $Q = \cos(\theta)$. Since it corresponds to negative TL lengths, this solution is obviously impossible in practice[1]. Therefore, the condition for the validity of the design expression is obtained by introducing $\tau = 0$ in (6.47), which yields:

$$2L_PC_S < \frac{1}{\omega_1^2\left(1-\cos(\theta)\right)} \tag{6.48}$$

This means that for a given design target phase shift $\theta = \beta_{equ}(f_1)\cdot d$, there is a maximum $2L_PC_S$

[1] It is possible to add a wavelength (calculated at f_1) to this negative TL length solution to obtain a positive, realizable value. By doing so, we indeed obtain the desired phase shift at f_1; however, this solution is not equivalent to the mathematical negative length TL for other frequencies than f_1 and is not satisfactory in terms of dispersion and space.

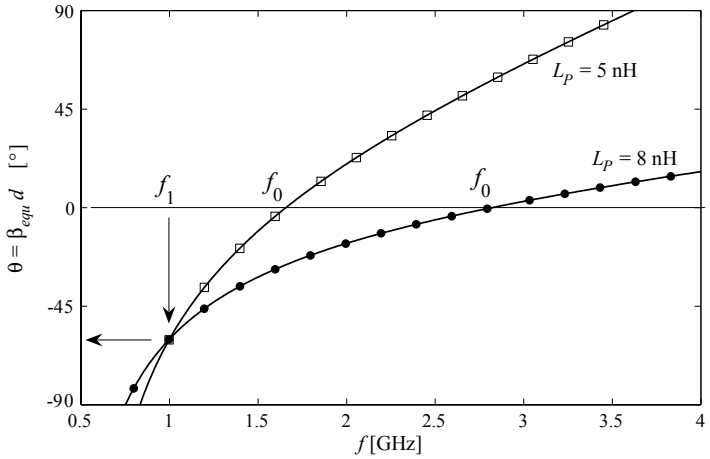

Figure 6.24: Unit cell phase shift for two CRLH-TLs with different inductance values (L_P = 5 nH and $L_P = 8$ nH) and same target phase shift of -60° at 1 GHz.

value given by (6.48) for which the CRLH-TL can be designed. However, let us note that this limitation only occurs for negative phase shift design (for $\beta_{equ}d > 0$, $f_1 > f_0$ and a design is always possible) and within a domain of parameters corresponding in practice to very large phase shifts and large L_P values. In this case, it was shown that f_0 is pushed to a frequency much higher than f_1. If so, there is no real use in enforcing a continuous phase shift at f_0 and designs with large and negative unit cell phase shifts $\theta = \beta_{equ}(f_1) \cdot d$ should thus rather be made free of the condition of continuous phase shift at f_0. Finally, let us remark that the limitation is here on the phase shift *per unit cell*; it is thus in practice possible to realize any total negative phase shift provided enough CRLH-TL cells are cascaded.

6.5.3. Application to antenna matching

a. Introduction

These theoretical results have been applied to the design of CRLH-TLs for the matching of antennas using multi-sectional QWTs, as sketched in Figure 6.25. Indeed, this application requires a simultaneous control of the phase shift and impedance of the CRLH-TLs at the antenna operation frequency. The study of this implementation was carried in the context of a Master thesis [74] supervised by the author of this thesis. Numerous practical results were obtained but we will here only summarize the main outcomes of this work.

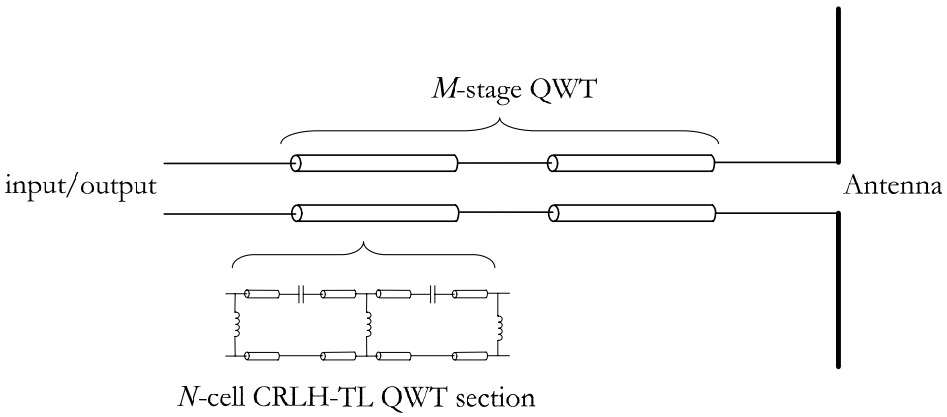

Figure 6.25: Illustration of the matching of an antenna using a CRLH-TL multi-sectional QWT. In the sketch, there are $M = 2$ stages in the QWT and $N = 2$ CRLH-TL cells in the QWT section whose circuit is detailed in the figure.

b. Results

General aspects

Some theoretical issues linked with the CRLH-TL-based QWTs were first studied in a general manner. For instance, we assessed the matching bandwidth as a function of the CRLH-TL dispersion or the number of sections in the QWTs (see Figure 6.26). In addition, many practical aspects arise in the context of concrete realizations. For instance, the impact of the following issues with regard to antenna bandwidth and size of the matching network were assessed:

- Selection of the type X or type Y unit cell.
- Use of 'forward' or 'backward' band to achieve the required phase shift (each QWT section can either incur a $+90°$ or $-90°$ phase shift).
- Choice of the number of cells N exhibiting a phase shift $\theta = \pm 90°/N$ to achieve the total $\pm 90°$ phase shift required in each QWT section.
- Other practical aspects: minimum size for the soldering of the SMT elements, maximum element value for layout implementations, etc.

The conclusion of theses studies are available in [74]. Concerning practical implementations, two different approaches in terms of technology and frequency were studied and are described in the next sections.

Low-frequency antenna matching based on SMT elements

We first studied the matching of a CPW-fed slot-loop antenna designed on a printed circuit board (PCB) substrate and whose second resonance —the one commonly employed in such a loop antenna— is at about 1.1 GHz. For that purpose, we designed a 2-stage QWT using SMT elements. The antenna and its matching network are shown in Figure 6.27. The matched antenna was measured, along with a reference design consisting of a 1-stage QWT using a conventional

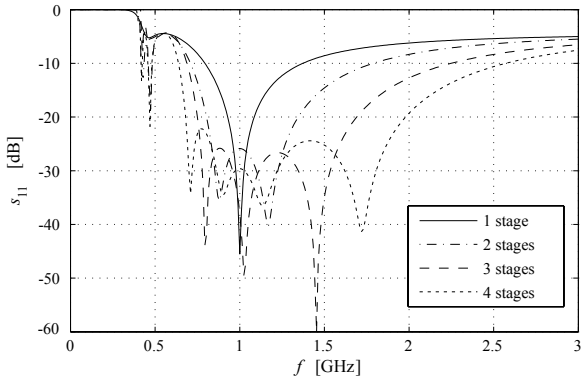

Figure 6.26: Performance of the CRLH-TL-based QWTs as a function of the number of QWT-sections (complete design for a load of 200 Ω with ideal lumped elements).

TLs instead of the CRLH-TL (a 2-stage QWT using a conventional TLs was not realized due to its prohibitive size). The results are presented in Figure 6.28; a slightly better bandwidth (25%) is obtained using the CRLH-TL-based match. More important, the matching network is 66% shorter than the classical 1-stage QWT. The radiation patterns of both antennas were also measured and proved to be very similar.

It should be noted that it was possible to use here SMT loading elements with large L and C values because the antenna was realized on PCB and especially as a result of its low operation frequency[1]. Consequently, the two CRLH-TLs designed here —one for each section of the QWT— are effective according to conditions (6.23) and (6.24). They could have thus, in contrast with the next demonstrator, been designed using the existing expressions based on the effective media assumption.

High-frequency antenna matching based on micromachining techniques

In a second step, we decided to match a similar slot-loop antenna, but operating at a much higher frequency (16 GHz). In this case it is not possible to use SMT elements and the loading elements thus have to be designed using a 'layout' approach (namely, interdigited capacitors and stub shunt inductors). The matching network and antenna were designed for an implementation using the 'Al-Quartz EPFL' process and a picture of the overall device is shown in the left hand side of Figure 6.29 (in the right of the figure is shown an example of a 2-port characterization of a QWT CRLH-TL section). The simulated and measured results are presented in Figure 6.30, along with the results for a QWT using conventional TLs. A larger bandwidth is observed for the realized CRLH-TL-matched antenna, whose matching network is also much smaller than for its conventionnal TL counterpart.

[1]SMT elements are in practice limited to a few GHz and a design at about 3 or 4 GHz would already be problematic.

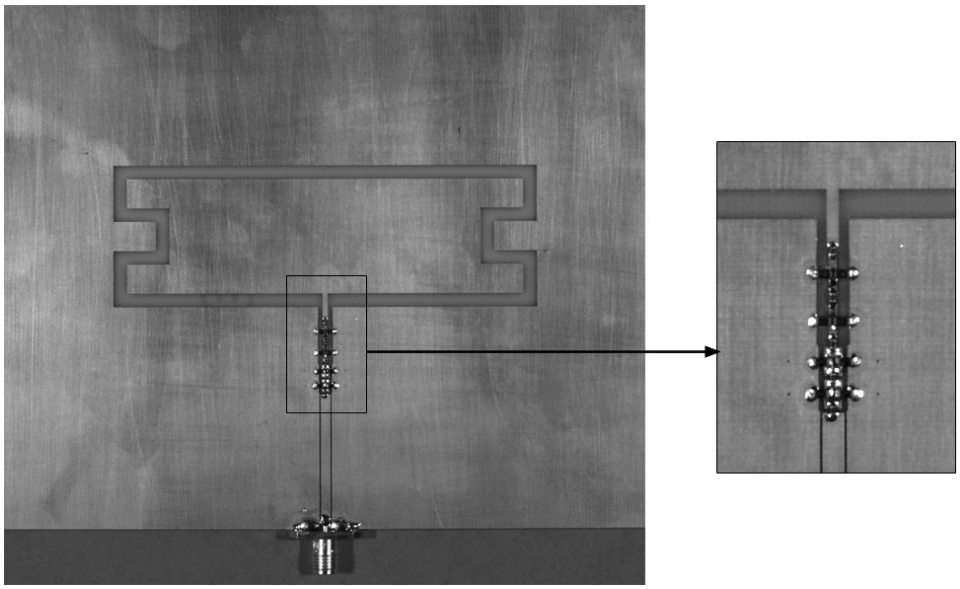

Figure 6.27: Picture of the low-frequency antenna demonstrator on PCB, with its 2-stage CRLH-TL QWT transformer using SMT elements (details available in [74]).

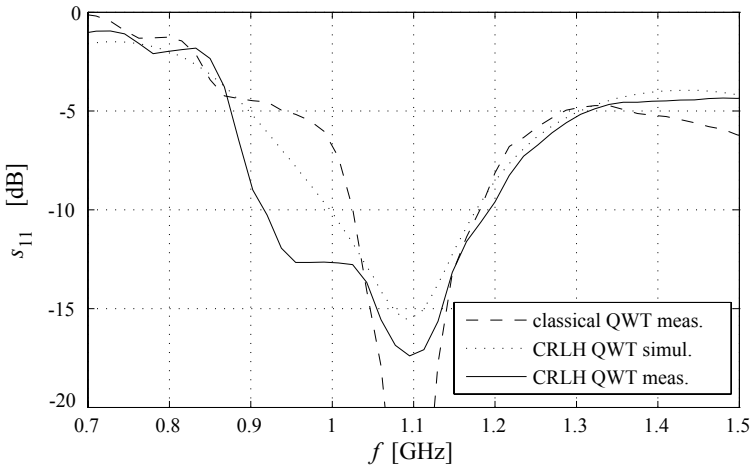

Figure 6.28: Matching results for the antenna of Figure 6.27.

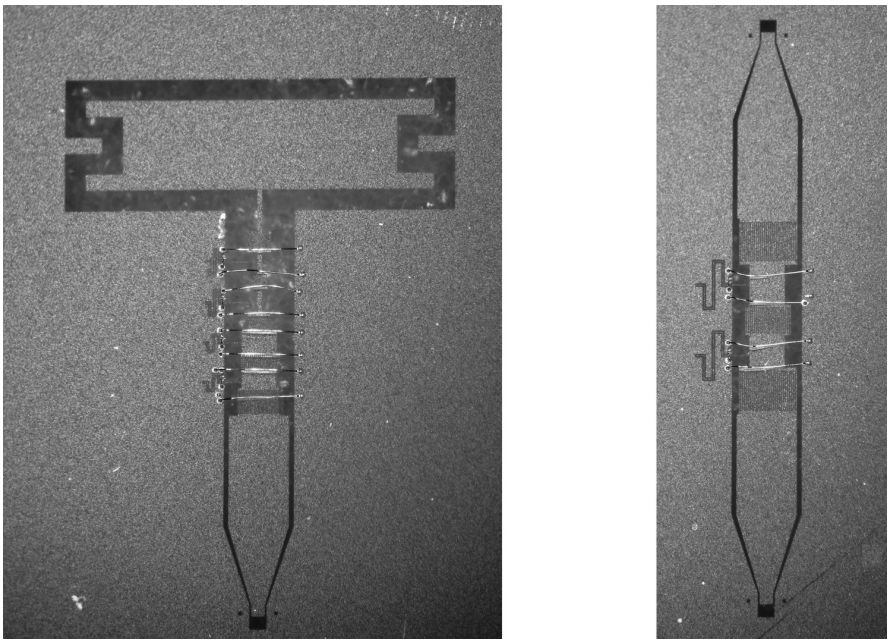

Figure 6.29: Left: Picture of the high-frequency micromachined antenna, with its 2-stage CRLH-TL QWT transformer using 'layout' elements. Right: 2-port characterization of a QWT CRLH-TL section (details available in [74]).

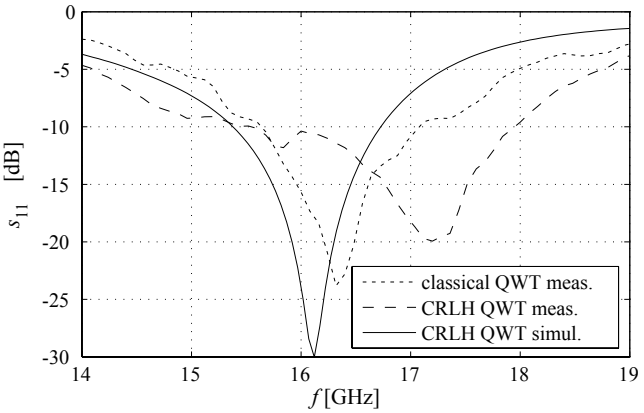

Figure 6.30: Matching results for the antenna of Figure 6.29.

c. Discussion on the antenna demonstrators

Although we showed that the CRLH-TL QWTs were surpassing the performances of their conventionnal counterparts, especially from a size point of view, it is probable that the antennas presented here could also be advantageously matched using other techniques (for instance, using a T-match, which allows achieving a wide bandwidth using a minimum space for the matching network [75]). Nevertheless, some advantage of the CRLH-TL QWT is that it is potentially dual-band since both the 'forward' and 'backward' regions can be used to achieve phase shifts of $+90°/N$ and $-90°/N$, respectively.

Due to the limited time available for this work, a more comprehensive benchmarking of the matching strategies and the extension to dual-band operation could not be completed. Nevertheless, these matching network implementations were first aimed at validating the design method presented in the second part of this chapter —that is to design CRLH-TLs with a non-zero phase shift and simultaneous control of the impedance– and have been successful from this point of view.

7. MEMS V-CRLH-TLs

7.1. Introduction

In Section 6.1.1 were listed numerous microwave devices where the use of CRLH-TLs allows surpassing the performances achievable with conventional, true-time delay TLs. In this context, it is obvious that the implementation of *variable* CRLH-TLs (V-CRLH-TLs) is of great interest since it would allow making such devices reconfigurable. V-CRLH-TLs based on diodes have been investigated in [76] in the case of leaky-wave antenna for scanning capabilities. Also, a CMOS active implementation has been proposed in [77]. However, MEMS-based V-CRLH-TL have —to the author's knowledge—not been reported yet, although MEMS technology has proved to allow challenging the performances of other types of phase shifters in terms of insertion loss, drive power, monolithic integration and cost (e.g.: the DMTL of Chapter 4). It was thus decided here to study the implementation of such MEMS V-CRLH-TLs, and corresponding results are reported in this chapter.

We present two different realizations of MEMS V-CRLH-TLs. In the first approach, we analogically control the series capacitance of the CRLH-TL alone, and this device is referred to the *analog* V-CRLH-TL. Second, in order to significantly extend the tunability range of the phase shifter while maintaining good performances in all states, we extend the initial concept by also controlling the shunt inductor of the CRLH-TL. In this case, both the C and L MEMS are digitally controlled, and the corresponding structure will be referred to as the *digital* V-CRLH-TL. We conclude the chapter by discussing in detail some new applications of the designed V-CRLH-TL, namely, the implementation of differential phase shifters with particular dispersion properties.

7.2. Analog MEMS V-CRLH-TLs

7.2.1. Description

First, we propose to achieve reconfigurability of the CRLH-TL by controlling the series capacitor C while letting the shunt inductor L fixed. As a result, it is clear that perfect phase shift continuity such as defined in Section 6.2.2 will not be achieved in all MEMS states. Nevertheless, this approach is sufficient if C is varied of a small relative amount and it will be shown that this results in satisfactory phase continuity within the whole range of analog variation of the MEMS series capacitance.

Figure 7.1 shows a 3-D view of the analog MEMS V-CRLH-TL. The detailed description of

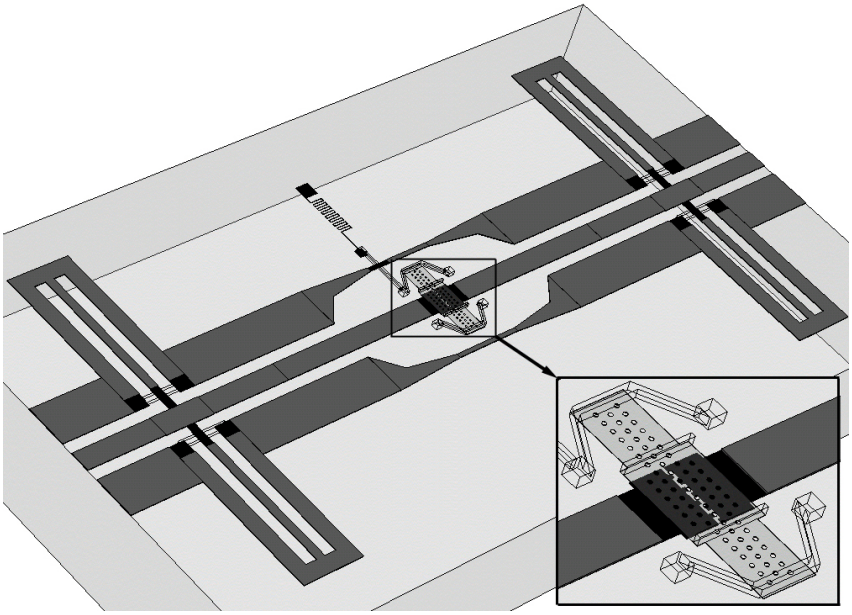

Figure 7.1: 1-cell MEMS-variable CRLH-TL (Black: 1st thin metal, dark grey: 2nd thick metal, light grey: bridge membrane, wireframe: bridge anchoring structure). The total length of the cell is 2.74 mm.

the MEMS capacitor designed for this application and visible in the inset of the figure was given in Chapter 3 and will thus not be repeated here. Nevertheless, note that in the context of this V-CRLH-TL application, the capacitor topology allows —thanks to the interdigited capacitor below the membrane— to independently tailor the value of the overall series capacitance in different MEMS bridge position.

The two shunt inductances in the CRLH-TL circuit are realized by a symmetrical arrangement of four short-circuited stubs. As a result, the CPW central conductors are DC grounded and it is possible to actuate the structure by applying a DC voltage to the bridge membrane, which is done here by means of the actuation pad visible in Figure 7.1. In the absence of a highly resistive material in the fabrication process to realize DC feed lines that do not impact on the microwave performances, the MEMS bridge is connected to the DC actuation pad by a narrow meander line using the thin 1st metal layer, in order to produce a high impedance. The length of this one-cell CRLH-TL is 2.74 mm.

7.2.2. Modeling and design

a. Circuit model

Figure 6.2 showed the circuit model of an *ideal* CRLH-TL structure. In the case of the MEMS design presented here, an accurate modeling requires the inclusion of parasitics linked with the integrated loading elements, as shown in Figure 7.2. The CPW-type stubs used to realize the

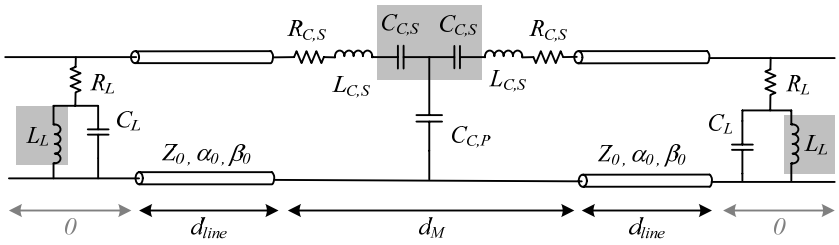

Figure 7.2: Comprehensive circuit model for the presented MEMS 1-cell CRLH-TL.

shunt L elements and visible in Figure 7.1 are represented by a combination of the desired L_L value, as well as R_L and C_L parasitics. This model is physically justified by representing the stub by the RLC model of an electrically short, short-circuited CPW section, where L_L and R_L are the series inductance and metal resistance of the CPW, respectively, while C_L accounts for the shunt capacitance. The circuit model for the MEMS capacitor was discussed in Chapter 3, and is represented in Figure 7.2 by the lumped elements $C_{C,S}$, $C_{C,P}$, $L_{C,S}$ and $R_{C,S}$.

b. Design procedure

Due the non-ideal circuit model required to model the structure, the electromagnetic design of the MEMS phase shifter cannot be made using simple design expressions such as derived in Chapter 6. In addition, it is not possible to tailor the C and L loading elements to any given value independently of the fabrication process constraints and electromechanical issues related with the actuation of the MEMS. Consequently, the approach employed here for the design of the phase shifters can be summarized as follow:

1. General topologies for the C and L loading elements are chosen according to process limitations and electromechanical issues.
2. These elements are separately simulated using HFSS.
3. Physical equivalent circuits for these elements are deduced by regression on the simulated data (see circuit of Figure 7.2).
4. The design and optimization of the phase shifter is done on a circuit level, using the extracted values as starting points.
5. Finally, some iterations of the 'simulation-extraction' process are made in order to update the loading elements geometries to match the required circuit elements values obtained in step 4.

For use in step 4., the S-parameters of the circuit model are computed by first cascading the five transmission matrices associated with the sub-elements of the circuit of Figure 7.2. By doing so, the S-parameters can be instantaneously plotted for any set of lumped elements values. Since the parasitics values weakly depend on the major circuit parameters such as the series capacitance $C_{C,S}$, the shunt inductance L_L, and the TL impedance and length, the optimization is based on the

latter alone to achieve the best phase shift continuity, matching and insertion loss at the frequency of interest. Finally, it is noticeable that step 5. can be done in a small number of iterations thanks to the physical model used here, which allows an easy link of the geometrical parameters of the loading elements with the lumped elements values. For example, the values of $C_{C,S}$ and L_L can be tuned by controlling the capacitance active surface and the stub length, respectively. Finally, let us note that some tradeoff between microwave performances and MEMS electromechanical behavior (low actuation voltage, reliability) must be considered in the design.

7.2.3. Results

The MEMS CRLH-TL structure depicted in Figure 7.1 was designed using the proposed design procedure and targeting a frequency of 0° phase shift $f_0 \approx 18$ GHz. The corresponding Bloch wave equivalent propagation constant and S-parameters are shown in Figure 7.3 and Figure 7.4, respectively. The results are shown for the two extreme positions of the bridge membrane in an analog mode of operation. The initial height of the bridge membrane is $h = 3$ μm and the minimal bridge position within the stable range for analog operation is thus of 2 μm (see Chapter 3).

For each bridge position, the graphs show both full-wave and circuit model results, which exhibit very good agreement. The values of the elements of the circuit model are given in Table 7.1, with reference planes locations within the unit cell chosen so that $d_M = 1000$ μm and $d_{line} = 870$ μm (see Figure 7.2). It is observed that the only parameter of the circuit that varies with the bridge membrane height is the capacitance $C_{C,S}$, thus confirming that the proposed circuit is a good *physical* model for the structure. It is also worth mentioning that, in contrast with the CRLH-TL circuit modeling proposed in [78], the element values are here frequency-independent (which is necessary for a *physical* model of an electrically small device, see Chapter 3).

Figure 7.3 shows the band structure of the designed CRLH-TL phase shifter. When losses are considered, as is the case here, the unit cell phase shift $\beta_{equ}d$ is never exactly 0° or −180° in the stopbands, while the attenuation $\alpha_{equ}d$ is not null in the passbands. As shown in Figure 7.3, the left-handed (LH) and right-handed (RH) propagation bands inherent to the CRLH-TL structure form here a single passband. Indeed, the design was made to achieve phase shift continuity at the transition f_0 between LH and RH bands, which also means that the stopband between LH and RH regions is 'closed'.

Due to the analog mode of operation, the overall series capacitance is varied of a relatively small amount, which results in a rather low variability, namely, about 300 MHz. However, this is also the reason why good phase shift continuity is achieved at $f_0 \approx 18$ GHz in all MEMS states, although the control of the CRLH-TL is made by the loading C element alone. Figure 7.4 also shows that the structure is matched over a very wide bandwidth since the -10 dB input return loss bandwidth is about 4 GHz. The insertion loss is -2 dB at the frequency of 0° phase shift $f_0 \approx 18$ GHz and smoothly decreases around f_0 within the input return loss bandwidth.

Table 7.1: Values of circuit elements for the presented MEMS CRLH-TL.

TL sections	$\alpha_0\,(20\text{ GHz}) = 0.16$ dB/mm
	$\beta_0\,(20\text{ GHz}) = 0.92$ rad/mm
	$Z_0 = 50 \qquad d_{line} = 870\ \mu$m
Inductive stubs	$L_L = 182$ pH $\quad C_L = 78$ fF $\quad R_L = 0.8\ \Omega$
MEMS capacitor	$C_{C,S}\,(h = 3\ \mu\text{m}) = 130$ fF $\qquad C_{C,S}\,(h = 2\ \mu\text{m}) = 140$ fF
	$C_{C,P} = 228$ fF
	$L_{C,S} = 176$ pH
	$R_{C,S} = 4.5\ \Omega$

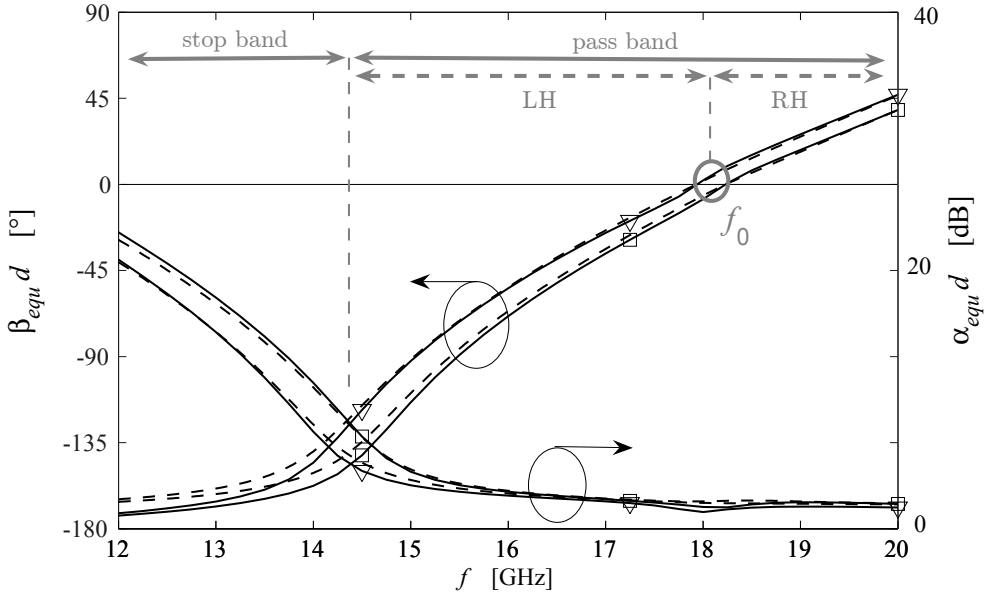

Figure 7.3: Bloch wave propagation constant of the MEMS CRLH-TL with $h = 3\ \mu$m (□) and $h = 2\ \mu$m (▽). For each state are shown full-wave HFSS simulation (—) and circuit model (- -) results.

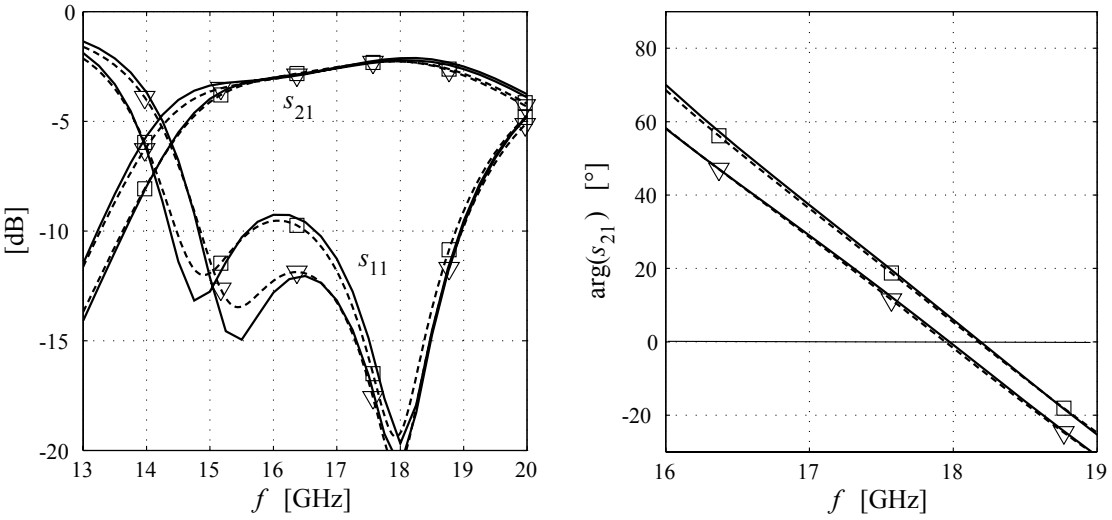

Figure 7.4: S-parameters of the MEMS CRLH-TL with $h = 3$ μm (□) and $h = 2$ μm (▽). For each state are shown full-wave HFSS simulation (—) and circuit model (- -) results.

7.2.4. Experimental validation

In order to measure the fabricated device under actuation, a DC probe was connected to the pad visible in Figure 7.1. Due to the availability of metal layers only to pattern bias lines in the 'Au-Si ISiT' process, the connection of the DC probe results in a degradation of the insertion loss from -2 dB to about -3.5 dB (taking into account the loss in the meander bias line path as well). However, it is observed in Figure 7.5 that measured phase and matching results are in close agreement with modeled ones. The DC voltage corresponding to the pull-in of the membrane is about 43 V and the phase shift can consequently be varied continuously between the two states shown in Figure 7.5 by applying a DC voltage between 0 V and 42 V, which correspond to bridge heights of about 3 μm and 2 μm, respectively.

Here we also present the measured results for another design. In this case, the optimization was made so that the matching and insertion loss bandwidth is centered around a frequency different from f_0. Indeed, we observe in Figure 7.1 that the optimal matching and insertion loss are obtained for a phase shift of about 30°. Such a design would be of use in applications where the CRLH-TL is operated at a frequency different from f_0, as is the case of several CRLH-TL-based couplers, baluns, or of the matching networks whose results where presented in Section 6.5 in a non-reconfigurable case. Indeed, for such devices, a 90° phase shift per section of CRLH-TL is required at the frequency of operation, and this could be achieved by cascading 3 unit cells as presented here since each of these presents about 30° of phase shift.

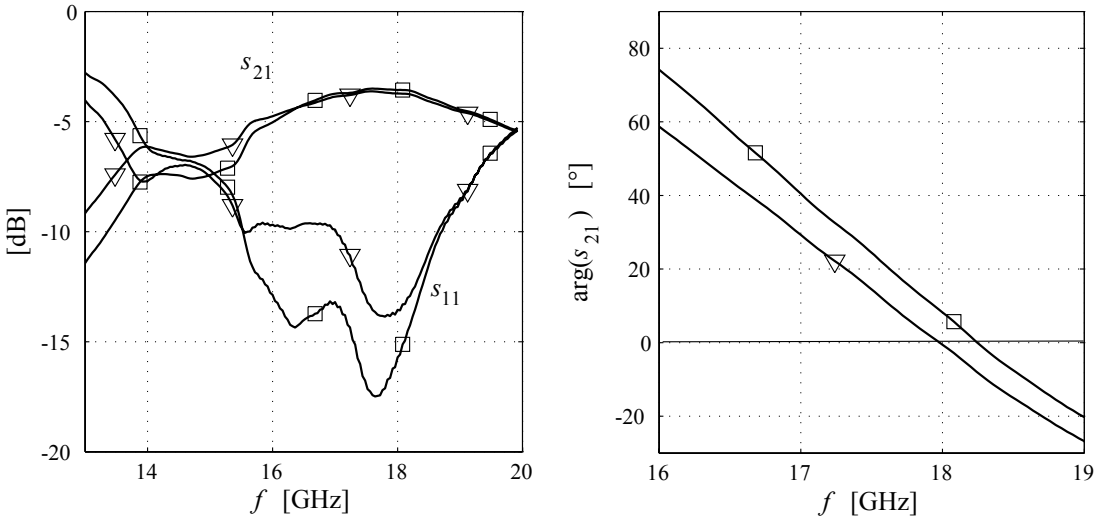

Figure 7.5: Measured S-parameters with actuation voltage of 0 V (□) and 42 V (▽).

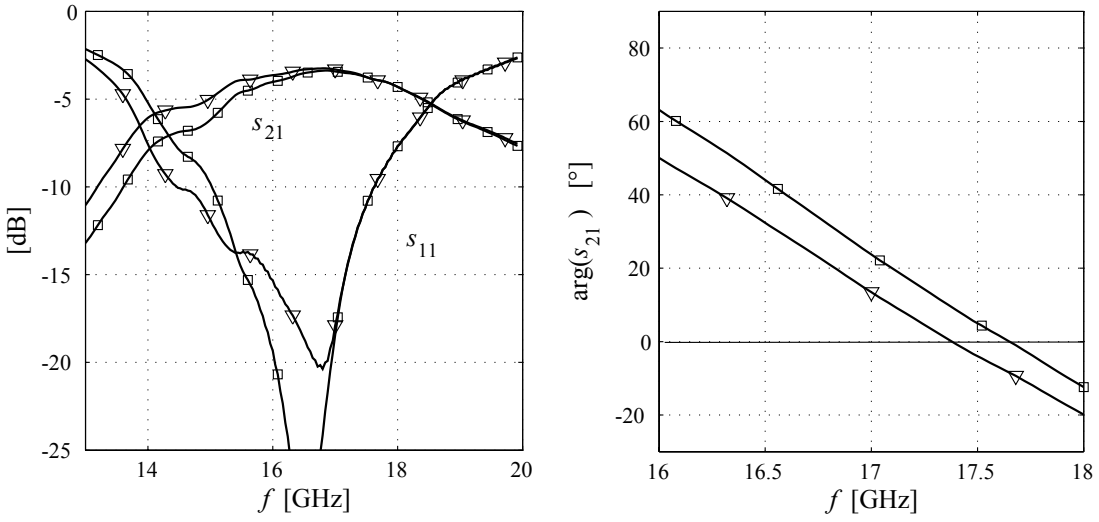

Figure 7.6: Measured S-parameters of an analog design with bandwidth optimized with actuation voltage of 0 V (□) and 46 V (▽).

7.3. Digital MEMS V-CRLH-TLs

7.3.1. Description

The digital-type phase shifter presented in this section consists in an evolution of the analog one and is depicted in Figure 7.7. First, Metal-Insulator-Metal (MIM) capacitors have been added in series with the MEMS central capacitor, following the same concept as in the case of distributed MEMS transmission lines (see Chapter 4). This allows operating the MEMS in two stable states while controlling accurately the overall series capacitance in each state. But more important, this topology allows achieving high capacitance ratios, which results in much higher tunability range than in the analog case; here, C is 26.8 fF and 57.3 fF when the bridge is in the Up and Down states, respectively, hence a capacitance ratio of 2.1. As a result, it is necessary to control also the shunt inductor element of the CRLH-TL in order to meet the CRLH-TL phase continuity condition in each state (see Section 6.2.2). Figure 7.7 shows that this is done here by means of MEMS bridges which allow changing the virtual length of the stubs and hence the shunt L value. In state A, the bridges of the series C and shunt L are in the up and down state, respectively. When state B is operated, both C and L values are increased to shift the phase response toward lower frequencies while maintaining phase shift continuity. This means that the C bridge is now in the Down state, whereas the L bridge is in the Up state.

The biasing of the structure is also shown in Figure 7.7. In this digital realization, the actuation of the C bridge is achieved by applying a floating DC voltage between both CPW central conductors, which are DC decoupled from the CPW grounds by the large MIM capacitor at the RF short of the stubs. Concerning the L bridges, the are actuated by a DC voltage applied on the actuation pad in the upper middle part of the figure. Finally, let us note that in order to facilitate the design and achieve better performances, the initial height of the membrane (namely, the thickness of the sacrificial layer in the MEMS process) was changed from 3 to 1 μm for the digital designs.

7.3.2. Modeling and design

Figure 7.8 shows the circuit employed to model the digital V-CRLH-TL depicted in Figure 7.7. Compared with the circuit model of the analog device, we observe that the capacitor is now modeled by a π-model rather than a T-model; the reason is that there is now no actuation pad, which made it preferable to model the analog capacitor by a T-model. In this new situation, it was observed that the element is more precisely modeled by a π-model. In the case of the inductor, some series parasitics inductances are now introduced to increase the overall precision of the model. Finally, it should be noted that, although a lot of lumped elements are present in the circuit, $L_{L,P}$ and $C_{C,S}$ are predominant and the structure still behaves in nature as a usual CRLH-TL. Concerning the design of the structure, it was made following the procedure explained in the case of the analog V-CRLH-TL.

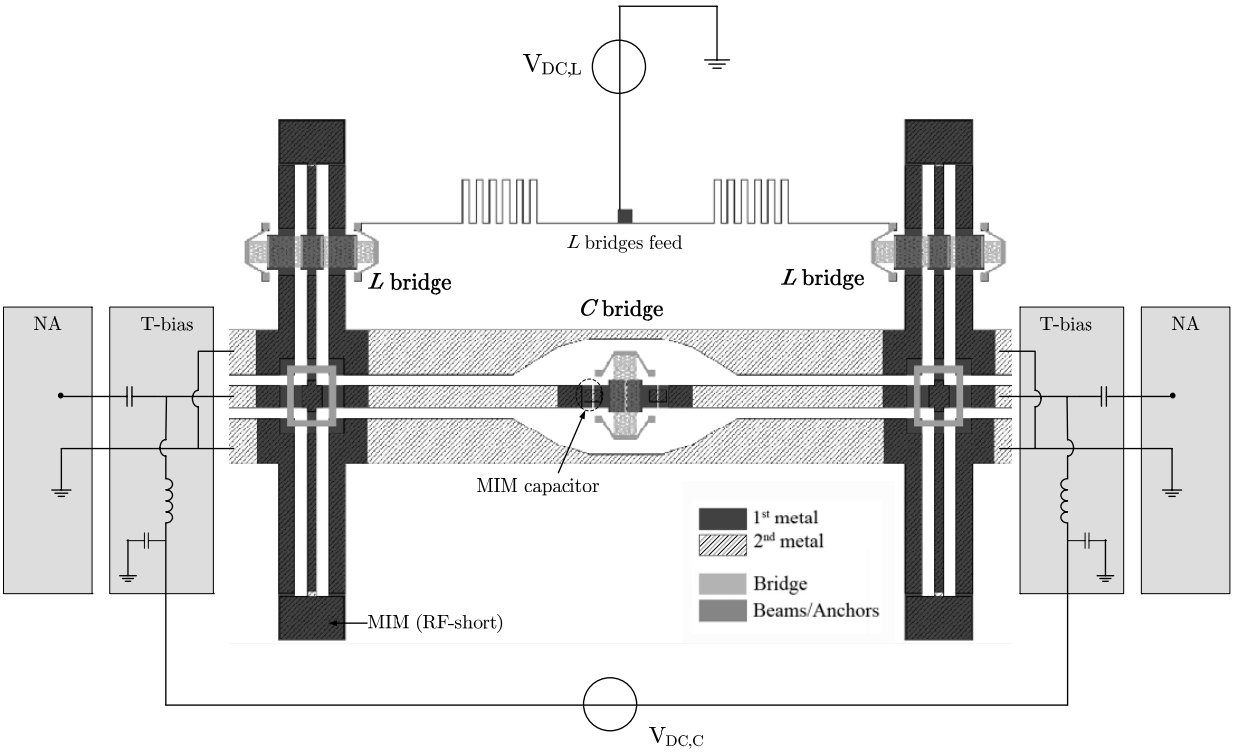

Figure 7.7: Layout of the presented digital CRLH-TL phase shifter (only conductive materials are shown here). The total length of the device is 2.80 mm.

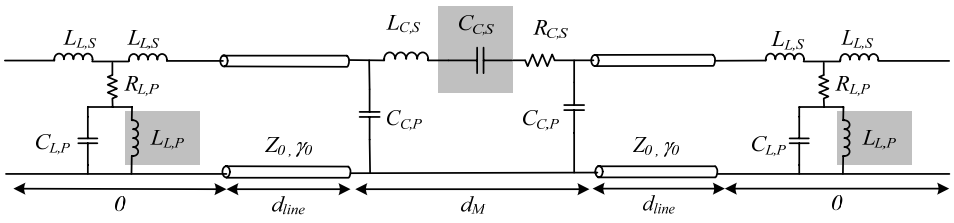

Figure 7.8: Physical equivalent circuit of the digital CRLH-TL phase shifter.

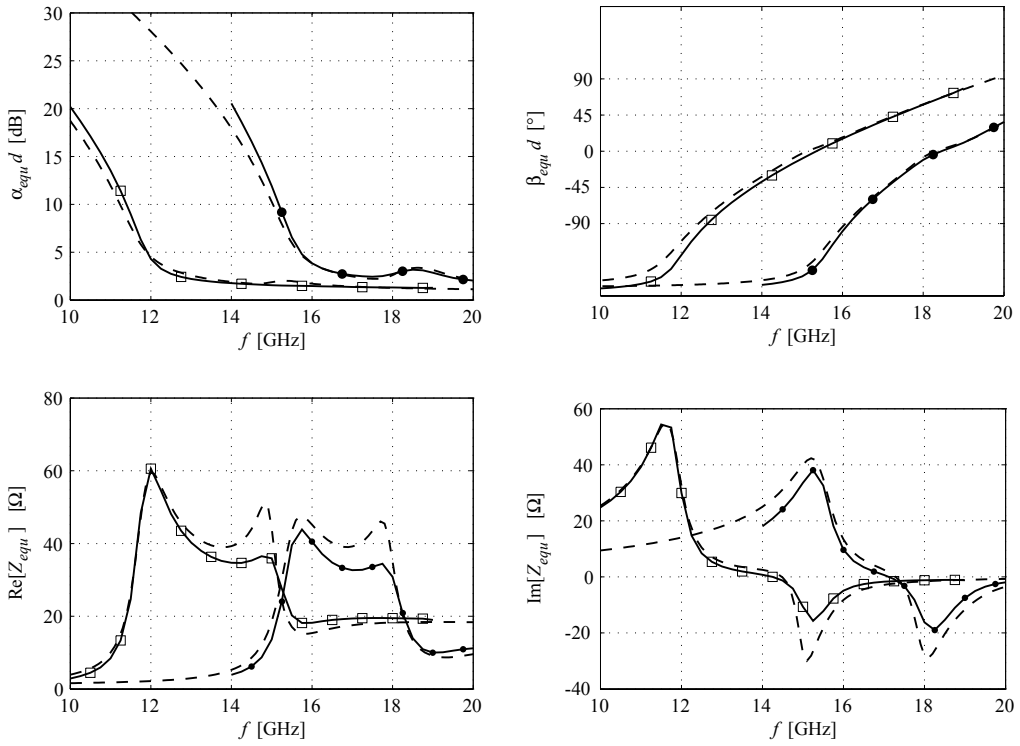

Figure 7.9: Bloch wave propagation constant and impedance in state A (•) and state B (□). Full-wave simulations (—), dashed lines: circuit model (- -).

7.3.3. Results

Figure 7.9 and Figure 7.10 show the results of the HFSS full-wave simulations of the whole structure, compared with results computed from the equivalent circuit of Figure 7.8. A very good agreement is obtained, except for a slight discrepancy in the phase shift outside the bandwidth, which is obviously no limitation here. The passband and stopband of the CRLH-TL structure in each state, as well as the phase continuity at the frequency of 0° phase shift f_0, are clearly identified in Figure 7.9. f_0 is 18 GHz and 15 GHz in state A and B, respectively, which means that the tunability is about 20% and hence much larger than for the analog device. However, for given applications such as the differential phase shifters to be presented in the next section, this tunability can rather be seen as a control of the phase shift at a given fixed frequency. Here, for instance, we can observe in Figure 7.10 that the phase shift can be controlled to -50° or +50° at 17 GHz.

Figure 7.9 shows that the equivalent impedance of the structure is close to 50 Ω around f_0 in each state. As can be seen in Figure 7.10, this results in good matching and insertion loss of the structure over a wide bandwidth around f_0. Finally, Figure 7.10 shows, in terms of S-parameters, that a good phase linearity is obtained in each state on relatively large bandwidth around f_0.

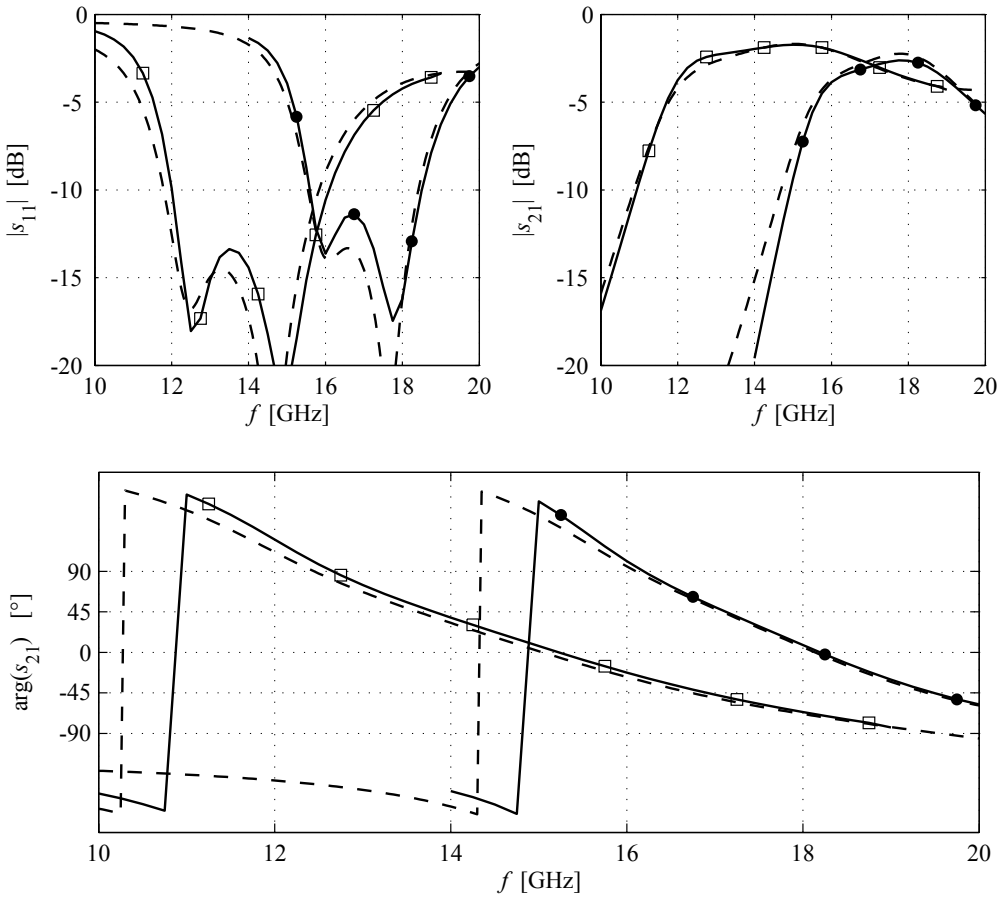

Figure 7.10: S-parameters in state A (•) and state B (□). Full-wave simulations (—), circuit model (- -).

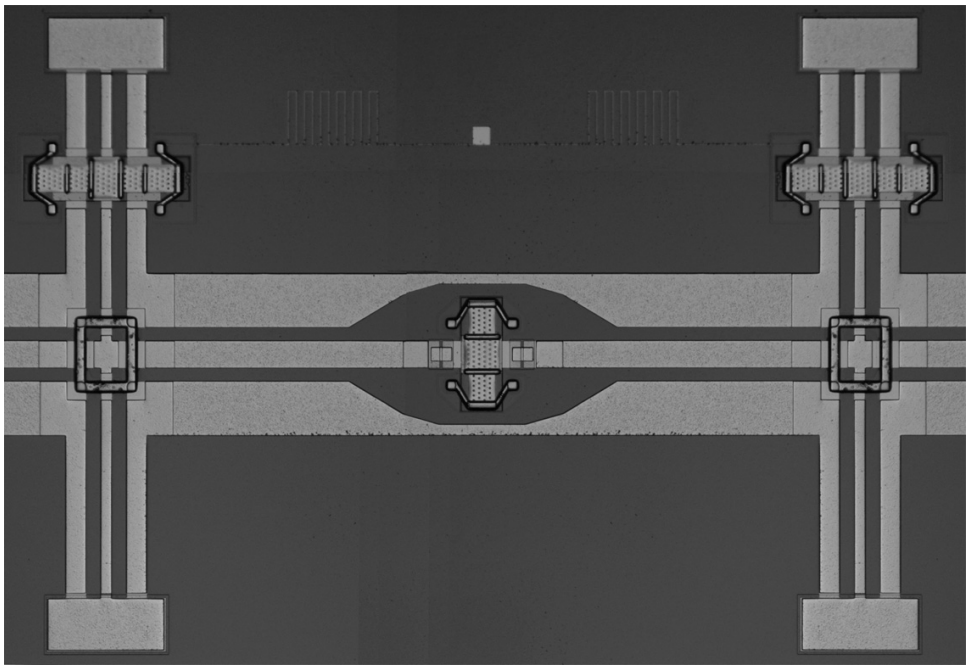

Figure 7.11: Picture of the fabricated digital V-CRLH-TL.

7.3.4. Experimental validation

The digital V-CRLH-TL was fabricated and a picture of the device is shown in Figure 7.11. However, some problems occurred with the second 'Au-Si ISiT' fabrication run for which the V-CRLH-TL had been designed (the first run was the one employed to fabricate the analog devices previously presented). This issue was extensively discussed when presenting the measured results of the series digital capacitor building bloc (Chapter 3) and will thus not be repeated here. However, it should be noted that the defects led to very significant discrepancies between simulated and measured results for both the C and L MEMS loading elements. Consequently, any proper functioning of the V-CRLH-TL could not be achieved and measured results for the digital device are not presented here. It is believed that a new run—possibly associated with some further work to design devices less sensitive to fabrication tolerances[1]— would have allowed obtaining satisfactory measured results. Such additional run could however not be performed, for reasons beyond the control of the author.

[1]Note that some steps were already taken in the first place to reduce this sensitivity (see Chapter 3). However, they obviously proved here to be insufficient to overcome unexpectedly large tolerances in the fabricated devices.

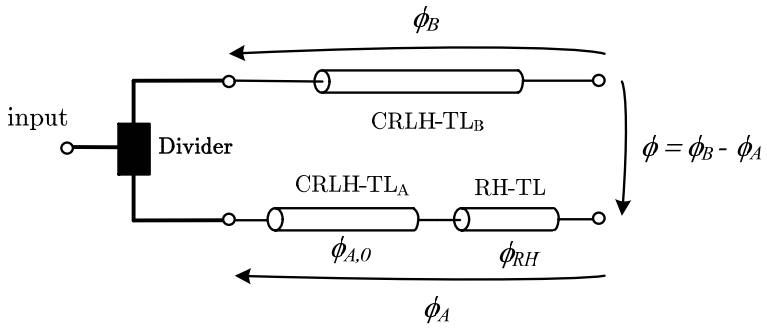

Figure 7.12: General topology of the differential phase shifters.

7.4. Applications

7.4.1. Introduction

The tunability of the presented V-CRLH-TLs can be seen either as a shift in frequency of their linear phase response or as a control of the phase shift at any given frequency in the bandwidth. In this context, such devices could be of use to achieve different reconfigurability capabilities in the various applications already demonstrated for fixed CRLH-TLs (see Section 6.1.1). Some other possible application concerns CRLH-TL leaky-wave antennas in *frequency scanning* operation (the use of the V-CRLH-TL for *fixed-frequency* phase scanning is already explained in [76] and thus not discussed here). In the case of frequency scanning, the reconfigurability of the CRLH-TL can be used for *interference reduction* purposes. Indeed, one drawback of frequency scanning antennas is that they are especially sensitive to noise and jamming since these interfering signals might exhibit high spectral density at the frequency corresponding to the desired scan angle [79]. In this case, a spectral analysis of the environment followed by an appropriate shift in frequency of the phase response of the V-CRLH-TL would allow reducing the undesired effect of the interferers [80].

In the rest of this section, we will study in detail some other new application of the designed V-CRLH-TL, namely, the implementation of differential phase shifters with particular dispersion properties.

7.4.2. Differential variable phase shifters

a. Introduction

Here We study the application of V-CRLH-TLs to 3-port phase shifters providing given *differential* phase shift functions between the two output ports of the device. The phase shifter structure is shown in Figure 7.12; first, the input signal is divided using a Wilkinson divider providing two outputs of same magnitude and phase. The outputs of the divider are connected to CRLH-TLs exhibiting different phase constants, thus providing a differential phase shift between the outputs of the phase shifter. The interest of the structure relies on the particular dispersion properties

and reconfigurability of the V-CRLH-TLs. Indeed, we will show that this phase shifter topology allows achieving versatile differential phase shift functions by adjusting the length and dispersion of each line section. In particular, we demonstrate two types of devices. In the first case, the phase shifter is designed to obtain a differential phase shift constant in frequency on a wide bandwidth. This device is thus referred to as the MEMS constant-phase shifter (M-CPS). In a second stage, we show that the topology of Figure 7.12 also allows achieving a tunable differential *group delay* which is frequency-independent on a significant bandwidth. This second device is referred to as the MEMS constant group delay shifter (M-CGDS).

The study is based on the simulated and measured performances of the V-CRLH-TL unit cells presented in the first part of this chapter. Since these CRLH-TLs were not designed targeting the application addressed in this section, it is expected that the performances of the phase shifters will be limited; a more efficient design approach would obviously consist in first designing CRLH-TL optimized for a particular phase shifter design. Nevertheless, we will show that interesting properties can be achieved even with this non-optimal approach, initially only meant to serve as a proof-of-concept.

b. MEMS constant-phase shifters (M-CPSs)

Principle

A phase shifter based on the topology of Figure 7.12 was presented in [81], where the two branches of the device are *fixed* balanced CRLH-TLs. If the two CRLH-TLs sections are designed to exhibit insertion phases that only differ by a constant phase in a given bandwidth, the differential phase shift ϕ between the outputs will be frequency-independent within this band. Note that the constant phase shift band can equivalently be in the left or right-handed band of the CRLH-TLs.

Reference [81] explains how to design two CRLH-TLs with the same slope, so that the differential phase shift ϕ is approximately constant in a significant bandwidth. This is quite easy provided the effective medium assumption is valid. Nevertheless, it is also possible to 'correct' a difference of slope in the phase response of the CRLH-TL by adding a right-hand transmission line (RH-TL) section to the appropriate branch. This is illustrated in Figure 7.12 and 7.13, where a RH-TL section of the right length was added to the 'A' branch of the phase shifter, so as to compensate for the smaller dispersion of the CRLH-TL in this branch. This is obviously an approximate solution and the differential phase shift will only be constant on a limited frequency band. Nevertheless, this is already the case without the RH line since the same dispersion for two different CRLH-TLs can only be rigorously satisfied at a single frequency (which is shown in [81] to be sufficient to obtain very good results). As mentioned above, the different CRLH-TLs designed here were not designed to exhibit the same dispersion in a given frequency band and we will thus make use of the additional RH-TL to achieve a pseudo-constant differential phase while using the V-CRLH-TLs previously designed. Finally, let us note that, in contrast with [81], the implementation considered here uses variable CRLH-TLs and the differential phase shift ϕ can thus be *dynamically controlled*. Examples of applications for such device are for phase comparison in receivers and in modulators [82].

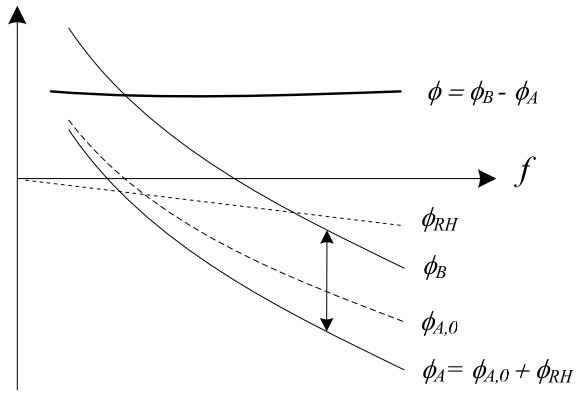

Figure 7.13: Sketch of the different phase shifts in the M-CPS.

Method

In order to calculate which differential phase shift would be achieved using our MEMS V-CRLH-TLs, we use the measured or simulated phase shifts $\phi_{A,0}$ and ϕ_B (see Figure 7.12). The power divider and the RH-TL section are considered ideal. The phase shift corresponding to the RH section can thus be written as $\phi_{RH} = -Kf$ (with $K = 2\pi\sqrt{\varepsilon_r}d/c_0$). If the structure is correctly matched, the differential phase shift is simply:

$$\phi = \phi_B - \phi_A = \phi_B - \phi_{A,0} - \phi_{RH} = \phi_B - \phi_{A,0} + Kf \tag{7.1}$$

Results analog M-CPS

First, we present the design of a M-CPS based on the measurements of the 2 different analog MEMS V-CRLH-TLs presented in Figure 7.5 and Figure 7.6. Using the measured phase shifts and an additional RH-TL section of 3.9 mm, we obtain the differential phase shift ϕ shown in Figure 7.14(a) and defined by (7.1). The results are plotted on a 5% fractional BW in the passband of the V-CRLH-TLs. The two curves in solid lines correspond to the maximum and minimum differential phase shifts; these states logically correspond to the situation were one V-CRLH-TL is not actuated while the other is in the state corresponding to the maximum deflection of the MEMS in the analog region. All intermediate phase shifts between these extrema can thus be achieved by applying the appropriate voltages to the V-CRLH-TLs. In Figure 7.14(a), the 3 curves in dashed lines represent intermediate states within this analog range. The range obtained is 55° at the center of the BW and the maximum phase error[1] is less than 3.5° (resp. 9°) on a on 5% BW (resp. 10% BW). Figure 7.14(b) shows the phase shifts in each branch of the phase shifter in the third state depicted in Figure 7.14(a), which illustrates well the principle of this M-CPS.

Figure 7.14 indicates that the differential phase obtained varies in a range that does not include a 0° differential phase shift, which is inconvenient in some particular applications. This is due to the addition of the RH-TL section in one branch of the phase shifter, itself due to the fact that these

[1] defined as the maximum difference between the phases at the center of the BW and at any frequency within the BW.

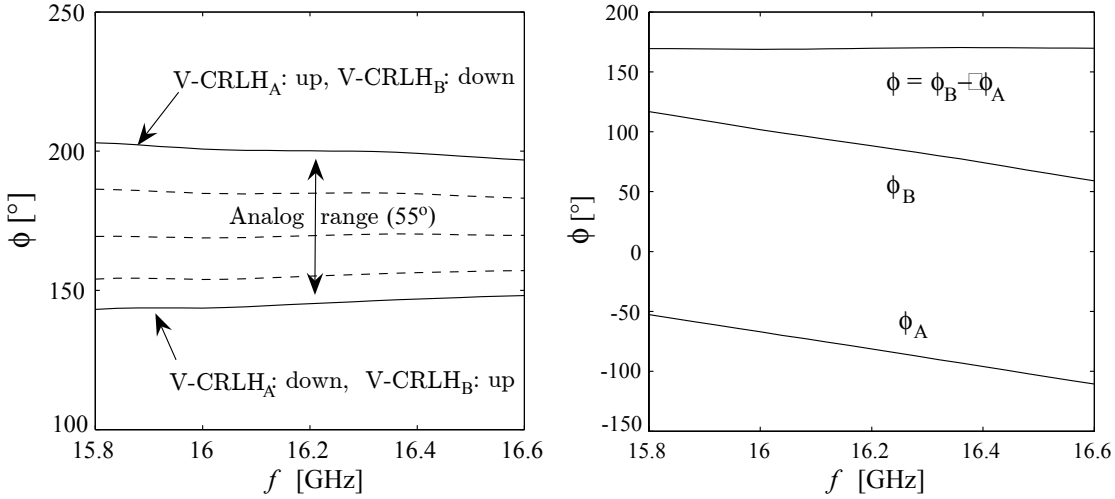

Figure 7.14: Analog M-CPS results: (a) differential phase shift analog range, (b) phase shift in each branch of the phase shifter and corresponding phase difference in one particular state.

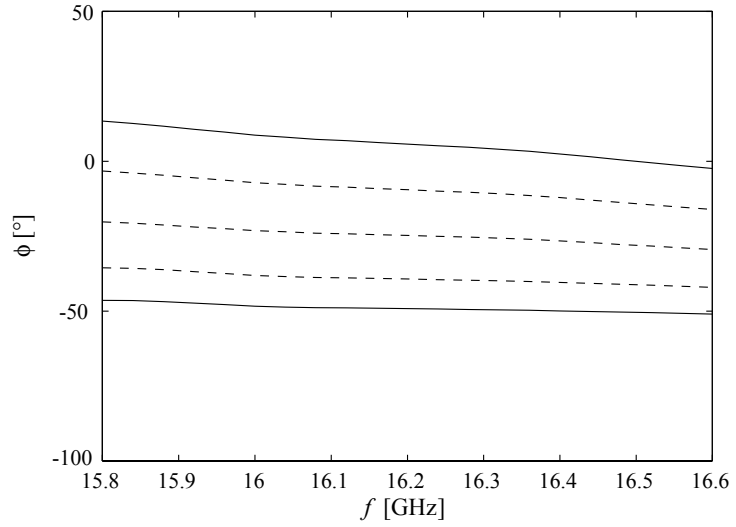

Figure 7.15: Analog M-CPS differential phase shift analog range, without the 'corrective' RH TL section.

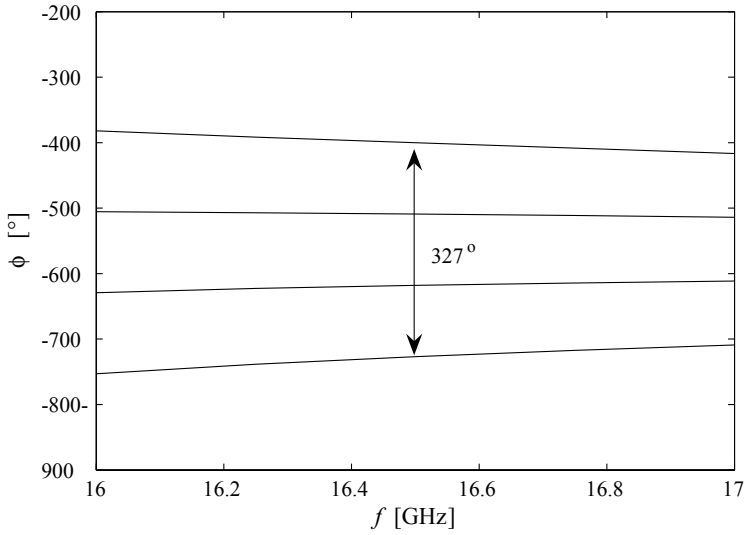

Figure 7.16: Digital M-CPS differential phase shift.

particular V-CRLH-TLs were initially not tailored for this application. Nevertheless, we observe that reasonable phase dispersion is obtained even without the RH-TL sections, while obtaining a phase range covering a 0° differential phase shift. The results are presented in Figure 7.15. It is observed that the maximum phase error is now 8°, whereas it was about 3.5° using the 'corrective' RH-TL section.

In order to extend the tuning range of the M-CPS (for a given number of V-CRLH-TL cells in the branches of the structure) and work in a digital control mode, we now make use of the digital V-CRLH-TL. As a result of the problems that occurred with the fabrication of these devices, we base the analysis on the simulated results shown in Figure 7.10 rather than measured ones. Corresponding results for the differential phase are shown in Figure 7.16, and there are now 4 different phase states that can be operated. A range of 327° is obtained by using 2 MEMS CRLH-TLs cells in each branch of the phase shifter.

c. MEMS constant group delay shifters (M-CGDSs)

Another interesting phase shifting property can be achieved based on the topology of Figure 7.12, namely, to obtain a controllable, frequency-independent *differential group delay*. For that purpose, the phase difference between the CRLH-TLs of each branch must now be linear within the bandwidth, such as depicted in Figure 7.17. In this case, the differential group delay d_g is given by (7.2):

$$d_g = d_{g,B} - d_{g,A} = -\frac{1}{2\pi}\frac{\partial\phi_B}{\partial f} + \frac{1}{2\pi}\frac{\partial\phi_A}{\partial f} = -\frac{1}{2\pi}\frac{\partial\phi}{\partial f} \tag{7.2}$$

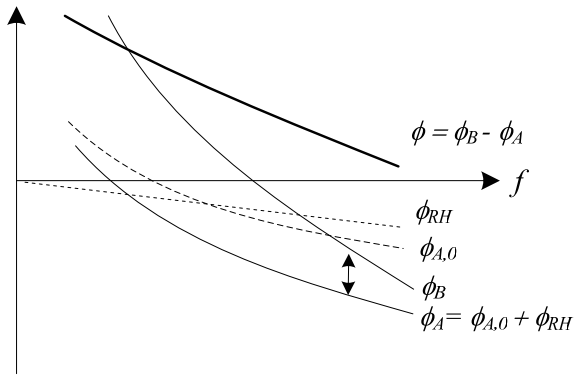

Figure 7.17: Sketch of the various phase shifts in the M-CGDS.

Type A

Let us first imagine that the two branches of the phase shifters are implemented with the *same* digital V-CRLH-TL. Each of the branches is controlled by a control voltage and there are therefore 4 states which will be referred to as AB, where A and B are the values of the bit controlling the A and B branches, respectively. In the states 01 and 10, there will be opposite differential group delays:

$$d_g(10) = -d_g(01) = d_{g,1} - d_{g,0} = -\frac{1}{2\pi}\frac{\partial\phi}{\partial f} \tag{7.3}$$

whereas when states 00 or 11 are operated, the differential group delay is zero: $d_g(00) = d_g(11) = 0$. As a result, this basic implementation allows controlling the differential group delay at the outputs of the phase shifter, which could for instance be utilized in time-domain modulation transceivers. Multibit operation can obviously be achieved as well, either by the connection of several phase shifters in a 'tree' manner (such as in a corporate feed network), or by cascading CRLH-TL corresponding to different bit weights in each of the two branches of the phase shifter.

Using the simulated results for the digital MEMS CRLH-TL presented earlier in this chapter, we obtain the differential phases and group delays shown in Figure 7.18. A differential group delay of 65 ps is achieved with a single V-CRLH-TL in each branch, and the maximum delay error is about 5 ps, which corresponds to a relative error of 8%.

Type B

In the case of the 'Type A' M-CGDS, the two branches of the phase shifters were implemented with the *same* digital MEMS CRLH-TL, which means that 3 different possible group delays could be achieved, with $d_g(10) = -d_g(01)$ and $d_g(00) = d_g(11) = 0$. Here, we show that it would also be possible to achieve other, more complex phase functions using different MEMS CRLH-TL in each branch. In this case, it is obvious that 4 *different* phase state are obtained (instead of 3 for Type A). For instance, let us imagine that we wish to achieve 4 differential group delays (temporarily referred to as a, b, c and d), which are equidistant according to (7.4) and as shown in Figure 7.19.

$$d_g(a) = \frac{1}{2}d_g(b) = \frac{1}{3}d_g(c) = \frac{1}{4}d_g(d) \tag{7.4}$$

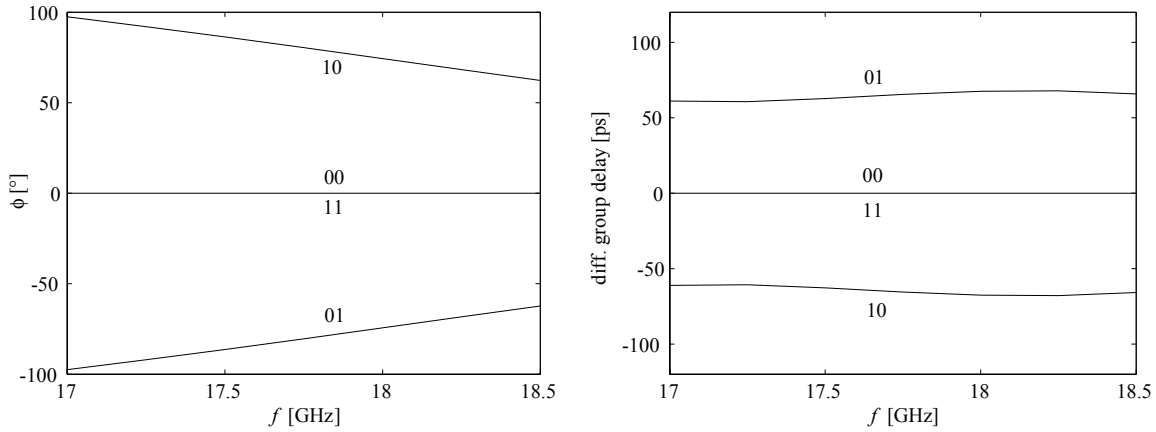

Figure 7.18: Digital M-CGDS differential phase shifts and group delays.

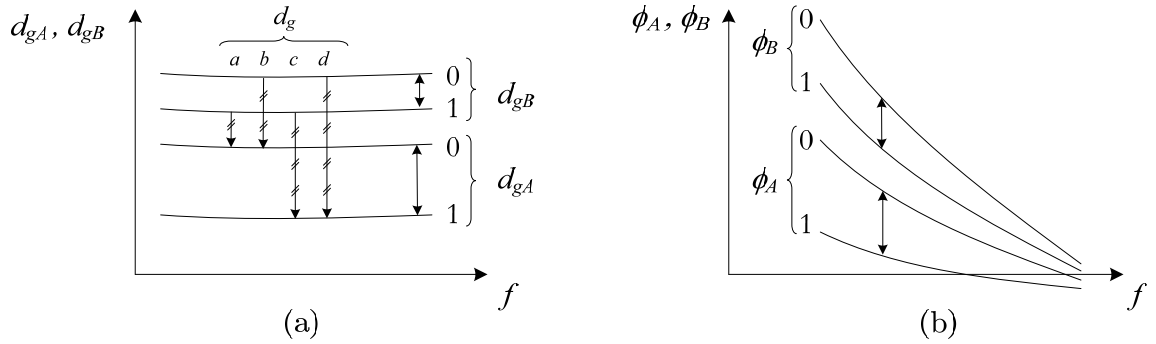

Figure 7.19: Graphical illustration of the group delays (a) and phase shifts (b) in the V-CRLH-TL for obtaining 4 equidistant differential group delays.

It is then quite simple to deduce the group delays in each branch that would allow obtaining the required differential group delays. The solution is graphically depicted in Figure 7.19(a), and the general shape of the corresponding phase shifts is shown in Figure 7.19(b).

In contrast with the cases presented above, this example is not implemented using the results of the MEMS V-CRLH-TL since devices exhibiting the required phase shifts were not designed. Nevertheless, it is believed that the required phase properties can quite easily be achieved. Indeed, we observe in Figure 7.19 that each branch A or B must be able to exhibit only a limited group delay variation [see the arrows in Figure 7.19(b)] with regard to the total differential group delays required. Moreover, it is again possible to make use of small RH section as shown in Figure 7.12 to make some correction of the group velocity in one of the branch.

Comparison with the DMTL

It is clear that the response of the devices studied here, namely, a controllable but frequency-independent differential group delay, can also be implemented using DMTLs such as designed in Chapter 4. In this case, the differential phase shifter has the same structure as the M-CGDS

of Figure 7.12, but with a DMTLs in each branch instead of the V-CRLH-TLs. Indeed, the DMTL, whose main purpose is to provide a controllable constant *phase* velocity in corporate feed network, do obviously also exhibits a constant group velocity. In contrast, it should be noted that the M-CGDS presented here can not substitute DMTLs in corporate feed networks aimed at very wideband application since the phase velocity is not constant. Nevertheless, it is relevant to compare the performances of both approaches in terms of devices providing a controllable constant differential group delay.

In order to do so, we will compare the results achieved in 'Type A' above (namely with identical MEMS V-CRLH-TL in each branch of the phase shifter), with a similar case but using the digital DMTL whose measured results are presented in Section 4.3.2. Although both kind of devices were not realized using the same fabrication process, the comparison in terms of losses is relevant since they are both realized on Hi-Res silicon wafers. The frequency for the comparison must obviously correspond as well, and is set here to 17.5 GHz. Table 7.2 shows the 3 principal figures of merit identified for the differential phase shifter, and in each case, corresponding numerical values. We first observe that the use of the V-CRLH-TL results in much better performance in terms of differential group delay over losses. Another significant advantage of this new approach is that it is much more compact than the somehow large DMTL structure. Indeed, the length of the line to be inserted in each branch is only 2.8 mm here, whereas it is 9.8 mm in the case of the DMTL. Taking into account that the differential delay is also larger with the new device, the performance in terms of delay per unit length is improved of a factor 10 by using the V-CRLH-TL-based M-CGDS. The main drawback to these advantages is the reduced bandwidth of the M-CGDS, which does not compete with the inherent very broadband DMTL.

Table 7.2: Comparison of the performances of the M-CGDS using V-CRLH-TLs or DMTLs.

	V-CRLH-TL	DMTL
Diff. group delay / losses	64 ps / 2.9 dB = 22 ps/dB	22.5 ps / 2 dB = 11 ps/dB
Bandwidth	$\sim 16 - 19$ GHz	$\sim 1 - 25$ GHz
Diff. group delay / length	64 ps / 2.8 mm = 23 ps/mm	22.5 ps / 9.8 mm = 2.3 ps/mm

7.5. Conclusions and perspectives

From a design perspective, the realization of MEMS V-CRLH-TLs requires a careful analysis of electromechanical issues, process limitations, and parasitics linked with this particular implementation. Nevertheless, we demonstrated that an efficient design can be achieved using accurate circuit models and a limited number of full-wave simulations.

Both analog and digital CRLH-TL phase shifters have been successfully designed. However, the fabricated digital devices suffer important defects, which prevented obtaining reasonably good measured results for this second class of devices. Concerning the analog devices, they suffer from a

rather low tunability; however, it is obviously possible to cascade digital and analog cells to achieve an analog control over a wide tuning range. The performance of the devices in terms of phase and matching are very good. The insertion loss, of about 3.5 dB, could be an issue in particular applications but is however quite good for *reconfigurable* phase shifters operating in the upper *Ku* band. Nevertheless, it was shown by simulation that this figure could be improved to about -2 dB by the use of high-resistive bias line, and some ions implementation in the silicon wafer to prevent the formation of a conductive layer at the Si-SiO_2 interface (see Chapter 3).

From a more general perspective, this work has shown that MEMS technology allows simultaneously adding variability, compactness, and monolithic integration to previously demonstrated capabilities of CRLH-TLs. In addition, we discussed in more details the application of our designs to differential phase shifter with particular dispersion properties.

8. Reconfigurable reflectarrays (RA) Cell Theory

8.1. Introduction

8.1.1. Objectives and organization of the chapter

The aim of this chapter is to provide all necessary theoretical aspects and to validate measurement and simulation methods for the MEMS RA cells presented in Chapter 9. First, we discuss in detail the various requirements for the design of MEMS-based reconfigurable RA cells, by integrating some well known issues linked with fixed-beam RAs with new ones related to the design of reconfigurable devices. We then discuss the theory and modeling of 2-D periodic structures interacting with a field in free space, based on Floquet's theorem. Then, a theoretical discussion of the possibilities and limitations in the simulations and measurements of such cells in an array environment is provided. Eventually, these developments and the simulation methods are validated using dedicated fixed test devices.

8.1.2. The reflectarrays (RA) antenna principle

The principle of the RA is well known and has been explained in several papers such as [83, 84]. In brief, it consists of a reflector antenna whose usual parabolic reflector is replaced by a planar or conformal surface, as shown in Figure 8.1. Thus, while the usual reflector uses the difference in the path length to control the phase of the reflected field, the RA is based on the control of the reflection phase on the reflecting surface. By appropriately tailoring this phase distribution, it is possible to form a given reflected radiation pattern out of the incoming wave on the reflector, which is produced by the feed of the RA (usually a directional antenna such as a horn). The RA is especially interesting for realizing pencil-beam high-gain antennas; in this case, the reflector is tailored to form a planar reflected field phase front perpendicular to a given pointing direction. Nevertheless, RAs are also used to achieve particular shaped-beams, for instance for the satellite multimedia coverage of a given earth area [85, 86].

The advantages and limitations of fixed-beam RA over parabolic reflectors and conventional fixed-beam TL-fed arrays have been extensively discussed (e.g. [84]). Compared to conventional fixed-beam TL-fed arrays, space feeding of the RA eliminates the complexity and losses of a TL feed network, which are especially problematic for high-gain and high frequency applications. Compared to parabolic reflectors, the RA system is advantageous in terms of size, weight and cost, since it is much easier to manufacture than a parabolic reflector. However, although the bandwidth (BW) of a RA is generally better than that of its planar array counterpart, it is much

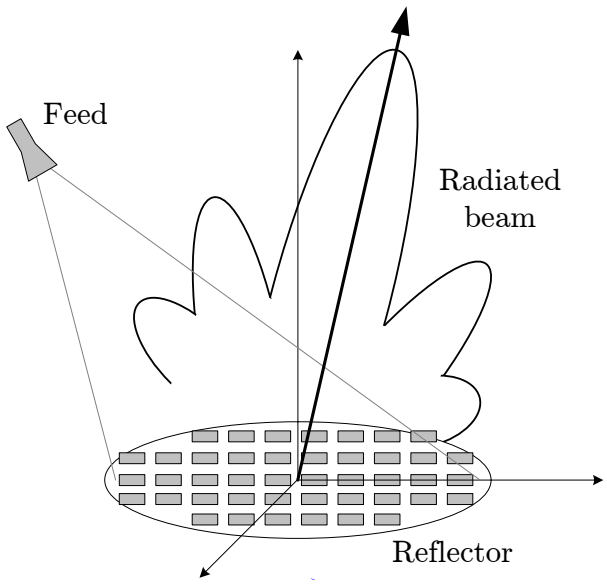

Figure 8.1: Symbolic representation of a RA system.

smaller than can be achieved with parabolic reflectors [84] (which provide a true-time delay, hence a very large BW). In contrast, the cross-polarization is generally low for dual-polarized RA, which can be designed so that each polarization operates at a different frequency [86].

Nevertheless, *as far as fixed-beam arrays are concerned*, the main advantages of the RA are not to be found in its electrical characteristics but rather in terms of size, weight and cost. It is thus clear that it is the application that will determine if a RA or a conventional parabolic reflector is to be implemented, depending on the tradeoff between electrical characteristics (BW, aperture efficiency, polarization purity), mechanical ones (space, weight), and cost.

8.1.3. Reconfigurable RAs

We can trace the origin of the RA antenna back to the 1960's [83], although most developments in terms of design, analysis and planar implementation of fixed beam RAs were performed in the last decade (e.g. [84, 85, 87, 88]). Nevertheless, there is at present a renewed interest in the RA structure, especially directed towards the implementation of *reconfigurable* RAs. Although we could think of reconfigurability in frequency for instance, the main interest at present is to form dynamically-controllable radiation patterns for beam-forming applications; namely, the RA counterpart of a TL-fed scan-phased array.

Compared to scan-phased arrays, reconfigurable RAs obviously present the same advantages as fixed-beam RA over fixed-beam TL-fed arrays (see previous section). However, the RA structure becomes even more interesting for applications requiring reconfigurability capabilities; indeed, it is clear that the beam produced by parabolic reflector can not be electronically steered, and mechanical steering cannot compete with electronic steering in terms of speed, vibration, etc.

In this context, very important applications for reconfigurable RA concern space applications, where high performances must be achieved on very low volume and mass budget [6]. Potential applications concern for instance earth observation, lunar/mars exploration, or orbital debris radar. More precisely, reconfigurable RA could serve as antennas mounted on low earth orbit (LEO) satellites that need the production of fixed spot beam on earth or serving as synthetic aperture radars (SAR) [89]. Reconfigurability however also concerns geosynchronous orbit (GEO) satellite systems, allowing to update some communication mission in-orbit, or to deal with the failing of an antenna by the reconfiguration of a spare one. In addition, the reflector of the RA can be mounted conformally onto a spacecraft. In the case of deployable reflectors, the reflecting surface, being flat, can be more easily and reliably deployed than curved reflectors. [86] presents another advantage of the RA structure over a parabolic reflector in a telecom satellite application, that is, the possibility of designing a reflecting surface scattering two different beams with only one reflector. Another interesting application of reconfigurable reflecting surfaces consists in the dynamic compensation of thermal or gravitational reflector distortion, for instance by the use of a reconfigurable sub-reflector [90]. As mentioned previously, the main limitation of RA is the limited BW. However, a significant number of communications satellite applications require only about 5% BW (e.g. direct broadcast satellites), which can be achieved by RA designs [85]. Finally, one can name non-spatial applications such as automotive cruise control (77 GHz), imaging applications or remote sensing (35 GHz, 94 GHz).

In this context, reconfigurable RA cells employing different techniques for microwave reconfigurability have recently been investigated by several groups, namely using:

- PIN diodes [89, 91–93].
- ferroelectric thin films [94].
- liquid-crystal [95].
- Photonically-controlled semiconductor [96].
- MEMS [97–99].

[89] and [91] present the results for a complete realized RA reconfigurable by means of PIN diodes. However, when compared to PIN-diodes based RA cells, MEMS will allow significantly reducing losses and intermodulation effects due to the non-linearity of PIN-diodes, while extending the high frequency limit of operation for such devices [98]. Concerning the other approaches listed above, they are at the moment not competitive with the MEMS and PIN diode approaches, mainly because they exhibit prohibitive losses with regard to most applications.

Concerning MEMS-based RAs, [98] presents the results for a RA unit cell only, and [97] presents the results for a fixed-beam RA structure while only providing the concept of an associated MEMS-based reconfigurable RA. In [100], a reconfigurable RA cell is studied by simulation and using ideal switching devices. In this case, an assessment of the performances that would be achieved for real MEMS or PIN-diode switches is necessary (real switching performance, parasitics, losses). The most comprehensive work on MEMS-based RA is, to the knowledge of the author, the one of [99], where both the fully operational MEMS unit cell and a 'static' RA demonstrator were measured.

From these observations we first conclude that a fully operational MEMS-based RA has not been implemented yet, due to the high complexity and cost of the design with a large number of MEMS unit cells, full biasing network, etc. For the same reason, it was decided in this thesis to design MEMS-based RA *unit cells* only. However, as will be explained later in this chapter, the RA design itself is quite independent from the design of a versatile reconfigurable RA cell. In other words, we can design a reconfigurable RA cell with good performances, which can then be used in most RA designs. Second, since there are numerous characteristics that must be *simultaneously* met for a high-performance reconfigurable RA cell (see section 8.2.1), satisfactory performances have not been fully demonstrated yet. Consequently, much work remains thus to be done in this field and we wish here to contribute to the development of new MEMS-reconfigurable RA unit cells.

8.2. Reconfigurable RA theory

8.2.1. Reconfigurable RA cell requirements

This section addresses the main requirements for the design of RA cells, first deduced in a qualitative way from the RA principle. Whether for fixed-beam or reconfigurable applications, the RA cell reflection phase is controlled by a given parameter p. In the case of fixed-beam RA, p is variable but not dynamically reconfigurable (e.g. length of patch, slot or tuning stub length). In the case of reconfigurable RA, the parameter p is dynamically controllable and is in general a DC control voltage (PIN-diode, MEMS, ferroelectric film and liquid crystal).

In both cases, we can plot the reflection phase as a function of frequency and for each p value, such as depicted in Figure 8.2(a). As shown in the figure, this graph will be referred to as the *frequency response* of the RA element. The companion graph is shown in Figure 8.2(b); in this case, the phase response of the element is plotted as a function of the control parameter p for different frequencies. This graph is referred to as the *phase diagram*, following the naming employed in [87]. As will be seen in many instances throughout this document, these two representations are very helpful to intuitively understand and quantify the different requirements for the design of high-performance RA cells.

a. Frequency phase error and BW

We define here the BW of a RA cell as the band within which the phase error (i.e. the phase difference with regard to the ideal phase response) is below a certain level. Indeed, the design of the RA is done so that the phase shift of the elements compensates for the different path length from the feed at the design frequency f_0 only. At $f_0 + \Delta f$ the phase of the elements does not in general match the phase of the propagation from the feed to the elements, which results in some loss in gain[1]. Since this requires some mathematical developments, the ideal reflection phase

[1]These remarks strictly concern pencil-beam RAs only. However, the same phenomenon obviously occurs for all RA since the radiation pattern will also be distorted for frequencies different from the design frequency.

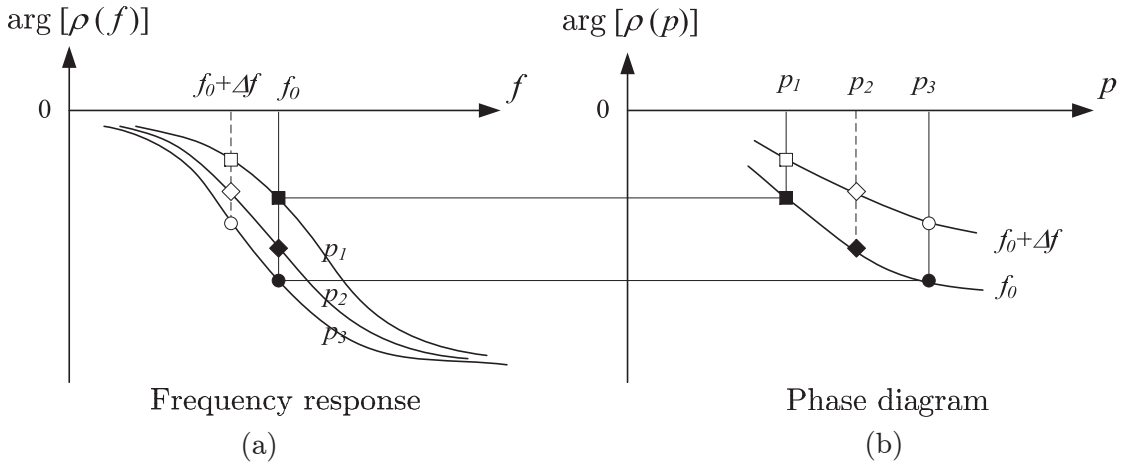

Figure 8.2: Frequency response and phase diagram representations of the reflection phase of a RA cell.

of a RA element for an optimal BW will be deduced later in this chapter in Section 8.2.4. The deviation from this ideal characteristic will determine the BW of a given RA, although we will in practice rather set the desired BW and characterize the phase error at the limits of the BW.

b. Sensitivity and range

The sensitivity s and range R are defined as:

$$s = \frac{\partial \left(\arg\left(\rho\right)\right)}{\partial p} \tag{8.1}$$

$$R = \max\left[\arg\left(\rho_i\right) - \arg\left(\rho_j\right)\right] \tag{8.2}$$

The sensitivity s corresponds to the slope of the phase diagram of Figure 8.2 and the range R to the difference of phase between the two extremes phases that can be obtained. For simplicity, let us first consider a fixed-beam RA. In this case, p is a variable but not dynamically reconfigurable parameter of the radiating element that is used to control the reflection phase. In other words, all elements in the array are different but non-variable. In practice, it is desirable that the sensitivity is small; indeed, the larger the sensitivity s, the larger the phase error to manufacturing and modeling tolerances. On the other hand, the range R should be large enough so that it is possible to achieve all required phases. Ideally, the range should be $R = 360°$ or more. The requirements on the sensitivity and range are contradictory since in general a lower sensitivity is associated with a smaller range (e.g.: rectangular patch [87]). In addition, *a high sensitivity is usually linked with a high frequency phase error*, which is a major limitation in RA design; for instance, increasing the substrate thickness in a microstrip patch allows reducing the frequency phase error (and thus increasing the BW), but also results in a reduction of the sensitivity and range [87]. A good study of the RA performances as a function of the shape of the radiating element and the parameter p varied is provided in [87] in the case of fixed-beam arrays.

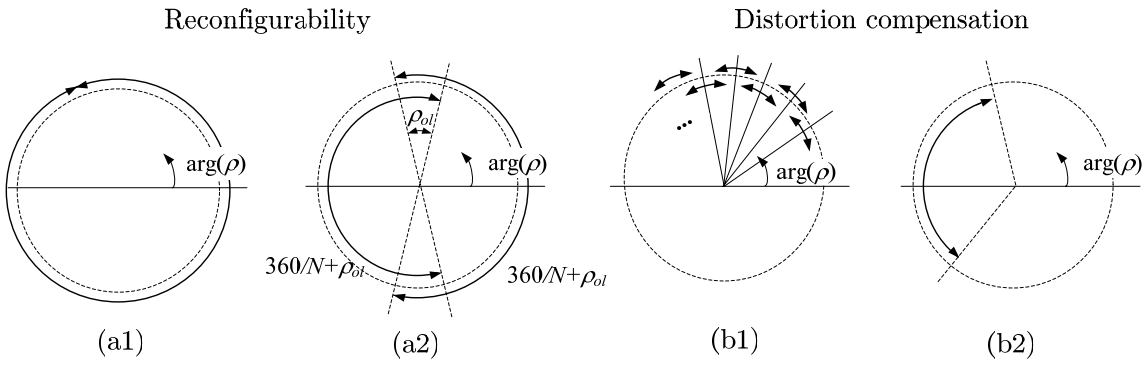

Figure 8.3: Diagrams illustrating the different possible approaches for the use of reconfigurable RA cells.

Let us now consider the case of reconfigurable RAs. As mentioned previously, the parameter p is in this case dynamically controllable and is in general a DC control voltage, as will be the case for the MEMS-based RA cells of Chapter 9. In order to comment on the requirements on sensitivity and range, we must separately treat different possible applications and approaches for the RA implementation. Ideally, a reconfigurable RA cell for scanning applications should obviously exhibit a $> 360°$ range so that any phase distribution can be achieved within the reflector surface[1]. This situation is symbolically sketched in Figure 8.3(a1). However, an intermediate approach might be envisioned if it is not possible to design a reconfigurable element with satisfactory performances on a $> 360°$ range. Indeed, we can subdivide the 360° range by N such as shown in Figure 8.3(a2) in the case $N = 2$. This means that we actually have to design N different elements which are meant to cover different areas of the 360° range [note that some overlap would then be necessary, as shown by ρ_{ol} in Figure 8.3(a2)]. This approach is however not as general as with a single element, because not all phase distribution can be achieved along the reflector surface. The possibility to use this approach thus depends on the application requirements (mainly on the scan angle range in the case of pencil-beam RAs).

A reconfigurable element might also be used for different purposes, that is, only to correct —or tune— the reflection phase of a fixed-beam array. This could be of use in large arrays such as satellite deployable RAs. Indeed, such structures will obviously not be perfectly flat and are also subject to some temperature and gravitational deformation, or even damaging. In this case, an interesting approach would be to design a pseudo fixed-beam array, but where the phase of the elements can be reconfigured on a small range, sufficient for an algorithm to dynamically correct for the non-ideal position of the elements [this case is depicted in Figure 8.3(b1)]. Another interesting approach for such surface distortion compensation is proposed in [90]. In this case, the main reflector of the array is not reconfigurable, and can be either a flat RA surface or a parabolic reflector. In order to compensate for the distortions in the reflector, a reconfigurable sub-reflector

[1] In the case of fixed-beam RA, it is possible to cope with ranges $< 360°$ by letting empty the elements locations requiring a phase that is unavailable with the considered cell [85]. However, in the case of reconfigurable RA, this is not possible in most cases since the location where the element should be 'removed' depends on the state operated.

is used between primary feed and fixed reflector. In this case, a good phase precision will be required; however, the necessary range will in general be smaller than 360°. This last situation is graphically depicted in Figure 8.3(b2).

As a result, the requirements on the range can be very different depending on the application and approach envisioned. Concerning the sensitivity, it should be small enough so that some imprecision in the control voltage has limited impact on the reflection phase. In a similar way as for the fixed-beam RA, there is here in general an inherent tradeoff between sensitivity and range. Nevertheless, we will show in Chapter 9 how this problem can be solved using MEMS technology, to achieve simultaneously a large range and a low sensitivity to the control voltage.

c. Uniform phase repartition

In the case of digitally-controlled RA elements, it is also important that a uniform phase reparation is obtained within the range, to limit to a minimum the discrepancy between the phase shifts required (by the array design) and the ones the designed element can provide. However, obtaining a phase repartition with good uniformity is not straightforward; indeed, the principle of all RA cells is to work the element close to one of its resonance, so that a full range of phases can be obtained by the variation of the control parameter. However, there will be in general (and especially if the resonance is too sharp) lots of states close to +180° or -180°, but very few in the region where the element resonates, namely, around 0°. The design of the element must thus be done considering this issue as well.

d. Summary of RA cells requirements

Here is a non-exhaustive list of the requirements for reconfigurable RA cells:

1. **Large phase range.**
2. **Uniform phase repartition.**
3. **Low frequency phase error (large BW).**
4. **Low reflection loss.**
5. **Low sensitivity to control voltage precision.**
6. **Polarization purity.**
7. **Small cell size.** Remark: It is useful to have radiating elements as small as possible, even below the limit set to rule out grating lobe (see Section 8.2.4), for phase quantization reasons.
8. **Broadbeam and incidence-independent element pattern.** As will be explained in Section 8.2.5 below, a weak dependence of the elements radiation pattern on the incident wave angle is preferred, so that these need not be taken into account in the array design. Second, a broadbeam reflected pattern is desired so that the gain of the RA do not degrades significantly when scanning the array away from broadside.
9. **(Small dependence on incidence angle.** Remark: This dependence is small close to broadside and becomes more important when the incidence angle becomes large. It can in principle be taken into account in the design and is thus not a major cause for concern.

However, it is clear that a significant dependence will increase the complexity of the design and the performances might consequently be slightly degraded.)

From a general perspective, the requirements for reconfigurable RA cells are basically the same as those for fixed-beam RA. However, in the case of the reconfigurable cell, we wish to have satisfactory performances *for all states* of a single element. From this point of view, the design of reconfigurable RA elements is much more demanding than in the case of its fixed counterpart.

8.2.2. RA fundamentals

The complicated issue of beamforming in RAs is treated for instance in [86], but is out of the scope of the present developments, since our aim is to design versatile elements that could potentially be employed for various RA implementations. Nevertheless, it is very important to discuss some fundamental principles and performances of RAs in order to select efficient radiating elements, based on particular figures of merit for the implementation of RAs. For the sake of simplicity, the rest of this chapter only concerns 1-D scanning (by a 1-D or 2-D reflector), although the concepts can be generalized to 2-D scanning as well. Figure 8.4 shows a 1-D representation of a RA and associated geometrical definitions used here. Note also that the reflecting surface is in general composed of a *discrete* number of equally spaced RA cells, such as sketched in Figure 8.4, and we employ the usual following discrete notation $var_m = var\,(x = md)$, where var is any of the considered variables. The right hand side of Figure 8.4 shows a zoom on some array elements and corresponding variables[1]. The lattice spacing d is in practice much smaller than the distance from the cell to the feed:

$$d \ll \sqrt{(x - x_f)^2 + (y - y_f)^2 + z_f^2} \tag{8.3}$$

so that the incident field has a *locally* nearly constant incidence angle, hence:

$$\theta_{i,m-1} \approx \theta_{i,m} \approx \theta_{i,m+1} \tag{8.4}$$

Here It should be emphasized that this condition does not means that we assume that $\theta_{i,m}$ is constant within the whole array, but only that it is slowly varying with regard to the lattice spacing, which is true if (8.3) is met. Using (8.4), the phase delay of the *incident* wave between successive elements is simply[2]:

$$\phi_{i,m} = +kd \sin \theta_{i,m} \tag{8.5}$$

However, the total phase delay between the *reflected* waves of successive array elements also includes the phase shift induced by the reflection on the elements. With $\Delta\rho_m$ given by (8.6) being

[1] The sketch of Figure 8.4 must be interpreted with care. Indeed, each reflected ray in the sketch —which corresponds to the maximum of radiation— should not be associated with a single element but with the overall reflection on a given number of elements in the x direction, locally in the array. Indeed, a single element is here in general not directive, whereas the directive beam results from the interference between elements.

[2] We chose here the convention $\theta_{i,m} < 0$. Note also the naming convention that θ angles are geometrical angles, whereas ϕ and ρ represent electrical phase shifts.

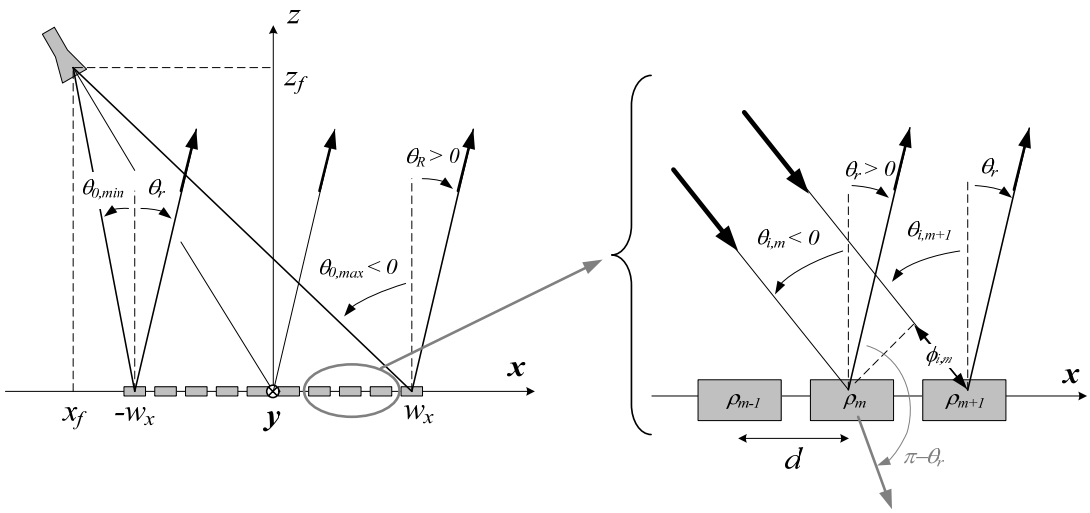

Figure 8.4: Variables definitions in a 1-D RA.

the difference between the reflection phase of successive array elements, this total phase delay $\phi_{it,m}$ is given by (8.7).

$$\Delta\rho_m = \arg(\rho_{m+1}) - \arg(\rho_m) \tag{8.6}$$

$$\phi_{it,m} = \phi_{i,m} + \Delta\rho_m = kd\sin\theta_{i,m} + \Delta\rho_m \tag{8.7}$$

Now, the locations of the main radiated beams are such that the waves reflected by each element interfere constructively in that direction. In other words, the total phase shift between two wave fronts is:

$$-kd\sin\theta_r^n - \phi_{it,m} = 2n\pi \tag{8.8}$$

with $n \in \mathbb{Z}$. We rewrite this expression as follows to give the location of the constructive reflection angles (location of the 'beams'):

$$\sin\theta_r^n = -\frac{\phi_{it,m}}{kd} - n\frac{\lambda_0}{d} \tag{8.9}$$

Note: Expression (8.9) shows that, as indicated in the right hand side of Figure 8.4*, there is identically always a solution $\pi - \theta_r^n$ and a solution θ_r^n, since $\sin\theta_r^n = \sin(\pi - \theta_r^n)$, which intuitively means that the locations of the beams are the same on both sides of the array plane. However, the element pattern is here obviously not accounted for and the array factor must be spatially modulated by the element pattern. The developments as written below are nevertheless general and account for both sides of the array. In the case of the RA application, there is always a ground plane to maximize the reflected power and the element patterns are null in the region 'below' the array (here $\theta \in \{\pi/2, 3\pi/2\}$).*

We are for the moment interested in the location of the *main lobe* of the array, which corresponds to $n = 0$ and we can write, using the simplified notation $\theta_r^{n=0} = \theta_r$:

$$\sin\theta_r = -\frac{\phi_{it,m}}{kd} \tag{8.10}$$

or also, using (8.7):

$$\sin\theta_r = -\left(\sin\theta_{i,m} + \frac{\Delta\rho_m}{kd}\right) \tag{8.11}$$

As expected, the reflection angle of the main beam is opposite to the incidence angle ($\theta_r = -\theta_{i,m}$) in the case where $\Delta\rho_m = 0$; namely, if all elements exhibit the same reflection phase. It should also be noted that there is a real solution for θ_r only if:

$$|\sin\theta_r| = \left|\frac{\phi_{it,m}}{kd}\right| = \left|\sin\theta_{i,m} + \frac{\Delta\rho_m}{kd}\right| \leq 1 \tag{8.12}$$

If this condition is not met, this does not necessarily mean that there is no constructive interference in real space, but only that the first beam appearing in real space is linked to the $n = 1$ or $n = -1$ (or any other) solution to (8.9). In practice, we can restrict our study to the case where (8.12) is true without loss of generality (if the main beam corresponds to $n = 1$ for instance, then the first GL will correspond to $n = 0$ or $n = 2$).

8.2.3. grating lobes (GLs)

a. Developments

In this section, we derive a general condition to rule out GLs in RAs, based on a simple calculation to deduce the location of the GLs with regard to the reflector inter-element spacing, the incidence angle, and the inter-element phase shift. We start with expression (8.9) from Section 8.2.2, which gives the angles θ_r^n where the waves reflected by the array elements interfere constructively. In (8.9), the main lobe normally corresponds to the solution $n = 0$. Thus, we can rewrite (8.9) as a function of the direction of the main lobe $\theta_r = \theta_r^{n=0}$ by introducing (8.10) in (8.9):

$$\sin\theta_r^n = \sin\theta_r - n\frac{\lambda_0}{d} \tag{8.13}$$

The condition to exclude any GLs is obtained by placing the first ones ($n = \pm 1$) in invisible space, namely:

$$\begin{cases} \left|\sin\theta_r^{+1}\right| > 1 \\ \left|\sin\theta_r^{-1}\right| > 1 \end{cases} \tag{8.14}$$

So we have, using (8.13):

$$\begin{cases} \left|\sin\theta_r + \frac{\lambda_0}{d}\right| > 1 \\ \left|\sin\theta_r - \frac{\lambda_0}{d}\right| > 1 \end{cases} \tag{8.15}$$

This system can be reduced as follows. First, let us use the reduced notation:

$$a = \sin\theta_r \quad \text{and} \quad b = \lambda_0/d \tag{8.16}$$

so that (8.15) writes:

$$\begin{cases} |a+b| > 1 \\ |a-b| > 1 \end{cases} \quad \text{with} \quad b \geq 0 \tag{8.17}$$

Using the property (8.18), this system can be reduced by treating separately 3 cases, as shown in Table 8.1.

$$|a+b| \geq |a-b| \quad if \quad sign\,(a) = sign\,(b) \tag{8.18}$$

Table 8.1: Resolution of system (8.17) by studying 3 cases separately.

	Case		
	$a > b$	$-b > a$	$b > a > -b$
Reduced form of (8.17)	$\begin{cases} a+b>1 \\ a-b>1 \end{cases}$	$\begin{cases} -a-b>1 \\ -a+b>1 \end{cases}$	$\begin{cases} a+b>1 \\ -a+b>1 \end{cases}$
After simplif. using (8.18)	$a-b>1$	$-a-b>1$	$-\lvert a\rvert+b>1$
After subst. using (8.16)	$\frac{\lambda_0}{d} < -1+\sin\theta_r$	$\frac{\lambda_0}{d} < -1-\sin\theta_r$	$\frac{d}{\lambda_0} < \frac{1}{1+\lvert\sin\theta_r\rvert}$

Let us now study the final solutions shown in the last row of the table. In the case $a > b$, we observe that the right member of the inequality is always negative or zero. Since λ_0/d is always positive, the inequality is never true and there will always be GLs in this first case. With a similar reasoning, we also find that the solution in the case $-b > a$ is never true and there will always be grating lobes in this case. Finally, in the case $b > a > -b$, the system reduces to:

$$\frac{d}{\lambda_0} < \frac{1}{1+|\sin\theta_r|} \tag{8.19}$$

We can thus conclude that, since there are no solution to avoid GLs in case 1 and 2, meeting condition (8.19) is the only way to rule out GLs. It is remarkable that condition (8.19) is similar to the one obtained in the case of a 'usual' array fed by TLs [101]. However, this result was shown here in the more general case of a RA and allowed us to demonstrate that the condition on the element spacing *depends only on the direction of the main reflected beam*, but not on the incident angle and inter-element phase shift (θ_i and $\Delta\rho_m$, respectively). This is due to the fact that $\Delta\rho_m$ and θ_i are not independent but that $\Delta\rho_m$ is tailored depending on the variation of θ_i within the array so that the overall field is coherent in the θ_r direction [according to (8.11)]. As a result, (8.19) is valid for any position x in the real array, despite the individual variations of θ_i and $\Delta\rho_m$ in that direction.

b. Influence of the cell radiation pattern

It is clear that the amplitudes of the main and grating lobes depend on the element radiation pattern. For instance, a GL close to $\theta = 90°$ might be almost cancelled out by the element pattern in the case of a grounded RA cell, as is almost always the case in practice (in order to maximize the reflection amplitude). In this case, we might consider that GLs located at $\theta > \theta_{lim}$ do not need be excluded, θ_{lim} being determined by the element pattern and the maximum GL level allowed by the application. In this case, the development presented in the first part of this section can be simply updated and (8.19) becomes:

$$\frac{d}{\lambda_0} < \frac{1}{L+|\sin\theta_r|} \tag{8.20}$$

with $L = |\sin\theta_{lim}|$. First, we observe that (8.20) is, as expected, equal to (8.19) in the case $\theta_{lim} = 90°$. Second, since $L \leq 1$, the elements can be spaced slightly further apart if we can live with GLs in the region $\theta > \theta_{lim}$.

8.2.4. RA element BW

In order to characterize the RA element BW, let us first rewrite (8.11) with explicit mention of the frequency dependence:

$$\sin\theta_r(f) = -\left(\sin\theta_{i,m} + \frac{\Delta\rho_m(f)}{kd}\right) \tag{8.21}$$

where

$$\Delta\rho_m(f) = \arg(\rho_{m+1}(f)) - \arg(\rho_m(f)) \tag{8.22}$$

represents the *variation* of the phase response of the cells over the array. First, we consider the dependence of $\Delta\rho_m(f)$ on the position m and at the design frequency only; since we want in general to have a reflection angle θ_r constant over the array for a maximum gain, it is clear from (8.21) that $\Delta\rho_m(f)$ is function of the location of the element m since the incidence angle $\theta_{i,m}$ from the feed is itself function of m. In practice, the exact relation between $\Delta\rho_m(f)$ and $\theta_{i,m}$ depends on the geometry of the RA (reflector and feed size and relative positions). These geometrical parameters thus determine the form of the curves in the phase diagram as a function of the position m in the array.

Now, let us consider a finite BW. We want θ_r to be frequency-independent so that the gain remains maximum within the whole BW (if it is not the case, not only some beam squint will occur, but the maximum gain will be degraded since the different elements will not radiate coherently anymore). A simple observation of (8.21) shows that θ_r is frequency-independent if $\Delta\rho_m(f)$ is proportional to f. This is the case if $\arg(\rho_m(f))$ is of true-time delay (TTD) (namely, proportional to f), although this is not the only solution for having $\Delta\rho_m(f) \sim f$), as shown in Figure 8.5(a). This means, considering now the phase diagram of Figure 8.5(b), that the derivative –in a discrete sense– of the curves is also proportional to f, as shown in (8.23), where $\arg(\rho_m(f))$ is written in its general ideal TTD form with arbitrary parameters A and B_m, and using the notation of (8.22).

$$\arg(\rho_m(f)) = A - B_m \cdot f \quad \rightarrow \quad \frac{\Delta\rho_m(f)}{\Delta m} = -\frac{\Delta B_m}{\Delta m} f \tag{8.23}$$

In the case of RAs, a BW of 5% is already considered rather large, and will never exceed 15% – 20%. Therefore, since f varies of a relatively small amount within such BWs, the ideal curves in the phase diagram almost only differ by a vertical offset, and the deviation of any real element phase response from this ideal case can be used as a measure of the phase error in the BW.

In the case of large arrays, there can be more than 360° of spatial phase delay from the feed between different locations in the array. For clarity, let us consider a location m_a where the spatial delay from the feed is ϕ_a and an another location in the large array m_b with $\phi_b = \phi_a + 2\pi$. If we consider the central frequency of operation only, the elements at m_a and m_b can be exactly the same since only the phase shift modulo 2π is relevant. In this case, it is only useful to achieve

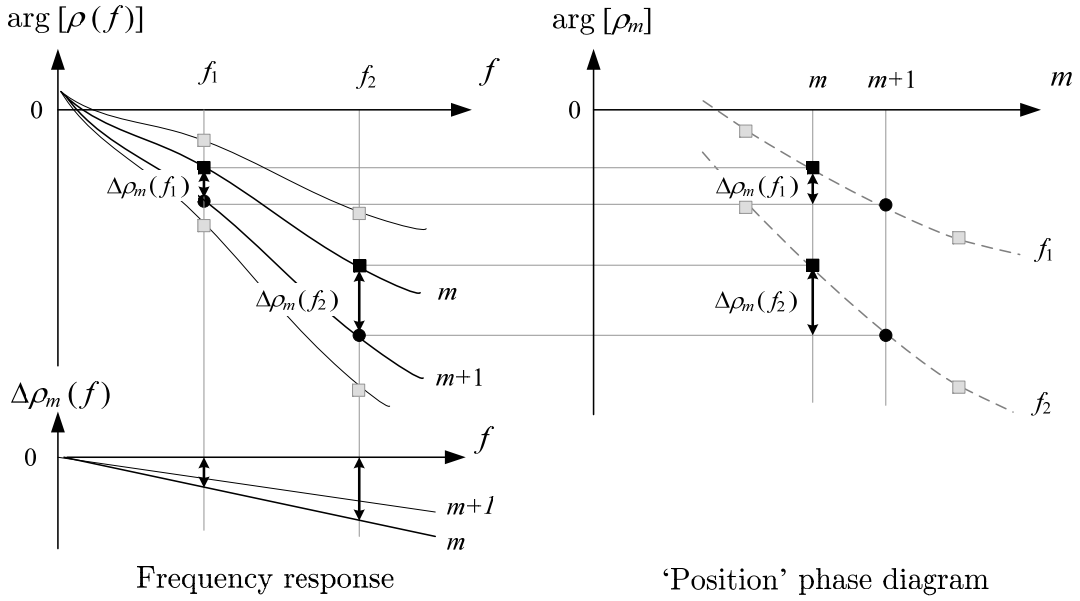

Figure 8.5: Ideal phase response of a RA element for a minimum frequency phase error (maximum BW).

elements with a reflection phase range of 360°. However, if we now consider a wideband design, the ideal frequency response *slope* is not the same for ϕ_b and ϕ_a. In this case there is the need for TTD responses in excess of 360° to achieve the ideal phase slope for each element, such as done in [102]. However, [103] shows that achieving a real TTD-type phase response only for the first 360° while reusing the same elements for phases in excess of 360° results only in a minor degradation of the gain with regard to the ideal solution, even for relatively large reflectors. This result is fundamental for reconfigurable RAs where we wish to use only a single reconfigurable element for the whole array; indeed, we only need to design an element with the appropriate phase responses within a range of 360°. If this was not the case, it would be necessary to have several states corresponding to the same phase modulo 2π but with different slopes of frequency response, which would be extremely complex in practice. In addition, in this case the approximation that the curves in the frequency response (and subsequently in the 'position' phase diagram, see Figure 8.5) are ideally almost parallel would not hold true anymore. Thus, a more complex criteria for the characterization of the frequency phase error would have to be used.

Finally, let us note that these developments were based on the reflection phase as a function of the position in the array m [hence the naming *position* phase diagram in Figure 8.5(b)]. However, when characterizing a RA element we will in practice rather plot its phase diagram as a function of its *state* p. Nevertheless, it is clear that if the curves in the position phase diagram are parallel, so will be those in the phase diagram as a function of the states of RA element used in the array. Thus, the frequency phase error defined by (8.27) can be employed to assess the BW of a RA element, based on the phase diagram as a function of the state p.

In summary of these observations, the ideal frequency response of the RA elements for achieving a large RA BW is such that $\Delta\rho_m(f) \propto f$ within the range from 0° to −360°. This means, by

approximation on a limited fractional BW, that the curves for different frequencies in the phase diagram should only differ by some offset, and that any deviation from this characteristic will limit the BW of the array.

a. Phase frequency error (BW) characterization

In order to assess the performance of different MEMS RA cells in terms of BW, we define here the *phase frequency error* as a measure of the imperfection of the phase response of the element at the limits $f_C + \Delta f$ and $f_C - \Delta f$ on a given BW. As explained above, the error for $f_C + \Delta f$ corresponds to the deviation of the curve at $f_C + \Delta f$ with regard to the curve at f_C in the phase diagram, except for a constant 'vertical' shift (with the assumption of a limited fractional BW). From a more intuitive perspective, this error is a measure of the 'non-parallelism'[1] of the curves at $f_C + \Delta f$ and f_C. So, we first define δ_m as the difference between the curves at $f_C + \Delta f$ and f_C [see Figure 8.5, this quantity should not be mistaken with (8.22)]:

$$\delta_m\left(f_C, \Delta f\right) = \arg\left(\rho_m\left(f_C + \Delta f\right)\right) - \arg\left(\rho_m\left(f_C\right)\right) \tag{8.24}$$

and the average distance on all M values of the parameter m (namely all states) represents the shift between both curves:

$$\bar{\delta}\left(f_C, \Delta f\right) = \frac{1}{M}\sum_{m}^{M} \delta_m\left(f_C, \Delta f\right) \tag{8.25}$$

So the average phase error of the response at $f_C + \Delta f$ can logically be defined as follows:

$$E_0\left(f_C, \Delta f\right) = \frac{1}{M}\sum_{m}^{M} \left|\delta_m\left(f_C, \Delta f\right) - \bar{\delta}\left(f_C, \Delta f\right)\right| \tag{8.26}$$

And we verify that the error E_0 is zero if $\rho_m\left(f_C + \Delta f\right)$ is parallel with $\rho_m\left(f_C\right)$ since in this case $\delta_m\left(f_C, \Delta f\right) = \bar{\delta}\left(f_C, \Delta f\right)$ for all m. In practice, we will calculate the average of the errors at the lower and upper frequency of the BW:

$$E\left(f_C, \Delta f\right) = \frac{1}{2}\left(E_0\left(f_C, +\Delta f\right) + E_0\left(f_C, -\Delta f\right)\right) \tag{8.27}$$

This finally yields (8.28), by substitution of (8.26) and (8.25) in (8.27), which will be the quantity used to assess the phase error of the presented RA cells at the limit of a given BW.

$$\begin{aligned} E\left(f_C, \Delta f\right) = \tfrac{1}{2M}\sum_{m}^{M}\Bigg[&\left|\delta_m\left(f_C, +\Delta f\right) - \tfrac{1}{M}\sum_{m}^{M}\delta_m\left(f_C, +\Delta f\right)\right| \\ &+ \left|\delta_m\left(f_C, -\Delta f\right) - \tfrac{1}{M}\sum_{m}^{M}\delta_m\left(f_C, -\Delta f\right)\right|\Bigg] \end{aligned} \tag{8.28}$$

[1] The term *parallelism* is here an abuse of the language since we deal here with curves that are not straight lines.

8.2.5. Element radiation pattern

The radiation pattern of a RA is mainly determined by the reflection phase of the RA elements, as discussed so far in this chapter. However, it is clear that the radiation pattern of the element also influences the total RA pattern, in a similar way as the pattern of an element in a conventional TL-fed array multiplies the array factor to yield the total radiation pattern. However, the situation is not exactly the same in the case of the RA; in order to discuss this issue and derive some requirements for the RA element pattern, we first recall formula (8.11):

$$\sin\theta_r = -\left(\sin\theta_{i,m} + \frac{\Delta\rho_m}{kd}\right) \tag{8.29}$$

where θ_r is the location of the *main lobe* of the array, $\theta_{i,m}$ the incidence angle on element m, and $\Delta\rho_m = \arg(\rho_{m+1}) - \arg(\rho_m)$ the difference between the reflection phase of successive array elements. First, let us imagine the case of a RA whose feed is far enough from the reflector so that the incidence angle $\theta_{i,m} = \theta_i$ can be assumed constant for all elements in the array, and thus independent from m (this is not realistic but helpful as a first step in the present discussion). In order to point the reflected beam in a given direction θ_r, (8.29) shows that the inter-element phase shift variation $\Delta\rho_m$ is also independent from m (but not necessarily zero). In other words, there is in this case a constant phase difference between successive elements in the array, and all elements have the same radiation pattern since illuminated under the same incidence. As a result, it is possible here to write the total pattern of the array as a product of the array factor and element pattern under θ_i illumination, in a similar way as in the case of a TL-fed array[1].

However, in practical RAs, the feed is too close to the reflector for the incidence angle to be assumed constant. In this case, (8.29) shows that the inter-element phase shift variation $\Delta\rho_m$ also changes with m. Second, all elements exhibit now a different radiation pattern since illuminated under a different incidence angle $\theta_{i,m}$. As a result, it is rigorously not possible to express the total field of the RA as a product of array factor and element pattern, although this could be done as a first approximation if the element pattern dependence on θ_i is assumed low enough.

Concerning the requirements on the RA element pattern, it is clear that a weak dependence on θ_i is preferred, so that the element radiation patterns do not be taken into account in the array design. Second, whichever the value of θ_i, a broadbeam reflected pattern is desired so that the gain of the RA do not degrades significantly when scanning the array away from broadside.

8.2.6. Design method

As explained previously, here we aim at designing RA elements but will not design a complete array. However, for the sake of completeness and to show that the design of a reconfigurable RA cell is, to a certain extent[2], independent from the RA design itself, we describe the general procedure for the design of a RA system [84]:

1. Selection of fixed parameters for the array (e.g. substrate, size of the reflector).

[1]Note that we also assumed in this reasoning that the incident field intensity is the same on all elements.
[2]The operation frequency and polarization of the cell must obviously be those intended for the complete RA.

2. Element design and characterization: The element is optimized and the reflection phase of the radiating element is computed as a function of the element control parameter p. All details about these issues are presented in Chapter 9.
3. Beamforming: For a given desired pattern, the required element phase shift as a function of the position of the element in the array is deduced from the path delays, which depend on all geometrical parameters shown in Figure 8.4. In the case of reconfigurable RAs, this calculation is done for each radiation pattern that the array must radiate. The incidence angle can be taken into account here if the phase of the element was computed for different incidences for each value of p.
4. Making use of the results of the two previous steps, a fixed-beam array is simply designed by placing the appropriate element at each position in the array to provide the required phase shifts. In the case of reconfigurable RAs, p is the command DC voltage and is deduced for each cell and for each state.

Since approximations were used in the design process, different steps can be employed to refine the design and predict the array pattern accurately (element radiation pattern, incident field amplitude, etc). More details about these issues can be found in [84] or [85].

8.3. Floquet's theorem and the periodic boundary conditions waveguide (PBC-WG)

8.3.1. Infinite periodic array approximation

In practical RA designs, the difference of reflection phase between successive elements, defined here as $\Delta\rho_m$ in (8.22), is small enough for the reflection phase of an element embedded in the array to be almost the same as if the element was embedded in an array of identical elements (for which $\Delta\rho_m = 0$). As a result, the reflection phase of the element is in general computed using an infinite array approximation, which allows simulating only one cell of the array by making use of periodic boundary conditions (PBCs). It should be noted that this approximation is necessary for design purposes since we need to first characterize the reflection phase of an element as a function of the control parameter p, before designing the array. Thus, the exact element environment is not known at the time of element characterization and the best possible approach is to compute the reflection phase in a infinite periodic array approximation. It is of course possible to carry out verification simulations once the array has been fully designed to assess the impact of this approximation.

8.3.2. Floquet's theorem

a. Introduction

Developments linked with Floquet's theorem were already presented in Chapter 2 to deduce the periodic structure Bloch equivalents of given two-port networks. In that case, we were interested in the characterization of the propagation of a wave *guided* by a periodic structure, namely with

identical networks connected together at their ports, where the fields can be decomposed into the modes supported by the TLs constituting the ports. Although we were in practice interested in 1-D structures, such approach can obviously be extended to 2-D ones as well. In these situations, the condition of periodicity was set at planes which are ports of the network that constitutes the unit cell of the periodic structure. The different Bloch wave propagation constants (one per Floquet's mode) found thus link the fields of input and output ports of the unit cell.

In the case of RAs, the situation is different since the planes of periodicity do not correspond to ports of the unit cell; there is an incident field exciting the structure and the condition of periodicity applies to the fields at periodic planes of the structure on which the incident wave impinges. In the rest of this section, we first recall Floquet's theorem and explain how it applies to the case of RAs of interest here. Although Floquet's theorem is referred to in numerous works, detailed information about this theorem, and especially the exact link with the periodic boundary conditions waveguide (PBC-WG) described in the next section, are not easily found. In this context, [104] proved to be a relevant source for the next developments, which are also further developed and interpreted in view of the analysis and design of the MEMS-controlled RA cell of Chapter 9. Finally, note that full demonstration of Floquet's theorem in the case of electromagnetic waves in periodic structures can be found in [105].

b. Floquet's theorem

The electromagnetic fields in an infinite periodic structure consist of a superposition of modes which are called Floquet's modes. *Each* of these modes can be expressed as follows:

$$U(\mathbf{r}) = U_p(\mathbf{r})\, e^{-\gamma\cdot\mathbf{r}} \tag{8.30}$$

with

$$U_p(\mathbf{r}+\mathbf{R}) = U_p(\mathbf{r}) \tag{8.31}$$

where $U(\mathbf{r})$ is any field component, $\mathbf{R}$ the lattice vector, $U_p(\mathbf{r})$ a periodic function in space (different for each Floquet's mode) and γ the equivalent propagation vector (different for each Floquet's mode). So, the field is the same in all cells of the structure, except for a propagation factor $e^{-\gamma\cdot\mathbf{r}}$, where $\mathrm{Re}[\gamma]$ is not necessarily zero. In other words, the Floquet's mode field is a travelling wave with $e^{-\gamma\cdot\mathbf{r}}$, modulated in space by the periodic function $U_p(\mathbf{r})$. Another form of this theorem can easily be obtained from (8.30) and (8.31) and writes:

$$U(\mathbf{r}+\mathbf{R}) = U(\mathbf{r})\, e^{-\gamma\cdot\mathbf{R}} \tag{8.32}$$

c. 2-D periodic structures and Floquet's spacial harmonics

In the case of reflectarrays, the structures are only periodic along two directions. With a periodicity along the x and y axes, the lattice vector $\mathbf{R}$ can be written as follows:

$$\mathbf{R} = m\, d_x \mathbf{e}_\mathbf{x} + n\, d_y \mathbf{e}_y, \quad m,n \in \mathbb{Z} \tag{8.33}$$

In this case, the periodic function $U(\mathbf{r}) = U_p(x, y, z)$ is only periodic along the x and y directions as well since (8.31) now writes:

$$U_p(x + m\,d_x, y + n\,d_y, z) = U_p(x, y, z) \tag{8.34}$$

Thus, the periodic function $U_p(\mathbf{r}) = U_p(x, y, z)$ can be expanded in a Fourier series as follows:

$$U_p(\mathbf{r}) = \sum_n^\infty \sum_m^\infty \left(a_{nm}(z) \exp\left[j\frac{2m\pi}{d_x} x \right] \exp\left[j\frac{2n\pi}{d_y} y \right] \right) \tag{8.35}$$

so that we can rewrite the total field, using (8.30) and the notation $\gamma = \gamma_x \mathbf{e_x} + \gamma_y \mathbf{e_y} + \gamma_z \mathbf{e_z}$:

$$U(\mathbf{r}) = \sum_n^\infty \sum_m^\infty \left(a_{nm}(z) \exp(-\gamma_z z) \cdot \exp\left[\left(-\gamma_x + j\frac{2m\pi}{d_x} \right) x \right] \cdot \exp\left[\left(-\gamma_y + j\frac{2n\pi}{d_y} \right) y \right] \right) \tag{8.36}$$

which means that *each Floquet's mode can be expressed as an infinite sum of traveling waves* of the form:

$$U_{mn}(\mathbf{r}) = a'_{nm}(z) \exp[-\gamma_{xm} x] \exp[-\gamma_{yn} y] \tag{8.37}$$

with:

$$\text{with} \quad \gamma_{xm} = \gamma_x - j\frac{2m\pi}{d_x} \quad \text{and} \quad \gamma_{yn} = \gamma_y - j\frac{2n\pi}{d_y} \tag{8.38}$$

and where the information about the dependence of the field in z (which is the normal direction to the periodic 'infinite' plane), is contained in $a'_{nm}(z)$. The traveling waves of the form (8.37) are called *Floquet's spatial harmonics*, and should not be mistaken with the Floquet's modes.

d. 2-D periodic structures illuminated by a plane wave

Let us now consider that the 2-D periodic structure is illuminated by a plane wave of propagation vector:

$$\mathbf{k} = -k_0 \begin{pmatrix} \cos\varphi \sin\theta \\ \sin\varphi \sin\theta \\ \cos\theta \end{pmatrix} \quad \text{with} \quad \begin{cases} 0 \le \theta < \frac{\pi}{2} \\ 0 \le \phi < 2\pi \end{cases} \quad \text{and} \quad k_0 = \frac{\omega}{c_0} \tag{8.39}$$

with the angles, the vector $\mathbf{k}$ and the associated incidence plane as depicted in Figure 8.6(a).

Now, we observe again from the form (8.32) of Floquet's theorem that the total fields in two successive cells of the structure only differ by some propagation factor $e^{-\gamma \cdot \mathbf{R}}$, and that this propagation factor is the same for all cells. As the structure is infinite and illuminated by a plane wave, it is clear that the only possible total field propagation factor between successive cells is that of the incident plane wave. Mathematically, this writes:

$$\gamma \cdot \mathbf{R} = j(\mathbf{k} \cdot \mathbf{R} + 2p\pi), \quad p \in \mathbb{Z} \tag{8.40}$$

Consequently, under illumination by a plane wave, the real part of the transverse components of γ is zero. This is not necessary in Floquet's theorem but stems here from the fact that the infinite structure being illuminated by an (also infinite) plane wave obviously 'carries' a field that do not

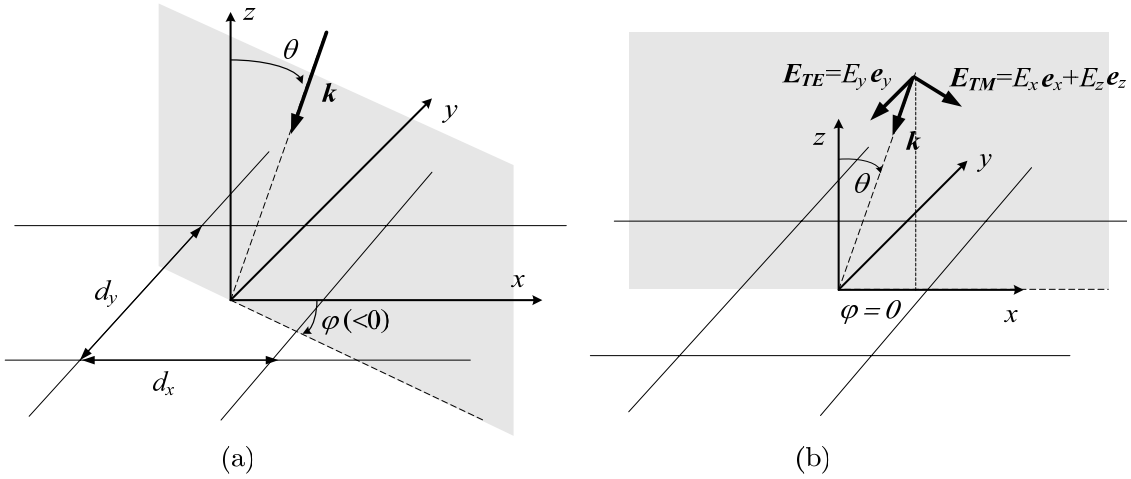

Figure 8.6: (a) Definition of the array cell dimensions, field incidence, and coordinates. (b) Decomposition of an incident field in TE and TM polarized waves (in the case $\varphi = 0°$).

decay in any direction along which the structure is infinite. Thus, Floquet's theorem becomes in this case:

$$U(\mathbf{r}+\mathbf{R}) = U(\mathbf{r})\, e^{-j\mathbf{k}\cdot\mathbf{R}} \tag{8.41}$$

In summary, in the case of a 2-D structure excited by an impinging plane wave, the Floquet's propagation vector γ in (8.30) only depends on the incident plane wave and is known. However, the form of the fields in a unit cell, or $U_p(\mathbf{r})$, depends on the structure of the cell itself and we explain in the next section how these fields can be determined.

8.3.3. periodic boundary conditions waveguide (PBC-WG) description

As a result of Floquet's theorem, the unit cell of the periodic structure can be seen as a waveguide with its axis in the z direction and its lateral walls subject to PBCs, as illustrated in Figure 8.7. The PBCs consist in enforcing that the field is the same on two opposite walls, except for a phase shift function of the frequency and incident wave angle [see (8.39)]:

$$\begin{cases} \phi_x = -k_x d_x = -(k_0 \cos\varphi \sin\theta)\, d_x \\ \phi_y = -k_y d_y = -(k_0 \sin\varphi \sin\theta)\, d_y \end{cases} \tag{8.42}$$

As a result, the considered 1-cell structure can be seen as a virtual waveguide along the z axis with PBC on its walls, and is hence referred to here as the periodic boundary conditions waveguide (PBC-WG). The analysis of such a waveguide is presented in [106] and will not be repeated here. The main practical results of this analysis are:

- The PBC-WG supports degenerated pairs of TE and TM modes (i.e. each TE mode propagation constant is also the propagation constant of a TM mode). As the boundary conditions of the PBC-WG are imposed by the direction of the incident plane wave, there is a PBC-WG with its own set of modes for each incidence angle.

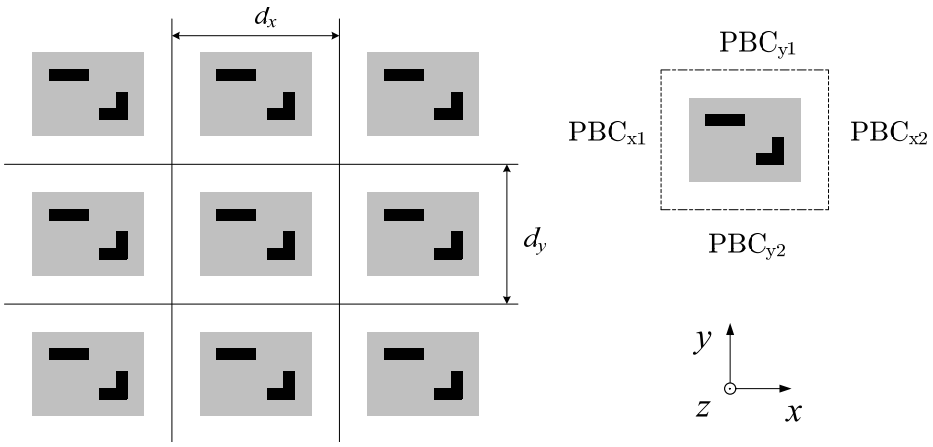

Figure 8.7: Modeling of an infinite periodic structure by its unit cell in a PBC-WG.

- In the particular case of normal incidence $\theta = 0$, both TE_{00} and TM_{00} modes become TEM modes.

Here, The convention for the TE and TM naming is the usual one used to describe the polarization of an incident wave on a surface; namely, the TE has a *perpendicular* polarization whereas the TM has a *parallel* polarization. As a result, a plane wave with any given polarization can always be decomposed in a TE and a TM polarized wave and analyzed by the PBC-WG approach. For instance, in the case $\varphi = 0°$ depicted in Figure 8.6(b), an incident plane wave with $\mathbf{E_i} = E_{ix}\mathbf{e_x} + E_{iy}\mathbf{e_y} + E_{iz}\mathbf{e_z}$ can be decomposed as $\mathbf{E_{i},}_{TE} = E_{iy}\mathbf{e_y}$ and $\mathbf{E_{i},}_{TM} = E_{ix}\mathbf{e_x} + E_{iz}\mathbf{e_z}$ so that $\mathbf{E_i} = \mathbf{E_{i},}_{TE} + \mathbf{E_{i},}_{TM}$.

It is shown in [104] that the modes of the PBC-WG correspond to the spatial Floquet's harmonics given by (8.37) on which the expansion of the concerned Floquet's mode was done. It is especially remarkable that:

- The dependence of the field in the dimensions of periodicity x and y, seen as a propagation along x and y in expression (8.41), is given by the *transverse* field of the PBC-WG modes.
- Concerning the dependence of the field along z, represented by $a_{nm}(z)$ in (8.41), it is determined by the PBC-WG modes propagation constant (these modes can be propagating or evanescent).

Consequently, the PBC-WG can be used to find the field distribution in the unit cell. However, in the case of the RA, we are mostly interested in the far field, which *is only determined by the modes of the PBC-WG which are non-evanescent.* Thus, the PBC-WG approach can be employed to compute the reflection phase that will determine the direction of the radiated beam(s) in a RA, since this reflection phase is the argument of the modal reflection coefficient of the non-evanescent mode(s) of the PBC-WG. Using the detailed mathematical description of the modes provided in [106], we can show that *the cutoff frequency of the 2^{nd} pair of PBC-WG modes corresponds to the limit frequency for a RA grating lobe to appear in visible space.* In conclusion, this means that a PBC-WG corresponding to an array whose dimensions were selected to rule out grating lobes

will have only one pair of TE/TM propagating mode, and the location of the main beam is thus linked with the reflection phase for this mode only.

It should finally be noted that, in contrast with the 'TL-type' periodic structures studied in chapter 2, the theory only allows here to deal with *infinite* periodic structures. This is due to the fact that in this case, the field at the periodicity planes cannot be decomposed into TL modes and connected to a given load where the structure is terminated.

8.3.4. PBC-WG in the case of normal incidence

In the case of a normal incidence $\theta = 0$, the phase shifts between PBCs given by (8.42) are obviously $\phi_x = \phi_y = 0$. If, in addition, the unit cell is symmetrical around both x and y axis and the excitation is linearly polarized along the y axis, the induced currents presents:

- A symmetry around the y symmetry axis of the cell, so the PBCx boundaries of Figure 8.7 are perfect magnetic conductor (PMC) boundaries.
- An antisymmetry around the x symmetry axis of the unit cell, so the PBCy boundaries of Figure 8.7 are perfect electric conductor (PEC) boundaries.

As a result, it is theoretically equivalent to simulate the structure with PBCs with $\theta = 0$ and PEC/PMC boundaries, and we will refer to the latter simulation setup as the perfect electric/magnetic conductor waveguide (PECPMC-WG). It is noticeable that PEC and PMC are simple (i.e. numerically efficient) boundary conditions and that the reflection coefficient in this case is the s_{11} of the TEM plane wave guided by the PECPMC-WG. As a result, it provides a simple tool to validate the PBC simulation setup and post-processing.

8.3.5. PBC-WG and linearly polarized arrays

This section discusses the interpretation and use of the aforementioned concepts in the case of RAs with linearly-polarized incident wave and antenna elements, as will be the case of the RA cells presented in Chapter 9. Let us consider linearly polarized elements designed to resonate along their y dimension. In this case, the most efficient method to illuminate such an array is to produce an incident TE-polarized wave with $\varphi = 0$. As a result, the incident wave in the PBC-WG is in this case purely TE polarized. In general, the reflected wave will however not be purely TE polarized, although only this contribution is desired with regard to the functioning of the RA.

As a result, the TE reflected wave can be seen as the co-polarization of the element while the TM contribution corresponds to 'lost' cross-polarized field. Finally, and as explained above, the array parameters are in practice chosen upon the condition that no GL appears and only the first degenerated TE/TM modes of the PBC-WG propagate. So we can write:

$$|\rho_{co}|^2 + |\rho_x|^2 + L_{mat} = 1 \tag{8.43}$$

where L_{mat} represents all material losses (metal and dielectric losses) and ρ_{co} and ρ_x are the reflection coefficient of the reflected TE and TM waves, respectively, with regard to the incident

TE polarized wave. Since the only useful reflected contribution is linked with ρ_{co}, we can identify the effective losses in the system as the sum of the material losses and losses by cross-polarization:

$$L = |\rho_x|^2 + L_{mat} = 1 - |\rho_{co}|^2 \tag{8.44}$$

Since ρ_{co} and ρ_x are both provided by the PBC-WG simulation, it is possible to identify individually cross-polarization losses L_x and material losses L_{mat}, so that $L = L_x + L_{mat}$.

$$L_x = |\rho_x|^2 \tag{8.45}$$

$$L_{mat} = 1 - |\rho_{co}|^2 - |\rho_x|^2 \tag{8.46}$$

8.4. Rectangular waveguide infinite array simulator (RWG-IAS)

8.4.1. Introduction

The measurement of array elements is especially inconvenient; indeed, the only way to measure such an element in its real array environment —namely, taking into account the coupling with the other active elements in the array— is to build the RA. Since building and measuring the array is particularly costly and time-consuming, this approach is extremely inefficient in a design stage since some updates of the element would mean that numerous arrays would have to be built and measured.

From a numerical simulation point of view, it is also extremely inefficient to simulate the whole array in the design stage; for that reason, PBCs were introduced to model the element in a periodic infinite environment (PBC-WG) and provide a computational effective way to simulate the array element in the design stage. In the case of measurements, PBCs can obviously not be artificially fabricated and the only easily available waveguide for the measurement is the usual rectangular waveguide (RWG). However, it was shown in [107] that such a waveguide can be used to simulate the behavior of an array element in an infinite array and *in an exact way* (upon some condition that will be exposed below). We will refer here to this approach as the rectangular waveguide infinite array simulator (RWG-IAS).

8.4.2. RWG-IAS description and theory

The RWG-IAS concept was introduced by Hannan and Balfour in [107]. Nevertheless, we will make in this section a complete but intuitive demonstration of the RWG-IAS principle and required assumptions, while limiting ourselves to the particular simple case of interest here (see below). The reason is twofold; first, [107] only provides very few theoretical justifications to the concepts presented, which do not allow answering practical questions arising when using the RWG-IAS in concrete situations. Second, we study different issues linked with the particular case of interest here, which will be used in this chapter for further developments and comparison with other methods of RA cell characterization. The particular case we are interested in here is sketched in Figure 8.8 and consists of:

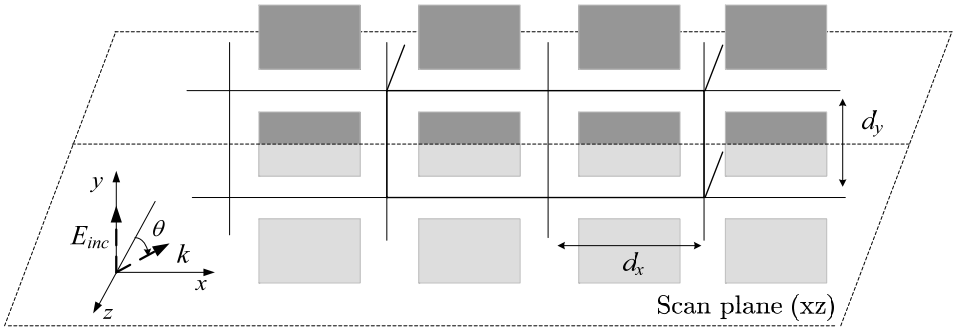

Figure 8.8: Definition of the array setup and incident wave for the present RWG-IAS developments.

- A rectangular array lattice with scanning in a single plane intersecting the array plane in one of the array axes. The array lattice spacing in that direction is d_x, as shown in the figure.
- TE incidence, also called H-polarization (namely, incident E field perpendicular to the scan plane and H field in the scan plane).
- The structure is to be characterized in a RWG and with the dominant TE_{10} mode only.

a. The RWG TE_{10} mode seen as a superposition of two plane waves

The principle of the RWG-IAS relies on the fact that the TE_{10} mode of a RWG can be decomposed into two particular plane waves, which we first write in the general forms:

$$\mathbf{E}_1 = \mathbf{E}_{1,0} \exp\left[-j\left(\mathbf{k_1} \cdot \mathbf{r} + \alpha_1\right)\right] \tag{8.47}$$

$$\mathbf{E}_2 = \mathbf{E}_{2,0} \exp\left[-j\left(\mathbf{k}_2 \cdot \mathbf{r} + \alpha_2\right)\right] \tag{8.48}$$

We will now re-write these planes waves so that:

- Their only non-null E field component is along the y axis and is the same for both plane waves: $\mathbf{E}_{1,0} = \mathbf{E}_{2,0} = E_y \hat{e}_y$.
- Their 'phase offset' are the same, and are set to zero here without loss of generality: $\alpha_1 = \alpha_2 = 0$.
- The planes waves propagation vectors are in the xz plane and with opposite angles θ and $-\theta$ relative to the RWG axis.

With these assumptions, we have:

$$\mathbf{E}_1 = E_y \hat{e}_y \exp\left[-jk_0\left(x \sin\theta + z \cos\theta\right)\right] \tag{8.49}$$

$$\mathbf{E}_2 = E_y \hat{e}_y \exp\left[-jk_0\left(-x \sin\theta + z \cos\theta\right)\right] \tag{8.50}$$

We can now sum these two plane waves and find:

$$\mathbf{E}_{tot} = \mathbf{E}_1 + \mathbf{E}_2 = E_y \hat{e}_y \exp\left(-jk_0 z \cos\theta\right) \cdot 2\cos\left(-k_0 x \sin\theta\right) \tag{8.51}$$

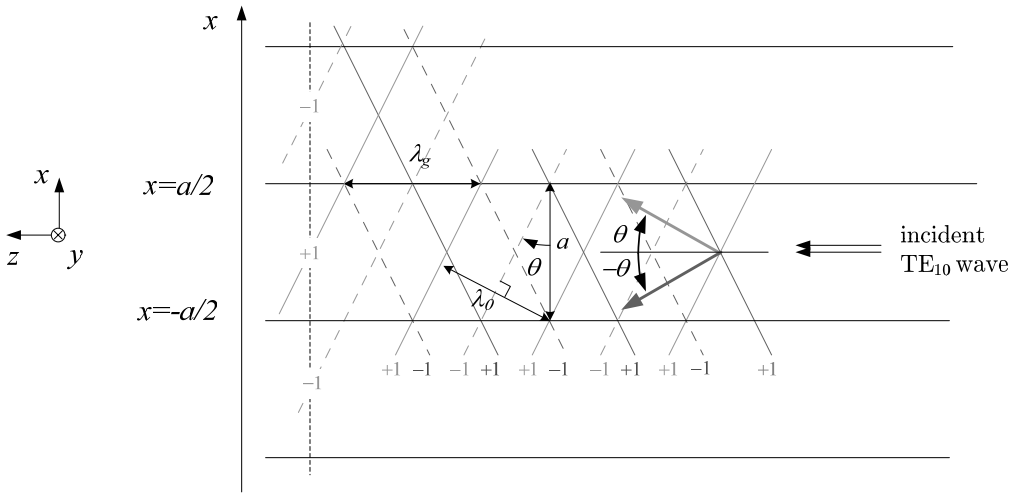

Figure 8.9: Illustration of the decomposition of the TE_{10} mode of a RWG into 2 plane waves.

Now, we want to find which condition on these plane waves is required so that the total field corresponds to the field of the TE_{10} mode of a RWG whose side walls are located at $x = -a/2$ and $x = +a/2$, as sketched in Figure 8.9. Since the tangential field must vanish at the PEC walls of the RWG, we have the condition:

$$\mathbf{E}_{tot}\left(x = +a/2\right) = \mathbf{E}_{tot}\left(x = -a/2\right) = 0 \tag{8.52}$$

Substituting these conditions in (8.51) yields:

$$|\sin\theta| = \frac{\pi}{k_0 a} = \frac{c_0}{2a \cdot f} \tag{8.53}$$

We now substitute (8.53) into the general expression for the total field (8.51) and obtain after some developments:

$$\mathbf{E}_{tot} = 2E_y\hat{e}_y \cdot \cos\left(\frac{\pi x}{a}\right) \exp\left(-j\sqrt{k_0^2 - \left(\frac{\pi}{a}\right)^2} \cdot z\right) \tag{8.54}$$

We observe that this is exactly the expression for the E field of the TE_{10} mode of RWG of width a (and with walls located at $x = -a/2$ and $x = +a/2$) [14], which concludes the demonstration.

Here we also provide an intuitive illustration of the above analytical developments. Figure 8.9 shows the two planes waves, symbolically represented in dark and light grey; phase fronts corresponding to maxima are represented by solid lines (+1) and the minima by dashed line (-1). In the situation sketched in the figure, the two plane waves add up in a destructive way on the RWG lateral walls (E field nulls) while they add constructively in the center of the guide, which complies with the TE_{10} mode. From simple geometrical considerations based on this figure, we can find again (8.53).

For following considerations, we also observe that the total field of the two plane waves which match the TE_{10} of the RWG are such that there is an 'antisymmetry' of this total field around

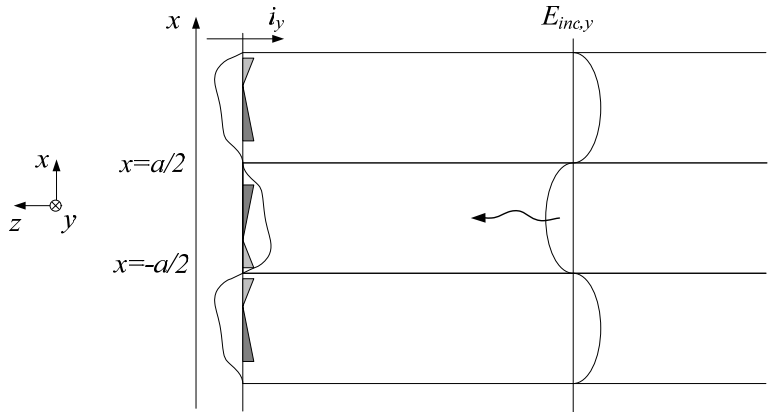

Figure 8.10: RWG and incident TE_{10} wave with $\mathbf{E} = E_y\hat{e}_y$ impinging on an asymmetrical load.

$x = -a/2$ and $x = +a/2$, namely $E_{inc,y}(x - a/2) = -E_{inc,y}(-x - a/2)$ and $E_{inc,y}(x + a/2) = -E_{inc,y}(-x + a/2)$. Concerning now the walls of the RWG in the xz plane, they also comply with the incident superposition of the planes; indeed, the E field is along the y axis and a PEC can thus be placed in the xz plane without perturbing the field.

b. Loaded RWG

We now place a load at one extremity of the RWG, which will be excited by the TE_{10} mode. There will now be some reflected wave and we will deduce *which infinite arrangement of this load under illumination by a plane wave is simulated by the loaded RWG*. The reasoning is based on Figure 8.10 and the load is, for the sake of generality, asymmetrical around the yz RWG symmetry plane. The total field simulated by the RWG necessarily satisfies the PEC condition at the RWG yz walls. For this condition to be verified, it is necessary that the total (incident and scattered) $E_{tot,y}$ and $E_{tot,z}$ components of the infinite structure simulated are 'antisymmetrical' around $x = -a/2$ and $x = +a/2$, which means here that $E_{tot,y}$ and $E_{tot,z}$ are of the form:

$$\begin{cases} E_{y/z}(x - a/2) = -E_{y/z}(-x - a/2) \\ E_{y/z}(x + a/2) = -E_{y/z}(-x + a/2) \end{cases} \tag{8.55}$$

Since the total field is the sum of incident and scattered fields and that the incident field is itself 'antisymmetrical' according to (8.55), we must only find which arrangement of loads in the simulated infinite structure will result in a scattered field satisfying (8.55). As depicted in the figure, we observe that this will be the case if the loads are placed so that there is a geometrical yz plane of symmetry at $x = -a/2$ and $x = +a/2$. In other words, the structure simulated is an infinite rectangular lattice, where the elements are repeated by *symmetry* (namely, not by *translation*).

Let us now consider the y dimension. Since the incident wave is polarized along y, we deduce that the infinite lattice arrangement whose scattered field will comply with the condition set by

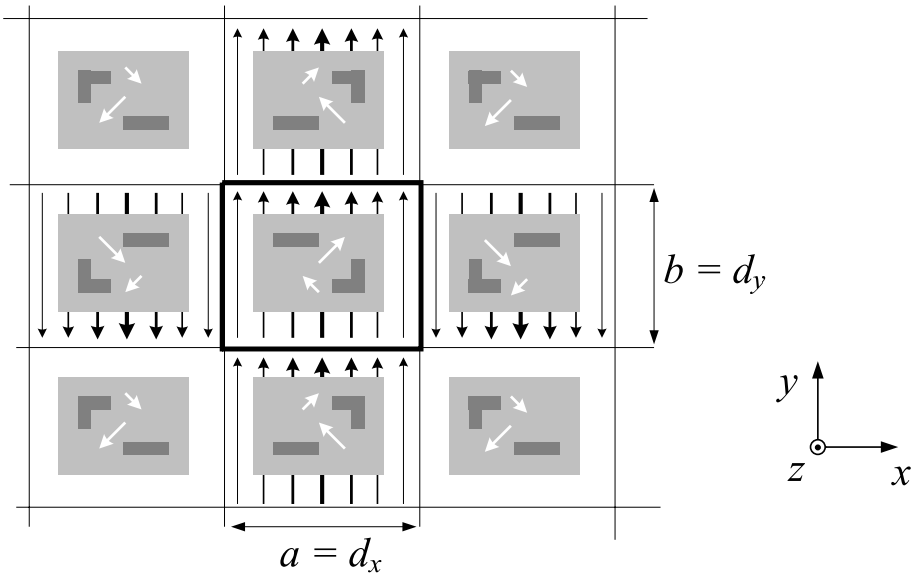

Figure 8.11: Illustration of the correspondence between the loaded RWG and the infinite arrangement, obtained by symmetry, that it simulates. White arrows represent currents in the elements whereas black ones represent the incident TE_{10} E field of the RWG.

the PEC walls is a repetition of the element by symmetry around the x axis, as illustrated in Figure 8.11. In conclusion, a load placed in the RWG and excited by the TE_{10} mode exactly models the incidence of two plane waves as described above on an infinite array of such loads, periodically repeated by symmetry around both array axes, as shown in Figure 8.11.

c. Loaded RWG for periodic array simulation

As mentioned in the introduction, our aim is to use the RWG to simulate an infinite array of the same radiating element, obtained by *translation* of this element. However, we showed that the RWG actually simulates an infinite array of elements, but where the infinite lattice is obtained by *symmetry* of the element with regard to the RWG lateral walls, such as depicted in Figure 8.11. As a result, the RWG-IAS can be employed to simulate the 'translation array' only in the particular case where both 'symmetry' and 'translation' arrangements are the same. Some inspection of Figure 8.11 shows that this is only possible if the two following conditions are met:

- The element must by symmetrical around both xz and yz symmetry planes of the RWG.
- The RWG height b must be a multiple of the array lattice half spacing in the y dimension d_y (E field direction).

$$b = \left(\frac{p}{2}\right) d_y \quad \text{with} \quad p \in \mathbb{N}^* \tag{8.56}$$

- The RWG width a must be related to the array lattice spacing in the x dimension d_x by:

$$a = \left(\frac{m}{2}\right) d_x \quad \text{with} \quad m \in \mathbb{N}^* \tag{8.57}$$

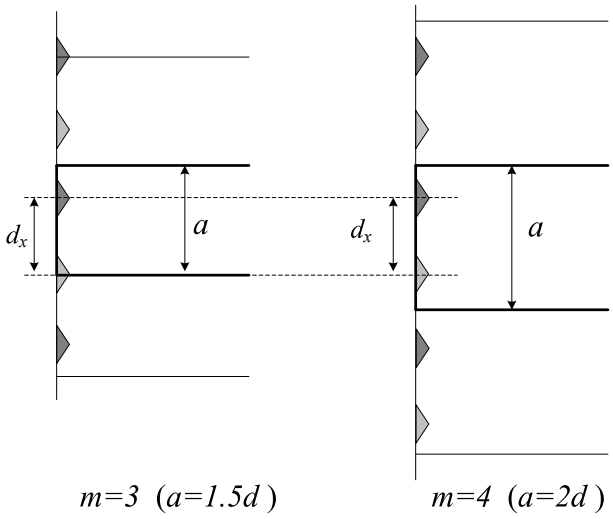

Figure 8.12: Simulation of the same RA with different RWG sizes.

where m is the number of 'half-elements' placed in the RWG in the x dimensions. Figure 8.12 illustrates how the same array (d_x is the same in both sketch) can be simulated by two different array lattices satisfying (8.57). Note that when m is odd, one element is cut in half (see the left hand side of Figure 8.12, where $m = 3$).

8.4.3. RWG-IAS and array grating lobes (GLs)

a. Developments

In this section, we link the above observations about the RWG-IAS to the issue of GLs addressed in Section 8.2.3. In order to do so, let us first recall the condition on the regular RA of lattice spacing d pointing in the direction θ so that no grating lobe occurs[1] [see (8.19)]:

$$\frac{d_x}{\lambda_0} < \frac{1}{1 + |\sin\theta|} \tag{8.58}$$

Now, we found the following relation between frequency and angle of incidence θ when using a RWG as RWG-IAS [written here as a function of m and d_x by substituting (8.57) in (8.53)]:

$$|\sin\theta| = \frac{\lambda_0}{m \cdot d_x} \tag{8.59}$$

Here, it should be noted that the formula for the RWG-IAS (8.59) consider an infinite array where all elements have the same reflection phase [namely with $\Delta\rho_m = 0$, see (8.22)], while the condition

[1] Remark: Here we recall that (8.58) is mathematically and physically equivalent to excluding higher order modes in a PBC-WG simulation. These superior modes should not be confused with the higher order modes of the RWG-IAS, which is the WG concerned here.

on the GL is valid without the need for this assumption; they are thus directly 'comparable'. In the case of a real RA, we have $\Delta\rho_m \neq 0$ but the developments hold true locally, thus for the element tested in the RWG-IAS. We can now introduce (8.59) in (8.58), which yield the new condition (8.60). This expression is written in terms of frequency rather than wavelength and the limit frequency where the first grating lobe appears is referred to as f_{GL}.

$$f < f_{GL} = \frac{c_0}{d_x}\frac{m-1}{m} \tag{8.60}$$

We will now introduce in this expression the cutoff frequency f_{10} of the RWG-IAS, which is first rewritten using (8.57) as:

$$f_{10} = \frac{c_0}{2a} = \frac{c_0}{m \cdot d_x} \tag{8.61}$$

which finally yields the condition on the frequency so that the array simulated by the RWG-IAS exhibits no grating lobe:

$$f < f_{GL} = (m-1)\, f_{10} \tag{8.62}$$

In principle, it can be envisioned to make a measurement in a multimodal region of the RWG by appropriate setup and mode cancelling. However, we will restrict our study to the simpler case where we wish to restrict our measurement to the fundamental TE_{10} band only (as will be done with the MEMS RA cells of Chapter 9). For RWGs with $a > 2b$, where a and b are the dimensions of the RWG, the second mode is the TE_{20} mode, so the frequency band where the only fundamental TE_{10} mode propagates is:

$$f_{10} < f < f_{20} = 2f_{10} \tag{8.63}$$

If we unify these two conditions, we find the band where the RWG-IAS can be employed in its fundamental mode to simulate an array without GL:

$$f_{10} < f < \min\left[2f_{10}\,,\ (m-1)\, f_{10}\right] \tag{8.64}$$

This formula and associated information are symbolically illustrated by the graph of the left of Figure 8.13. Now, let us study the band as a function of the parameter m, namely, the number of half-elements placed in the RWG-IAS [see (8.57)]:

- for half a cell or a single cell embedded in the RWG-IAS ($m = 1$ and $m = 2$, respectively), there is no frequency where the first mode of the RWG propagates for a RA without GL.
- for $m = 3$, which means that 1.5 cell is embedded in the RWG-IAS, the first grating lobe appears at the same frequency as the 2^{nd} mode of the RWG, so the whole $f_{10} < f < f_{20} = 2f_{10}$ band can be used.
- For $m > 3$, the limiting factor for the upper band of the frequency range measured is the appearance of the 2^{nd} mode of the RWG, so we always have in this case $f_{10} < f < f_{20} = 2f_{10}$.

b. Influence of the cell radiation pattern

As explained in Section 8.2.3, the element pattern might in practice cancel, or at least reduce to a low level, the amplitude of a GL close to $\theta = 90°$. If such a GL is 'tolerated', this means that the

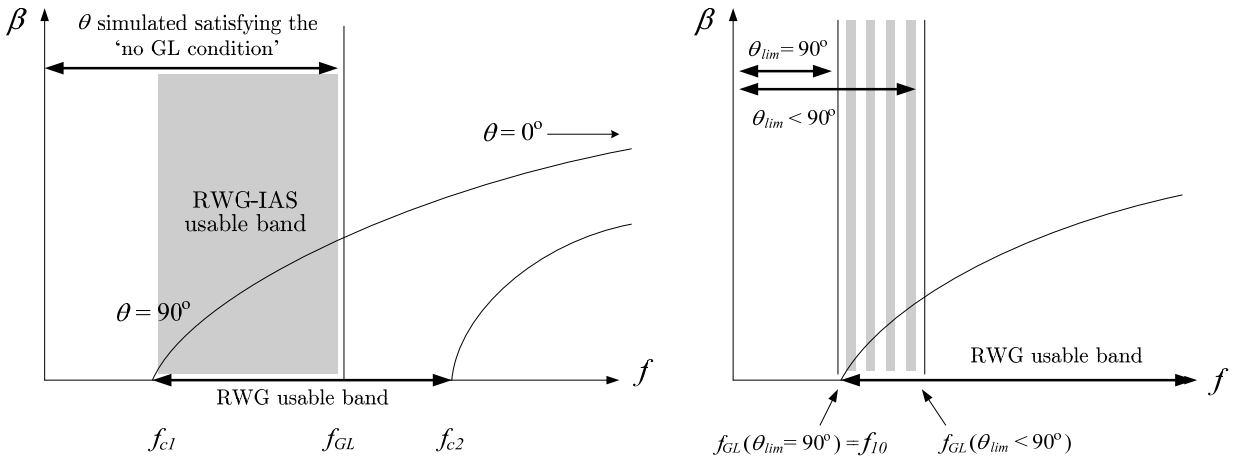

Figure 8.13: Illustration of the band usable for the RWG-IAS measurement of a RA cell with no GLs, limited by the RWG mode structure and the condition that no GL exists (Left: general case. Right: $m = 2$). f_{c1} and f_{c2} represent the two first cutoff frequency of the RWG.

upper limit frequency f_{GL} for the measurement is slightly larger than the value given by (8.60), as suggested in the right hand side of Figure 8.13, which corresponds to the case $m = 2$ (where $f_{GL} = f_{10}$). We see that in this case, there is a small band just above f_{10} where the measurement of the cell can be taken. However, this band corresponds to very large incidence angles, where the reflection coefficient is strongly dependent on θ. In other words, the reflection coefficient obtained here is a bad approximation of the reflection close to normal incidence, which can thus not be measured with reasonable accuracy with $m = 2$. As a result, we can conclude that even if the GL condition is slightly relaxed, it is still necessary to choose $m > 2$ in the great majority of practical RA designs. In this case, a measurement for incidence angles down to $\theta = 30°$ represents a good approximation of the reflection for normal incidence (see Section 8.6.2).

8.4.4. Practical RWG-IAS summary and conclusions

A conventional RWG with $a > 2b$ operated in its fundamental TE_{10} mode can be used to simulate the reflection of an H-polarized plane wave of incidence θ on an infinite array of symmetrical elements and constant lattice spacing d according to [substitution of (8.57) in (8.53)]:

$$|\sin\theta| = \frac{\lambda_0}{m \cdot d} = \frac{c_0}{m \cdot d \cdot f} \tag{8.65}$$

where the width of the RWG a is linked to d by:

$$a = \left(\frac{m}{2}\right) d \quad \text{with } m \in \mathbb{N}^* \tag{8.66}$$

In order to simulate an infinite array without GL, it is necessary to choose $m \geq 3$. This means, for a RWG-IAS with $a > 2b$, that the band available for monomodal measurement corresponding

to an array free of GL is:

$$f_{10} < f < 2f_{10} \quad \text{with} \quad f_{10} = \frac{c_0}{m \cdot d} \tag{8.67}$$

So, for a given array lattice spacing d, the only free parameter here is m, which is twice the number of array elements placed in the RWG-IAS. We showed that m must necessarily be equal to or larger than 3 for the measurement of an array without grating lobe and that the choice of m determines the relation between frequency and angle θ. However, the maximum and minimum incidence θ angle that can be simulated do not depend on the choice of m and are $\theta_{\max} = \theta(f_{10}) = 90°$ and $\theta_{\min} = \theta(f_{20}) = 30°$ (a multimodal approach would be necessary in order to simulate angles $\theta < 30°$). This is due to the fact that when m is increased for a given array lattice spacing d, the limit frequency f_{20} reduces linearly with m, which exactly compensates for the m factor in (8.65). Finally, let us note that more than one incidence angle can be tested at the same frequency if several RWG-IASs, corresponding to different m values, are built. Nevertheless, even in this case, the frequency and incidence angle for characterization cannot be independently chosen, since $m \in \mathbb{N}^*$.

8.5. Summary of RA cell simulations/measurements possibilities

Table 8.2 summarizes the possibilities and necessary assumptions to characterize, either by simulation or measurement, a linearly polarized RA cell under illumination by an H-polarized wave with different incidence angles. In all cases, the assumption of an infinite array of the same element is required.

In conclusion, the choice of a simulation setup depends on the incidence angle range, on whether the element is symmetrical or not, and on the simulator capabilities (e.g. availability of PBCs). It is of course possible to do some approximation; for instance, an element with a limited asymmetry could be simulated with the PECPMC-WG and measured with a RWG-IAS with a limited error. In such a case, this error should be quantitatively assessed by a comparison between PECPMC-WG and PBC-WG simulations.

Table 8.2: Summary of RA cell simulations/measurements possibilities.

	Type of WG (Boundary conditions)	WG mode	Condition on element	Availability
$\theta = 0$	PBC-WG with $\theta = 0$	TEM	-	Simul. only (requires PBC)
	PECPMC-WG	TEM	Double symmetry	Simul. only (requires PMC)
$\theta \neq 0$	PBC-WG with $\theta \neq 0$	Floquet's modes	-	Simul. only (requires PBC)
	RWG-IAS	TE_{10}	Double symmetry	Simul. + Measurement

8.6. Validations

8.6.1. Test structures description

In order to validate the previous developments and test measurements and simulation accuracy, four test RA cells were designed and fabricated. The corresponding layouts, printed on a lossy 0.1 mm-thick epoxy substrate ($\varepsilon_r = 4.4$, $\tan\delta = 0.01 - 0.02$), are shown in Figure 8.14(a). In order to have a thick substrate with reasonably low losses, the PCB is then stuck to a 3 mm-thick foam ($\varepsilon_r = 1.07$, $\tan\delta \approx 0.001$) and the whole structure is backed by a ground plane. All elements are designed to resonate within X-band under TE incidence with $\mathbf{E}_{inc} = E_{inc,y}\mathbf{e}_y$ [the y axis is vertical in Figure 8.14(a)]. Cell D is a simple rectangular patch, while A, B and C can be seen as 2 pairs of dipoles, or a pair of rings split in their E-plane symmetry axis. The array lattice spacing is 11.43 mm and 10.16 mm in x and y directions, respectively. The dimensions of these demonstrators were chosen here so that the measurements could be carried out using an existing usual X-band RWG. In practice, it is clear that it is the array lattice that is set by the array requirement, and a RWG complying with that lattice must be built especially for this purpose.

As explained in Section 8.4.3, the exact measurement of such a cell using the RWG-IAS in a case where no grating lobe is radiated requires that at least 1.5 cells are placed in the RWG. Here we chose to place 2 cells in the measurement setup ($m = 4$), which sets which pairs f , θ will be characterized. The left of Figure 8.14(b) shows the four fabricated pairs of cells. The right of the figure shows one pair of cells in the RWG section, backed by a RWG short accounting for the array ground plane. It is noticeable that this setup maintains the RWG continuity so that no leakage occurs.

With the conventional X-band R100 RWG used here (10.16×22.86 mm), we have $f_{10} =$ 6.56 GHz, $f_{20} = 13.12$ GHz and $f_{01} = 14.76$ GHz. Thus the theoretical fundamental mode band is 6.56 GHz -13.12 GHz[1]. It can be verified with (8.65) and (8.58) that we have indeed no GLs for the angle and frequency of this RWG-IAS measurement.

8.6.2. Simulated performances (PBC-WG)

Here, the aim was not to design high-performance RA elements but to demonstrate the theoretical developments and test the simulation and measurements accuracy. Thus, we do not provide the phase diagram or other consideration linked with the design of a RA using these elements. Nevertheless, we first show the simulated reflection of the cells in a PBC-WG, which is the determining parameter of the unit cell for the design of the RA. In the latest version of HFSS available at the time of this work (HFSSv10), only the magnitude of the reflection coefficient for such a PBC-WG was provided by the software. Therefore, a dedicated post-processing of the fields computed by HFSS was programmed to deduce the reflection phase.

[1]Note that the recommended band for this RWG is 8.2 GHz -12.15 GHz (limited by the dispersion and the proximity to higher modes, respectively). However, as will be verified below, here we can use the full theoretical BW since the RWG is not used for the transmission of a signal.

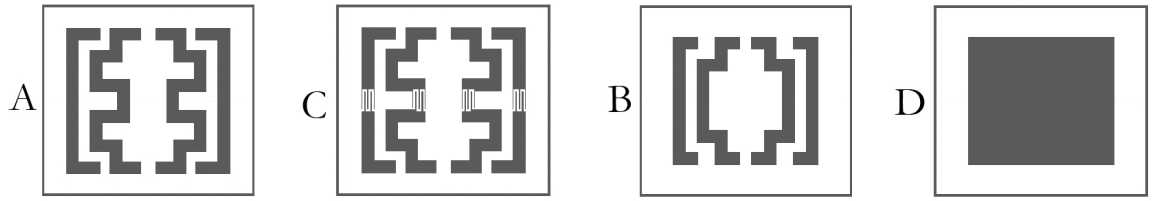

(a) layout of the cells.

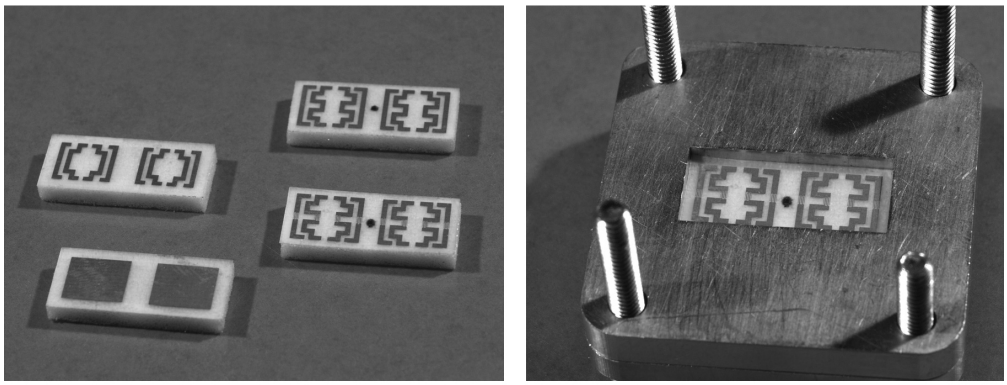

(b) Left: picture of the fabricated RA cells on the additional foam substrate. Right: a cell placed in a RWG shortcut for measurement (the RWG shortcut simulates the RA ground plane).

Figure 8.14: Passive RA cell measurement.

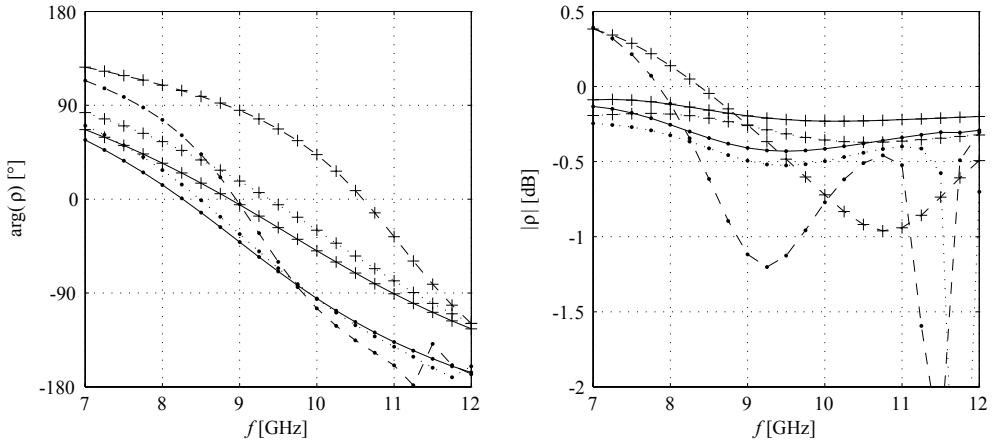

Figure 8.15: Computed reflection coefficients for cells C (•) and D (+) of Figure 8.14(a) for different incidence angles 0°(—), 30°(· · ·) and 60°(– –).

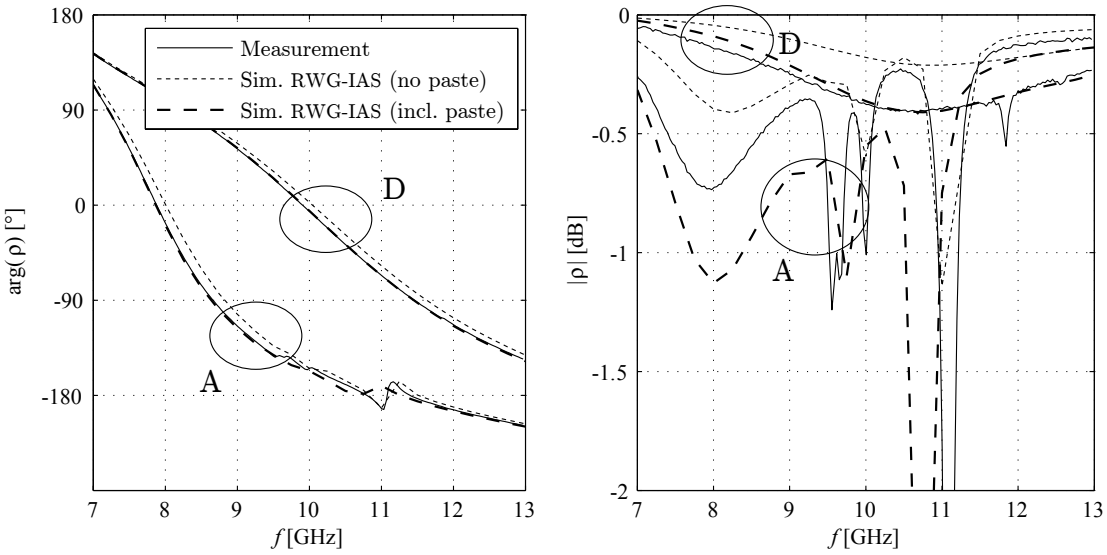

Figure 8.16: Measured and simulated reflection phase of devices A and D from Figure 8.14(a).

The results are shown in Figure 8.15 for different incidence angle (0°, 30°, and 60°). It is observed that, as expected, the reflection phase becomes highly dependent on this angle for incidences far from normal (in other words, the difference between the phases for 30° and 60° is much larger than between 0° and 30°). Concerning the magnitude, we observe that unphysical results, namely, $|\rho| > 0$ dB, are obtained under the 60° incidence for all four devices (although only the results for cells C and D are shown in the figure for clarity purpose), while this never occurs for 0° and 30°. This shows a limitation of HFSSv10 to compute the losses with PBC conditions for large incidence angles.

8.6.3. Experimental validation (RWG-IAS, simulation vs measurement)

Figure 8.16 shows the phase and amplitude measured in the RWG-IAS for 2 of the 4 fabricated RA cells test devices, namely devices A and D from Figure 8.14(a). These results are compared to simulated ones. For a first direct comparison, we also simulate the 2-cells device in the RWG rather than in the PBC-WG, while making use of a symmetry plane for computation time saving.

First, we plot the result simulated with the materials definitions provided by the manufacturer (for the PCB substrate, we used the maximum value in the range provided, namely, $\tan\delta \approx 0.02$). These results are referred to as 'no paste' in the legend of the figure. There is a good agreement between the phase of measured and simulated results, except for a slight shift. Concerning the magnitude of the reflection coefficient, it is observed that the losses are underestimated by the simulation but that the general measured behavior of the losses is well accounted for. This discrepancy might be due to variation of the material properties but is rather thought to be the due to the epoxy paste used to glue the PCB substrate on the foam. The curves denoted as 'incl. paste' in the graphs corresponds to the same simulation definition, except for the insertion of a thin layer

meant to account for the epoxy paste ($t = 0.025$ mm, $\varepsilon_r = 4.4$, $\tan\delta = 0.1$). The thickness of the layer is not known and has been fitted here to match the reflection phase. We observe that the new curves almost exactly match measured results, even though the discrepancy that was previously observed is not constant with frequency. Consequently, we can assume that the inclusion of the paste as done here in the simulation indeed accounts well for the real fabricated device.

Finally, it should be noted here that the agreement between curves does not degrade when approaching the cutoff frequency $f_{10} = 6.56$ GHz, which shows that the large dispersion of the TE_{10} mode in the lowest part of the band does not affect the accuracy of the measurement and simulation. The same remark applies when approaching the cutoff frequency of the first superior mode ($f_{20} = 13.12$ GHz).

8.6.4. Verification of RWG-IAS theory

a. Comparison with PBC-WG results (and PECPMC-WG)

The previous section showed a direct comparison between simulation and measurements in the RWG. However, the determining reflection coefficient for the design of a RA is the one corresponding to the PBC-WG. Thus, we must link PBC-WG simulations and RWG-IAS results according to the developments of Section 8.2 to validate the theory as well as the PBC-WG simulation setup and post-processing.

Figure 8.17 first shows measured and simulated results in the RWG-IAS for cell D (these are the same curves as in Figure 8.16, where the simulation includes the epoxy paste definition). The previous developments showed that these RWG-IAS results are exactly equivalent to PBC-WG ones, but only for the particular incidence angles θ given by (8.65). Here, we have $m = 4$ and $d = 11.43$ mm and these angles are $\theta\,(7\text{ GHz}) = 69.9°$, $\theta\,(8\text{ GHz}) = 55.1°$, and so on until $\theta\,(13\text{ GHz}) = 30.3°$, as shown on the top of the graphs of Figure 8.17. So, the simulations with the PBC-WG were carried out for each of these pairs f , θ. The corresponding results can now be directly compared to the RWG results, as done in Figure 8.17. It is observed that a very good agreement is obtain for the phase, while the discrepancy in terms of magnitude is also quite small. Similar results are found for the three other cells, as shown in Figure 8.18 to Figure 8.20. In all cases, it is observed that a better agreement is obtained for the phase than for the magnitude.

Finally, we also plotted on the same graphs the reflection phase for normal incidence, namely using the PECPMC-WG, which was shown to be in this case exactly equivalent to the PBC-WG with 0^o phase shift between boundaries. As expected, the difference with the other curves is rather small in the highest part of the band, since it corresponds to small incidence angles. However, the phase simulated for normal incidence becomes very different from the one obtained with the RWG-IAS for lower frequencies, where a discrepancy as high as 90^o is observed for the 4 devices. Since these results are computed for a RWG and a PBC-WG of same width a, the difference can only be attributed to the angular dependence of the reflection coefficient. This means that, in contrast with the statement expressed in [95], the RWG measurement cannot *in general* be considered as fairly good approximation of the case of normal incidence.

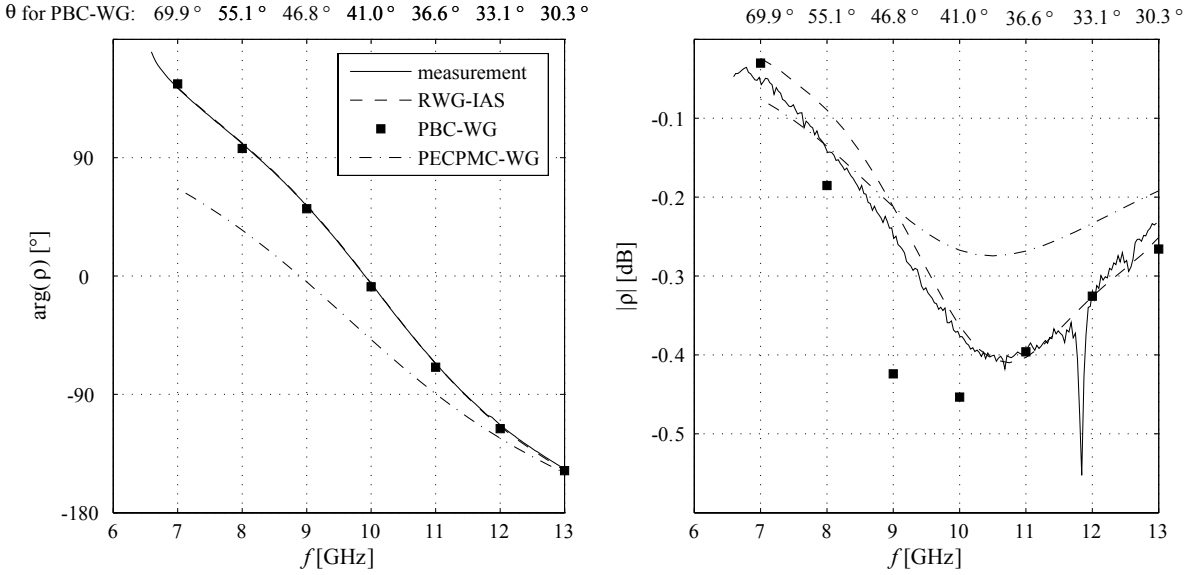

Figure 8.17: Measured and simulated reflection coefficient (cell D).

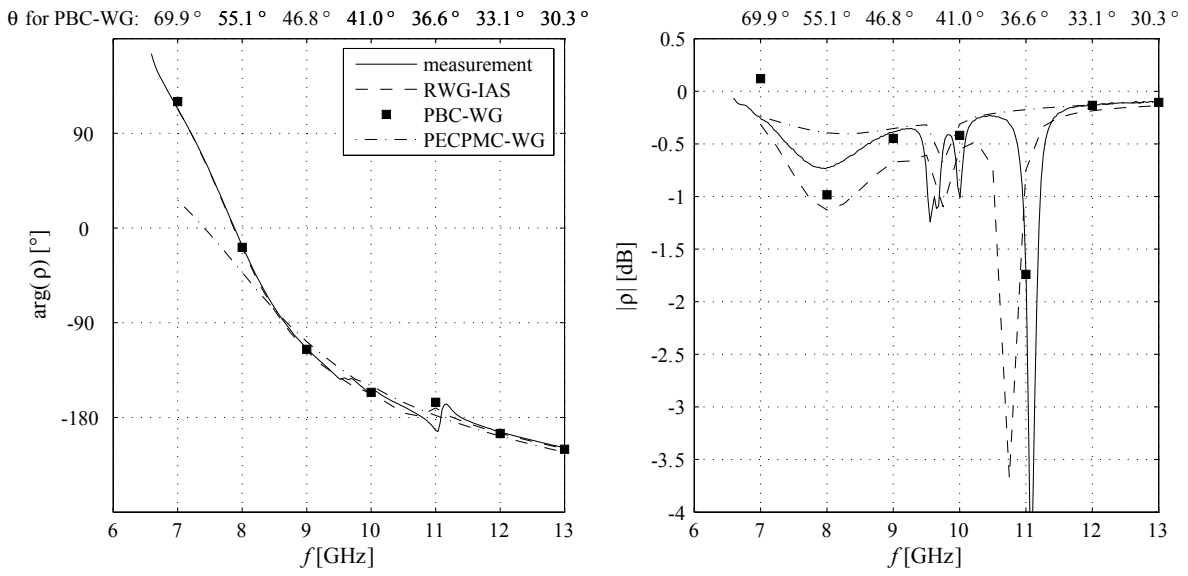

Figure 8.18: Measured and simulated reflection coefficient (cell A).

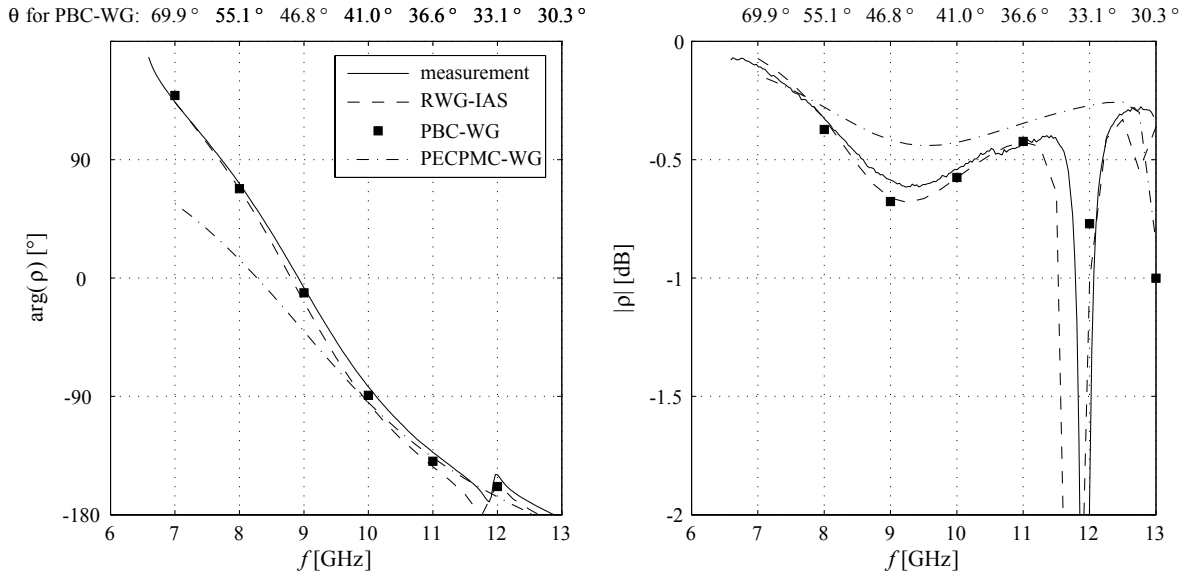

Figure 8.19: Measured and simulated reflection coefficient (cell B).

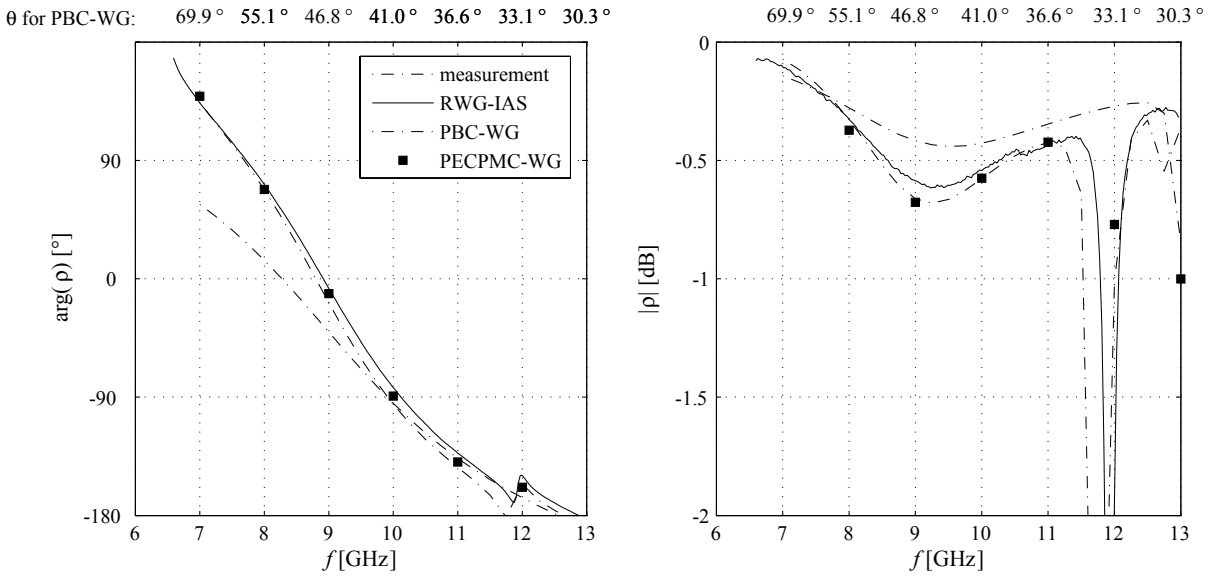

Figure 8.20: Measured and simulated reflection coefficient (cell C).

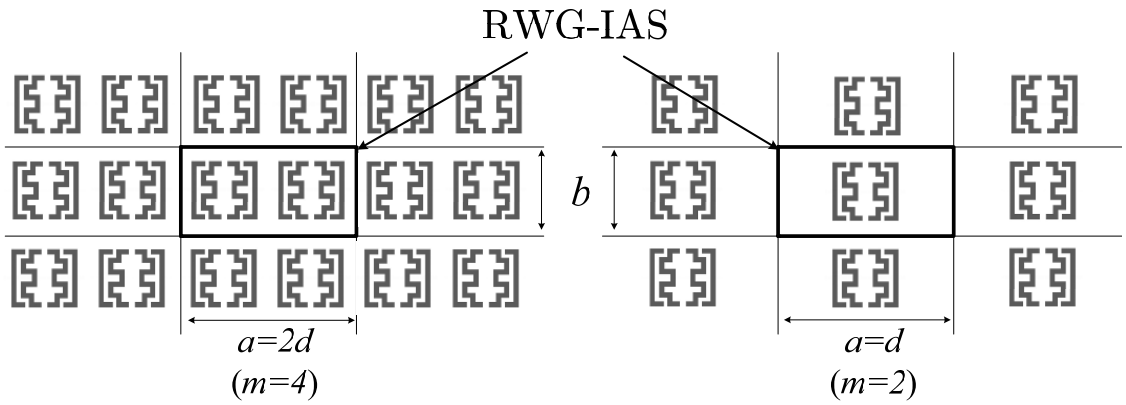

Figure 8.21: RWG-IAS setup with 2 (left) or 1 (right) embedded RA unit cells, and corresponding infinite arrays simulated.

b. Comparison with RWG-IAS results for a single embedded cell

In [100], for instance, the same X-band RWG as used for the measurement presented in the previous section is employed, but with only one cell embedded in the RWG ($m = 2$). This situation is sketched in the right of Figure 8.21 using our element A, together with the corresponding infinite array that the RWG-IAS simulates. In the aforementioned reference, the measurement is done at $f = 9.8$ GHz and, as rightly pointed out in [100], this corresponds to an incidence angle of $\theta\,(f = 9.8\text{ GHz}) = 42°$ using (8.65). However, as demonstrated above, the corresponding infinite array that the RWG-IAS simulates necessarily exhibits GLs at the frequency and angle of measurement. This angle can be calculated using (8.13):

$$\sin\theta_{r,\pm1} = \frac{\lambda_0}{d}\left(\pm\frac{1}{m} \pm 1\right) \tag{8.68}$$

and we find that in the case corresponding to a single cell embedded in the RWG-IAS ($m = 2$, or $a = d$), the first GL is opposite to the main one so it is here located at the angle $-42°$. As a result, although the measurement done in [100] is perfectly valid, it corresponds to an array which exhibits a GL. It is noticeable that although we considered here isotropic elements for the determination of the GL location, the element pattern will in this case not cancel or limit this first GL level. Indeed, RA elements generally radiate broadbeam patterns and the gain of the antenna for such an angle is still close to its azimuthal maximum. Anyhow, the element concerned here exhibits symmetrical patterns around the lattice axes (this is required for scanning both negative and positive angles with regard to azimuth). Therefore, in the case $m = 2$—where the first GL location is simply opposite to the main radiated beam, the level of the GL will be exactly that of the main lobe.

In order to determine if the measurement with $m = 2$ is useful for the design of the real array (which should not exhibit GLs), the results thereby obtained should be compared with the case where the lattice spacing is small enough so that no GL occurs. These two situations, in the cases $m = 2$ and $m = 4$, are depicted in Figure 8.21. The difference is small if the coupling

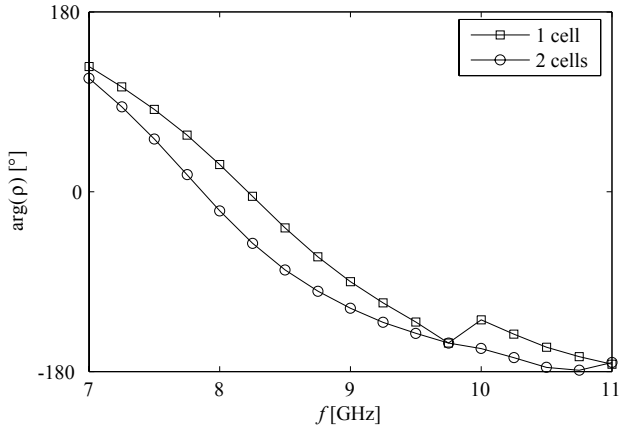

Figure 8.22: Comparison of the simulated reflection phase for 1 and 2 cells embedded in the same RWG-IAS and as depicted in Figure 8.21.

between elements in the actual array is low, and if extending the GP around the element does not influence much the reflection phase. This was quantitatively tested here by simulation in the case of structure A of Figure 8.14(a) and the results for the reflection phase are plotted in Figure 8.22. Although the general behavior of both setups is similar, there is a substantial difference in the phase obtained (the difference is larger than 50^o for the majority of frequencies simulated), which demonstrates the necessity of choosing the size of the RWG to be used as RWG-IAS according to (8.57).

8.7. Conclusions

In this chapter, we first explained what are the multiple requirements for reconfigurable RA cells, based on simple considerations using RA theory. Then, we characterized in detail the different measurement and simulation methods for RA cells, in the particular case of interest for the following MEMS RA cell designs (although most of these considerations are valid or could be extended to other cases as well). These developments were validated by measurements and comparison between the different simulation methods, which also allowed assessing the precision of these characterization techniques. This chapter thus paved the way for the design of the MEMS cells of Chapter 9 both from a design point of view (determination of the requirements) and characterization (analysis of the different simulation and measurements approaches).

9. MEMS Reflectarray Cells

9.1. Introduction

We addressed in Chapter 8 the principal prerequisites for the design of reconfigurable RA cells; namely, modeling and measurements issues, as well as the description of the various requirements for such cells. In addition, some introduction on the need for reconfigurable RA cells and corresponding state-of-the-art was made and will thus not be repeated here. As a result, this chapter focuses on the design of a particular MEMS-reconfigurable RA cell, making extensive use of both modeling and requirement issues previously exposed.

It was decided here to design MEMS RA cells operating in X-band and linearly polarized, as needed, for instance, in synthetic aperture radar (SAR) applications [89]. Concerning the MEMS technology platform, it was possible —for the first time in this thesis— to choose among different fabrication processes made available by the AMICOM EU network of Excellence (see Chapter 1, [11]). In this context, it was decided to design the RA cell based on the 'Al-Quartz VTT' platform described in Appendix A, for the two following main reasons; first, this process is based on quartz wafers, which, as shown in Chapter 3, exhibit better loss performances than Hi-Res silicon wafers. Second, this process comprises a highly resistive layer dedicated to the patterning of biasing lines which do not degrade microwave performances.

9.2. Description

9.2.1. General element shape

The basic topology of the RA element studied here consists of single-layer ring elements backed by a ground plane, such as depicted in Figure 9.1. The element is to operate in single, linear polarization with E field along the y axis of Figure 9.1(a) and will be reconfigurable to achieve scanning in its H-plane (xz plane). In this case, if not centered, the feed of the RA should be placed in the H-plane of the array to minimize the cross-polarization and reflection phase dependence on the relative position of the element in the array. In other words, this means that the incident field on the array element is TE polarized with a wave vector $\boldsymbol{k}$ in the H-plane of the element[1].

RA cell ring elements have been studied in [108] and [109] in the case of fixed-beam RA. Such elements exhibit smaller resonant size than rectangular patches which allows the reduction

[1]This is exact only for the elements that are in the plane perpendicular to the array surface and that contains the feed. For other elements in the array, $\boldsymbol{k}$ has a small non-zero component outside their H-plane.

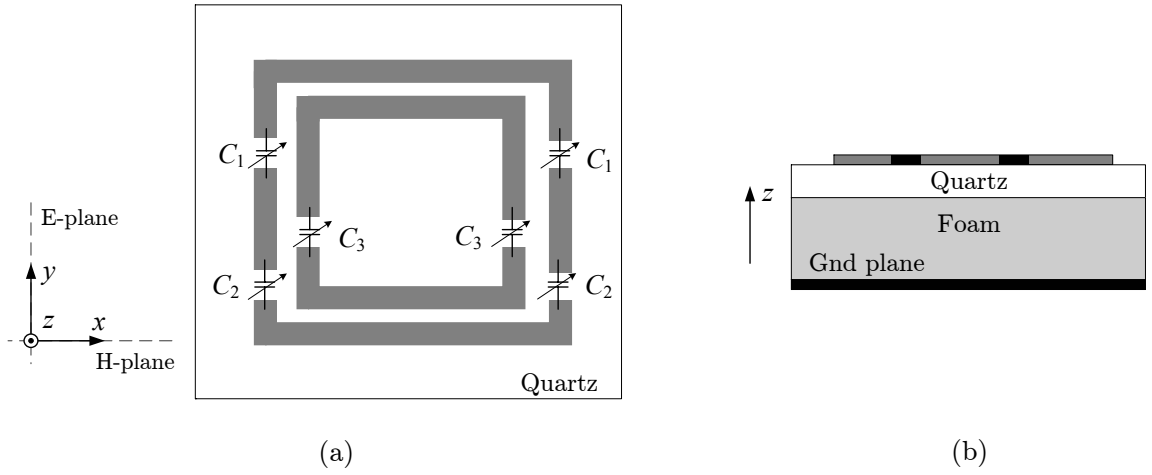

Figure 9.1: Schematic description of a double ring RA cell loaded with variable capacitances. (a) top view. (b) side view.

of the phase quantization error in a RA. In addition, [109] states that this results in a reduced dependence on the incidence angle. Finally, although this work only concerns single linear polarized elements, it is noticeable that ring elements are good candidates for an extension to dual frequency operation [108], as well as circular or dual-linear polarization.

It is well known that the substrate permittivity and thickness greatly impact on the BW and range of the reflection coefficient of printed RA cells [87]. Since we will implement our device in MEMS technology, the choice of the substrate characteristic is extremely limited. In order to overcome this limitation, the fabricated device is to be placed on a foam layer mimicking air, which is itself backed by the ground plane, as depicted in Figure 9.1(b).

9.2.2. Reconfigurability approach

In order to achieve reconfigurability, the rings are loaded with variable series MEMS capacitors, as shown in Figure 9.1. Indeed, the resonance of such rings loaded with capacitors shifts towards lower frequencies with increasing capacitances values, thus enabling to dynamically reconfigure the reflection phase at a given frequency by control of the MEMS.

As suggested by Figure 9.1(a), the capacitors are placed by pairs so that the symmetry of the element around the E-plane is preserved. This is useful to reduce the cross-polarization to a minimum (the cross-polarization is zero in the E-plane, for a normal incidence). This is at the cost of doubling the number of loading elements. Nevertheless, the whole RA cell is to be fabricated in a monolithic process and the number of MEMS devices is not an issue in the case of a reliable process. In contrast, the cell is not symmetrical around the H-plane. Indeed, this would mean that the number of MEMS would again have to be doubled, which would be problematic here because of the limited space to accommodate the MEMS in the rings in the y dimension of the cell (this problem does not occur when doubling the elements around the E-plane). Finally, let

us remark that although the locations of the MEMS loading elements present some asymmetry, the general shape of the radiating element does not. Thus, the cross-polarization in the H-plane should remain small as well. These assumptions will be quantitatively assessed in the case of the designed structure.

A reflectarray cell loaded with a single pair of MEMS is proposed in [98]. In this case, the control of the MEMS capacitance, and thus of the reflection phase, is of *analog* type. The approach proposed here is different in the sense that N pairs of *digital*-type MEMS are implemented, so that 2^N discrete states can be operated [$N = 3$ in Figure 9.1(a)]. There are different advantages to this approach with regard to the analog one. First, let us note that the MEMS used here will be operated as switches, namely, with an Up state corresponding to a zero voltage ($V_{Up} = 0$ V control voltage, and a Down state corresponding to a pulled-in MEMS membrane ($V_{Down} > V_{Pull-in}$). Thus, the two states of the MEMS are mechanically stable and insensitive to control voltage imprecision, since this voltage is zero in the Up state and that a variation of voltage in the Down state will only induce a negligible error in the capacitance value, as the MEMS membrane is in this case already pulled-in. This is especially important for the design of RA cell, for the following reason. In fixed-beam reflectarrays, the requirements on the sensitivity and range are contradictory, since a lower sensitivity is associated with a smaller range (e.g.: rectangular patch [87]). This problem also occurs for analogically-controlled reconfigurable RA (e.g. [94, 98]) and particularly in the case of an analog MEMS control. First, let us note that a single-gap MEMS analog capacitance ratio is only 1.5 and that the corresponding $V(C)$ characteristic becomes highly non-linear above a capacitance ratio of about 1.3 [7] (larger ratios can be obtained using more complex fabrication processes [98], but the general limitation remains the same). In order that this small capacitance ratio leads to a large range of reflection phase, it is necessary to design an element very sensitive to some variation of MEMS capacitance. However, such a design will necessarily be very sensitive to the precision of the control voltage, as well as fabrication tolerances and temperature drift. This problem is solved using a multi-bit digital control as proposed here, since, as explained above, the capacitances are in this case insensitive to the DC voltage precision. Intuitively, this improvement consists in preserving a high sensitivity as defined by (8.1)—hence a large range, while *decoupling the precision of the state* p *operated from the precision or noise of the control voltage and fabrication variability.*

From a biasing circuit point of view, the digital case requires a single voltage V_{Down} and some DC switching matrices, whereas the analog type requires the supply of a variable and precise voltage, and this independently for each cell in the RA. Finally, a very interesting feature of the digital approach is linked with the functioning of the loaded ring resonator. It can be observed that there is a limit lower (resp. larger) capacitance value for which it acts as an open-circuit (resp. short-circuit). Thus, if the two discrete values of the digital capacitance are chosen so that they are beyond these limit values, the design can be made insensitive to discrepancies in the fabricated MEMS capacitance values, which is a major cause for concern in the design of MEMS microwave devices. It is however clear that the digital approach does not allow a continuous control of the phase. Nevertheless, a sufficiently good phase quantization can be achieved with a limited number of MEMS (here $N = 5$ bits and thus there are 32 states available, hence an average $360°/32 < 12°$ step between successive available phases).

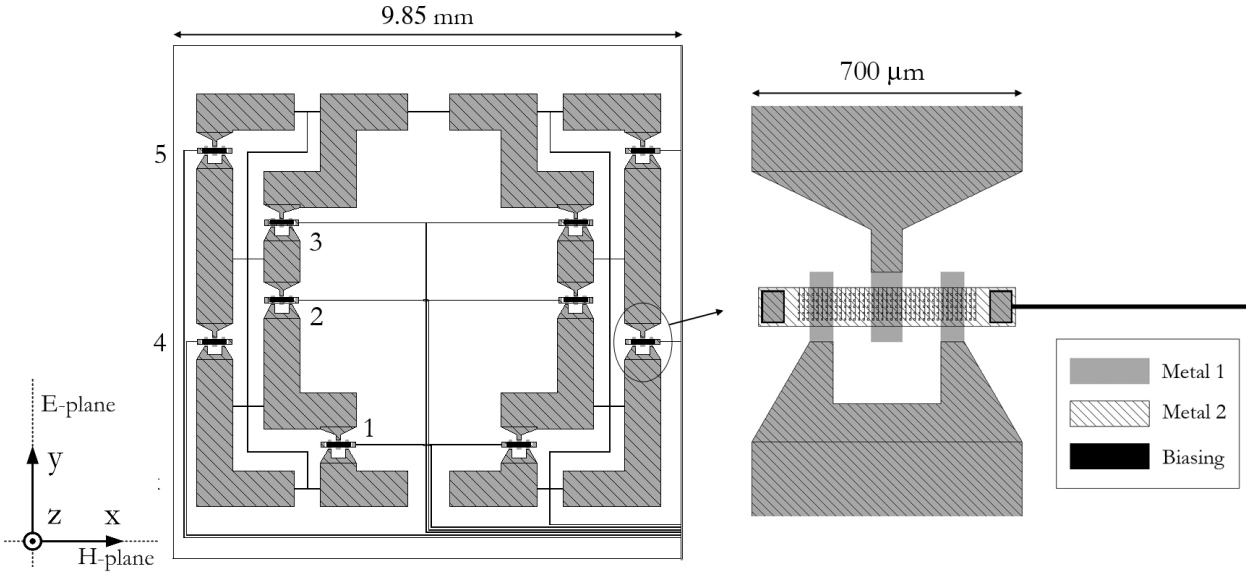

Figure 9.2: Reflectarray cell layout with numbering of the MEMS bits (dielectric and sacrificial layers are not shown here).

9.2.3. Implementation

As explained in the introduction, we base our design on an existing MEMS micromachining process, described in detail in [110] and in the Appendix as the 'Al/quartz VTT' process. Deposited on fused silica quartz wafers, the first metal layer consists of 500 nm-thick gold. The second metal layer, used for the free-standing parts or to cover the first metal, is 1500 nm-thick aluminum. Finally, the high-resistivity bias lines are patterned out of polysilicon.

The left hand side of Figure 9.2 shows the layout of a designed RA cell based on this technology, where only metal layers and biasing lines are shown. The 5 pairs of MEMS, to achieve 32 phase states, are clearly seen in the figure. It is observed that the radiating elements are not properly speaking closed loops; concerning the center element (the one loaded by MEMS 1, 2, and 3 in the figure), it is actually similar to a closed loop since the openings at the top and bottom of the ring are located in current nulls, as a result of the incident E field polarization. The openings were made here to allow an easier layout for the biasing lines. The second element could be seen as a loop with larger openings, or even like two dipoles. Here again, it was observed that the openings have a small impact on the reflection phase when compared to a closed loop.

The MEMS structure can be seen in the right hand side of Figure 9.2. The membrane of the MEMS, made out of 'metal 2', is connected to the bias line and the capacitance between the conductors on each side of the MEMS can be controlled by the actuation of the membrane. In order to have an attraction force on the membrane when a voltage is applied to the bias line, all radiating element parts (namely all metal parts apart from the bridge membrane) are connected to DC ground bias lines.

9.3. Modeling and design

9.3.1. RA cell full-wave simulation

The modeling and optimization of the RA cell requires a very large number of intensive simulations. Indeed, there are here 32 different MEMS states to be simulated for several frequency points and incidence angles. In addition, in a process of tests and optimization, such simulations must be repeated for each variation in the design, which is practically prohibitive. In this context, this section describes the major steps taken to dramatically reduce the computation time of the RA cell using Ansoft HFSS, which allowed to efficiently optimize the presented device.

a. Use of PEC and PMC boundaries

As explained in Section 8.3, the only strictly valid way to simulate an asymmetric RA cell in an infinite array obtained by translation of the cell is to use the periodic boundary conditions waveguide (PBC-WG). With this method, we can compute the results for any incidence angle and frequency. However, the approach employed here for the design consists in optimizing the element under normal incidence and subsequently characterizing it under oblique incidence. In this case, it is possible to reduce the computation time by replacing the PBCs by simple PEC and PMC boundaries (PECPMC-WG, see Section 8.3.4). Since the element is symmetrical around its E-plane (Fig. 9.2), the PBCs boundaries parallel to this plane can be replaced by PMC walls in an exact way for normal incidence characterization. In contrast, the element exhibits a small asymmetry around its H-plane. Thus, replacing the PBC boundaries parallel to the H-plane by PEC boundaries amounts to neglecting the small H-plane asymmetry.

The impact of this approximation on the results was assessed by comparing the results obtained with the PBC-WG under normal incidence and with the PECPMC-WG, as shown in Figure 9.3 for 4 different MEMS states of the cell shown in Figure 9.2 (two of the 4 states tested here are the 'most asymmetrical' ones). The agreement is good and we can thus conclude that the PBCs can be replaced by PEC and PMC boundaries for the characterization of our element under normal incidence. In terms of computation time, the advantage is twofold. First, PEC and PMC boundaries are treated much more efficiently than PBCs in the software used here, namely, Ansoft HFSS. Second, since the cell is symmetrical around its E-plane, the structure simulated in the PECPMC-WG can be cut in half to reduce the computation effort even further. Finally, let us recall that PBC-WG simulations can be performed for all states once the optimization is completed, in order to characterize the element without the aforementioned symmetry assumption and under oblique incidence as well.

b. Lumped MEMS modeling in full-wave simulation

Including the detailed MEMS geometry in the full-wave cell simulations leads to very intensive simulations (there are 5 MEMS in the PEC/PMC boundaries simulation and 10 in the PBCs simulations). However, the small electrical size of the MEMS makes it possible to model these

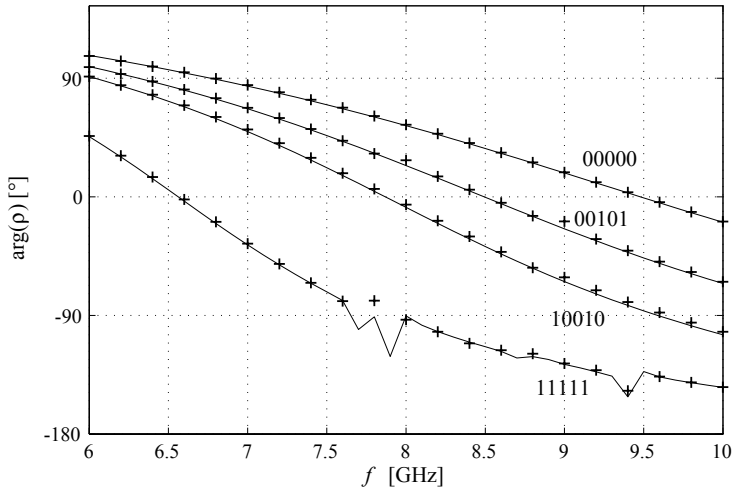

Figure 9.3: Comparison of the reflection phase of the asymmetric RA cell with PBCs under normal incidence (+) and with PEC/PMC boundaries (—), $t_{foam} = 3\,\text{mm}$.

by lumped circuits. Since it is possible to include lumped elements in most full-wave simulators, (in HFSS, this can be done using the so-called *RLC* boundaries), the simulation time can be highly reduced if the MEMS geometries are replaced by accurate but simple lumped models. The modeling of the MEMS used here by such lumped elements was described in detail in the 'building blocks' Section 3.8 and will thus not be repeated here. Let us however recall that it is modeled by a single capacitor in the Up state, and by a series *RLC* network in the Down state.

Validation of this simplification process was made in Chapter 3 by introducing the equivalent lumped models in two-port simulations using *RLC* boundaries, and comparing with the simulations of the detailed MEMS geometry. Here, we make the same comparison but for the complete structure of interest, namely, the RA cell. In the simulation setup of Figure 9.4(a), the MEMS geometry is detailed whereas in Figure 9.4(b), it has been replaced by 3 *RLC* boundaries connected in series, since a single *RLC* boundary in HFSS can only handle *RLC* circuits in *parallel*. A routine was programmed to set the right numerical values to the various *RLC* boundaries as a function of the state being computed.

The computed reflection phases are shown in Figure 9.5 (for clarity, only 7 states are shown here but a similar behavior is found for all 32 states). We observe that the simulation including the *RLC* models developed accounts very well for the phase response of the 'exact' structure. The reflection loss is plotted in Figure 9.5 for the 2 extreme states. We observe a rather good agreement, except for the location of the dips in the 11111 state curve, which correspond to small ripples in the phase plot. In conclusion, the MEMS can be replaced by a carefully developed lumped model to characterize and optimize the phase very quickly and accurately. More attention must be paid with regard to the interpretation of the loss obtained using the lumped model, although this approach still provides some good assessment of the losses. Nevertheless, a more accurate but intensive computation of the losses, obtained by a complete definition of the MEMS geometry, can be carried out once the design is completed.

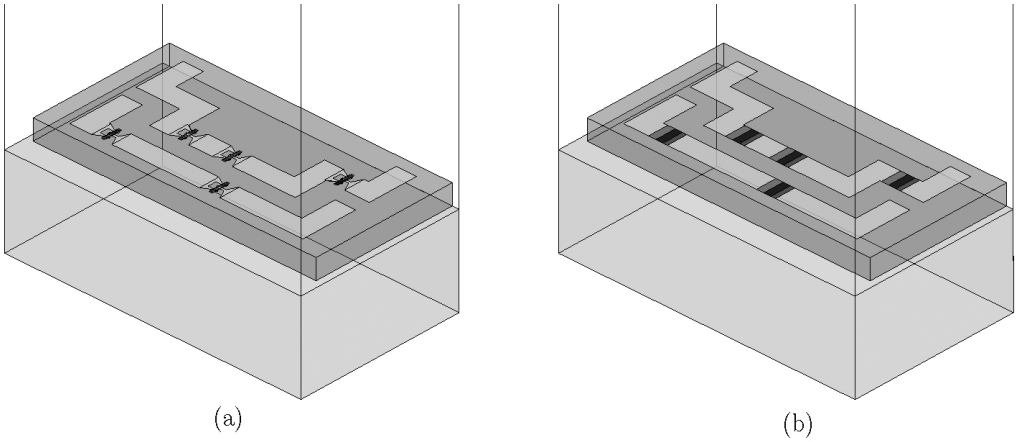

Figure 9.4: RA cell simulation setups with: (a) detailed MEMS geometries and (b) MEMS lumped models using *RLC* boundaries. Note that only the half-cell actually simulated is shown here.

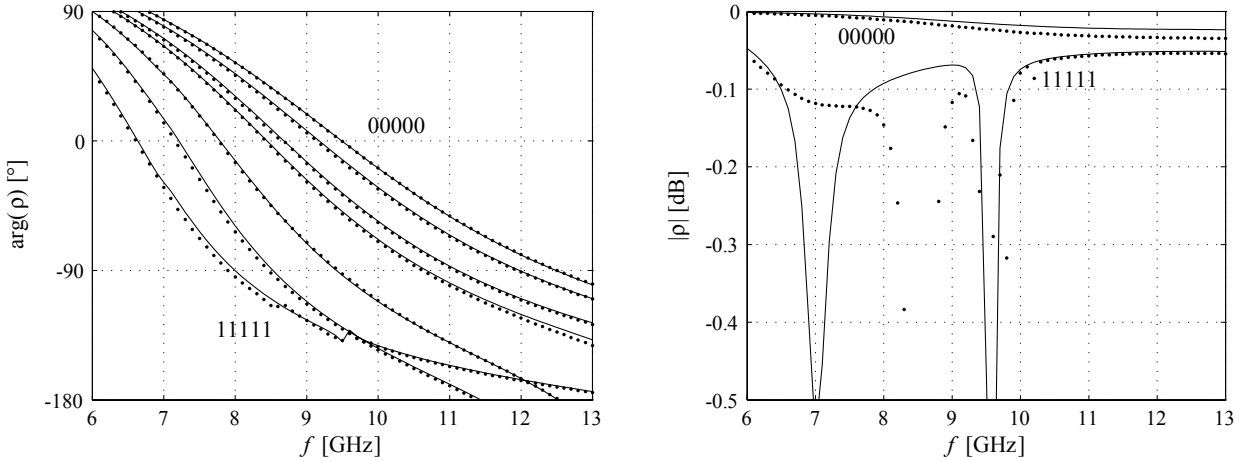

Figure 9.5: Comparison of the computed reflection coefficient with exact MEMS geometry (—) and lumped model *RLC* boundaries ($\cdots$). For clarity, only some of the computed states are plotted here.

Finally, let us note that the conjunction of these two simplifications (PECPMC-WG and MEMS lumped element modeling) proved to reduce the computation time by a factor of at least 20. In the case of the exact geometry definition with PBCs, the required mesh to obtain sufficiently accurate results leads to large RAM memory requirements (in excess of 2 GB), and days of computation time.

c. DC biasing network

The biasing network visible in Figure 9.2 is a very complex part of the RA cell from a full-wave simulation point of view (in particular, the crossing of lines corresponding to different bits result in complex multi-layer geometries). Thus, it was first tested if the resistance per unit length of these lines is sufficient for these to be neglected in the simulations. The lines are 10 μm-wide and patterned from 1 kΩ/sq polysilicon; simulations showed that the corresponding resistance is large enough for the bias network to have no visible impact on the microwave performances of the cell. By contrast, it was observed that the effect becomes non-negligible starting from a surface resistance of 100 Ω/sq, and eventually very large for 10 Ω/sq. In conclusion, the patterned DC biasing network can be removed from the simulations without impacting on the precision of the results.

9.3.2. Design/optimization of the MEMS geometry and locations

The strategy employed here to design the MEMS geometry and select optimized locations for the different MEMS can be summarized as follows:

1. Simulations of 'isolated' generic/possible MEMS geometries are carried out in a two-port configuration (see Section 3.8). The S-parameters obtained are then treated to extract equivalent circuits for the MEMS in Up and Down states for the different variations, thereby providing the range of possible values for the MEMS lumped elements.
2. The RA cell response is then studied for the range of lumped element values deduced in step 1. The adequate lumped element values being selected, the corresponding MEMS exact geometry is found with the two-port simulations of Step 1.
3. The location of the MEMS is optimized to achieve good relative repartition of the different states phases.

The approach presented requires some comments:

- The efficiency of the method relies on the use of lumped elements models for the MEMS in the full-wave RA cell simulation. Indeed, this allows separating step 1 and 2 and thus simulating the exact MEMS geometry only in an 'isolated' configuration while running the much more intensive RA cell simulation with lumped models only.
- The selection of the MEMS geometry (step 2.) was made prior to the MEMS location (step 3). The reason is that the range and BW of the RA cell are strongly dependant on the *MEMS equivalent circuit*, while in contrast, the *MEMS locations* have limited impact on

these figures but influence the relative repartition of the phases. Therefore, we first choose the MEMS geometry for a large range and BW, and subsequently optimize the MEMS locations to improve the phase repartition.

- As mentioned in Section 9.2.2, it was shown that there is a limit Up state (resp. Down state) capacitance value for which the MEMS load behaves as an open-circuit (resp. short-circuit). Thus, two discrete values of the digital capacitance can be chosen in Step 2 beyond the aforementioned limit values, in order to make the design insensitive to discrepancies in the fabricated MEMS capacitor. The drawback is that the range achieved can not be simply extended by increasing the ratio between the capacitance in the Up and Down states.

9.4. Results

9.4.1. Current visualization

Both pseudo-ring radiating elements composing the RA cell were designed to resonate in the same frequency range, which helped achieving good range and phase repartition. This can be shown by plotting the induced surface currents in two particular states, such as done in Figure 9.6. In the first one, state 00011, all the MEMS of the inner pseudo-ring are in the Up state while the ones of the outer shape are in the Down state. Plotting the surface current where the reflection phase is approximately zero, here at 7.5 GHz, we observe that the outer element is in a classical half-wavelength resonance mode, while the inner one presents much lower current levels, since all corresponding MEMS are in the Up state. We can now compare this plot to the one obtained for state 11100, the reflection phase of which is also close to zero at this frequency. We observe that the inner ring is now in resonance while the outer one is poorly excited, illustrating how both shapes resonate at around 7.5 GHz for this foam thickness when the corresponding MEMS are all in the Down state.

9.4.2. Reflection phase characterization

Figure 9.7 shows the reflection phase as a function of frequency for all 32 states, with a foam thickness $t_{foam} = 3\,\text{mm}$. This graph confirms that the resonant frequency decreases when the loading capacitors values increase. Thus, the state corresponding to the highest resonant frequency is 00000 (all MEMS in Up state), and the state with the lowest frequency is 11111 (all MEMS in Down state).

In order to better observe the phase distribution at a given frequency of operation, we plot the phase as a function of the state operated (phase diagram). In order to assess the relative repartition of the phase states within the range, the states are sorted according to the phase, as is done in Figure 9.8 for an operation frequency $f_C = 8.5$ GHz. Such plot allows characterizing the range while visualizing the relative repartition of the 32 states, which should be as uniform as possible —namely, forming a linear curve in the phase diagram— to minimize phase quantization errors on the array reflector surface. It is observed that for the frequency and thickness considered

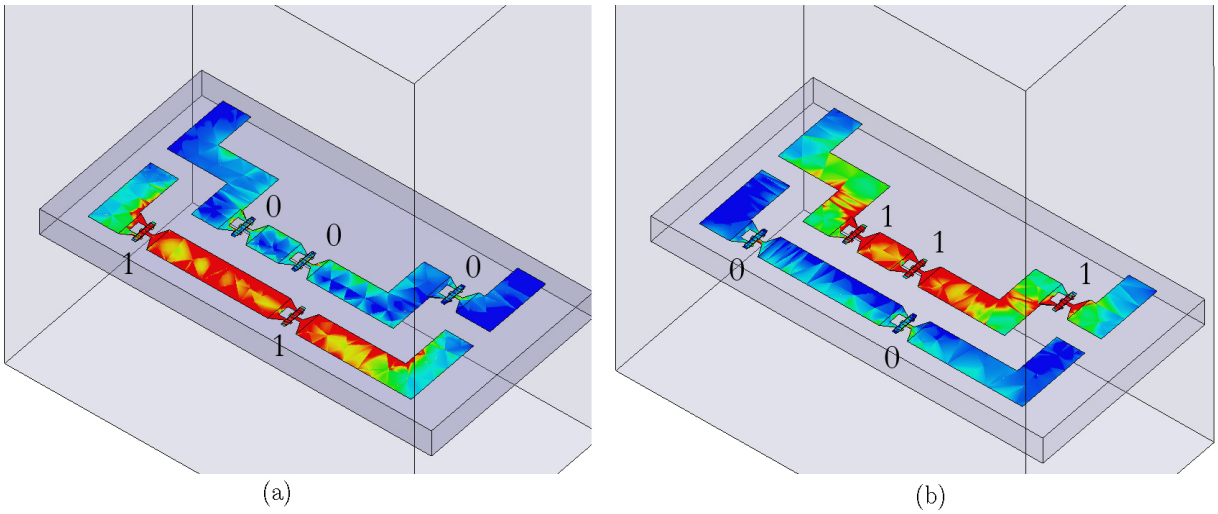

Figure 9.6: Computed surface current at 7.5 GHz in states 00011 (a) and 11100 (b), $t_{foam} =$ 3 mm. The same scale is used for both plots.

here, a range of 147° and good phase repartition are obtained. The losses are shown in the same graph, and are very low since below 0.2 dB in all states.

Nevertheless, as explained in Chapter 8, a comprehensive characterization of such element requires the assessment of the phase not only at the central frequency but on a certain BW. Indeed, it is in practice easy to design a RA cell that presents good range and phase repartition by operating it around high resonances, namely where the phase dispersion is very high. However, this would lead to very large frequency phase errors, hence very narrow BWs. In addition, such a design would also be extremely sensitive to fabrication tolerances, control voltage imprecision, and temperature drift.

Here, for simplicity, we address the BW issue by first setting the desired fractional BW and plotting the corresponding phase error at the lower and upper limits of the band, referred to as f_L and f_H, respectively. We use a reference fractional BW of 5% (this is a typical 'large' BW for RAs [85]), and the results for f_L and f_H are plotted in Figure 9.8 along with f_C. It should be emphasized here that these curves must not be sorted according to their own phase, but using the same 'sorting index' as for f_C. Indeed, we must characterize the phase difference state-by-state. In most cases, sorting each curve independently wrongly suggests a better BW than is actually the case.

In order to quantitatively assess the dependence of the phase on the frequency, we employ the definition of the frequency phase error $E\left(f_C, BW\right)$ introduced in Section 8.2.4. We obtain an average phase error at the limits of a 5% BW of only 1°. It is also noticeable that, even for a very large BW of 20%, this error remains low since it is only 10° (a limit phase error as high as 30° is sometimes used in the design of RA [86]).

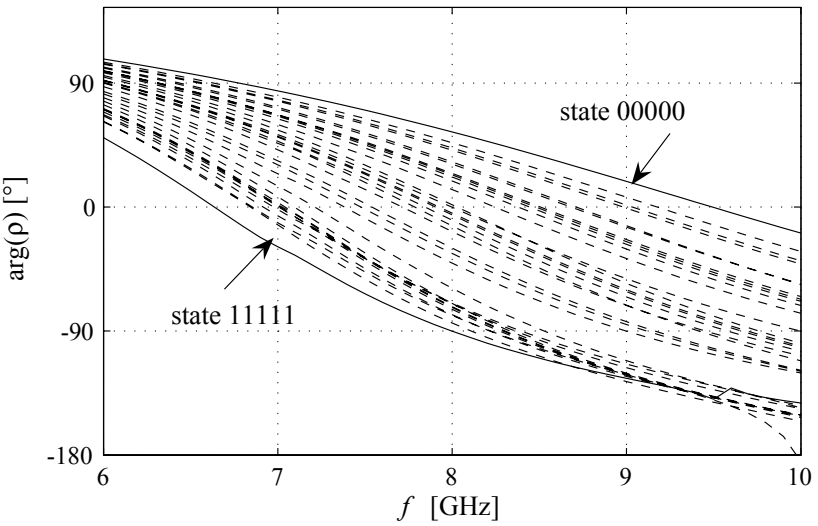

Figure 9.7: Reflection phase as a function of frequency for all 32 states, $t_{foam} = 3\,\text{mm}$.

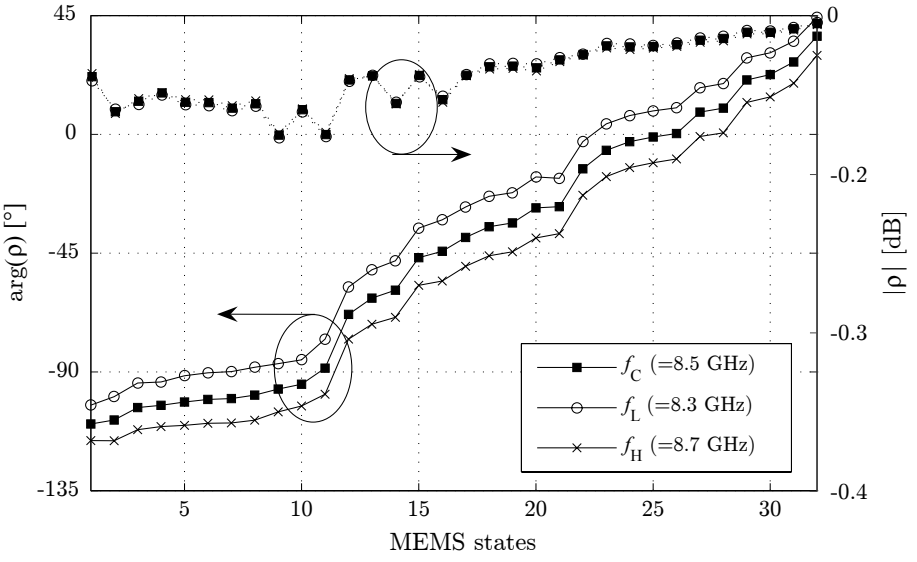

Figure 9.8: Reflection phase and loss as a function of the MEMS states (phase diagram) at the center and limits of a 5% BW around $f_C = 8.5$ GHz, for $t_{foam} = 3\,\text{mm}$.

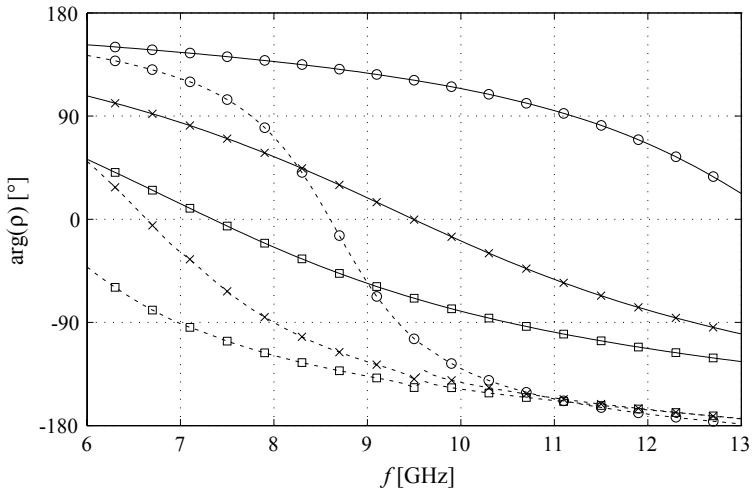

Figure 9.9: Effect of the foam thickness t_{foam} on the reflection phase. (—): state 00000, (- -): state 11111. (○): $t_{foam} = 1\,\text{mm}$, (×): $t_{foam} = 3\,\text{mm}$, (□): $t_{foam} = 5\,\text{mm}$.

Table 9.1: RA element performances overview and influence of the foam substrate thickness.

Substrate thickness t_{foam}	1 mm	2 mm	3 mm	4 mm	5 mm
Frequency f_C	12 GHz	10 GHz	8.5 GHz	7 GHz	6 GHz
Range $R(f_C)$	360°	218°	147°	118°	94°
Phase error $E(f_C, BW = 5\%)$	7°	4°	1°	1°	1°
Phase error $E(f_C, BW = 10\%)$	15°	7°	2°	2°	2°
Cell size d	$< 0.47\lambda$	$< 0.39\lambda$	$< 0.34\lambda$	$< 0.28\lambda$	$< 0.24\lambda$
Average loss	< 0.3 dB	< 0.2 dB	< 0.1 dB	< 0.1 dB	< 0.05 dB

9.4.3. Foam substrate thickness

Figure 9.9 illustrates the dependence of the reflection phase on the foam substrate thickness. For clarity, only states 00000 and 11111 are shown but the same trend is observed for each state. First, we note that the resonance of the element —which approximately corresponds to the frequency where the range is the largest— is shifted towards lower frequencies when the foam thickness t_{foam} increases. In order to fairly compare other performances of the element (BW, loss, electrical size) as a function of the foam thickness, we compute these at the 'largest range' frequencies, which are reported in the second row of Table 9.1.

The fractional BWs chosen for the comparison are 5% and 10%, and Table 9.1 indicates that the average phase error $E(f_C, BW)$ reduces as the foam thickness increases. This was already suggested by Figure 9.9, where we observe that the slope of the reflection phase decreases with

t_{foam}, which generally means a lower frequency phase error. As mentioned in Chapter 8, the cost of an enhancement in the element BW is in general associated with a reduced range. This is clearly verified here since the improvement in terms of phase error achieved by increasing the substrate thickness is at the cost of a severe reduction of the range $R(f_C)$. Finally, the losses are higher for thin foam thicknesses, which is due to the sharper resonances occurring in this case.

Finally, we graphically illustrate some results obtained for the two extreme foam thicknesses $t_{foam} = 1\,\text{mm}$ and $t_{foam} = 5\,\text{mm}$ (the results for $t_{foam} = 3\,\text{mm}$ were shown in Figure 9.8). Figure 9.10(a) shows the performances of the cell with the thin $t_{foam} = 1\,\text{mm}$ foam substrate at 12 GHz. In this case, the full 360° range is covered, while the average phase error at the limit of the 5% BW is still very low, namely, about 7°. The graph is necessary to assess the phase repartition, which is rather good, except that few states exhibit phases between -45° and -135°. Now, some inspection of the magnitude of the reflection coefficient shows that higher losses occur for particular states and frequencies, due to some sharp resonances of the element (here, this occurs only for states 23 and 32 and especially at the frequency of 12.3 GHz). Although the level of losses is acceptable even for these states, a practical solution to overcome this problem is simply to exclude the states leading to prohibitive losses, which is not a problem if there is some redundancy in the available phases.

The results obtained for $t_{foam} = 5\,\text{mm}$, at 6 GHz, are shown in Figure 9.10(b) on a 10% BW. The corresponding very low phase error (2°) reported in Table 9.1 stems from the fact that some change in frequency mainly results in some offset of the phase curve in the graph. We also observe that very good phase repartition and loss are obtained.

9.4.4. Incidence angle

a. Introduction

The phase results presented so far correspond to a normal incidence $\theta_i = 0°$. However, it is clear that in an actual RA, the different cells all 'see' the feed under different incidence angles, depending on their locations on the reflector surface. As a result, this incidence angle must be taken into account in the RA design when selecting the state to be operated at a given cell location and for a given scan angle. Consequently, the design of the reconfigurable RA requires the characterization of the cell reflection phase for each state, for different frequencies in the BW, but also for the various possible incidence angles from the feed to the reflector surface. Here, this is possible thanks to the development of the PBC-WG setup in HFSS, and this section studies the influence of the incidence angle on the phase diagram and BW, from an array design and performances points of view.

In [92], the design of a pin diode based reconfigurable reflectarray was carried out by characterizing the element for an incidence of about 50° alone[1]. The design of the RA itself was thus made by assuming that this reflection phase is independent from the incidence angle. As rightly pointed out in this reference, this assumption probably led to the observed significant loss of efficiency of the array, since the assumption results in phase characterization errors of "up to 45° for

[1]This angle was not chosen for a particular reason but set by the cell characterization method of [92].

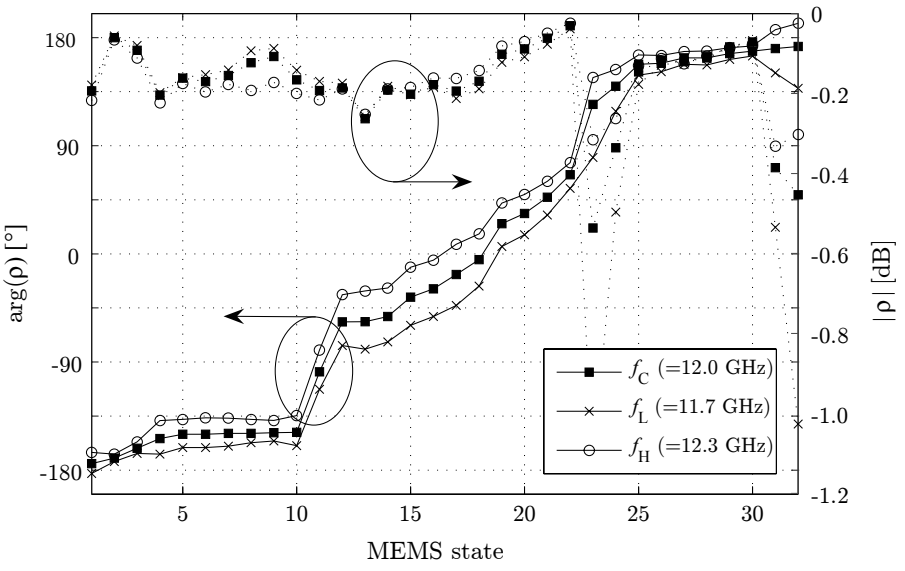

(a)

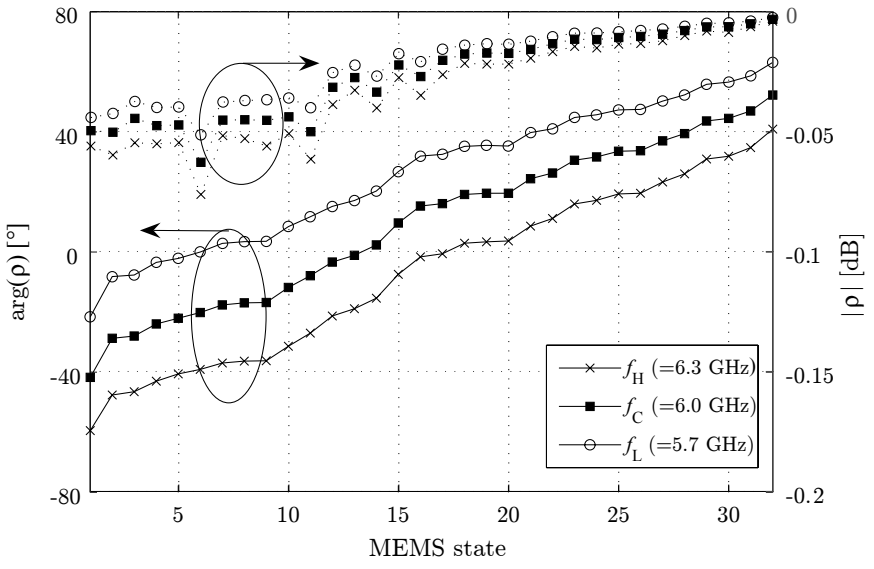

(b)

Figure 9.10: Reflection phase and loss as a function of the MEMS states. (a): at the limits of a 5% BW at 12 GHz with $t_{foam} = 1\,\text{mm}$. (b): at the limits of a 10% BW at 6 GHz with $t_{foam} = 5\,\text{mm}$.

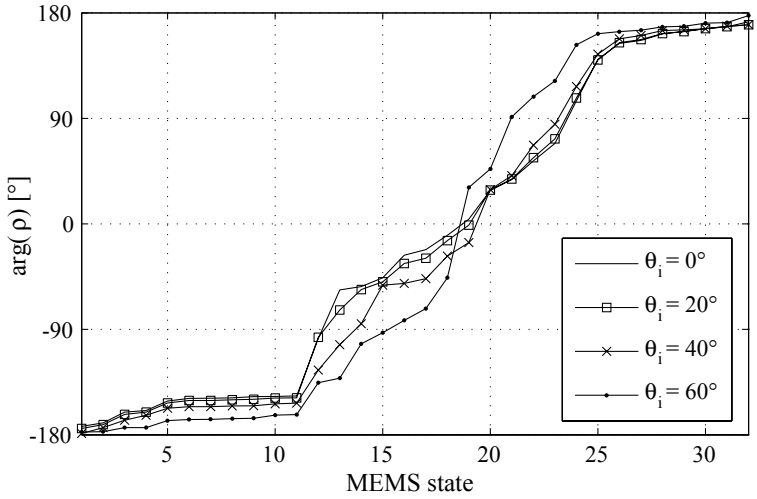

Figure 9.11: Phase diagram of the MEMS RA cell for different incidence angles, with $t_{foam} = 1\,\text{mm}$ and at 12 GHz.

incidence angles as small as $\theta_i = 25°$, compared to the case of normal incidence $\theta_i = 0°$". In [100] and [95] as well, RA elements are characterized in usual RWGs only, which means that the element is only characterized for given pairs of frequency and incidence angles (see Section 8.4).

b. Effect of incidence angle on phase and range

When characterizing the BW of a RA element such as done Section 9.4.2, we explained the requirement that the curves obtained at different frequencies only differ by some phase offset. However, there is no such requirement for the curves obtained under different incidence angles, at a given frequency. Indeed, in this case these curves correspond to different element locations on the reflector, and not to the variation of phase with frequency for a given array location. Consequently, *the dependence of the incidence angle on the phase is not a limitation, provided it is taken into account in the design.* Nevertheless, although the phase responses for different angles need not be the same, it is clear that large range and good phase repartition should be achieved for all possible incidence angles. As an example, Figure 9.11 depicts the phase diagrams for 4 different incidence angles between 0° and 60°. We observed that the 360° phase range is preserved even for very large incidence angles, and that the phase repartition is not significantly degraded.

c. Effect of incidence angle on BW

Similarly to the range and phase repartition, the BW should be assessed for the different incidence angles under which the reflector surface is illuminated by the feed. This is done here in Figure 9.12, where the phase diagram on a 5% BW is shown for both normal incidence and $\theta_i = 40°$. A moderate degradation of the frequency phase error is observed, namely, from an average of about 7° to 17°. It should however be noted that these figures are very sensitive to the large errors

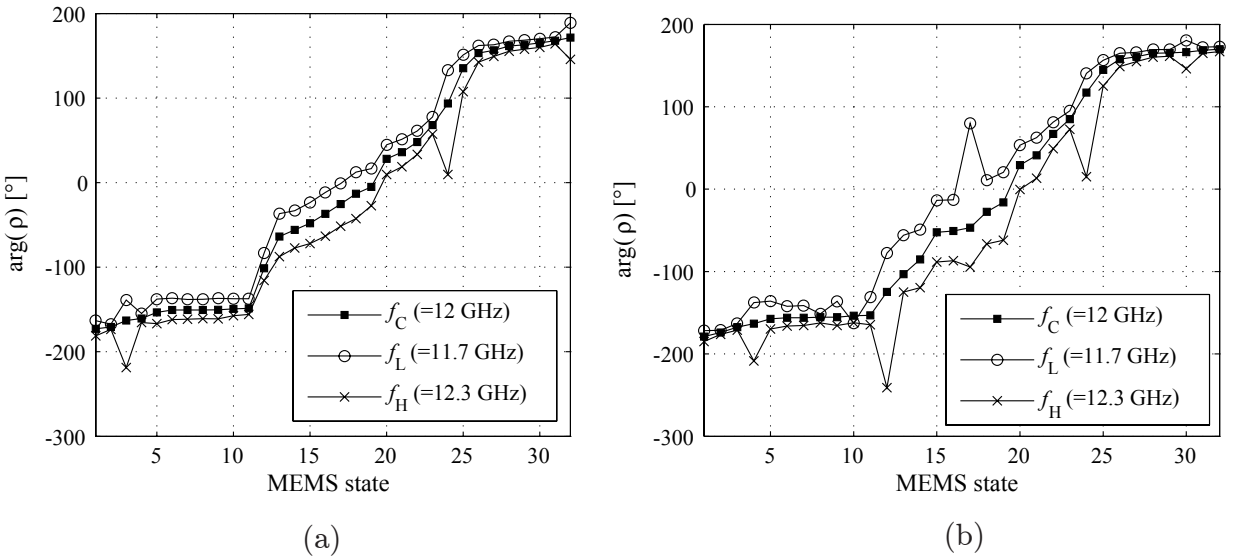

Figure 9.12: BW characterization plots for different incidence angles (a) $\theta_i = 0°$ (b) $\theta_i = 40°$, with $t_{foam} = 1\,\text{mm}$, at 12 GHz.

occurring in particular states (see the 'peaks' in the graphs of Figure 9.12(b) in states 12, 17 and 24). Nevertheless, it was observed that these peaks are not easily repeatable by the simulation, even for very stringent convergence criteria, which is linked to the limited precision of HFSS using PBCs for large incidence angles.

9.4.5. Element radiation patterns

As explained in Section 8.2.6, a weak dependence of the element radiation patterns on the incidence angle θ_i is preferred, so that these patterns do not need to be taken into account in the array design. Second, whichever the value of θ_i, a broadbeam reflected pattern is desired to limit the degradation of the RA gain when scanning the array off broadside. Here, a problem is to characterize the element pattern when embedded in the array (so-called *active* pattern). In a TL-fed array, it would be possible to carry out some simulation or measurement of an active element, surrounded by some other elements matched to the reference impedance of the system. This is not possible in the case of the RA, because we cannot 'match' the surrounding elements, as they will necessarily all be excited by the incident wave as well. Another approach employed for TL-fed arrays to deduce the active pattern is using the isolated element pattern and the the reflection coefficient at the input of the element in the array environment as a function of the scan angle [101]. This is again impossible in the case of the RA and here we will, for simplicity, only simulate the radiation patterns of the element in an *isolated* configuration. It is thus clear that the coupling between elements is not taken into account and that related effects such as array blindness are not assessed [101]. However, the idea here is simply to observe the effect of the incidence angle on the patterns and to compare the results with a reference rectangular patch RA element, although some methods for obtaining

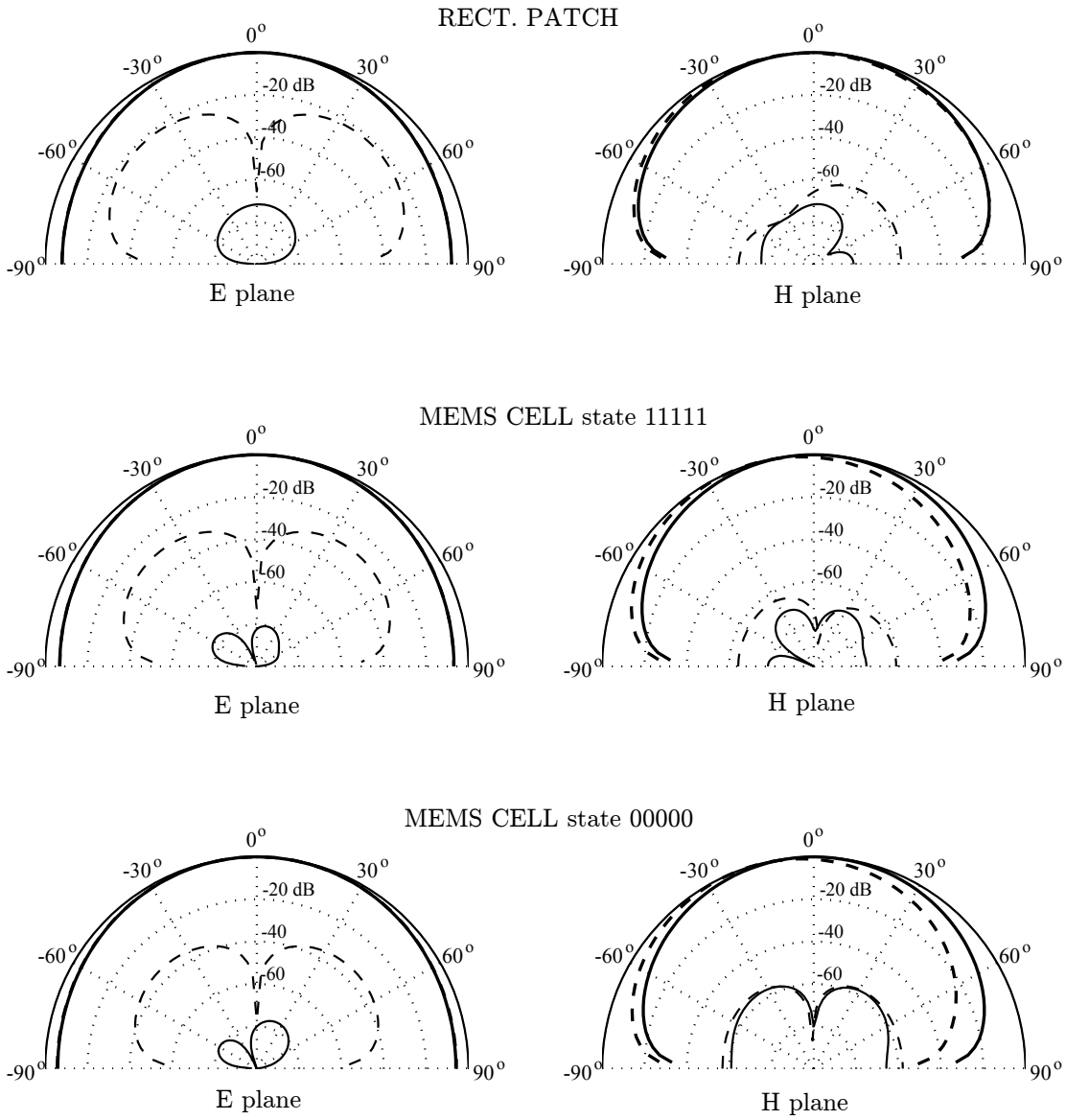

Figure 9.13: Simulated element radiation patterns as a function of incidence angle θ_i, at 12 GHz for $t_{foam} = 1\,\text{mm}$. (thick lines): Co-pol, (thin lines): Cross-pol. (—): $\theta_i = 0°$, (- -): $\theta_i = 40°$.

the active patterns should be studied in future work on the topic (note that publications on the design of RA generally do not address this question). The different 2-D patterns computed are described in the following table:

	E plane ($\phi = 90°$)	H plane ($\phi = 0°$)
Co-polarization	E_θ	E_ϕ
Cross-polarization	E_ϕ	E_θ

The results are shown in Figure 9.13, and have been computed for states 00000 and 11111 with a foam thickness $t_{foam} = 1\,\text{mm}$ at 12 GHz, in order to correspond to the phase results presented in Figure 9.10 and Figure 9.12. Figure 9.13 first shows the patterns for a reference rectangular patch on the same substrate, which was designed to resonate at about 12 GHz, too. We observe that:

- The E-plane co-polarization very weakly depends on the incidence angle θ_i.
- The E-plane cross-polarization for $\theta_i = 0°$ is extremely low, and is actually only related to the limited precision of the simulation, since this is theoretically zero in the whole E-plane. For an oblique incidence $\theta_i = 40°$, the currents induced in the element are no longer symmetrical around the E-plane, and the simulation shows that the cross-polarization is now about -20 dB.
- The H-plane co-polarization pattern is influenced by the incidence angle θ_i; more precisely, the maximum directivity approximately corresponds to the angle of specular reflection (here, $\theta_i = 40°$ so this maximum is at about $-40°$).
- The H-plane cross-polarization is very low for both simulated incidence angles.

As is clearly seen in Figure 9.13, all these observations apply to the MEMS ring element as well. The worst cross-polarization level is about -30 dB, which is even better than the -20 dB obtained in the case of the reference rectangular patch and good enough for most applications. The co-polarization patterns are very broadbeam. Thus, the directivity in a wide range of angle around broadside is only weakly dependent on the incidence angle. As a result, we can conclude that the designed element can be employed for RAs scanning large angles off broadside. Also, a comparison with a rectangular patch antenna shows that the pattern are not degraded by the use of more complicated radiation element shapes, which were here required to achieve the desired reflection phase properties.

9.4.6. Experimental validation

a. Introduction

Figure 9.14 shows a fabricated device, as well as some close views on a MEMS series capacitor and the bias lines distribution network. In the picture, the MEMS device is placed on the thinnest (1 mm) foam additional substrate. The foams were fabricated to exhibit thickness tolerances below 0.05 mm for a good reflection phase precision. Figure 9.15 shows a symbolic representation of a fabricated device embedded in a RWG-IAS for experimental characterization. Here, two cells

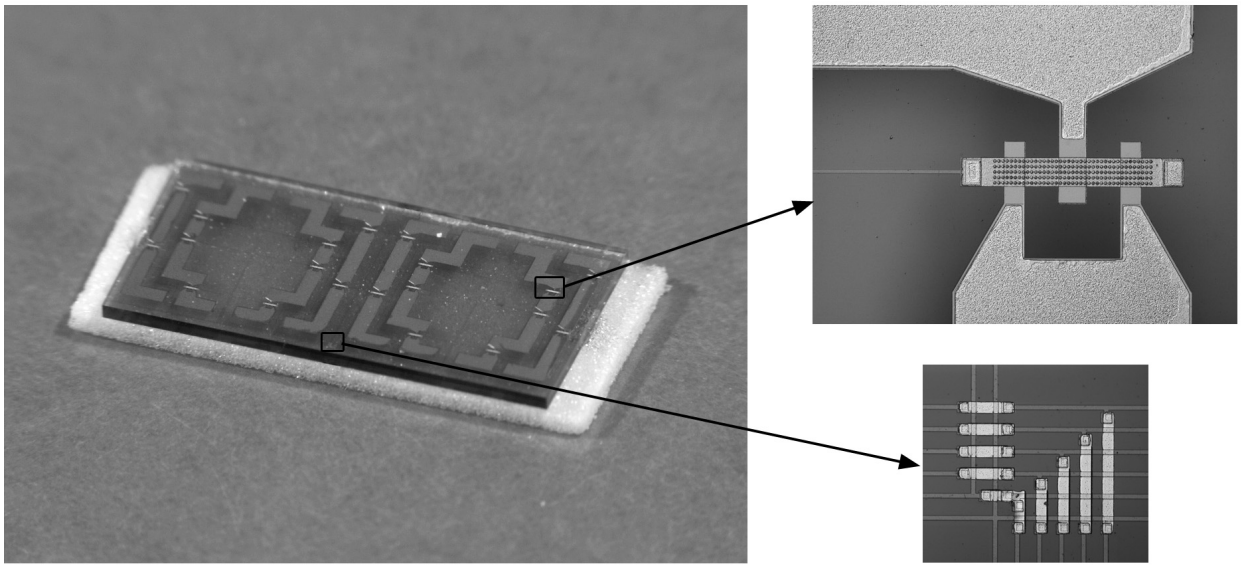

Figure 9.14: Pictures of a fabricated RA 2-cell on a 1 mm foam additional substrate. The insets show close views on a MEMS series capacitor and the bias lines distribution network.

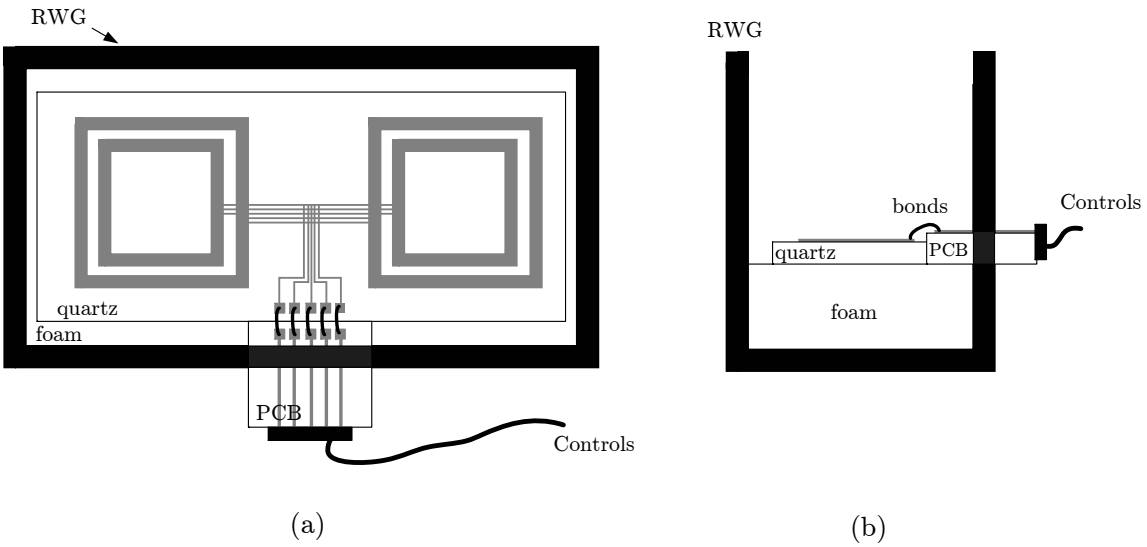

Figure 9.15: Sketch of a proposed 'active' RWG-IAS measurement of the RA cell.

are actually measured, for the reasons explained in detail in Section 8.6 in the case of the PCB cells measurements. As shown in the sketch, it is however necessary here to drive the DC control voltages inside the RWG. There are several possible ways to do this, with different pros and cons. The solution shown in Figure 9.15 is to mechanically fix the device to a PCB where lines and connectors were previously printed and mounted, respectively. The lines are then connected to the MEMS device by wirebonding, as shown in the drawing. Finally, the whole structure is inserted in the RWG-IAS, which must include some opening to accommodate the PCB.

It is clear that the opening carried out in the RWG should not perturb the measurement. This issue can be addressed by carefully selecting its size and location with regard to the fields and currents in the RWG. However, more problematic here is the fabrication issue. Indeed, although quite simple in principle, realizing the proposed setup is difficult in practice, in particular because of the stringent criteria on the size of the MEMS chip to be fabricated (this one could not be freely chosen to allow printing some dedicated pads for the wirebonding). As a result, it was decided to test the device in 'frozen' states, where all MEMS are either in the Up or Down state. The measurements are thus carried for the states 00000 and 11111 only, for the 5 considered substrate thicknesses and on the whole X-band, which should be sufficient to confirm simulated results. Indeed, if good correlation between simulations and measurements is confirmed for states 00000 *and* 11111, this means that the MEMS structure is well modeled *both* the Up state and the Down state. Since all other RA cell states can be seen as combinations of these two extreme states, it can safely be assumed that a good agrement between simulations and measurements would be obtained for the other states as well.

b. Results

Figure 9.16 exhibits measurement results for 3 foam thicknesses (1 mm, 3 mm, and 5 mm) and for both states considered. In each case, two different instances of the device were measured to assess the repeatability of the results, which proves to be very good both in terms of phase and loss. The graphs also show simulated results in the same configuration and same location of the reference plane for the computation of the reflection phase. Concerning the phase, an excellent agreement between simulations and measurements is observed, taking into account the inherent measurement imprecision such as the centering of the RA cells in the RWG and the accuracy of the foam substrate thickness. In particular, we can note that the difference between the two measured devices is sometimes larger than the difference between simulation and measurements. It is believed that the good agrement is partly due to the fact that the design was done so that moderate discrepancies in the MEMS capacitance values would not impact on the reflection phase precision (see Section 9.3.2).

More complicated is the issue of loss, because of the limited knowledge in the conductivity of the deposited materials. Some tuning of the metal conductivity in the simulations showed that the actual conductivity of the deposited metal is much lower than that of pure aluminium (of a factor of about 100). However, this very large change in the conductivity does not lead to a great degradation of the reflection loss, nor to the presence of new resonances in the reflection loss, as shown in the right hand side of Figure 9.17. In addition, the left hand side of Figure 9.17 shows

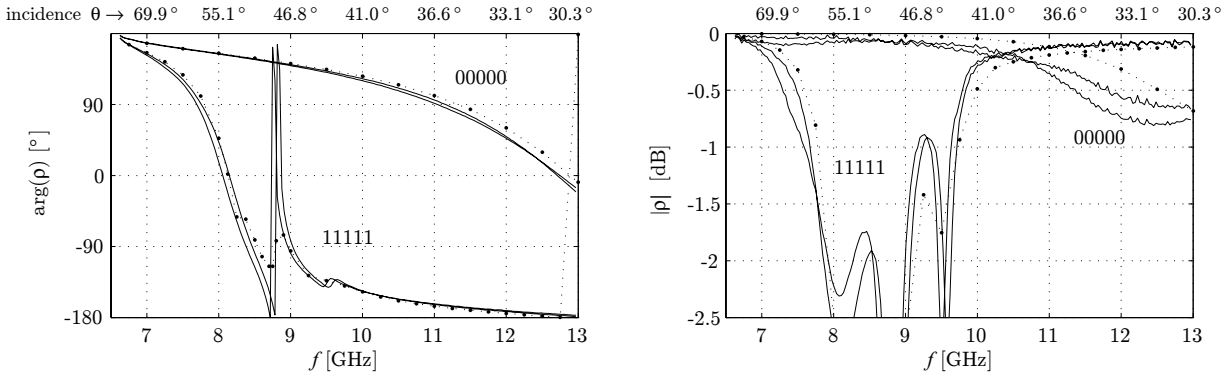

(a) $t_{\text{foam}} = 1$ mm

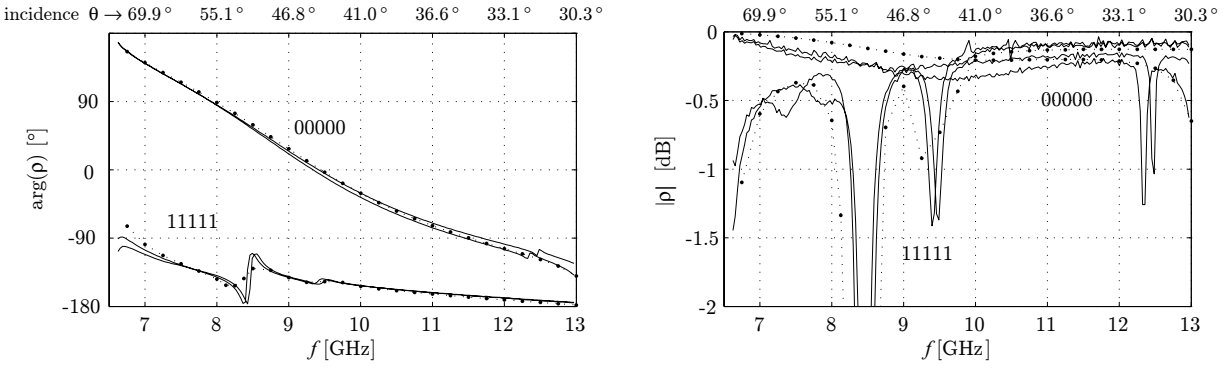

(b) $t_{\text{foam}} = 3$ mm

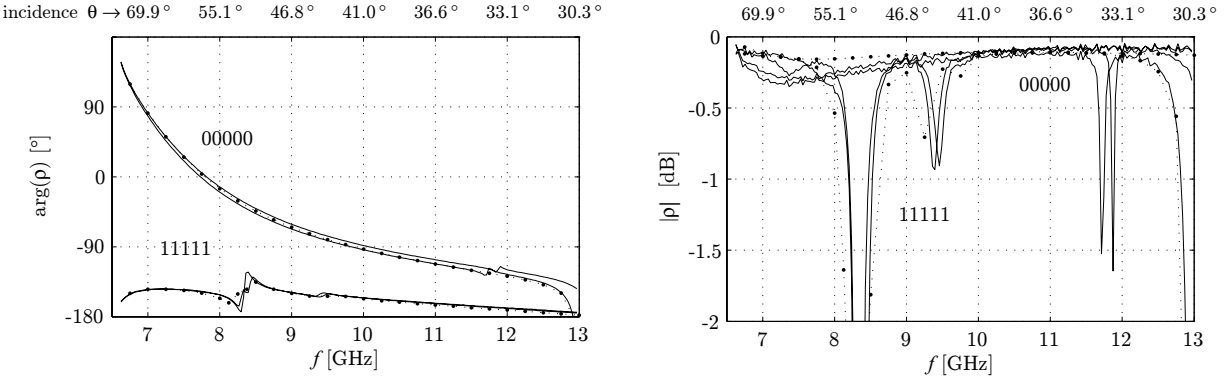

(c) $t_{\text{foam}} = 5$ mm

Figure 9.16: RWG-IAS measurements results of the MEMS RA cell (—), compared with simulations ($\cdots\bullet\cdots$). The plane wave incidence angle θ corresponding to the different frequencies of the RWG-IAS measurement are shown on the top of each graph.

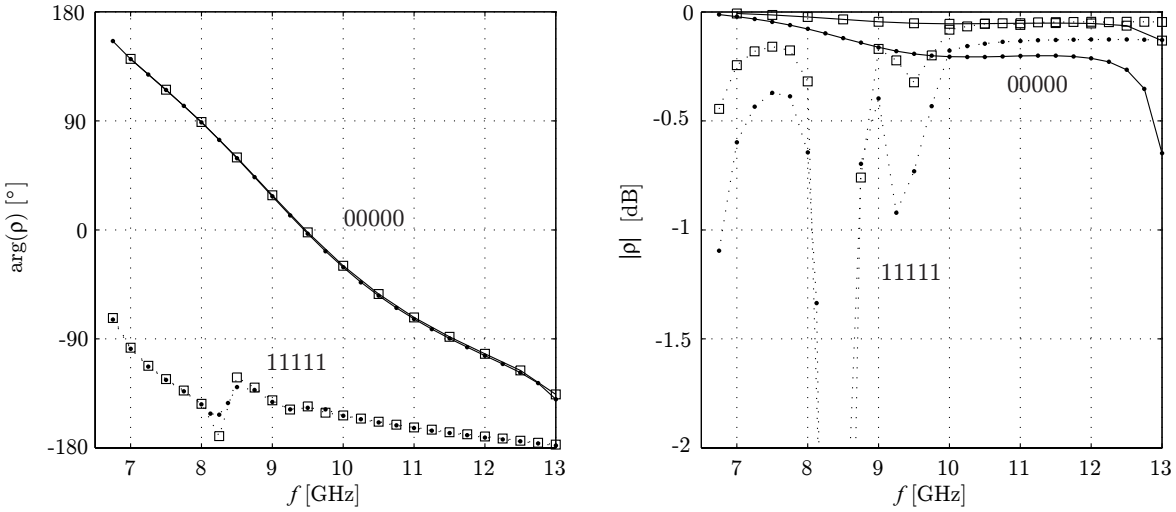

Figure 9.17: Comparison of the simulated results with a metal conductivity of σ = 4e7 S/m (□) and σ = 5e5 S/m (•), for $t_{foam} = 3\,\text{mm}$.

that the reflection phase is totally insensitive to the conductivity of the metal, which is especially convenient for the design of RA cells. Finally, let us note that although the cell might exhibit rather large losses in some parts of the measured band, this does not mean that the actual RA cell in operation will exhibit such losses. For instance, let us observe the loss of the cell on the 1 mm foam [Figure 9.16(a)]; although the losses are larger than -2 dB below 10 GHz, they are much lower in the frequency range where this cell is intended to be used. Indeed, the phase diagram for this structure shown in Figure 9.10(a) corresponds to an operation frequency of 12 GHz, where the worst case measured loss is below -0.7 dB. As a result, the losses remain excellent with regard to state-of-the-art, even for a significant degradation of the metal conductivity.

9.4.7. Application examples

This section presents the application of the designed MEMS RA cell to reconfigurable RA designs. The idea is to show in a simple but quantitative way how the element could be employed in concrete reconfigurable RAs, but especially to illustrate the corresponding *phase quantization*. Indeed, the phase distribution that can be achieved using the RA element differs from the ideal phase required on the reflector surface since:

1. The actual reflector surface is discretized according to the cell size d, whereas the required phase shift is a continuous function.
2. Only 2^N phase states can be achieved by the actual element, although the required phase shift at a given element location can take any 'analog' value. So, there will necessarily be some differences between the required theoretical phase and the selected state of the cell for this location. We will refer to this imperfection, which degrades the gain of the RA, as the *phase quantization error*.

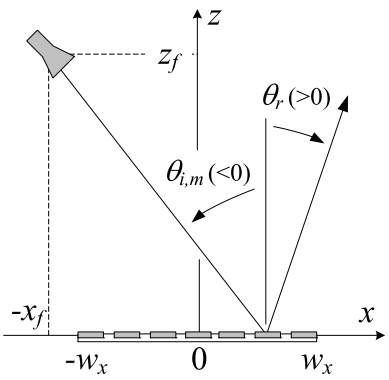

Figure 9.18: RA geometry with $[-x_f; z_f] = [180\,\text{mm}; 360\,\text{mm}]$ and $2w_x = 320\,\text{mm}$.

Here, we first calculate the required phase distributions for a given array geometry and some scan angles. Second, we study how these phase distributions can be approximated using the designed MEMS RA cell. For simplicity, we consider here 1-D scanning and will only determine the required phase on the axis of the array in the scan plane (note that the phase within the whole array can be easily deduced too). Figure 9.18 shows the RA geometry and associated definitions. Here the idea is to get 'maximum gain' scanning in the xz plane, with an angle θ_r with regard to broadside. The feed is located at $[-x_f; z_f]$ and the reflecting surface width is $2w_x$. The numerical values are provided in the caption of the figure and correspond to the fixed-beam RA presented in [111]. This array geometry was chosen first because it operates in the same band as our RA elements (X-band). Second, the electrical dimensions of the array at the operation frequency are such that an element covering the full 360° range is required, because different elements in the array are subject to more than one wavelength of difference of path length from the feed. For the following calculations, the surface of the array is discretized according to the grid spacing d so that $x = m \cdot d$ with $m \in \mathbb{Z}$. As the reflector is located within $x \in [-w_x, w_x]$, we have $m \in [-M, M]$, with M being the largest integer with $M \leqslant w_x/d$.

In order to determine the required phase distribution, let us first re-write (8.11) in the following form:

$$\Delta\rho_m = -kd\,(\sin\theta_r + \sin\theta_{i,m}) \tag{9.1}$$

and recall that $\theta_{i,m}$ is the incidence angle on element m (see Figure 9.18), and $\Delta\rho_m$ the difference of reflection phase between successive elements: $\Delta\rho_m = \arg(\rho_{m+1}) - \arg(\rho_m)$. We express $\theta_{i,m}$ as a function of the array geometry:

$$\theta_{i,m} = -\text{arctg}\left(\frac{x_f + md}{z_f}\right) \tag{9.2}$$

Then we substitute (9.2) in (9.1) and obtain, after some trigonometric simplification:

$$\Delta\rho_m = -kd\left(\sin\theta_r - \frac{\alpha_m}{\sqrt{1+\alpha_m^2}}\right) \tag{9.3}$$

with $\alpha_m = (x_f + md)/z_f$. Finally, the desired reflection phase for $\arg(\rho_m)$ is deduced from (9.3) by the following recursion:

$$\arg(\rho_m) = \Delta\rho_m + \arg(\rho_{m-1}) \tag{9.4}$$

There is obviously an infinity of solutions $\arg(\rho_m)$, which only differ by a constant phase offset. This is very interesting in the sense that, in practice, we can select which offset to give to the ideal phase response to get a minimal quantization error using a given reconfigurable RA element. However, for simplicity, we choose in this first example to set $\arg(\rho_{m=0}) = 0$, namely, to fix the phase to zero at the center of the array. We have now deduced the ideal phase reflection in the array axis, which is given by (9.4) and (9.3). Using the array geometry described above and for an operation frequency of 12 GHz, we obtain the results shown in solid lines in Figure 9.19, for 4 different scan angles.

Now, we want to approximate this ideal phase distribution using the designed MEMS element. For that purpose, we use the 32 phases obtained in the case of a 1 mm-thick foam, in order to cover the full 360° range required here. First, we observe how finely the ideal curve is discretized along the reflector dimension x, which only depends on the element size d. Here, $d = 11.43$ mm and there are 28 elements in the considered array axis. A routine was programmed to automatically select the best state at each element location, and plot the corresponding phase as shown in Figure 9.19, in comparison with the ideal solution. We observe here that the element allows implementing a phase profile that accounts well for the ideal solution. The largest discrepancies obviously occur in the regions of the phase diagram where few states are available. The average and maximum quantization phase errors are also calculated; for the four scan angle studied here, the average quantization phase error is between 6° and 10°, while the maximum error is less than 30°.

It is interesting to compare these figures with the average frequency phase error defined in Section 8.2.4 and reported in Table 9.1 for this RA element. We observe that the phase quantization error is in general larger than the frequency phase error. This means that the degradation of the phase response due to a change of frequency in the considered BW is small with regard to the error already present at the design frequency because of phase quantization.

As explained in Section 8.2.1, another application for reconfigurable reflecting surfaces is for the dynamic compensation of surface distortion [90]. Let us imagine that our surface is now a sub-reflector that must exhibit the typical phase profile shown in Figure 9.20(b)[1]. In this case, since the range is only about 60°, it is preferable to use an element with a limited range but better phase repartition to minimize the phase quantization errors. Using a foam thickness of 5 mm, we obtain the phase diagram of Figure 9.20(a), and Figure 9.20(b) plots the optimal phases obtained at each element location. Note that we made use of the fact that, as explained above, any offset of the ideal phase reflection is also an ideal solution. Thus, we purposely selected the ideal phase response that is within the range of our element [see the arrow in Figure 9.20(a)], so that the required phase distribution is well accounted for by the real surface.

[1]This profile was chosen arbitrarily, for the sake of illustration, but is typical of a sub-reflector compensation of some parabolic antenna thermal distortion [90].

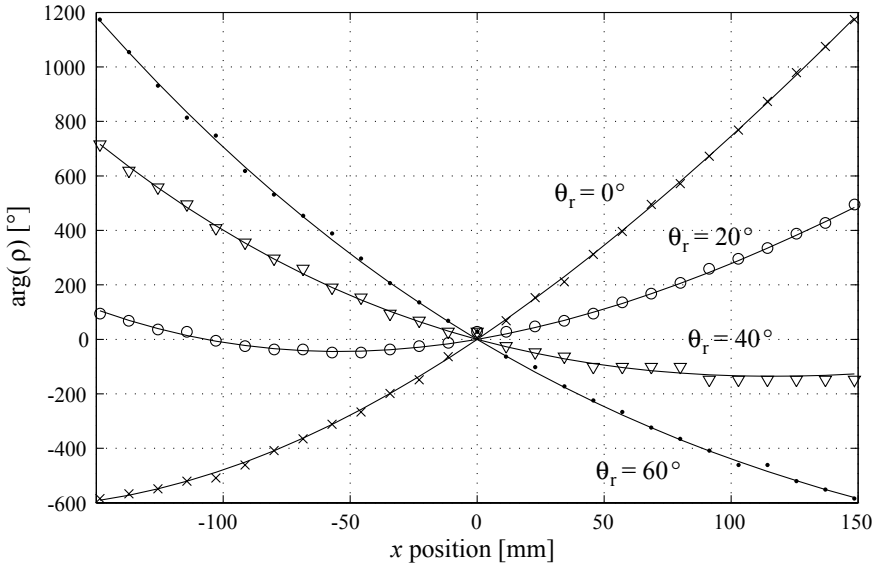

Figure 9.19: (—): ideal phase responses for the array of Figure 9.18, (markers): implementation using the presented MEMS RA cell with a 1 mm-thick foam, 12 GHz.

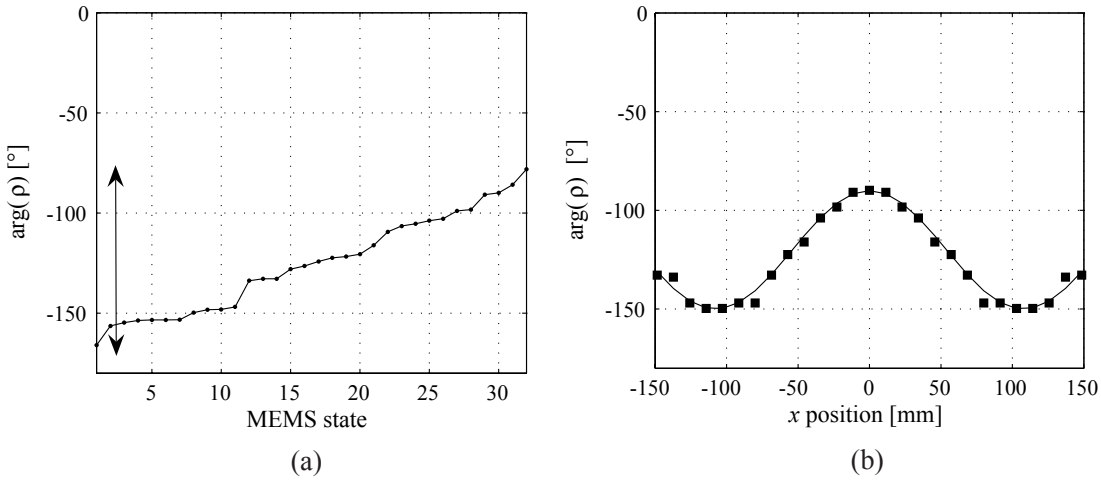

Figure 9.20: Use of the RA element for phase distortion compensation at 10 GHz. (a): Phase diagram of the RA element with a 5mm-thick foam. (b): Ideal phase compensation (—) and implementation using the RA element (■).

9.5. Results summary and performances discussion

This section gives an overview of the results obtained with the designed MEMS cell, with regard to the various requirements for reconfigurable RA cells addressed in this work. Theses performances are also discussed in the light of the results achieved for other reflectarray cells, whether based on MEMS or on other technologies for reconfigurability.

Phase range

As shown in Table 9.1, The range of the designed MEMS cell can be controlled by means of the foam substrate thickness. The full 360° range is covered in the case $t_{foam} = 1\,\text{mm}$, with all other performances satisfactory. Nevertheless, in cases where a smaller range is sufficient, it is possible to use a thicker substrate to further increase the BW. For instance, [112] calculates a required range of 300°, while even smaller ranges could be sufficient for some error compensation application. For comparison with the results achieved in the literature, one must separately treat the case where the phase shift is achieved by a TL connected to the radiating elements, or when the phase shift originates from a modification of the radiating area itself. In the first case, achieving a 360° is rather straightforward since this only depends on the length of the TL. In this context, RA cells such as presented in [92, 113, 114] all achieve the required phase shift. However, in the case of the modification of radiating shape itself, it is observed that [95] and [98] demonstrate smaller ranges of 280° and 230°, respectively. The cell designed here belongs to this second category and thus presents very good range with regard to the aforementioned values.

Phase repartition

In principle, the best method to achieve uniform phase repartition is using TL phase shifters, since the different phases can be uniformly distributed in a simple way by varying the electrical length of the TLs of *constant increments*. However, note that having a sufficient number of bits might be problematic here if the principle is to switch between TLs of different length, such as done in [114]. Indeed, in this case complicating switching network would have to be implemented (in [114], a 2-bit resolution is achieved by using SP3T switches). Nevertheless, we demonstrated here that good phase repartition can be achieved as well by integrating the control element into the radiating shape itself; in this case, the principle can be extended to virtually any number of bits.

Bandwidth (BW)

Table 9.1 shows the very small average phase error obtained with the designed element. In most published works presenting reconfigurable RA cells (e.g. [93, 95, 98, 100]), a unique phase diagram at the design frequency and for a given incidence angle is used to characterize the element. It is therefore not possible to compare our design to these references where the BW was not characterized. In contrast, some phase error information can be found in [92] and inspection of Figure 2 in this reference shows that the element presents larger phase error than the extremely small figures obtained for our element and reported in Table 9.1. Reference [113] also shows the phase obtained at different frequencies around the center frequency of the element. In this case, an average phase error as large as 50° is obtained in a BW of less than 10%, which is much larger than typical phase

errors obtained here.

Reflection loss

The losses of the RA cell depend on the foam thickness, and the worst case here corresponds to the largest phase range 360º, namely, using the thinnest 1 mm foam substrate. Even in this case, very low losses were measured, namely, inferior to -0.7 dB at 12 GHz for all states and chips measured. In the case of the rather new approaches for RA reconfigurability based on liquid-crystal [95], ferrite ground plane [94], or the photonically-controlled semiconductor of [96], the losses are in the range of -6 dB to -10 dB, which seems prohibitive with regard to most applications. The diode-based designs of [92] and [93] exhibit better performances, namely, about -2.5 dB and -3.5 dB, respectively. However, these figures are already much higher than the loss reported in this work. In addition, such loss performances are obtained for operation frequencies of 5.4 GHz and 5.8 GHz, whereas the 'worst case' -0.7 dB obtained here correspond to an operation frequency of 12 GHz. Since the difference between both approaches in terms of losses increases with frequency, the advantage of the MEMS implementation would be even more advantageous for higher frequencies, which is fundamental considering the millimeter waves applications envisioned for reconfigurable RAs [e.g. automotive cruise control (77 GHz), imaging and remote sensing (35 GHz, 94 GHz)]. Finally, some measured loss results for a MEMS implementation were presented in [98] and range from -1 dB to -3 dB at 5.8 GHz, for a limited range of 230º. References [115] and [114] provide some loss assessment too; however, these only correspond to the loss in the TL to be used as a reflective phase shifter at the 'ouput port' of the radiating element. Corresponding results are already of about -1 dB in both cases, but still have to be evaluated for the complete RA cell (as well as confirmed by measurement in the case of [115]). Finally, some good loss figure is obtained with the MEMS RA cell of [99], namely, between -0.6 dB and -1 dB.

Sensitivity to control voltage precision

The approach employed in this work to reduce (and virtually eliminate) the influence of noise/imprecision of the control voltage on the microwave performances was to operate the MEMS in a digital mode. In contrast, designs based on an analog control necessarily suffer such limitation (e.g. diodes [92], ferrite [94], liquid crystal [95], and MEMS [98]). The sensitivity of these analog designs depends on the technology and detailed design, and cannot be easily quantified; however, it will clearly be much more important than for the digital design presented here. In addition, and as explained in Section 9.2.2, the sensitivity is especially problematic in the case of the MEMS analog implementation, as a result of the very large slope of the $C(V)$ curve for large capacitance ratios.

Reflected pattern

Some radiation patterns for the designed element were presented in Figure 9.13. We could thereby show that a broadbeam pattern is obtained, with a maximum cross-polarization level of about -30 dB for an incidence angle of 40º. The performance of the element was compared with a reference rectangular patch in a similar setup and it was found that the MEMS element cross-polarization is even lower than that of the patch element. It is not possible to compare these results to other RA cell since no pattern characterization was found in the corresponding references.

Incidence angle effect

The effect of the incidence angle was tested both in terms of the phase response and of the reflected pattern. Concerning the phase response, it was observed that the range, the phase repartition, and the BW are good even for incidence angles as large as 60°. The radiation pattern dependence on the incidence angle was found comparable to that of a rectangular patch. Here again, no similar results for comparison could be found in the literature.

Cell size

The cell designed here is smaller than $\lambda/4$ at the maximum operating frequency, thus ruling out grating lobes for any angle scanned by the array. In addition, the even smaller electrical sizes of the element reported in Table 9.1 allow the reduction of phase quantization errors on the reflector surface. This is an advantage over RA elements based on TL phase shifters, which can suffer from the space required to accommodate the TL in the unit cell [111, 113].

Complexity

The complexity of the designed structure is obviously also an issue, mainly for reliability and cost reasons. In this context, [96] certainly presents the more costly solution, as a result of the photonical excitation of the substrate. Concerning MEMS-based cell, a monolithic approach as presented here is the most reliable and cheap, since no difficult mounting and wirebonding must be carried out (e.g. [112]). Finally, as explained in Section 9.2.2, the DC biasing circuit of the digital MEMS approach is much simpler than it is the case of an analog implementation.

Other issues

In addition to the points discussed above and linked to the RA operation, MEMS based RA cells inherently present the usual advantages of MEMS over established technologies. One can name: a fundamental very high upper frequency limitation, very low drive power, and excellent linearity with regard to diodes.

9.6. Conclusions and perspectives

From a general perspective, we demonstrated that MEMS technology is a very promising solution for the implementation of reconfigurable RAs with state-of-the-art performances. This solution is particularly suitable for high frequencies, which is especially important considering envisioned applications for reconfigurable RA in satellite communication, automotive cruise control, and remote sensing. In general, MEMS reconfigurable RA presents the same pros and cons as other MEMS-based microwave devices (e.g. cost, reliability; see Chapter 1). However, the digital MEMS control proposed here allowed solving the main limitation linked with any analog implementation, namely, a severe tradeoff between range and sensitivity to control voltage precision, temperature drift and fabrication tolerances. In addition, the numerous other requirements for RA cells were addressed and the very good performances of the device from these different points of view were highlighted.

An efficient design method was employed to design the MEMS RA cell, based on physical

insight, circuit modeling of the MEMS, and full-wave simulations. Since a very large number of intensive simulations is required in this process, particular steps were taken and validated to reduce the computational time.

The presented reconfigurable RA cell exhibits excellent performances with regard to the fragmented results available today in the literature concerning reconfigurable RA cells. However, here are some potential directions for further work on this topic:

- Study the effect of MEMS packaging: this is rather straightforward since this would only require running similar simulations as carried out here, while adding the package in the setup.
- Investigate multilayer topologies, which were shown in [88] to potentially improve the BW of fixed-beam reflectarrays.
- Increase or decrease the number of bits (depending on the application), while maintaining good range and phase repartition.
- Investigate dual-polarized reconfigurable elements.
- Develop some algorithm for the automatic optimization of some of the element parameters. This would be particularly useful for the fine tuning of the MEMS elements locations, which mainly determine the quality of the phase repartition.
- Finally, it is clear that the implementation of a full, operating MEMS RA should eventually be carried out. The main issue here is technological, namely, to fabricate a large number of RA cells, and to manage the mounting, biasing, and control of the whole structure.

10. Conclusions and perspectives

10.1. Summary

The theory of periodic TL structures has been revisited in the light of its application to the development of circuit-based design methods for micromachined and MEMS circuits. The first outcome of these developments was to show that Bloch wave modeling can be rigorously employed even in the case of finite periodic structures. Second, particular attention was paid to the mathematical and physical interpretation of the sign ambiguities in the computation of the fundamental parameters of the periodic structure. Finally, the approach was generalized for the multimode description of the structure's unit cell.

Methods based on this theory were then developed for the design of distributed MEMS transmission lines (DMTLs), along with different contributions to the analysis of such structures. Analog and digital devices were fabricated, showing excellent agreement with the circuit modeled results. In a next step, a new topology for the reduction of the mismatch in multi-bit implementations was introduced. An analytical proof of the superiority of the approach over the conventional one was then presented, along with some design method for the new topology.

The next results presented mainly consisted in theoretical developments on the composite right/left handed transmission lines (CRLH-TLs) structure, carried out to overcome the limitations of existing modeling based on the effectively homogenous media assumption, which was shown to be inappropriate in the case of micromachined or MEMS CRLH-TL implementations. Devices were successfully designed based on the new theory, which also allowed the demonstration of the possibility to design especially low/high impedance CRLH-TLs.

Next, MEMS implementations of variable CRLH-TLs were presented. Analog and digital devices were designed, and excellent agreements between full-wave simulations and circuit models were obtained in both cases. For fabrication reasons, only the analog device could be measured to exhibit the expected performances. Eventually, new differential phase shifters were designed using the MEMS CRLH-TLs as building blocks. The devices exhibit reconfigurable frequency-independent differential phase shift, or group delay, on wide bandwidths.

The last part of the thesis concerned the reflectarray application. We first presented a comprehensive assessment of the numerous requirements for a reflectarray cell, which required several considerations related to the functioning of a reconfigurable reflectarray. Simulations and measurement issues were also extensively discussed and validated. The designed reflectarray cell was then introduced and characterized considering all aforementioned requirements.

10.2. Discussion

This thesis addressed various issues linked with the development of microwave or millimeter wave devices reconfigurable by means of MEMS, both from a practical and a theoretical point of view.

Different types of devices have been designed to illustrate the versatility of the developed methods. In addition, the choice of the devices studied was also made to illustrate the various potentialities of MEMS in microwave applications. The first device studied, the DMTL, was an already popular MEMS device and the new contributions here mainly consisted in the improvement of existing design methods as well as proposing some new topology for multi-bit operation. The second TL structure that was selected, the CRLH-TL, was much more challenging and constitutes —to the author's knowledge— the first implementation of a MEMS-reconfigurable metamaterial structure. This research area is especially promising, as a result of the demonstrated capabilities of non-variable metamaterial and the efficiency of MEMS for reconfigurability. Finally, noting that the two first classes of structures designed were based on TL, it was decided to implement some MEMS-variable radiating structure as well. The reflectarray application was selected, as an advantageous solution for reconfigurable low-cost antennas that would especially benefit from MEMS technology.

When designing microwave MEMS, considerations related to fabrication, reliability, and electromechanical issues must be considered along with the electromagnetic design —on which the emphasis was put in the present work. In this context, there is the requirement of some 'practical' know-how for addressing all these issues in reasonable time, which was progressively acquired through the various designs presented. It is actually interesting to note that many published works on microwave MEMS have somehow neglected theoretical issues to the profit of the time-consuming practical and technological issues to be addressed as well. However, it was shown in many instances in this thesis that a careful electromagnetic theoretical approach is also required for an efficient design and optimized performances. It is also obvious that the V-CRLH-TL could not have been designed without the Bloch modeling approach employed, and that the performances of the reflectarray cell would not have been achieved without the setup of a very effective simulation method, which relied on the clear understanding of various theoretical concepts. A last and fundamental example of the necessity of a careful theoretical analysis of a MEMS device is linked with the major limitation of MEMS with regard to industrialization, namely, the precision and reliability of microwave MEMS. Indeed, the presented MEMS reflectarray cell was designed in order to alleviate the impact of the limited precision in the MEMS device on the electromagnetic performances.

In several instances, these theoretical contributions did not fully constitute new theoretical concepts, but rather consisted in revisiting or extending some existing theory in the light of our targets. It is however noticeable that several theoretical developments presented are not restricted to micromachined and MEMS devices, but could be of use for many other microwave designs. This is for instance the case of the multimode periodic theory, the interlaced bit topology for the reduction of the mismatch, the analysis and design of non-effectively homogeneous CRLH-TLs, or the requirements and modeling of reconfigurable reflectarray cells. Nevertheless, it is believed

that a main contribution of this thesis relies in the setup of a common approach to the design of different MEMS structures. Indeed, all presented designs relied on the completion of three main steps:

- Setup of efficient full-wave simulations of MEMS blocks.
- Development of physical, compact and accurate circuit models.
- Full-wave – circuit model hybrid design methods based on periodic structure Bloch wave modelling.

From a general perspective, the designed components exhibit very good simulated and measured performances, with the exception of the digital V-CRLH-TL, the poor measured results of which were clearly attributed to fabrication issues. Concerning the DMTL, the performances obtained were not as good as state-of-the-art. However, this is a consequence of the use of a standard silicon wafer rather than quartz, which is again linked to fabrication issues rather than modeling ones. Concerning the micromachined fixed CRLH-TLs, they are the first structures operating at such high frequencies, and the devices realized on quartz wafer shows excellent properties, as is also the case of the low-impedance demonstrator. Regarding now the MEMS V-CRLH-TLs, they are limited mainly by the insertion loss; it is however noticeable that it is likely that no better performances would be achieved using technologies other than MEMS at similar frequencies. In addition, the achieved losses could be significantly reduced by passivation of the silicon substrate or, preferably, the use of quartz wafers. However, the most performing structure of this thesis with regard to state-of-the-art is certainly the reflectarray cell; indeed, it exhibits excellent performances in comparison with similar MEMS reconfigurable reflectarray cell in the literature, as well as dramatic loss reduction with regard to other reconfigurability technologies used for that purpose.

10.3. Perspectives

Research on microwave MEMS such as done in this thesis and by other groups has recently confirmed that this technology outperforms other solutions, not only in the case of basic devices such as the MEMS switch, but also for more advanced applications such as metamaterials, filters, phase shifters or reconfigurable antennas. However, the picture is somewhat different regarding the commercialization of such products, since the only available device on the market today is the simplest MEMS microwave device, namely, a switch. The reason is probably linked to—in addition to the natural delay between research and industrialization—the issue of reliability and yield of MEMS fabrication. However, in the light of the aforementioned breakthrough in the potentialities and performances of reconfigurable microwave devices, it is believed that effort should be maintained to overcome theses difficulties so that more MEMS devices can be employed in real-life applications. In addition, it is clear that the trend towards higher frequency operation, for instance in imaging/sensing and communication applications, will further encourage MEMS solutions in the future. However, the issue of tolerances and reliability is also a concern of the electromagnetic designer of MEMS devices, since this one should also contribute to leverage the impact of the fabrication problems on the microwave performances.

Once these issues are solved, it is likely that MEMS will establish themselves as a standard technology for reconfigurable microwave designs, as is today the case of MMICs or diodes. However, one should distinguish here two possible approaches: in the first case, MEMS can be used as surface mount elements, in a similar way as diodes are employed in PCB circuits. However, a preferred approach for advanced designs is obviously to implement the whole microwave device in a monolithic MEMS process. In this case, some MEMS technology platforms should be made available to the designers. One of the key advantages of this approach is that it would be possible to freely design the MEMS themselves, rather than only the circuit they are part of, thereby achieving much better performances and versatility. However, such approach obviously requires particular knowledge of the designer with regard to the analysis and design of the MEMS structure itself. In this context, the methods presented in this thesis have proved to constitute an efficient way to achieve this goal, and could consequently be used for the design of a wide range of MEMS microwave or millimeter wave devices.

A. Appendix: Fabrication processes

A.1. Al-Si EPFL process

A.1.1. Introduction

Here we describe the fabrication process developed at the Center of MicroNanoTechnology (CMI) of EPFL to realize Aluminium-based MEMS devices on high-resistivity silicon wafer. This fabrication process was presented in [116] and is referred to here as the *Al-Si EPFL* process. It was employed for the design of the DMTLs of Chapter 4, as well as for some of the fixed CRLH-TLs presented in Chapter 6. In summary, this process involves 5 photolithographic steps and one chemical mechanical planarization (CMP) step. It has a low thermal budget, making it compatible with CMOS post-processing for *above-IC integration* of RF-MEMS devices.

A.1.2. Process description

Figure A.1 shows the complete fabrication process sequence for the *Al-Si EPFL* process. The MEMS structures are fabricated on 525 μm-thick high resistivity silicon substrates ($>$ 8 kΩcm), which are first thermally oxidized (500 nm-thick) [Figure A.1(a)-(b)]. A 1 μm or 1.5 μm-thick Al-Si (1%) layer (Metal1) is then deposited by sputtering [Figure A.1(c)] and patterned by dry etching in a standard Cl_2/BCl_3 gas mixture using a photoresist mask [Figure A.1(d)]. Then, a 200 nm-thick sputtered silicon dioxide layer is deposited at 200^o as an insulating layer [(Figure A.1(e)]. A 4 μm-thick amorphous silicon (a-Si) layer is then sputtered [Figure A.1(f)]. Prior to planarization, the a-Si layer is etched with continuous SF_6/C_4F_8 anisotropic process to have access to the alignment structures in Metal1 and to monitor the a-Si thickness during CMP (this step is not shown in Figure A.1). It is then planarized by CMP to a thickness that will determine the nominal gap of the suspended membranes (2 μm here) [Figure A.1(g)].

The a-Si sacrificial layer is now patterned by chlorine-based chemistry using a photoresist mask [Figure A.1(h)]. The second step is to pattern the mechanical anchors and the Metal1-to-Metal2 contacts [Figure A.1(i)]. The SiO_2 insulating layer plays the role of etch stop layer for the chlorine chemistry in this latter step. It is then etched at 0^o in carbon/fluorine plasma, which is selective to aluminum. A 2 μm or 4 μm-thick Al-Si (1%) structural layer (Metal 2) is deposited by sputtering [Figure A.1(j)] and patterned by dry etching in a standard Cl_2/BCl_3 gas mixture using a photoresist mask [Figure A.1(k)]. For wafers, which will be wafer-level packaged afterwards, annealing is done at 300^o for 20 min in N_2/H_2 forming gases. The aluminum membranes releasing is done in SF_6 plasma with a high selectivity to both SiO_2 and aluminum at room temperature

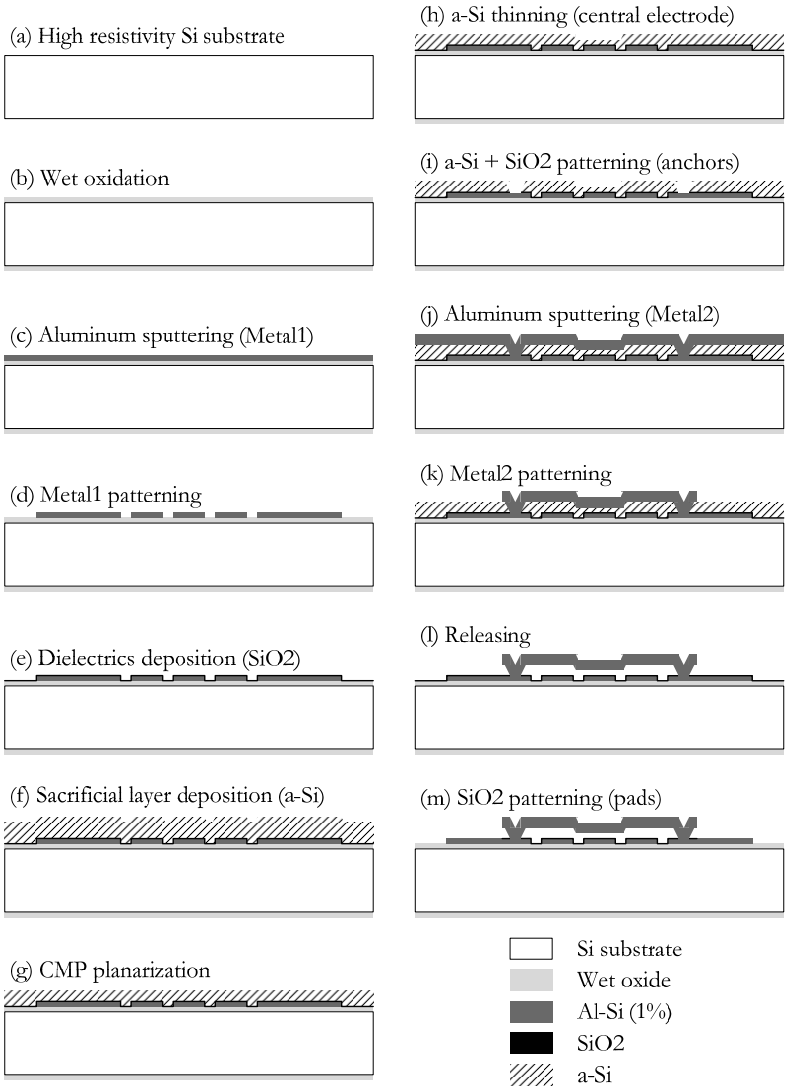

Figure A.1: Al-Si EPFL process complete fabrication sequence

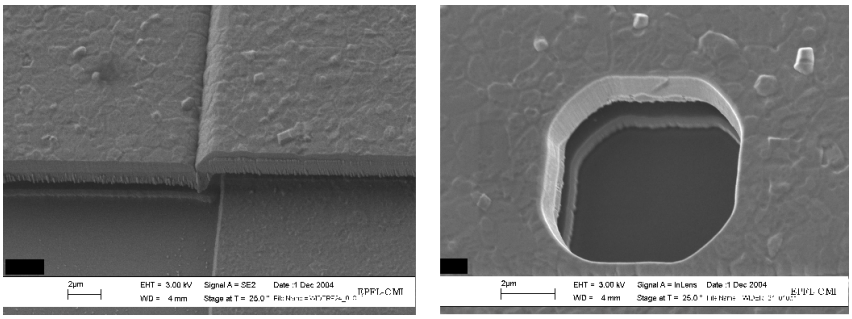

Figure A.2: SEM detail pictures of devices on the Al-Si EPFL process. (left: suspended Metal2 membrane over Metal1 step, right: etching hole in Metal2)

[Figure A.1(l)]. Finally, the SiO_2 insulating layer over Metal1 is etched in carbon/fluorine plasma where it is not covered by Metal2 [Figure A.1(m)], in order to reduce the losses as explained in Chapter 3.

Figure A.2 shows two close SEM views of particular details of DMTL bridges realized with this process. We also show here an example of profilometer measurements of an analog shunt capacitor loading a CPW realized on this process. In the case of the bridge shown here, a significant bending in the 'H cut' direction is observed (see Figure A.3), while the membrane over the central conductor of the CPW is very flat in the 'V cut' despite the large dimension of the suspended structure in that direction (about 600 μm).

A.2. Au-Si ISiT process

A.2.1. Introduction

Here we describe the fabrication process developed at the Franhofer Institute for Silicon technology (ISiT), Itzehoe, Germany, to realize gold-based MEMS devices on High-Resistivity silicon wafer [117]. This process was used for the realization of the analog and digital MEMS CRLH-TLs presented in Chapter 7, in the framework of a multi-project run launched within the AMICOM European network of excellence.

A.2.2. Process description

This process is based on high-resistivity silicon wafers ($> 3k\Omega cm$) with an insulator oxide of 2 μm. Figure A.4 shows the different process step for this *Au-Si ISiT* process, which are described as follows:

1. Lithography (UPATH) and fabrication of a Ti/ Pt/ Au/ Pt underpath by lift-off.
2. Deposition of the first dielectric layer (300 nm PECVD nitride), lithography (PASS 1) and RIE. Deposition of the second dielectric layer (300 nm AlN or PECVD nitride) and lithography (PASS 2) and structuring by wet etching or RIE.
3. Deposition of a Ti/Cu plating base and electroplating of the sacrificial Cu layer (4500 nm).
4. Polishing of the sacrificial Cu layer and correction to a final thickness of about 3 μm (by sputtering of Cu). Evaporation of the 900 nm thick Au/Ni/Au or 850 nm thick Ni membrane. Lithography (BRIDGE) and structuring by ion-milling.
5. Lithography (OS 1) and wet etching of the sacrificial Cu. Deposition of a Ti/Au plating base layer. Lithography (LINES) and electroplating of the Au lines (about 2 μm thick).
6. Lithography (SPRING) and electroplating of the Ni anchoring and, if required, the stiffening bars on the membrane (about 15 μm thick). Removal of the oxide from the back side of the substrate (optional).
7. Removal of the Ti/Au plating base by wet etching and wet etching of the Ti/Cu sacrificial layer and rinsing with isopropanol. Supercritical drying and annealing at 350^o under vacuum.

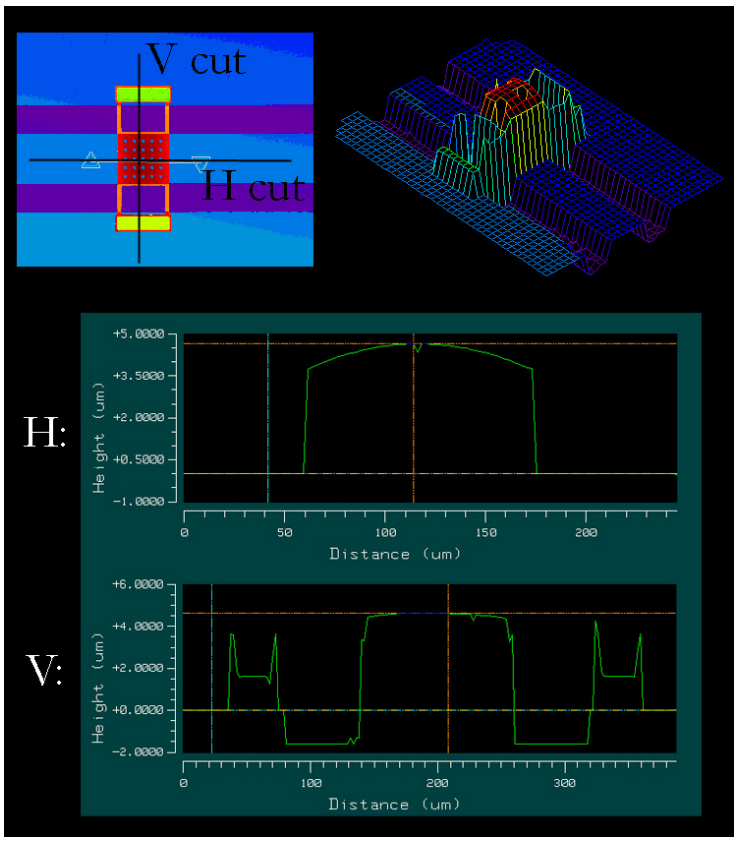

Figure A.3: Measured profile of an analog shunt capacitor loading a CPW.

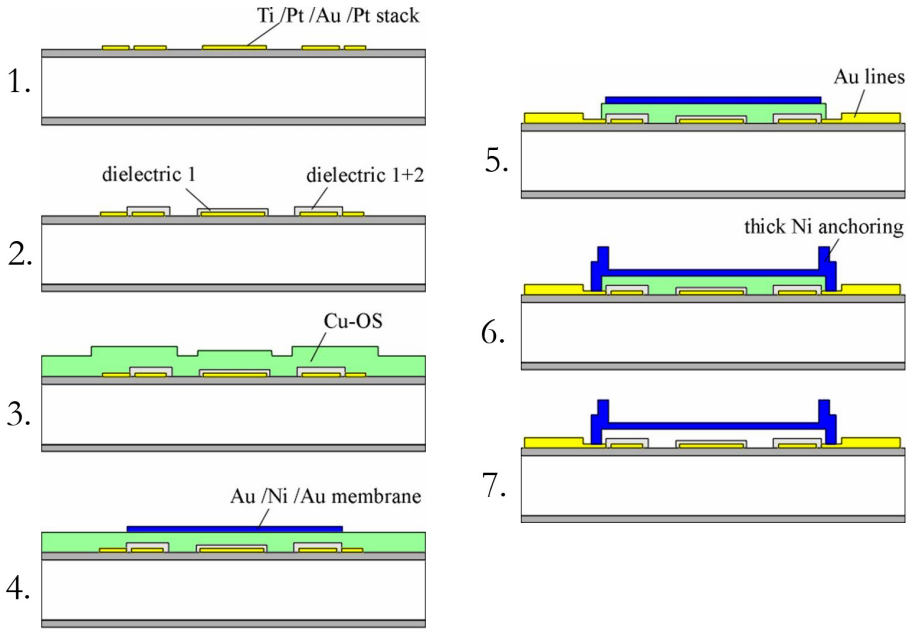

Figure A.4: *Au-Si ISiT* process fabrication sequence.

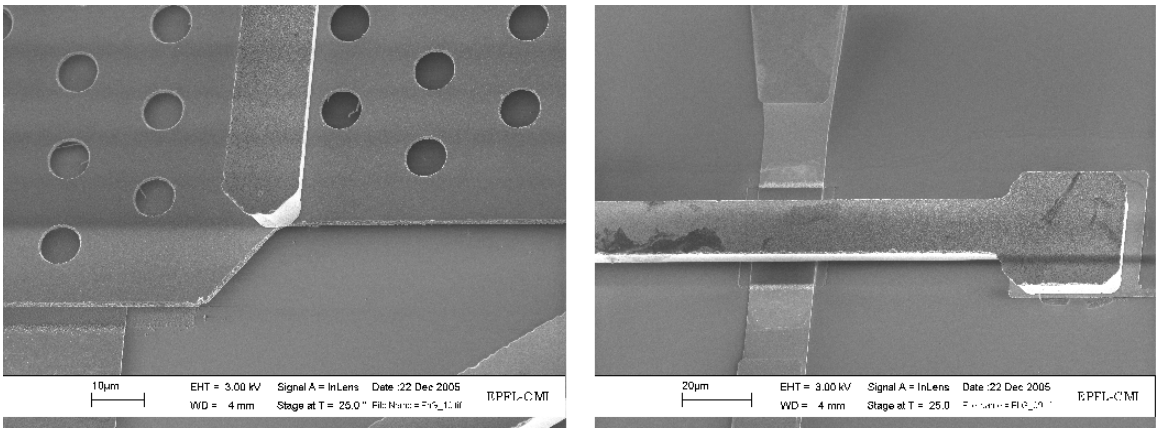

Figure A.5: SEM detail pictures of devices on the *Au-Si ISiT* process.

Table A.1 lists the 7 standard lithography layers available for this process in more detail, along with some material properties. Finally, Figure A.5 shows some SEM views of particular details of the MEMS CRLH-TLs realized with this process.

A.3. Al-Quartz VTT process

A.3.1. Introduction

This section describes the fabrication process developed at VTT-Millilab, Finland, to realize Aluminum-based MEMS devices on fused silica quartz wafer [110]. It also provides high resistance bias lines, which was not the case of the previous *Al-Si EPFL* and *Au-Si ISiT* processes. The *Al-Quartz VTT* process was used for the realization of the monolithic MEMS reflectarray cells presented in Chapter 9. This fabrication was made possible in the framework of a multi-project run launched within the AMICOM European network of excellence.

A.3.2. Process description

Figure A.5 summarizes the main steps of the *Al-quartz VTT* fabrication process and Table A.2 describes the resulting layers. The process is based on fused silica substrates with a permittivity of 3.8. High resistivity bias lines (about 1 kΩ/square) are made of polysilicon and are used in order to prevent coupling between RF signal and biasing circuits. The bottom electrodes of MEMS structures are made of Gold or Aluminium/Molybdenum (500 nm). Plasma enhanced chemical vapor deposited (PECVD) silicon oxide (200 nm) is used as the dielectric layer. A 1100-1200 nm photoresist is then deposited to serve as sacrificial layer. It is possible to use two sacrificial layers to get about 2400 nm total thickness. Sputtered aluminium (1500 nm) is then used as the structural layer. As the last step, the sacrificial layer is removed in oxygen plasma without the need of critical point drying.

Layer	Object	Material	Structuring	Properties
UPATH	underpath metallization	evaporated Ta/Pt/Au/Pt	lift-off with resist mask	$<$ 0.10 Ω/sq
PASS 1	additional dielectric on the act. electrodes	PECVD Si_3N_4	RIE	300 nm, $\varepsilon = 7.5$
PASS 2	dielectric in the active area	sputtered AlN	wet etching	300 nm, $\varepsilon = 10$
OS 1	main sacrificial layer	electroplated Cu	wet etching	$\sim$ 3 μm (after CMP)
LINES	lines and interconnections	electroplated Au		$\sim$ 3 μm
BRIDGE	movable membrane	evap. stack Au/Ni/Au	ion-beam etching	900 nm, $\sim$ 0.06 Ω/sq, $\sim$ 5e8 Pa stress
SPRING	anchoring structures and stiffening bars	electroplated Ni		$\sim$ 16 μm, $\sim$ 0 stress

Table A.1: *Au-Si ISiT* process layers.

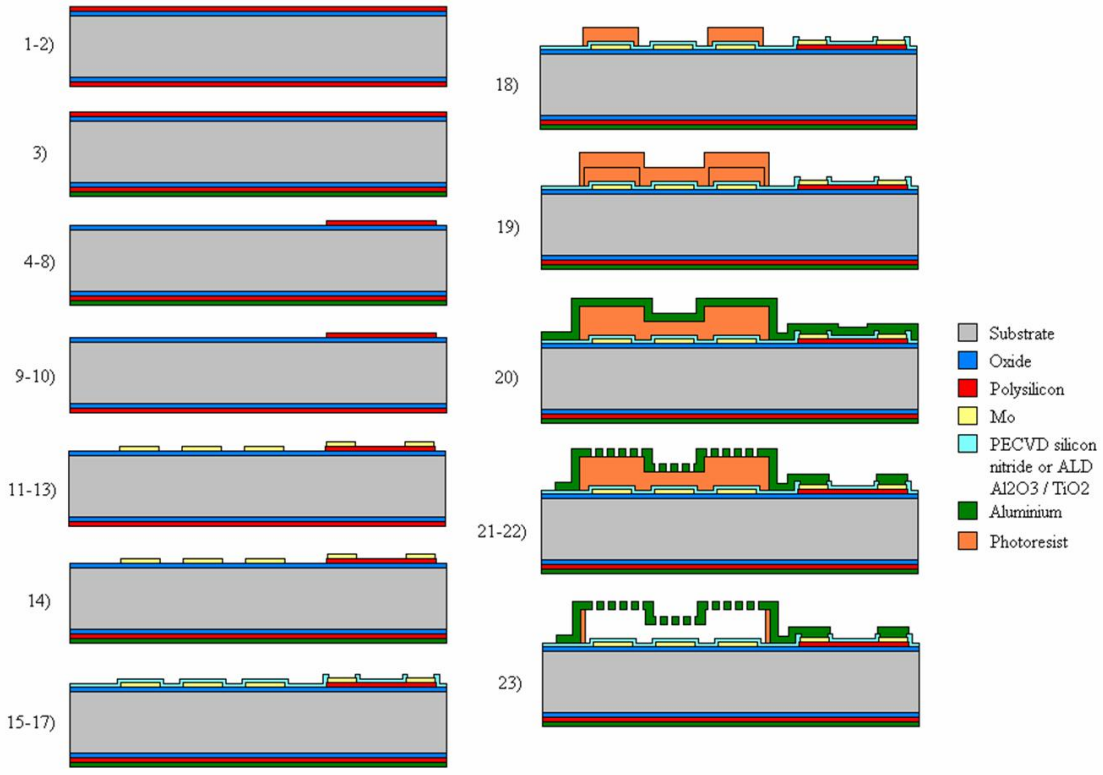

Figure A.6: *Al-quartz VTT* process fabrication sequence.

	Name	Material	(Default) function	Thickness	Sheet resistance
1	bias	Polysilicon	Bias lines	500 nm	$> 1000\ \Omega$
2	cont	(Ion implantation)	Doping for polySi-metal contact	-	$70\ \Omega$
3	met1	Au	Metal layer	500 nm	-
4	diel	PECVD Si-N	Dielectric layer	200 nm	-
5	sacr1	Photoresist	Sacrificial layer	1100-1200 nm	Insulator
6	sacr2	Photoresist	Sacrificial layer	1100-1200 nm	Insulator
7	bridge	Aluminium	Structural layer	1500 nm	$< 0.03\ \Omega$

Table A.2: *Al-quartz VTT* process fabrication sequence.

A.4. Al-Quartz EPFL process

In contrast with the three processes presented above, the *Al-Quartz EPFL* process is not a MEMS process but a very simple micromachining one for non-controllable circuits. This process was employed for the realization of most of the micromachined CRLH-TLs demonstrators of Chapter 6.

It mainly consists in a lithography of aluminum on fused silica quartz wafers. First, the 1.5μm-thick, pure Al layer is deposited on the wafer by sputtering at room temperature. Some amorphous Si was temporarily deposited on the back of the wafer for clamping the quartz substrate and the Al is dry etched. Since some bridges were needed in the designs to realize shunt inductances in the CPWs, precision gold wirebonding was employed as a last step of the fabrication.

A. Appendix: MEMS biasing, actuation, and power handling

A.1. Preliminary considerations

A.1.1. Introduction

In this thesis, it was decided to put limited effort into electromechanical aspects of MEMS, to the profit of electromagnetic considerations; in the various demonstrators presented, electromechanical issues, and in particular the actuation voltage of MEMS devices, were approximated by simple formulas or by appropriate 'scaling' strategies using measured actuation voltages in conjunction with analytical formulas [7]. These calculations were done in the sole goal of obtaining functioning devices with reasonable actuation voltages and was not reported in the present document. Indeed, due to the complexity of electromechanical modeling of MEMS structures taking into account complex but non-negligible material stress as well as charging effects, the electromechanical modeling of MEMS devices is a research topic of its own. In this context, there is sustained effort in the MEMS community to address this issue and related information can be found for instance in [7, 118, 119].

Nevertheless, we will address here some electromechanical issues in a way that useful information can be obtained without considering mechanical aspects in detail. As will be shown below, the power handling capability of a microwave device based on MEMS is directly linked to electromechanical aspects, and more particularly to the actuation voltage and the topology employed for the biasing of the MEMS. Therefore, we will deduce in this section, working on an electric circuit level, the relation between MEMS *biasing topologies*, *actuation voltage* and *power handling*.

A.1.2. Network analyzer and T-bias

Before dealing with biasing and power issues, we recall how RF and DC signals are decoupled in a network analyzer when T-bias are connected to both its ports. Figure A.1 shows the basic schematic of the network analyzer with its device under test. We see that the low pass filter constituted by the T-bias helps not short-circuiting the RF signal. The remaining influence of this DC access on the RF signal is removed by calibration since the T-bias are also connected during calibration. From the DC point of view, the capacitances are open-circuits, which results in a direct transmission of the DC voltage at the ports of the network analyzer, provided that the other terminal of the DC source is grounded.

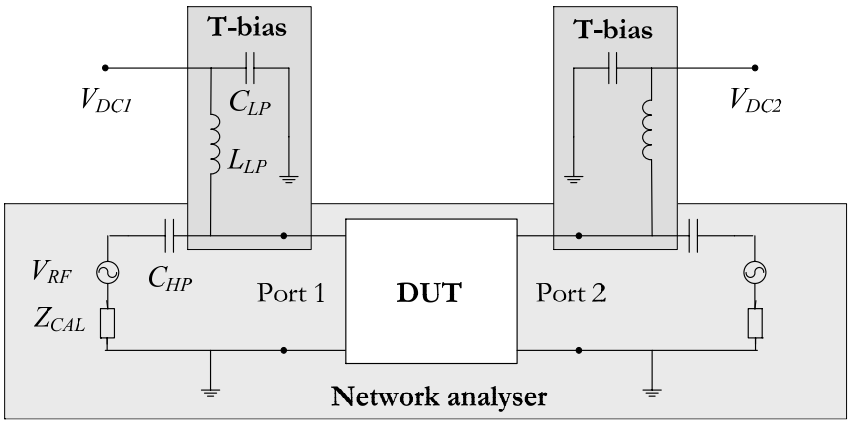

Figure A.1: Schematic of the network analyzer, including T-bias, with its device under test (DUT).

A.1.3. Parallel plate capacitance electrostatic force

Although there exist different geometries for the actuation part of a MEMS, the most common by far, which is also the only one employed in this thesis, simply consists of two parallel plates. In general, one of the plates is fixed while the other is mobile and can thus be actuated by an electrostatic force resulting from a voltage applied between the plates. An electrostatic parallel plate capacitor model can be used to account for this force since the gap g between plates is always much smaller that the longitudinal dimensions of the capacitor. Moreover, the fringe effects can be taken into account in the computation of an effective plate surface A. So, using the definition of the electric energy density w_E, the total energy W_E between the plates of surface A and distant from g, as a function of the voltage applied V, is given by:

$$w_E = \frac{1}{2}\varepsilon E^2 = \frac{1}{2}\varepsilon\left(\frac{V}{g}\right)^2 \quad \rightarrow \quad W_E = Agw_E = \frac{1}{2}\frac{\varepsilon A V^2}{g} \tag{A.1}$$

and the force between plates is:

$$F = \frac{\partial W_E}{\partial g} = (-)\,\frac{1}{2}\frac{\varepsilon A V^2}{g^2} \tag{A.2}$$

The minus sign is not important as we know that the force is always an attractive force between electrodes, regardless of the voltage polarity (no net charge in the capacitor). We can also write this last expression as a function of the capacitance C and we finally obtain the force as a function of the capacitance and voltage at the terminals of the capacitance:

$$F = \frac{1}{2}\frac{C}{g}V^2 \tag{A.3}$$

A.2. Basic topologies analysis

In this section, we study 4 different MEMS and actuation topologies to deduce relevant information about the actuation voltage and power handling.

A.2.1. Case 1: single capacitor, direct actuation

We call *direct actuation* the situation where the DC voltage actuation of the MEMS is directly applied at the RF ports. This is straightforwardly done by means of T-bias, as shown in the circuit of Figure A.1. If we analyze the resulting circuit [see Figure A.2(a)] by means of the superposition principle, and consider the low-pass filter to be ideal, we obtain:

$$V_M(t) = V_{DC} + V_{RF}(t) \tag{A.4}$$

The instantaneous electrostatic force (A.3) between the parallel plates of the capacitance C_M is here:

$$F_{Case1}(t) = \frac{1}{2}\frac{C_M}{g}V_M^2(t) \tag{A.5}$$

We calculate the square of the total voltage (A.4) and with the definition of the RMS voltage $V_{RF,rms}$ according to $V_{RF}(t) = V_{RF,rms}\sqrt{2}(\sin\omega t)$, we obtain:

$$V_M^2(t) = V_{DC}^2 + V_{RF,rms}^2 + 2\sqrt{2}V_{DC}V_{RF,rms}(\sin\omega t) - V_{RF,rms}^2(\cos 2\omega t) \tag{A.6}$$

So the total force (A.5) is:

$$F_{Case1}(t) = \frac{1}{2}\frac{C_M}{g}\left[V_{DC}^2 + V_{RF,rms}^2 + 2\sqrt{2}V_{DC}V_{RF,rms}(\sin\omega t) - V_{RF,rms}^2(\cos 2\omega t)\right] \tag{A.7}$$

The two last terms in (A.7) are alternative forces at the frequency (and twice the frequency) of the RF signal. These frequencies are well above the mechanical resonances of typical MEMS devices and the corresponding terms need not be considered when calculating the displacement of the bridge. The resulting force is thus time independent and we have:

$$F_{Case1} = \frac{1}{2}\frac{C_M}{g}\left[V_{DC}^2 + V_{RF,rms}^2\right] \tag{A.8}$$

This result is fundamental in the sense that it shows that *the RF signal yields a DC component in the total force between plates*, which is the principal cause of the power handling limitations of MEMS devices. A numerical example linked with this issue is presented below.

A.2.2. Case 2: double capacitor, direct actuation

The structure studied here is referred to as a *double* capacitor and only differs from the previous case by the addition of a total *fixed* capacitance C_L in series with the variable one C_M. This situation is illustrated in Figure A.2(b), where the capacitance C_L is actually implemented using two capacitors $2C_L$ in parallel, and corresponds to the digital shunt MEMS capacitor on CPW presented in Chapter 3. The voltage at the ports of the variable capacitance C_M is now:

$$V_M(t) = \left(\frac{C_L}{C_M + C_L}\right)\left[V_{DC} + V_{RF}(t)\right] \tag{A.9}$$

and the force is:

$$F(t) = \frac{1}{2}\frac{C_M}{g}V_M^2(t) \tag{A.10}$$

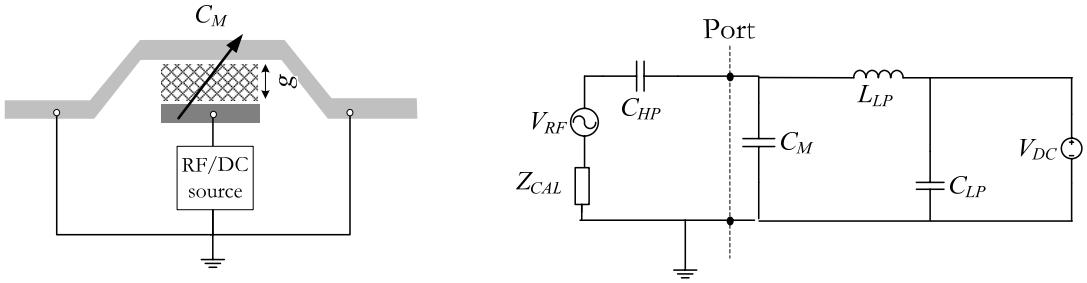

(a) Case 1: single capacitor, direct actuation.

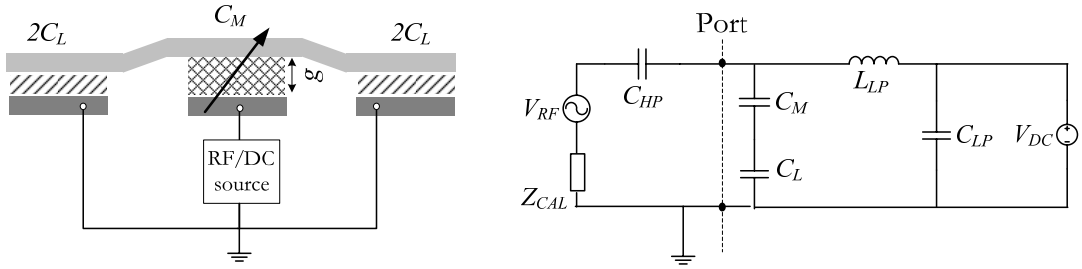

(b) Case 2: double capacitor, direct actuation.

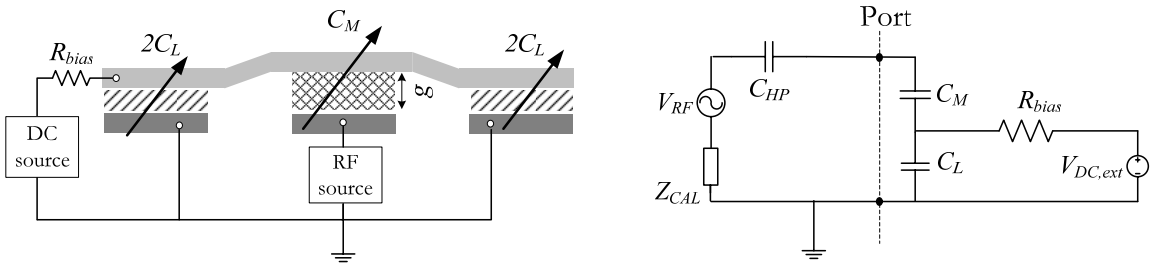

(c) Case 3: double capacitor (variable 2nd capacitor), separate actuation.

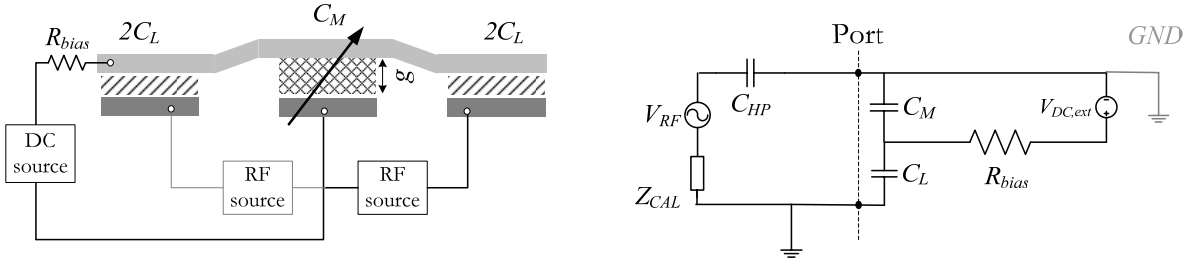

(d) Case 4: double capacitor (fix 2nd capacitor), separate actuation.

Figure A.2: Different capacitor structures and actuation strategies studied.

With a calculation similar to the previous case, we find:

$$F_{Case2} = \frac{1}{2}\frac{C_M}{g}\left(\frac{C_L}{C_M + C_L}\right)^2 \left[V_{DC}^2 + V_{RF,rms}^2\right] \tag{A.11}$$

If we compare this expression to the one obtained for the single capacitor, given in (A.8), we observe that:

- The DC actuation voltage must be increased of $(C_M + C_L)^2 / C_L^2$ in order to produce the same force on bridge.
- The relative effect of V_{RF} and V_{DC} on the force remains the same as in the single case. This is due to the fact that both voltages are reduced by the same factor at the terminals of the variable capacitor.

A.2.3. Case 3: double capacitor (variable 2nd capacitor), separate actuation

In general, it is also possible to apply the actuation voltage by means of separate feeds from the RF access, as shown in Figure A.2(c). In this case, the most efficient solution to avoid detrimental effects of the DC bias circuit on the RF performances is to place high resistances in the DC signal path and close to the RF circuit (for instance by plating narrow line with a material of high resistivity), which act as open circuits for the RF signal while allowing driving the DC voltage to the electrodes.

This structure was proposed in [120] but its analysis in terms of power handling capabilities presented suffers inaccuracy and would even prove to be erroneous for other geometries than the one studied (see details below). However, we will see here that this problem can be addressed very simply by the circuit approach proposed. First, let us write the voltages V_M and V_L applied to the two capacitances C_M and C_L:

$$V_M(t) = V_{RF}(t)\frac{C_L}{C_M + C_L} \tag{A.12}$$

$$V_L(t) = V_{DC} + V_{RF}(t)\frac{C_M}{C_M + C_L} \tag{A.13}$$

As shown before, the forces for each capacitance write:

$$F_M(t) = \frac{1}{2}\frac{C_M}{g}V_M^2(t) \tag{A.14}$$

$$F_L(t) = \frac{1}{2}\frac{C_L}{g}V_L^2(t) \tag{A.15}$$

We now write the squares of the voltages using again the notation $V_{RF}(t) = V_{RF,rms}\sqrt{2}(\sin\omega t)$, and neglecting again the alternative terms for the reason previously explained, we obtain:

$$V_M^2 = \left(\frac{C_L}{C_M + C_L}\right)^2 V_{RF,rms}^2 \tag{A.16}$$

$$V_L^2 = V_{DC}^2 + \left(\frac{C_M}{C_M + C_L}\right)^2 V_{RF,rms}^2 \tag{A.17}$$

The two forces are parallel and directed in the same direction. Therefore, the resulting force on the plate is easily obtained and we find after some simplifications:

$$F_{Case3} = F_M + F_L = \frac{1}{2}\frac{C_L}{g}\left[V_{DC}^2 + \left(\frac{C_M}{C_M + C_L}\right) V_{RF,rms}^2\right] \tag{A.18}$$

a. Comparison with the 'direct actuation' (case 1)

Following the choice made in [120], so as to appropriately compare our results with this reference, we decide to compare both situations case 1 and case 3 *with* C_M *constant*. This means that, for a same RF power, the actuation DC voltages are linked as follows [this expression is deduced from (A.8) and (A.18)]:

$$V_{DC,Case3} = \sqrt{\frac{C_M}{C_L}}\sqrt{V_{DC,Case1}^2 + \left(\frac{C_M}{C_M + C_L}\right) V_{RF,rms}^2} \tag{A.19}$$

We will now comment these results with regard to the observations made in [120] on this capacitor topology. Expression (9) of [120] means that the RF force on the bridge is well approximated by the force due to the capacitance C_M only. However, (2.42) shows that the force is actually related to the capacitance $C_M C_L/(C_M + C_L)$ and the result given in [120] thus only holds true when $C_L \gg C_M$. As in the particular case studied in [120], $C_L \approx 8C_M$, the condition $C_L \gg C_M$ is roughly satisfied and the error is not detected (it is also mingled with the uncertainty in the capacitances values).

When discussing the advantage of this improved switch over a 'direct' actuated switch, [120] states that "the actuation voltage is reduced by a factor of $\sqrt{8}$ for a given maximum RF power" [n.b.: The $\sqrt{8}$ figure actually stands for $\sqrt{C_L/C_M}$ in (A.19)]. However, looking at (A.19), we observe that this observation is only true if no RF power is transmitted (or if it is low enough to result in a negligible actuation force).

A.2.4. Case 4: double capacitor (fixed 2nd capacitor), separate actuation

If the lateral capacitors are fixed, the above feeding configuration is obsolete since no actuation occurs, as the DC voltage is only applied to the fixed capacitors. Consequently, the bias voltage source must be connected between the terminals of C_M, as depicted in Figure A.2(d). This source can be floating, but we can also ground it by means of the connections GND in the figure. If we do so, one terminal of C_M is DC grounded and the DC source sees the capacitances C_M and C_L connected in *parallel*. In this case only the force related to the capacitance C_M actuates the bridge:

$$F_M(t) = \frac{1}{2}\frac{C_M}{g} V_M^2(t) \tag{A.20}$$

where the voltage V_M is:

$$V_M(t) = V_{DC} + V_{RF}(t)\frac{C_L}{C_M + C_L} \tag{A.21}$$

which yields:

$$F_{Case4} = \frac{1}{2}\frac{C_M}{g}\left[V_{DC}^2 + \left(\frac{C_L}{C_M + C_L}\right)^2 V_{RF,rms}^2\right] \tag{A.22}$$

Again, we compare this expression to the one obtained for the 'direct actuation case' (case 2) written in a suitable form:

$$F_{Case2} = \frac{1}{2}\frac{C_M}{g}\left[\left(\frac{C_L}{C_M + C_L}\right)^2 V_{DC}^2 + \left(\frac{C_L}{C_M + C_L}\right)^2 V_{RF,rms}^2\right] \tag{A.23}$$

and observe that the relative effect of the RF power on the actuation is reduced by a factor $(C_M + C_L)^2 \Big/ C_L^2$ as a result of the decoupling of the actuation voltage from the RF signal. Consequently, when choosing values for C_L and C_M in a such a design, one should keep in mind the impact on the power handling of this structure, which is determined by the factor $(C_M + C_L)^2 \Big/ C_L^2$. Finally, we also observe that the actuation voltage does not need now be increased when compared to the single case (case 1).

A.3. Examples and remarks

Formulas (A.8), (A.11), (A.18) and (A.22) express the force on the MEMS membrane in 4 possible configurations as a function of DC voltage and RF power. This allows carrying out calculations for a given topology about the actuation with RF power taken into account, or to compare two topologies, for instance, from a power handling point of view for the same actuation voltage and with the same overall capacitances in 'Up' and 'Down' states. In this section, we present some calculation example and remarks resulting from the developments presented in this appendix.

A.3.1. RF power and single capacitor (case 1)

We saw that in case 1 above, the attraction force is related to an *equivalent DC* voltage defined as follows:

$$V_{equ} = \sqrt{V_{DC}^2 + V_{RF,rms}^2} \tag{A.24}$$

The relation between *incident* RF power and voltage in a line of characteristic impedance Z_0 is:

$$P_{RF,inc} = \frac{V_{RF,rms,inc}^2}{Z_0} = \frac{V_{RF,rms}^2}{(1+\rho)\,Z_0} \tag{A.25}$$

where ρ is the reflection coefficient due to the obstacle, which accounts for the fact that the tension V_{RF} is the superposition of incident and reflected voltage, the incident power being directly linked to the incident voltage only. These last two equations allow taking the RF signal effect into account in the electromechanical static modeling of the bridge. If we plot the equivalent RMS tension for a line of 50 Ω characteristic impedance as done in Figure A.3, we can for instance observe that an RF power of 100 mW will induce a force on the bridge which is equivalent to the one obtained with a DC actuation voltage of 2 V and no RF power (for the sake of simplicity, $\rho = 0$ is considered in the example, which approximately correspond to the reflection coefficient of a shunt capacitor

in the 'Up' state). This characterizes the non-linearity of the device with regard to RF power. In contrast, the equivalent voltage decreases when the power is reduced and we can neglect the effect of the RF power when this power is less than about 10 mW. In general and in order to make appropriate assumptions and calculations in the design, an assessment of the *relative* importance of the two following parameters must be made:

- RF power handling requirement in the target application.
- DC actuation voltage chosen for the design.

In other words, the lower the actuation voltage of a parallel capacitor on CPW, the more limited the power handling of the MEMS. Depending on the priorities in the design, the best topology can be chosen using the results presented in this appendix.

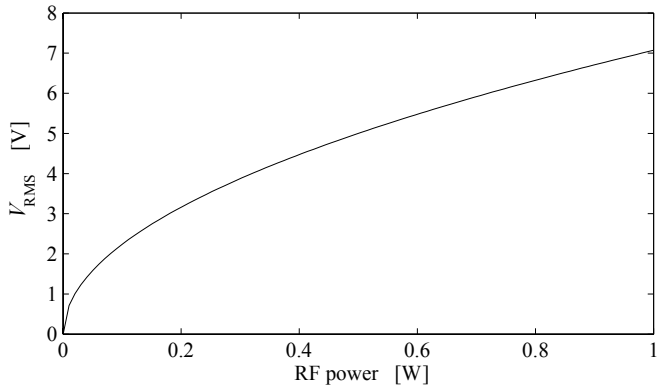

Figure A.3: Equivalent actuation voltage as a function of RF power for a 50 Ω line.

A.3.2. Stiction

In the 'Down' state, one of the capacitance plate is pulled-in to the other (in practice it is stuck to the thin insulator layer between the conductors), which means that the pull-in actuation voltage has been reached. In this particular case, the contribution of the RF power to the actuation force will obviously not influence the position of the bridge. However, another problem might happen in this case, which has been addressed in [119] and called stiction (or latching). In brief, stiction might occur in the case of a switching from the 'Down' to the 'Up' state when the RF power is maintained during switching ('hot' switching). Just after the switching, the equivalent voltage is only due to the RF voltage since V_{DC} is switched to zero but the membrane is still in its 'Down' position. If the equivalent actuation voltage due to the RF power is large enough, the membrane will remain in the 'Down' position, causing a failure of the device. In practice, the condition for stiction in any of the four cases presented can be simply deduced from the results provided since the pulled-in capacitances values are known and that the DC voltage is simply zero in this case.

A.3.3. Intermodulation

We calculated the capabilities in terms of power handling versus actuation voltage and thus neglected alternative terms in the total force on the membrane. Nevertheless, these terms actually translate into intermodulation effects, which are out of the scope of this appendix. However, this issue is treated in [119]. From a general point of view, it is noticeable that intermodulation effects are much smaller in MEMS devices than in their solid state counterparts [98, 119].

List of Acronyms

BW bandwidth

CMP chemical mechanical planarization

CPW coplanar waveguide

CRLH-TL composite right/left handed transmission line

CSRR complementary split ring resonator

DMTL distributed MEMS transmission line

EM electromagnetic

FEM finite elements method

FET field effect transistor

FSS frequency selective surface

GL grating lobe

IRL input return loss

LTCC low temperature co-fired ceramics

LWA leaky wave antenna

MAM metal-air-metal

M-CGDS MEMS constant group delay shifter

M-CPS MEMS constant-phase shifter

MEMS MicroElectroMechanical Systems

MIM metal-insulator-metal

MMIC monolithic microwave integrated circuit

MoM method of moments

PBC periodic boundary condition

PBC-WG periodic boundary conditions waveguide

PCB printed circuit board

PEC perfect electric conductor

PECPMC-WG perfect electric/magnetic conductor waveguide

PMC perfect magnetic conductor

QWT quarter-wavelength transformer

RA reflectarrays

RF radio frequency

RWG rectangular waveguide

RWG-IAS rectangular waveguide infinite array simulator

SEM scanning electron microscope

SMT surface-mount technology

SRR split ring resonator

TEM transverse electromagnetic

TL transmission line

TRL through-reflect-line

TTD true-time delay

TTDL true-time delay line

UWB ultra wideband

V-CRLH-TL composite right/left handed transmission line

V-TTDL variable true-time delay line

Bibliography

[1] http://www.allaboutmems.com/.

[2] Yole-Développement, "Status of the MEMS industry report," *http://www.yole.fr*, 2007.

[3] S. Lucyszyn, "Review of radio frequency microelectromechanical systems technology," *Proc. IEE Science, Measurement and Technology*, vol. 151, no. 2, pp. 93–103, March 2004.

[4] Y.-W. Lin, S. Lee, S.-S. Li, Y. Xie, Z. Ren, and C.-C. Nguyen, "Series-resonant VHF micromechanical resonator reference oscillators," *IEEE Journal of Solid-state Circuits*, vol. 39, no. 12, pp. 2477 – 2491, Dec. 2004.

[5] A. El-Fatatry, B. Knoblich, F. Coccetti, H. Tilmans, and J. Bouchaud, "EU position in RF MEMS," *Deliverable D3.2 of EU project ARRRO: Applied Research Roadmap for RF micro/nano systems Opportunities (www.amicom.info/arrro)*, 2007.

[6] O. Vendier, M. Paillard, H. Legay, C. Schaffauser, S. Forrestier, G. Caille, C. Drevon, and J. Cazaux, "Main achievements to date toward the use of RF MEMS into space satellite payloads," in *European Gallium Arsenide and Other Semiconductor Application Symposium (EGAAS 2005)*, 2005, pp. 285–288.

[7] G. Rebeiz, *RF MEMS, theory, design and technology*, ser. Wiley-Interscience. New York: John Wiley and Sons, Inc., 2003.

[8] J. Laskar, S. Pinel, D. Dawn, S. Sarkar, B. Perumana, and P. Sen, "The next wireless wave is a millimeter wave," *IEEE Microw. Magazine*, vol. 50, no. 8, pp. 22–32, Aug. 2007.

[9] "WIDE-RF: Innovative MEMS for wideband reconfigurable RF microsystems." *European Union framework program FP6, Information and communication technology (ICT) project, http://www-g.eng.cam.ac.uk/epec/WIDERF/default.htm.*

[10] "NanoTIMER: Nanotechnology in mechanical-electrical resonators," *European Union framework program FP6, Information and communication technology (ICT) project, http://www.hitech-projects.com/euprojects/nanotimer/index.htm.*

[11] "AMICOM: European network of excellence on RF MEMS and RF microsystems." *European Union framework program FP6, Information and communication technology (ICT) Network of Excellence, http://www.amicom.info/.*

[12] "RARPA: Reflectarrays and reconfigurable printed antennas." *European Union framework program FP6, Information and communication technology (ICT), North Star project within the AMICOM Network of Excellence, http://www.amicom.info/.*

[13] R. Collin, *Foundations for microwave engineering, 2nd Edition.* New-York: McGraw-Hill, 1992.

[14] D. Pozar, *Microwave engineering.* Reading, MA: Addison-Wesley, 1990.

[15] D. R. Smith, S. Schultz, P. Markov, and C. M. Soukoulis, "Determination of effective permittivity and permeability of metamaterials from reflection and transmission coefficients," *Phys. Rev. B 65*, p. 195104, 2002.

[16] F. Gardiol, *Electromagnétisme, Traité d'électricité.* Lausanne: Presses Polytechniques et Universitaires Romandes, 1999.

[17] J. Li, "Novel filter using composite right/left-handed transmission line," *Microw. and Optical Tech. Lett.*, vol. 48, no. 10, pp. 2013–2015, Oct. 2006.

[18] A. Nagra and R. York, "Distributed analog phase shifters with low insertion loss," *IEEE Trans. Microwave Theory Tech.*, vol. 47, no. 9, pp. 1705 – 1711, Sept. 1999.

[19] R. Collin, *Field theory of guided waves, 2nd Edition.* IEEE Press, 1991.

[20] J. Jackson, *Classical Electrodynamics, third Edition.* New-York: John Wiley and Sons, Inc., 1999.

[21] O. Siddiqui, M. Mojahedi, and G. Eleftheriades, "Periodically loaded transmission line with effective negative refractive index and negative group velocity," *IEEE Trans. Antennas and Propagat.*, vol. 51, no. 10, pp. 2619 – 2625, Oct. 2003.

[22] E. L. Bolda, R. Y. Chiao, and J. C. Garrison, "Two theorems for the group velocity in dispersive media," *Phys. Rev. A 48*, pp. 3890 – 3894, Nov. 1993.

[23] D. Mercier, J.-C. Orlianges, T. Delage, C. Champeaux, A. Catherinot, D. Cros, and P. Blondy, "Millimeter-wave tune-all bandpass filters," *IEEE Trans. Microwave Theory Tech.*, vol. 52, no. 4, pp. 1175 – 1181, April 2004.

[24] T. Vaha-Heikkila and G. M. Rebeiz, "A 4-18-GHz reconfigurable RF MEMS matching network for power amplifier applications," *Int. Journal of RF and Microw. Computer-Aided Engineering*, vol. 14, no. 4, pp. 356 – 372, June 2004.

[25] K. Michalski and J. Mosig, "Multilayered media green's functions in integral equation formulations," *IEEE Trans. Antennas and Propagat.*, vol. 45, no. 3, pp. 508–519, March 1997.

[26] Agilent-Technologies, "Product note 8510-8a, Agilent network analysis, applying the 8510 TRL calibration for non-coaxial measurements."

[27] R. Marks and D. Williams, "Characteristic impedance determination using propagation constant measurement," *IEEE Microwave Guided Wave Lett.*, vol. 1, no. 6, pp. 141 – 143, June 1991.

[28] Y. Wu, S. Gamble, B. Armstrong, V. Fusco, and J. Stewart, "SiO2 interface layer effects on microwave loss of high-resistivity CPW line," *IEEE Microwave and Guided Wave Lett.*, vol. 9, no. 1, pp. 10–12, Jan. 1999.

[29] M. Spirito, F. De Paola, L. Nanver, E. Valletta, B. Rong, B. Rejaei, L. de Vreede, and J. Burghartz, "Surface-passivated high-resistivity silicon as a true microwave substrate," *IEEE Trans. Microwave Theory Tech.*, vol. 53, no. 7, pp. 2340 – 2347, July 2005.

[30] N. Barker and G. Rebeiz, "Distributed MEMS true-time delay phase shifters and wide-band switches," *IEEE Trans. Microwave Theory Tech.*, vol. 46, no. 11, pp. 1881–1890, Nov. 1998.

[31] J.-J. Hung, L. Dussopt, and G. Rebeiz, "Distributed 2- and 3-bit W-band MEMS phase shifters on glass substrates," *IEEE Trans. Microwave Theory Tech.*, vol. 52, no. 2, pp. 600–606, Feb. 2002.

[32] K. Topalli, M. Unlu, H. Sagkol, S. Demir, O. Civi, S. Koc, and T. Akin, "A new model for distributed MEMS transmission lines," in *Antennas and Propagation Society Symposium. IEEE*, vol. 3, 20-25 June 2004, pp. 2855 – 2858.

[33] R. Simons, *Waveguide circuits, components, and systems*, ser. Wiley-Interscience. New York: John Wiley and Sons, Inc., 2001.

[34] J. Hayden and G. Rebeiz, "Low-loss cascadable MEMS distributed X-band phase shifters," *IEEE Microwave and Guided Wave Letters*, vol. 10, no. 4, pp. 142–144, April 2000.

[35] K. Hettak, T. Laneve, and M. Stubbs, "Size-reduction techniques for CPW and ACPS structures," *IEEE Trans. Microwave Theory Tech.*, vol. 49, no. 11, pp. 2112 – 2116, Nov. 2001.

[36] S. Ramo, J. R. Whinnery, and T. Van Duzer, *Fields and waves in communication electronics*, 2nd ed. New York: John Wiley and Sons, Inc., 1967.

[37] M. Kim, J. Hacker, R. Mihailovich, and J. DeNatale, "A DC-to-40GHz four-bit RF MEMS true-time delay network," *IEEE Microwave and Wireless Let.*, vol. 11, no. 2, Feb 2001.

[38] C. Shafai, S. Sharma, L. Shafai, and D. Chrusch, "Microstrip phase shifter using ground-plane reconfiguration," *IEEE Trans. Microwave Theory Tech.*, vol. 52, no. 1, pp. 144 – 153, Jan. 2004.

[39] J. Hayden, A. Malczewski, J. Kleber, C. Goldsmith, and G. Rebeiz, "2 and 4-bit DC-18 GHz microstrip MEMS distributed phase shifters," in *Microwave Symposium Digest, 2001 IEEE MTT-S International*, vol. 1, 2001, pp. 219 – 222.

[40] R. C. Johnson, *Antenna Engineering Handbook*. New-York: McGraw-Hill, 1984.

[41] A. Hajimiri, A. Komijani, A. Natarajan, R. Chunara, X. Guan, and H. Hashemi, "Phased array systems in silicon," *IEEE Communications Magazine*, vol. 42, no. 8, pp. 122–130, Aug. 2004.

[42] M. Rodwell, S. Allen, R. Yu, M. Case, U. Bhattacharya, M. Reddy, E. Carman, M. Kamegawa, Y. Konishi, J. Pusl, and R. Pullela, "Active and nonlinear wave propagation devices in ultrafast electronics and optoelectronics," *Proceedings of the IEEE*, vol. 82, no. 7, July 1994.

[43] J. Krupka, J. Breeze, A. Centeno, N. Alford, T. Claussen, and L. Jensen, "Measurements of permittivity, dielectric loss tangent, and resistivity of float-zone silicon at microwave frequencies," *IEEE Trans. Microwave Theory Tech.*, vol. 54, no. 11, pp. 3995 – 4001, Nov. 2006.

[44] N. Barker and G. Rebeiz, "Optimization of distributed MEMS transmission lines phase shifters, U-band and W-band designs," *IEEE Trans. Microwave Theory Tech.*, vol. 48, no. 11, pp. 1957–1966, Nov. 2000.

[45] B. Lakshminarayanan and T. Weller, "Design and modeling of 4-bit slow-wave MEMS phase shifters," *IEEE Trans. Microwave Theory Tech.*, vol. 54, no. 1, pp. 120 – 127, Jan. 2006.

[46] J. Hayden and G. Rebeiz, "Very low-loss distributed X-band and Ka-band MEMS phase shifters using metal-air-metal capacitors," *IEEE Trans. Microwave Theory Tech.*, vol. 51, no. 1, pp. 309–314, Jan. 2003.

[47] F. De Flaviis, N. Alexopoulos, and O. Stafsudd, "Planar microwave integrated phase-shifter design with high purity ferroelectric material," *IEEE Trans. Microwave Theory Tech.*, vol. 45, no. 6, pp. 963 – 969, June 1997.

[48] T.-Y. Yun and K. Chang, "A low-loss time-delay phase shifter controlled by piezoelectric transducer to perturb microstrip line," *IEEE Microwave and Guided Wave Lett.*, vol. 10, no. 3, pp. 96–98, March 2000.

[49] V. Veselago, "The electrodynamics of substances with simultaneously negative values of permittivity and permeability," *Soviet Physics Uspekhi*, vol. 10, no. 4, pp. 509–514, 1968.

[50] J. Pendry, A. Holden, D. Robbins, and W. Stewart, "Low frequency plasmons in thin-wire structures," *J. Phys.: Condens. Matter*, vol. 10, no. 22, pp. 4785–4809, June 1998.

[51] ——, "Magnetism from conductors and enhanced nonlinear phenomena," *IEEE Trans. Microwave Theory Tech.*, vol. 47, no. 11, pp. 2075 – 2084, Nov. 1999.

[52] G. Eleftheriades and K. Balmain, *Negative-Refraction Metamaterials: Fundamental Principles and Applications.* Hoboken, NJ: Wiley - IEEE Press, 2005.

[53] C. Caloz and T. Itoh, *Electromagnetic Metamaterials, Transmission Line Theory and Microwave Applications.* Hoboken, NJ: Wiley - IEEE Press, 2005.

[54] A. Lai, C. Caloz, and T. Itoh, "Composite right/left-handed transmission line metamaterials," *IEEE Microwave Magazine*, vol. 5, no. 3, pp. 34 – 50, Sept. 2004.

[55] J. Garcia-Garcia, F. Martin, F. Falcone, J. Bonache, J. Baena, I. Gil, E. Amat, T. Lopetegi, M. Laso, J. Iturmendi, M. Sorolla, and R. Marques, "Microwave filters with improved stopband based on sub-wavelength resonators," *IEEE Trans. Microwave Theory Tech.*, vol. 53, no. 6, pp. 1997 – 2006, June 2005.

[56] M. Gil, J. Bonache, J. Selga, J. Garca-Garca, and F. Martin, "Broadband resonant-type metamaterial transmission lines," *IEEE Microwave and Wireless Comp. Lett.*, vol. 17, no. 2, pp. 97–99, Feb. 2007.

[57] G. V. Eleftheriades, "Analysis of bandwidth and loss in negative-refractive-index transmission-line (NRI-TL) media using coupled resonators," *IEEE Microwave and Wireless Comp. Lett.*, vol. 17, no. 6, pp. 412–414, June 2007.

[58] A. Lai, K. Leong, and T. Itoh, "Novel series divider for antenna arrays with arbitrary element spacing based on a composite right/left-handed transmission line," in *2005 European Microwave Conference*, Paris, France, 2005, pp. 145– 148.

[59] I.-H. Lin, M. DeVincentis, C. Caloz, and T. Itoh, "Arbitrary dual-band components using composite right/left-handed transmission lines," *IEEE Trans. Microwave Theory Tech.*, vol. 52, no. 4, pp. 1142 – 1149, April 2004.

[60] S. Otto, A. Rennings, C. Caloz, and P. Waldow, "Dual mode zeroth order ring resonator with tuning capability and selective mode excitation," in *2005 European Microwave Conference*, Paris, France, 2005, pp. 149– 152.

[61] M. Antoniades and G. Eleftheriades, "A broadband wilkinson balun using microstrip metamaterial lines," *IEEE Antennas Wireless Propagat. Lett.*, vol. 4, pp. 209–212, 2005.

[62] A. Grbic and G. Eleftheriades, "Experimental verification of backward-wave radiation from a negative refractive index metamaterial," *J. Appl. Phys.*, vol. 92, no. 10, pp. 5930–5935, Nov. 2002.

[63] G. Eleftheriades, A. Iyer, and P. Kremer, "Planar negative refractive index media using periodically L-C loaded transmission lines," *IEEE Trans. Microwave Theory Tech.*, vol. 50, no. 12, pp. 2702 – 2712, Dec. 2002.

[64] M. Antoniades and G. Eleftheriades, "Compact linear lead/lag metamaterial phase shifters for broadband applications," *IEEE Antennas Wireless Propagat. Lett.*, vol. 2, no. 7, pp. 103 – 106, 2003.

[65] T. Koschny, P. Markov, D. R. Smith, and C. M. Soukoulis, "Resonant and antiresonant frequency dependence of the effective parameters of metamaterials," *Phys. Rev. E 68*, p. 065602(R), 2003.

[66] D. R. Smith, S. Schultz, P. Markov, and C. M. Soukoulis, "Experimental verification of a negative index of refraction," *Science*, vol. 292, pp. 77–79, 2001.

[67] D. R. Smith, D. C. Vier, T. Koschny, and C. M. Soukoulis, "Electromagnetic parameter retrieval from inhomogeneous metamaterials," *Phys. Rev. E 71*, p. 036617, 2005.

[68] T. Koschny, P. Markov, N. Economou, D. R. Smith, D. C. Vier, and C. M. Soukoulis, "Impact of inherent periodic structure on effective medium description of left-handed and related metamaterials," *Phys. Rev. B 71*, p. 245105, 2005.

[69] A. Grbic and G. Eleftheriades, "Periodic analysis of a 2-D negative refractive index transmission line structure," *IEEE Trans. Antennas and Propagat.*, vol. 51, no. 10, pp. 2604 – 2611, Oct. 2003.

[70] S. Lim, C. Caloz, and T. Itoh, "Metamaterial-based electronically controlled transmission-line structure as a novel leaky-wave antenna with tunable radiation angle and beamwidth," *IEEE Trans. Microwave Theory Tech.*, vol. 52, no. 12, pp. 2678 – 2690, Dec. 2004.

[71] M. Gil, I. Gil, J. Bonache, J. Garcia-Garcia, and F. Martin, "Metamaterial transmission lines with extreme impedance values," *Microw. and Optical Tech. Lett.*, vol. 48, no. 12, pp. 2499–2505, Dec 2006.

[72] M. Antoniades and G. Eleftheriades, "A metamaterial series-fed linear dipole array with reduced beam squinting," in *IEEE Intl. Symposium on Antennas and Propagation*, Albuquerque, NM,, 2006, pp. 4125–4128.

[73] Y. Kwon, H.-T. Kim, J.-H. Park, and Y.-K. Kim, "Low-loss micromachined inverted overlay CPW lines with wide impedance ranges and inherent airbridge connection capability," *IEEE Microw. and Wireless Comp. Lett.*, vol. 11, no. 2, pp. 59 – 61, Feb. 2001.

[74] A. Diaz Bolado, "Application of composite right/left-handed transmission lines to antenna matching, Master thesis," Tech. Rep., 2006.

[75] J. Perruisseau-Carrier, D. Llorens del Rio, and J. Mosig, "A new integrated match for CPW-fed slot antennas," *Microw. and Optical Tech. Lett.*, vol. 42, no. 6, pp. 444–448, Sept. 2004.

[76] S. Lim, C. Caloz, and T. Itoh, "Electronically scanned composite right/left handed microstrip leaky-wave antenna," *IEEE Microwave and Wireless Comp. Let.*, vol. 14, no. 6, pp. 277– 279, June 2004.

[77] M. A. Y. Abdalla, K. Phang, and G. V. Eleftheriades, "A 0.13-μm CMOS phase shifter using tunable positive/negative refractive index transmission lines," *IEEE Microwave and Wireless Comp. Lett.*, vol. 16, no. 12, pp. 705–707, Dec. 2006.

[78] J. Gao and L. Zhu, "Characterization of infinite- and finite-extent coplanar waveguide metamaterials with varied left- and right-handed passbands," *IEEE Microwave and Wireless Comp. Lett.*, vol. 15, no. 11, pp. 805 – 807, Nov. 2005.

[79] M. Shelley, A. Mason, and K. Markus, "Frequency scanning antennas for aeronautical communications," in *IEE Colloquium on Satellite Antenna Technology in the 21st Century*, 1991, pp. 12/1 – 12/4.

[80] P. Bradsell, "Phased arrays in radar," *Electronics and Communication Engineering Journal*, vol. 2, no. 2, pp. 45–51, April 1990.

[81] M. Lapine, I. Nefedov, J. Saily, and S. Tretyakov, "Artificial lines with exotic dispersion for phase shifters and delay lines," in *36th European Microwave Conference.*, Manchester, UK, 2006, pp. 427–430.

[82] R. Garver, "Broad-band diode phase shifters," *IEEE Trans. Microwave Theory Tech.*, vol. 20, no. 5, pp. 314– 323, May 1972.

[83] D. Berry, R. Malech, and W. Kennedy, "The reflectarray antenna," *IEEE Trans. Antennas and Propagat.*, vol. 11, no. 6, pp. 645– 651, Nov. 1963.

[84] D. Pozar, S. Targonski, and H. Syrigos, "Design of millimeter wave microstrip reflectarrays," *IEEE Trans. Antennas and Propagat.*, vol. 45, no. 2, pp. 287 – 296, Feb. 1997.

[85] D. Pozar, S. Targonski, and R. Pokuls, "A shaped-beam microstrip patch reflectarray," *IEEE Trans. Antennas and Propagat.*, vol. 47, no. 7, pp. 1167 – 1173, July 1999.

[86] J. Encinar, L. Datashvili, J. Zornoza, M. Arrebola, M. Sierra-Castaner, J. Besada-Sanmartin, H. Baier, and H. Legay, "Dual-polarization dual-coverage reflectarray for space applications," *IEEE Trans. Antennas and Propagat.*, vol. 54, no. 10, pp. 2827 – 2837, Oct. 2006.

[87] M. Bozzi, S. Germani, and L. Perregrini, "Performance comparison of different element shapes used in printed reflectarrays," *IEEE Antennas and Wireless Propagation Letters*, vol. 2, no. 1, pp. 219 – 222, 2003.

[88] J. Encinar, "Design of two-layer printed reflectarrays using patches of variable size," *IEEE Trans. Antennas and Propagat.*, vol. 49, no. 10, pp. 1403 – 1410, Oct. 2001.

[89] C. Apert, T. Koleck, P. Dumon, T. Dousset, and C. Renard, "ERASP a new reflectarray antenna for space applications," in *1st European Conference on Antennas and Propagation (EuCAP 2006)*, Nice, France, 2006.

[90] S. Xu and Y. Rahmat-Samii, "Sub-reflectarrays for main reflector surface distortion compensations," in *URSI 2007, North American Radio Science Meeting URSI - CNC/USNC*, Ottawa, Canada, 2007.

[91] D. Sievenpiper, J. Schaffner, H. Song, R. Loo, and G. Tangonan, "Two-dimensional beam steering using an electrically tunable impedance surface," *IEEE Trans. Antennas and Propagat.*, vol. 51, no. 10, pp. 2713 – 2722, Oct. 2003.

[92] M. Riel and J.-J. Laurin, "Design of an electronically beam scanning reflectarray using aperture-coupled elements," *IEEE Trans. Antennas and Propagat.*, vol. 55, no. 5, pp. 1260 – 1266, May 2007.

[93] S. V. Hum, M. Okoniewski, and R. J. Davies, "Modeling and design of electronically tunable reflectarrays," *IEEE Trans. Antennas and Propagat.*, vol. 55, no. 8, pp. 2200–2210, Aug. 2007.

[94] R. Romanofsky, "Special issues and features of a scanning reflectarray antenna based on ferroelectric thin film phase shifters," in *1st European Conference on Antennas and Propagation (EuCAP 2006)*, Nice, France, 2006.

[95] A. Moessinger, R. Marin, J. Freese, S. Mueller, A. Manabe, and R. Jakoby, "Investigations on 77 GHz tunable reflectarray unit cells with liquid crystal," in *1st European Conference on Antennas and Propagation (EuCAP 2006)*, Nice, France, 2006.

[96] M. Chaharmir, J. Shaker, M. Cuhaci, and A.-R. Sebak, "Novel photonically-controlled reflectarray antenna," *IEEE Trans. Antennas and Propagat.*, vol. 54, no. 4, pp. 1134– 1141, April 2006.

[97] J. Gianvittorio and Y. Rahmat-Samii, "Reconfigurable patch antennas for steerable reflectarray applications," *IEEE Trans. Antennas and Propagat.*, vol. 54, no. 5, pp. 1388 – 1392, May 2006.

[98] S. Hum, G. McFeetors, and M. Okoniewski, "Integrated MEMS reflectarray elements," in *1st European Conference on Antennas and Propagation (EuCAP 2006)*, Nice, France, 2006.

[99] H. Legay, B. Pinte, E. Girard, R. Gillard, M. Charrier, and A. Ziaei, "A low loss and steerable reflectarray antenna in Ka band," in *27th ESA Antenna Technology Workshop on Innovative Periodic Antennas*, Santiago de Compostela, Spain, 2004, pp. 281–288.

[100] H. Rajagopalan and Y. Rahmat-Samii, "Reconfigurable reflectarray element characterization," in *1st European Conference on Antennas and Propagation (EuCAP 2006)*, Nice, France, 2006.

[101] R. Hansen, *Microwave Scanning Antennas.* Los Altos CA: Peninsular Publishing Company, 1986.

[102] E. Carrasco, M. Barba, and J. Encinar, "Reflectarray element based on aperture-coupled patches with slots and lines of variable length," *IEEE Trans. Antennas and Propagat.*, vol. 55, no. 3, pp. 1662 – 1664, March 2007.

[103] D. Pozar, "Bandwidth of reflectarrays," *Electron. Lett.*, vol. 39, no. 21, pp. 1490 – 1491, Oct. 2003.

[104] R. Collin and F. Zucker, *Antenna Theory, Part 2*, ser. Inter-University Electronics Series. New-York: McGraw-Hill, 1969.

[105] M. Gans, "A general proof of floquet's theorem (correspondence)," *IEEE Trans. Microwave Theory Tech.*, vol. 13, no. 3, pp. 384 – 385, May 1965.

[106] M. Bozzi, L. Perregrini, J. Weinzierl, and C. Winnewisser, "Efficient analysis of quasi-optical filters by a hybrid MoM/BI-RME method," *IEEE Trans. Antennas and Propagat.*, vol. 49, no. 7, pp. 1054 – 1064, July 1999.

[107] P. Hannan and M. Balfour, "Simulation of a phased-array antenna in waveguide," *IEEE Trans. Antennas and Propagat.*, vol. 13, no. 3, pp. 342– 353, May 1965.

[108] N. Misran, R. Cahill, and V. Fusco, "Design optimisation of ring elements for broadband reflectarray antennas," *Proc. IEE Microw. Antennas Propag.*, vol. 150, no. 6, pp. 440– 444, Dec 2003.

[109] M. Chaharmir, J. Shaker, M. Cuhaci, and A. Ittipiboon, "A broadband reflectarray antenna with double square ring cell elements," in *1st European Conference on Antennas and Propagation (EuCAP 2006)*, Nice, France, 2006.

[110] M. Ylanen, T. Vaha-Heikkila, and H. Kattelus, "Amorphous metal alloy based MEMS for RF applications," *Sensors and Actuators A: Physical.*, vol. 132, no. 1, pp. 283–288, 2006.

[111] M. Bialkowski, A. Robinson, and H. Song, "Design, development, and testing of X-band amplifying reflectarrays," *IEEE Trans. Antennas and Propagat.*, vol. 50, no. 8, pp. 1065 – 1076, Aug. 2002.

[112] G. Lissorgues, F. Flourens, A. Phommahaxay, F. Marty, L. Rousseau, C. Papon, P. Nicole, and T. Dousset, "A dual-gap tunable RF MEMS capacitor for reflectarray applications," in *MEMSWAVE 2007*, Barcelona, Spain, 2007, pp. 71–74.

[113] B. Mencagli, R. Gatti, L. Marcaccioli, and R. Sorrentino, "Design of large mm-wave beam-scanning reflectarrays," in *European Microwave Conference*, Paris, France, 2005.

[114] C. Siegel, V. Ziegler, B. Schoenlinner, U. Prechtel, and H. Schumacher, "RF-MEMS based 2-bit reflective phase shifter at X-band for reconfigurable reflect-array antennas," in *MEMSWAVE 2007*, Barcelona, Spain, 2007, pp. 165–167.

[115] B. Mencagli, P. Farinelli, L. Marcaccioli, R. V. Gatti, B. Margesin, F. Giacomozzi, and R. Sorrentino, "Design and realization of a MEMS tuneable reflectarray for mm-wave imaging application," in *MEMSWAVE 2007*, Barcelona, Spain, 2007, pp. 115–118.

[116] R. Fritschi, S. Frederico, C. Hibert, P. Fluckiger, P. Renaud, D. Tsamados, J. Boussey, A. Chovet, R. Ng, F. Udrea, J.-P. Curty, C. Dehollain, M. Declercq, and A. Ionescu, "High tuning range AlSi RF MEMS capacitors fabricated with sacrificial amorphous silicon surface micromachining," *Microelectronic Engineering*, vol. 73-74, pp. 447–451, June 2004.

[117] T. Lisec, C. Huth, M. Shakhhray, B. Wagner, and C. Combi, "Surface-micromachined capacitive RF switches with high thermal stability and low drift using Ni as structural material," in *MEMSWAVE 2004*, Uppsala, Sweden, 2004, pp. C33–C36.

[118] O. Bochobza-Degani, E. Socher, and Y. Emirovski, "On the effect of residual charges on the pull-in parameters of electrostatic actuators," *Sensors and Actuators A: Physical.*, vol. 97-98, pp. 563–568, 2002.

[119] L. Dussopt and G. Rebeiz, "Intermodulation distortion and power handling in RF MEMS switches, varactors, and tunable filters," *IEEE Trans. Microwave Theory Tech.*, vol. 51, no. 4, pp. 1247 – 1256, April 2003.

[120] D. Peroulis, S. Pacheco, and L. Katehi, "RF MEMS switches with enhanced power-handling capabilities," *IEEE Trans. Microwave Theory Tech.*, vol. 52, no. 1, pp. 59–68, Jan. 2004.

Julien Perruisseau-Carrier

CONTACT INFORMATION

Laboratoire d'Electromagnétisme et d'Acoustique
Ecole Polytechnique Fédérale de Lausanne
Station 11, 1015 Lausanne
Switzerland

☎ +41.76.402.23.71
+41.21.693.26.73
julien.perruisseau.a3@epfl.ch

NATIONALITIES

Swiss and French

RESEARCH & ACADEMIC EXPERIENCE

Ecole Polytechnique Fédérale de Lausanne, Laboratoire d'Electromagnétisme et d'Acoustique, Switzerland. ***(2003 - 2007)***

PhD thesis

- Microwave Periodic Structures Based on MicroElectroMechanical Systems (MEMS) and Micromachining Techniques.

EU-funded research

- WIDE-RF: Innovative MEMS for Wideband Reconfigurable RF Microsystems.
- NanoTIMER: Nanotechnology in Mechanical-electrical Resonators.
- RARPA: Reflectarrays and Reconfigurable Printed Antennas.
- AMICOM: European Network of Excellence on RF MEMS and RF Microsystems.

Other activities

- Assistantship, supervision of bachelor/master theses.
- Support to other EPFL groups in the modelling of RF devices.

University of Birmingham, Communication group, UK. ***(2002 - 2003)***

- Exchange EPFL M.Sc thesis 'Wide bandwidth dual-polarized scan phased array', followed by a short-term scientific visit.

EDUCATION

- B.Sc and M.Sc in Electrical Engineering, CGPA 5.84/6.00, Ecole Polytechnique Fédérale de Lausanne (EPFL), Switzerland. *(1998 - 2003)*
- 'Certificat de Maturité', Gymnase de la Cité, Lausanne. *(1995 - 1998)*

HONOURS

- *Young Scientist Award* at URSI-EMTS 2007, International Symposium on Electromagnetic Theory, Ottawa, Canada.
- *Best Results* and *English* prizes for the 'Cértificat de Maturité', Gymnase de la Cité, Lausanne, Switzerland
- Reviewer for the IET *Proceedings on Microwave, Antennas and Propagation.*

SKILLS

Languages

- French: Mother tongue.
- English: Spoken and written, Cambridge Certificate in Advanced English, mark 'A'.
- German: Good knowledge.
- Spanish: Good knowledge.
- Turkish: Basic.

Computing

- Ansoft HFSS/Designer, Agilent ADS, ANSYS, Mathematica, Matlab, misc.

PUBLICATIONS

Journal Papers

- J. Perruisseau-Carrier, and TBD. *"Design and Characterization of a 5-bit MEMS-reconfigurable Monolithic Reflectarray Cell,"* to be submitted to the IEEE Trans. Antennas and Propagat.

- J. Perruisseau-Carrier and A. K. Skrivervik, *"Design of Wideband High and Low Impedance Meta-Transmission Lines,"* Microw. and Optical Tech. Lett., vol. 49, no. 8, August 2007, pp. 1926-1929.

- J. Perruisseau-Carrier and A. K. Skrivervik, *"Bloch Wave Approach to the Design of Optimally Matched Non-Effective Medium Composite Right/Left Handed Transmission Lines,"* Proc. IET Microw., Antennas Propag., vol. 1, no. 1, pp. 50-55, Feb. 2007.

- J. Perruisseau-Carrier, T. Lisec and A. K. Skrivervik, *"Circuit Model and Design of Silicon-Integrated CRLH-TLs Analogically Controlled by MEMS,"* Microw. and Optical Tech. Letters, vol. 44, no. 12, Dec. 2006, pp. 2496-2499.

- J. Perruisseau-Carrier and A. K. Skrivervik, *"Composite right/left handed transmission line metamaterial phase shifters (MPS) in MMIC technology,"* IEEE Trans. Microwave Theory Tech., vol. 54, no. 4, no. 1, April 2006, pp 1582 - 1589.

- J. Perruisseau-Carrier, R. Fritschi, P. Crespo-Valero, and A. K. Skrivervik, *"Modeling of periodic distributed MEMS, application to the design of variable true-time delay lines,"* IEEE Trans. Microwave Theory Tech., vol. 54, no. 1, Jan. 2006, pp. 383 - 392.

- J. Perruisseau-Carrier, D. Llorens del Río, J.R. Mosig, *"A new integrated match for CPW-fed slot antennas",* Microw. and Optical Tech. Letters, vol. 42, no. 6, September 2004, pp. 444-448.

- J. Perruisseau-Carrier, T.W. Hee, P.S. Hall, *"Dual-polarized broadband dipole",* IEEE Antennas and Wireless Propagation Letters, vol. 2, issue 21, 2003, pp. 310-312.

- M. Fernández-Bolaños, J. Perruisseau-Carrier, P. Dainesi and A.M. Ionescu *"RF MEMS Capacitive Switch on Semi-Suspended CPW using Low-Loss High-Resistivity Silicon,"* submitted to Microelectronic Engineering.

Conferences Papers, 1^{st} author

- J. Perruisseau-Carrier and A. K. Skrivervik, "*Requirements and challenges in the design of high-performance MEMS reconfigurable reflectarray cells*," 2^{nd} European Conference on Antennas and Propagation (EuCAP 2007), Edinburgh, UK, 2007.

- J. Perruisseau-Carrier, H. Legay, J. Lenkkeri, J.-P. Polizzi, E. Jung, and A. K. Skrivervik, "*Design and realization of a MEMS-tuned reflectarray on LTCC substrate*," MEMSWAVE 2007, Barcelona, Spain, 2007.

- J. Perruisseau-Carrier, F. Bongard, and A. K. Skrivervik, "*Wideband Digitally MEMS-Controlled Reflectarray Cells*," EMTS 2007, International Symposium on Electromagnetic Theory, Ottawa, Canada, 2007.

- J. Perruisseau-Carrier and A. K. Skrivervik, "*Tunable Differential Phase Shifters Using MEMS Positive/Negative Phase Velocity Transmission Lines*," URSI 2007, North American Radio Science Meeting URSI - CNC/USNC, Ottawa, Canada, 2007.

- J. Perruisseau-Carrier and A. K. Skrivervik, "*Non-effective Medium Composite Right/Left Handed Transmission Lines- Design and Applications*," 1st European Conference on Antennas and Propagation (EuCAP 2006), 6 - 10 November 2006, Nice, France.

- J. Perruisseau-Carrier, T. Lisec and A. K. Skrivervik, "*Analog and Digital MEMS-Variable Composite Right/Left Handed Transmission Lines*," 2006 ANTEM, International Symposium on Antenna Technology and Applied Electromagnetics and URSI/CNC Canadian Radio Sciences Conference, Montréal, Canada, 2006.

- J. Perruisseau-Carrier, T. Lisec and A. K. Skrivervik, "*Silicon-Integrated Composite Right/Left Handed Transmission Lines Controlled by MEMS Loading Elements*," Third Workshop on Metamaterials and Special Materials for Electromagnetic Applications and TLC, Rome, Italy, 2006.

- J. Perruisseau-Carrier, R Fritschi and A Skrivervik, "*Design of Enhanced Multi-Bit Distributed MEMS Variable True-Time Delay Lines*", IEEE PRIME 2005, 2005, Lausanne, Switzerland, pp. 163-166.

- J. Perruisseau-Carrier and A.K. Skrivervik, "*A new topology for the reduction of mismatch in multi bit distributed MEMS true time delay lines*," MEMSWAVE 2005, Lausanne, Switzerland, pp. 53-56.

- J. Perruisseau-Carrier, "*Distributed MEMS Variable True-Time Delay Lines*", Center of MicroNanotechnology annual review meeting, May 2005, EPFL, Switzerland (invited).

- J. Perruisseau-Carrier, T.W. Hee, J. R. Mosig and P. S. Hall, "*Ultra Broadband Dipole Antennas Using Fractal Geometries*", Latsis symposium 2005, March 1-2, Lausanne, Switzerland.

- J. Perruisseau-Carrier, R Fritschi and A Skrivervik, "*Controllable True-Time Delay Line and Left-Handed Transmission Lines in MMIC technology*", Latsis symposium 2005, March 1-2, Lausanne, Switzerland.

- J. Perruisseau-Carrier, J.R. Mosig and P.S. Hall, "*Plain and Fractal, Single and Dual-Polarized Ultra Broadband Dipole*", Journées Internationales de Nice sur les Antennes (JINA'04), Nice, 8-10 novembre 2004.

- J. Perruisseau-Carrier, R. Fritschi, P. Crespo Valero, C. Hibert, J.-F. Zürcher, Ph. Flückiger, A. Skrivervik and A.M. Ionescu, "*Fabrication Process and Model for a MEMS parallel plate capacitor above a CPW line*", MEMSWAVE 2004, Uppsala, Sweden, June 30-July 2, 2004.

Conferences Papers, other

- A. K. Skrivervik, J. Perruisseau-Carrier, *"MEMS in antennas: an overview,"* Proc. IEEE Seminar on Advances in Applied Electromagnetics: Antennas and Microwave Engineering (invited paper), Zagreb, Croatia, 2007.

- H. Legay, Y. Cailloce, G. Caille, J. Perruisseau-Carrier, M. Lathi, JP. Polizzi, U. Oestermann, P. Pons, N. Raveu, *"Satellite Antennas Based on MEMS Tunable Reflectarrays,"* 2nd European Conference on Antennas and Propagation (EuCAP 2007), Edinburgh, UK, 2007.

- M. Fernández-Bolaños, J. Perruisseau-Carrier, P. Dainesi, A.M. Ionescu, *"RF MEMS Capacitive Switch on Semi-Suspended CPW using Low-Loss HRS"*, MNE07, 33rd International Conference on Micro and Nano-Engineering, Copenhagen, Denmark, 2007.

- F. Bongard, J. Perruisseau-Carrier, A. K. Skrivervik and J. R. Mosig, *"Review of EPFL-LEMA activities on Metamaterials,"* Metamaterials'2007: The First International Congress on Advanced Electromagnetic Materials for Microwaves and Optics, Rome, Italy, 2007.

- H. Legay, E. Girard, G. Caille, O. Vendier, N. Raveu, H. Aubert, P. Pons, R. Gillard, J. Polizzi, M. V. d. Voorst, J. Perruisseau-Carrier, A. K. Skrivervik, J. Lenkkeri, and E. Jung, *"MEMS controlled Reflectarray Elements,"* 29$^{\text{th}}$ ESA Antenna Workshop on Multiple Beams and Reconfigurable Antennas, Noordwijk, The Netherland, April 2007.

- A. K. Skrivervik and J. Perruisseau-Carrier, "MEMS tuneable Antennas and Arrays," MEMSWAVE 2007, Barcelona, Spain, 2007.

- A. D. Bolado, F. Bongard, J. Perruisseau-Carrier, J. R. Mosig, *"Application of Composite Right/Left Handed Transmission Lines to Antenna Matching,"* 1$^{\text{st}}$ European Conference on Antennas and Propagation (EuCAP 2006), 6 - 10 November 2006, Nice, France.

- A. K. Skrivervik, J. Perruisseau-Carrier, *"Design and characterization of distributed MEMS phase shifters for microwave and mm-wave applications,"* Mediterranean Microwave Symposium 2006, Genova, Italy, Sept.19-21, 2006.

- A. Jourdain, H. Tilmans and J. Perruisseau-Carrier, *"Wafer-level Packaging of MEMS resonators,"* NanoTimer Workshop on Micro-Electro-Mechanical Resonators: From Technology to Applications, Feb. 2, 2006, Lausanne, Switzerland.

- M. Mazza, D. Badila, J. Perruisseau-Carrier, A. M. Ionescu and A. Skrivervik, *"Nanogap MEMS resonators and adapted oscillator design,"* NanoTimer Workshop on Micro-Electro-Mechanical Resonators: From Technology to Applications, Feb. 2, 2006, Lausanne, Switzerland.

- P.S. Hall, T.W. Hee and J. Perruisseau-Carrier, *"Ultra wideband Array Elements"*, in the APS digest of the 2004 IEEE International Symposium on Antennas and Propagation and USNC/URSI National Radio Science Meeting, Monterey, California, USA, June 20-26, 2004.

- D. Llorens del Rio, J. Perruisseau-Carrier and J.R. Mosig, *"The T-match: an integrated match for CPW-fed slot antennas"*, Journées Internationales de Nice sur les antennes (JINA'02), Nice, 12-14 novembre 2002, vol. II, pp. 347-350.